

Transformation of Multidirectional Sea  
Field and Computational Study

Suzana Ilić

A thesis submitted to the University of Plymouth  
in partial fulfilment for the degree of

Doctor or Philosophy

School of Civil and Structural Engineering  
Faculty of Technology

July 1999

LIBRARY STORE

REFERENCE ONLY

UNIVERSITY OF PLYMOUTH	
Item No.	9004013636
Date	24 SEP 1999 T
Class No.	T 551.4702 I LI
Contl. No.	X703932607
LIBRARY SERVICES	

90 0401363 6



## Copyright Statement

*This copy of the thesis has been supplied on condition that anyone who consults it is understood to recognise that its copyright rests with its author and that no quotation from the thesis and no information derived from it may be published without the author's prior consent.*

## Abstract

A computational model based on the evolution equation for water waves (Li, 1994b) derived from the original Berkhoff's (1972) "Mild Slope Equation" is tested against multidirectional sea data. The model accounts for reflection as well as diffraction-refraction processes, which is important for applications involving coastal structures. The accuracy and convergence of the numerical solution, as well as the possibility of the implementation of an adaptive numerical scheme are investigated and implemented. The model was firstly tested using laboratory measurements (Briggs *et al*, 1995) of random directional wave diffraction around a semi-infinite breakwater on a flat bottom. These tests confirm the need to use "directional modelling" (using the principle of linear superposition) for the prediction of wave heights behind the breakwater.

The model was then tested using directional wave data records, which were chosen from 4500 wave records collected in the field campaign, by the University of Plymouth and the University of Brighton, at Elmer - Sussex, UK from September 1993 – January 1995. The results showed that the representation of the measured random sea by monochromatic wave runs can introduce a significant error in wave height predictions shoreward of the breakwaters in the diffraction region, thus confirming the importance of directional modelling for random wave simulation. Evidence strongly suggests that non-linear wave effects have a significant influence (40-60%) on the accuracy of the model. Consequently, further tests are needed, which should also consider the influence of wave-current interaction, wave breaking, bed friction and transmissive boundaries. Over all the model predictions are more accurate for the controlled environment in the laboratory (5-13%), than for field conditions where the directional modelling accuracy varied from 8 - 32%.

A summary of the data, collected by the author as a member of the University of Plymouth Research Team and a database of spectral and directional parameters is also presented in this thesis. Field validation of the numerical model required accurate estimates of measured data. Emphasis was placed on identifying a suitable directional analysis method, which accurately predicted direction and directional spread in the far-field from structures where reflection is still present. The non-phase-locked (NPL) methods developed for a homogeneous sea are found to be appropriate. The analysis of two NPL methods, the Maximum Likelihood Method (MLM) and Bayesian Directional Method (BDM), directional estimates for simulated data shows that both methods can predict accurate incident wave height and direction. Both methods tend to overpredict directional spread and give non-accurate reflection estimates. The MLM method is easier to implement than the BDM method, which is sensitive to the chosen starting value of the hyperparameter  $u$ . As the difference between estimates of the two methods for numerical data is small, the MLM method's estimates were chosen for model testing.



# List of contents

Abstract	iii
List of contents	iv
List of symbols	vii
List of tables	xi
List of figures	xiii
Acknowledgements	xix
Author's declaration	xxi
The project background	xxiv

## Chapter 1

<i>Introduction</i>	1
---------------------	---

## Chapter 2

<i>Literature and Background</i>	6
2.1 Introduction	6
2.2 Offshore Breakwaters and Field Examples	7
2.2.1 History	7
2.2.2 General operation of detached breakwaters	8
2.2.3 Monitoring Examples	10
2.3 Mild Slope Equation - wave transformation model	12
2.3.1 Introduction	12
2.3.2 Development	14
2.3.3 Mild Slope Equation	16
2.3.3.1 Elliptic forms	16
2.3.3.2 Parabolic forms	18
2.3.3.3 Hyperbolic forms	19
2.3.3.4 Other forms	21
2.3.4 Boundary conditions for MSE	22
2.3.5 Applications and verifications	22
2.3.5.1 Regular waves	22
2.3.5.2 Irregular and random waves	26
2.4 Directional Analysis	29
2.4.1 Introduction	29
2.4.2 Measuring devices	29
2.4.3 Basic definitions	31
2.4.4 Stochastic analysis methods for homogeneous wave field	32
2.4.4.1 Maximum Likelihood Method	34
2.4.4.2 Maximum Entropy Method	35
2.4.4.3 Bayesian Directional Method	36
2.4.5 Stochastic methods for a reflective field	37
2.4.5.1 Modified Maximum Likelihood Method	38
2.4.5.2 Applicability of the phase locked and non-phase locked methods	38
2.4.6 Stochastic methods for a field with currents	39
2.5 Objectives of study	40

## **Chapter 3**

<b><i>Field work</i></b>	<b>43</b>
3.1 Introduction	43
3.2 Field Site Description	44
3.2.1 General	44
3.2.2 Background	45
3.2.3 Available data	49
3.3 Instrumentation	51
3.3.1 The Inshore Wave Climate Monitor	51
3.3.2 Offshore Wave Recording System (WRS)	53
3.4 Deployment and measurements	55
3.4.1 Offshore wave measurements	56
3.4.2 Inshore wave measurements	57
3.4.3 Other measurements	61
3.5 Summary	63

## **Chapter 4**

<b><i>Data processing and analysis</i></b>	<b>65</b>
4.1 Introduction	65
4.2 Data processing and measurements comparisons	66
4.2.1 Data processing considerations	66
4.2.2 Existing data processing comparison	70
4.2.3 Evaluation of WRS and IWCM spectral analysis	72
4.2.4 Measurements comparison	81
4.2.4.1 Spectral analysis	81
4.2.4.2 Comparison	83
4.2.4.3 Conclusion	90
4.3 Uniform data processing routine	92
4.4 Wave data summary	94
4.4.1 Processing and archiving of wave data	94
4.4.2 Spectral and directional analysis of wave data	95
4.4.3 Summary of results contained within the Database	95
4.5 Summary	104

## **Chapter 5**

<b><i>An assessment of methods for the evaluation of multidirectional wave parameters</i></b>	<b>106</b>
5.1 Introduction	106
5.2 Raw spectra	108
5.3 The validation of the non-dimensional frame work	110
5.3.1 Theoretical framework	110
5.3.2 Tests and results for offshore field data	112
5.4 Numerically generated data	124
5.4.1 Results of the analysis for the numerically generated data	126
5.5 Directional analysis of field data	142
5.5.1 Offshore data	143
5.5.2 Inshore field data	150
5.6 Influence of currents	155
5.7 Summary, discussion and conclusion	165

<b>Chapter 6</b>	
<i>Validation of the Mild Slope Evolution Equation Computational Model</i>	<b>171</b>
6.1 Introduction	171
6.2 Computational model	173
6.2.1 Governing equation based on the velocity potential	173
6.2.2 Numerical solution, accuracy and stability	175
6.2.3 Model convergence	179
6.2.4 Dynamic Alternating Direction Implicit (DADI) Method	189
6.3 Validation of the model on laboratory data	192
6.3.1 Physical model	192
6.3.2 Numerical model tests and results	195
6.4 Validation from field data	209
6.4.1 Computational set up	210
6.4.2 Tests and results	214
6.4.3 Discussion	222
6.5 Conclusions	237
<b>Chapter 7</b>	
<i>Summary and conclusions</i>	<b>240</b>
<i>References</i>	<b>248</b>
<i>Appendices</i>	<b>263</b>
Appendix A - Derivation of the Mild Slope Equation	1-7
Appendix B - Linear Stability Analysis	1-6
Appendix C - Truncation Error Analysis	1-5
Appendix D - Theory of Spectral Analysis Summarised	1-7
Appendix E - Cross-spectral Analysis Theory Summarised	1-4
Appendix F - Generation of Synthetic Wave Data	1-4
Appendix G - Evaluation and Validation of the Mild Slope Evolution Equation Model Using Field Data	(pp 149-160)
Appendix H - Directional Results Summary	1-5
Appendix I - Bispectral Analysis Theory Summarised	1-3

# List of Symbols

$A_n$	Fourier Coefficient
<b>B</b>	biamplitude
$B(f)$	bias function
$b(f_j, f_k)$	bicoherence
$B(f_j, f_k)$	bispectrum
$B_n$	Fourier Coefficient
$c$	phase celerity
$c_g$	wave group celerity
$c_n$	amplitude or oscillation height
$\tilde{c}_k$	Fourier coefficient
co	co-spectrum
$Cr(f)$	frequency dependent reflection coefficient
$Cr_x$	non-dimensional number $Cr_x = \frac{cc_g}{2\omega} \frac{\Delta t}{\Delta x^2}$
$Cr_y$	non-dimensional number $Cr_y = \frac{cc_g}{2\omega} \frac{\Delta t}{\Delta y^2}$
<b>D</b>	characteristic diameter of rock armour $(W_{50}/\rho)^{1/3}$ in non-dimensional number R
<b>D</b>	matrix of distances
<b>d</b>	water depth
$D(f, \theta)$	wrapped normal directional spreading in 6.3.1
$D_i$	incident main direction
difrms	quantitative difference $\frac{\sqrt{\sum \left( \frac{H_m - H_c}{H_m} \right)^2}}{N}$
$D_n$	amplitude
$ D^i(\omega) $	filter gain function
$d_t$	water depth at the toe of the breakwater
<b>E</b>	energy
$E(f)$	spectral energy

$E_i$	incident energy
$E_r$	reflected energy
$F(i\omega_0)$	Fourier coefficient
$f(t)$	periodic function
$f_0$	fundamental frequency
$f_N$	Nyquist frequency
$f_s$	sampling frequency
$G$	non-dimensional number $G = \frac{1}{2} k_c^2 \frac{\Delta t c c_g}{2\omega}$
$G(\theta/f)$	directional spreading function
$H$	Hamiltonian
$h$	water depth
$H$	wave height
$H_c$	calculated wave height
$H_i$	incident wave height
$h_m$	function related to $H_m$
$H_m$	measured wave height
$H_m(k, \omega)$	is the transfer function from the water surface elevation to m-the wave property
$H_{m0}$	significant wave height
$i$	imaginary unit
$Im$	imaginary part of function (or imag)
$k$	is the wave number vector
$k_0$	wave number, $k_c$ wave number for waves on currents
$K_{\eta\eta}(\tau_i, \tau_k)$	two dimensional autocorrelation function
$K_d$	diffraction coefficient in Chapter 6
$K_{dsm}$	measured diffraction coefficient
$K_{dsp}$	predicted diffraction coefficient
$K_r$	reflection coefficient
$K_{xx}$	coherence
$L$	the time of wave travel to the reflector and back in Chapter 5
$m_n$	spectral moments
$N$	number of tests
$P$	cross-power spectrum matrix
$P_{mn}(\sigma)$	cross-power spectrum between m-th and n-th wave properties (properties measured at m & n station)

Q	pseudo flux
q	quadrature spectrum
r	complex reflection coefficient
R	non-dimensional parameter $R = \frac{d, L_o^2 \tan \beta}{H, D^2}$
R(f)	frequency response function, transfer function
$r_{xy}^2$	coherence function
Re	real part of function
S	the length of time series in seconds in Chapter 5
$S'_{\eta\eta}(t)$	spectrum estimate
$S_{\eta\eta}(t)$	true spectrum
S(f)	spectral energy density
S(k,ω)	directional spectrum as a function of wave number and angular frequency
SE	Shennan's information entropy
$S_i$	incident directional spreading
$S_{xx}, S_{yy}$	auto spectrum
$S_{xy}$	cross-spectrum
T	kinetic energy in Appendix A
t	time
T	time period or length of time series
T(f,θ)	transfer function from hydrodynamic pressure to surface elevation
tanβ	slope of the breakwater
TP	residual parameter
u	hyperparameter in Bayesian Directional Method
u	parabolic function in 6.2.4
U(0,π)	uniform distribution
$U_c$	current velocity
$U_r$	Ursell number $U_r = \frac{H_i}{2d(k_d)^2}$
V	potential energy in Appendix A
v	velocity
w(θ,θ')	window function
	wave property
$W_{ss}$	window function
$W_{50}$	characteristic weight of rock armour

$X$	location vector
$x(t)$	sample function
$x_k$	values of estimates in Bayesian Directional Method
$x_m$	location vector of the wave probe for the m-th wave property
$y(t)$	sample function
$\bar{y}_{xy}$	random variable
$z$	vertical elevation
$\alpha$	angle; proportionality constant in 2.4.4.1; confidence level in Appendix E
$\alpha$	$=2\pi/N_x$ , where $N_x$ is the number of grid points per wave length
$\beta$	$=2\pi/N_y$ , where $N_y$ is the number of grid points per wave length
$\beta(f_j, f_k)$	biphase
$\gamma$	$=2\pi/T$
$\varepsilon$	residual
$\Phi(x,y,t)$	complex wave potential function
$\phi(x,y,t)$	$\phi(x, t) = \text{Re} \{ \Phi(x) e^{-i\omega t} \}$ ; velocity potential
$\eta(t)$	wave profile; surface elevation
$\varphi$	$\varphi = \psi \sqrt{cc_g}$ ; complex velocity potential
$\vartheta$	phase angle or phase shift, random phase; $\bar{\vartheta}_{xy}$ - phase lag
$\kappa$	proportionality constant
$\lambda_0 \dots \lambda_4$	Lagrange's multipliers
$\nu$	degree of freedom
$\theta_n$	direction of wave propagation; wave angle
$\theta_M$	mean direction
$\rho_{x,y}$	cross-correlation
$\sigma$	variance in Chapter 4
$\sigma_m$	circular standard deviation in radians 6.3.1
$\sigma_\theta$	spreading function in Chapter 5
$\omega$	$\omega^2 = (2\pi f)^2 = gk \tanh kd$ angular frequency
$\xi_k^n$	Fourier coefficient
$\Xi_{x,y}$	cross-covariance
$\psi$	$\psi(x, y, t) e^{-i\omega t} = \Phi(x, y, t)$ ; complex velocity potential
$\tilde{\psi}$	complex wave potential function
$\zeta$	surface elevation

# List of Tables

## Chapter 2

Table 2.1 Summary of the some of the developed models and their validation Part 1; FDS stands for finite difference scheme, FE stands for finite elements and CG for conjugate gradient method (* stands for application only)	23
Table 2.2 Summary of the some of the developed models and their validation Part 2; FDS stands for finite difference scheme, FE stands for finite elements and CG for conjugate gradient method	24

## Chapter 4

Table 4.1 In the first column the MWD for IWCM data is given. $H_s$ is calculated for IWCM data. Diff1 is the difference between MWD and visual observation. Diff2 is the difference between MWD for IWCM and MWD for WRS data.	84
Table 4.2 Field data and database summary	94

## Chapter 5

Table 5.1 Summary of tests performed using different segment lengths and different number of frequency bins	113
Table 5.2 Tests program for the numerical simulation where P-M stands for Pierson-Moskowitz frequency spectra	126
Table 5.3 Summary of spectral analysis test cases (case 3a for 5 sensors, case 3b for 6 sensors, case 5 for 5 sensors); *The effective L/S is 1.08 and 2.54 respectively	127
Table 5.4 Percentage difference and root mean square values where (cor.) means corrected values – the frequencies which were not resolvable were not taken in account ( $K_r$ greater than 1.0)	141
Table 5.5 The method with the closest estimates to the target values	142
Table 5.6 Percentage difference between BDM and MLM significant wave height estimates	143
Table 5.7 Percentage difference between BDM and MLM direction estimates	145
Table 5.8 Percentage difference between BDM and MLM directional spreading estimates	147
Table 5.9 Percentage difference between the BDM and the MLM reflection coefficient estimates.	147
Table 5.10 L/S values for the inshore field data	154
Table 5.11 Percentage of differences between BDM and MLM parameter for the inshore data	155

## Chapter 6

Table 6.1 Summary of tested conditions for flat bed	180
Table 6.2 a The parameters for tests on the sloping bed and grid size $\Delta x=1.0$ m	183
Table 6.2 b The parameters for tests on the sloping bed and grid size $\Delta x=2.0$ m	184
Table 6.2 c The parameters for tests on the sloping bed and grid size $\Delta x=5.0$ m	185
Table 6.3 Description of laboratory simulated wave conditions	193
Table 6.4 Parameters for TMA spectra and directional wrapping function (where $\alpha$ is Philip's constant and $\gamma$	



is peak enhancement factor)	194
<b>Table 6.5</b> Summary of the tests performed for five different wave conditions generated in the laboratory (M4, N1, N2, B1 and B2)	197
<b>Table 6.6</b> The <i>rms</i> values when the MSE and DIRSPDF predictions are compared to the measurements	205
<b>Table 6.7a</b> The percentage error difference – absolute values (case 1- mono; case 2 - all frequencies and one direction, case 3 - directional; case 4 - reduced directional)	206
<b>Table 6.7b</b> The percentage error difference between MSE and DIRSPDF model predictions and measurements – relative values (case 1- mono; case 2 - all frequencies and one direction, case 3 - directional; case 4 - reduced directional)	206
<b>Table 6.8</b> Summary of offshore wave conditions used as input for model validation – <i>monochromatic case</i>	212
<b>Table 6.9</b> The summary of inshore wave conditions used for the model validation. <i>The parameters are given for the position shoreward of the gap unless stated otherwise. H** and WD** are given for 3 positions, first for the shoreward of the gap, second for the lee of the breakwater and third for the gap</i>	213
<b>Table 6.10</b> Summary of results for monochromatic case - (case 1 - peak frequency and principal direction with reflection, case 2 - mean frequency and mean direction with reflection, case 3 - same as case 1 without reflection)	216
<b>Table 6.11</b> Summary of results for directional wave modelling	221

# List of Figures

## Chapter 2

- Figure 2.1** The general operation of detached breakwater for the shore protection (after Dally and Pope, 1986) 9
- Figure 2.2** Flow chart for morphological modelling (after Bos *et al*, 1996) 10

## Chapter 3

- Figure 3.1** The location map 46
- Figure 3.2** Elmer site and the equipment locations 48
- Figure 3.3** Transducer positions and connections at Elmer offshore (marked as offshore WRS in Figure 3.2):  
a) surveyed co-ordinate of the array deployment B; b) surveyed co-ordinate of the array deployment D;  
where  $R=3m$  59
- Figure 3.4** The equipment positions at Elmer: a) surveyed coordinate of the pressure transducer array offshore - deployment 9 (marked as offshore WRS in Figure 3.2); b) surveyed coordinates of the inshore start array (marked as IWCM array in Figure 3.2 - inset); where  $R=3m$  60

## Chapter 4

- Figure 4.1** a) Cosine – bell window where T stands for a length of whole series; b) Its influence on time series; c) Subseries prepared for spectrum computation where M stands for a length of segment (number of points) and overlap is 20 %; 68
- Figure 4.2** The weighting function for transfer of pressure to surface elevation 71
- Figure 4.3** The wave recorder position scheme ( the dotted lines connect the transducers which were taken into comparison) 73
- Figure 4.4** Comparison of spectral energy normalised results obtained using cosine bell and triangular window (data measured near the breakwater) 76
- Figure 4.5** Comparison of spectral energy normalised results obtained using cosine bell and triangular window (data measured on the beach, notice smoothing) 76
- Figure 4.6** Comparison of spectral energy normalised results obtained using cosine bell window - starting points 0; 148; 296 (data measured near the breakwater) 77
- Figure 4.7** Comparison of spectral energy normalised results obtained using cosine bell window - starting points 0; 148; 296 (data measured on the beach) 77
- Figure 4.8** Comparison of spectral energy normalised results obtained using triangular window - 1 and 3 FFT segments (data measured near the breakwater) 79
- Figure 4.9** Comparison of spectral energy normalised results obtained using triangular window - 1 and 3 FFT segments (data measured on the beach) 79
- Figure 4.10** The side effects of window from Davidson (1993) 81
- Figure 4.11** The spectral energy density for IWCM and WRS data measured on 18/6/93 using MATLAB program specopt4 with cosine bell window 85
- Figure 4.12** The spectral energy density for filtered IWCM and WRS data measured on 18/6/93 using MATLAB program specopt4 with cosine bell window 86
- Figure 4.13** Spectral energy density results for IWCM and WRS data recorded on 11/06/93, using specopt4 and Hanning ( - - ), Welch ( : ) and cosine bell windows (—) 87
- Figure 4.14** Cross-spectral analysis results for IWCM and WRS data recorded on 11/06/93 at 17.26, using specopt4 program; a) cross-spectrum, b) coherence, c) transfer function, d) phase 88
- Figure 4.15** The coherence confidence intervals for IWCM and WRS data measured on 11/6/93 89

<b>Figure 4.16</b>	The phase confidence intervals for IWCM and WRS data measured on 11/6/93	89
<b>Figure 4.17</b>	Wave excursions for filtered IWCM and WRS data recorded on 14/06/93	91
<b>Figure 4.18</b>	The scheme of new spectral and directional program	93
<b>Figure 4.19</b>	Mean water depths offshore and inshore during October 1994. For locations refer to Figures 3.2, 3.3b and 3.4b	96
<b>Figure 4.20</b>	Spectral energy offshore during the October 1994	96
<b>Figure 4.21</b>	Comparison of spectral significant wave heights offshore and inshore in October 1994	98
<b>Figure 4.22</b>	Comparison of wave periods offshore and inshore in October 1994	98
<b>Figure 4.23</b>	Significant wave heights plotted against mean water depths-for channel 1 offshore: a) during deployment 9; b) during deployment B; c) during deployment D (see section 3.4.1) and d) for channel 6 inshore (in the gap between two breakwaters)	100
<b>Figure 4.24</b>	Comparison of wave direction offshore and inshore	100
<b>Figure 4.25</b>	Histogram of wave directions, Elmer offshore, February 1994 - January 1995	102
<b>Figure 4.26</b>	Wave height/period scatter diagram for Elmer	102
<b>Figure 4.27</b>	Wave periods at Elmer: Comparison of prediction and measurements	103
<b>Figure 4.28</b>	Occurrence of low frequency spectral peaks at Elmer	103
 <b>Chapter 5</b>		
<b>Figure 5.1</b>	Energy spectra measured at five offshore positions (see Figures 3.2 and 3.3b), the bar indicates lower and upper 95 % confidence levels for energy density = $10 \text{ m}^2\text{s}$	108
<b>Figure 5.2</b>	An example directional spectrum measured at the offshore position	109
<b>Figure 5.3</b>	The practical guideline for effective use the MMLM and the MLM method related to L/S ratio (courtesy Huntley and Davidson, 1998). The line which separates PL and non-PL regions is vertical as a result of assuming that waves are in shallow water. If the dispersion is taken in account, the line will curve to the right with increasing L/T. The inclined lines are the locations of spectral frequency estimates.	111
<b>Figure 5.4</b>	Time lag L / segment length S ratio for the field data. The marker, $\square$ , stands as an indication of L/S and L/T values for frequency estimates (S is here number of points [2 s/points])	113
<b>Figure 5.5</b>	Directional spectra contour plots given in the percentage of the peak energy when MLM was applied. For cases 1,2,3,4 respectively spectral smoothing was used. For cases 5,6,7 respectively frequency smoothing was used. ( - 1,2,3 and 5% ; — 10:10:100 %)	115
<b>Figure 5.6</b>	Directional spectra contour plots given in the percentage of the peak energy when the MMLM was applied. For cases 1,2,3,4 spectral smoothing was used. For cases 5,6,7 respectively frequency smoothing was used. ( - 1,2,3 and 5% ; — 10:10:100%)	116
<b>Figure 5.7</b>	Directional distribution for the energy summed over all frequencies ( - ), and only for frequencies < 0.2 Hz ( - - ), case 2	119
<b>Figure 5.8</b>	Directional contour plot for narrow frequency spectra, case 2 ( - 1,2,3 and 5% ; — 10-100% with an interval of 10%)	119
<b>Figure 5.9</b>	Directional contour plot for bimodal spectrum, case 2 ( - 1,2,3 and 5% ; — 10-100% with an interval of 10%)	120
<b>Figure 5.10</b>	Directional contour plot for wide spread spectrum, case 2 ( - 1,2,3 and 5% ; — 10-100% with an interval of 10%)	120
<b>Figure 5.11</b>	Frequency dependent reflection coefficient for cases 1-7 when the MLM was applied. Reflection coefficient is given by 'o' and the energy spectra normalised by the maximum value is given in the background (—)	122
<b>Figure 5.12</b>	Energy spectra for case 4 for offshore field data measured at the five positions (see Figure 3.2 and 3.3b). The bar indicates lower and upper 95% confidence levels for energy density = $10 \text{ m}^2\text{s}$	123

<b>Figure 5.13</b> Offshore array layout used for generation of synthetic wave data	125
<b>Figure 5.14</b> Predicted $H_s$ versus normalised target ( $H_s=1.0m$ ) values when MLM and BDM were applied for both spectral analysis cases for a) SW; b) S and c) SE direction. MLM0 and BDM0 stand for a case of purely incident waves. Notice the poor performance of the field array when waves are incident from the SE.	130
<b>Figure 5.15</b> Percentage difference between BDM and MLM $H_s$ estimates and target values and BDM and MLM estimates for $T=8sec$ , $s=25$ , for case 5 in the upper row and for case 3 in the lower row. The percentage difference is given in the legend.	131
<b>Figure 5.16</b> Percentage difference between BDM and MLM $H_s$ estimates and target values and BDM and MLM estimates for case 5 and for $T=8sec$ in the upper row and $T=4 sec$ in the lower row; $s=10$ . The percentage difference is given in the legend.	132
<b>Figure 5.17</b> Percentage difference between BDM and MLM direction estimates and target values and BDM and MLM estimates for $T=8sec$ , $s=25$ , for case 5 in the upper row and for case 3 in the lower row. The percentage difference is given in the legend.	134
<b>Figure 5.18</b> Percentage difference between BDM and MLM direction estimates and target values and BDM and MLM estimates for case 5 and for $T=8sec$ in the upper row and for $T=4 sec$ in the lower row; $s=10$ . The percentage difference is given in the legend.	135
<b>Figure 5.19</b> Percentage difference between BDM and MLM directional spreading estimates and target values and BDM and MLM estimates for $T=8sec$ , $s=25$ for case 5 in the upper row and for case 3 in the lower row. The percentage difference is given in the legend.	136
<b>Figure 5.20</b> Percentage difference between BDM and MLM directional spreading estimates and target values and BDM and MLM estimates for case 5, for $T=8sec$ in the upper row and for $T=4 sec$ in the lower row; $s=10$ . The percentage difference is given in the legend.	137
<b>Figure 5.21</b> Predicted reflection coefficient versus target values when MLM and BDM were applied for both spectral analysis cases for a) SW; b) S and c) SE direction	138
<b>Figure 5.22</b> Frequency dependent reflection coefficient predicted by MLM method (predifined reflection coefficient = 0.4)	139
<b>Figure 5.23</b> Frequency dependent reflection coefficient predicted by BDM method (predifined reflection coefficient = 0.4)	139
<b>Figure 5.24</b> BDM and MLM estimates of significant wave height for case 5 and case 3 normalised to the MLM estimates the case 5.	144
<b>Figure 5.25</b> BDM and MLM estimates of directions for case 5 and case 3	146
<b>Figure 5.26</b> The MLM and BDM directional distribution; a) MLM case 5; b) MLM case 3; c) BDM case 5; d) BDM case 3; ( - 5% ; — 10-100% with an interval of 10%)	148
<b>Figure 5.27</b> BDM and MLM estimates of reflection coefficient for case 5 and case 3	149
<b>Figure 5.28</b> The MLM and BDM frequency dependent reflection coefficient estimates and frequency spectrum normalised to the peak spectral energy; a) MLM case 5; b) MLM case 3; c) BDM case 5; d) BDM case 3	151
<b>Figure 5.29</b> BDM estimates of significant wave height normalised to the MLM estimates (inshore field data)	152
<b>Figure 5.30</b> The MLM and BDM directional distribution for inshore data ( - 5% ; — 10-100% with an interval of 10%)	153
<b>Figure 5.31</b> The MLM and BDM frequency distribution for inshore data dependent reflection coefficient estimates for inshore data	153
<b>Figure 5.32</b> The ratio of wave number with currents included and wave number without currents included versus relative angle for a current speed of 1 m/s in a water depth of 7 m	158
<b>Figure 5.33</b> The ratio of wave number with currents included and wave number without currents included versus relative angle for a current speed of 0.5 m/s in a water depth of 7 m	158
<b>Figure 5.34</b> The ratio of wave number with currents included and wave number without currents included versus current speed for relative angle of $0^\circ$ in the water depth of 7 m	161

<b>Figure 5.35</b> The ratio of pressure transfer function with currents included and pressure transfer function without currents included versus relative frequency in a water depth of 7 m and $u=0.5$ m/s	161
<b>Figure 5.36</b> The MLM directional distribution for offshore data combined swell and wind frequency spectrum: a) with no currents, b) currents - speed 0.5 m/s (crossing currents), c) currents - speed 0.5 m/s (following currents) and narrow frequency spectrum: d) no currents, e) currents - speed 0.5 m/s (crossing currents), f) currents - speed 0.5 m/s (following currents); ( - 5% ; — 10-100% with an interval of 10%)	162
<b>Figure 5.37</b> The MLM directional distribution for offshore data broad frequency spectrum: a) with no currents, b) currents - speed 0.5 m/s (crossing currents), c) currents - 0.5 m/s (following currents) and bimodal frequency spectrum: d) with no currents, e) currents - speed 0.5 m/s (crossing currents), f) currents - 0.5 m/s (following currents); ( - 5% ; — 10-100% with an interval of 10%)	163
<b>Figure 5.38</b> The sum of energy over all frequencies for cases given in Figures 5.36 and 5.37: a) combined swell and wind frequency spectrum, b) narrow frequency spectrum, c) broad spectrum and d) bimodal frequency spectrum); with no currents —, currents - speed 0.5 m/s (crossing currents) ---; currents - speed 0.5 m/s (following currents) -	164
<b>Figure 5.39</b> Array layout and corresponding co-array and co-array lags: a) offshore, b) inshore; where $R=3$ m	168
 <b>Chapter 6</b>	
<b>Figure 6.1</b> The computational domain schematisation where $\Delta x_2=v\Delta x_1$ ; $\Delta x_3=v\Delta x_2$ etc.	175
<b>Figure 6.2</b> The residuals difference versus the number of time steps for the conditions of the flat bed	181
<b>Figure 6.3</b> Residuals difference plotted versus number of time steps for sloping bed	185
<b>Figure 6.4</b> Standard deviation of the solutions as a function of $L/\Delta x$ and $T/\Delta t$ ; — contours for standard deviation every 0.0001 from 0 to 0.001, every 0.0002 from 0.001 to 0.002 and every 0.002 from 0.002 to 0.014; - contours for number of steps (details in Figure 6.5)	186
<b>Figure 6.5</b> The number of time steps required for the calculation as a function of $L/\Delta x$ and $T/\Delta t$ ; — contours for number of steps; every 100 from 0 to 1000 and every 200 from 1000 to 2000	187
<b>Figure 6.6</b> $N/N_s$ a function of $L/\Delta x$ and $T/\Delta t$ (calculated); — contours for $N/N_s$ every 1 from 0 to 20, every 2 from 20 to 40, every 4 from 40 to 80, every 10 from 80 to 120	188
<b>Figure 6.7</b> TP values (upper curve), residuals between two time steps ( $2\Delta t$ -middle curve) and residuals between two time steps ( $\Delta t$ -lower curve) as a function of the number of time steps ( $\Delta x = \Delta y = 2.0$ m, $Cr=1.0$ , $T=6.0$ s)	191
<b>Figure 6.8</b> Layout of physical model test. Measurements are taken in the area behind the breakwaters at distances of $x/L_p = 1 ; 2 ; 3$ from the tip of the breakwater. $L_p$ is the nominal wavelength for the modelled wave period.	192
<b>Figure 6.9</b> Diffraction coefficients contours for the monochromatic wave, - measured; --- predicted by DIRSPDF model; - predicted by MSE model. Only the area behind the breakwater is plotted here (contours in 0.1 intervals).	199
<b>Figure 6.10</b> Diffraction coefficients contours for the N1 directional waves, - measured; --- predicted by DIRSPDF model; - predicted by MSE model. Only the area behind the breakwater is plotted here (contours in 0.1 intervals).	200
<b>Figure 6.11</b> Diffraction coefficients contours for the N2 directional wave, - measured; --- predicted by DIRSPDF model; - predicted by MSE model. Only the area behind the breakwater is plotted here (contours in 0.1 intervals).	201
<b>Figure 6.12</b> Diffraction coefficients contours for the B1 directional wave, - measured; --- predicted by DIRSPDF model; - predicted by MSE model. Only the area behind the breakwater is plotted here (contours in 0.1 intervals).	202
<b>Figure 6.13</b> Diffraction coefficients contours for the B2 directional wave, - measured; --- predicted by DIRSPDF model; - predicted by MSE model. Only the area behind the breakwater is plotted here	

(contours in 0.1 intervals).	203
<b>Figure 6.14</b> The measured diffraction contours for four directional cases; --- wave condition N1; --- wave condition N2; - wave condition B1; - wave condition B2. The area behind the breakwater is only plotted here.	208
<b>Figure 6.15</b> The model bathymetry and measurement positions	211
<b>Figure 6.16</b> Typical model output (file 64 - directional modelling results)	215
<b>Figure 6.17</b> The percentage of difference for monochromatic and directional case-(a) lee of breakwater, (b) shoreward of breakwater gap, (c) breakwater gap	217
<b>Figure 6.18 a-f</b> Directional results summary – File 64 –a) sum of energy over all frequencies versus direction (line plot) and energy in directional bands chosen for modelling offshore (bar plots); b) sum of energy over all frequencies versus direction (line plot) and energy in directional bands chosen for modelling inshore (bar plots); c) measured inshore (line plot) and model predicted energy versus direction (circles plots); d) sum of energy over all directions versus frequency (line plot) and energy in frequency intervals chosen for modelling offshore (bar plots); e) sum of energy over all directions versus frequency (line plot) and energy in frequency intervals chosen for modelling inshore (bar plot); f) measured inshore (line plot) and model predicted energy versus frequency (bar plot)	218
<b>Figure 6.18g-h</b> Measured directional spectra – g) directional spectrum offshore; h) directional spectrum inshore;	219
<b>Figure 6.19</b> The bispectrum and bicoherence for the offshore measured data set 65; a) real part of bispectrum; b) imaginary part of bispectrum; c) absolute value of bispectrum; d) bicoherence	225
<b>Figure 6.20</b> The bispectrum and bicoherence for the inshore measured data set 65; a) real part of bispectrum; b) imaginary part of bispectrum; c) absolute value of bispectrum; d) bicoherence	226
<b>Figure 6.21</b> The bispectrum and bicoherence for the offshore measured data set 73; a) real part of bispectrum; b) imaginary part of bispectrum; c) absolute value of bispectrum; d) bicoherence	227
<b>Figure 6.22</b> The bispectrum and bicoherence for the inshore measured data set 73; a) real part of bispectrum; b) imaginary part of bispectrum; c) absolute value of bispectrum; d) bicoherence	228
<b>Figure 6.23</b> The results of the sensitivity tests for the position in the lee of the breakwater; a) sensitivity on change of beach reflection; b) sensitivity on change of breakwater reflection; c) sensitivity on change of breakwater transmission; d) sensitivity on change of frequency and direction	231
<b>Figure 6.24</b> The results of the sensitivity tests for the position shoreward of the gap a) sensitivity on change of beach reflection; b) sensitivity on change of breakwater reflection; c) sensitivity on change of breakwater transmission; d) sensitivity on change of frequency and direction	232
<b>Figure 6.25</b> The results of the sensitivity tests for the position in the gap between breakwaters; a) sensitivity on change of beach reflection; b) sensitivity on change of breakwater reflection; c) sensitivity on change of breakwater transmission; d) sensitivity on change of frequency and direction	233
<b>Figure 6.26</b> The wave height contours in the bay for file 73: a) original bathymetry with no transmission and no beach reflection taken into account; b) rotated bathymetry with no transmission and no beach reflection taken into account; c) rotated bathymetry with added transmission effect and no beach reflection taken into account (grid points are given on axis, contours are at 0.1 m interval)	236

## Appendices

<b>Figure A.1</b> Definition scheme for the Mild Slope Equation derivation	A-1
<b>Figure B.1</b> The computational domain schematisation where $\Delta x_2 = \nu \Delta x_1$ , $\Delta x_3 = \nu \Delta x_2$ , $\Delta x_4 = \nu \Delta x_3$ , $\Delta x_5 = \nu \Delta x_4$ etc.	B-2
<b>Figure C.1</b> The ADI scheme used by Li (1994b)	C-1
<b>Figure I.1</b> Plan view of a unique bifrequency space	I-1
<b>Figure H.1</b> Directional results summary – File 64 –a) sum of energy over all frequencies versus direction (line plot) and energy in directional bands chosen for modelling offshore (bar plots); b) sum of energy	

over all frequencies versus direction (line plot) and energy in directional bands chosen for modelling inshore (bar plots); c) measured inshore (line plot) and model predicted energy versus direction (circles plots); d) sum of energy over all directions versus frequency (line plot) and energy in frequency intervals chosen for modelling offshore (bar plots); e) sum of energy over all directions versus frequency (line plot) and energy in frequency intervals chosen for modelling inshore (bar plot); f) measured inshore (line plot) and model predicted energy versus frequency (bar plot)

	H-1
<b>Figure H.2</b> Same as for Figure H.1 – Directional results summary – File 69	H-2
<b>Figure H.3</b> Same as for Figure H.1 – Directional results summary – File 72	H-3
<b>Figure H.4</b> Same as for Figure H.1 – Directional results summary – File 73	H-4
<b>Figure H.5</b> Same as for Figure H.1 – Directional results summary – File 75	H-5

## List of Plates

<b>Plate 3.1</b> The aerial survey of the Elmer site	47
<b>Plate 3.2</b> Pressure transducers prepared for the offshore deployment	58
<b>Plate 3.3</b> Pressure transducer and its housing prepared for offshore deployment	58
<b>Plate 3.4</b> Assembling of IWCM on the top of the beach	62
<b>Plate 3.5</b> IWCM and one of satellite probes during deployment in Elmer	62
<b>Plate 4.1</b> WRS and IWCM deployed at Felpham beach during June 1993	82
<b>Plate 6.1</b> Numerical model results for file 64; directional modelling results above, mono run results below	239

# Acknowledgements

I would like to give thanks

To my supervisors

Andrew Chadwick, of School of Civil and Structural Engineering, University of Plymouth for his support, encouragement, patient reading of the manuscript, care, guidance with respecting my independence; Mark Davidson of Institute of Marine Studies, University of Plymouth, for teaching me oceanography, enthusiasm, stimulating discussions and much appreciated suggestions.

To my examiners

Prof. Brian O'Connor, Department of Civil Engineering, University of Liverpool and Prof. Phil Dyke, School of Mathematics and Statistics, University of Plymouth, for agreeing to be my examiners and for detailed attention given to the thesis.

To my 'collaborators' on the Elmer project

Phil Axe for collecting and quality checking data, for sharing his ideas and views, long discussions and mugs of coffee in endless working hours; Li Bin for kindly providing me with his model, his interest, useful suggestions and approachability; Chris Fleming making this possible and for his interest and encouragement; Jacob-Helm Petersen for sharing his software with me, following my ideas and answering an enormous number of questions; David Simmonds being so helpful and generous, a real 'soul-mate'

To the 'field-guys'

Paul Bird, technical staff and divers from School of Civil and Structural Engineering, University of Plymouth, David Pope, Richard Brown, Bob Gayler from Civil Engineering Department, University of Brighton, Roger Spencer and Ian Trayner from Arun District Council for a help in field deployment and collection of vast number of data.

To David Huntley for beneficial discussions and his time.



To Lynne Saunders for helping me out with wordprocessor puzzles, printing, giving me such great support in editing this thesis, her patience and good will.

To colleagues from School of Civil and Structural Engineering for nice working ambience. Special thanks to Mike R, Dave, Rob for helping me out after my PC and 'back ups' were devastated. To 'freshers' Erik, Brian, Elisa, Ken, Kathryn... for company.

To the 'coastal ladies'

Francoise Ozanne for chats on nonlinearities and Brekfast in America, Jaqui Kelly for letting me use her computer and coastal weekends, Travis Mason for her advice and support, Karen Stapleton for encouragement and herbal drops, Yollanda Foote for idle chats and being in touch.

Thanks to Nic, Mercedes, Mike F and Ed for yoga, salsa, sailing and philosophical discussions which kept me going.

To my friends

Alison, Angela, Adam, David, Ed, Chris S, Chris M, Mike W, Nic, Sue, Sarah H, Giovanni, Vedrana and Jaime, Ester and David, Amira and Leo, Branka, ..., my Croatian friends, my friends from Delftse Dagen for seeing and helping me and being in touch through all these years; particularly to Sarah B and Neil being so kind to me in long writing days. To Paul and Antonio for support via e-mail and virtual roses.

To my family

Nono for stories about huge ocean waves and New World, nona for being always ready to help financially, to mama, tata and Natasa for their understanding, support and love.

To all who helped me, to all who offered me help and to all who did not help but made me stronger

HVALA!

## **Author's declaration**

The work described in the thesis was carried out in the School of Civil and Structural Engineering at the University of Plymouth. At no time during the registration for the degree of Doctor of Philosophy has the author been registered for any other University award. All the material described herein is the original work of the author unless otherwise acknowledged.

This study was financed with the support of the Engineering and Physical Sciences Research Council through research grants GR/H74360, GR/J5947, GR/H2969 and GR/K48587, Arun District Council and The Standing Conference on Problems Associated with the Coastline (SCOPAC).

A programme of advanced study was undertaken, which included attendance at several one-day short courses. The SCSE and IMS seminars and four conferences detailed below were attended. The consulting company, Halcrow, whose numerical model was used was visited for consultation purposes.

### Courses attended:

Hydroinformatics, HR Wallingford, 1993

Physical Modelling (F. Raichlen, S. Hughes, W. Kamphuis), Sediment Transport (O. Madsen) and Field Measurement Techniques (E. Thornton), ICCE '96, Orlando, September 1996

### Conferences attended:

Coastal Dynamics '95, Gdansk, Poland

First Croatian Conference on Water, 1995, Dubrovnik, Croatia

ICCE '96, Orlando, USA

Coastal Dynamics '97, Plymouth, UK

Publications:

- Axe, P.G., Ilic, S., Chadwick, A.J., 1996, Evaluation of Beach Modelling Techniques Behind Detached Breakwaters, Proc. of 25th Inter. Conf. on Coastal Engineering, Orlando 1996, USA, ASCE, pp 2036-2047
- Bird, P.A.D., Davidson, M.A., Ilic, S., Bullock, G.N., Chadwick, A.J., Axe, P.G., Huntley, D.A., 1995, Wave Reflection, Transformation and Attenuation Characteristics of Rock Island Breakwaters, Proceedings ICE Conference Coastal Structures and Breakwaters '95, London, UK, pp
- Chadwick, A.J., Pope, D.J., Borges, J., Ilic, S., 1995, Shoreline Directional Wave Spectra. Part 1. An Investigation of Spectral and Directional Analysis Techniques, Proc Instn Civ Engrs, Water Maritime and Energy, Vol 112, Issue 3
- Chadwick, A.J., Pope, D.J., Borges, J., Ilic, S., 1995, Shoreline Directional Wave Spectra. Part 2. Instrumentation and Field Measurements, Proc Instn Civ Engrs, Water Maritime and Energy, Vol 112, Issue 3
- Ilic, S., Chadwick, A.J., Li, B., Fleming, C., 1997, Composite Modelling of Offshore Breakwaters, Proc. Conf. Coastal Dynamics '97, Plymouth, UK, ASCE, pp 684-693
- Ilic, S., Chadwick, A.J., Davidson, M.A., Bird, P.A.D., Huntley, D.A., 1997, Directional Analysis of Partially Reflected Waves, Proc. Seminar on Multidirectional Waves and their Interaction with Structures, 27th IAHR Congress, San Francisco, USA, pp 323-337
- Ilic, S., Chadwick, A.J., 1995, Evaluation and Validation of the Mild Slope Evolution Equation Model Using Field Data, Proc. Conf. Coastal Dynamics '95, Gdansk, Poland, ASCE, pp 149-160
- Ilic, S., Axe, P.G., Chadwick, A.J., Davidson, M.A., Bird, P.A.D., Bullock, G.N., Pope, D.J., 1995, The Role of Offshore Breakwaters in Coastal Defence, Proc. 1st Croatian Conference on Water, Dubrovnik, Croatia, pp 325-332

External contacts

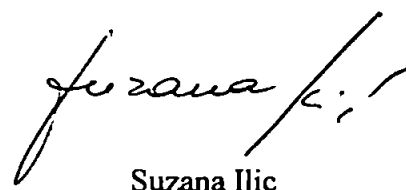
Bin Li and Chris Fleming, Halcrow, UK

Arun District Council

SCOPAC

Civil Engineering Department, University of Brighton, UK

Jacob Helm-Petersen, Civil Engineering Department, Aalborg University, Denmark



Suzana Ilic

## The project background

This PhD thesis arose from a collaborative research project between the University of Plymouth and the University of Brighton 'The Role of Offshore Breakwaters in Coastal Defence'.

In this project, fieldwork was required for the provision of data for the evaluation of numerical models of wave shoaling, refraction, diffraction and reflection. Shoreline survey data for the study of shoreline changes was also required.

An extensive field measurement programme has been successfully carried out over a one year period from September 1993 until January 1995. This programme consisted of concurrent offshore and inshore directional wave measurements and aerial and beach surveys at a new offshore breakwater scheme located in a macro-tidal environment with a renourished mixed sand/shingle beach at Elmer, West Sussex, UK. The new scheme consisted of eight breakwaters, six of which were built in 1993. The other two breakwaters were built in 1992 as an emergency measure and were enlarged when the other breakwaters were built (see Plate 1).

Two different types of wave measurement equipment were deployed for concurrent field measurements. The first, the University of Brighton Inshore Wave Climate Monitor (IWCM) consisted of six surface piercing wave resistance staffs, four configured in a star array with the other two acting as independent satellites. The IWCM measured wave activity behind one of the breakwaters enabling measurement of the effects of diffraction, refraction and shoaling. The second type of equipment, the University of Plymouth Wave Recording System (WRS) consists of six pressure transducers arranged in an array on the sea bed extending over an area of 60x16 metres, deployed offshore of the breakwaters, giving incident wave conditions.

All the field data have been archived and all the wave data have been analysed using spectral and directional analysis. A database of spectral and directional wave parameters has been assembled.

In the early stage of the field campaign, Dr Andrew Chadwick and the author of this thesis

moved from the University of Brighton to the University of Plymouth, hence the data processing and analysis were carried out at the University of Plymouth.

In 1992 and 1994, Davidson *et al* (1996) undertook fieldwork at this site, measuring the reflection performance of one of the breakwaters. In summer 1992, IWCM was also deployed in the lee of the two original breakwaters. Additionally, both measurement systems were deployed at the same position at Felpham beach. Some of the data collected in the 1992 campaign at Elmer and the data collected at Felpham were used by the author in this thesis.

#### **Candidate responsibilities:**

- Planning of deployment and deployment of equipment as a member, firstly of University of Brighton team and later University of Plymouth team
- Amendments to spectral and directional analysis software for IWCM to enable processing of data at the site
- Deployment and surveying of equipment deployed in Felpham
- Comparison of measurements by IWCM and WRS and evaluation of its compatibility
- Compilation and further development of spectral and directional software, originally developed by Paul Bird, Andrew Chadwick and Mark Davidson, for the analysis of data collected by IWCM and WRS
- Spectral and directional analysis of all data collected offshore and inshore
- Assembling database of spectral and directional wave parameters

#### **Contributions:**

**Philip Axe:** field deployment, offshore wave data collection and calibration, statistical analysis of processed offshore wave data, analysis of beach changes and photo record of beach changes

**David Pope:** further development of Inshore Wave Climate Monitor, field deployment at

**Elmer and Felpham, data login software for Inshore Wave Climate Monitor**

**Richard Brown:** further development of Inshore Wave Climate Monitor, field deployment at Elmer and Felpham, inshore wave data collection, video and photo records of the site

**Paul Bird:** field deployment at Elmer and Felpham, data logging software for offshore Wave Recording System

**Mark Davidson:** software for converting pressure data to surface elevation time series

**Technical staff University Plymouth and University of Brighton:** field deployment at Elmer and Felpham

**Diving team University of Plymouth:** field deployment at Elmer

**Additional software which was used in this thesis:**

**Jacob Helm-Petersen:** directional analysis software based on the Bayesian Method and software for generation of synthetic wave data

**Bin Li:** numerical model based on the Mild Slope Equation

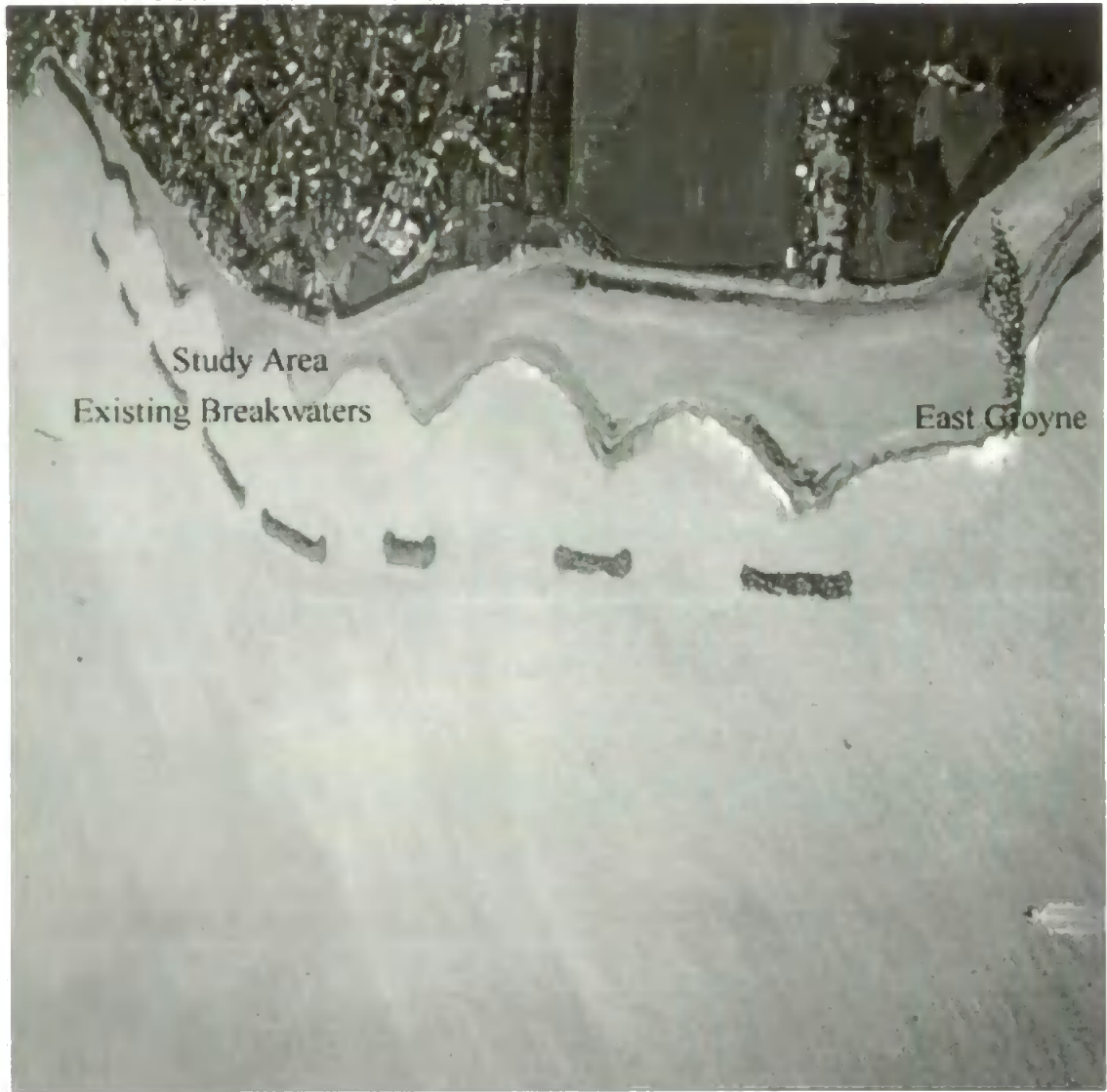


**Plate 1** Aerial survey of new breakwater scheme at Elmer (supplied by Arun District Council)



# Chapter 1

## Introduction

*It is then seen that this other way in which the numbers are beginning to function has little or nothing to do with science-as-such at all, but it clearly has quite a lot to do with how science is applied in our world of name and form. Correspondingly, research in this 'other way of functioning of the numbers', which is of the essence of research in hydroinformatics, is NOT SCIENTIFIC RESEARCH, even though it can be construed as research upon how science is applied, or how it participates in the 'bringing forth' that is technology. In this way, as 'research into revealing', hydroinformatics research belongs very essentially to RESEARCH IN TECHNOLOGY.*

*M Abbott (1991a)*

The development of numerical models for wave transformation, wave hydrodynamics and morphological changes has proceeded at a fast pace during the last thirty years. The creators of these models have exclusively used them in the late sixties and seventies. Most computation and interpretation of results was performed in some of the leading computational centres. With the development of PC's, the models are now being used by a number of clients outside the development centres. At the same time the development of computing hardware and new numerical methods means that once impossible solutions now become possible (e.g. new numerical methods enable solution of the Navier-Stokes equation) and that data assimilation; inverse modelling or Genetic Algorithms (GA) can be used to tune the existing models. Also the unknown parameters and processes which cannot be described in the traditional way through physics and mathematics are being replaced with so called black boxes and solved by some of the new techniques such as

Neural Networks (NN)<sup>1</sup>. Through the use of such tools, with their graphical user interfaces, the coastal engineer, the environmental scientist, the oceanographer and most others involved in analysis, planning, design and management of water-based assets have become the manipulators of numbers and symbols.

*This research is, then, concerned with the 'where' and the 'how' of the coming to presence and the bringing forth of this other way of functioning of the numbers in our outer world. It has to do, at least initially, with how works are currently designed and how they might better be realised in the future, with how complete systems are currently MANAGED AND HOW THEY MIGHT BETTER BE MANAGED IN THE FUTURE, and so on. Although it must always start from where those that it serves, its clients, are presently situated, it must also always seek to lead these that it serves to another, higher place. As we shall see, one of the places where this process begins is in simulation using numerical models, even as it already proceeds much further, into areas that have apparently very little to do with simulation using numerical models.*

*M Abbott (1991a)*

With the widespread use of models and with ever faster computers, the most often asked questions are how accurate and how applicable are the models. The clients, engineers, planners and managers wish to know where and how to apply the models. The developers wish to know the limitations of existing models. The answer to these questions lies in the validation of the numerical models using physical model data<sup>2</sup> and field data. The validation of models is then research in technology, verifying the capabilities and limitations of the tools, in this case numerical models. The result of research will provide guidelines for the model's applications. This can also be useful in the future when the numerical models are envisaged to be used through the internet or intranet. A database of the existing models with their applicability and limitations will assist a design engineer in making a choice of a proper model for the particular project. Most such research these days is based on verifying not only numerical models but also indirectly the existing theory behind them<sup>3</sup>. Therefore, new projects (such as the new European projects e.g. COAST3D and NICOP) place emphasis on numerical model validation. Such studies are in hand for straight and parallel contour beaches<sup>4</sup>. However, situations such as the area around detached breakwaters are more complicated and will take a few years to be completely validated.

---

<sup>1</sup> They are also used with hydrodynamic models.

<sup>2</sup> It is interesting to mention that with the wide use of numerical models physical models were abandoned by researchers and practitioners. In recent years, there has been a new boom in the use of physical models as part of composite modelling which also incorporates numerical modelling and field measurements. One purpose of physical models is to provide the data for the numerical model validation. Another is to understand physical processes better.

<sup>3</sup> Most of the models are based on Newtonian principles.

<sup>4</sup> The COAST3D studies are also planned for a beach with a structure.

Shore-parallel or offshore breakwater units or schemes have been used for the shore protection or beach protection since the beginning of this century. They alter the nearshore wave climate and hence sediment transport. Their local effect on the coast is to form salients or tombolos. The main design consideration is which of these shapes will develop, but not only in terms of visual aspects or water quality aspect but also of their impact on the longshore transport budget and the influence on the downstream coast. When a tombolo develops the longshore transport through the scheme will be stopped or redirected seaward of the structure, which again completely changes the shoreline equilibrium.

Detached breakwaters were only recently built in the UK. Existing design guidelines are based on experience in other areas of the world, with the most recent publications being the CERC Technical Report '*Engineering Design Guidance for Detached Breakwaters as Shoreline Stabilisation Structures*' and '*Beach Management Manual*' (Simm *et al*, 1996). Firstly these methods are empirical methods which did not prove to be satisfactory in the past and very often they needed to be accompanied by expensive physical modelling. Shoreline change or beach response numerical models can be used instead. However to model the wave field around breakwaters a series of parameters need to be taken into account and it is not possible to include them all in such numerical models. Apart from that, the majority of research and experience relates to sand beaches in a microtidal environment (tidal range <4m) . Hence they are not applicable to UK situations where the conditions are macrotidal (tidal range >4m) and the many of the beaches are shingle beaches.

Alternatively, breakwater design can be based on a morphological model which consists of a wave transformation model, a current model<sup>5</sup>, a sediment transport model and a bed evolution model. The development of morphological models is currently at the stage that the simulation can be performed over a period of time long enough to approach equilibrium conditions. Models of wave induced currents, which gives the input for sediment transport are based on the results of wave models.

As wave transformation modelling is the starting point of morphological calculations, the validation of an appropriate tool for a design will start with this model. In the context of the present study, a few considerations motivated the choice of wave transformation model based on the Mild Slope Equation (MSE). The MSE model is applicable for the situation in

---

<sup>5</sup> Alternatively one numerical model which predicts wave heights and current field can be used.

which strong diffraction, refraction and reflection are all present. Those processes are believed to be the main physical processes around breakwaters. It is also a linear type of model, which is easy to implement and is economical in use of CPU time. It has already been used in industry for the design of harbours and other coastal structures. Because of its linear character it can be applied to random waves using superposition of results obtained for computations for a series of frequencies and directions. Finally, MSE models are also included in some of the existing morphological models produced by research centres such as HR Wallingford and Danish Hydraulic Institute.

The first generation of wave transformation models assumed regular waves with height and period being the same as those of significant waves. Neumann (1953) was the first in proposing a functional form of wave spectrum<sup>6</sup> to account for randomness. While engineers continued to design coastal structures assuming wave transformation of regular waves, measurements of ocean wave spectra were carried on and the importance of considering the full directional wave spectrum was gradually realised and started to be used for engineering applications first in Japan in the 1970's.

*Since around 1990, coastal and port engineers in the world seem to have finally realised the necessity to introduce the directional wave spectrum into wave analysis for design works.*

*It will not be far away when various technical manuals in the world will list the directional wave analysis as the standard approach to the engineering design.*

*Goda (1998)*

Vincent and Briggs (1989) carried out laboratory experiments using directional random (short crested) waves for wave diffraction-refraction over an elliptic mound and Briggs et al (1995) for wave diffraction around a breakwater. They illustrated the importance of incorporating directional spread in wave transformation modelling. The data from these studies among the others (e.g. Sand *et al*, 1983 and O'Connor *et al*, 1995) are providing a basis to calibrate numerical schemes for directional spectral calculations.

Developments in information technology have resulted in the use of computational models for design and decision making purposes. Also it has enabled the development of analysis for random waves measurements and the simulation of random seas in the laboratory. A further step is the use of numerical models for random sea simulation, which have still not been validated against field data.

---

<sup>6</sup> The wave spectrum describes how the wave energy is spread over frequencies and directions.

Therefore the aim of this thesis is to evaluate a Mild Slope Equation model that predicts the wave transformations caused by refraction, diffraction and reflection using field data with emphasis on the transformation of random directional seas.

The study is presented as follows

Chapter 2 - gives the necessary background information on detached breakwaters, the numerical model used in this thesis and directional analysis enabling the definition of the objectives of the study.

Chapter 3 - describes the field site and deployment

Chapter 4 - consists of field data processing and analysis of results

Chapter 5 - evaluates directional estimates from numerical and field data

Chapter 6 - provides results of the numerical model validation

Chapter 7 - gives final conclusions of the study and the guidelines for future work

By this means, this thesis can be viewed as a contribution to the following aims identified by Goda (1998):

*It will be a task for researchers to clarify physical mechanisms, to provide numerical schemes easy to use, and to prepare technical manuals based on the random wave approach. By doing so, the random wave approach can truly become a design tool of practitioners*

*Goda (1998)*

# Chapter 2

## Literature and Background

*Try to learn something about everything and everything about something*

*Text on the memorial of Thomas Henry Huxley*

### 2.1. Introduction

The evaluation of a wave transformation computational model using field data can be divided into three parts. The first part is the field deployment and measurements of wave properties. The choice of the equipment and deployment location offshore and nearshore is facilitated by prior general knowledge of main physical processes for the specific site, accompanied by computational model information. In the second stage the appropriate processing and analysis technique needs to be chosen to minimise the uncertainty of wave data accuracy. The third part is wave transformation simulations using the computational model. The input and boundary conditions are taken from the field measurements at the offshore position. Once the computation is finished, the results are compared to the inshore measurements and qualitative and quantitative comparisons are made.

This chapter begins with a short description of offshore (shore-parallel) breakwaters and discusses their general operation and design consideration. Then the necessary background

and literature review for the evaluation of the computational model using the field data collected around an existing scheme of offshore breakwaters is presented. The computational model, which was chosen, is of the linear type derived on the basis of the Mild Slope Equation. The "Mild Slope Equation" is a differential equation of elliptic form. The main consideration in the last twenty years has been to find a very rapid means for solving this equation. A history of the derivation and modelling of the Mild Slope Equation is, therefore, briefly presented in section 2.3. The different forms of the original equation, boundary conditions and solution techniques are summarised. The section finishes with a short description of examples of validation and evaluation of Mild Slope Equation models.

The data collected offshore of the detached breakwater scheme at Elmer and in the lee of one of the breakwaters were processed using spectral and directional analysis. Spectral and directional analysis techniques using linear wave theory are now well established and are succinctly described in Isobe and Kondo (1984), Goda (1985) and Benoit *et al* (1997). However, their practical application is quite complex and in section 2.4, short summaries on the relevant theory and its practical application are presented. The emphasis is on stochastic methods in homogeneous fields and fields with reflection and currents present. The chapter concludes with the aim and objectives of this study.

## **2.2. Offshore<sup>1</sup> breakwaters and field examples**

### **2.2.1 History**

The first offshore breakwaters in UK were built back to the last century. The main purpose of those structures was to protect harbours (e.g. Plymouth rubble mound offshore breakwater). The use of offshore breakwaters for beach protection is more recent. The earliest application of a single unit breakwater was at Venice, California, 1905 (Dally and Pope, 1986). A single breakwater was built near the shoreline to protect an alongshore amusement pier.

Since then, offshore or detached breakwaters have been widely used for beach protection, particularly in areas with small tidal oscillations. They have been extensively built in the Mediterranean region. Hundred of kilometres of Italian coast have been protected by

---

<sup>1</sup> Offshore breakwaters are also described as shore-parallel or detached breakwaters in the literature.

offshore breakwaters (Liberatore, 1992) and they have also been employed and monitored in Israel (Nir, 1982). A few examples of detached breakwaters schemes protecting artificial beaches can be found on the Mediterranean coast of France and Spain. There is also considerable evidence of construction and monitoring during the seventies and eighties in Japan. Sawaragi (1992) wrote that 630 km of detached breakwaters were constructed in Japan. Dally and Pope (1986) summarised the multiple units schemes built in USA<sup>2</sup> The largest of these, at Presque Isle, on Lake Erie (1978), comprises the scheme of 52 units. It was constructed along with a sand beach fill to protect an 11 km long sand spit. Similar schemes were also built in Denmark, Australia and more recently in the UK.

The first offshore structure for beach protection in the UK, a single breakwater, was built at Leasowe Bay in 1976 (Barber and Davies, 1985). Other schemes have been built, at Happisburgh and Winterton (MAFF, 1994), at Monks Bay, on the Isle of Wight, and most recently at Sidmouth in Devon (Axe, 1999). A scheme of eight breakwaters, constructed to provide protection from flooding and beach erosion at Elmer, in 1993, was chosen for the field study.

### **2.2.2 General operation of detached breakwaters**

Detached breakwaters protect the beach from direct wave action and transform the incoming waves. Their effect on wave propagation is similar to the combination of effects caused by natural shore parallel sand bars or reefs and artificial islands. The wave energy is dissipated on or reflected from the structure and the diffraction of waves around the breakwater ends results in a lateral spread of wave energy as it reaches the shore. The wave energy is significantly reduced in the area immediately behind the breakwater – in the shadow zone. The net effect is the entrainment of sediment in the energetic regions which is subsequently transported by mean flows into the shadow zone. This causes the development of salients along the shore. If the salient becomes connected to the structure, it is called a tombolo as illustrated in Figure 2.1.

The advantage of detached breakwaters compared to other more traditional shoreline structures (e.g. groynes) is that, in generally they actually decrease the heights of incoming waves, and reduce offshore losses. They control not only longshore transport<sup>3</sup> but also cross-shore transport. Even though the main aim of these schemes is to protect the

---

<sup>2</sup> They can be found in Massachusetts, Virginia, Louisiana and Ohio.

<sup>3</sup> Some material is still transported through the scheme.



shoreline and the beach from erosion, sometimes such schemes introduce additional side effects. A potential problem is the formation of tombolos behind the structures, which may interrupt longshore sediment transport, and cause additional erosion further alongshore. Some problems connected with the use of detached breakwaters are reported by Toyoshima (1976, 1982)<sup>4</sup>.

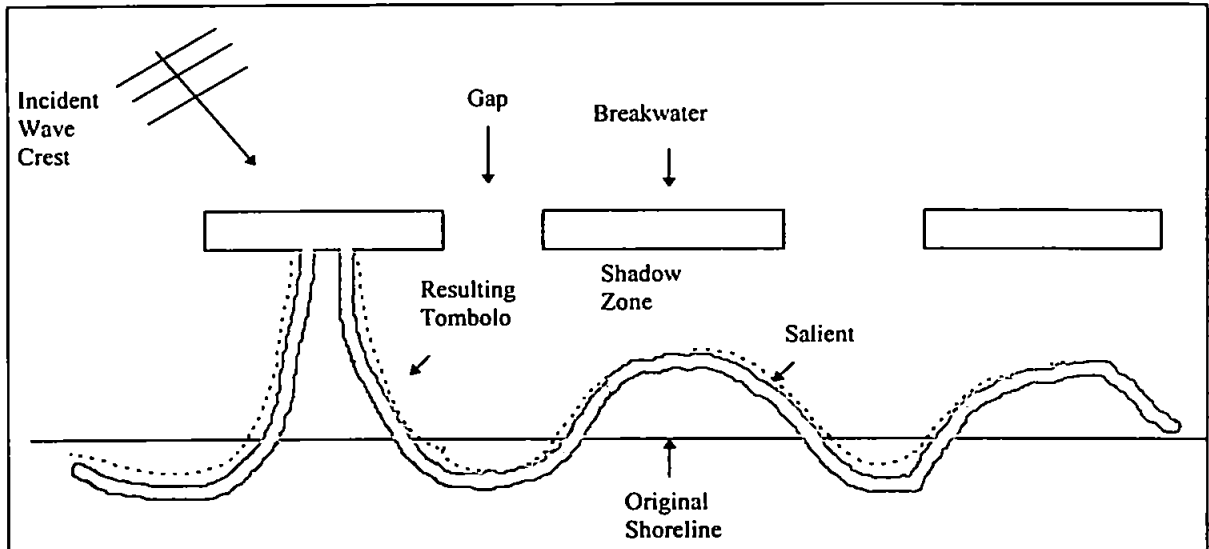


**Figure 2.1** The general operation of detached breakwater for the shore protection (after Dally and Pope, 1986)

The primary interest to the coastal engineer when designing a detached breakwater scheme is the equilibrium beach plan form and the stability of the salient whilst minimising the side effects. The design procedure is still rather empirical, although the understanding of the behaviour of such systems is slowly progressing. There are several design methods available. First, there are empirical methods (characterised as rules of thumb by Bos *et al* 1997), based on field and laboratory experience<sup>5</sup>. Summary of geometrical plan-form models can be found in Axe *et al* (1996). These methods can be used as a first estimates but it is advisable to support them with physical model and pilot cases prior to construction (Dally and Pope, 1986).

The second method is the application of so-called one line numerical models. These models work on the assumption that the coastal profile is more or less constant in slope and the longshore transport is related to the local angle of incidence of waves. One of the most

<sup>4</sup> Therefore, in Italy and in Japan, surface piercing breakwaters were replaced with submerged breakwaters and beach nourishment in the eighties.

<sup>5</sup> For example, Sawaragi (1992) summarised the empirical knowledge about wave heights behind a group of detached breakwaters and transmission coefficient through the structure.

used one line numerical models is the GENESIS<sup>6</sup> shoreline model (Hanson, 1989), Hanson and Kraus, 1989). The model does not take cross shore transport into account and assumes an equilibrium profile. Recently more complex 'area models' have been developed taking into account waves, currents, sediment transport and bed evolution simulations (e.g. O'Connor et al 1992, Pechon and Teisson, 1996, Zyserman *et al*, 1998 ). They can be run over a period which is long enough to approach equilibrium conditions (Johnson *et al*, 1994). The new morphological models integrate the wave, currents and sediment transport and bottom changes model. A flow diagram of a morphological model components is given in Figure 2.2.

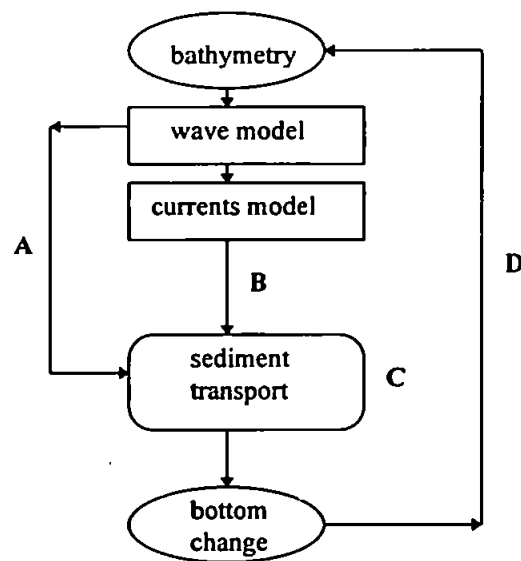


**Figure 2.2** Flow chart for morphological modelling (after Bos *et al*, 1996)

Firstly a wave transformation computation is carried out for a given bathymetry (A), followed by currents calculation (B). The wave and current model can be then iterated for wave-current interactions. This is used as an input to a sediment transport module (C). After each run the bathymetry can be updated (D) and computation can proceed, ideally, until a beach equilibrium is obtained<sup>7</sup>. However, the result of testing contemporary morphological models with laboratory data and its intercomparison (Nicholson *et al* 1997, Pechon *et al* 1996) show good results and form the basis for further development.

<sup>6</sup> A generalised shoreline change numerical model

<sup>7</sup> This is sometimes very difficult to achieve.

### 2.2.3 Monitoring examples

Dally and Pope, (1986) advised the monitoring of the existing schemes in order to help with the design of new schemes and to better understand physical processes. There are several published examples of field monitoring offshore breakwater schemes.

Kraus (1983) validated his shoreline evolution model on data collected at a breakwater protected beach at Oarai in Japan. Wave data was recorded for seven and a half months with wave gages deployed at 21.8 m depth. Wave breaking near the shore was also measured. Hanson *et al* (1989) evaluated GENESIS, which included transmission using field data measured at Holly Beach, Louisiana. The monitoring programme consisted of periodic vertical aerial photography, quarterly beach profile surveys and visual observation of local waves and nearshore circulation. A five year monitoring program for a project site at Lakeview Park, near Lorrain Harbour, at Lake Eire, was reported by Pope and Rowen (1983). Aerial photographs and bathymetric surveys were taken on regular basis. Monitoring information was also used to validate the wave transmission coefficient in the GENESIS model (Hanson *et al*, 1989 and Hanson and Kraus, 1990). To form a one year representative wave data set, hindcasting was used from Lorain. There are also examples of monitoring in Israel (e.g. Nir, 1982) and Spain (e.g. Galofre and Montoya, 1999). The emphasis was mostly on the shoreline change behind the breakwaters, less information on the wave and currents transformation around detached breakwaters is available.

#### *Summary*

The effect of surface piercing breakwaters on incoming waves, wave induced currents, and the transport and deposition of sediment is a complex three dimensional phenomenon. In many circumstances, the accurate prediction of shoreline change behind those structures is still beyond the present state of knowledge. The evaluation of existing models from field data can help in further understanding of the processes around offshore breakwaters and give guidelines for further model developments and design tools. As the computation of morphological changes starts with a wave transformation model, the field measurements and evaluation of wave transformation models is firstly required. In the morphological models the wave transformation is still computed mostly by linear wave models. One of the most developed and used linear models is based on the Mild Slope Equation. In the next

section the development, advantages and disadvantages of Mild Slope Equation models are given.

## **2.3 Mild slope equation - wave transformation model**

### **2.3.1 Introduction**

A wave transformation model transforms wave properties (e.g. wave height, period, and direction) from one position at sea to another due to physical processes. The main physical processes causing wave transformations are

- Shoaling, the change in wave length and amplitude due to spatial variations in depth
- Refraction, the change in the direction and amplitude of wave propagation due to spatial variation in depth
- Diffraction, the transmission of energy in a direction perpendicular to the wave rays, caused by structures and by seabed features
- Energy dissipation due to sea bed friction and wave breaking
- Interaction of waves and currents and seabed changes
- Refraction of waves due to currents
- Wave breaking due to depth, bed slope and currents
- Wave reflections from submerged and surface piercing objects
- Energy gain and loss due to winds and spectral evolution due to wave-wave interaction

Linear and non-linear models can describe wave transformation processes from offshore to inshore. The non-linear models are still being developed (e.g. MacDonald, 1998). Also they are usually computationally demanding and not so simple to apply in the practical engineering field. Unlike the non-linear models, linear models are mostly developed, and they are easier to implement. Most of the linear models are already installed on PCs and notebooks and used for design and consultancy purposes. Great care is however required in

the use of models of this kind in view of the whole chain of assumptions that are made. The modeller should be aware of those restrictions and as Abbott (1991b) said:

*"An analogy is sometimes made between instability and a "nervous breakdown". If a person is obliged to do something but at the same time is constrained in his actions in such way that he cannot in fact possibly do it, then a common consequence is a nervous breakdown."*

Linear models are derived from linear wave theory. They are based on the assumption that waves amplitudes never become very large for a given water depth, so that wave profiles can be approximated to a reasonable degree of accuracy by the familiar sinusoidal shape. It should be taken in account that linear theory will fail when wave heights become very large (and wave profiles differ markedly from the sinusoidal shape) or when waves break. Also they cannot accurately predict shallow water processes such as wave-wave interactions. The non-linear models, e.g. those based on the Navier - Stokes Equation, and weakly non - linear models, based on Boussinesqu Equation, should be used instead in such conditions.

Assuming that diffraction, refraction and reflection govern the wave transformation processes around detached breakwaters and that non-linear processes have only a minor effect; linear wave period - averaged diffraction-refraction models can be used to predict wave heights around those structures. Most of the wave models are monochromatic. To simulate a real sea, however, a range of components (directions + frequencies) is usually needed. The advantage of linear models is that they can model random sea as a series of monochromatic waves. The final result is a summation of results for each component. Using such techniques, energy transfer between components is not possible. However, in conditions where those processes might be of second order, the implementation of a linear model has the advantage that it is simpler and quicker to run than a non-linear model.

The most frequently used linear diffraction-refraction models in the last twenty years or so are the wave transformation models based on Mild Slope Equation. There are a vast number of publications describing developments of these models, their application in case studies or research. The results of these kind of models as well as other types of wave models are also used as a starting point in the morphological modelling (e.g. O'Connor *et al* 1992, Nicholson *et al* 1997). In the next section a summary of the development and applications will be given.

### 2.3.2 Development

Possibly, one of the first mathematical models for wave transformation was developed at the University of California in about 1939 (Goda, 1998). These models were further developed during the Second World War<sup>8</sup>. By 1960, it was quite common, at least in the USA, to use calculations to predict wave refraction. Those first models were based on the concept of wave rays. They are still used today but have been improved in recent times to include many processes including diffraction (e.g. Yoo and O'Connor (1986a,1988a)), wave current interaction (see e.g. Yoo *et al* (1988b)).

On the other hand, diffraction around breakwaters was calculated using diagrams, based on optical theory. With the development of computers and numerical schemes, the modelling of wave transformation equations became ever more advanced. Refraction models were not able to simulate diffraction, and produced caustics. It was therefore necessary to develop a new model capable of dealing with refraction and diffraction.

To overcome the limitation of refraction models in the treatment of caustics where diffraction becomes important, combined refraction-diffraction models have been developed. Berkhoff (1972, 1976), developed the so-called "Mild Slope Equation" (MSE), which was the first attempt to formulate and solve numerically, an equation of linear short wave transformation<sup>9</sup>. The original Berkhoff equation was derived taking energy conservation in account and applying the Galerkin method (Booij 1981). He showed that the equation could be reduced to forms of the wave-ray method (see also Yoo *et al* (1989)).

The Mild Slope Equation can also be derived following slightly different principles than Berkhoff originally used<sup>10</sup>. Booij (1981) and Dingemans (1997) derived the transient form<sup>11</sup> of the mild slope equation using Luke's variational method and the Hamiltonian variational principle respectively. It is assumed that the waves are almost periodic with a frequency in the neighbourhood of the main angular frequency. Berkhoff's original harmonic form can be retrieved from this equation and the full derivation is given in Appendix A. Behrendt and Jonsson (1984) obtained the mild slope equation by requiring

---

<sup>8</sup> A wave refraction model was first used for D-day landings in 1943.

<sup>9</sup> There were attempts to derive mild slope type of equation before. Eckart (1952) was the first to propose a form of the mild slope equation.

<sup>10</sup> Independently, Smith and Sprinks (1975) and Lozano and Meyer (1976) in their studies of wave scattering by circular islands gave a much clearer derivation of the equation than originally Berkhoff did. They all derived the steady state, elliptic equation for harmonic waves.

<sup>11</sup> The transient form of the MSE is the hyperbolic time dependent equation and it is for nearly harmonic waves

conservation of wave energy. Two different functionals were constructed in a way which leads to a better physical understanding. Copeland (1985a) used the assumption that the rate of change of wave energy is equal to the rate at which work is done by external pressure and obtained the transient form of the Mild Slope Equation.

The models based on the Mild Slope Equation are rapidly replacing ray refraction models for areas with complex topography and structures, although they must be applied with care due to assumptions made in their derivation. They are:

- The fluid is an ideal fluid (no viscosity).
- The fluid is incompressible and homogeneous.
- Gravity is the restoring force.
- Motion is irrotational, which leads to a potential formulation.
- Infinitesimally small amplitude waves.
- A motion which is only simple harmonic in time.

To by-pass restrictions imposed by the derivation of the model a number of different mild-slope equations have been derived, where the difference is due to assumptions in bottom geometry (smooth bed/rippled bed) or the inclusion of further physical processes (i.e. current refraction or inclusion of evanescent modes).

Booij (1981) included the effects of refraction by a nonuniform current in an extended form of the MSE. Kirby (1984) corrected his derivation and therefore Kirby's version of the extended equation was used further<sup>12</sup>. Massel (1993) and Dingemans (1997) extended the MSE considering the evanescent modes.

During early applications and verifications of the models it was found that including non-linearities in the model produced better results in non-linear environments such as behind a shoal. Booij (1981) included the influence of non-linearity on the phase and group velocities by taking Hedges (1976) simple formulation of the dispersion relation. Kirby and Dalrymple (1986) extended Booij's work and proposed a dispersion relation for

---

<sup>12</sup> Yoo *et al* (1989) and O'Connor and Yoo (1988) incorporated dissipative processes and wave current interactions in the energy approach of Copeland (1985a) and showed that in shallow water the resulting equations were almost equivalent to Kirby's (1984) elliptic equation.

monochromatic wave models in order to model non-linear effect over a broad range of depths. The non-linear modification to the time-dependent form of the linear Mild Slope Equation provides a smooth prediction of wave parameters for the entire range of water depth even in the case of weakly non-linear waves. In shallow water the Hedges simple formulation is obtained and the limit for deep water is the second order Stokes formulation<sup>13</sup>. Later a time dependent model which preserves wave group behaviour and it is applicable for bounded and free long waves was developed (Kirby *et al*, 1992).

It was also found necessary to include dissipative processes by bottom friction and wave breaking when the model was used for design purposes (Booij, 1981). Dingemans (1985) and Kirby (1986a) took the effects of a ripple bed in account whereas, Rojanakamthon *et al* (1990) derived an equation for waves propagating over a porous bed under the mild-slope assumption<sup>14</sup>.

Further information on the MSE and related approaches can be found in reviews presented by Copeland (1985a), Yoo *et al* (1989), McDowell (1988), Liu (1990), Dodd and Brampton (1995). The validity of the equation is given by Jonsson (1979,1981) and Dingemans (1985). Most recently, Dingemans (1997), summarised his latest work on the MSE and compared it with other existing models. He also describes all additional parameters (e.g. bottom friction, wave breaking) and the manner in which they may be included into the original equation.

## 2.3.3 Mild Slope Equation forms

### 2.3.3.1 Elliptic forms

The original mild slope equation derived by Berkhoff (1972) is a differential equation of elliptic form , given by

$$\nabla(cc_g \nabla \Phi) + cc_g k^2 \Phi = 0 \quad (2.1)$$

where:

c = phase celerity,  $c_g$  = group celerity, k = wave number,  $\Phi$  = complex wave potential function

<sup>13</sup> Zhao and Anastasiou (1993) made their expression for dissipation more explicit.

<sup>14</sup> Yoo and O'Connor (1986b) included both dissipation processes, wave current interaction and wave breaking in alternative refraction-diffraction model.



Very often the elliptic equation is slightly modified in order to speed convergence and execution time. With the transformation

$$\Phi = \tilde{\psi} (c c_g)^{-1/2} \quad (2.2)$$

the MSE (2.1) may be written in the form of a Helmholtz equation

$$\nabla^2 \tilde{\psi} + k_c^2 \tilde{\psi} = 0 \quad (2.3)$$

The Helmholtz equation for purely harmonic waves is also elliptic.

The elliptic model needs boundary conditions for the whole domain and simultaneous solution over the whole area. Any error occurring at a boundary will be manifested throughout the entire solution domain, which makes the whole solution prone to error.

### Numerical solutions

The elliptic mild slope equation can be solved numerically in two ways. One way is to use the finite element method and the second is to use iterative numerical methods. In both cases the large number of equations needed to be solved makes the implementation of the elliptic models difficult. Therefore, a few authors have worked on the development of numerical techniques in order to improve and speed up the computation.

Berkhoff's (1972) numerical solution of the original equation was based on the finite hybrid element method. Behrendt and Jonsson (1984) using the functional derived from the MSE improved the finite element solution<sup>15</sup>. The first functional is based on a finite/infinite element formulation and the second one on a hybrid finite element formulation. Austin and Bettes (1982) used the finite element method for solving the equation with the formulation of a 'damping' boundary, which absorbs the wave and so removes any artificial reflections from the boundary.

The iterative methods, which were used to solve the elliptic MSE, avoid using a direct Gauss elimination matrix method to solve the system of linear equations, which requires larger computer storage. Panchang *et al* (1988) has developed a model of the elliptic type based on the "Error Vector Propagation" method. A further development was the

---

<sup>15</sup> Bettes and Zienkiewicz (1977), Houston (1981) and Tsay and Liu (1982) among others have also worked on the numerical solution by applying finite element methods.

introduction of a conjugate gradient iterative method for solving the original equation (Panchang *et al*, 1991). To accelerate the speed of convergence the preconditioning method should be used, which increases the computer storage requirements. A further contribution was the introduction of a Gauss transformation in order to produce a stable conjugate gradient scheme for the linear system of the elliptic mild slope equation (Li, 1994a)<sup>16</sup>.

Li and Anastasiou (1992) presented two models based on the mild slope equation. Both formulations are solved using a modified form of the multigrid method which was originally developed by Brandt (1977). Accurate solutions were obtained using only two or three points per wavelength. The accuracy and the small computer storage requirement enables the model to be used for a number of practical problems.

### 2.3.3.2 Parabolic forms

In the early 1970's, computational difficulties existed in modelling larger coastal areas using the elliptic differential equation. These problems lead to the derivation of a parabolic approximation by Radder (1979). The derivation was based on the use of a splitting matrix, which divides the wave field into transmitted and reflected components. It is assumed that wave propagation takes place mainly in one direction, then wave diffraction in that direction can largely be ignored but in the direction normal to the main wave direction it is kept in the formulations. This results in following equation

$$\frac{\partial A}{\partial x} = \frac{1}{2kcc_g} \frac{\partial}{\partial y} \left( cc_g \frac{\partial A}{\partial y} \right) - \frac{(kcc_g)_x}{2kcc_g} A \quad (2.4)$$

where A is an amplitude function and  $\Phi(x, y) = A(x, y)e^{ikx}$

The equation is usually solved in this form since the amplitude is much less rapidly-varying than the exponential form (which contains the 'waviness' of the basic incident wave). The implication is that this equation can not be used in a field with strong diffraction. For an uneven bottom, the wave field is to be split into a forward scattering field and a backward-scattering field. Hence the parabolic approximation consists in neglecting the backward field and to some extent the effects of varying bathymetry or reflection will not be taken in account.

---

<sup>16</sup> Tozer and Lawson (1994) used the conjugate gradient scheme as well.

However, the main advantage of this approach is in consuming two times less computational effort, because the parabolic equation uses a marching method with boundaries at the initial line, and along the lateral sides. Therefore, large number of authors have used Radder's approach and tried to modify and improve the solution through the 70's and 80's. This resulted in further developments of parabolic approximations to the mild slope equation and suitable methods to solve them.

Tsay and Liu (1982) and Liu and Tsay (1983) improved the parabolic approximation of the MSE combining the approximation for the forward scattered wave with that for the backward scattered wave to form a more general solution. They could even study weak reflections from a submerged shoal. Firstly Kirby (1986b) and then Dalrymple and Kirby (1988) and Dalrymple *et al* (1989) extended the parabolic model for refraction and diffraction to 90 degrees including irregular bathymetry. The new parabolic model presented by Li (1997) does not have the angle limitation either. Kirby and Dalrymple (1986) applied a non-linear modification to the parabolic equation for refraction and diffraction in order to include non-linear effects. Nonlinearity is incorporated in the model by correcting the wave parameters iteratively using an empirical non-linear dispersion relationship.

### Numerical solutions

The most used numerical scheme to solve parabolic equations is the finite difference Crank - Nicolson scheme. Generally, the scheme is unconditionally consistent and stable. It is also an inexpensive higher - order accurate scheme. It has an error of  $O(\Delta t^2, \Delta x^4)$  with properly chosen weighting. Unfortunately this scheme can lead to unrealistic oscillating solutions when the forward step  $\Delta x$  is large. Booij (1981) and Radder (1979) used an implicit higher order scheme with separate discretisations in x and y directions to overcome these problems.

#### 2.3.3.3 Hyperbolic forms

The MSE given by expression 2.1 for purely harmonic motion is elliptic. A hyperbolic form of the purely harmonic case is obtained noting that for harmonic motion with frequency  $\omega$  it can be shown that

$$\zeta = \frac{-1}{\omega^2} \frac{\partial^2 \zeta}{\partial t^2} \quad (2.5)$$

And using equation 2.5 for the last term of 2.1, Copeland (1985a,b) obtained a hyperbolic equation

$$\nabla(cc_g \nabla \zeta) - \frac{c_g}{c} \frac{\partial^2 \zeta}{\partial t^2} = 0 \quad (2.6)$$

He split equation 2.6 into a system of two first order hyperbolic equations

$$\nabla Q + \frac{c_g}{c} \frac{\partial \zeta}{\partial t} = 0 \quad (2.7)$$

$$\frac{\partial Q}{\partial t} + cc_g \nabla \zeta = 0 \quad (2.8)$$

where Q is introduced as a pseudo flux and the time co-ordinate is treated as an iteration parameter. His model includes internal boundaries of arbitrary reflective properties and a driving boundary of transmissive and reflective waves.

Madsen and Larsen (1987) provided a more efficient solution of Copeland's equations by extracting harmonics from the system of equations. They included internal generation of waves and partial reflection from breakwaters in their model.

At this point it is worth mentioning a transient form or the time dependent form of the Mild Slope Equation which can be derived using the Luke or Hamiltonian Variational Principle. This type of equation is for nearly harmonic waves, thus some small modulation of  $\omega$  and  $k$  are permitted. As given by Dingemans (1997).<sup>17</sup>

$$-\frac{\partial^2 \phi}{\partial t^2} + \nabla(cc_g \nabla \phi) - (\omega^2 - k^2 cc_g) \phi = 0 \quad (2.9)$$

where  $\phi(x, t) = \text{Re}\{\Phi(x)e^{-i\omega t}\}$

For the surface excursion equation 2.9 becomes

$$-\frac{\partial^2 \zeta}{\partial t^2} + \nabla(cc_g \nabla \zeta) - (\omega^2 - k^2 cc_g) \zeta = 0 \quad (2.10)$$

---

<sup>17</sup> Kirby *et al* (1992) derived their own time dependent MSE model.

## Numerical solutions

Madsen and Larsen (1987) used the Alternative Directions Implicit (ADI) finite difference scheme rather than the explicit scheme, which Copeland (1985a,b) or Yoo *et al* (1989) used previously to solve the system of hyperbolic equations. It was also necessary to introduce a time varying time step, the so-called Dynamic Alternative Directions Implicit method (DADI). To decide when the solution reaches the steady state, an additional condition was applied as the average of the residuals between the present and previous solution steps. Larger time steps were used at the beginning of the calculations and were reduced when the solution almost reached the steady state. Dissipation due to wave breaking also had a beneficial effect on the convergence towards a steady state and is easy to implement because of the marching solution technique. The disadvantage of hyperbolic models is that they require very high grid resolution of at least 10 points per wavelength.

### 2.3.3.4 Other forms

Ebersole (1985) modified the original equation in order to obtain a system of three equations. These three equations along with the dispersion relation are used to describe the refraction-diffraction phenomena, under the assumptions that the bottom slopes are small, the waves are linear, harmonic and irrotational, wave reflection is negligible, and any energy losses due to bottom friction or wave breaking are neglected. He used an iterative method to solve the system of equations. Kim (1992) modified Ebersole's approach to include wider angle diffraction and interfaced it with analytical diffraction solutions for within harbour predictions.

Li (1994b) derived a new parabolic model. He used the perturbation method to obtain a time dependent evolution equation, which is also based on the original mild slope equation. A two-dimensional parabolic equation is derived by assuming that the second derivative of the amplitude function with the respect to the slow time variable is negligible. Exclusion of harmonic time in the model enables a fast convergence. However, this model is parabolic in time and therefore unlike previous mentioned parabolic models is capable of dealing with refraction, diffraction and reflection. Li (1994b) used a time<sup>18</sup> iterating approach applying the Alternative Directions Implicit finite difference scheme. The advantage of the

---

<sup>18</sup> Time is here a time for iteration and is not time of evolution, so that the solution converges to a steady state.

model is an easier implementation compared to the hyperbolic model, particularly in respect of boundaries. Also the solution is quicker compared with the full elliptic model.

### **2.3.4 Boundary conditions for MSE**

The following types of boundary conditions are required for applications

1. Radiation conditions at open boundaries for application to harbour waves and oscillations there is also a need for
2. Reflection (partial) against structures like quays, breakwaters.
3. Wave transmission (partial), through permeable breakwaters boundaries; (see Kostense *et al*, 1986)
4. A wave-maker conditions for verification purposes in laboratory to be able to test the model on different laboratory experiments

### **2.3.5 Applications and verifications**

The previous section illustrates the large activity in the MSE model development and accompanying publishing. However, there are only a few examples of MSE model validation from field data, which were undertaken (or published), in the last two decades. Berkhoff *et al* (1982) verified a model using a laboratory experiment of wave transformation around an elliptic shoal. This set of results became the standard test to verify all new models. Tables 2.1 and 2.2 give a brief summary of some of the models and their application and verification.

#### **2.3.5.1 Regular waves**

Most of the models have been applied for regular waves. Here only the few applications and verifications which may be relevant to offshore breakwater study will be outlined. Dalrymple *et al* (1986) used their own MSE model to study waves trapped by breakwaters. The numerical results were compared with laboratory measurements and good agreement was found. Pos and Kilner (1987) investigated experimentally and numerically (using the MSE model) the influence of the breakwater gap on the wave height in the shadow zone.

<i>Author</i>	<i>Equation</i>	<i>Additional parameters</i>	<i>Numerical scheme</i>	<i>Waves</i>	<i>Validation</i>
Kostense et al (1986)	Elliptic	+dissipation with combined reflective and transmissive boundaries	Standard FE	Regular	Physical model of harbour oscillations
Pos and Kilner (1987)	Elliptic		FE (finite/infinite)	Regular	Physical model of diffraction through the gap
Hurdle et al (1989)	Elliptic	+ currents, breaking/bottom dissipation + reflective/ transmissive boundaries	FE with CG method	Random	Harbour Ijmiden, Venice Lagoon, Rotterdam Port*
Izumiya (1990)	Elliptic	+ dissipation	FDS	Regular	Physical model of transmission over submerged breakwater
Rojanakamthon et al (1990)	Elliptic	+ breaking criteria	FDS	Regular	Elliptic shoal lab experiment
Panchang et al (1991)	Helmholtz	+ nonlinear effects	Second order FDS + CG	Regular	Elliptic shoal lab experiment
Li and Anastasiou (1992)	Helmholtz	+ currents and wave breaking criteria	Multigrid Method	Regular	Elliptic shoal lab experiment and comparison with other models
Al-Mashouk et al (1992)	Elliptic		Multigrid Method	Random	Elliptic shoal lab experiment with random waves
Tsay and Liu (1982)	Parabolic		Crank-Nicholson FDS	Regular	Experimental data- breakwater perpendicular on shore, shoal,
Liu and Tsay (1983)	Parabolic	+ weak reflection	Numerical Iterative Scheme	Regular	Comparison to the results of the other models
Kirby and Dalrymple (1984)	Parabolic	Stokes waves	Crank-Nicholson FDS	Regular	Elliptic shoal lab experiment
Dingemans et al (1984)	Parabolic	+ currents, dissipation due to breaking and bottom		Regular	Elliptic shoal lab experiment Field data from Haringvliet
Kirby (1986b)	Parabolic	Wide angle of approach	Crank-Nicholson FDS	Regular	Circular shoal lab experiment Shore attached breakwater exp.
Dalrymple et al (1986)	Parabolic		Crank-Nicholson FDS	Regular	Lab experiment of trapping waves by breakwater

**Table 2.1** Summary of the some of the developed MSE models and their validation Part I; FDS stands for finite difference scheme, FE stands for finite elements and CG for conjugate gradient method (\* stands for application only)

<i>Author</i>	<i>Equation</i>	<i>Additional parameters</i>	<i>Numerical scheme</i>	<i>Waves</i>	<i>Validation</i>
Dalrymple and Kirby (1988)	Parabolic	Wide angle of approach	Spectral Fourier Method	Regular	Physical model of diffraction around breakwater
Dalrymple <i>et al</i> (1989)	Parabolic	Wide angle of approach + irregular bathymetry + nonlinear effects	Spectral Fourier Method	Regular	Circular shoal lab experiment
Panchang <i>et al</i> (1990)	Parabolic			<b>Random</b>	Elliptic shoal lab experiment with random waves
O Reilly and Guza (1991)	Parabolic		FDS ?	<b>Random</b>	<b>Random waves elliptic shoal exp.</b>
Ozkan and Kirby (1993)	Parabolic	+ wide angle + currents + breaking criteria + nonlinear effects	FDS ?	<b>Random</b>	Random waves elliptic shoal exp. Random waves beach exp.
O Hare and Davies (1993)	Parabolic (coupled)	Extended for ripple bed	Crank-Nicholson	Regular	Laboratory data for ripple bed
Li (1997)	Parabolic	+ currents	FDS	Regular	Elliptic shoal lab experiment and comparison with other models
Copeland (1985 a,b)	Hyperbolic		FDS	Regular	<b>Field data from detached breakwater scheme</b>
Smallman and Tozer (1990)	Hyperbolic Parabolic		Explicit FDS Evolutionary FDS	<b>Random</b>	Physical model of harbour entrance
Kirby <i>et al</i> (1992)	Hyperbolic	Linear and nonlinear version	Higher order FDS	<b>Irregular</b>	Random waves elliptic shoal exp.
Helm-Petersen and Brorsen (1997)	Hyperbolic		Explicit FDS	<b>Random</b>	Physical model of harbour
Ebersole (1985)	Modified elliptic		Forward and central FDS	Regular	Lab experiment for linear refraction
Li (1994b)	Parabolic in time		ADI	Regular	Elliptic shoal lab experiment Semi infinite breakwater analit.

**Table 2.2** Summary of the some of the developed MSE models and their validation Part 2; FDS stands for finite difference scheme, FE stands for finite elements and CG for conjugate gradient method



They found that measured wave heights in the shadow zone are larger than ones predicted theoretically due to the secondary waves generated at the breakwater tips and wave orthogonal spreading near the gap centreline.

They concluded that the linear theory provides conservative wave height estimates outside the shadow zones, but underpredicts the wave height estimates in the shadow zone as a function of breakwater gap and wavelength ratio<sup>19</sup>.

The results of model comparisons are helpful when the choice of an appropriate model needs to be made. Smallman and Tozer (1990) validated the hyperbolic MSE (Copeland, 1985b) and parabolic MSE (Dodd, 1988) on physical model data for a typical harbour approach bathymetry. The results were also compared with a refraction ray model. The refraction ray model performed better for shorter period waves and incident directions, which were not aligned with the line of the channel. For longer period waves and where the waves were directly incident along the channel, the parabolic model gave a good representation. However, it does require the grid alignment to be coincident with the main wave propagation direction. The hyperbolic model did not appear to offer any significant advantages in terms of accuracy over the parabolic model and its run-times were significantly longer.

Dong and Al-Mashouk (1989) compared hyperbolic and elliptic model results to the analytical solution of the classical fully open harbour. The two models were in good agreement for long wave propagation. For shorter waves, the imperfect boundary for the hyperbolic model tended to distort the results more severely. One of the reasons was an inadequate explicit scheme accompanied with not enough time to reach the steady state. Thus, the problem with numerical solutions of hyperbolic models was highlighted.

Examples of field validation of the MSE models are rarely found in the literature. However, Dingemans' *et al* (1984) validation of the parabolic model on laboratory data and field data collected at Haringvliet became a foundation for such work. They presented a summary of the quantitative verification work, calculating bias, percentage error and rms error (Wilmott, 1981). Copeland (1985a) verified his model on field data collected around the offshore breakwater at Leasowe Bay UK. While, Kim (1992) and O'Connor *et al*

---

<sup>19</sup> Yoo and O'Connor (1986b) validated their model with laboratory data from detached breakwater experiment (Gourlay, 1974).

(1992) found good agreement using the modified elliptic approach with wave buoys data from an open beach situated at Chukpyon Harbour, Korea. Further guidelines for model verification and validation can be found in Dingemans (1997).

### 2.3.5.2 Irregular and random waves

In nature the incident wave field is random and has directional spreading. A number of authors, Mobarek and Wiegel (1966), Goda (1978,1985), Briggs *et al* (1995), Girolamo (1995), indicated the importance of calculating diffraction taking into account irregular waves and directional spreading. Diffraction coefficients calculated, taking only regular waves into account, are underpredicted in the shadow zone or in the lee of the breakwater.

Vincent and Briggs (1989) conducted experiments on wave propagation over an elliptic shoal using multidirectional waves. They showed the importance of including (spectral) multiple frequencies and directions in wave transformation models. It was concluded that the degree of directional spreading was a more significant parameter than the spread of energy in frequency space. Briggs *et al* (1995) found similar results when the diffraction of multidirectional waves around a semi-infinite breakwater was measured in the laboratory. Hence a need for the development of numerical spectral models exists. The behaviour of multidirectional waves can be described by solving governing equation for a number of frequencies and directions using linear superposition. This is an advantage of linear models like the MSE and therefore the MSE models started to be used for directional modelling in the 90's. However, these models are still time consuming and therefore there are only few examples of 'directional modelling'.

Isobe (1987), Panchang *et al* (1990), Grassa (1990) and Li *et al* (1993) have each developed models, which operate by first discretising the spectrum into individual monochromatic directional components and then running each component in a separate parabolic model. Results from the segmental runs are superimposed in order to obtain estimates of statistical wave heights<sup>20</sup>. O'Reilly and Guza (1991) have further extended this formulation and have pointed out that the model could be used (in linear form) to develop a transfer function between onshore and offshore conditions. Thus, the incident spectrum can be simply transformed using the computed transfer function. This is however, valid for

---

<sup>20</sup> Hurdle *et al* (1989) used the same principle for the full elliptic equation when the modelling for a harbour at Ijmuiden was performed. Kirby *et al* (1992) applied a linear and non-linear version of the time dependent form of the MSE for wave transformation of irregular waves around a circular shoal. The non-linear model gave better agreement between measured and predicted wave heights.

beach conditions and not around the structures where reflection is present which depends on wave height and frequency.

Firstly, they validated their model on laboratory measurements of regular and irregular wave transformations around a circular shoal. Further, the model was validated using field data from the beach in San Diego California with smooth coastal bathymetry. The importance of directional wave spreading in wave transformations over simple bathymetry was found. Also, the accuracy of the field measurements appeared to have a significant role in the model validation.

The 'directional' or 'spectral' modelling was further used to study specific wave conditions which is illustrated in the following three examples. Al Mashouk *et al* (1992) applied a spectral model to Li's (1992) multigrid version of the MSE. The elliptic equation was solved for a set of frequency and direction bins and computing time was reduced even in comparison with a parabolic equation. Firstly, the model was validated on laboratory data from Vincent and Briggs (1989) experiment. The application of the model to the Marsexlokk bay showed overestimation of wave heights when only the regular wave model was used.

Ozkan and Kirby (1993) used the parabolic MSE to determine breaking directional spectral waves in the nearshore zone. The two dimensional spectrum was divided into discrete components which were simultaneously computed using the parabolic model. Statistical quantities were computed at each forward step in the parabolic scheme and used to construct a statistical wave-breaking model. The breaking criteria based on energy of all components rather than wave height limit<sup>21</sup> is built into the model. Computed results for cases without breaking showed good results. However, the model did not accurately predict the shoaling and decay of the wave height for a multidirectional random sea. This might be caused by the incorporated energy dissipation model, which does not account for directional effects, or because of pronounced non-linear effects. More studies need to be done to understand breaking and non-linear processes.<sup>22</sup>

Helm-Petersen and Brorsen (1997) using the time dependent MSE (Kirby *et al*, 1992) for random waves studied reflective boundaries and reflection from a rubble mound breakwater.

---

<sup>21</sup> The wave breaking criteria which is used for regular waves does not have any effect when directional modelling is applied. The wave height of each component is small compared to the water depth. However, the waves do break in the field.

<sup>22</sup> This work was improved even though it still has limitations

The numerical results were verified with physical model data of Grenaa Harbour. Hence a further application of the model for wave reflection prediction is demonstrated.

As for the case of regular waves there are not many cases of validation of the model from field data presented in the literature<sup>23</sup>. One of the reasons is that the main effort in the past twenty years was on the model development and accordingly its numerical solutions. Also, the field campaigns are expensive and rare.

### *Summary*

The Mild Slope Equation provides a solution for one given frequency at a time, but is applicable in both deep and shallow water and applies to all frequencies. It can model refraction, diffraction and also reflection with properly chosen boundary conditions. By introducing the effects of wave breaking, bed friction and wave-current interaction it can even be used over the whole coastal zone. The models based on the MSE can also be used to obtain estimates of the radiation stress tensor of periodic waves hence the longshore current.

All of the models based on the MSE suffer from some restrictions. The full elliptic models solved by the finite element method cannot be applied to large coastal areas because of the large computer memory requirements. The more economic multigrid model for the elliptic equation could not produce accurate solutions in wave fields with strong reflection. Parabolic models have physical restrictions (like for example they are not able to model reflection or other rapid changes). Hyperbolic models need large numbers of iterations and a very fine grid solution and also special treatment of boundaries. This suggests that there is still a need to find a fast and accurate solution to the original elliptic equation or find a suitable compromise. Li's (1994b) time parabolic model seemed to be the best choice at the time the present study started. The model accounts for reflection which is important for a field with structures. Also, the numerical solution is stable and is thus easy to implement. The model is owned and used for consultancy purposes by Halcrow, UK.

The examples given in section 2.3.5.2 indicate that MSE model predictions are more accurate when random directional wave modelling is applied. There is however a lack of the validation of these models using field data. Therefore, the time evolution parabolic model (Li, 1994b), which can model refraction, diffraction and reflection in its random

---

<sup>23</sup> Some of the validations are probably not published and might be only available in internal reports of some Institutes.

mode, will be validated using field data. The validation of the random model requires accurate directional estimates of measured data. In the next section a review of directional methods for field data analysis will be given.

## 2.4. Directional analysis

### 2.4.1. Introduction

One of the priorities of field measurements of wave climate has been to obtain accurate estimates of directional wave spectra by using directional analysis. A range of directional analysis techniques have been developed and published in the literature. The most prominent of these have most recently been reviewed and classified by Benoit *et al* (1997). The methods were classified as stochastic methods (in which the phase of individual components is randomly distributed), deterministic methods (which retain the phase information inherent in the data set) and time domain analysis methods (which use time domain variables to estimate the directional spreading function (DSF) rather than frequency domain variables).

Panicker and Borgman (1970,1974) probably developed the first deterministic methods<sup>24</sup>. Except for recent work by Prislun *et al* (1996) all deterministic methods were confined to single point measurements. Even though some of the methods gave good results, the physics behind it was questionable. Two new methods – Single Direction Analysis and Double Direction Analysis – by Schaffer and Hyllested (1994) gave results comparable with the Maximum Entropy stochastic method. The time domain analyses are quite sparse in operational application. Therefore, the stochastic methods have developed faster and are more commonly applied to the analysis of field data (e.g. O'Reilly and Guza (1991), Hashimoto *et al* (1988) and others). Here, the emphasis will be given to stochastic methods.

### 2.4.2 Measuring devices

The measuring devices for directional seas can be classified into three groups (Benoit *et al* 1997)

---

<sup>24</sup> There are still doubts whether this method is being used in practice (Benoit *et al* (1997)).

- A single point system measures simultaneously at the same location (horizontal and vertical) several properties of the waves. The most widely used are the heave-pitch-roll buoy and a two component current-meter associated with a pressure sensor or wave elevation probe.
- Gauge arrays comprise several sensors set up at various locations over a fixed frame. The sensors may be identical or of various types including for instance currents meters and pressure transducers.
- Remote-sensing systems are based on spatial rather than time correlation. The common principle is to make an "image" of the wave field over a given area. The Fourier transform of the surface elevation field is used to produce a directional spectrum assuming a homogeneous wave field over an "image area". These systems include microwave radar, aerial stereo-photography techniques and video imaging (ARGUS). They have been significantly developed in recent years for example with the use of Synthetic Aperture Radar (SAR), on the satellite ERS-1 and 2.

Remote sensing systems are sparse and expensive<sup>25</sup> for field campaigns. Also, the analysis of the images is still time and computational demanding. Thus, the choice of measuring device is commonly between single point and multiple point measurements devices. O'Reilly and Guza (1991) addressed the problem of predicting an accurate directional spectrum using single point measurement by pitch-roll buoy. Young (1994) showed the superior performance of multipoint gauge arrays compared to single point measurements. A laboratory comparison of measurements and analysis techniques carried out by Benoit and Teisson (1994) led to the same conclusion. Bird (1993), Bird *et al* (1994) and Chadwick *et al* (1995a,b) demonstrated the satisfactory performance of an array of pressure transducers and wave probes respectively. It should be noted that it is beneficial to choose irregular transducers positions and that effort should be made to maximise the different spatial lags between transducers in order to reduce data redundancy and maintain good directional resolution (e.g. Davis and Regier, 1977). Taking into account the experience of Bird and Chadwick; the multipoint gauge arrays have been chosen for field deployment in the present study. Hence, the analysis methods based on temporal analysis of wave signals at a limited number of locations will be further considered.

---

<sup>25</sup> Video imaging techniques are probably an exception.

### 2.4.3 Basic definitions

Multidirectional waves can be described as an infinite sum of sine<sup>26</sup> waves with different amplitudes, frequencies and phases (obeying a dispersion relationship between wave frequency, wave length and water depth). However a more complete description of a two-dimensional wave field must recognise that every sine wave is travelling in a different direction. Hence, surface elevation,  $\eta(x,y,t)$ , of a given point is a function not only of time but also of its space co-ordinates relative to an arbitrary axis  $[x,y]$

$$\eta(x,y,t) = \sum_{m=1}^M c_m (k_m x \cos \theta_m + k_m y \sin \theta_m - \omega_m t + \vartheta_m) \quad (2.11)$$

In this expression surface elevation is written as superposition of M elementary sine wave, and each component satisfies the linear dispersion relationship  $\omega_m^2 = gk \tanh(k_m d)$  where g is specific gravity, k is a wave number and d is water depth.

Under the assumption that the phases  $\vartheta_m$  are randomly distributed over  $[0, 2\pi]$ , the following relationship holds between the directional variance spectrum and the amplitudes of the wave components in the two dimensional range  $[f, f + df] \times [\theta, \theta + d\theta]$

$$\sum_f^{f+df} \sum_\theta^{\theta+d\theta} \frac{1}{2} c_m^2 = S(f, \theta) df d\theta \quad (2.12)$$

The directional variance spectrum  $S(f, \theta)$  is proportional to the energy spectrum  $S(f, \theta) = E(f, \theta) / \rho g$ . The directional energy spectrum represents the energy distribution over both frequency and direction of propagation.

It should be noted that the directional variance spectrum may alternatively be expressed as a function of wave number and direction  $(k, \theta)$

$$S(f, \theta) = \frac{2\pi}{c_g} S(k, \theta) \quad (2.13)$$

<sup>26</sup> They are usually called sine waves even though the cosine functions are included in equations.

## 2.4.4 Stochastic analysis methods for a homogeneous wave field

The stochastic methods for directional analysis are based on a mathematical relationship between the directional spectrum and the cross-power spectra. Isobe and Kondo (1984) define the relationship between cross spectra and directional spectra for each of two arbitrary wave properties with following equation

$$P_{mn}(\omega) = \int_k H_m(K, \omega) H_n^*(K, \omega) \exp\{-iK(X_n - X_m)\} S(K, \omega) dK \quad (2.14)$$

In this equation,  $\omega$  is an angular frequency,  $K$  is the wave number vector,  $P_{mn}(\omega)$  is the cross-power spectrum between  $m$ -th and  $n$ -th wave properties (properties measured at  $m$  &  $n$  station).  $H_m(K, \omega)$  is the transfer function from the water surface elevation to  $m$ -th wave property,  $i$  is an imaginary unit,  $X_m$  is location vector of the wave probe for the  $m$ -th wave property,  $S(K, \omega)$  is a directional spectrum as a function of wave number and frequency (\* denotes conjugate complex). The wave dispersion equation is given by the equation:

$$\omega = (2\pi f)^2 = gk \tanh kd \quad (2.15)$$

Equation 2.14 can be rewritten as a function of the frequency and the direction of wave propagation

$$P_{mn}(f) = \int_0^{2\pi} H_m(f, \theta) H_n^*(f, \theta) \left[ \cos\{k(x_{mn} \cos\theta + y_{mn} \sin\theta)\} - i \sin\{k(x_{mn} \cos\theta + y_{mn} \sin\theta)\} \right] S(f, \theta) d\theta \quad (2.16)$$

The directional spectrum  $S(f, \theta)$  can also be expressed as a product of the frequency spectrum,  $S(f)$ , and directional spreading function,  $G(f, \theta)$

$$S(f, \theta) = S(f)G(f, \theta) \quad (2.17)$$

The directional spreading function (DSF) satisfies two important properties

$$G(f, \theta) \geq 0 \quad \text{over} \quad [0, 2\pi] \quad (2.18)$$



$$\int_0^{2\pi} G(\theta|f) d\theta = 1 \quad (2.19)$$

The first condition defines that the DSF is a non-negative expression and the second is a consequence of the following relationship

$$\int_0^{2\pi} S(f, \theta) d\theta = S(f) \quad (2.20)$$

The transfer function,  $H_m(f, \theta)$ , is usually given in the following form

$$H_m(f, \theta) = h_m(f) \cos(\alpha_m \theta) \sin(\beta_m \theta) \quad (2.21)$$

For the water surface elevation - function  $h_m(f)=1$  and parameters  $\alpha_m$  and  $\beta_m$  are equal to zero. For the other properties refer to Hashimoto *et al* (1987) and Benoit *et al* (1997).

The directional methods proceed in two steps

1. Spectral analysis of the recorded time series is performed resulting in computing the cross-spectra between each pair of signals. The details on a spectral and cross-spectral analysis are given in Appendices D and E.
2. The determination of the directional spectrum  $S(f, \theta)$  can then be achieved by the inverse of the equation 2.14. As the measuring devices have a limited number of measuring points (usually 3-10, Benoit *et al* (1997)), the mathematical problem is not fully defined and some additional assumptions need to be introduced. In practice, this is not straightforward and several methods have been developed to solve this problem.

The IAHR working group (Benoit *et al*, 1997) stated that in the case of multidirectional incident sea states the stochastic methods comprising the Maximum Likelihood Method, the Maximum Entropy Method and the Bayesian Directional Method offer superior resolving power when applied to spatially separated multipoint wave gauge arrays. Hence, a brief description of each of these methods is given.

#### 2.4.4.1 The Maximum Likelihood Method (MLM)

The Maximum Likelihood Method, MLM, was originally developed by Capon *et al* (1967) for the analysis of seismic waves with a sensor array. It was later adapted to obtain the directional wave spectrum. It is designed to minimise the variance of the difference between the estimate and the true spectrum under the constraint that the amplitude of unidirectional plane waves, with no contamination by noise, is passed without bias, as described by Pawka (1983).

The MLM is based on the assumption that the estimate of the DSF may be expressed as a linear combination of the cross-spectra

$$\hat{G}(f, \theta) = \frac{1}{\hat{S}(f)} \sum_{m,n} \alpha_{mn}(f, \theta) P_{mn}(f) \quad (2.22)$$

Where,  $P_{mn}^{-1}$  is an  $mn$  element of the inverse matrix  $P^{-1}(\omega)$  and  $\alpha$  is a proportionality constant.

The estimates are related to the actual DSF by following relationship

$$\hat{G}(f, \theta) = \int_0^{2\pi} G(f, \theta) w(\theta, \theta') d\theta' \quad (2.23)$$

Where

$$w(\theta, \theta') = \sum_{m,n} \alpha_{mn}(f, \theta) H_m(f, \theta') H_n^*(f, \theta') \quad (2.24)$$

Hence, the MLM estimate may be seen as a convolution product of the actual DSF by a window function  $w(\theta, \theta')$ . This estimate will approach the actual DSF as the window function tends towards a Dirac function.

The estimate that best satisfies this condition is given by Isobe *et al* (1984).

$$\hat{G}(f, \theta) = \kappa / \left[ \sum_m \sum_n P_{mn}^{-1}(f) H_n^*(f, \theta) H_m(f, \theta) \right] \quad (2.25)$$

This expression includes the transfer function  $H_m(f,\theta)$ , thus enabling directional spreading estimates from measurements of different properties.

Tests on numerical and laboratory data (Benoit and Teisson, 1994) show that this method usually produces broader directional peaks compared to the target directional spectra particularly in the case of single point measurements. The cross-spectra computed from the MLM estimates differ from the cross-spectra computed from wave measurements. Pawka (1983) and then Oltman-Shay and Guza (1984) proposed an iterative refinement to the MLM in order to get a consistent estimate. It does require more computing time, but it is recommended for use with the single point measurements.

Chadwick *et al* (1995a,b) found that the MLM provides good estimates when applied to a star array with at least four measuring sensors and when suitable spectral analysis are performed. The MLM method usually exhibits acceptable estimates with relatively short CPU time and is therefore widely used (Benoit, 1993).

#### 2.4.4.2 Maximum Entropy Method (MEM)

The Maximum Entropy Method has been adapted from the theory of probability to directional wave analysis due to similarities between a DSF and a probability density function (PDF). The principle of these methods is to define an ‘entropy’ function, which has to be maximised under the various constraints given by the cross-spectra equations. Two such methods have been proposed depending on the definition used for the entropy (Benoit *et al*, 1997).

The first definition for entropy was proposed by Barnard (1969) and then adapted to the single point measurements systems by Lygre and Krogstad (1986) (MEM1). The MEM1 estimates are consistent with the cross-spectral data, but the method overpredicts the height of directional peaks, and sometimes gives two peaks for unidirectional cases. Benoit *et al* (1997) advised to use this method only for comparison purposes.

The Maximum Entropy Method proposed by Kobune and Hashimoto (1986) is based on Shannan’s definition of entropy (SE). The entropy which needs to be maximised is:

$$SE = - \int_0^{2\pi} \hat{G}(f, \theta) \ln \hat{G}(f, \theta) d\theta \quad (2.26)$$

The estimate of  $G(f,\theta)$  which maximises SE is called the maximum entropy estimate. For the single point measurement, it is given by following equation:

$$\hat{G}(f, \theta) = \exp\{-\lambda_0 - \lambda_1 \cos \theta - \lambda_2 \sin \theta - \lambda_3 \cos 2\theta - \lambda_4 \sin 2\theta\} \quad (2.27)$$

Where the coefficients  $\lambda_0 \dots \lambda_4$  are the Lagrange's multipliers which are determined by solving non-linear equations as given by Kobune and Hashimoto (1986).

The method is iterative and for the case of three measured elements, the solution is quite straightforward. However, it has the disadvantage of not converging for very narrow spreading functions. Nwogu *et al* (1987) extended the Maximum Entropy Method to improve convergence for narrow spreading functions. Their analysis is based on a 3-sensor array consisting of 1 elevation sensor and a biaxial current sensor. The final equation is similar to equation 2.27, but is extended for four properties.

The method is not simple to implement (especially for wave probe arrays) and requires more computing time due to the iterative procedure of solving non-linear equations. Recently Kim *et al* (1994) proposed some approximations to the numerical scheme in order to remove convergence problems, which may occur for real data. The MEM is recommended for single point measurements by Benoit *et al* (1997).

The extended MEM (EMEM) derived by Hashimoto *et al* (1994) improves the technique for array measurements. Tests on numerical data sets show that results for an array are now comparable to the other methods.

#### **2.4.4.3 The Bayesian Method (BDM)**

This method is based on the Bayesian technique used in probability theory. Akaike (1973) introduced the Bayesian approach for regression analysis problems where the number of parameters to be determined was large compared with the sample size. The estimation of the directional spectrum can be considered as a regression analysis, to find the most suitable model from limited data. Therefore, the Bayesian approach can be useful to obtain the most reasonable model (directional spreading function) which best approximates the sample (cross-power spectrum) and which also satisfies the nature of the physical phenomenon, i.e. continuous and smooth variation of its value.

Hashimoto *et al* (1987) applied this principle to directional wave analysis. The method is not easy to implement but has powerful capabilities in resolving the DSF shape with no *a priori* assumptions. The so-called, hyperparameter,  $u$ , is introduced to take into account the balance of the two requirements imposed on the model, that is, to maximise the likelihood of the model given by equation 2.14 and to include smoothness conditions.

It is assumed that the directional spreading function is expressed as a piecewise - constant function over each segment of the directional range from 0 to  $2\pi$  ( $k\Delta\theta=2\pi$ ). It is defined by a series of  $K$  values  $x_k$  (each corresponds to the logarithm of the constant value of the BDM estimate of each segment):

$$\ln[\hat{G}(\theta_k)] = x_k(f), \quad (k = 1, \dots, k) \quad \text{when} \quad \theta_k = (k - 1/2)\Delta\theta \quad (2.28)$$

$$\hat{G}(\theta) = \sum_{k=1}^K \exp(x_k) I_k(\theta) \quad \text{with} \quad I_k(\theta) \begin{cases} 1 & \text{if } (k-1)\Delta\theta \leq \theta \leq k\Delta\theta \\ 0 & \text{otherwise} \end{cases} \quad (2.29)$$

The system of non-linear equations given by the co- and quad spectra (see Appendix E) is completed by the smoothness condition of the estimated DSF. This is mathematically expressed by the following relationship between three consecutive values of the estimate

$$\sum_{k=1}^K (x_{k+1} - 2x_k + x_{k-1})^2 \rightarrow 0 \quad (2.30)$$

The most suitable values of the hyperparameter,  $u$ , is determined as the one which minimises the ABIC (Akaike Bayesian Information Criterion, (Akaike, 1973)).

Due to its large number of degrees of freedom, the BDM is able to represent almost all kinds of DSF shapes. Its main applicability is to a multi-component array and it is considered to be a most powerful technique.

#### 2.4.5 Stochastic methods for a reflective field

Reflective wave fields caused by coastal structures can be usefully divided into a near structure field and a far field. The near structure field is characterised by the formation of partially standing waves caused by phase locking of incoming and outgoing (reflected) waves. All the stochastic methods were originally developed for a homogeneous field and therefore fail to give accurate directional spectra estimates in the near field. Two methods,

the Modified Maximum Likelihood Method (MMLM) (Isobe *et al*, 1984), and Modified Bayesian Directional Method (MBDM) (Hashimoto and Kobune, 1987) take into account not only the relative distance between sensors but also their position relative to the reflector. The MMLM has previously been successfully used to analyse measurements taken in the near structure environment (Bird *et al*, 1994). A brief summary of the method will be given in the next section.

#### 2.4.5.1 Modified Maximum Likelihood Method (MMLM)

Isobe and Kondo (1984) proposed an equation to estimate the directional spectrum. It is given by the equation:

$$\hat{S}(k, \omega) = \kappa / \left[ \sum_m \sum_n P_{mn}^{-1}(\omega) H_m^*(k, \omega) H_n(k, \omega) \exp(ik(x_n - x_m)) - Z \right] \quad (2.31)$$

where

$P_{mn}^{-1}$  - mn element of the inverse matrix  $P^{-1}(\omega)$

$\kappa$  - proportionality constant

$$Z = - \frac{\left\{ \sum_m \sum_n P_{mn}^{-1}(\omega) \left[ e^{ik(x_n - x_m)} + e^{ik(x_{nr} - x_{mr})} \right] \right\}^2}{4 \sum_m \sum_n P_{mn}^{-1}(\omega) e^{-ik(x_{nr} - x_{mr})}} \quad (2.32)$$

where  $x_{nr}$  and  $x_{mr}$  are distances from the reflector.

However, this phase sensitive method tends to produce spurious peaks when applied to the data measured far from the reflector. Huntley *et al* (1995) described the sensitivity of the MMLM used for co-located sensors and the problems in applying the method. Davidson *et al* (1998) subsequently demonstrated that this method could produce very accurate estimates in the near field for multipoint measurements, provided that the effective reflection line is iteratively determined.

#### 2.4.5.2 Applicability of the phase-locked and non phase-locked methods

For the far field, Huntley and Davidson (1998) postulated that the frequency dependent node/antinode structure implies that for random wave field, phase locking between

incoming and outgoing waves is linked to the frequency resolution (bandwidth) used in the spectral analysis. If the frequency bandwidth is wide enough to encompass frequencies with both nodes and antinodes of the partially standing waves at the sensor location then in effect the node/antinode structure is smoothed over. This would allow the use of non-phase-locking methods (NPL) for data analysis. On the other hand if the frequency bandwidth is small compared to the frequency interval between a standing wave node and antinode, the phase locking effect is significant and a phase-locked method (PL) must be used. Huntley and Davidson (1998) show further that, since the node/antinode frequency interval is determined by the time of wave travel to the reflector and back,  $L$ , and the frequency bandwidth in spectral analysis is determined by the length of time series used,  $S$ , then the ratio,  $L/S$ , can be used to determine whether or not a phase-locked method should be used.

Their analysis did not take into account directional spreading which will tend to decrease the phase locking between incident and reflected waves. Inclusion of directional spreading might extend the applicability of non phase-locking methods.

#### 2.4.6 Stochastic methods for a field with currents

All previous mentioned methods were developed for analysis of random (directional) seas in the absence of currents. However in reality, waves rarely propagate on quiescent water. The presence of a tide or other current alters the speed of the wavelength and the observed wave period (see for example Hedges *et al* 1992, 1993). Thus the proper wave number needs to be taken into account in directional analysis. Nakagawa *et al* (1996) proposed a modified directional analysis taking the effects of currents into account by altering the linear dispersion equation.

The dispersion relation given as

$$\omega^2 = (2\pi f)^2 = gk_o \tanh k_o \quad (2.33)$$

calculates the wave number in directional analysis when no current is present. However, when a current is present, the dispersion relation becomes

$$(\omega - U_c k_c \cos \theta_r)^2 = gk_c \tanh k_c \quad (2.34)$$

However, their solution is limited to a homogeneous field, which implies uniform currents in space, and in time e.g. tidal or large-scale currents. Thus, the wave number also depends on the direction and magnitude of the currents. The problem of refraction associated with wave encountering sheared flow from quiescent water to water with a current, or from a field of one current speed to a field with another current speed is not taken in account. This would have an influence on the shape of directional distribution (see for example Hedges *et al* (1993)).

### *Summary*

In the field around offshore breakwaters where a certain amount of reflection can be expected, a proper choice of directional analysis needs to be made. The most verified methods are methods for homogeneous fields or the so called non-phase-locked methods. However they can fail in the estimation of DSF when they are applied in other circumstances (Teisson and Benoit, 1994). The validation of the methods was performed in the laboratory. The field measured data give the opportunity to test which method, phase-locked (PL) or non-phase-locked (NPL), is more applicable for field data analysis taking into account Huntley and Davidson's (1998) recommendation. The MLM method, which gives accurate estimates when the proper spectral analysis is applied, will be considered as the NPL method. It is easy to implement and uses a small amount of CPU time compared to the other methods. As the PL method, the MMLM method will be considered. The NPL estimates are also compared with the BDM method estimates. The BDM method was found by Teisson and Benoit (1994) to be the most powerful method in laboratory validation.

## **2.5 Objectives of the study**

With the exception of a few examples (e.g. Kraus *et al* 1983) monitoring of offshore breakwater schemes have mostly concentrated on shoreline change. Wave measurements were mostly taken offshore or for only short periods of time. Also, most of the schemes were built in a microtidal environment and therefore there is a need to monitor the new macrotidal schemes and their influence on hydrodynamics and morphology. The newly constructed scheme at Elmer, West Sussex, offered an opportunity to measure directional wave transformation. Two different measuring systems were deployed. An array of pressure transducers was deployed offshore and an array of wave probes was deployed in the shallow water in the lee of the breakwaters. The measurements of both equipment prior



to deployment were compared in order to verify the compatibility of the two measuring systems. Also there was a need to utilise the same spectral analysis to analyse both data sets.

Wave transformation models have been mostly used for regular wave fields. There is evidence from field and laboratory measurements taken to date that the diffracted wave field for regular waves is overpredicted compared to diffracted random waves. The linear model based on the Mild Slope Equation can be used for a random field by superposition of separate frequency and direction computational results. There is little information in the literature on validation of these models from field data. So far they have been validated for regular waves or for random waves on a plane beach. In order to improve the wave transformation model effectiveness more validation with field data particularly on complex bathymetries and around structures is necessary. The MSE model chosen for validation from field data is Li's (1994b) model. Li (1994b) has already verified his model with laboratory measurements for the regular waves. In the present work, verification of Li's model will be extended using 'directional modelling'. Firstly, the model will be verified using laboratory measurements of the diffraction of random waves. The next step is to validate the model from field data taking the multidirectional sea into account. Possible non-linear effects might also be detected when applying this linear model to such a complex environment.

When validation of the model from field data is performed, there are two uncertainties – the accuracy of the model and the accuracy of the data. It is therefore worth repeating O'Reilly and Guza (1991) statement:

*Accurate estimation of the incident wave spectrum will be a vital component in any field tests of refraction-diffraction models.*

Therefore, a proper directional analysis needs to be applied to obtain accurate directional estimates. So far, the non-phase-locked (NPL) methods have been carefully checked in the non-reflected field. Also, phase-locked (PL) methods seem to give accurate results when applied in the areas of strong reflection, close to the reflector, providing the reflection line distance is known. However, in the present study the measurements are to be taken offshore of and behind the breakwaters. The locations are not in the vicinity of the reflector but still a certain amount of reflection can be expected. The applicability of the PL and

NPL methods needs to be investigated first. Then the sensitivity of the chosen method can be checked with validation from numerical data sets and compared with another PL or NPL method, such as BDM or modified BDM.

To summarise, the objectives of the present study were as follows:

- to organise field deployment of equipment and to collect data for a year
- to test the compatibility of two different measuring systems (pressure transducers and wave probes)
- to develop a single spectral analysis software package for both measuring devices, to allow a comparison of data
- to investigate the applicability of phase- (PL) and non-phase-locked (NPL) directional analysis methods
- to check the sensitivity of the directional analysis method using simulated data and field data with respect of – direction, directional spread, wave height, reflection and currents
- to validate the Li's (1994) MSE numerical model in a multidirectional measured sea
- to check sensitivity of the model with respect to a size of the grid and number of time steps to bring the solution to steady state
- to check the prediction of the model for pure diffraction
- validate Li's model from field data with a search for non-linear effects

# Chapter 3

## Field work

*In the field of observation, chance only favours those minds which have been prepared.*

*Louis Pasteur (1822-1895)*

### 3.1 Introduction

Dally and Pope (1986) highlighted the need for post-construction field monitoring of detached breakwater schemes to evaluate their performance. The primary reason to choose the Elmer site, West Sussex for such a monitoring exercise was that the scheme was completed in September 1993. Therefore, it was possible to monitor wave transformation and concurrent beach evolution from an early stage of the scheme. The other reason to choose the Elmer scheme for the field campaign was the existence of previous wave measurements and beach monitoring data. Arun District Council (ADC) and the National River Authority (NRA) have been monitoring the shoreline changes at Elmer through the 1980's and the University of Plymouth has measured reflection characteristics of one of the two original breakwaters (see Chapter 1). These data together with the data collected in the course of this study can provide a valuable resource for the future evaluation of different defence techniques.

The field monitoring campaign has spanned over more than a year. The measurements were concentrated on wave transformation and shoreline change. Two different wave measurement systems were deployed offshore of the breakwaters and in the lee of the breakwaters. A pressure transducer array was deployed about 500 m offshore of the breakwaters. A wave probe array and two satellite probes were deployed in the lee of the breakwater, the gap and shoreward of the gap, respectively. The measurements were continuous for more than a year and more than 4500 data sets were collected. Aerial surveys of the shoreline change were taken on a regular three monthly basis.

The present chapter starts with a brief description of the new scheme in section 3.2.1. The history of the coastal defence works at Elmer is described in section 3.2.2. A summary of available data is given in section 3.2.3. The two wave measurement systems are described in section 3.3.

The field deployment and details of the concurrent measurements are summarised in sections 3.4.1. and 3.4.2. Additional measurements are given in section 3.4.3. and the chapter concludes with a summary in section 3.5.

## **3.2 Field site description**

### **3.2.1 General**

The fieldwork took place at Elmer, which lies, on the South coast of the UK, 38 km west of Brighton, in West Sussex (Holland and Coughlan, 1994). The Elmer coast forms part of the Sesley Bill to Beachy Head coastal cell (Figure 3.1). The average beach line at Elmer has a bearing of  $76^\circ$  over a distance of some 12km. This is the most seaward protrusion of an almost straight stretch and acts as a headland feature (Figure 3.1). The defence scheme, which protects 2 km of headland area from flooding and beach erosion, was completed in September 1993.

The scheme, which is shown in Plate 3.1 and Figure 3.2, is based on a soft defence philosophy and consists of 8 shore-parallel rock island breakwaters and a terminal groyne protecting a renourished sand/shingle beach. The structures are low-crested 'reef' type rubble mound breakwaters. The structural form of the breakwaters is quite simple and

consist of rock armour placed on a modest bedstone layer to provide a permeability transition to the beach. The bedstone layer was laid on the chalk platform. The breakwater lengths vary between 70 m and 140 m and the length of the gaps between them vary from 70 m to 152 m. Crest elevations are 4.5 m above Ordnance Datum, with the exception of the two easternmost breakwaters which are 1m lower. This is in order to reduce the downdrift impact of the scheme. The breakwaters have a slope of 1:2 (seaward) and 1:1.5 (landward faces), respectively, with a widened roundhead at each end of the structure with a slope of 1:2.5. The rock armour blocks used were of Norwegian syonite, with an effective mean weight of between 7.5 and 8.5 tonnes. A minimum rock density of 2.6 tonnes/m<sup>3</sup> was specified for the single layer armourstone and bedstone.

The newly renourished beach consists of 139 000 m<sup>3</sup> of mixed sand and shingle, supplied from offshore dredging areas. The upper beach consists mainly of shingle ( $D_{50}=11.0$  mm) with a gradient of 1:7 overlying a sandy toe ( $D_{50}=115\mu\text{m}$ ) of gradient 1:50. The defences at Elmer were commissioned jointly by ADC and the NRA. A fuller description of the site and details of the construction may be found in Holland and Coughlan (1994).

### **3.2.2 Background**

The new scheme provides protection for residential areas and for agricultural land. The previous coastal protection was reinforced concrete seawalls, timber breastworks and timber groynes. Groynes with a terminal groyne on the Eastern end can be seen on the Ordnance Survey Map dating back to 1879. However the residential area was built only just before, and after the First World War. Concrete sea walls were built in the 1960's to protect a new residential area. Pool Place groyne (Eastern terminal or end groyne in Figure 3.2) acted as a terminal feature ensuring the stability of the updrift shingle beach and bank. The beach nourishment started from the 70's onwards. Despite beach nourishment, erosion continued. Additionally, some of the existing defences along the frontage were coming to the end of their useful life in the late 1980's. Erosion of the shingle beach in front of the sea walls and breastworks highlighted the very real risk of a breach in the defences. In addition the lower beach levels allowed considerable overtopping of the defences in storm conditions, causing extensive flooding to properties. An upper wave return shaped face wall was constructed in 1988.

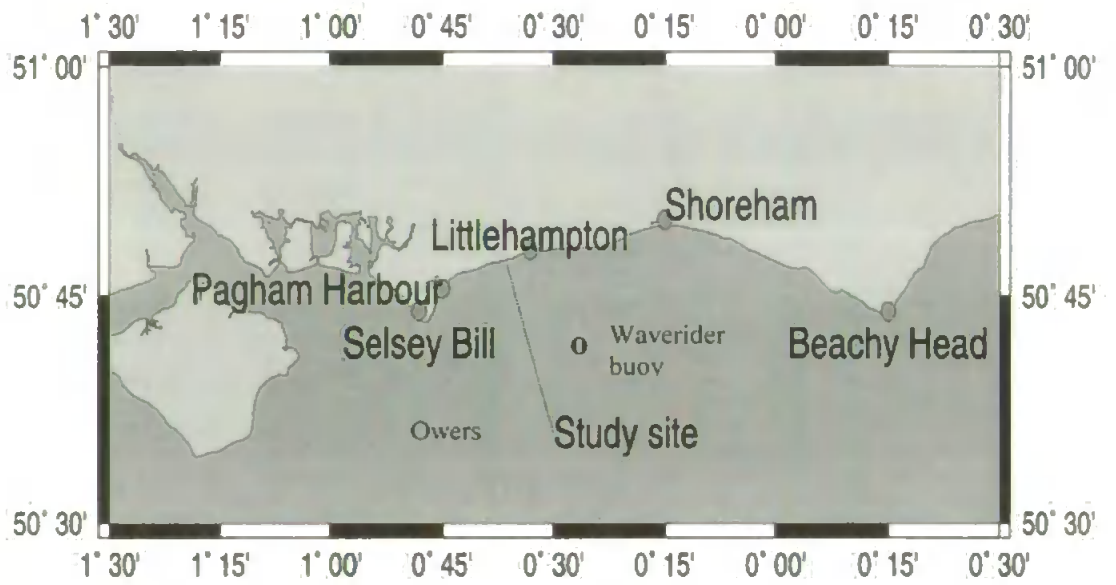


**Figure 3.1** The location map

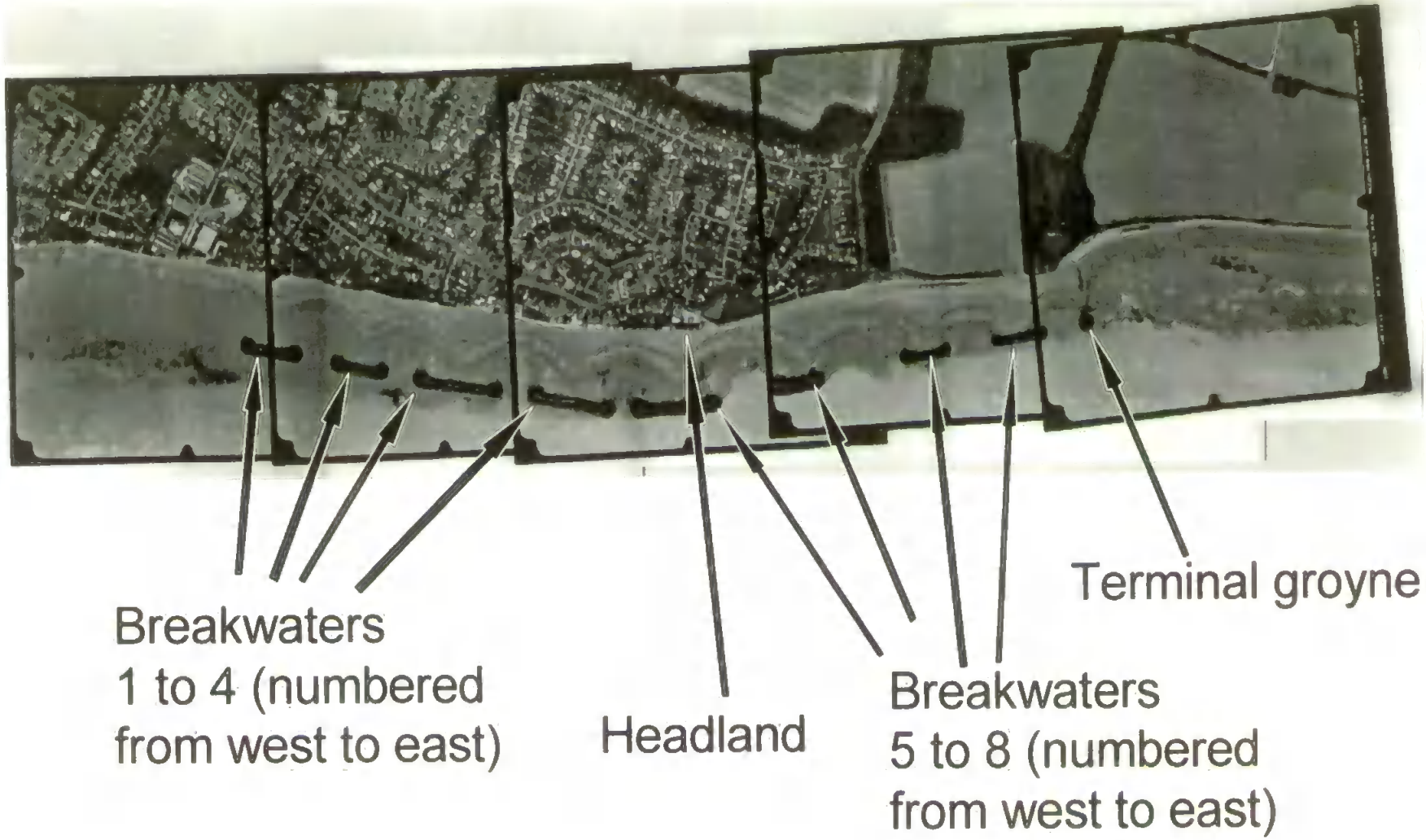


Plate 3.1 The aerial survey of the Elmer site

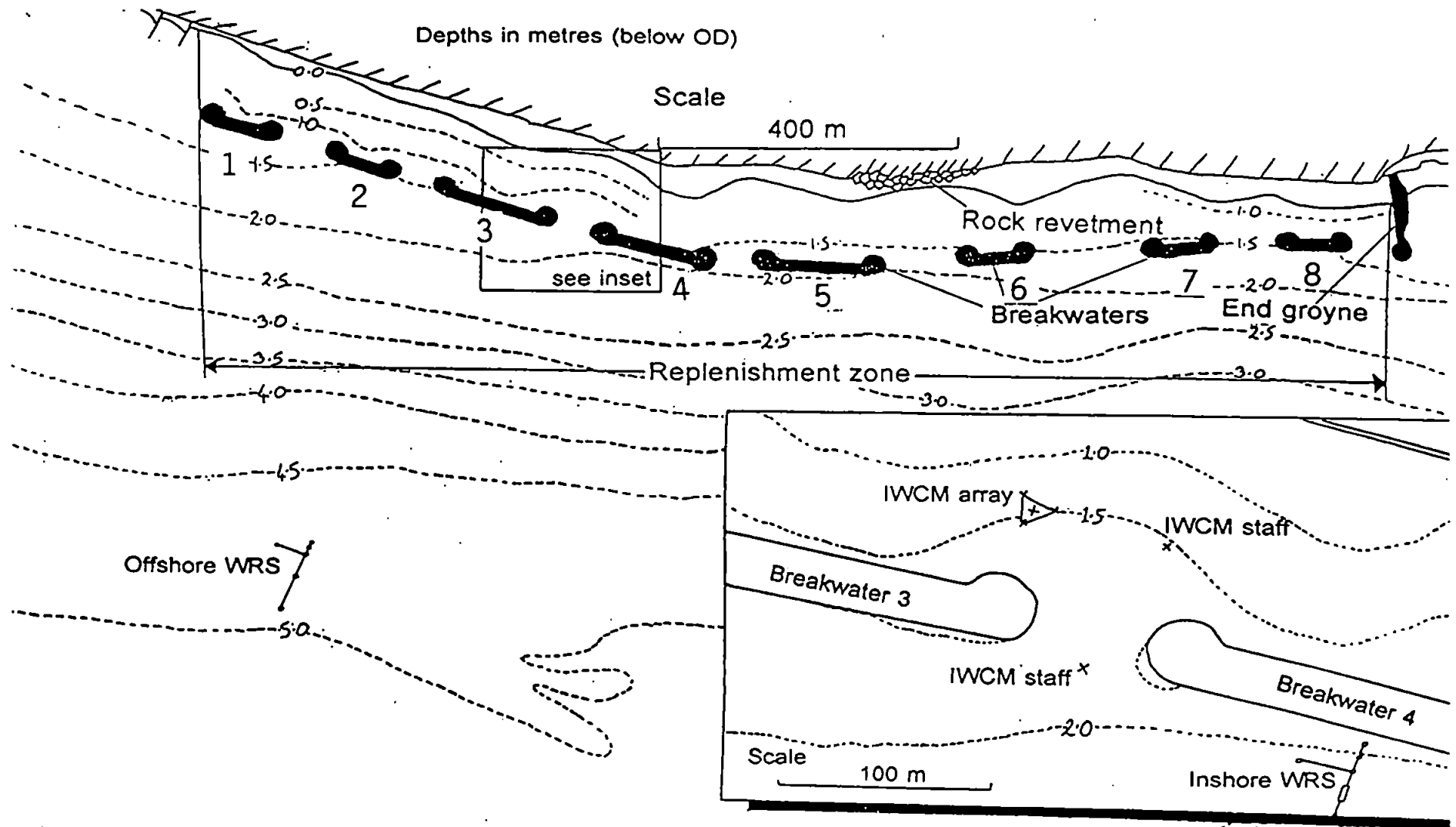


Figure 3.2 Elmer site and the equipment locations



However, the shingle beach crest in the front of the walls was low and did not provide protection against overtopping. Following a flood in 1989/1990 ADC and NRA built short-term protection (two shore-parallel breakwaters and a rock revetment) with a view to incorporate this work into a long-term strategy.

Subsequently a 3D physical model with a mobile bed was constructed in a wave basin at HR Wallingford (1990-1992) to find the optimum shore protection scheme. An area of approximately 2.65 km by 0.65 km was modelled at a scale of 1:80. A mobile anthracite beach was included together with facilities for measuring wave overtopping. Several layouts were tested, comprising offshore breakwaters, rock groynes and a recharged beach. They were tested under random wave conditions from three offshore wave directions and with sea states representing storm events with joint probability return periods ranging from 1 in 5 years to 1 in 200 years. It was found (HR, 1992) that the offshore breakwater scheme was the most effective in terms of reducing both wave overtopping and shoreline recession. Given the disadvantages of physical modelling related to scaling problems, it was desirable to monitor the performance of the new scheme in the field. A one year monitoring programme was set up by, Coastal Research Team from the University of Plymouth and the University of Brighton following the completion of the scheme.

### **3.2.3 Available data**

#### *Geology*

Generally, the natural coast at Elmer comprises a clay (brick earth) cliff deposit overlying chalk whereas the shingle beach overlies a thin veneer of sand on the top of the chalk platform.

Robert West and Partners (RWP), consulting engineers examined number of trial pits and analysed historical maps prior to the construction of the brekwaters. The findings were summarised in their report (RWP, 1991) in which beach deposits on the frontage were identified as follows<sup>1</sup>

a) fine, medium and coarse shingle (2 - 60mm)

b) sand intermixed with a relatively small proportion of shingle (0.6 - 2.0mm)

---

<sup>1</sup> Grain sizes are given in accordance with British Standard Material Size Classification (e.g. Simm *et al*, 1996).

- c) fine and medium sand (0.06 - 0.6mm)
- d) soft to firm alluvial silt deposits (0.002 - 0.06mm)
- e) in situ upper chalk (grade 5 or 6 (RWP, 1991)).

Shingle and sandy shingle was found to be present to a depth of approximately 3m below Ordnance Datum while approximately 1m of sand was found to lie between the shingle and chalk. The seabed was found to consist of a wave cut platform of Cretaceous chalk, with occasional exposed flint nodules. The indications were that the chalk rises from an approximate lowest level of 1.5 m OD to a level of approximately 1m AOD at the far eastern end of the surveyed area. The seabed slope approaching the shingle bank and seawalls was of an average order value of 1 : 115 in the central surveyed area. However, the chalk platform had a very mild slope of approximately 1:180 in the central part.

#### *Tidal levels*

The tidal levels can be found from two available tidal stations at Littlehampton and Bognor Regis, respectively. The tidal range varies from 2.9 - 5.3m on neap and spring tides, respectively (RWP, 1991).

#### *Wave conditions offshore*

The coast at Littlehampton is orientated from east to west and is thus open to wave action from the south-west, south and south-east. Beachy Head and Sesley Bill shelter the areas from the east and west respectively. The Isle of Wight reduces wave fetches in the directions between 255 - 270°<sup>2</sup> and the greatest fetch lies to the south of 255°. The coastline is subject to swell from the Atlantic and also to the storm and wind waves generated locally along the English Channel. The swell waves are generally small due to diffraction along the English Channel. The wave activity is mostly caused by onshore winds. However, surges occur during strong offshore winds. It was observed by RWP (1991) that the overtopping along the frontage was related to the occurrence of surge.

HR Wallingford (1986) operated a non-directional wave rider buoy off Littlehampton in 1985/86. The buoy was located just east of Kingmere rocks approximately eight and half km offshore of Littlehampton and in 10 m of water. This recorded a max. wave height of

---

<sup>2</sup> South equals 270°.

3.3 m with a zero upcrossing period of 5.8 s. It was found that wave heights measured less at Littlehampton due to shallow water effects, refraction across the Ower Bank Shoals and some shelter from the southwest by the Isle of Wight.

### *Currents*

Both tidal and wave-induced currents exist on the Elmer foreshore. However, tidal currents inshore rarely exceed 0.7 m/s ( RWP, 1991) and they generally run parallel to the coast. RWP (1991) carried out float tracking at Elmer and the results were very close (RWP, 1991) to those measured by HR Wallingford (method unknown) off the entrance to Littlehampton Harbour. Easterly currents were found not to exceed 0.3 m per second and to reverse approximately 2 hours before high water.

## **3.3 Instrumentation**

Selection of an appropriate technique for wave measurements depends on several factors such as the environment, site access and cost. The sensors for the present study were to be deployed at three positions just above lowest astronomical tide, in the tidal zone and offshore in deep water. Considering the advantages and disadvantages of the measuring equipment given in Chapter 2, a pressure transducer system, was chosen by Research Team, for the offshore measurements only. The simple and well established wave gauge or staff was selected for the inshore or shallow water measurements.

### **3.3.1 The inshore wave climate monitor**

The Inshore Wave Climate Monitor (IWCM) had been previously designed to meet the following criteria (Brown, 1994 and Chadwick *et al*, 1995b):

- a) accurate measurement of shoreline directional wave spectra;
- b) capability of long term measurements with on-site data storage and analysis;
- c) robust design capable of withstanding breaking storm waves on a beach;
- d) portability and transportability allowing rapid erection/dismantling on any beach site;

- e) to be structurally self contained such that beach movements do not affect the integrity of the device.

Additionally, IWCM measures instantaneous depth and it is easily fabricated at low cost.

### **Sensor and Acquisition Systems**

The wave gauge consists of a 6 metre resistive sensor mounted on an aluminium scaffold tube held vertically from the seabed, on a triangular base frame. The triangular sensor support frame is constructed from readily available aluminium scaffold tubes held by cadmium plated steel swivel fittings. Once on site, erection of the IWCM takes less than an hour and scaffold tubes driven into the beach material effect attachment to the seabed.

Each sensor was formed by a helical winding of 80 metres of resistance wire on a non-conducting support previously treated with anti-fouling paint to reduce contamination by marine organisms. A small sensor excitation and signal conditioning module was mounted directly on the top of each sensor to provide a filtered +/-5V signal directly proportional to water surface elevation. All sensor modules included an on board filter to attenuate the signal noise at source. Prior to measurement, each signal was passed through a 6 pole anti-aliasing low pass Bessel filter<sup>3</sup>. All modules were directly connected by armoured cable to a central termination unit also mounted on the sensor support frame. A larger marine cable was used to connect the sensor array to a secure base station well above the high water mark. In the absence of mains electricity supplies the complete sensor array can be operated from two 12-volt batteries.

A remote microcomputer-based data acquisition system was used to control timing, measurement and storage of data, followed immediately by on line spectral and directional analysis of waves incident on the shoreline. The flexibility of the microcomputer-based system allowed instant on site modification to data acquisition or analysis software and immediate logging of unscheduled events of particularly interesting activity. Graphical visualisation of wave activity during recording was also useful for verification of correct operation and calibration checks.

The data acquisition software was written by David Pope, from the University of Brighton, in compiled BASIC. Before each logging event a check on still water level and wave height

---

<sup>3</sup> Bessel filter has a cut-off frequency of 2Hz and roll off at 36dB/octave effectively passing all wave data with frequencies less than 0.75 Hz and with 80% attenuation at 4 Hz.

was made to avoid storage of unnecessary data files. An Amplicon PC74 A/D card in the differential mode was used to discretely sample the analogue output from the signal filters and each sensor was selected sequentially and read within a period of 10msec. All raw data were stored in encoded form to reduce disk space and all file names reflected the date and time of each event.

Initial static calibration of each wave sensor is achieved by graduated immersion of the complete sensor and module in still seawater. Dynamic response was tested in the laboratory and the sensor was found to be dynamically accurate. Further details of the calibration may be found in Borges (1993).

### **3.3.2 Offshore wave recording system (WRS)**

This system had been designed by Paul Bird and previously deployed at a few locations e.g. Plymouth breakwater, Elmer's original emergency two breakwaters scheme (Bird, 1993). The system was designed to be self contained and situated on the seabed, measuring pressure at several locations. Taking account of functionality, purpose and working environments the following criteria were met:

- a) It measures water pressures at several locations simultaneously, therefore also the directional wave spectra and also records times and dates of measurements.
- b) It has sufficient data and battery capacity to record pressure data over a fairly long period<sup>4</sup>.
- c) It is robust enough to survive storms, and can be located to avoid unauthorised interference.
- d) Performance specification provides accuracy limits for the steady component of - +/- 1% of the pressure reading and for the varying component - +/- 1% of the pressure reading or 5 mm.
- e) It is seabed mounted with integral power supply and data store.
- f) The only communications link to the user is a cable link normally lying on the seabed that can be hauled or lifted aboard a boat. The operator needs to visit the site

---

<sup>4</sup> The envisaged capacity was about 4 million readings and battery life of four months.

boat, haul aboard the cable and connect it to a personal computer to download the data onto the computer's disc. However, the measuring cycle needs to be an automatic operation and subject to pre-set timing (typically 17 min every 3 hours, but alterable). Thus, it should enable the user to set up measurement parameters, and to check for the correct operation from time to time, without full recovery of the equipment.

The wave recording system consists of eight separate units: six transducer assemblies, the recorder and a portable computer interface unit. Interfaces are in analog form via marine Subcon connectors and cable. Six transducers are seabed mounted in a linear array with one offset transducer.

### **Sensor and Acquisition systems**

The PDCR 130 pressure sensor from Druck was chosen by Paul Bird to record the absolute pressure (Bird, 1993). Correction to each record from a barograph is added at the analysis stage. It was decided to place only pre-amplifiers with the pressure transducers and to link the high level analog signals to a central recorder unit which would contain all the other functions. Plate 3.3 shows the pressure transducer and its housing.

The functional sections of the wave recorder (WR) are a signal conditioning unit, power supply, microcomputer and data storage. The signal conditioning units convert the information in six analog signal inputs into a stream of binary numbers, which can be then read by the microprocessor. The microprocessor's role is to control the track/hold circuit, multiplexer, programmable gain amplifier and analog to digital converter on a signal conditioning board. The power supply section consists of a printed circuit board assembly and battery pack. Its function is to provide electrical power for the six remote transducers and the analog digital circuitry. A pack of twenty-eight D size alkaline-manganese cells provide the wave recorder's electrical power requirements for approximately four months. A battery-backed static random access memory was chosen for data storage.

Signals from all sensors are sampled simultaneously by a track and hold circuit to avoid any delay between readings taken at the different locations. The first operation after the signal enters the signal-conditioning unit is to put the signal through a low pass filter, which removes any 'high' frequency content (above one Hertz)<sup>5</sup>. Analog signal

---

<sup>5</sup> Its characteristics are as follows less than +/- 0.02 dB attenuation up to 0.4 Hz, less than +/- 0.1 dB up to 0.5 Hz and

conditioning is complete at the output of the amplifier and the signal is then ready for conversion into digital form. The controlling program handles measurements (scheduling transducer readings), measurement processing (compressing the readings, time and date stamping the records), memories, power supply and the communication link.

The wave recording electronics and pressure transducers were fitted into watertight pressure housings capable of reliable long-term sealing to a depth of 100 metres in seawater. The recorder housing is of tubular construction, with removable end caps sealed by 'O' rings and retained by nuts and bolts through the flanges. Connectors for the transducers are fitted to the end caps and also sealed using 'O' rings. The materials, which were used, are all corrosion resistive and enable a good seal. Aluminium alloy was selected for the housing as it is easy to machine and weld and it is light and cheap. The high corrosion rate was overcome by the application of a hard anodic oxide coating. Three elastomeric torodial sealing rings seal the joint between each end cap and the tube. The transducers are made from stainless steel, which can corrode, badly after prolonged immersion in seawater. A special casing was therefore designed for the transducers.

The laptop personal computer (PC) acts as a terminal to the wave recorder's microcomputer and provides mass storage to collect the data. A proprietary communications package is run on the PC, giving the user control over its serial interface<sup>6</sup> and disc drive.

The offshore wave recording system is calibrated at a number of stages in order to give the greatest possible assurance that the readings obtained are accurate. Each part of the system is firstly tested and calibrated separately. Then the system as a whole is set to take the record at ambient pressure and compared to mercury-in-glass precision aneroid barometer. More details can be found in Bird (1993).

### **3.4 Deployment and measurements**

As the currents are relatively small (less than 0.7 m/s) and the monitoring budget was limited it was decided by Research Team to give an emphasis on the directional wave measurements. The wave measurements offshore and inshore were accompanied by an aerial surveying of the shoreline change. The positions of the equipment was located

---

greater than 40 dB at 1Hz and above.

<sup>6</sup> (800 kb/hour about 265kb/rampack; 16 rampacks takes about 3h and 36 min )

considering natural site conditions described in section 3.2.3., capabilities of equipment and requirements of numerical model.

### **3.4.1 Offshore wave measurements**

The deployment of the WRS took place on 23 September 1993. A team from the University of Plymouth deployed it 650 m offshore and about 500-m from the completed breakwater scheme (see Figure 3.2). The mean water depth offshore was 6 m. The location was chosen to provide the seaward boundary for the numerical model. For the WRS array design, the recommendations of Isobe and Kondo (1984) were followed: a linear array of exponentially increasing spacing, with values chosen to suit the range of wavelengths expected. In addition, one extra sensor was placed off-line to determine the wave directions different to the orientation of the array.

A rectangular steel platform of about 400-kg was provided for the recorder and six smaller platforms of concrete and steel<sup>7</sup> for the transducers. These platforms minimise the movement and tilting of recorder and transducers. Transducers with cables attached were bolted on to platforms. The chain, which connects the wave recorder platform and transducer platforms, was pre-cut to define the spacing. Cables were tied up to the chain. First, the steel recorder platform and transducers on concrete transducer mounting blocks were deployed. Plates 3.2 and 3.3 show the transducers prepared for the deployment. They were dragged by the vessel and cut free and sunk at the appropriate locations. Divers adjusted the final position on the sea bed. In the next stage the recorder was taken down to its platform and bolted on. The cables were then unrolled from the transducers to the recorder and tied at intervals to the chain. Finally the connectors were mated at the recorder, and the locking rings tightened. After deployment a survey was made to establish the actual locations and connections of the WRS (see Figures 3.3 a, b) and 3.4 a).

The system was visited regularly by Philip Axe in order to download data until early November 1993. Between this lattermost time and early January '94, bad weather prevented the system from being downloaded and restarted. In January '94, it was found that the mooring line had been fouled by fishing equipment, and had to be replaced. This was repaired at the beginning of February '94 and the system restarted again. The system was successfully operated between this lattermost date and 16th January 1995. A

---

<sup>7</sup> concrete filled tyres



'deployment', a term, which will be used further on is the period normally limited by battery life. The batteries were changed twice during the field campaign resulting in three 'deployments'. Deployment 9 ran from 23rd September 1993 until 10th of March 1994 (715 pressure records collected). Deployment B followed from 11th of March until 23rd of July 1994 (916 pressure records collected). Deployment D started with the last change of batteries on 4th of August 1994 and lasted until 14th January 1995 (1147 pressure records collected).

A 'measurement operation' is defined as the period between two start commands, which is limited by the memory or full data store. After every measurement operation, data had to be downloaded by PC. Downloading of data usually took about 2-3 hours. Each operation is composed of a number of measuring cycles (rampacks) lasting typically 3 hours each. Data from each transducer in the offshore system were collected every 3 hours 6 minutes with a sampling frequency of 2 Hz. The recorder was switched on for 10 - 20 min in each cycle. In this case it was switched on for 11.3 min. The WRS was comprehensively calibrated before and after deployments, and was found to have changed very little over the period. Any small corrections were incorporated into the data analysis procedure.

### **3.4.2 Inshore wave measurements**

Inshore deployment was completed on the 5th October 1993. The Research Team deployed an IWCM in the lee of breakwater number three to record directional wave spectra and two satellite probes to record simultaneous spectral wave data at nearby locations (see Figure 3.2). The array geometry of the IWCM was based on the four guidelines as described in Goda (1985) and is repeated here.

- i) No pair of wave gauges should have the same vector distance between gauges
- ii) The vector distance should be distributed uniformly in as wide a range as possible
- iii) The minimum separation distance between a pair of wave gauges should be less than one half of the smallest length of the component waves for which the directional analysis is to be made
- iv) The greater the number of probes the greater the resolution



**Plate 3.2** Pressure transducers prepared for the offshore deployment



**Plate 3.3** Pressure transducer and its housing prepared for the offshore deployment

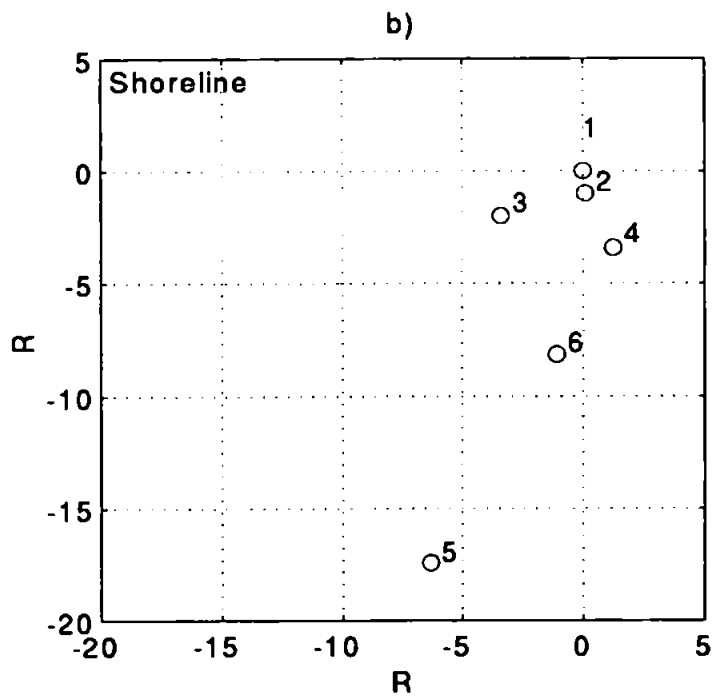
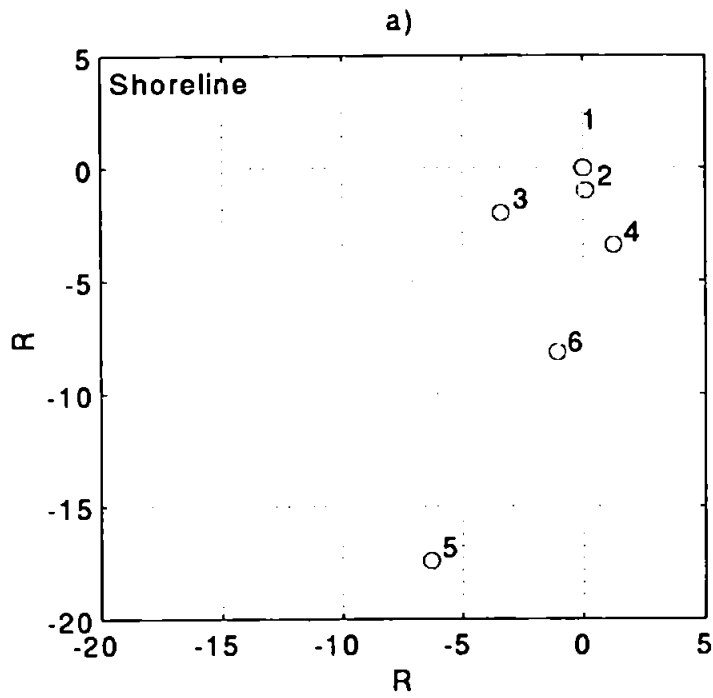


**Figure 3.3** Transducer positions and connections at Elmer offshore (marked as offshore WRS in Figure 3.2): a) surveyed co-ordinate of the array deployment B; b) surveyed co-ordinate of the array deployment D; where  $R=3m$

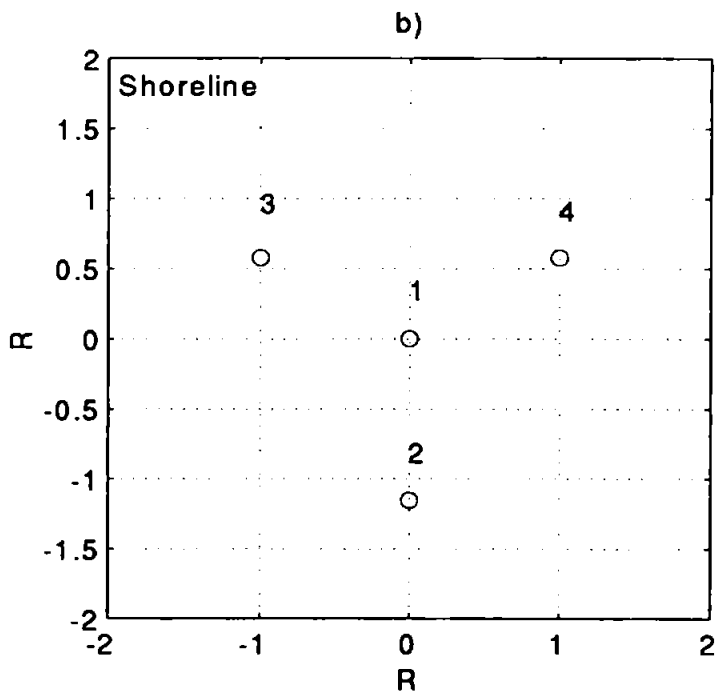
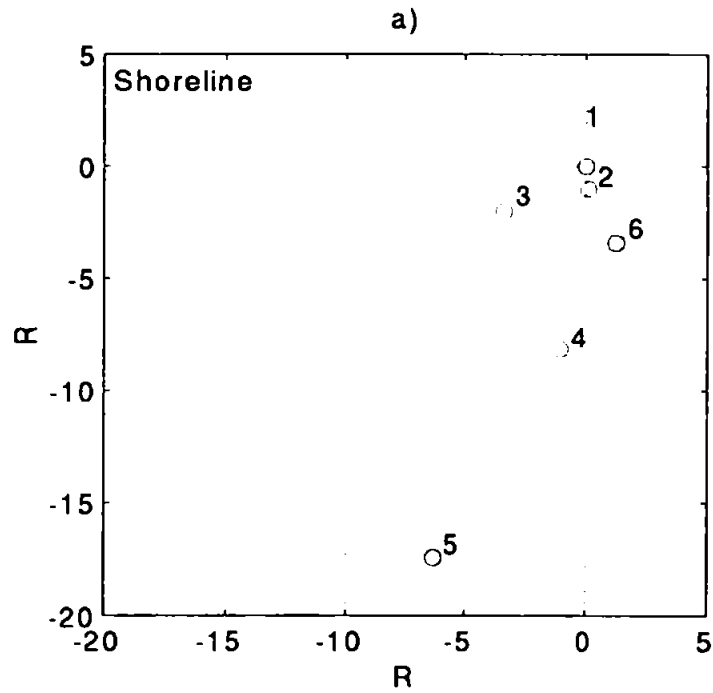


**Figure 3.4** The equipment positions at Elmer: a) surveyed coordinate of the pressure transducer array offshore - deployment 9 (marked as offshore WRS in Figure 3.2); b) surveyed coordinates of the inshore starr array (marked as IWCM array in Figure 3.2 - inset); where  $R=3m$

The star array satisfies condition (i) and is sufficient for condition (ii). Condition (iii) is met by limiting the cut-off frequency and condition (iv) for a star array produces six independent pairs of cross-correlation measurements.

The star array and two satellites were firstly assembled on the top of the beach. The triangular support frames constructed from aluminium scaffold tubes were assembled around the measuring poles. The frames were moved to the lower beach after completion. Once on the site, they were attached to the seabed by scaffold tubes driven into the beach material. The marine cables (length of 150m) which connect the sensor array and the PC station were buried in prepared trenches. The data logging system was placed in a shed in the garden of a nearby resident for the whole duration of the field campaign. Plates 3.4 and 3.5 show assembly of IWCM on the top of the beach and the final position of the system in the lee of the breakwater.

A schedule of site visits every one to two weeks was followed throughout the monitoring period. At each visit data was collected, synchronisation times adjusted and, if tidal conditions allowed, a through inspection was made of all sensors and supports. Calibration checks of all sensors were made at suitable times throughout the monitoring exercise and small adjustments made where necessary. Occasional interruptions to the logging sequence occurred, resulting in the loss of a few days of data due to power supply disturbances. The locations of the star array in the lee of the breakwater and the satellite probe shoreward of the gap were swapped between 13th to 16th July 1994. Logging was re-established on the 24th July. The star array stopped recording on 2 November 1994, but the two satellite probes continued recording data until 13th December 1994 (1550 data sets collected). Data were collected every 3 hours 6 minutes (when the IWCM was in more than 0.5 m of water) for 17 minutes with a sampling frequency of 4Hz.

The WRS and IWCM systems measured data simultaneously. The position of both inshore and offshore equipment was surveyed during the operation.

### **3.4.3 Other measurements**

#### *Beach surveying*

The length of the coastline under investigation precluded the use of traditional leveling techniques for beach surveying. It was decided instead to use aerial stereo-photogrammetry.



**Plate 3.4** Assembling of IWCM on the top of the beach

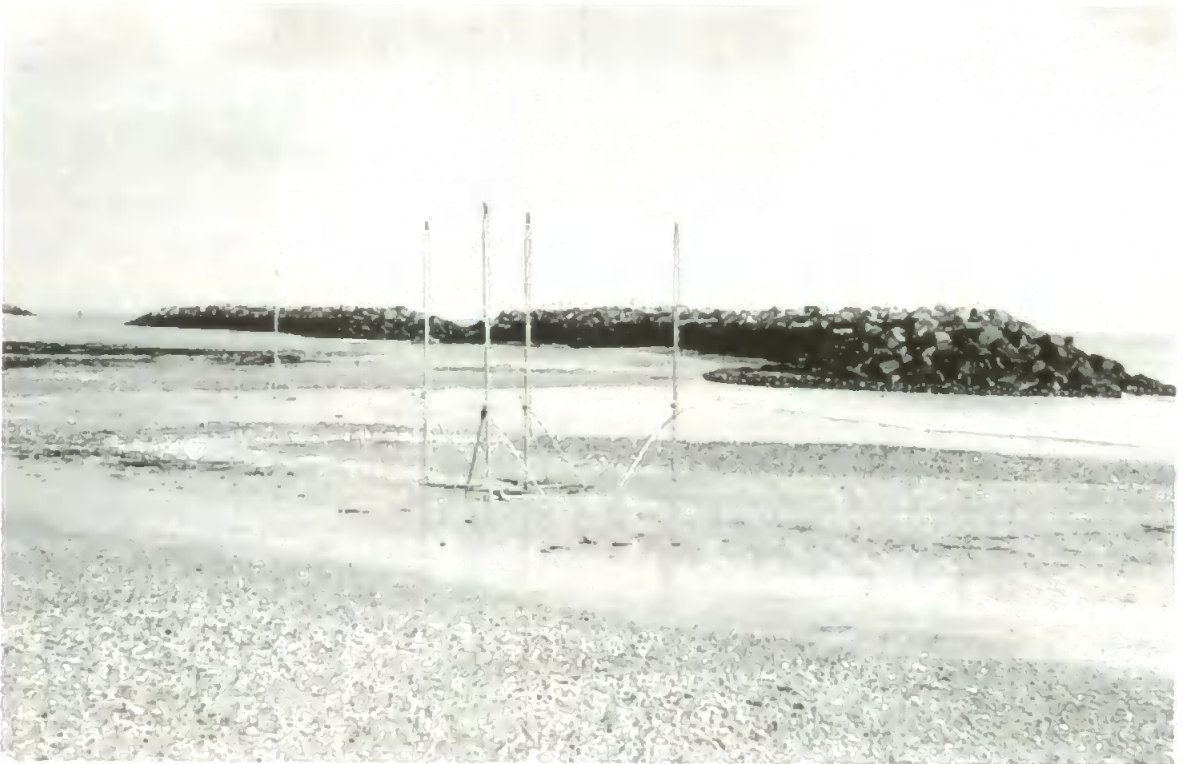


**Plate 3.5** IWCM and one of satellite probes during deployment in Elmer

After the breakwater scheme contractor-completion survey, flights were flown at quarter year intervals at low tide, giving four aerial surveys over the wave-recording period. Surveys included information on surface material (mud, sand, shingle, concrete or rock), in addition to the beach level information.

Sediment size distributions were studied by the analysis (to BS 812) of 22 beach samples taken in the bay between breakwaters 3 and 4 by Philip Axe. Twelve of these were 'random' samples, giving a description of the overall beach composition (Axe, 1994). The other ten were to show any variation in particle size with distance from the salient tip.

### **Video recording and photographs**

At each visit to the site, photographs of beach features along the entire frontage were taken by Philip Axe and Richard Brown. More than 350 photographs have been studied, and form the basis of an internal report by Axe (1994). Richard Brown was taking video recordings of particularly interesting wave conditions (storm events) and their effects on the beach.

## **3.5 Summary**

The field campaign involving wave measurements and beach changes started immediately after the new defence scheme was completed. The advantage of such an early start is that the development of the equilibrium beach profile related to the measured wave conditions could be observed. The field measurements were taken almost continuously for more than a year. The equipment resisted several major storms without any damage and all together about 4500 wave data sets were collected. The aerial surveying captured the rapid beach changes in the early stage until equilibrium was almost achieved. The wave data and the beach surveying data form a uniquely valuable database. This will allow the validation of existing wave transformation and morphological numerical models and evaluation of the effectiveness of the beach protection scheme.

The IWCM and WRS systems incorporated data recording, ease of deployment and very precise data handling. However, there are some limitations in both systems, which should be improved in the future.

The deployment of offshore pressure transducers by divers becomes very difficult in deep

water, particularly with low subsurface visibility. To fix the transducers at the proper position and to connect the cables to the right transducers is very difficult. A new offshore deployment technique should be investigated. The measuring cycles and time for the WRS is automatically pre-set. The IWCM measuring time was set up manually. In concurrent measurements like this, it is very important to have the same recording time offshore and inshore. Unfortunately, this was not working properly during the whole field campaign time. It was impossible to access the offshore wave recorder during high storm conditions. The possibility of a single operation system for both devices should be investigated. Also, the measurement cycle offshore was limited by the constraints of the control programme software. It should be extended from the existing 11 min to at least 17 min. Downloading of the data offshore from the boat takes about 2 to 3 hours (maximum 5 hours). Bad weather conditions can prevent the downloading operation. The gap in the measurements occurred in the winter 1993 for the same reason. Therefore there is a need for the development of a telemetric operation system. The array shape can influence the directional analysis. Special care should be given to the array design in the future.



# Chapter 4

## Data processing and analysis

*Science is spectrum analysis. Art is photosynthesis.*

*Karl Kraus (1868-1952)*

### 4.1 Introduction

Measured wave properties are stochastic processes by their character. Thus the choice of an optimal spectral analysis routine is very complex. Different spectral analyses with different degrees of freedom and confidence levels can produce different results (Sand, 1985). Two devices, the IWCM and the WRS deployed at Elmer, measure different wave properties - surface elevation and pressure respectively. Existing original data processing routines, for these two devices were also different. Thus the measured wave climates offshore and inshore could contain differences arising from the measurements and analysis techniques.

It is important to minimise the input errors for the computational model validation. The input data needs to be accurately pre-processed and also needs to be comparable in accuracy to the data which are used for the validation. Thus, evaluation of different spectral analysis techniques is essential. However, measurements of different wave properties can influence the final comparison results. It was decided to compare measurements and different analysis techniques before the field campaign started in

September 1993.

In section 4.2 first the existing IWCM and WRS spectral analysis routines are compared. This is followed by a comparison of the measurements taken at the same location by the two measurement devices. These lattermost analyses highlighted a future need for a uniform data processing technique to be able to compare the offshore and inshore measurements. The uniform processing procedure is outlined in section 4.3. A summary of data collected and analysis results are given in section 4.4. The chapter is summarised in section 4.5.

## **4.2 Data processing and measurements comparisons**

### **4.2.1 Data processing considerations**

Spectral analysis (see Appendix D) not only gives cross-spectral (see Appendix E) information as the basis for the directional analysis but can also be used to derive frequency domain statistical parameters, such as significant wave height and peak period. However, for stochastic processes, spectral computations require an enhanced degree of attention. Considering a stationary stochastic process, that is a time series of length  $T$ , the spectrum of the whole stochastic process should be determined. The real, true spectrum is unknown, hence by use of statistical methods the true spectrum should be estimated. From one time series, it is possible to calculate several different spectra (illustrated later in section 4.2.3). Therefore it is necessary to compare the reliability of the given estimates.

The important concepts related to the spectral estimates are as follows:

- variance of spectrum values
- bias of a smoothed estimator
- spectral window
- spectral bandwidth
- data window
- degree of freedom
- confidence interval

Each of these is outlined in turn

#### *Variance of spectrum values*

By means of Parseval's theorem (e.g. Press *et al*, 1986) the variance of the process can be

expressed in terms of  $A_n, B_n$  as

$$\sigma = \frac{1}{2} \sum_{n=1}^{\infty} (A_n^2 + B_n^2) \quad (4.1)$$

since the spectrum relates the variance as a function of frequency. The first raw estimate (sample spectrum) becomes:

$$S'_{\eta\eta}(f) = \frac{1}{2} (A_n^2 + B_n^2) / \Delta f \quad (4.2)$$

$S'_{\eta\eta}(f)$  is an estimator of the true spectrum  $S_{\eta\eta}(f)$ . From (4.1) it can be concluded that the area under the spectrum equals the variance of the process, and is constant. On the other hand the variance of a certain spectrum value may vary

$$\text{Var}(S'_{\eta\eta}(f)) \neq \text{const.} \quad (4.3)$$

$S'_{\eta\eta}(f)$  varies considerably even inside a small band of the raw spectrum. Therefore a smoothing procedure must be introduced to reduce the variance  $\text{Var}(S'_{\eta\eta}(f))$ .

#### *Bias of a Smoothed Estimator*

By smoothing over a certain number of frequencies, the difference between estimates and the true spectrum is influenced by the adjacent frequencies. The difference, or the error, between the smoothed estimate and the true one is given by

$$B(f) = E\{S'_{\eta\eta}(f)\} - S_{\eta\eta}(f) \quad (4.4)$$

and is called bias. Smoothing decreases variance but on the other hand increased bias, therefore the balance between variance and bias should be found in each specific situation.

#### *Spectral window*

Smoothing is very often performed by a spectral window on the spectral estimate in the frequency domain. The Bartlett spectral window is very often used which corresponds to splitting up the actual time series into  $p$  subseries each of length  $M=T/p$  and calculating

$$\bar{S}'_{\eta\eta}(f) = \frac{1}{p} \sum_{i=1}^p S^i_{\eta\eta}(f) \quad (4.5)$$

where  $\bar{S}'_{\eta\eta}$  is a smoothed spectral estimator.

This last technique is the so called ensemble averaging and is widely used because with the development of computing technology, it is quite quick to perform the FFT on large numbers of subseries. The advantage of the method is that it reduces the variance and smoothes the estimate proportionally to the number of subseries. The overlapping of the subseries can be from 10 - 75 % (Welch, 1967).

### *Spectral Bandwidth*

The spectral bandwidth,  $b$  is the width of a spectral window for smoothing. Smoothing over a larger number of frequencies widens the spectral bandwidth which corresponds to length of subseries ( $M$ ) in ensemble averaging.

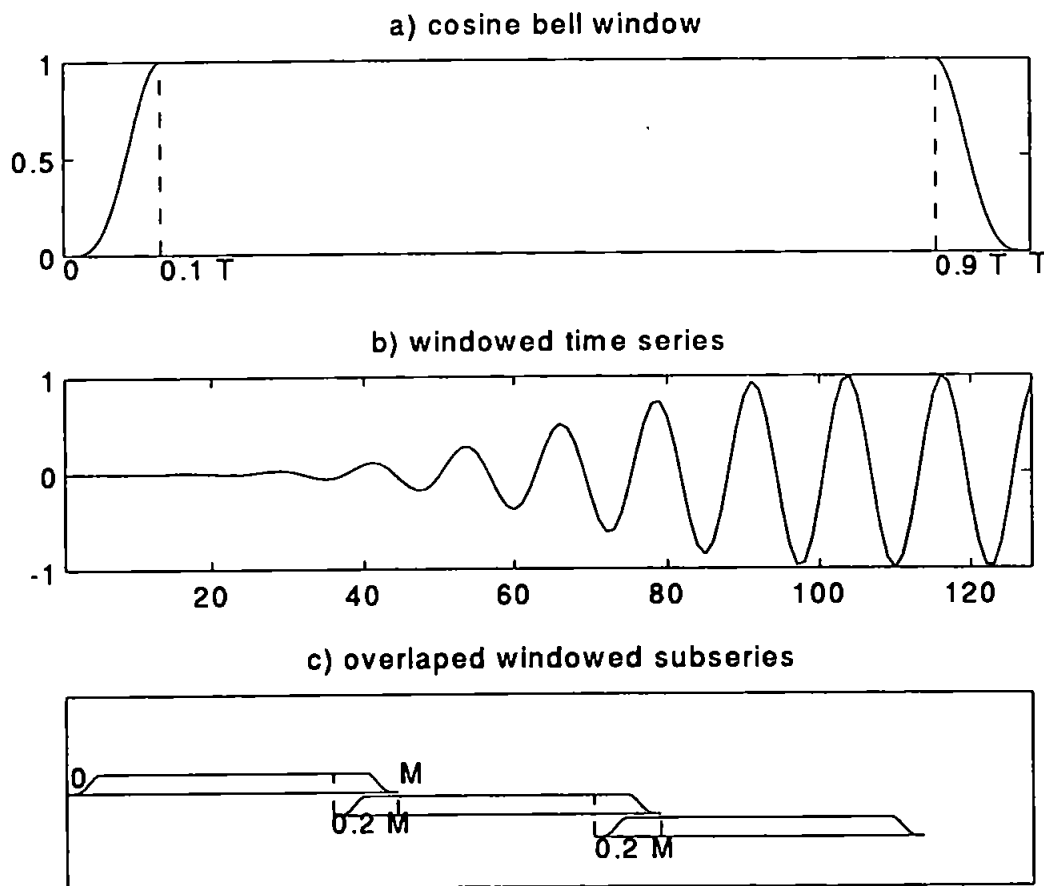


**Figure 4.1** a) Cosine – bell window where  $T$  stands for a length of whole series; b) Its influence on time series; c) Subseries prepared for spectrum computation where  $M$  stands for a length of segment (number of points) and overlap is 20 %;

### *Data Window*

If a difference between the end and start values appears in any of the subseries (i.e. if a discontinuity is present) when ensemble averaging is performed, the Fourier coefficients of a given frequency will be spread over neighbouring frequencies. This contributes to the total error or bias of the estimate. Therefore, it is advisable to equalise the boundary values before the Fourier transformation by means of a data window. A taper window which has a value of unity over 60 - 80 % of the series, and decreasing to zero at the end is widely used. One such window is a cosine bell window which is illustrated in Figure 4.1.

### *Degrees of Freedom*

The spectrum estimator is a stochastic variable and it can be shown that it is  $\chi^2$  (chi-squared) distributed. The distribution has  $\nu$  degrees of freedom, where  $\nu$  is the number of linearly independent or "free" squares entering the expression ( $\nu=2$  for the raw spectrum). Degrees of freedom are interpreted as a measure of the stability of the estimate. Increasing  $\nu$  corresponds to increasing the stability and decreasing the variance of the spectral estimate.

Generally, combined frequency smoothing and ensemble averaging gives spectral estimates with  $2lp$  degrees of freedom, where  $p$  is the number of segments for ensemble averaging and  $l$  is the number of adjacent frequency bins. Some authors (Jenkins and Watts, 1968 and Goda, 1985) take in account the percentage of segments overlapping in ensemble averaging or the influence of the window.

### *Confidence interval*

The  $\chi^2$  distribution is also used to calculate confidence limits for the true spectrum  $S_{\eta\eta}(f)$  i.e.

$$\text{Prob} \left\{ A < \bar{S}'_{\eta\eta}(f) - S_{\eta\eta}(f) \leq B \right\} = 1 - \alpha \quad (4.6)$$

The probability that the true parameter  $S_{\eta\eta}$  is in interval  $\bar{S}'_{\eta\eta} - B$  and  $S'_{\eta\eta} - A$  corresponds to  $1 - \alpha$ . This interval is called a confidence interval for  $S_{\eta\eta}(f)$ .

## 4.2.2 Existing data processing comparison

Two different spectral analysis routines had been previously developed independently by Bird and Chadwick for each of the measurement systems. Both spectral analysis techniques were performed on surface elevation data. As mentioned in the previous section, different spectral techniques will give different estimates, therefore it was desirable to compare the methods performance on the same measured record. A short summary of the existing methods is given in the next two sections.

### The existing processing method for WRS data

The usual number of data points sampled was 1356, with a sampling interval of 0.5 sec. They were stored as coded and compressed files as outlined in Chapter 3. Two Fortran programs **paginate** and **decode**, were written to convert coded and compressed dump files into pressure records in standard form Bird (1993). The role of **paginate** is to split the dump file up into files containing one measurement record each. It also forms six columns of data, one for each transducer. **Decode**'s function is to work out the actual pressure readings from the compressed values in the Paginated files, applying to those the values of the amplifier gain and offset settings, the transfer function and the pressure transducer characteristic.

The decoded pressure data are converted to surface elevation time series by the program **psurf** (Davidson, 1992). The program also takes the calibration factors into account. It operates by applying a spectral weighting function (based on linear wave theory) to Fourier components of the pressure time series, then reverse transforms the data back to the time domain. The routine has several advantages over the alternative time domain approach. These are as follows:

- phase is perfectly preserved
- much less data is lost
- the spectral gain function of the filter can be rigidly controlled.

The maximum value of the weighting function is set to a value of 10. The value of 10 was chosen to limit the steepness of the function and thus to control the impulse response characteristics. Also, if the factor is allowed to be higher than 10, it might lead to noise amplification.

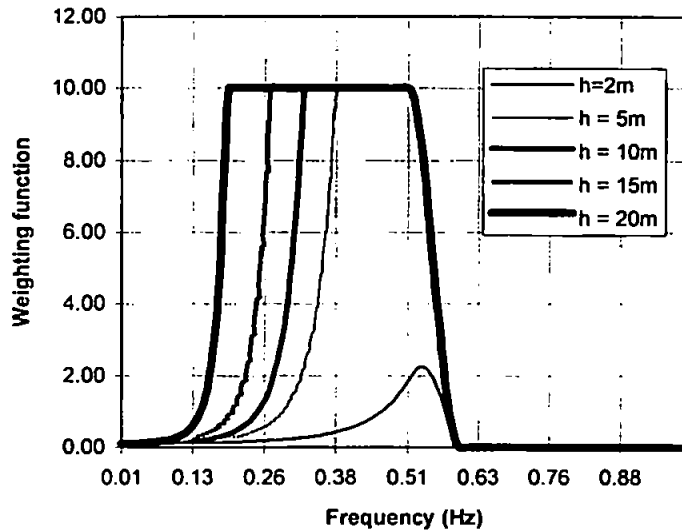


**Figure 4.2** The weighting function for transfer of pressure to surface elevation

The frequency limits depend on the overall water depth and the height of the transducer above the seabed. As the water depth increases the frequency limit decreases<sup>1</sup>. This implies in an incorrect transfer of pressure to the surface elevation if there is a significant energy contribution from frequencies above the limit. Therefore, the weighting function is reduced linearly with frequency down to zero for frequencies greater than 0.33 Hz (0.5 Hz in the new weighting function as is illustrated in Figure 4.2). The main purpose of the ramp is to control the impulse response characteristic. Sharp vertical edges in the frequency domain filter lead to a ringing in the time domain (see Press *et al*, 1986). The ramp, which is chosen, gives function values equal to zero for frequencies greater than 0.56 Hz. The upper depth limit to the application of the software is about 15-20 m.

Spectral analysis was then carried out on the surface elevation series. The spectral procedure was as follows

- subtract the mean from the data series
- apply a Parzan (triangular) window
- Fourier Transform the data using a routine from NAG library (bandwidth was  $1.479 \times 10^{-3}$  Hz)
- average 5 adjacent frequency bins to smooth the spectrum (after frequency smoothing over 5 bins, the bandwidth became  $7.396 \times 10^{-3}$  Hz. This yields 10 degrees of freedom,

<sup>1</sup> The frequency limit of 0.33 Hz is reached at a water depth of 7 m.

and 0.48-3 as lower and upper 95% confidence limits)

- the output spectral estimates were expressed as a peridiogram where the sum of the Fourier components to the Nyquist frequency is equal to the time domain variance

### The existing processing method for the IWCM data

The usual number of data points sampled was 2048, with a sampling interval of 0.5 sec. The stored data were coded and compressed. A BASIC program, **diran4**, was written to process the data (Chadwick *et al*, 1995 a). It consists of a decoding routine and spectral and directional analysis routine. The spectral analysis consisted of the following procedures

- detrend the data to eliminate the tidal influence; splitting wave records into segments and calculating change in mean water depth using Goda's (1985) polynomial function
- demean the data
- cosine bell window applied (first order cosine function, 10% taper)
- ensemble averaging (3 FFT segments with 50% overlap)
- average adjacent frequencies (smoothing over 2 adjacent frequency bins. This yields in bandwidth of  $3.9 \cdot 10^{-3}$  Hz; 12 degrees of freedom, and 0.5 and 2.75 as the lower and upper 95% confidence limits), respectively.
- the spectra estimates were normalised to the time domain variance ( $\sigma$ ) in the frequency domain, by the following relationships

$$S_{n'} = S_n \left( \frac{\sigma}{m_0} \right) \quad (4.7)$$

$$m_0 = \sum_{n=0}^{f_N} S_n \Delta f \quad (4.8)$$

$$\sigma = \frac{1}{N} \sum_{i=1}^N (\eta_i - \bar{\eta})^2 \quad (4.9)$$

where  $m_0$  is frequency domain variance and  $\eta$  a surface elevation.

### 4.2.3 Evaluation of WRS and IWCM spectral analysis

As spectral analysis for the data collected by the WRS and IWCM differ from each other, prior to the field measurement campaign and data processing, both techniques were compared and analysed. The data chosen for analysis were recorded at the same site where the new field exercise was planned. Both measurement devices were deployed at Elmer in the summer of 1992. The WRS was deployed in front of the one of the two original



breakwaters and the IWCM was deployed on the beach in the lee of the two original breakwaters.

### Comparison of the spectral energy

First, the comparison between total variance (or energy) obtained by time series analysis and first spectral moment  $m_0$  (or energy) obtained by the spectral analysis was made. The spectral analysis routine was the WRS routine, which comprises triangular window without normalisation<sup>2</sup>. Seven files were compared. The total variances for four chosen pressure transducers for six data files were larger than the total variances obtained by time series analysis. One of the reasons is that the wave excursion data files prepared by **psurf** contain the tide elevation. If the mean surface level is not properly adjusted then the spectral estimate near  $f=0$  appears large which will have an influence on the total energy value. However the energy can also leak to other neighbouring frequencies which is difficult to discern.

### Influence of windows, starting points, FFT length

The spectral analysis procedure for the IWCM was then applied to the WRS data measured in the front of the breakwater. As the IWCM analysis was developed for a star array and four measurement points only the data from transducers 2,3,4 and 6 were taken for comparison purposes as it outlined in Figure 4.3.

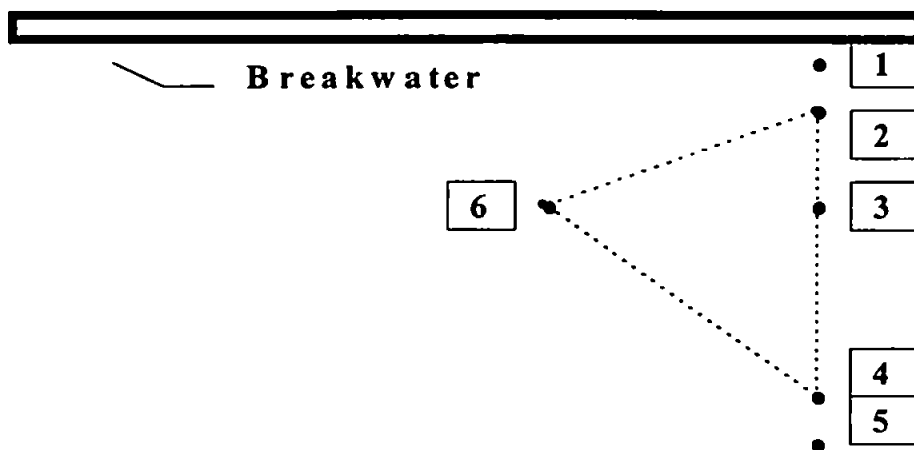


**Figure 4.3** The wave recorder position scheme ( the dotted lines connect the transducers which were taken into comparison)

According to the considerations outlined in the section 4.1, the influence of the following

<sup>2</sup> The results are not unwinded nor normalised on the time series variance.

parameters and their combinations were investigated

- application of the data windows
- starting points for the data analysis<sup>3</sup>
- FFT segment length and corresponding number of segments, which influences the degrees of freedom
- energy normalisation to time series variance ( $\sigma$ )

Two different windows were applied

- a) Cosine bell window
- b) Triangular window

Natural wave records are non-stationary. Therefore it is intuitive that the resulting spectrum will be dependent to some extent on the start point of the FFT within the record. The difference between number of recorded data (1320) and those chosen for analysis (1024) allowed different starting points. Starting points (ST) were chosen as follows

- a) ST = 0
- b) ST = 148
- c) ST = 296

Further two different FFT segment lengths were examined

- a) segment length - 1024 data points (1 segment), and averaging over 4 adjacent frequencies which gave a frequency interval of 0.0078 Hz, 8 degrees of freedom and 0.46-3.6 as the lower and upper 95% confidence limits
- b) segment length - 512 data points (3 segments), and averaging over 2 adjacent frequencies which again gives a frequency interval of 0.0078 Hz, but in this case, 12 degrees of freedom and 0.5-2.75 as the lower and upper 95% confidence limits

The data measured in the front of the breakwater showed more spatial and time variation than the data measured on the beach, which may be due to the presence of reflection. The influence of the same parameters on the spectral analysis results for IWCM data, measured on the beach, were tested as follows:

- a) segment length - 2048 data points (1 segment), and averaging over 12 adjacent frequencies which gives a frequency interval of 0.0234 Hz, 24 degrees of freedom 0.6-1.9 as the lower and upper 95% confidence limits

---

<sup>3</sup> Only 2<sup>n</sup> data are considered for the FFT analysis. Thus in case when number of points differ from 2<sup>n</sup>, the different starting point can be chosen.

b) segment length - 1024 data points (3 segments), and averaging over 6 adjacent frequencies which again gives frequency interval of 0.0234 Hz, but in this case, 36 degrees of freedom and 0.65-1.7 as the lower and upper 95% confidence limits

#### *Comparison of different windows*

The results obtained after the applications of the triangular and cosine bell window were compared. The starting point and the number of segments were kept constant. The comparison was performed for data collected in the front of the breakwater and on the beach. The total energy is 1.2 - 1.6 times lower when the cosine bell window without normalisation was applied and about 3 times lower when the triangular window without normalisation was applied. The bigger discrepancies were noticed for the data measured near the breakwater. This highlighted a necessary normalisation or unwinding procedure. When the results were normalised by ratio  $V/m_0$ , the differences were not significant. It can be concluded that both windows can be applied when the data are normalised<sup>4</sup> as it is shown in Figures 4.4 and 4.5.

#### *Comparison of different starting points*

The influence of the choice of starting point for both sets of data measured near the breakwater and on the beach was also investigated. From Figures 4.6 and 4.7, it can be seen that for the data measured near the breakwater, the choice of the starting point has an influence on the energy distribution over frequencies and on the energy magnitudes for both applied windows. Whereas, the shifting of the starting points applied on the data measured on the beach caused only slight changes. Thus, the choice of the starting point has a larger influence on the data measured near the breakwater than measured on the beach. This can be explained by the presence of reflection near the breakwater which caused larger variations in the wave excursion time histories.

#### *Comparison of different number of segments for the Fast Fourier Transform Method*

As was expected, a different number of segments for spectral analysis cause a change in the energy distribution for both data sets. The energy spectra become smoother for larger number of segments of FFT.

---

<sup>4</sup> It is well known that when a window is applied the data needs to be normalised.

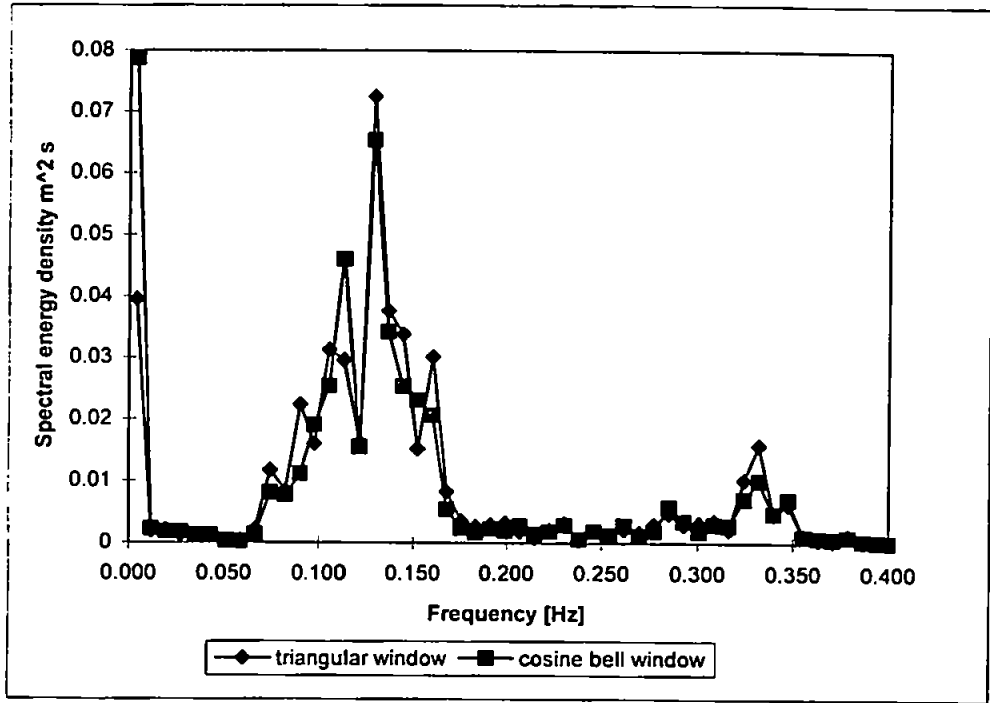


**Figure 4.4** Comparison of spectral energy normalised results obtained using cosine bell and triangular window (data measured near the breakwater)

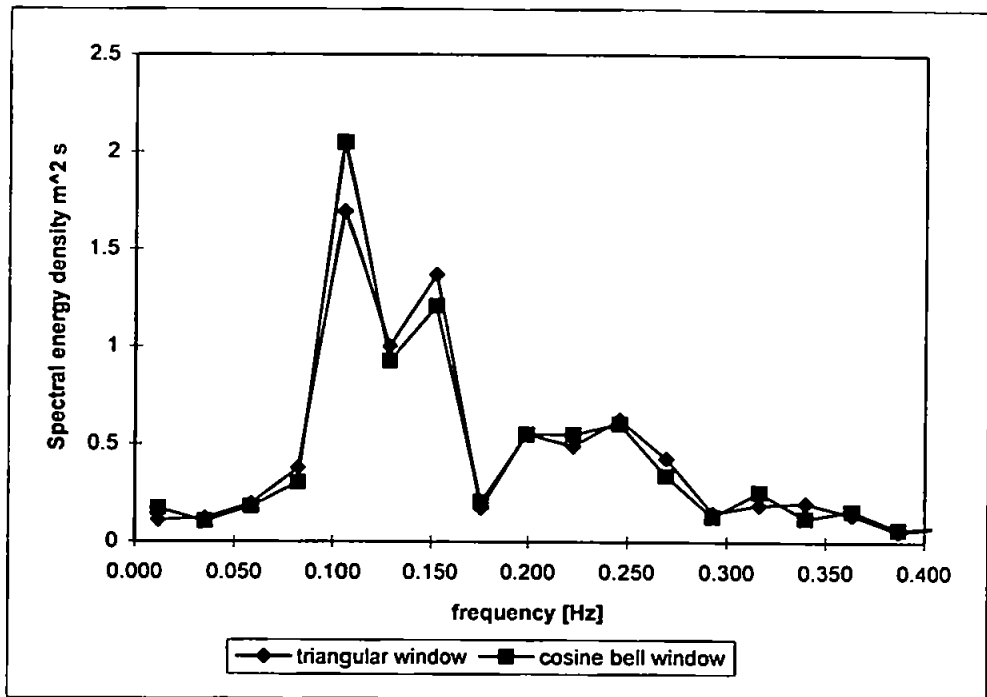


**Figure 4.5** Comparison of spectral energy normalised results obtained using cosine bell and triangular window (data measured on the beach, notice smoothing)

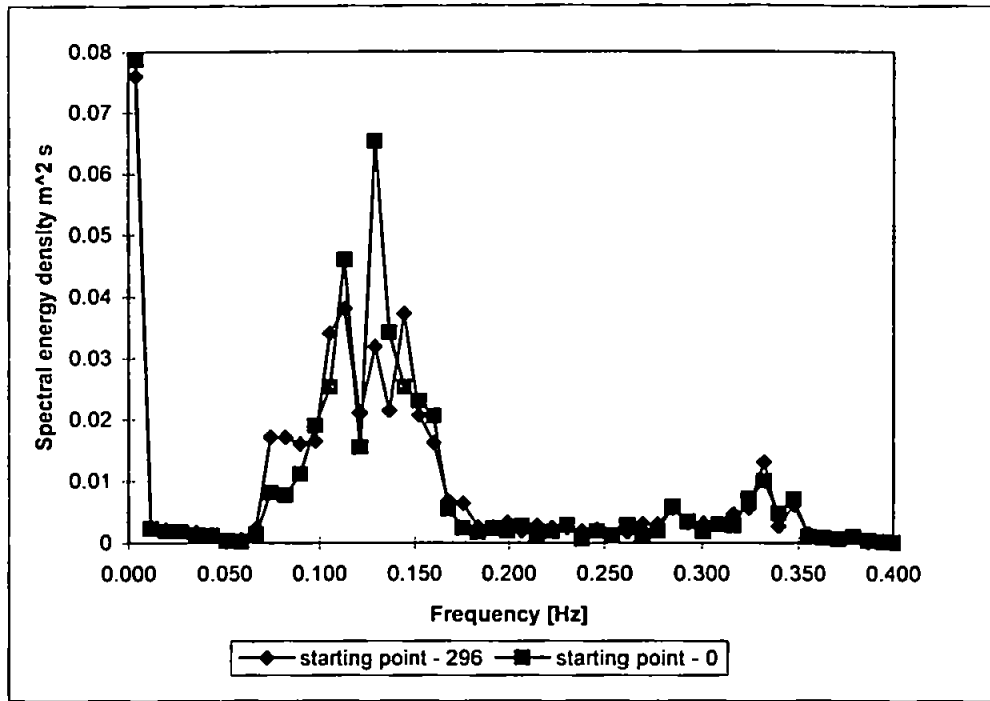


**Figure 4.6** Comparison of spectral energy normalised results obtained using cosine bell window - starting points 0; 148; 296 (data measured near the breakwater)

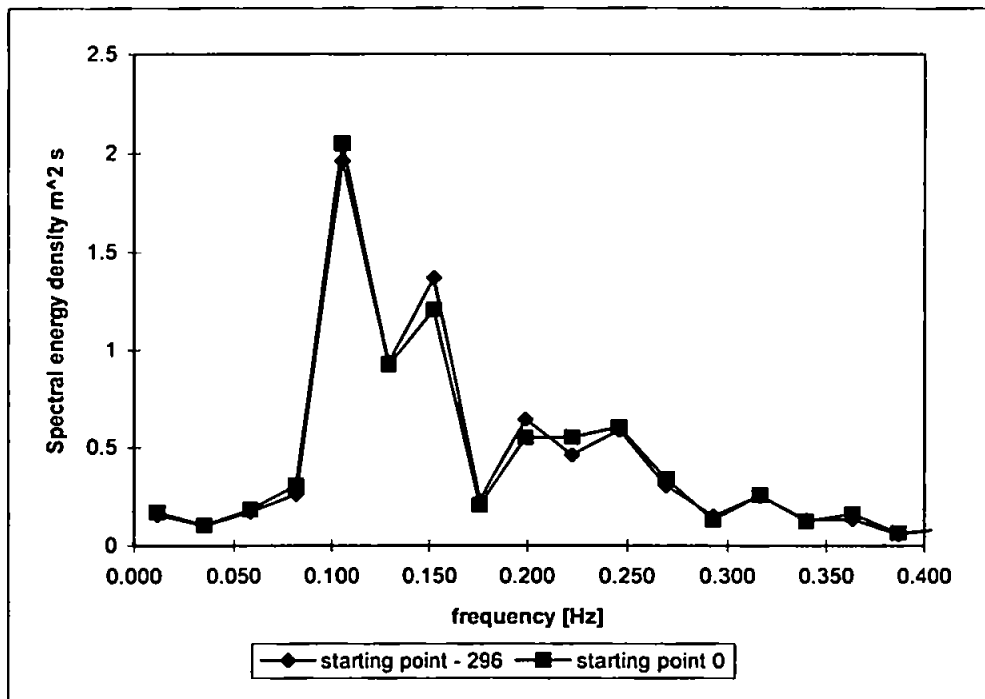


**Figure 4.7** Comparison of spectral energy normalised results obtained using cosine bell window - starting points 0; 148; 296 (data measured on the beach)

At the same time, the degrees of freedom are increasing and hence the confidence levels. There is a lower limit to the segment size of a record and therefore the number of segments into which a record may be split. This is of course governed by the maximum bandwidth of a frequency bin that is permissible in the spectral estimate, and additionally by the lowest energetic frequency present in the spectrum. However, the WRS (near the breakwater) results were additionally averaged over four and two adjacent frequency bins for 1 FFT and 3 FFT segments respectively. The IWCM (on the beach) results were averaged over twelve and six adjacent frequency bins for 1 FFT and 3 FFT respectively. Thus the frequency intervals remained the same and confidence levels increased for larger number of segments. The results are plotted in Figures 4.8 and 4.9. The changes in spectral energy distribution can be observed from both figures. Thus the combination of ensemble averaging and frequency averaging can produce different results which effects the directional wave analysis.

Even though the same detrending routine was applied for the data measured near the breakwater and on the beach, the presence of low frequency energy can be observed for the data measured near the breakwater (Figures 4.4, 4.6 and 4.8). This was possibly due to the method for transferring pressure to surface elevation records.

Both spectral analysis techniques with varying, windowing technique, starting point of analysis and number of segments for FFT, were applied on one data file measured in the front of the breakwater and examined. The observed result difference might be related to the different smoothing technique or to different cut off frequencies in both programs. As it was expected, the difference disappears with the normalisation. Details are given in Ilic (1993).

The analysis and comparisons of the results obtained by two different analysis techniques opened some additional questions such as which data points should be included in the analysis or where to start with the data windows and which window gives more accurate results. The method of analyses (i.e. window function and spectral smoothing technique used) has an effect on the form of the resulting spectrum. This seems to be particularly true in reflective wave fields.

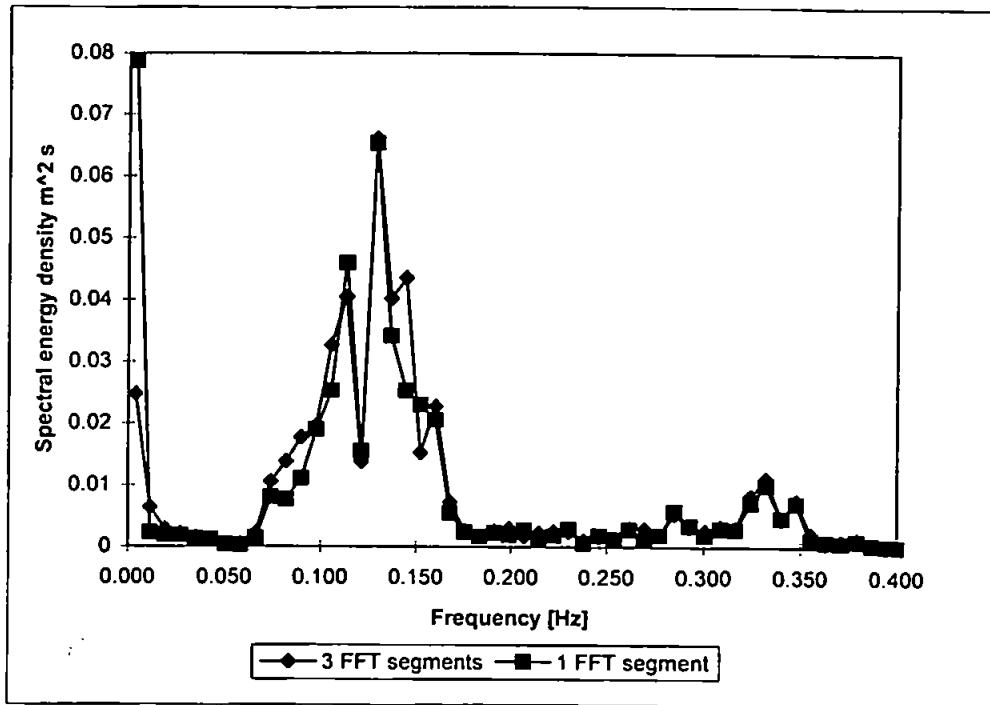


**Figure 4.8** Comparison of spectral energy normalised results obtained using triangular window - 1 and 3 FFT segments (data measured near the breakwater)

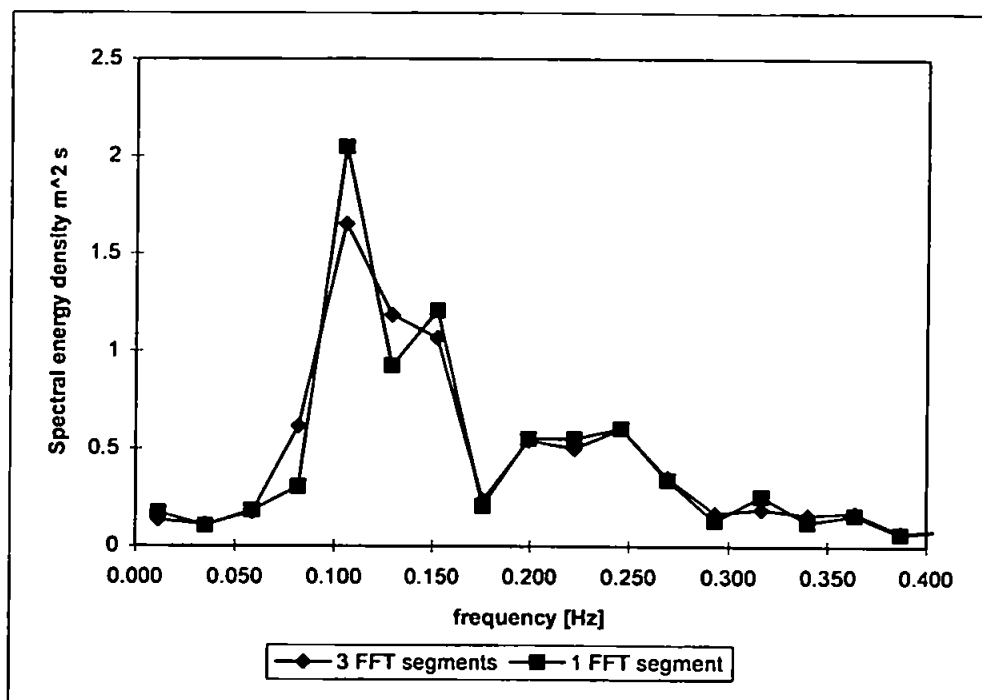


**Figure 4.9** Comparison of spectral energy normalised results obtained using triangular window - 1 and 3 FFT segments (data measured on the beach)

## Recommendation

One recommendation can be given on the basis of the presented analysis. A full triangular window applied across the whole record will waste too much data. Many of the alternative 10% windows (e.g. cosine bell) however, exhibit poor leakage characteristics. Since, the selection of an appropriate window is a subtle 'trade-off' between making the central frequency as narrow as possible and minimising leakage to side-lobes. Thus, the full data windows are recommended as optimal data windows (for e.g. Hanning). For more details see Harris (1978).

Peridiogram estimates must be normalised in accordance with the type of window functions used. There are two possible approaches:

- Normalise the peridiogram estimate with the variance of the record computed in the time domain (Parseval's Theorem).
- Compute the theoretical normalisation factor using the following expression for the window squared and summed (Press *et al*, 1986)

$$W_{ss} = N \sum_{i=1}^{i=N} w_i^2 \quad (4.10)$$

Where  $w$  is the time domain window function. Note that this reduces to  $N^2$  for no window (box-car window). The total variance is then given by

$$\sigma = \frac{2}{W_{ss}} \sum_{i=0}^{i=N/2} (\text{Re}_i^2 + \text{Im}_i^2) \quad (4.11)$$

The second technique may result in incorrect estimates in the total variance if the record is not perfectly stationary or if there is significant energy with periods of similar length to that of the data segment. It may be favourable therefore to adopt the first method in the future for normalisation of spectra. However the first method might lead to problems in directional analysis and prediction of reflection coefficients.

It would be appropriate to composite a unique spectral routine for IWCM and WRS devices taking the mentioned recommendations in account.



## 4.2.4 Measurements comparison

The compatibility of the spectral results for two measurement systems will not only depend on the spectral analysis routine but also on differences between measured data. Therefore a comparison of the two measurements systems (WRS, IWCM) was undertaken prior to the main field deployment.

The deployment of the pressure transducers system at Felpham beach in spring 1993 (Axe and Bird, 1994) was used for the comparison exercise. One of the IWCM probes was deployed next to the most shoreward pressure transducer through June 1993. The data were recorded simultaneously. Visual observations of the sea level by video recorder and surveying were undertaken subsequently with data recording. Richard Brown and Philip Axe were responsible for these tasks. Plate 4.1 shows both devices during the Felpham field exercise. The measurement comparison also enabled a test of the new spectral analysis routine unique for both devices. Thus, this section will start with its description.

### 4.2.4.1 Spectral analysis

Davidson (1993) investigated the effect of different data windows and different smoothing on computation of wave spectra. In order to test the performance of the windows, a synthetic data set was produced (details are given in Davidson (1993)). Six different windows were examined including the; boxcar (no window), 10 % Cosine bell, Bartlett (triangular window), Hanning, Hamming and Blackman windows. This study concluded that either Bartlett, Hanning or Hamming window should be selected in order to minimise the side-lobe leakage.

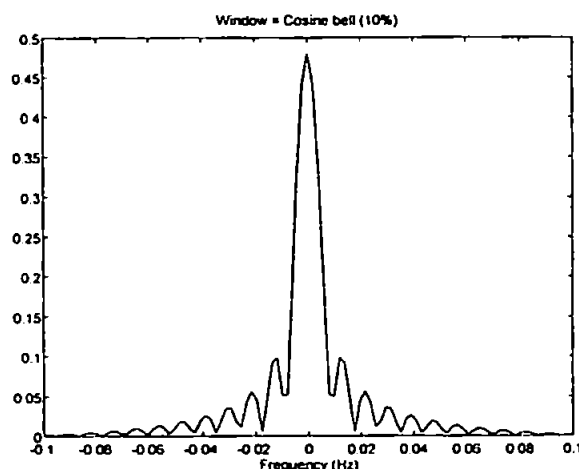


**Figure 4.10** The side effects of window from Davidson (1993)



**Plate 4.1** WRS and IWCM deployed at Felpham beach during June 1993

Three different smoothing techniques were compared in the same study. Ensemble averaging, frequency smoothing and the combination of both were taken in account. The combination of ensemble averaging and frequency smoothing produced the most satisfactory results. Those findings were implemented in a new spectral analysis routine for WRS data. The new program, **specopt4**, uses Matlab routines for the FFT (Davidson, 1993).

The new spectral analysis program **specopt4** were used to analyse data recorded by WRS and IWCM. To enable a detailed comparison, a cross-correlation analysis was performed using the cross-spectrum routines from the **specopt4** program.

Both surface elevation records contain the influence of tide level variation. To correct the

data, **specopt4** uses a linear detrending routine from MATLAB. It also provides analysis using different windows - cosine bell, Hanning and Welch with unwinding. Thus the calculated spectrum in **specopt4** is modified as follows:

$$S_{n'} = S_n \frac{I}{W_{ss}} \quad (4.12)$$

**Specopt4** were based on 1024 points and 3 FFT segments, chosen for both data sets (in this case every second point from the IWCM data set was chosen as it recorded at 4 Hz). Frequency smoothing which simply means addition, (not averaging) of spectral estimates from adjacent frequency bins was applied over six frequency bins for both data sets (6 x 2 Hz/512). This gives 36 degrees of freedom and 0.65-1.70 the lower and upper 95 % confidence limits for both data sets.

#### 4.2.4.2 Comparison

The comparison consisted of several steps, which are described, consecutively in the following paragraphs.

##### *Data logging*

The IWCM probe was deployed only for several days (from 09/06 to 18/06 1993) during the WRS deployment in Felpham in the spring of 1993. All together, fifteen readings were taken simultaneously with the pressure transducer readings. The WRS measurement cycle was three hourly and the sampling frequency was 2Hz. The IWCM measurement device operated simultaneously in those cycles with 4Hz sampling frequency. Visual observations of the surface levels were taken parallel with IWCM data logging on 11<sup>th</sup>, 14<sup>th</sup>, 15<sup>th</sup>, 17<sup>th</sup> and 18<sup>th</sup> of June 1993.

##### *Pressure to surface elevation transformation*

The pressure data were transformed to the water surface elevations using program **psurf\_b1** (Davidson, 1992) as described in section 4.2.2.

##### *Time series analysis*

Time series analysis was performed on the IWCM raw measured data and on WRS surface elevation data. For these analyses previously described program **diran4** (section 4.2.2) was

used. The calculated mean water depths were plotted and compared. Differences in the range from 5 to 18 cm were observed. There are at least two possible reasons for the difference to occur. There was no site device to measure atmospheric pressure. The variations in the atmospheric pressure were included in the transformation procedure. However the difference of 1mb in the pressure can cause 1-cm difference in the water level. Beside, the IWCM sensors are subject to a small drift in the zero voltage offsets, which is temperature dependent. However, the combination of both can increase the difference.

*IWCM mean water level and wave excursion*

The IWCM surface elevation time series were analysed. The minimum and maximum water levels were obtained and compared with visual observations. The calculated mean water depths (MWD) differed from the visually observed water levels. There was the possibility of an error in the visual readings. The video recording and surveying were taken from the shore. The distance and weather conditions could influence the accuracy of readings. This was supported by the fact that the readings, which were taken during a clear day, have the lowest difference. Taking this in account together with tidal effect and IWCM offset, the four data sets given in Table 4.1 were chosen for further analysis and comparison. The summary of analysis is given in Table 4.1.

<i>time</i>	<i>MWD</i>	<i>Hs</i>	<i>Diff1</i>	<i>Diff2</i>
11/06/1993 17h 26 min	3.55	0.33	0.11	0.18
18/06/1993 14h 26 min	1.06	0.35	0.11	0.08
18/06/1993 11h 26 min	3.38	0.74	0.02	0.17
14/06/1993 11h 26 min	0.82	0.42	0.17	0.14

**Table 4.1** In the first column the mean water depth (MWD) for IWCM data is given. *Hs* is calculated for IWCM data. *Diff1* is the difference between MWD and visual observation. *Diff2* is the difference between MWD for IWCM and MWD for WRS data.

The average difference between the IWCM measured mean water depth and the visual observation are smaller than the average difference between IWCM and WRS measured mean water level. However, the IWCM measured mean water level is an average 10 cm higher than the WRS measured water level.

### *Cross-correlation*

When the calculated excursions<sup>5</sup> for both devices were plotted, firstly a time lag was observed, secondly the amplitudes were slightly different because the wave excursion shapes differed from each other. The WRS data were filtered with a weighting function which is zero for frequencies higher than 0.33 to 0.4 (depending on the water depth). The use of such a filter smoothed and attenuated the wave excursion curves.

The first task was to find and define the time lag. The cross-correlation function was used to calculate the time difference between the two series. Time differences were in the range from a few seconds to some minutes. Thus the measured WRS and IWCM records (1320 and 2250 measured points respectively) were long enough to select a sufficient number of points which were collected at the same time, for further analysis.

### *Spectral analysis*

Figure 4.11 shows the difference in spectral energy density for the IWCM and WRS data measured at the same time and analysed using the same spectral analysis routine. Comparing the spectral energy density graphs for the IWCM and WRS data, there is a clear difference in the energy for frequencies higher than 0.4 Hz which was the cut off frequency in the filter technique used in the transformation of the data from pressure to surface levels.

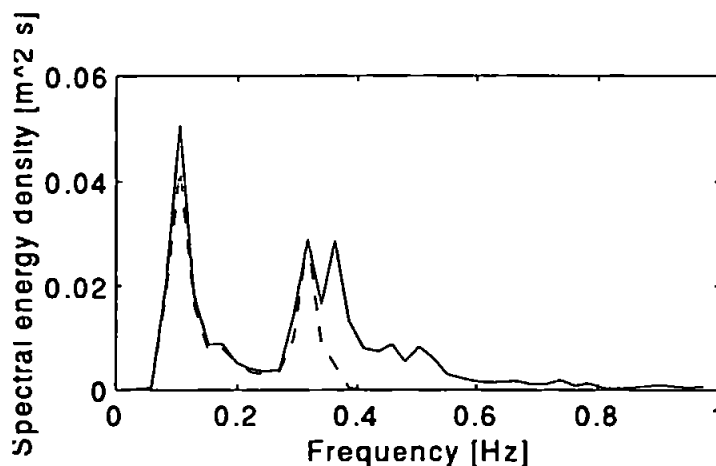


**Figure 4.11** The spectral energy density for IWCM and WRS data measured on 18/6/93 using MATLAB program `specopt4` with cosine bell window

---

<sup>5</sup> Obtained by `diran 4`.

The slight difference in the infragravity band can be caused by different treatment of the tidal influence in the `psurf` and `specopt4` programs or with the measurement devices themselves. Figure 4.12 shows the spectral energy density for WRS data and filtered (described later in this section) IWCM data. There is very small difference present.

The spectral energy density was then calculated using `specopt4` with different windows - cosine bell, Hanning and Welch, for IWCM and WRS data sets. Comparisons of the results showed no or minor differences using those three windows as are illustrated in Figure 4.13. Also, the sum of spectral energy density varies only slightly as a function of the windowing technique.

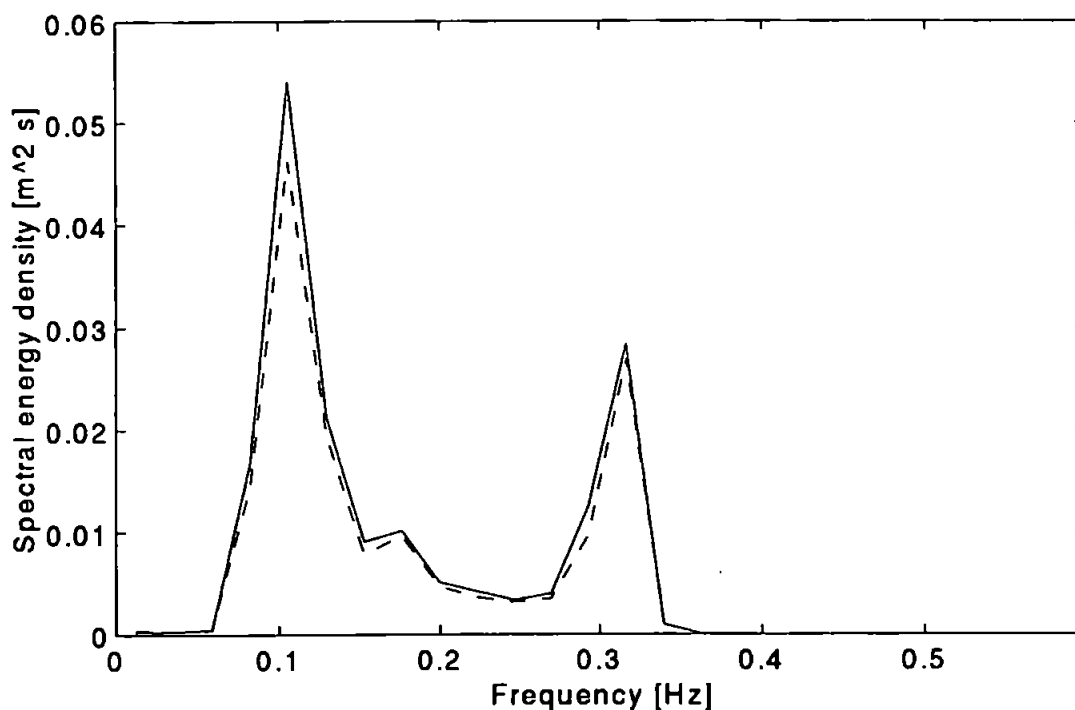


**Figure 4.12** The spectral energy density for filtered IWCM and WRS data measured on 18/6/93 using MATLAB program `specopt4` with cosine bell window

The spectral energy densities in the gravity band (frequencies greater than 0.05 Hz) for IWCM and WRS data were compared. For the spectra with clearly defined peak (e.g. swell spectra with peak frequency  $\sim 0.1$ ), there is small difference (13 - 15 %) in the sum of the spectral energy density (SED) between the two data sets. For broad spectra, there is a larger

difference in SED between the two data sets (40%)<sup>6</sup>. However, the time series variances were calculated for unfiltered IWCM data and for filtered WRS data. Thus the differences indicate the energy contained in frequencies greater than 0.33 Hz.

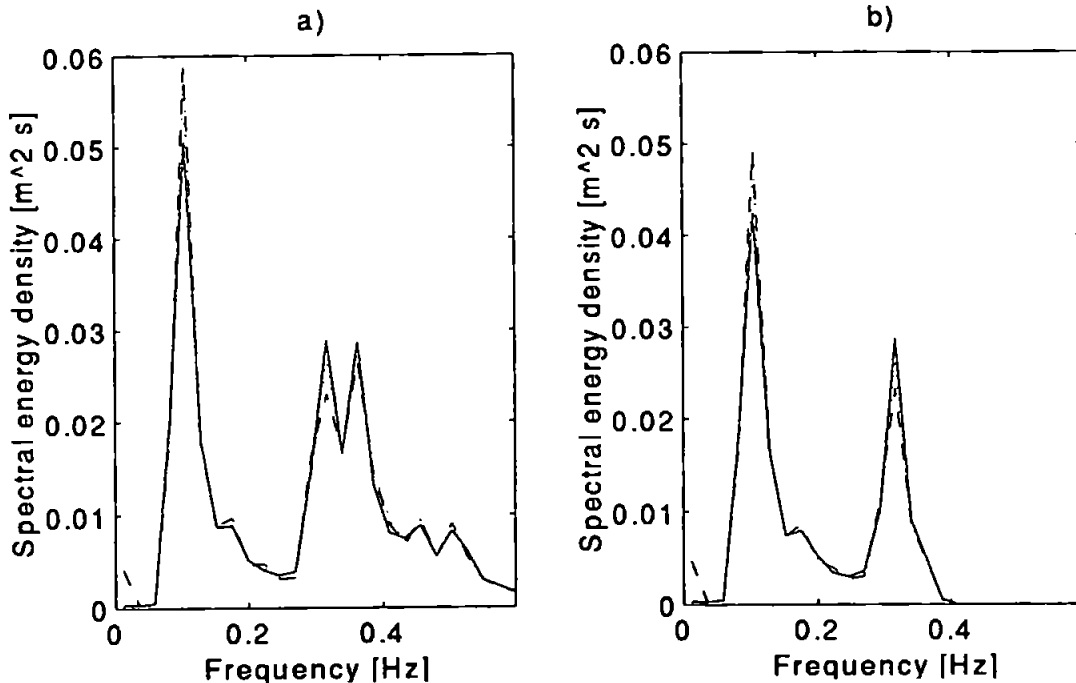


**Figure 4.13** Spectral energy density results for IWCM and WRS data recorded on 11/06/93, using *specopt4* and Hanning (---), Welch (· · ·) and cosine bell windows (—)

#### *Cross-spectrum analysis between two measurements*

Coherence, transfer function or amplification function and phase lag were calculated from the cross-spectrum between two measured surface elevation series, performed by *specopt4*. This is illustrated in Figure 4.14. It was evident that within the gravity band 0.05 - 0.33Hz, the value of coherence is very high and almost equal to 1, and it drops slightly in the infragravity band. The value of transfer function or amplification factor is also around 1 but varies more than coherence, and its range is from 0.9 to 1.3 for the different data sets. The phase difference is less than  $\pi$  or higher than  $-\pi$  in the gravity interval. From the phase lag the time delay was calculated. The time delay is less than  $\pm 0.2$  sec what is acceptable, as the measuring time intervals were 0.25 and 0.5 sec. This indicates that the data are highly correlated.

<sup>6</sup> This high difference occurs for the data when the most energy is present in higher frequencies, thus is influenced by cut off frequency

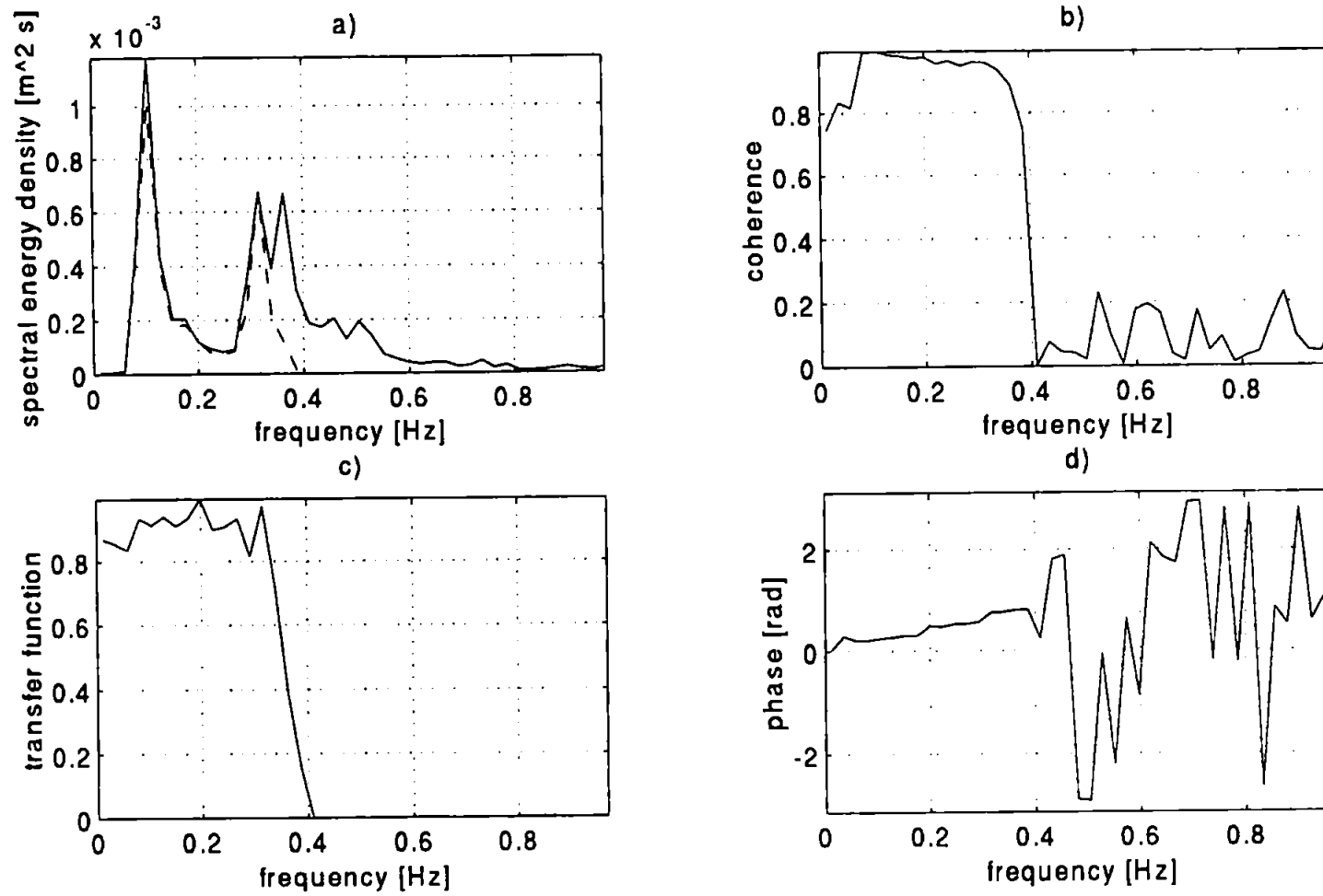


**Figure 4.14** Cross-spectral analysis results for IWCM and WRS data recorded on 11/06/93 at 17.26, using `specopt4` program; a) cross-spectrum, b) coherence, c) transfer function, d) phase



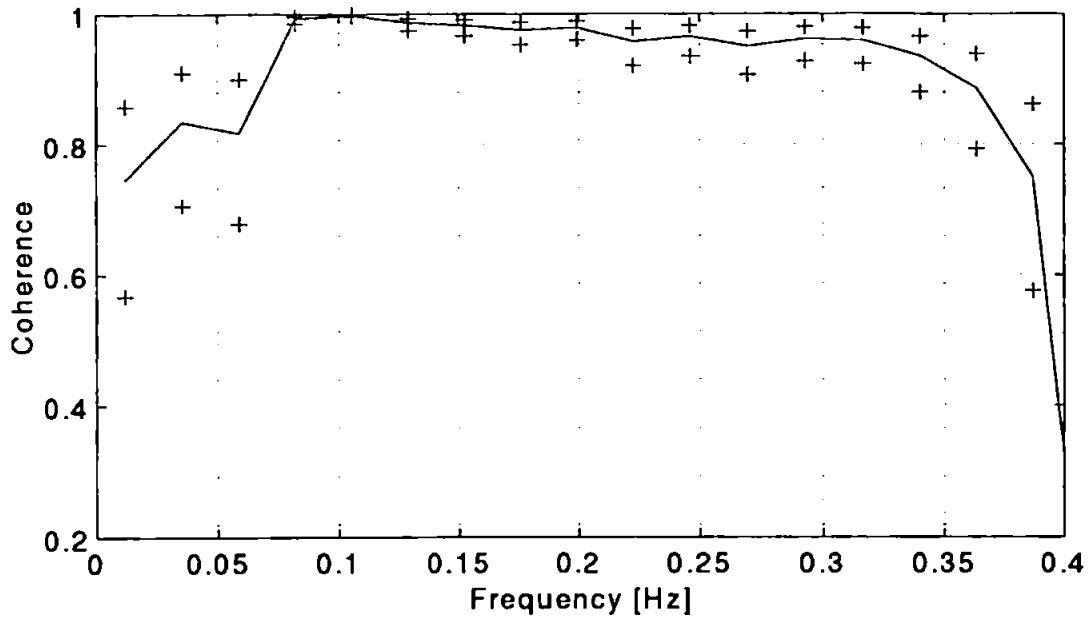


**Figure 4.15** The coherence confidence intervals for IWCM and WRS data measured on 11/6/93

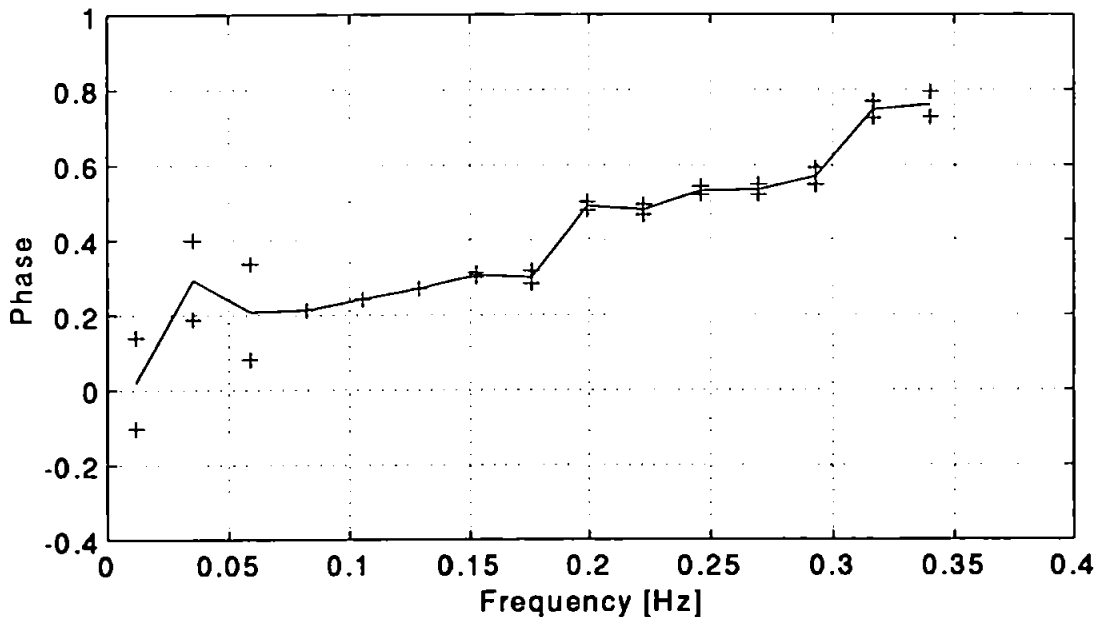


**Figure 4.16** The phase confidence intervals for IWCM and WRS data measured on 11/6/93

The confidence intervals for smoothed coherence and phase were calculated (Appendix E) as illustrated in Figures 4.15 and 4.16. The confidence intervals were calculated with 36 degrees of freedom. The coherence confidence intervals are significantly different than the zero coherence upper limit confidence interval, which is 0.162, calculated by following

equation:

$$c^2 = 1 - \frac{\alpha^2}{n-2} \quad (4.13)$$

where  $n$  is number of degrees of freedom and  $\alpha = 0.05$  for 95% level.

The confidence limits are uniformly distributed with frequency. However, there are significant differences between confidence limits for infragravity and gravity band<sup>7</sup>. The small difference between lower and upper confidence limits show that the calculated coherence and phases are most likely very close to the real values. From Figure 4.16 it can also be seen that the phase is almost linearly dependent on frequency which produces a constant time delay.

#### *Data filtering*

To try to define how different the spectral results are in the gravity band both data sets were filtered using a sharp weighting function. The cut off frequency was 0.33 Hz for both data. Wave excursions for both filtered data sets as shown in Figure 4.17, had the same shape and amplitude. The energy density spectra for filtered data coincide with each other (Figure 4.12). Whereas, coherence and transfer function values differ from 1. Phase difference results show quite a lot of disturbances. It can be concluded that filtering interfered the high correlation between data sets and the value of correlation significantly decreased. The complete analysis is given in Ilic (1994).

#### **4.2.4.3 Conclusion**

It may be concluded that the measured data from the two different devices are highly correlated and coherent. The influence of different windows using unwinding or normalisation technique, on the spectral energy density results has been shown to be very small. The observed differences in the time series analysis and in the spectral analysis can be attributed to analysis methods rather than to the measurements. However, given that the two devices produce equivalent measurements, it is still necessary to use the same analysis procedures for both devices.

---

<sup>7</sup> After Kinsman (1965), the infragravity band applies to wave periods between 5 min and 30 s (for frequencies between 0.00333 Hz and 0.0333 Hz) and the gravity band to wave periods between 30s and 1s (for frequencies between 0.0333 Hz and 1 Hz).

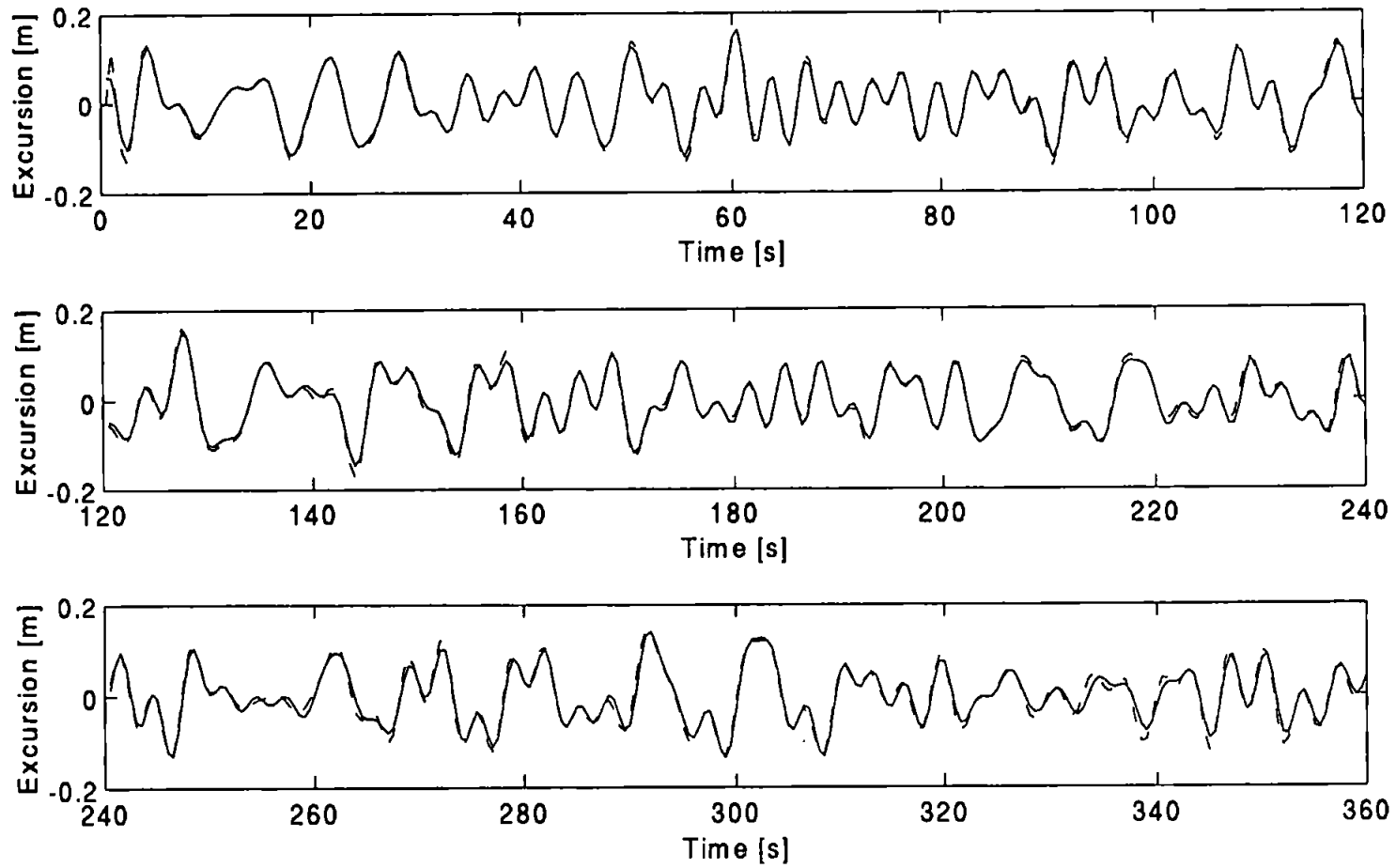


**Figure 4.17** Wave excursions for filtered IWCM and WRS data recorded on 14/06/93

## 4.3 Uniform data processing routine

### *Spectral analysis*

The measurements and data processing comparisons summarised in sections 4.2.2 and 4.2.3 showed a need for a uniform set of spectral analysis routines for offshore and inshore wave data. This would enable a direct comparison of results. Conclusions from section 4.2.3 resulted in creating a new MATLAB<sup>TM</sup> spectral analysis routine, which consists of the following items:

1. Detrending of instantaneous depth to produce instantaneous excursion using Goda's (1985) second order polynomial method to discard tidal effect
2. Spectral analysis using Welch (full) window<sup>8</sup>, ensemble-averaging with 50% overlap and frequency smoothing over two frequency intervals. It was proposed to use adjustable overlap for the WRS to enable the whole-recorded data set to be used. This yields 16 and 28 degrees of freedom for WRS and IWCM data respectively. The lower and upper 95% confidence limits are 0.55-2.3 and 0.62-1.8 of the calculated value for WRS and IWCM respectively.
3. Statistical analysis in accordance with IAHR proposal (Darras, 1987) to calculate spectral parameters in frequency band from 0.05Hz to the chosen cut off frequency.

### *Directional analysis*

The preliminary analysis showed that at the measurement positions, offshore (500 m from the breakwaters) and inshore in the lee of the breakwater, there will not be any phase-locked wave components. Therefore, non-phase locking methods were considered for the directional analysis. Considering the number of data sets to be processed, the accuracy and advantages of different NPL methods given in Chapter 2, the MLM has been chosen as the most suitable method. A summary of the data processing routine using the MATLAB package is given in Figure 4.18.

It should be noted that spectral and directional analyses rely on the application of linear wave theory. In shallow water, significant wave non-linearities arise which might be expected to invalidate the results. In particular, waveforms become asymmetric which

---

<sup>8</sup> Also, cosine bell, Hanning, Hamming, Bartlett, triangular windows were included.

when transformed into the frequency domain produce harmonics in the frequency spectra.

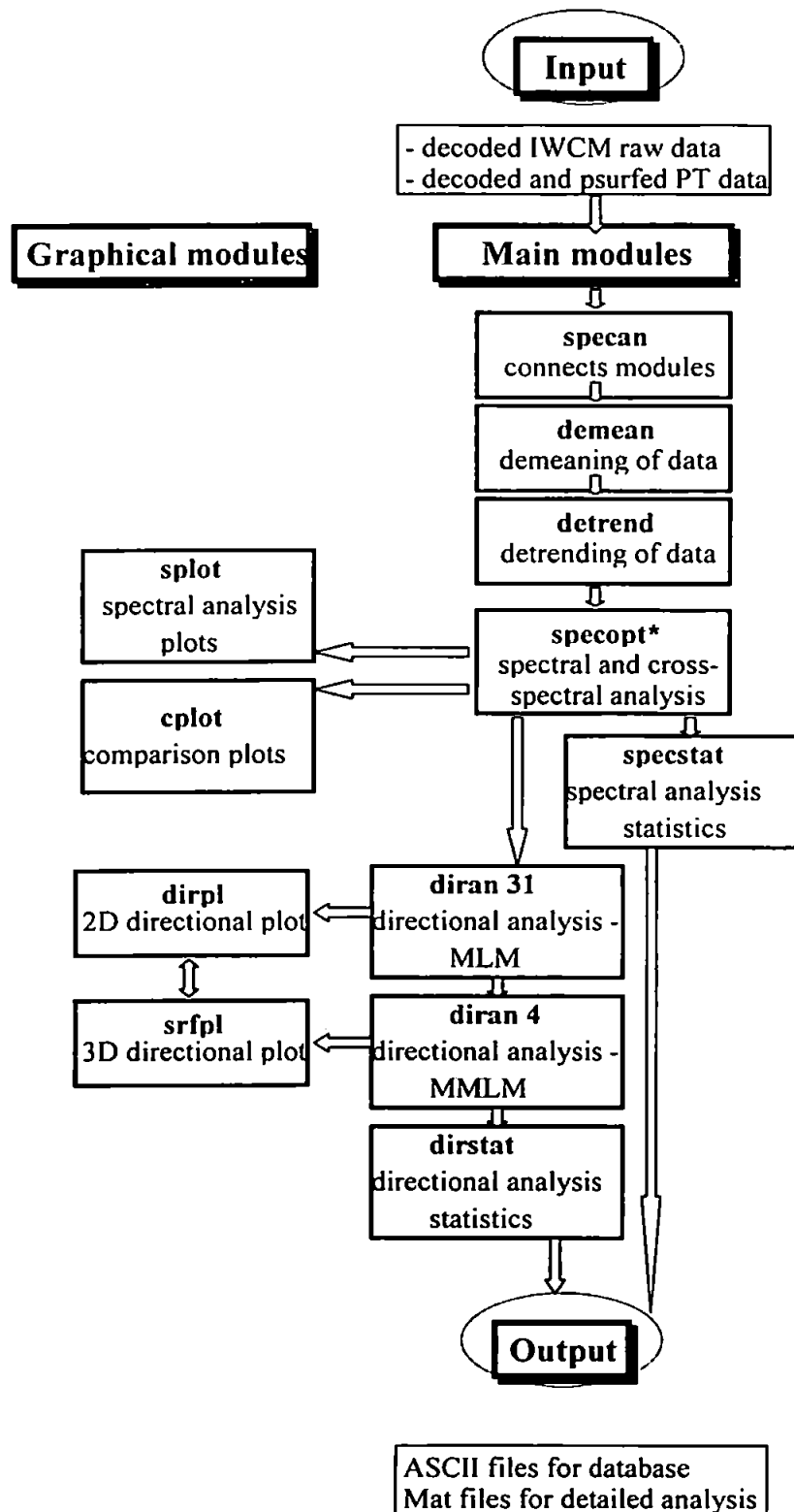


**Figure 4.18** The scheme of new spectral and directional program

Guza and Thornton (1980) who analysed the field data from the Torrey Pines Beach, San Diego, investigated this phenomenon. They concluded, however, that using linear theory produced errors of less than 20% in calculating total variance and energy density in a particular frequency band both inside and outside the surf zone, except in the immediate vicinity of the breakpoint.

This offers some reassurance that the application of linear theory to shoreline measurements will still produce realistic results with the possible exception of when measurements are taken at the initial wave breakpoint.

## 4.4 Wave data summary

### 4.4.1 Processing and archiving of wave data

A large amount of data were collected and processed during the measurement programme, which are summarised in Table 4.2. The IWCM data were originally compressed and stored on diskettes. The compressed WRS data were retrieved on diskettes and then stored on tape. Subsequently, the results from the wave data analysis were stored in the spreadsheet package EXCEL, enabling additional analyses of these results. This approach enables easier manipulation of the data, including comparisons between data and results collected at different locations recorded at the same time.

<i>Deployment period</i>	<i>Location</i>	<i>Equipment</i>	<i>No of records collected</i>
June-Aug 1992	Seaward of breakwater 4	WRS 2	586
June-Aug 1992	Inshore of breakwater 3	IWCM	296
Sept 1993-Jan 1995	Offshore	WRS 2	2,776
Oct 1993-Dec 1994	Inshore of breakwaters 3 and 4	IWCM and Satellites	1,550
Feb - Apr 1994 <sup>9</sup>	Seaward of breakwater 4	WRS 1	364

**Table 4.2** Field data and database summary

<sup>9</sup> Directly seaward of one breakwater, another WRS was deployed between February and April 1994 for the reflection studies.

#### 4.4.2 Spectral and directional analysis of wave data

All records were processed using spectral and directional analysis. The basic statistics were computed in accordance with IAHR guidelines (Darras, 1987) which give the following parameters for each record: mean water depth (MWD) (m); signal variance ( $\sigma^2$ ) ( $m^2$ ); spectral moments  $m_0$  to  $m_4$  ( $m^2/s^n$  where  $n$  is from 0 to 4) from which various spectral wave parameters have been derived including spectral significant wave height  $H_{m0}$  (m), peak frequency  $f_p$  (Hz), average periods  $T_{01}$  (s) and  $T_{02}$  (s), spectral peakedness and width parameters -  $Q_p$ ,  $e_2$ ,  $e_4$ ; principal wave direction  $\theta_p$  (degrees); incident and reflected spectral moments -  $m_{0,i}$ ,  $m_{0,r}$  ( $m^2$ ) and incident and reflected spectral significant wave heights -  $H_{m0,i}$  and  $H_{m0,r}$  (m); reflection coefficient  $K_r$ - breakwater position only.

#### 4.4.3 Summary of results contained within the database

Once the database was formed, some basic analysis of recorded and processed data were made. Here, only a brief summary is given which then can be used as a guideline for the selection of the data for the computational model validation or design purposes.

##### Mean water depth (MWD)

Figure 4.19 shows a comparison of the mean water depths for the offshore pressure transducers and the following IWCM poles, sensor 6 - in the gap between breakwaters 3 and 4, sensor 5 - part of the star array shoreward of breakwater 3, sensor 1 - directly shoreward of sensor 6, during 6 days in October 1994 (see Figure 3.2). The full set of graph show a maximum mean water depth of 8.3 metres offshore and 4.5m between the two breakwaters recorded in early April 1994. Minimum mean water depth recorded offshore was 2.1 metres. The water depth in the lee of the breakwater was about 3m for the high tide and about 1.5 m for intertidal measurements<sup>10</sup>. For the linear wave propagation validation only the data collected during high tide will be considered.

##### Spectral energy ( $m_0$ )

The maximum energy recorded offshore was  $0.55 m^2$ . The corresponding energy recorded in the breakwater gap was  $0.34 m^2$ , while in the breakwater lee it was  $0.09 m^2$ .

---

<sup>10</sup> Assuming a period of 10 sec, the ratio between water depth and deep water wave length for 3 m water depth is 0.019 and for 1.5 m water depth is 0.0096 which is less than 0.01.

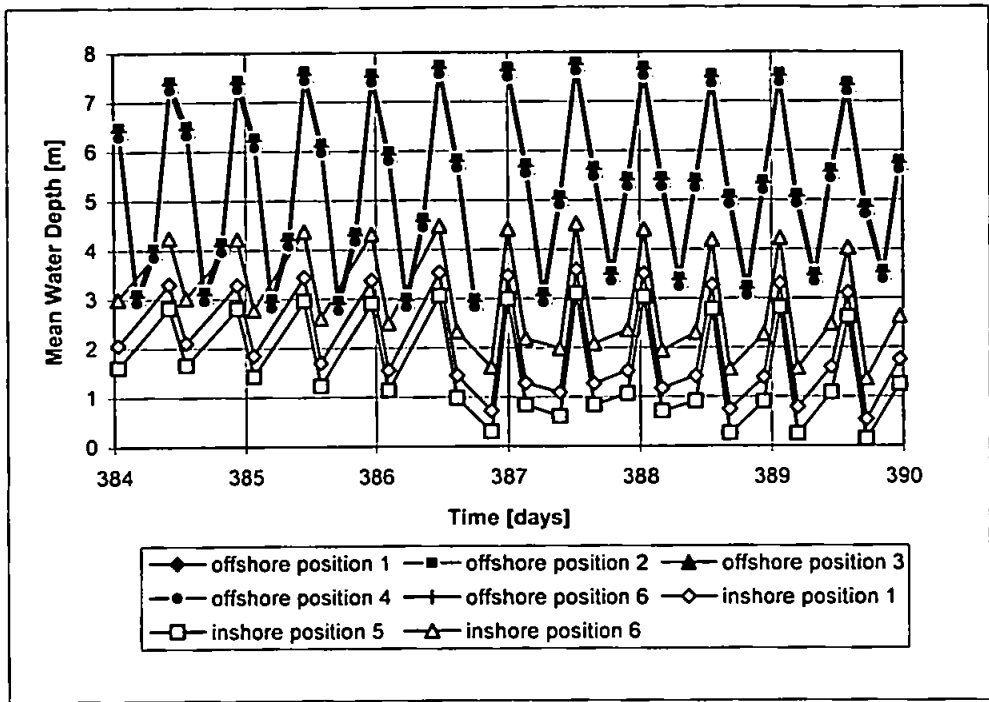


Figure 4.19 Mean water depths offshore and inshore during October 1994. For locations refer to Figures 3.2, 3.3b and 3.4b

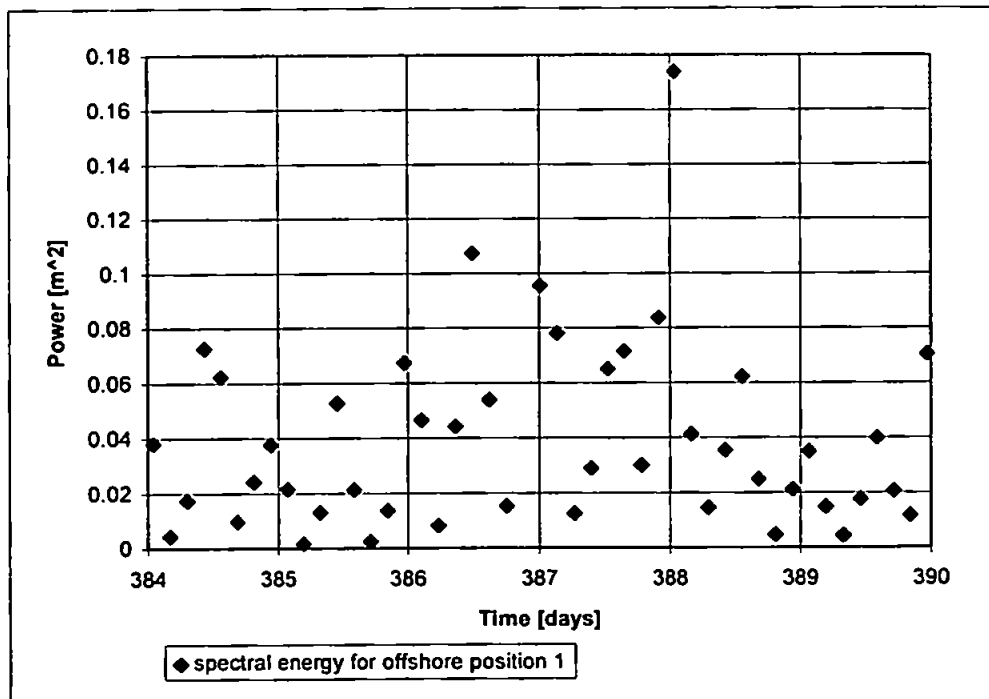


Figure 4.20 Spectral energy offshore during the October 1994



Thus, the energy measured offshore was reduced six times in the lee of the breakwaters. Large storm events occurred in December 1993 and in March, April, June and December 1994. Figure 4.20 shows spectral energy recorded at channel 1 offshore during six days in October 1994.

### **Significant wave height ( $H_{m0}$ )**

The maximum significant wave height recorded offshore was 2.85 m. The corresponding wave height between the two breakwaters was 2.32 m, and in the lee of the breakwater was 0.45 m. The reduction in wave height between the two breakwaters, when compared with the offshore wave height ranges between 6 and 35%. Wave height in the lee of the breakwater is 38-75% of that recorded offshore. This however depends on incoming wave direction, mean water depth and frequency, thus also wave breaking. Figure 4.21 shows a comparison of the spectral significant wave height measured offshore and inshore at the positions in the gap and shoreward of the gap during October 1994.

### **Peak Period ( $T_p$ )**

A wide range of peak wave periods (2 to 20 seconds) was recorded. Large numbers of events had peak period of about 10 seconds (about 10% in the water depth higher than 5.8 m). Higher wave periods were associated with swell waves. The largest storm event which was recorded in April 1994 had a peak period of 10 s. There is an evidence of a change in the spectral peak period as the wave propagate inshore which is illustrated in Figure 4.22. Figure 4.22 also shows the wide range of wave periods recorded both offshore and inshore in October 1994. The change of peak period in the lee of the breakwater can be associated with diffraction (Goda, 1985). However there is a possibility of non-linear processes in the gap which might change the peak period and this could be further investigated.

### **Significant wave height versus mean water depth ( $H_{m0}$ versus MWD)**

Figure 4.23 shows graphs of significant wave height plotted against mean water depth. The limiting ratio of 0.33 between significant wave height and mean water depth offshore indicates that no depth-limited waves were recorded at this position. In between the breakwaters, the wave heights are limited to 0.53 of the mean water depth. At this point, the waves became depth limited on a large number of occasions, and the gap between breakwaters lay within the surf zone, thus in those the processes can not be explained by linear theory.

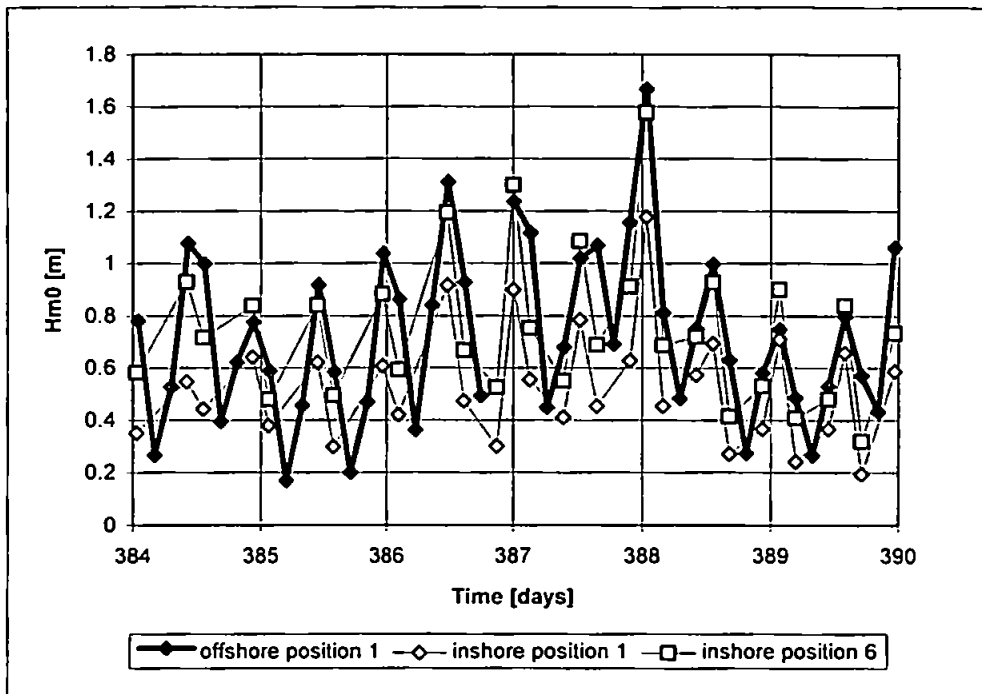


Figure 4.21 Comparison of spectral significant wave heights offshore and inshore in October 1994

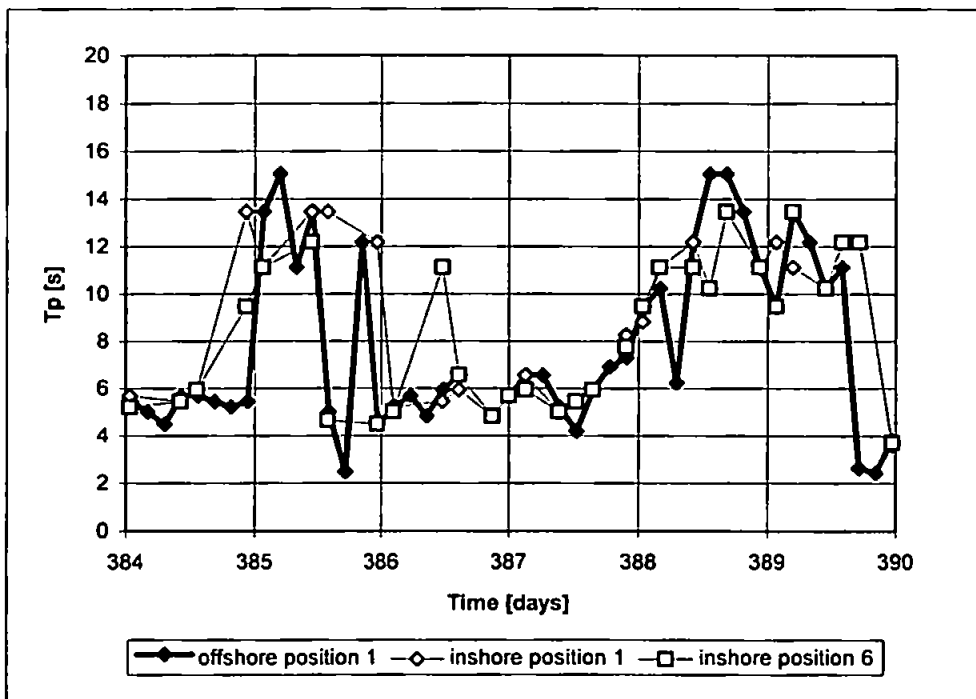


Figure 4.22 Comparison of wave periods offshore and inshore in October 1994

### **Principal Wave direction ( $\theta_p$ )**

Principal wave directions recorded offshore during the field programme varied from  $-60^\circ$  (Southeast) to  $-104^\circ$  (Southwest). Nearly 50% of the waves comes from south ( $-90^\circ$  or shore normal direction), which indicates that the waves approaching the shore are already refracted. Also, as mentioned in Chapter 3, the Island of Wight protects the shore from most westward approaches. Behind breakwater 3 (see Figure 3.2) in the wave diffraction zone, waves from  $-40^\circ$  to  $-100^\circ$  were recorded. Refraction-diffraction processes cause the difference in the principal direction. Figure 4.24 shows the comparison of the recorded wave directions during October 1994 for offshore and inshore positions.

### **Additional analysis**

Once the database was formed by the author, it allowed additional analysis. An example is additional statistical analysis which were performed by Philip Axe (see Chadwick *et al*, 1997) for the beach evolution study. Here only a brief summary of this statistical analysis will be given. More details can be found in Chadwick *et al*, 1997.

### *Histogram of wave height and direction*

A complete histogram of wave directions (referred to compass bearings) is shown in Figure 4.25. For each directional increment ( $12^\circ$ ), the percentage of occurrence of waves in class intervals of 0.5 m is given, derived from the offshore measurements during the period February 1994 to January 1995. Nearly 50% of the waves came from due south which also contained all waves greater than 2 m. The other two most frequent directions are only  $12^\circ$  east or west from the beach normal direction. Thus for the numerical model validation, these lattermost directions need to be considered. The data used to compose this figure is particularly valuable for future coastal evolution studies as it contains a complete year of directional wave data.

### *Wave height/period scatter plot*

A scatter plot of wave height/wave period is shown in Figure 4.26, which also provides lines of equal wave steepness, number of occurrences of particular wave height and period and a contouring of the number of occurrences. Only 21% of the data have a wave height above 1.0m. The most frequent waves have 5-7s period. Thus during the measurement period of a year, the most frequent were low energy wind waves.

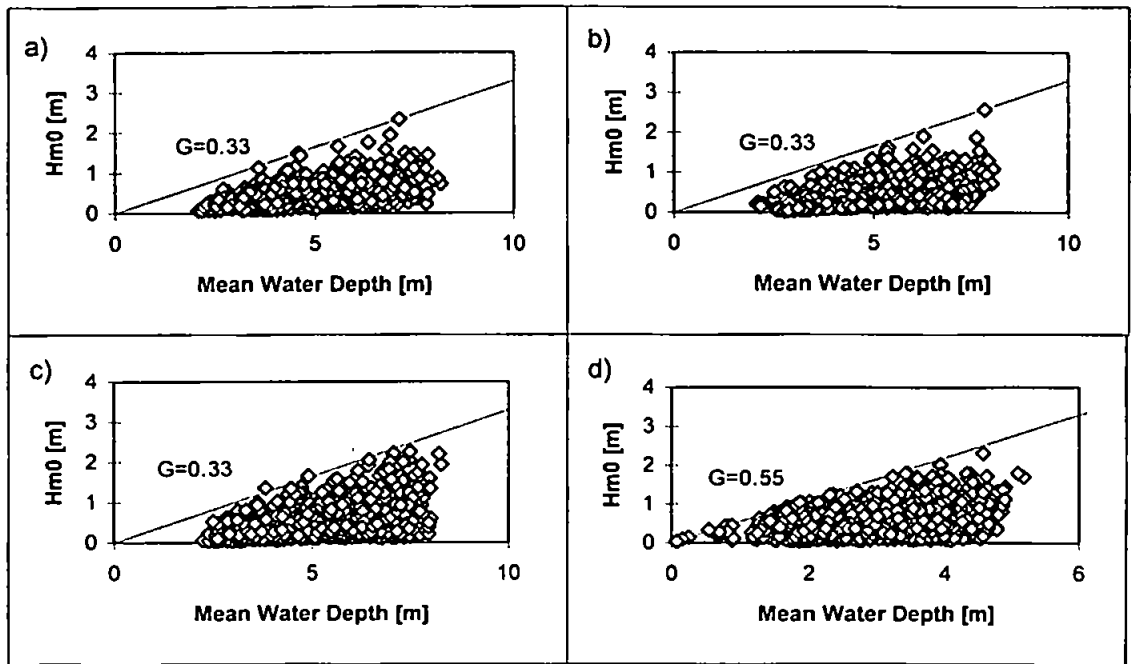


**Figure 4.23** Significant wave heights plotted against mean water depths-for channel 1 offshore: a) during deployment 9; b) during deployment B; c) during deployment D (see section 3.4.1) and d) for channel 6 inshore (in the gap between two breakwaters)

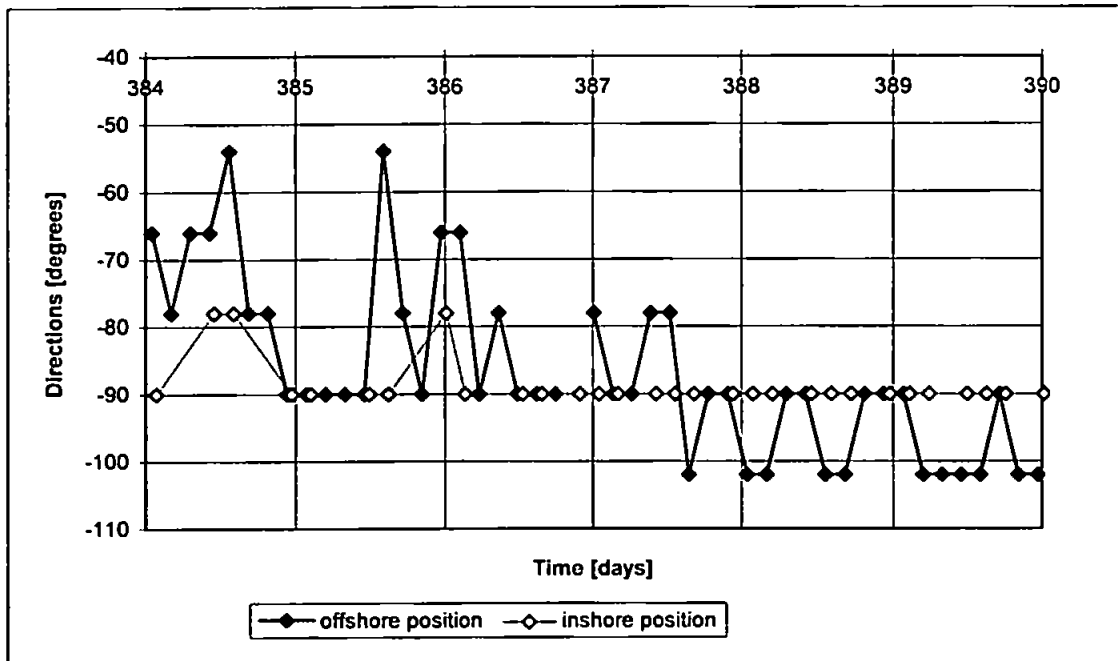


**Figure 4.24** Comparison of wave direction offshore and inshore

However this figure clearly shows the existence of some large period swell waves which cannot have been generated in the English Channel due to the short fetch, which need to be taken in account in beach evolution or for design purposes.

#### *Wave periods: comparison with HR data and seasonality*

Figure 4.27 shows a comparison of the relative occurrence of waves with peak period lying between 4 and 20 seconds as supplied to Arun District Council for their "Contractors' Guide" by HR Wallingford (1994). This clearly shows that the HR estimates significantly underestimate wave periods in excess of 8 seconds and do not predict any wave periods in excess of 15 seconds, which in reality are present. The highly seasonal occurrence of the low frequency waves are illustrated in Figure 4.28, which shows the number of occurrences of waves with periods in excess of 14 seconds and their associated heights plotted against time. Most of these waves are present between October and March. Generally, the higher wave periods and heights both occur between October and March.

#### *Extreme value analysis of wave heights*

Axe (see Chadwick *et al*, 1997) investigated 5 statistical distributions (Weibull, Fisher-Tippet, Frechet, Gumbel, Gompertz) with the probabilities being calculated using the observed 0.25m class intervals. The Weibull, Fisher-Tipper and Gumbel distributions all produce good fits to the data with the predicted 100 year return period wave heights varying between about 3.5m and 4.2m. Given that the measured wave heights were taken in transitional/shallow water, the absolute maximum wave height will be controlled by depth. In this case the maximum depth is of the order of 8 m which will limit the maximum significant wave height to the order of 4.4m (neglecting any extreme surge levels).

Histogram of wave directions. Elmer Offshore.  
February 1994- January 1995

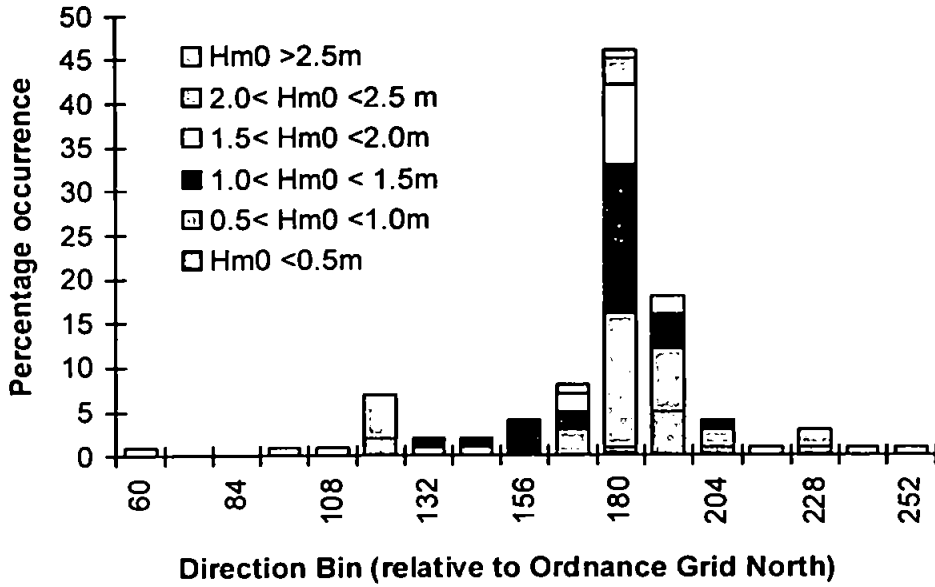


Figure 4.25 Histogram of wave directions, Elmer offshore, February 1994 - January 1995

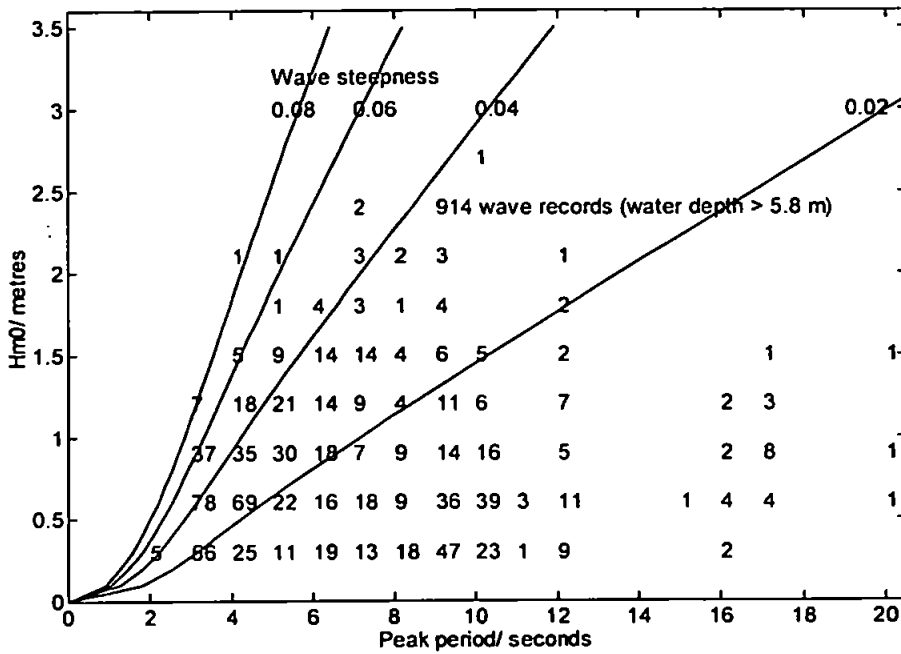


Figure 4.26 Wave height/period scatter diagram for Elmer

### Wave Periods at Elmer: Comparison of Prediction and Measurements

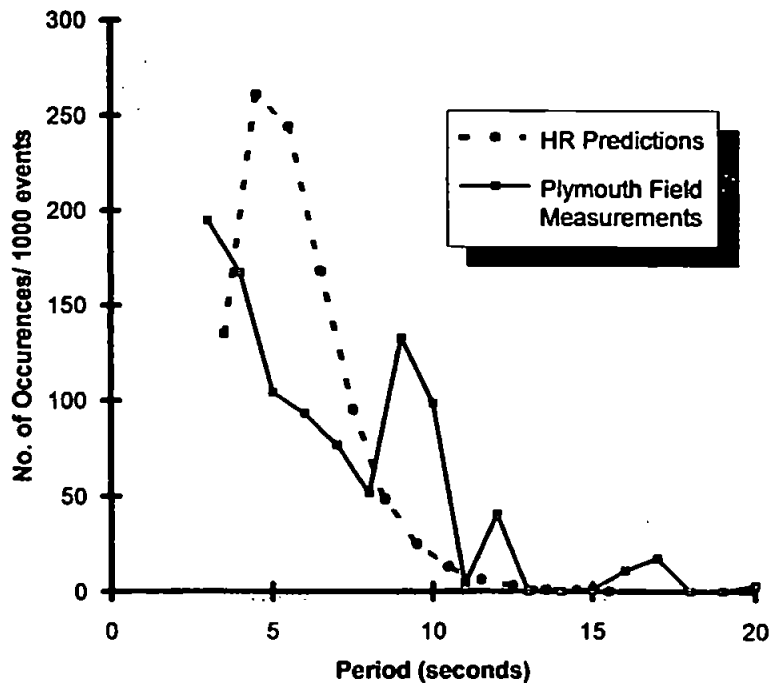


Figure 4.27 Wave periods at Elmer: Comparison of prediction and measurements

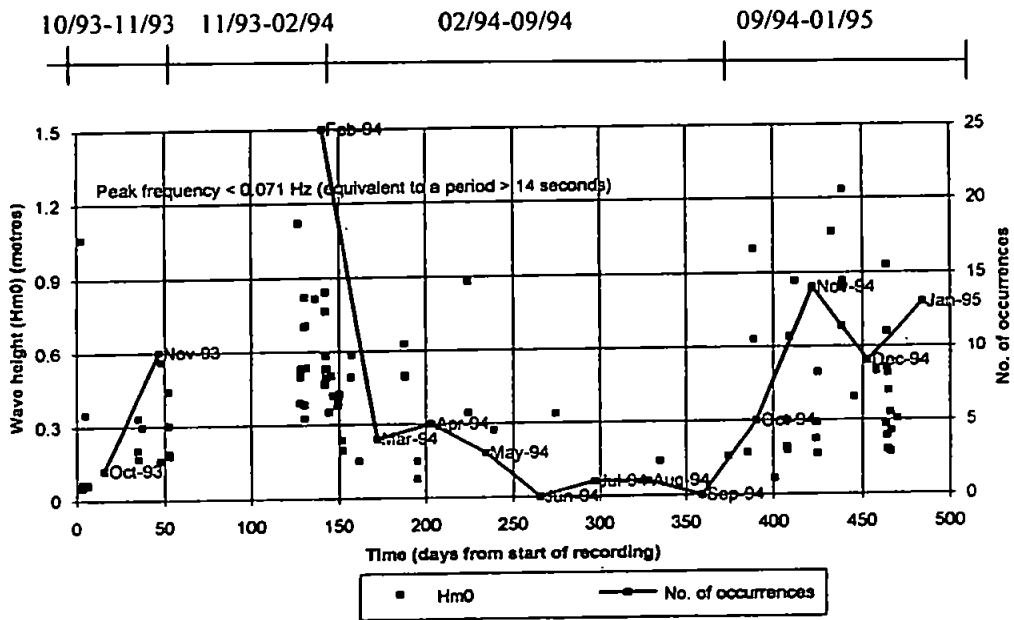


Figure 4.28 Occurrence of low frequency spectral peaks at Elmer

## 4.5 Summary

Firstly, the data collected at Elmer in the summer of 1992 were analysed by the author using two different spectral analysis techniques (IWCM and WRS spectral techniques). Also, the parameters such as different types of windows, different starting points, different number of segments for FFT and normalisation of spectra energy with time domain variance was investigated.

It was found that the use of a triangular window in comparison with a cosine-bell window reduced the measured energy. A different starting point for the FFT resulted in different total energy and distribution in the front of the breakwater whereas in the lee of the breakwater it did not demonstrate such an influence. The difference in the influence of the starting point for data in front and in the lee of the breakwater could be connected to spectral analysis technique and the measured time series itself. Those series include the partially standing waves caused by the presence of the reflector.

As was expected, a higher number of FFT segments smoothed the spectra distribution, increased the degrees of freedom and confidence levels. It was recommended to normalise spectral energy. It was concluded that the same spectral routines should be implemented on both data sets. This would enable their further comparison and make them suitable for computational model validation.

The WRS and IWCM deployment at Felpham during spring 1993 gave an opportunity to test whether the two device's measurements were equal or comparable. Data sets, which were measured at the same time, were chosen and compared. They were analysed by a newly developed spectral analysis routine which took into account the recommendation from the comparison of WRS and IWCM spectral techniques.

The WRS measured pressure data are transformed to surface elevation using a weighting function. When the IWCM surface elevation data were filtered in the same way as the WRS data, the data records were equal. Again, it was shown that full comparison could only be made when the same spectral routines are applied to both data sets.

The conclusion and recommendation from the two comparison exercises (measurements by WRS and IWCM and spectral analysis for IWCM and WRS) were the foundation for the new spectral analysis routine applicable to both data sets. This was then applied to a large



number of data sets, which were collected in the field campaign at Elmer from September 1993 - January 1995. The processed data were stored in an EXCEL database. A summary of the main wave parameters found from the analysis has been given as a guideline for the selection of data selection for numerical model validation.

# Chapter 5

## **An assessment of methods for the evaluation of multidirectional waves parameters**

*Some problems are just too complicated for rational logical solutions. They admit of insights, not answers.*

*By Jerome Bert Wiesner*

### **5.1 Introduction**

The validation of the wave transformations models using field measurement of multidirectional waves requires an accurate input of its parameters. Those models usually require the accurate input of incident significant wave height and reflection coefficient at the boundaries. When directional modelling is applied, the accuracy of the direction and directional spread estimates become important as well. Therefore, for the purpose of this study it is necessary to discern these parameters with the maximum possible accuracy.

The determination of the directional spectrum of real sea waves is a heterogeneous problem, requiring careful consideration of a number of factors. These include the nature of the sea state categorised, the type and detailed design of the wave measuring system, and the spectral and directional analysis techniques to be employed. Each of these factors can have an interactive effect with the others. The difficulties are compounded by the fact that at full scale, the sea state is unknown, *a priori*, and thus cannot be used directly to ascertain

the accuracy of the derived directional spectra.

It is desirable to utilise a measuring system and associated spectral and directional analysis techniques that are capable of accurately determining the true directional spectrum for complex sea states. Such sea states may encompass simple unimodal incident waves, bimodal incident waves, multidirectional incident waves and combinations of such incident waves with reflected waves from either coastal structures or beaches. These reflected waves may or may not be phase-locked to the incident waves at the measurements position.

In section 5.3, a new non-dimensional framework for application of phase-locked (Modified Maximum Likelihood Method - MMLM) and non phase-locked (Maximum Likelihood Method - MLM ) methods is investigated. In section 5.4, further study has been carried out using two non-phase-locked directional analysis methods - Maximum Likelihood Method (MLM) and Bayesian Directional Method (BDM) - to determine the directional spectrum from the measured data. Their capabilities are first compared using a range of synthetically generated data composed of both incident and reflected waves. The effects of varying the spectral analysis techniques are highlighted in this part of the study and are placed within a theoretical framework enabling an informed choice of spectral analysis technique to be made. The tests using synthetically generated data also provides a means by which the accuracy of the two methods may be quantitatively determined. The results of these tests are summarised and conclusions drawn. Section 5.5 presents the results from an investigation of over 80 data sets measured at the same time offshore and inshore in the lee of the breakwaters, covering a wide range of environmental conditions.

In applying these techniques to field data, another important consideration is the effects of currents. Such currents may comprise tidal and/or wave-induced currents. Consequently, the influence of currents on the field measured directional spectra is investigated in section 5.6. The results are very clear and were found to follow the same trends discerned from the simulation tests, allowing conclusions to be drawn in section 5.7.

## 5.2 Raw spectra

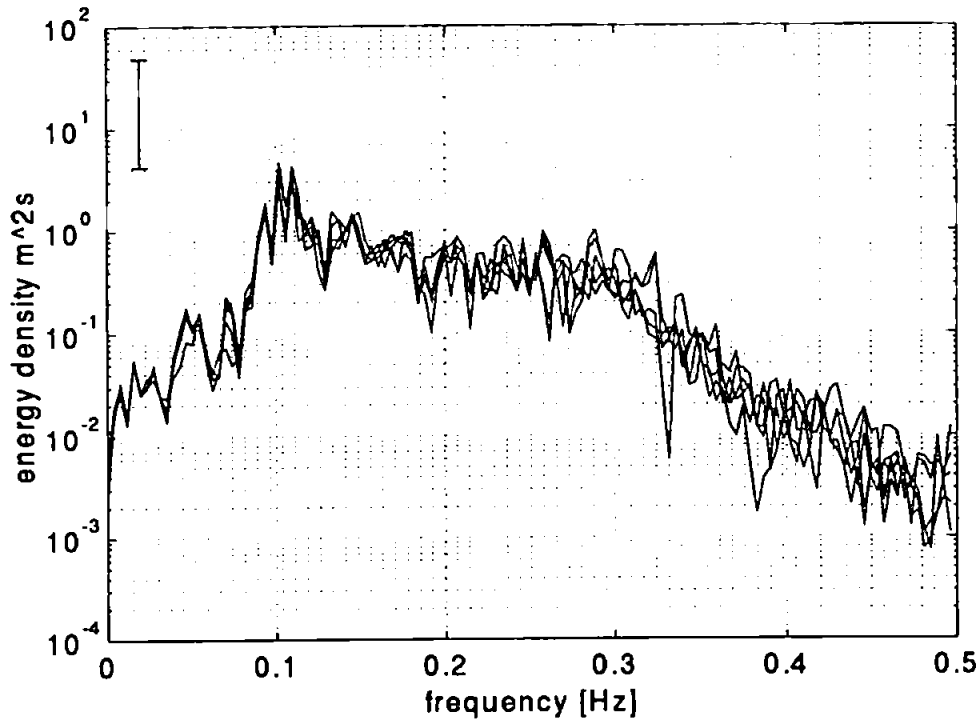


**Figure 5.1** Energy spectra measured at five offshore positions (see Figures 3.2 and 3.3b), the bar indicates lower and upper 95 % confidence levels for energy density =  $10 \text{ m}^2\text{s}$

The methods used to predict directional spectra have been developed for either a sea state with dominant phase-locking between incident and reflected waves (near reflectors) or for a non-phase-locked sea state further offshore (far from the influence of the reflector). When the measurements are taken in the area between these two extremes an appropriate choice of the method must be made. Usually in such conditions where only partial phase-locking occurs both methods fail to give accurate estimates. It was initially assumed that incident and reflected waves are not phase-locked at the measurement positions offshore and inshore in the lee of the breakwaters. Database analysis revealed a certain amount of reflection measured offshore of the breakwater and inshore in the lee of the breakwater.

Figure 5.1 shows an example of energy spectra measured at 5 different positions offshore. From the figure it can be seen that for some frequencies there is more variation in the spectral density functions between different locations than for the other frequencies. This

can be caused by uncertainties associated with the spectral analysis technique used, limited record length, non-stationarity<sup>1</sup> and the presence of the reflection. The variation becomes pronounced for frequencies greater than 0.2 Hz which is caused by non-stationarity.

Figure 5.2 is an example of a directional spectrum measured at the offshore position and obtained using the MLM method. The incident wave field is in the direction interval from -180 to 0 and the reflected wave field in the direction interval from 0 to 180 degrees. In this example the measured reflection coefficient offshore was between 0.5 - 0.8. However, at the same time, 2D analysis for the data measured right in the front of the structure (Davidson *et al* 1996) estimated reflection coefficients of 0.2 - 0.6. It was anticipated that the reflection coefficient offshore would be less than that inshore as a proportion of the incident waves penetrates through the breakwater gaps and dissipates on the beach and also attenuates with offshore propagation. As the apparent reflection coefficient offshore was greater than that measured inshore this raises the question as to how accurate were the reflection coefficients as determined by the MLM. This illustrates the difficulty in interpreting the 'reflected' wave field offshore which may be associated with directional ambiguity rather than with actual reflection.

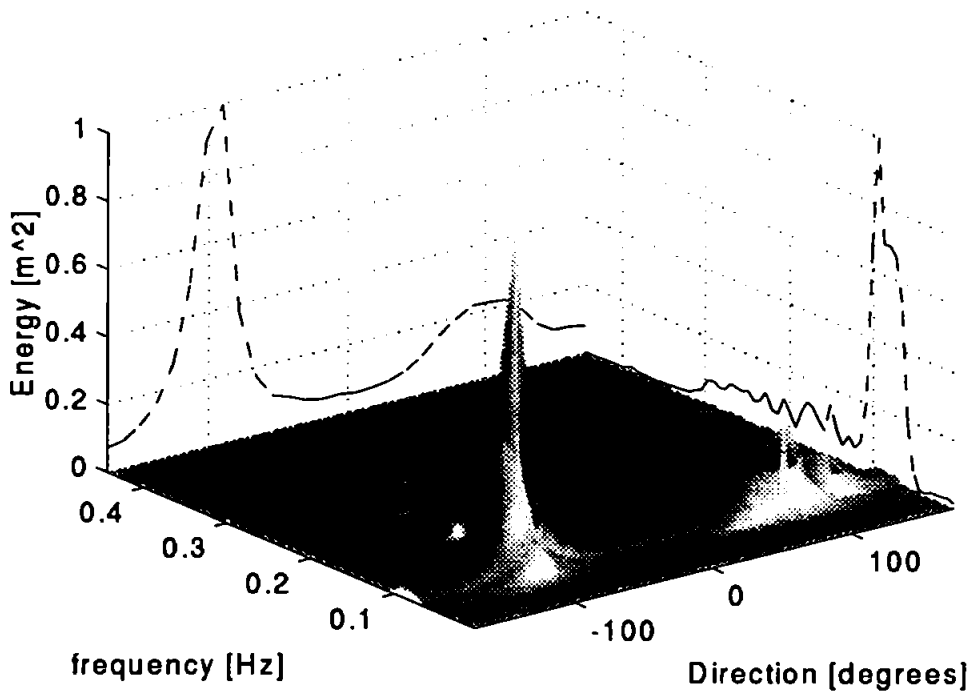


**Figure 5.2** An example directional spectrum measured at the offshore position

<sup>1</sup> This is probably the dominate influence for the frequencies greater than 0.2 Hz and the reflection is the dominate influence for frequencies smaller than 0.2 Hz.

The Modified Maximum Likelihood Method (MMLM) developed by Isobe and Kondo (1984) has been successfully applied to the data collected in the strongly reflective wave field, in the front of the breakwater (Davidson *et al*, 1997). However this was not the case when the method was applied by the author for the data measured at the offshore position. This method takes into account the reflected wave by introducing the known distance from the reflector to the WRS. It was observed that the MMLM is very sensitive to the position of the reflection line. At large distances offshore from the reflector, the MMLM can produce spurious peaks leading to potential difficulties with the method when dealing with a partially reflected wave field. Therefore, the method is not used in such conditions.

### **5.3 The validation of the non-dimensional frame work**

The purpose of this section is to assess, the performance of phase-locked and non-phase-locked methods in determining the directional spectrum from field data measured offshore. The assessment is related to the measurement locations and the frequency bandwidth used in the spectral analysis.

#### **5.3.1 Theoretical Framework**

The reflected wave field around the structures can be divided into a near structure field and a far field. The near structure field is characterised by the formation of partially standing waves caused by phase locking of incoming and outgoing (reflecting) waves. Methods, such as the MLM (Capon *et al*, 1969), which were developed for a homogeneous field fail to give accurate directional spectra estimates in such an environment. Subsequently the MMLM (Isobe and Kondo, 1984), which takes into account not only the relative distance between sensors, but also their position relative to the reflector, was developed, and was successfully used to analyse measurements taken in the near structure environment. However, this phase sensitive method tends to produce spurious peaks when applied to the data measured far from the reflector<sup>2</sup>. On the other hand, any phase-locking which is still present closer to the reflector affects the accuracy of the MLM method.

---

<sup>2</sup> Huntley *et al* (1996) described the sensitivity of the MMLM used for co-located sensors and the problems in applying the method.

Huntley and Davidson (1998) show that ratio,  $L/S$ , can be used to determine whether or not a phase-locked method should be used. Where  $L$  is the time of wave travel to the reflector and back which determines the node/antinode frequency interval.  $S$  is the length of time series used for spectral analysis which determines the bandwidth of this spectral analysis.

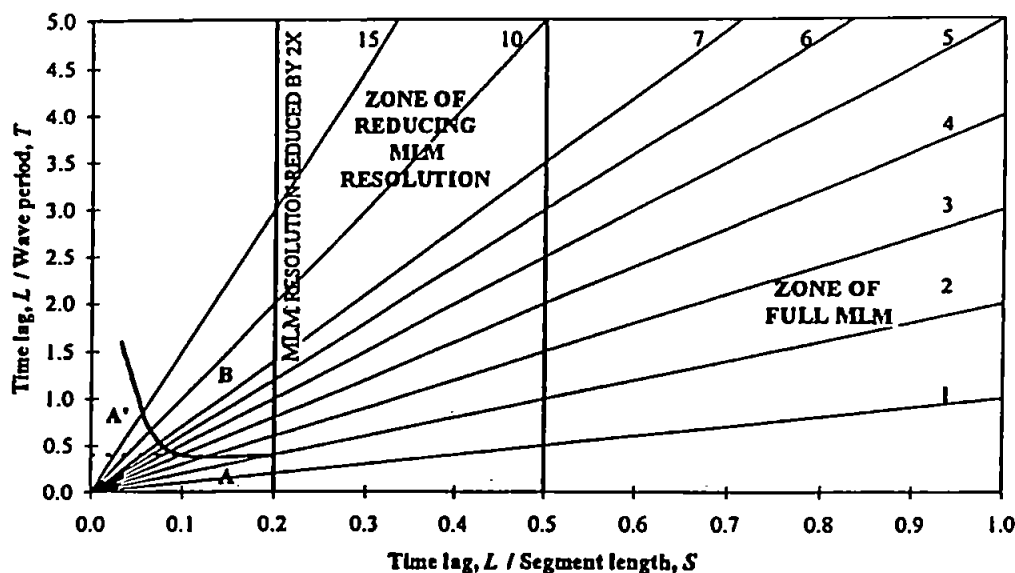


**Figure 5.3** The practical guideline for effective use the MMLM and the MLM method related to  $L/S$  ratio (courtesy Huntley and Davidson, 1998). The line which separates PL and non-PL regions is vertical as a result of assuming that waves are in shallow water. If the dispersion is taken in account, the line will curve to the right with increasing  $L/T$ . The inclined lines are the locations of spectral frequency estimates.

There are two possible ways of increasing the bandwidth. The first one is to decrease the FFT segment length, thus to increase the number of segments and bandwidth. The second one is a frequency smoothing which also increases the bandwidth. Huntley and Davidson (1998) using unidirectional simulated data showed for both a co-located and spatially distributed array that if the time of each FFT segment is shorter than the time for a wave to travel to the reflector and back, then the segment will not contain any phase-locked waves. The summary of their investigation and a practical guideline is given in Figure 5.3. On the basis of the ratio  $L/S$ , the domain of applicability is divided into the PL region (where PL methods are more applicable) and into the NPL region (where NPL methods are more appropriate). The PL region,  $L/S$  smaller than 0.2, is divided into three subsection A, B and A'. If one needs to distinguish real reflection from spurious peaks,  $L/S$  need to be less than

0.025 and the  $L/T$  criterion can be relaxed (zone A'). If  $L/S$  is between 0.025 and 0.2, the same result can be obtained if  $L/T$  is less than 0.4 (zone A). The spurious peaks will be obtained for  $L/S$  and  $L/T$  from zone B. Changing the segment size, they were able to use successfully both methods. In the case of a spatial array, the MLM method had full resolution for  $L/S$  greater than 0.5. The MMLM method worked well for a wider range of frequencies when  $L/S$  less than 0.1.

### 5.3.2 Tests and results for offshore field data

Data measured at the offshore position during high tide were selected which implies intermediate or deep water conditions<sup>3</sup>. The length of segments for the spectral analysis was reduced in order to minimise the effect of possible phase locking. The effects of both varying the length of the FFT segments and frequency smoothing were tested.

The Fast Fourier Transform was performed using a Welch Window and 50% overlapping segments. Firstly the spectral smoothing influence was investigated. Four different cases were tested with varying length of segments,  $S$ . The segment lengths were 512, 256, 128 and 64 points (cases 1-4 in Table 1). Additionally frequency smoothing was introduced to enlarge the frequency bandwidth to encircle the frequencies with possible nodes and antinodes for the data measured offshore (cases 5-7 in Table 5.1).

Using a segment length of 512 points, three different cases were investigated with smoothing over 2, 4 and 8 adjacent frequency bands respectively. The time lag,  $L$ , for all seven cases was calculated depending on frequency due to the dispersive effect of the waves in intermediate depths. These values varied slightly from file to file depending on the measured water depth. The  $L/S$  ratio was recalculated by the author using Huntley and Davidson's (1998) guideline. Their graph was modified by the author, taking dispersion in account, to suit field data and it is given in Figure 5.4. From Figure 5.4, it can be noticed that for all four chosen segment lengths,  $L/S$  is greater than 0.5, which is classified as in the NPL region. Thus  $S$  equal to 128 or less should be used for accurate estimates. Table 5.1 gives the summary of all these seven cases for the offshore array (WRS).

---

<sup>3</sup> For average water depth of 7.5m,  $D/L$  greater than 0.5 for 3s waves, which implies deep water conditions. For same water depth,  $0.05 < D/L < 0.5$  for 6s and 12s waves, which implies intermediate water conditions.



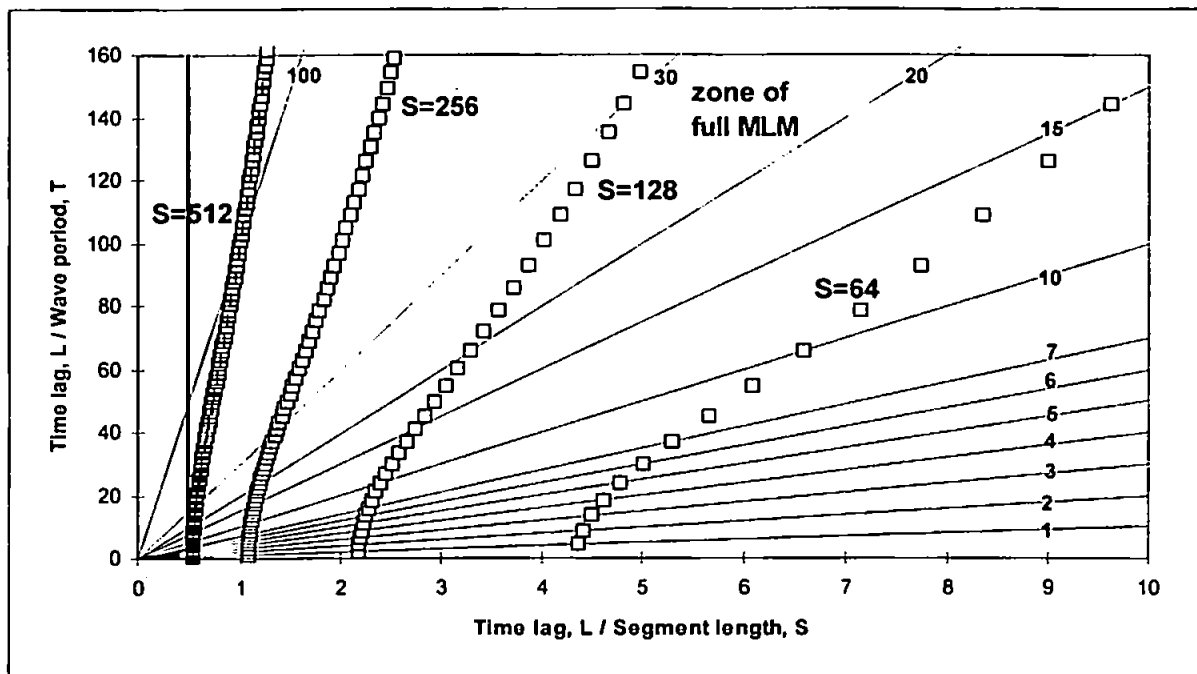


**Figure 5.4** Time lag  $L /$  segment length  $S$  ratio for the field data. The marker,  $\square$ , stands as an indication of  $L/S$  and  $L/T$  values for frequency estimates ( $S$  is here number of points [2 s/point])

Case No	$S$ (sec)	smoothed frequ. bins	Limits Lower $f$	of $L/S$ Highest $f$	$df$	Degrees of freedom	95% confidence limits
1	256	1	0.54	1.27	0.0039	6	0.42-4.8
2	128	1	1.09	2.53	0.0078	14	0.54-2.4
3	64	1	2.17	4.97	0.0156	30	0.63-1.8
4	32	1	4.36	9.63	0.0313	62	0.73-1.4
<i>Smoothed frequency bins</i>							
5	256	2	0.54*	1.27*	0.0078	12	0.5-2.7
6	256	4	0.54*	1.26*	0.0156	24	0.6-1.9
7	256	8	0.54*	1.24*	0.0313	48	0.7-1.6

**Table 5.1** Summary of tests performed using different segment lengths and different number of frequency bins<sup>4</sup>.

Both MLM and MMLM methods, with directional resolution of  $12^\circ$ , were then applied and the directional results compared.

### The influence of spectral smoothing

The offshore data have a broad frequency distribution with an evidence of both swell (peak frequency  $\sim 0.1$  Hz) and wind energy (peak frequency greater than 0.1 Hz). Figures 5.5 and

<sup>4</sup> \* stands for absolute values of  $L/S$ . To obtain the effective  $L/S$ , segment length  $S$  needs to be divided by the number of averaged frequency bins. Thus effective  $L/S$  become, for lower  $f = 1.08$  and for highest  $f = 2.54, 2.52$  and  $2.48$  respectively.

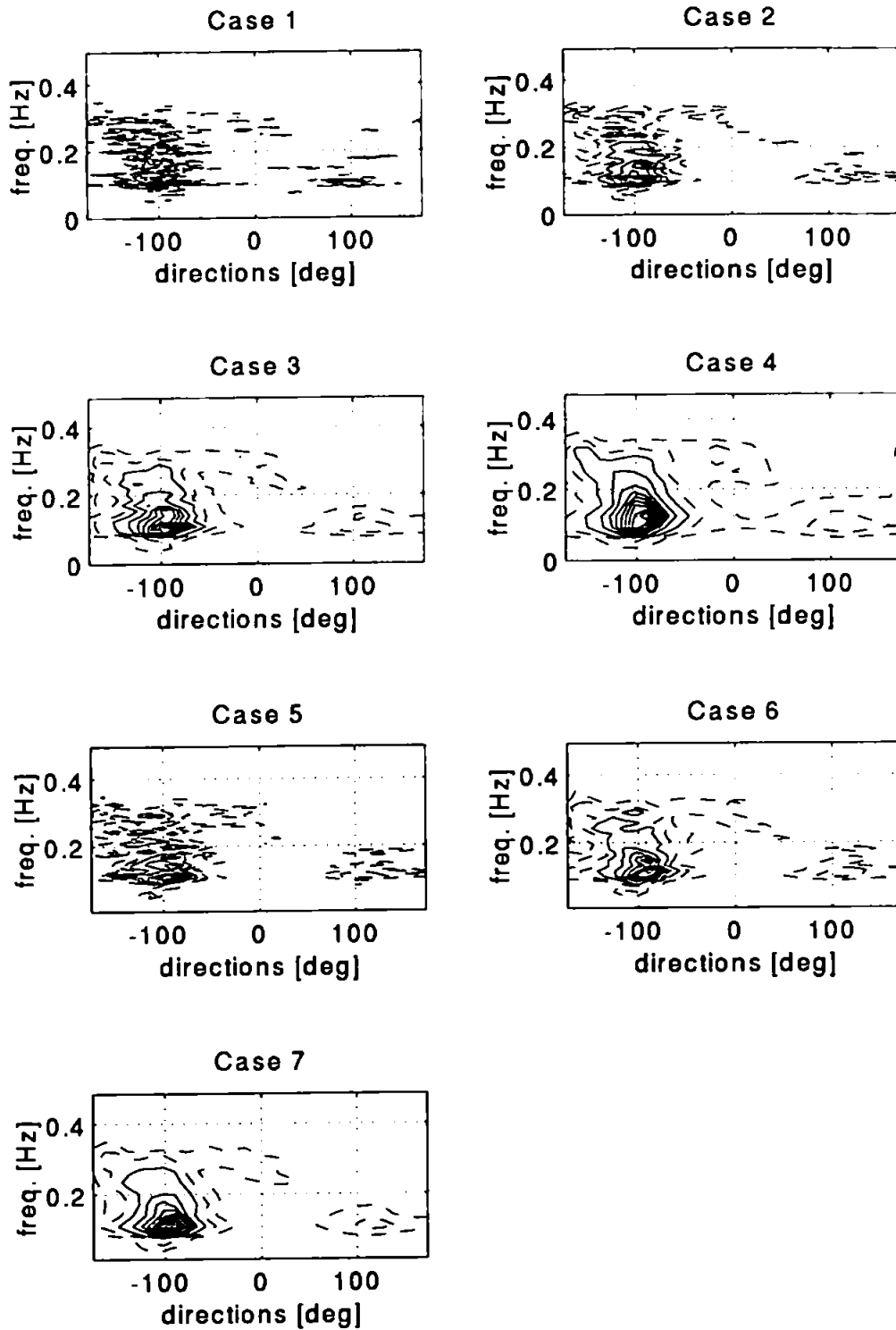
5.6 illustrate typical energy contour plots for all seven cases when the MLM/MMLM methods respectively were applied. The solid line contours are given in intervals of 10 % of the peak energy and the dashed line contours are 1, 2, 3 and 5% of the peak energy. There is evidence of a small amount of energy (less than 5% of the peak, dashed line contours) randomly distributed for frequencies above 0.2 for all cases in Figures 5.5 and 5.6. The directional results from both the MLM and the MMLM showed the presence of reflected energy (in interval of  $0^\circ - 180^\circ$ ).

Figure 5.5, cases 1-4, show the sensitivity of MLM to the chosen segment length. With a reduction of the segment length, there is still an indication of the reflected energy. With decreasing segment length, the energy is concentrated in frequency bands lower than 0.2 Hz. Also the incident peak is more distinguished with the reduction of the segment length. The reduced segment length does not noticeably improve the resolution of the reflected wave energy. The sum of energy for all frequencies versus direction reveals the presence of a small amount of background energy evenly distributed over all directions (Figure 5.7). If only the energy for frequencies less than 0.2 Hz is summed, then the background energy diminishes (Figure 5.7). Thus also the ratio of reflected/incident energy decreases.

When the MMLM method was applied (Figure 5.6, cases 1-4,) there is an evidence of increase of spurious peaks with decreasing segment length. The MMLM was applied outside its zone of applicability. The results proved that MMLM can not be accurately applied for  $L/S$  greater than 0.5. With larger distance from the reflector and also with decreasing of segment length, the phase-locking effects are encompassed. Huntley and Davidson (1998) found that in such conditions the MMLM amplifies strongly the noise in the cross-spectrum at locations predicted to be nodes.

### **The influence of frequency smoothing**

The directional spectra contour plots for different frequency smoothing are given in Figure 5.5 (cases 5-7) when the MLM was applied. Comparing those three cases with cases 1-4, a very similar trend in the change of directional distribution of energy with decreasing  $S$  or increasing number of frequency bins can be observed. The frequency interval,  $df$ , was similar in those cases. However, the degrees of freedom and confidence levels were different (see Table 5.1). The representative frequencies for the frequency bandwidth differed from those used in cases 1-4.



**Figure 5.5** Directional spectra contour plots given in the percentage of the peak energy when MLM was applied. For cases 1,2,3,4 respectively spectral smoothing was used. For cases 5,6,7 respectively frequency smoothing was used. ( - 2 and 5% ; — 10-100% with an interval of 10%)

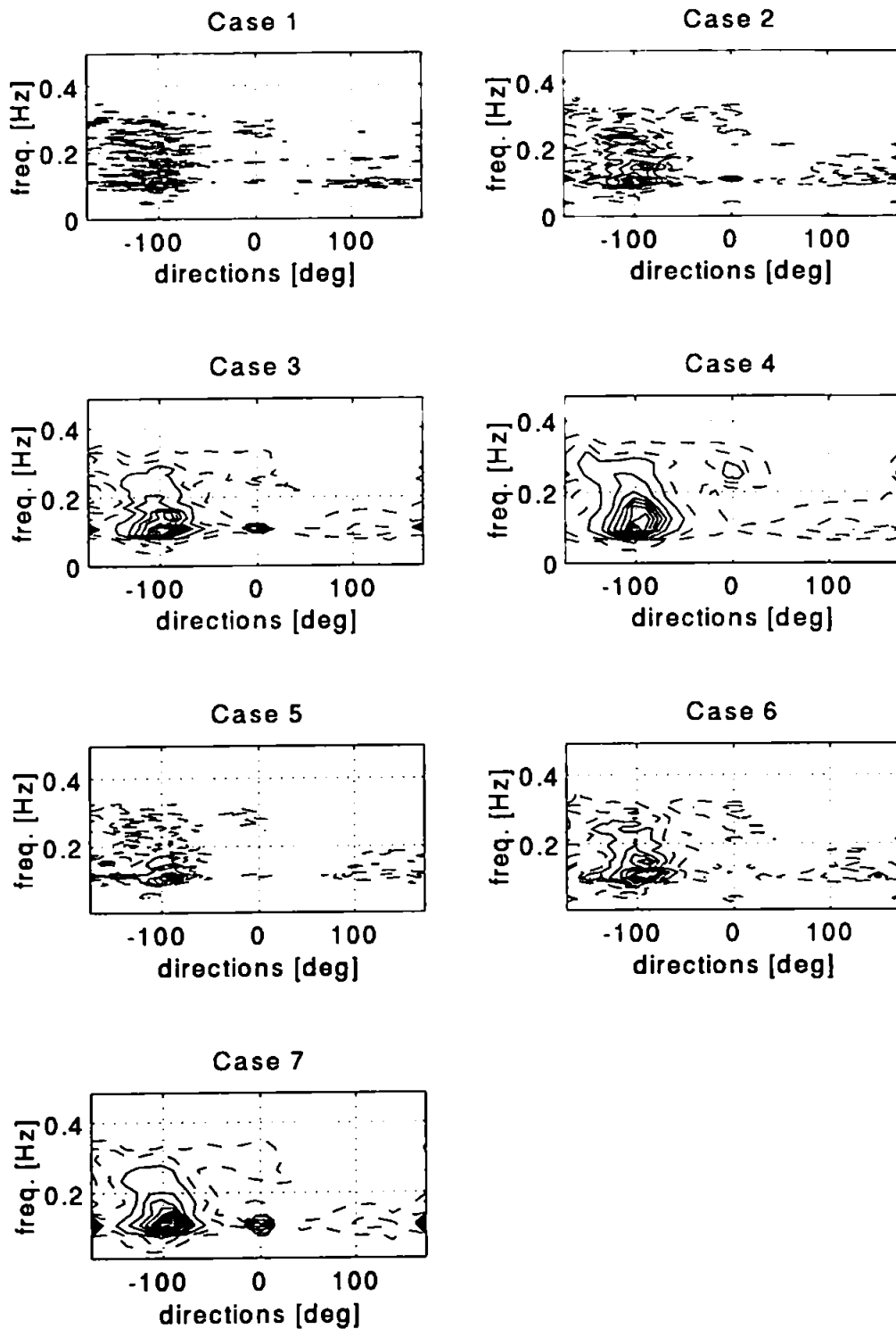


**Figure 5.6** Directional spectra contour plots given in the percentage of the peak energy when the MMLM was applied. For cases 1,2,3,4 spectral smoothing was used. For cases 5,6,7 respectively frequency smoothing was used. ( - - 2 and 5% ; — 10-100% with an interval of 10%)

Figures 5.6 (cases 5-7) are contour plots for directional spectra when frequency smoothing and the MMLM were applied to data. The different representative frequencies and thus the different wave numbers used in the directional analysis made the spurious peaks more or less distinctive. Thus for the MMLM accuracy not only the value of  $L/S$  but also the value of  $L/T$  is important. In the last case when frequency smoothing over 8 frequencies was used the spurious peaks became the most pronounced. In this case, the representative frequency and wave number had more influence on results than the frequency interval,  $df$ .

The  $L/S$  ratios for all cases were larger than those recommended for applicability of the MMLM. Thus, as was expected, the MMLM failed to give accurate directional analysis estimates. The MMLM was successfully applied in the front of the structure where the ratio between segment length and time lag,  $L/S$ , was 0.02. It was found that the offshore data set needed to be larger in order to obtain the same  $L/S$ . This was a limitation that precluded further analysis.

#### Main direction and spreading width

The main direction and spreading width were calculated for each of seven MLM cases in accordance with the IAHR guidelines for multidirectional waves (Frigaard *et al* 1997). The main direction is defined as the expected value of the stochastic variable, direction as a function of frequency, having a probability density function determined by the corresponding spreading function, that is:

$$\theta_{M_I} = E[\Theta_I(f)] = \frac{\sum_{k=1}^{K/2} \theta_k G(f, \theta_k) \Delta\theta}{\sum_{k=1}^{K/2} G(f, \theta_k)} \quad (5.1)$$

$$\theta_{M_R} = E[\Theta_R(f)] = \frac{\sum_{k=K/2+1}^K \theta_k G(f, \theta_k) \Delta\theta}{\sum_{k=K/2+1}^K G(f, \theta_k)} \quad (5.2)$$

The spreading width is defined as the standard deviation of the same directional spreading function.

$$\sigma_{\theta_l}^2 = \frac{\sum_{k=1}^{K/2} (\theta_k - \theta_{M_l})^2 G(f, \theta_k) \Delta\theta}{\sum_{k=1}^{K/2} G(f, \theta_k)} \quad (5.3)$$

$$\sigma_{\theta_R}^2 = \frac{\sum_{k=K/2+1}^K (\theta_k - \theta_{R_l})^2 G(f, \theta_k) \Delta\theta}{\sum_{k=K/2+1}^K G(f, \theta_k)} \quad (5.4)$$

The difference between main incident directions varied from 0-12 degrees, using different FFT segments, when the MLM was applied (cases 1-4). The directional interval was 12 degrees<sup>5</sup>, thus an error of 12 degrees could be expected. The directional spreading width varied from 26-33 degrees when the MLM was used to analyse data for cases 1-4. The minimum spreading width was found for case 1 and maximum spreading width for case 4. This confirms that the spreading width increases with decreasing FFT segment size.

The difference in the main incident direction estimates varied from 0-10 degrees, when the MLM was applied using different frequency smoothing (cases 5-7). The directional spreading width varied from 23-34 degrees (cases 5-7). The minimum value was found for case 5 and the maximum value for case 7. Again, as for cases 1-4, the spreading width increases with increasing frequency smoothing. Spreading width depends on the way in which it is estimated, and is a function of the content of the energy in a particular frequency bin (equations 5.3 and 5.4). From Figures 5.7 and 5.8, it can be seen that there is a certain amount of 'background noise' present in the directional distribution. This noise is usually associated with frequencies above 0.2 Hz and with frequencies which contain small amount of energy (Figure 5.5). The energy content in each frequency bin becomes larger with increasing smoothing. When smoothing is applied, 'noise' becomes associated with frequencies containing more energy and influences the directional spreading results.

---

<sup>5</sup> The first analyses were performed on 486 PC, therefore the directional interval was only 12 degrees to speed up the computation.

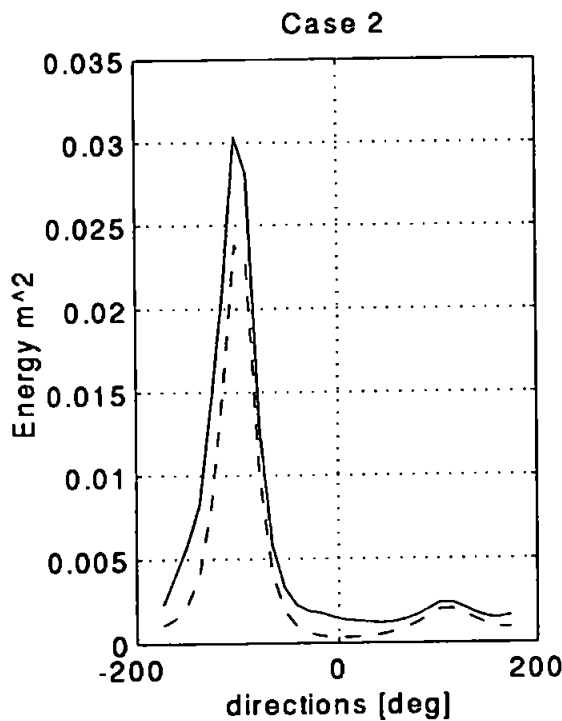


**Figure 5.7** Directional distribution for the energy summed over all frequencies (-), and only for frequencies < 0.2 Hz (-), case 2

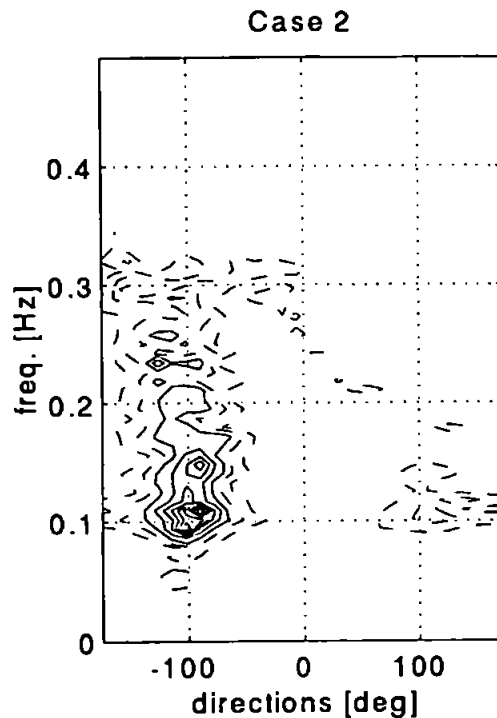


**Figure 5.8** Directional contour plot for narrow frequency spectra, case 2 (- - 2 and 5% ; — 10-100% with an interval of 10%)

### Frequency spectra shape

Even though all the measured frequency spectra have a broad distribution they can be classified into three groups - narrow frequency spectra when swell waves dominate wind waves<sup>6</sup>, bimodal with swell and wind waves, and broad frequency spectra when wind waves dominate swell waves<sup>7</sup>.

The influence of energy spectra shape on directional distribution was also investigated. For the narrow frequency spectra, the energy was concentrated between 0.05-0.12 Hz. Those were usually swell dominated waves and some reflection from the structure was expected.

<sup>6</sup> Most of the energy is contained within frequencies below 0.1 Hz.

<sup>7</sup> Most of the energy is contained within frequencies above 0.1 Hz.

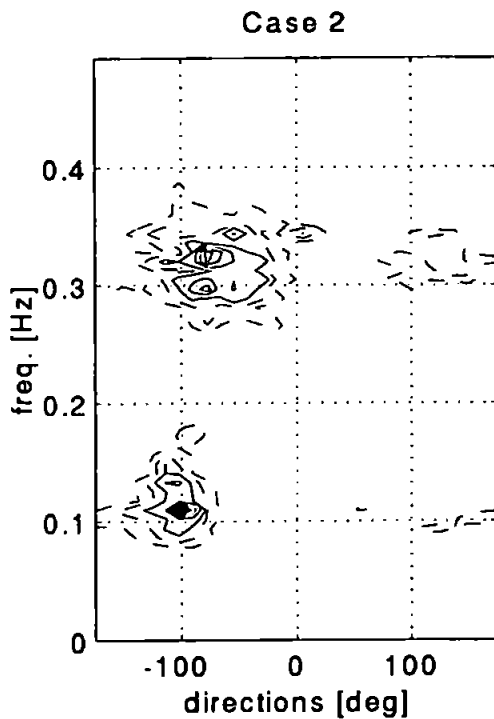


**Figure 5.9** Directional contour plot for bimodal spectrum, case 2 ( - 2 and 5% ; — 10-100% with an interval of 10%)

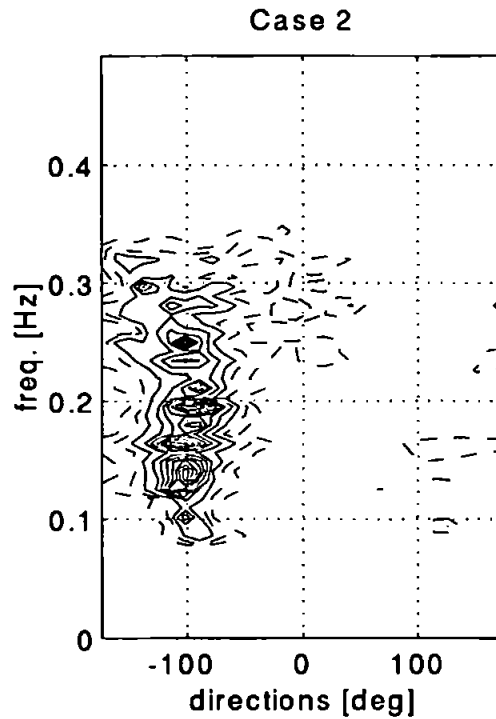


**Figure 5.10** Directional contour plot for wide spread spectrum, case 2 ( - 2 and 5% ; — 10-100% with an interval of 10%)

The directional distribution for case 2 (see Table 5.1) type analysis ( $S=128s$ ) was used to show the presence of energy in reflected directions (see Figure 5.8). Also, there is evidence for energy present at frequencies above 0.2 Hz, which is randomly spread in different directions. Decreasing the segment length, there is still evidence of energy in the reflected directional intervals. However, the sum of reflected energy over all frequencies and directions decreases with increasing smoothing.

Bimodal seas with two distinguished peaks (usually swell and wind peaks) generally have two different main directions. It was possible to detect those peaks applying the MLM and MMLM. Even when more smoothing was introduced by reducing segment length, different directional peaks were still preserved (Figure 5.9). Decreasing the segment length caused the estimate of the reflected energy to also decrease. This was a similar trend to the case of the narrow frequency spectra.

Broad frequency spectra were measured when waves were generated by strong local winds (short fetches). Broad frequency spectra were also obtained when swell waves were



accompanied with strong wind. The directional distribution obtained using the MLM show the presence of 'reflected' energy. However, it is still not clear what is the real reflection or what is the background noise for the higher frequencies. In the case when energy was almost equally distributed over the wider range of frequencies, the directional spread was higher (Figure 5.10). The method cannot accurately resolve the frequencies above 0.2 Hz.

### Reflection

As the MLM can be potentially used for the estimation of incident and reflected wave height and subsequently for the estimation of the reflection coefficient, the frequency dependent reflection coefficient was investigated. Figure 5.11 shows the frequency dependent reflection coefficient for all seven cases (see Table 5.1) when the MLM was applied. The coefficient was only calculated for frequencies with energy greater than 5% of peak energy. In general, frequency-averaged reflection coefficient estimates decreased with increasing smoothing. The smaller estimates were also closer to the estimates obtained using the 2D method for the data measured at the structure (between 40%-60% from Davidson *et al* (1996)).

On closer observation of all seven cases and the different amounts of smoothing, it was found that the reflection coefficient is not only a function of frequency but also energy dependent. Higher coefficient estimates were obtained for the widely spread frequency spectra when the energy was evenly spread over all frequencies. Also, it is observed that the method overpredicts the amount of reflection for smaller energies. The trend of increasing reflection coefficient for frequencies above 0.2 Hz was observed. It was expected from the measurements at the structure that the reflection coefficient for such frequencies would be in the range around 0.2/0.3 because those waves are most likely to break and reflect less energy back. The reflection coefficient values are higher for frequencies which contain lower amounts of energy than for the adjacent frequencies which contain higher amounts of energy.

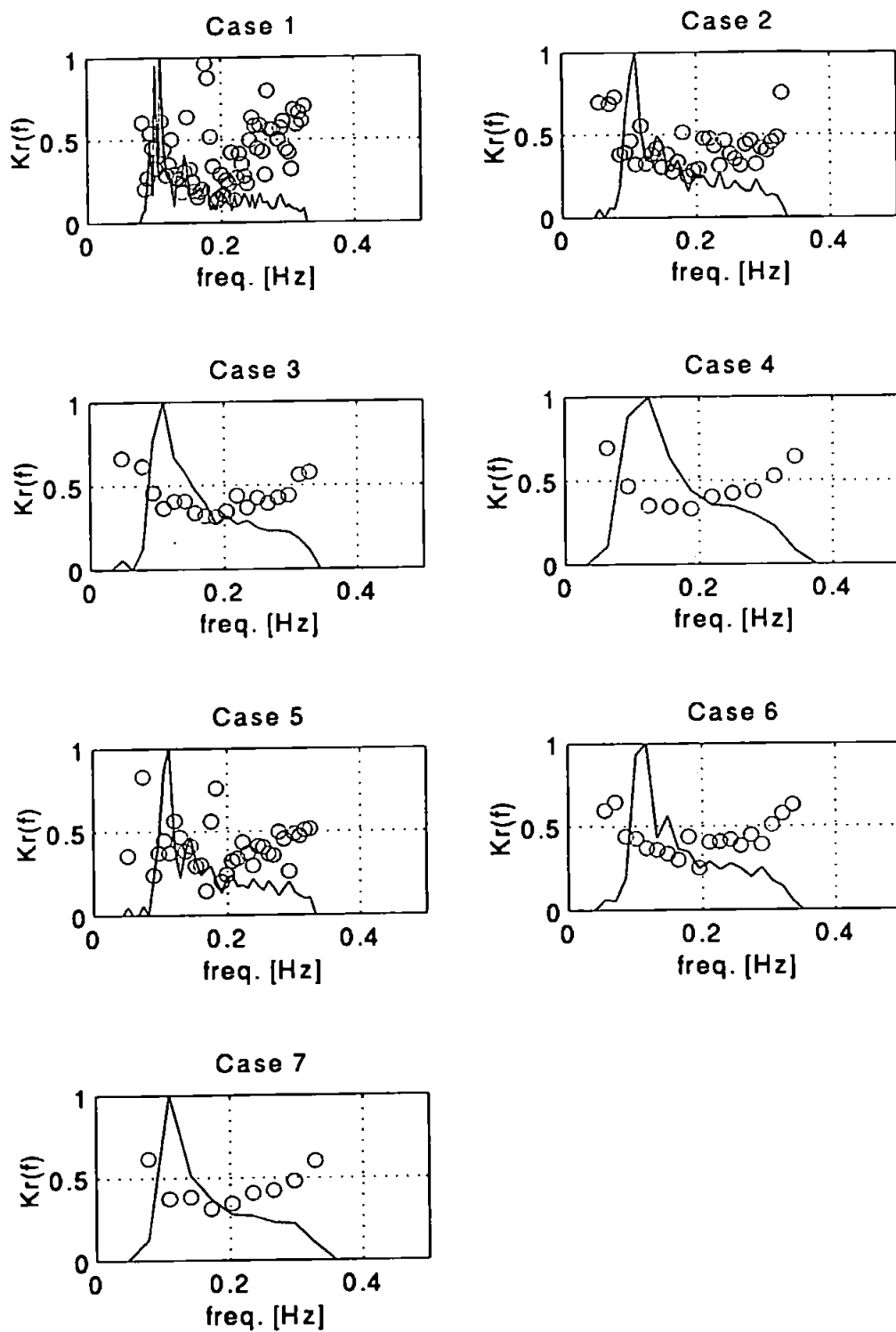


**Figure 5.11** Frequency dependent reflection coefficient for cases 1-7 when the MLM was applied. Reflection coefficient is given by 'o' and the energy spectra normalised by the maximum value is given in the background (—)

## Summary

The results agreed in general with the concept tested on simulated data by Huntley and Davidson (1998). For all chosen lengths of segment, the value of  $L/S$  is larger than 0.5, which is in the NPL region. As it was expected the MLM gave stable results and the MMLM produced spurious peaks. These analyses showed that the non-phase locked method is more applicable to analyse offshore field measured data.

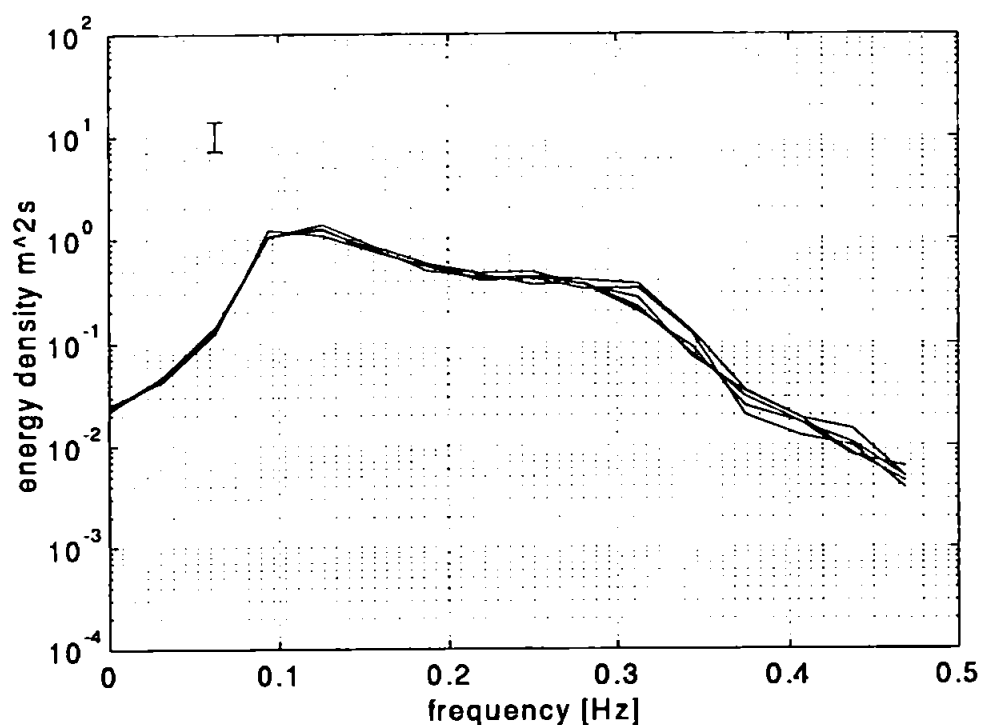


**Figure 5.12** Energy spectra for case 4 for offshore field data measured at the five positions (see Figure 3.2 and 3.3b). The bar indicates lower and upper 95% confidence levels for energy density =  $10 \text{ m}^2 \text{ s}$

Figure 5.12 shows the energy spectra for case 4 ( $L/S = 4.36 - 9.63$ ). If this energy spectra is compared to the energy spectra in Figure 5.1 for case 1 ( $L/S = 0.54 - 1.27$ ) then it can be seen that with increasing smoothing the spatial variation in energy has decreased but the spatial difference in energy is still present for the frequencies greater than 0.2. This can be related to the array size or non-stationarity, which will be addressed later in the present chapter.

The directional estimates varied with increasing smoothing thus  $L/S$  ratio. The accuracy of the method's prediction is still not clear. The choice of a segment length, which increases  $L/S$ , clearly results in a significant reduction in spectral resolution. As it was envisaged that

it is more useful to have a larger number of components for the directional modelling of random waves, it was chosen to proceed with results from case 5.

Considering the MLM limitations, it was thought desirable to test the performances of the other non-phase locked method and compare the estimates from both methods. The Bayesian Directional Method (BDM) as one of the most powerful technique available was chosen for a comparison. The BDM method is also a NPL method, however it can estimate directional distribution in the front of the reflector. Unfortunately, it has been found that its frequency dependent reflection coefficient estimates are not accurate in such environment (Helm-Petersen, 1995).

## 5.4 Numerically generated data

In order to compare the two non-phase-locked methods of prediction (MLM and BDM), synthetic directional wave data sets were created composed of an incident directional spectrum and the corresponding partial reflections from a reflector at a distance of 500m. Surface elevations were created for an array of six transducers using the geometry from offshore deployment 9 (Figure 5.13).

Surface elevation time series were generated by means of white noise filtering in the time domain. The software is courtesy of Jacob Helm Petersen (personal communications (1994)) from Aalborg University and details are given in Appendix F. Digital filters were designed to provide proper phase locking between incident and reflected waves. The time lag between incident and reflected waves takes in account the array locations in the field. The filter length was 245 elements. Linear wave theory was applied. To ensure wave directionality, incident waves were generated in 40 directions over a range of 180 degrees. Time series with a duration of 640 seconds<sup>8</sup> were generated with a sampling frequency of 2 Hz. Wave energy spectra were applied as discussed in the next paragraph. It was considered desirable to obtain simulated data similar to the measured data.<sup>9</sup> The length of time series used and the array configuration were, therefore, fixed by the field measurements. It is less likely to have the phase-locked components offshore. However, this simulated data containing phase-locked components will provide a more rigorous test for both methods.

---

<sup>8</sup> This gives approximately 83 waves in the case of 8 sec waves and 165 waves in the case of 4 sec waves.

<sup>9</sup> Consequently the coherence between signals measured at different sensors was not high and the same was observed for the coherence between simulated signals.

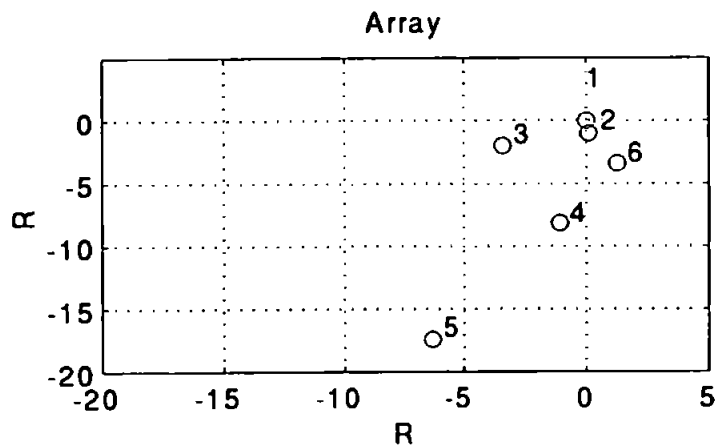


**Figure 5.13** Offshore array layout used for generation of synthetic wave data

The Jonswap and Pierson Moskowitz frequency spectra were chosen to cover a wide range of measured wave spectra and The Mitsuyasu directional spreading function (Mitsuyasu *et al*, 1975) was applied to these frequency spectra, with values of  $s=25$  for swell with short decay distance and  $s=10$  for wind waves. A wave period of 8.0s was chosen to simulate swell and 4.0s to simulate wind waves conditions and significant wave heights of 0.5, 1.0 and 1.5m were selected. Three different main directions were investigated, normal incidence ( $-90^\circ$ ) corresponding to southerly direction at the field site, slightly oblique towards the south-west direction ( $10^\circ$  to normal) and more oblique towards the south-east direction ( $25^\circ$  to normal).

The frequency independent wave reflection coefficient values of 0.2, 0.3, 0.4 and 0.6 were chosen to simulate reflective components of time series. Combinations of these different parameter values yielded 45 different wave data sets to be tested. Additionally, three other data sets were created with a reflection coefficient equal to zero, a Jonswap frequency spectrum, a wave height of 1 m and three different directions ( $-100^\circ$ ,  $-90^\circ$ ,  $-65^\circ$ ).

Table 5.2 summarises the parameters used for numerical simulations.

<i>Label</i>	<i>Spectrum</i>	<i>Hsi</i> <i>m</i>	<i>Tp</i> <i>s</i>	$\theta$ <i>deg</i>	<i>s</i>	<i>Kr</i>
1110	Jonswap	1.0	8.0	-100	25	0
1120	Jonswap	1.0	8.0	-90	25	0
1130	Jonswap	1.0	8.0	-65	25	0
1111/2/3	Jonswap	1.0	8.0	-100	25	0.6/0.4/0.3
1121/2/3	Jonswap	1.0	8.0	-90	25	0.6/0.4/0.3
1131/2/3	Jonswap	1.0	8.0	-65	25	0.6/0.4/0.3
1211/2/3	Jonswap	1.5	8.0	-100	25	0.6/0.4/0.3
1221/2/3	Jonswap	1.5	8.0	-90	25	0.6/0.4/0.3
1231/2/3	Jonswap	1.5	8.0	-65	25	0.6/0.4/0.3
2111/2/3	Pierson- Moskowitz	0.5	4.0	-100	10	0.4/0.3/0.2
2121/2/3	Pierson- Moskowitz	0.5	4.0	-90	10	0.4/0.3/0.2
2131/2/3	Pierson- Moskowitz	0.5	4.0	-65	10	0.4/0.3/0.2
2211/2/3	Pierson- Moskowitz	1.0	4.0	-100	10	0.4/0.3/0.2
2221/2/3	Pierson- Moskowitz	1.0	4.0	-90	10	0.4/0.3/0.2
2231/2/3	Pierson- Moskowitz	1.0	4.0	-65	10	0.4/0.3/0.2
2311/2/3	Pierson- Moskowitz	1.0	8.0	-100	10	0.4/0.3/0.2
2321/2/3	Pierson- Moskowitz	1.0	8.0	-90	10	0.4/0.3/0.2
2331/2/3	Pierson- Moskowitz	1.0	8.0	-65	10	0.4/0.3/0.2

**Table 5.2** The input parameters for the numerically generated wave data

## 5.4.1 Results of the analysis for the numerically generated data

### Spectral analysis of the numerical simulations

Spectral analysis was performed using the Fast Fourier Transform applying a Welch Window, 50% overlapping segments<sup>10</sup> and normalisation of the resulting spectral variance to the time domain variance. Two segment lengths were used, 512 points with additionally frequency smoothing over two frequencies (case 5) and 128 points (case 3a) for 5 sensors.<sup>11</sup> Additionally the analysis was performed for all 6 sensors, with segment length of 128 points (case 3b). The three cases investigated (with different L/S values) are summarised in Table 5.3 and named in accordance with Table 5.1.

<sup>10</sup> The overlapping varied slightly to enable the use of the whole data set as described in Chapter 4.

<sup>11</sup> For most of the field data, only 5 sensors were operational.

Case No	S (sec)	smoothed frequ. bins	Limits Lower f	of L/S Highest f	df	Degrees of freedom	95% confidence limits
3 (a,b)	64	1	2.17	4.97	0.0156	30	0.63-1.8
5	256	2	0.54*	1.27*	0.0078	16	0.55-2.3

**Table 5.3** Summary of spectral analysis test cases (case 3a for 5 sensors, case 3b for 6 sensors, case 5 for 5 sensors); \*The effective L/S is 1.08 and 2.54 respectively

### Directional analysis of the numerical simulations

Initially the Maximum Likelihood Method (MLM) and Bayesian Directional Method (BDM) were applied to case 5 spectral analysis results. The results were evaluated by considering the prediction of the incident significant wave height, the main direction, the directional spreading and the reflection coefficient. These were only evaluated over the frequencies with an energy content greater than 5% of the maximum energy content.

The incident significant wave heights obtained by directional analysis were compared to the 'normalised target' values<sup>12</sup>. The 'normalised target' values were calculated using Goda and Suzuki's (1976) recommendation for the significant incident wave height,  $H_{si}$ , for irregular waves. The  $H_{si}$  is defined as follows:

$$H_{si} = \frac{4\eta_{rms}}{\sqrt{1+K_r^2}} \quad (5.5)$$

where  $\eta_{rms}$  is the average root-mean-square water surface displacement measured at all offshore positions at all offshore locations and  $K_r$  is the reflection coefficient. The main direction and directional spreading were calculated using equations 5.1-5.4.

### Results for incident significant wave height with purely incident waves

The incident significant wave height ( $H_{si}$ ), calculated by BDM was very close to the target as shown in Figure 5.14. From Figure 5.15, it can be seen that the best BDM estimate was obtained for SW direction and the least accurate for the S direction. The MLM slightly underpredicts  $H_{si}$  for the S, gives accurate predictions for the SW direction and underpredicts for SE. Predicted  $H_{si}$  differed by less than 6% of the normalised target values over all data sets and both methods used. The direction of wave propagation and array orientation appeared to influence the amount of incident energy detected by both methods.

<sup>12</sup> The significant wave height for the simulated time series differ from the target values. It was reduced for the SW and the S direction. This indicates that the direction of wave propagation and array orientation along with the amount of reflection had an influence on the amount of energy simulated.

However, the wave heights predicted by MLM and BDM for these conditions were very similar and the percentage difference is less than 1% (also shown in Figure 5.15).

#### **Results for main direction with purely incident waves**

The main direction predicted by both the MLM and BDM differed only by  $\pm 2^\circ$  from the target direction over all data sets (see Figure 5.17). Correspondingly, the BDM/MLM percentage differences were only up to 4 % in the SW direction and -1- -1.72 %<sup>13</sup> in other two directions. Given that the directional interval used for analysis was  $12^\circ$ , these errors do not appear to be significant.

#### **Results for directional spreading with purely incident waves**

The directional spreading predicted by the MLM was 25-41% larger than the target spreading (see Figure 5.19). The largest difference was for waves from the southerly direction and the smallest difference was for waves from the SE. The difference between estimated and target values was 40-60% for all directions when the BDM was applied. The BDM/MLM percentage differences were -1.7 % -13% (see Figure 5.19).

#### **Results for reflection coefficient with purely incident waves**

The expected reflection coefficient was equal to 0 for all three data sets. Both methods predicted some reflection. The predicted reflection coefficient using the MLM method was from 4.1% in S direction to between 6.9% and 7.1% in the SW and SE direction respectively. The reflection coefficient calculated by the BDM was between 7.3% and 7.6% for the S and SW directions and 8.5% for the SE direction (see Figure 5.21).

#### **Results for Incident significant wave height in partially reflective wave field**

Both methods gave quite similar results (1.4% and 1.3% average difference) and it is difficult to distinguish which one gives the best estimates. The influence of the Jonswap and Pierson-Moskowitz frequency spectra, used for numerical simulation, on the results was investigated. No obvious influence of these frequency spectra shapes on results was found. However, the influence of the simulated wave direction on the prediction of incident wave height was found to be significant. The best match between predicted and target values is obtained for the SW direction. The predicted values start to deviate from the

---

<sup>13</sup> The positive percentage values mean overprediction and the negative percentage values mean underprediction.



target values for the S direction and the difference increased for the SE direction. The results are plotted in Figure 5.14. The MLM produces the lower estimates. Underestimation is in the range of -16 to -2 % for both methods. Thus, it was concluded that the array shape and orientation combined with the main wave propagation direction was influencing the results, which will be addressed later in this chapter. It also became apparent that the reflection coefficients, wave period as well as the directional spread were influencing the prediction of wave height. This is illustrated in Figures 5.15 and 5.16, where percentage difference between predicted and target values are plotted versus direction and the value of the simulated reflection coefficient for different periods.

For a wave period of  $T=8$  sec and directional spread of  $s=25$  (Figure 5.15), the BDM gave the best estimate for the SW direction. The MLM estimates became closer to the normalised target value when waves were from the SW and the reflection coefficient was 0.6. The closest estimates were obtained with the BDM method for a wave period of  $T=8$ sec and directional spread,  $s=10$ . Also, the largest difference between BDM and MLM was observed for this case (up to 8%).

For a wave period of  $T=4$  sec and directional spread width,  $s=10$  (Figure 5.16), the percentage difference between both methods estimates and normalised values increase. The estimates were more influenced by direction than by reflection.

### **Results for main direction in a partially reflective wave field**

Very good agreement was found between the predicted main directions using the MLM and BDM and target directions. The differences were in the range of  $\pm 12^\circ$ , which was the directional interval used for the analysis, therefore the error is within the limits expected. The maximum observed difference is  $14^\circ$  in two cases when BDM was used. The average difference between two methods is only -2 to 3.5 % in most cases. The influence of the chosen frequency spectra for data simulation on the prediction of the main direction has no obvious influence. It appears that the direction of incoming waves had more influence on the prediction of the main direction. The percentage difference between the predicted main directions obtained by the two methods and the target values and also the differences between predictions as functions of direction and reflection are plotted in Figures 5.17 and 5.18.

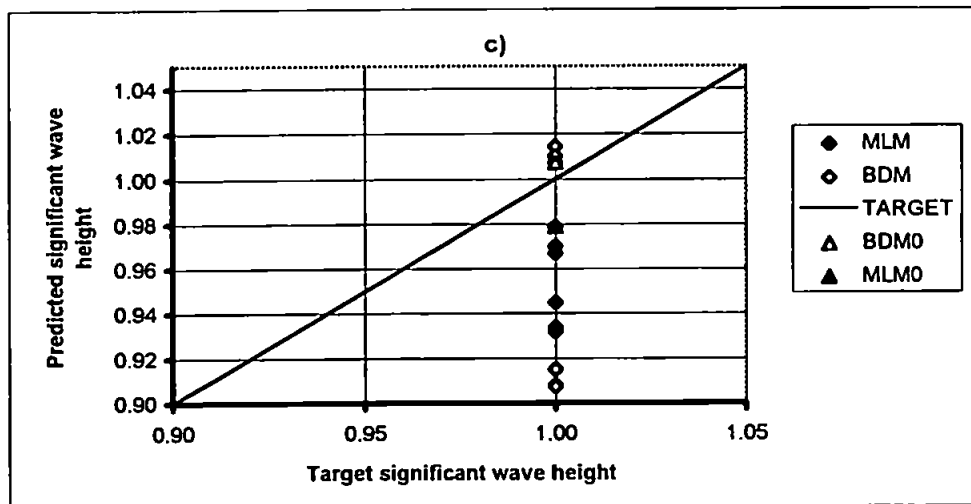
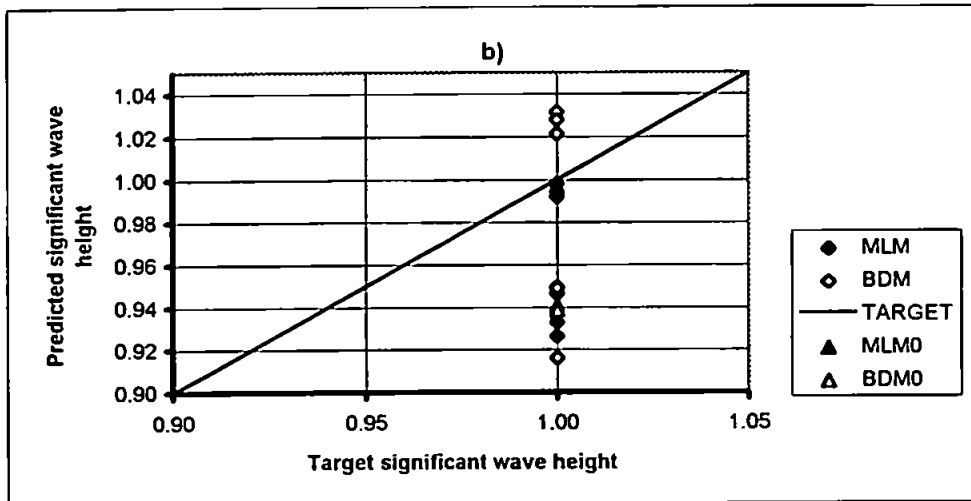
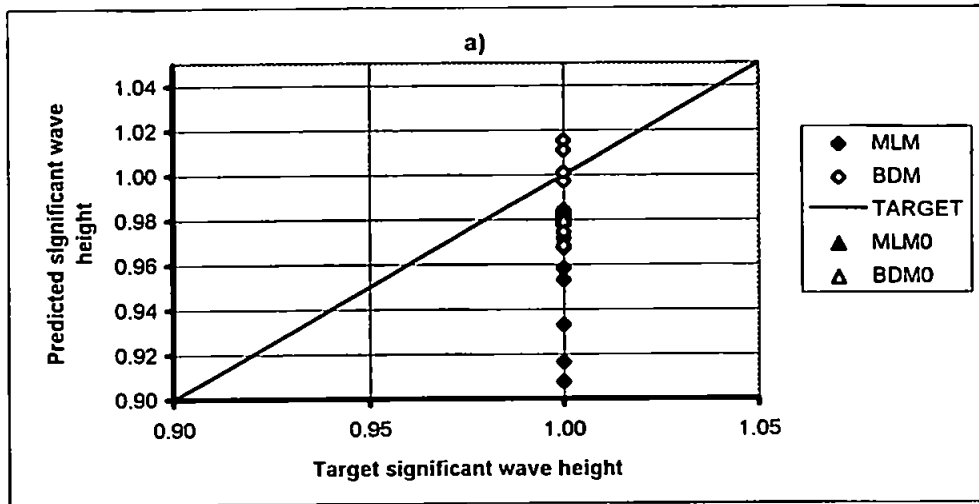


**Figure 5.14** Predicted  $H_s$  versus normalised target ( $H_s=1.0\text{m}$ ) values when MLM and BDM were applied for both spectral analysis cases for a) SW; b) S and c) SE direction. MLM0 and BDM0 stand for a case of purely incident waves. Notice the poor performance of the field array when waves are incident from the SE.

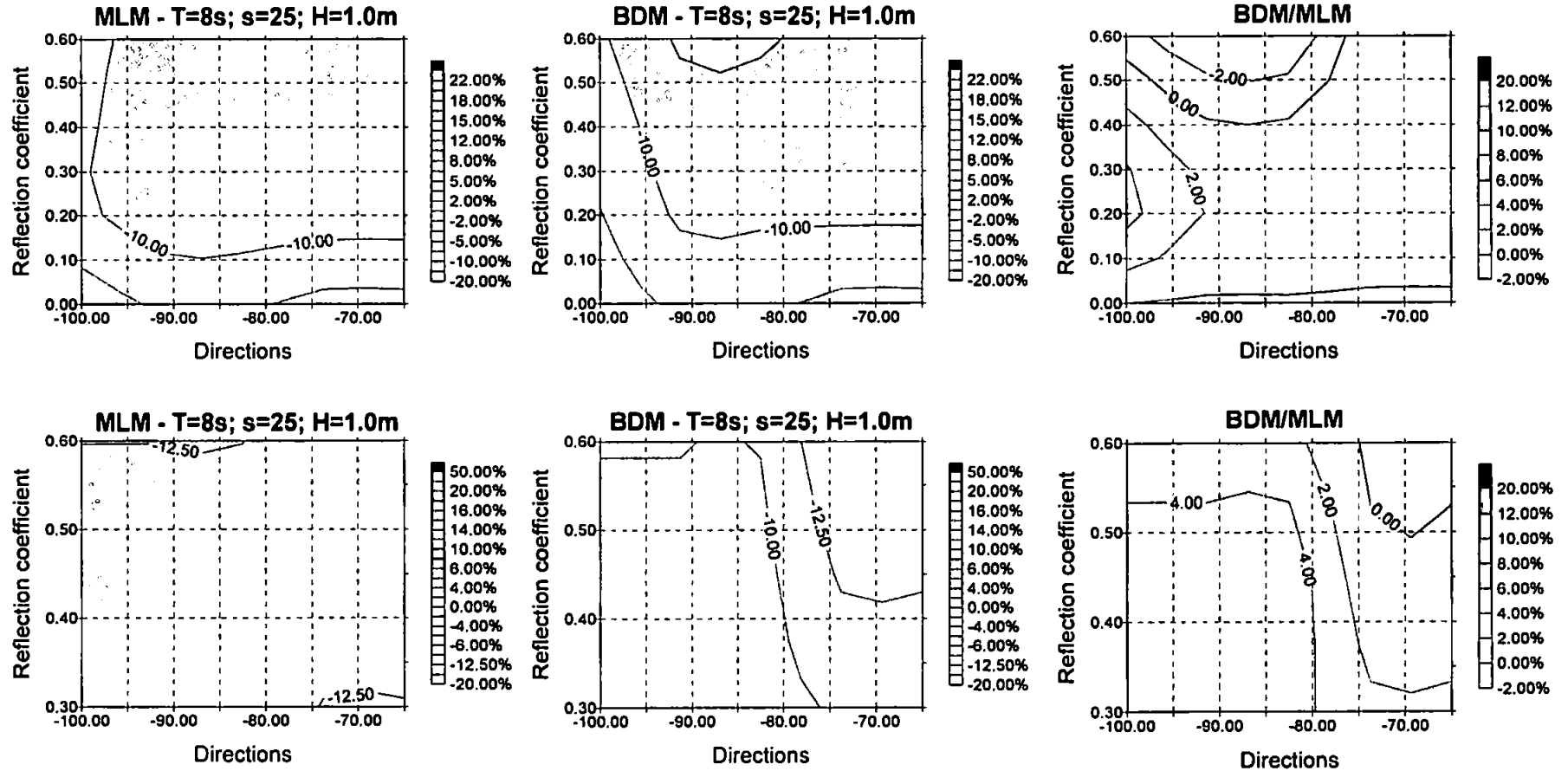


**Figure 5.15** Percentage difference between BDM and MLM  $H_s$  estimates and target values and BDM and MLM estimates for  $T=8\text{sec}$ ,  $s=25$ , for case 5 in the upper row and for case 3 in the lower row. The percentage difference is given in the legend.

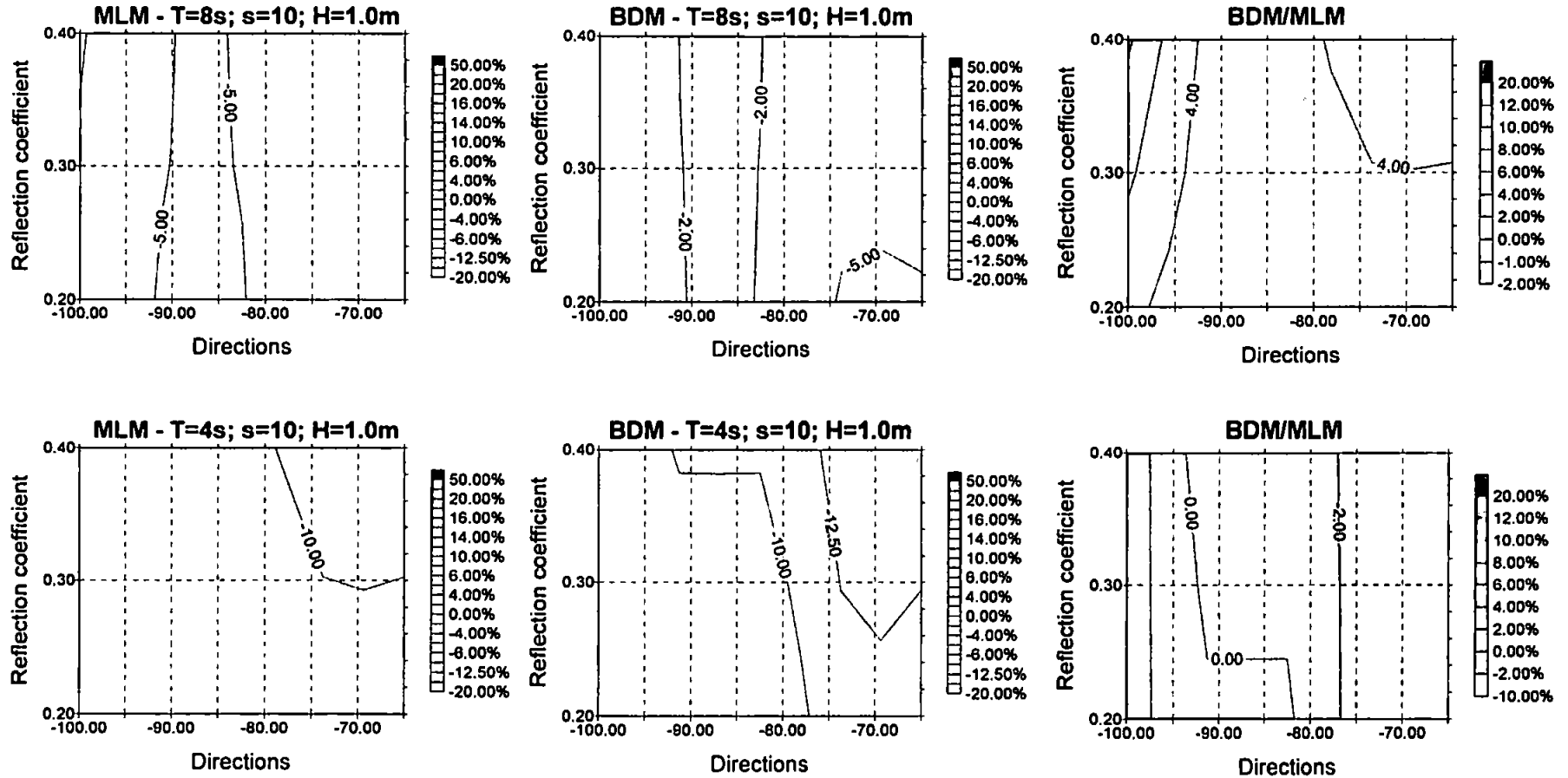


**Figure 5.16** Percentage difference between BDM and MLM  $H_s$  estimates and target values and BDM and MLM estimates for case 5 and for  $T=8sec$  in the upper row and  $T=4$  sec in the lower row;  $s=10$ . The percentage difference is given in the legend.

The smallest percentage difference is found for the wave period  $T=8$  sec and directional spread  $s=10$  (the MLM for the SW direction 1%). For a wave period of  $T=8$  sec and a directional spreading of  $s=25$ , both methods underpredict for the SW direction (-3 to 2%) and overpredict for the SE. The largest percentage difference is for the wave period of  $T=4$  sec (Figure 5.18) and directional spread  $s=10$  (up to 19% for the BDM).

### **Results for directional spread in a partially reflective wave field**

The percentage difference between results obtained by the two methods and target values and also the percentage differences between the two predictions are plotted in Figures 5.19 and 5.20. For a wave period of  $T=8$  sec and directional spread of  $s=25$ , both methods introduced the largest overprediction with the MLM providing the better estimates. For wave periods of  $T=8$  sec and  $T=4$  sec and a directional spread of  $s=10$ , the smallest differences are observed for the BDM.

Overall, both methods overpredict the directional spread and it is evident that both methods give better estimates for a broad directional spread. This overprediction is related to the directional ambiguities for some frequencies in the case of the MLM and failure of the BDM for the same frequencies.

### **Results for reflection coefficient in a partially reflective wave field**

The MLM generally overpredicted the reflection coefficient values<sup>14</sup>. The difference between predicted and target values was between -18 and 120%. The biggest discrepancies occurred in analysing data sets with the lowest reflection coefficient. The influence of spectral energy shape on prediction of reflection coefficient was investigated and found not to be significant. Figure 5.21 shows the influence of main direction of incident wave approach on the relation between predicted and target reflection coefficient. The differences between predicted and target value increases with changing directions from the SW to SE. Generally there is overprediction of the reflection of all three directions using the MLM method. The BDM reflection estimates are closer to the target in the case of the SW direction than in the case of the S and SE direction. The results show that both methods are not reliable in predicting reflection coefficient for the simulated field situation.

---

<sup>14</sup> Firstly, the reflection coefficient at each frequency is computed as the ratio of the reflected and incident energy. The averaged reflection coefficient is calculated then taking into account the amount of energy in each frequency.

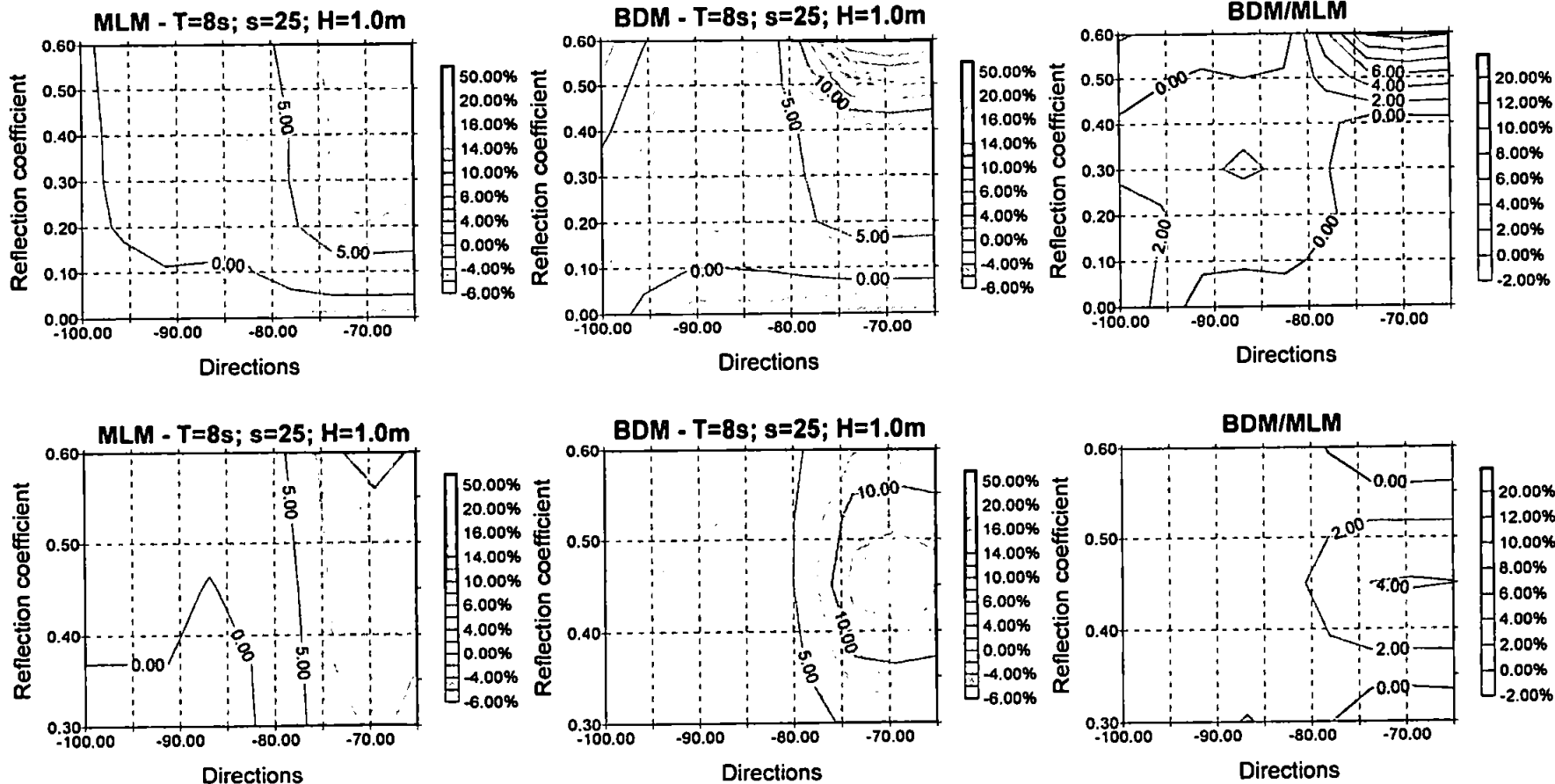


**Figure 5.17** Percentage difference between BDM and MLM direction estimates and target values and BDM and MLM estimates for  $T=8\text{sec}$ ,  $s=25$ , for case 5 in the upper row and for case 3 in the lower row. The percentage difference is given in the legend.

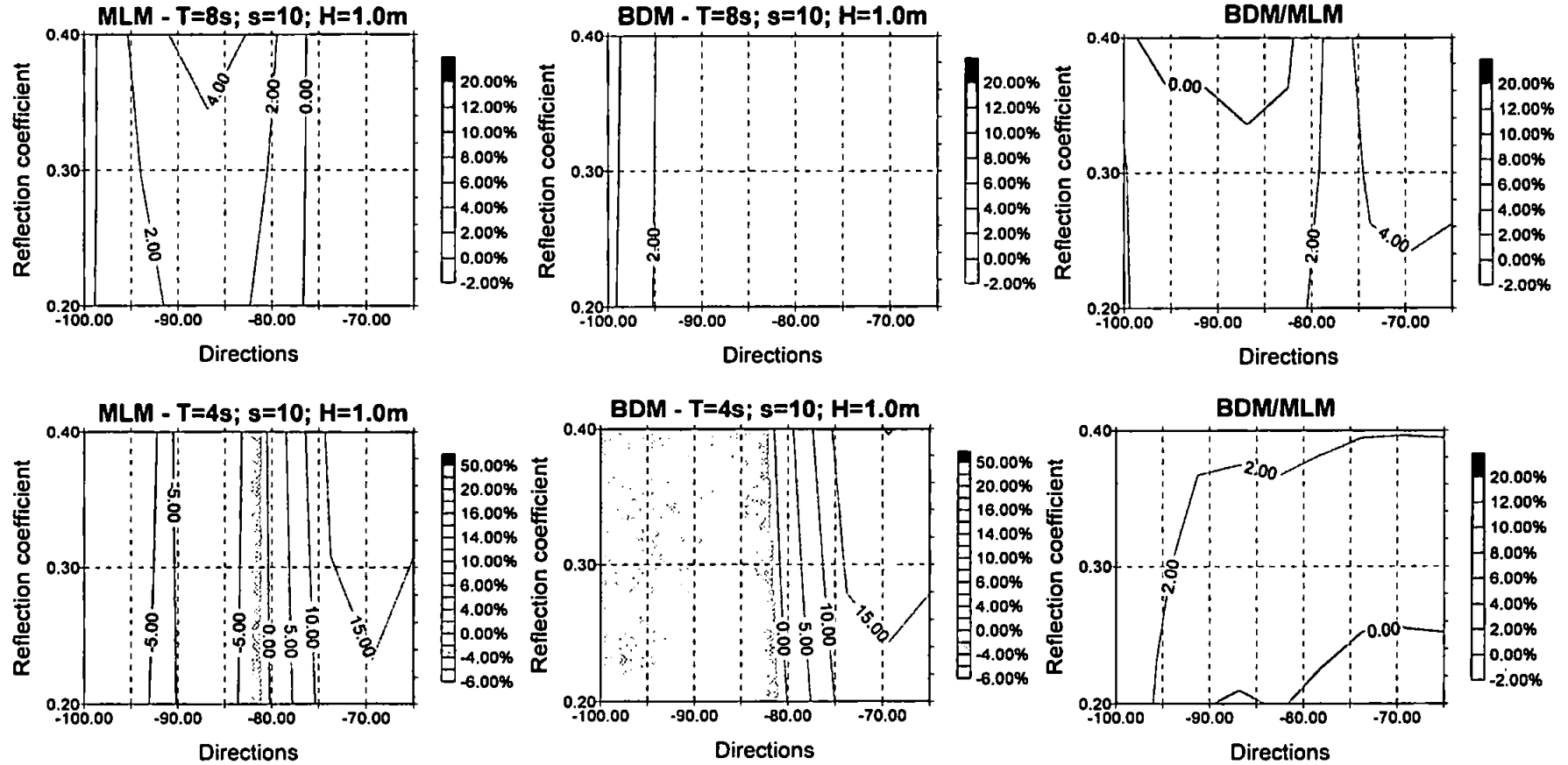


**Figure 5.18** Percentage difference between BDM and MLM direction estimates and target values and BDM and MLM estimates for case 5 and for  $T=8s$  in the upper row and for  $T=4s$  in the lower row;  $s=10$ . The percentage difference is given in the legend.

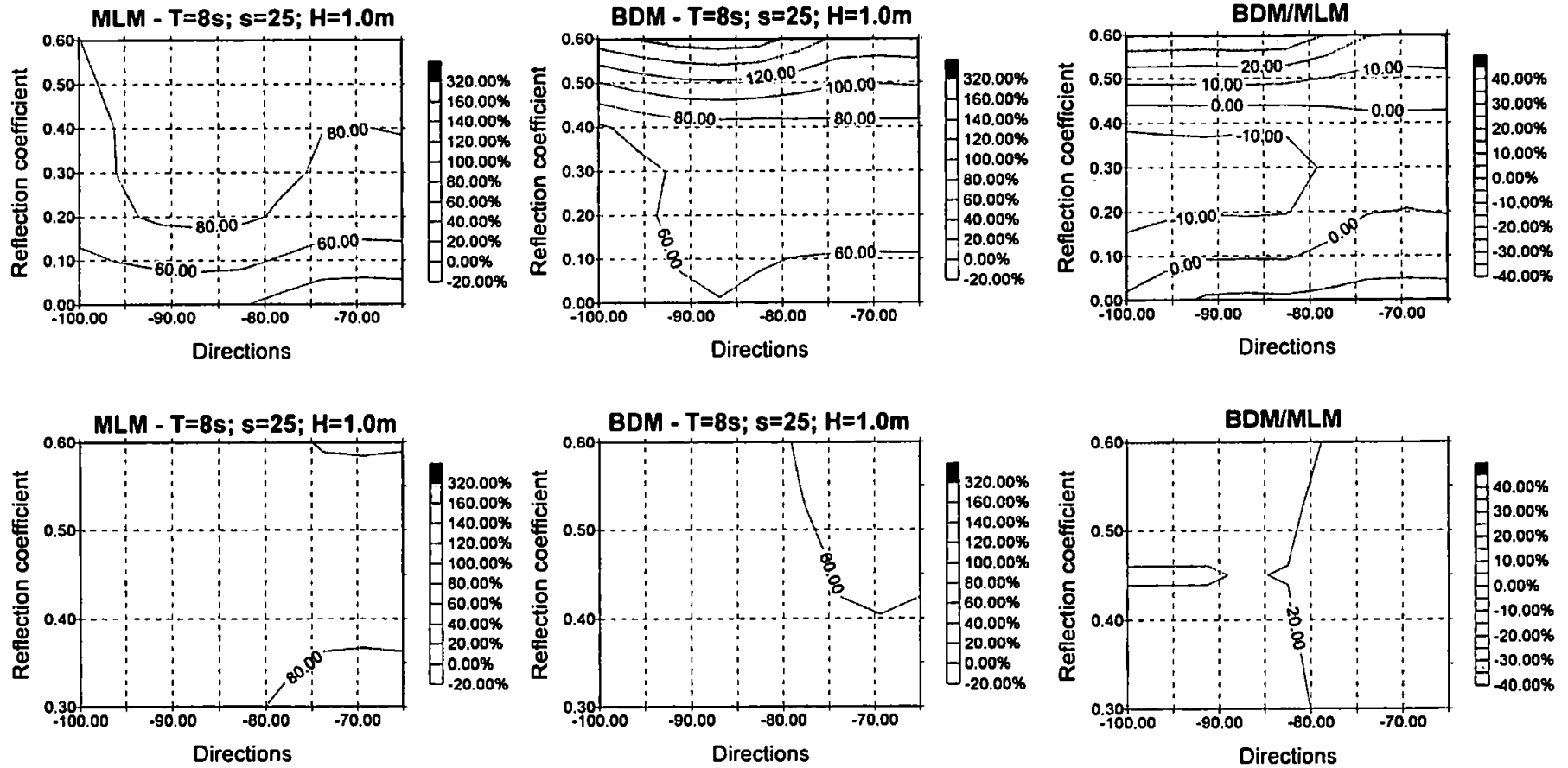


**Figure 5.19** Percentage difference between BDM and MLM directional spreading estimates and target values and BDM and MLM estimates for T=8sec, s=25 for case 5 in the upper row and for case 3 in the lower row. The percentage difference is given in the legend.



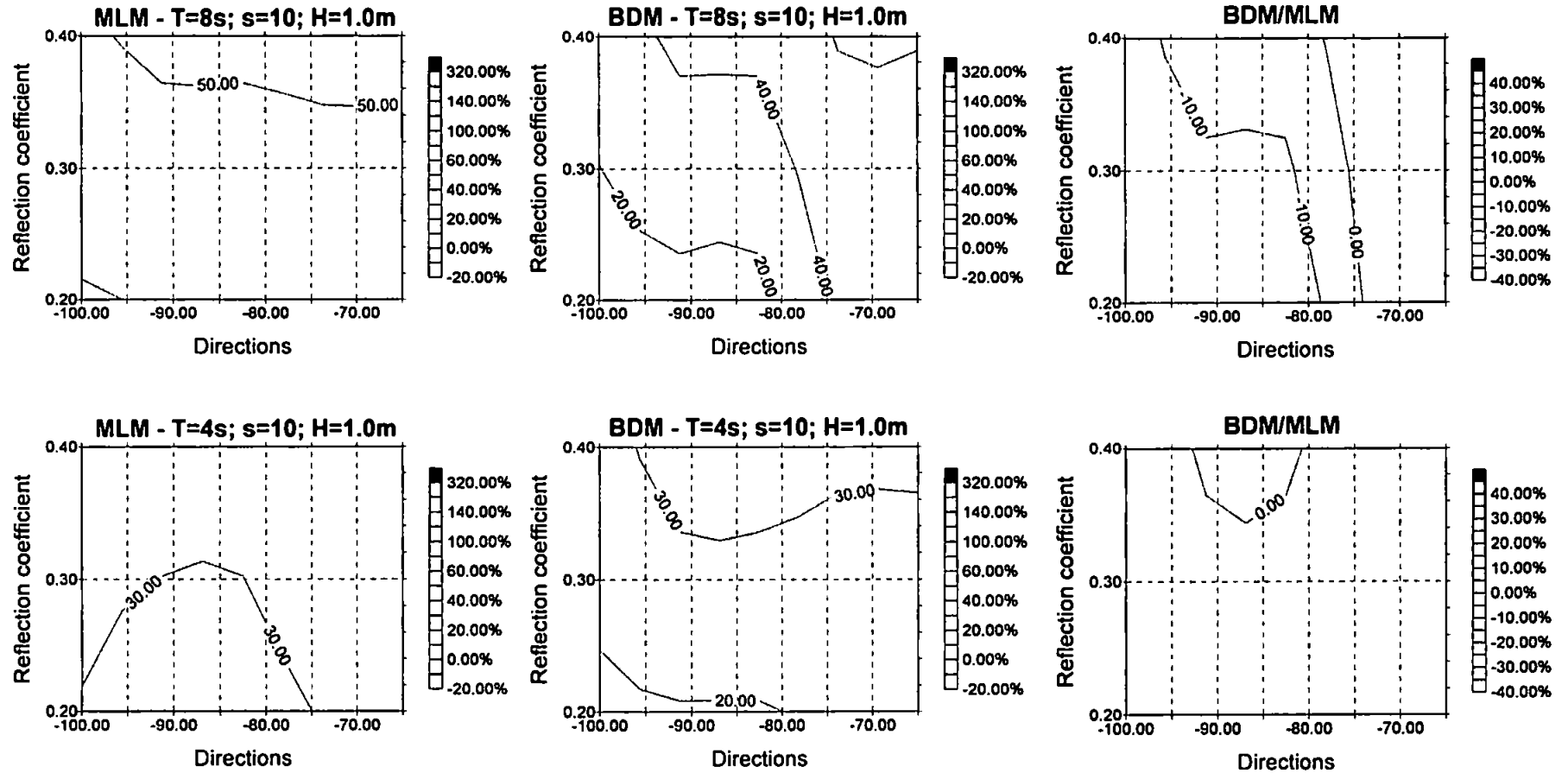


**Figure 5.20** Percentage difference between BDM and MLM directional spreading estimates and target values and BDM and MLM estimates for case 5, for  $T=8$ sec in the upper row and for  $T=4$  sec in the lower row;  $s=10$ . The percentage difference is given in the legend.

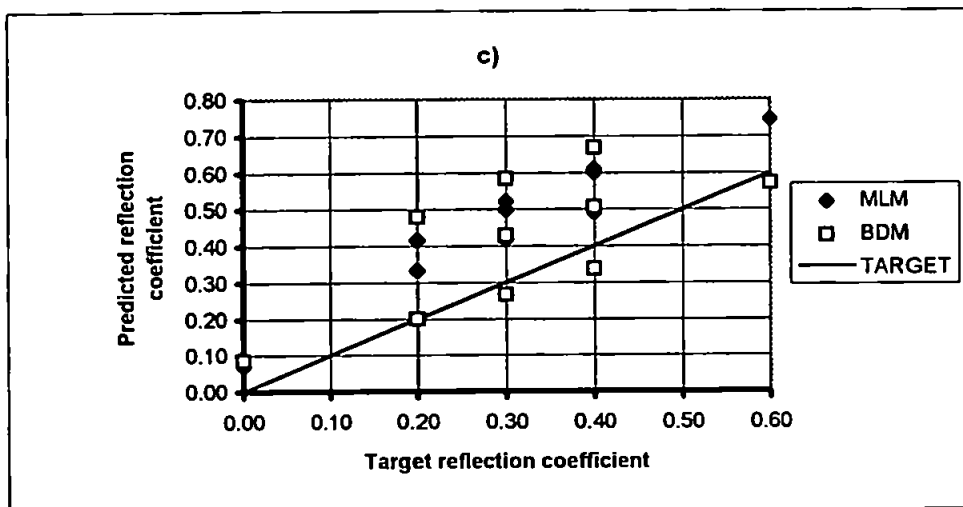
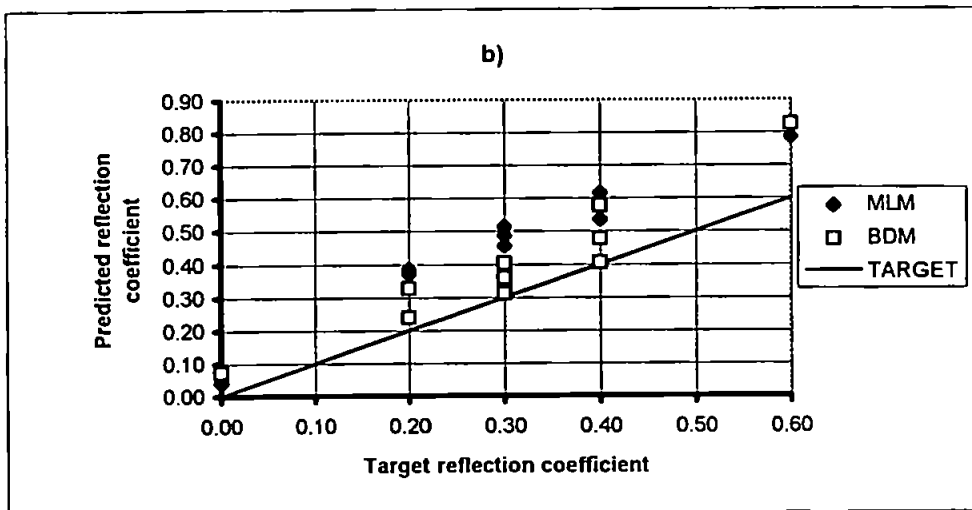
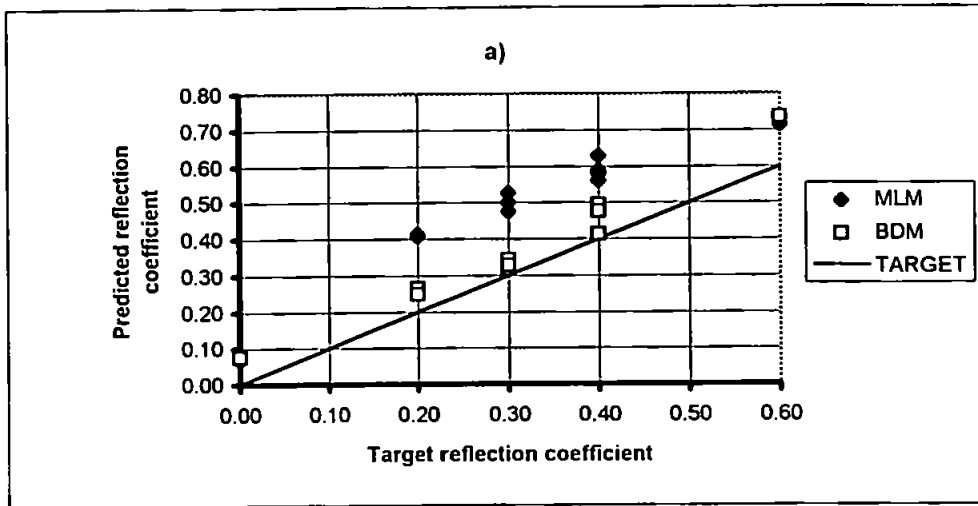


**Figure 5.21** Predicted reflection coefficient versus target values when MLM and BDM were applied for both spectral analysis cases for a) SW; b) S and c) SE direction

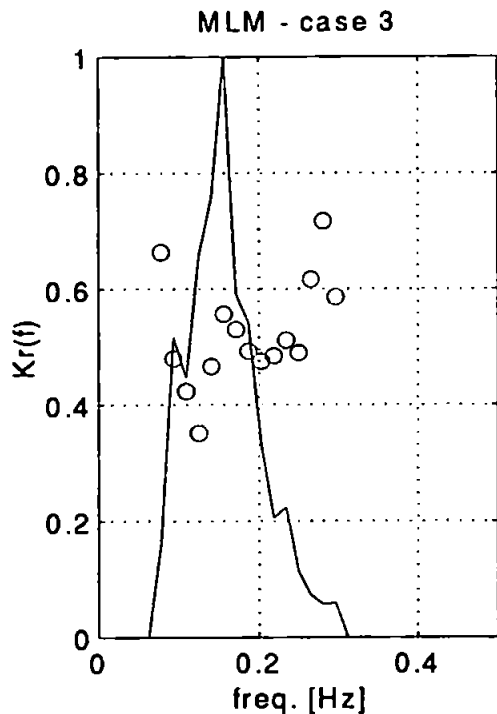


**Figure 5.22** Frequency dependent reflection coefficient predicted by MLM method (pre-defined reflection coefficient = 0.4)

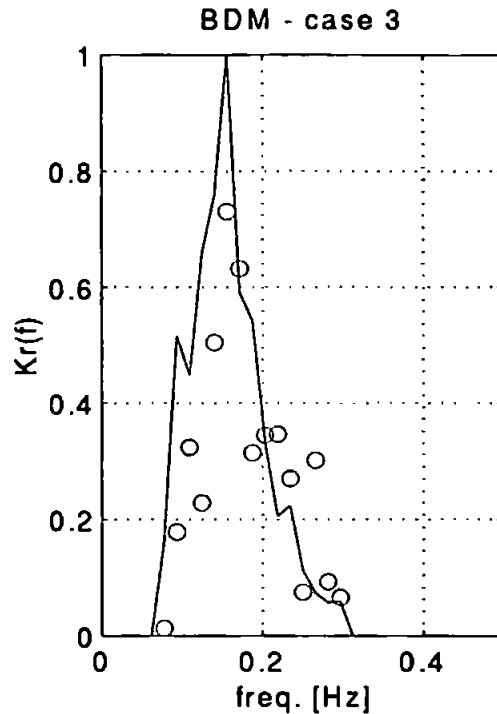


**Figure 5.23** Frequency dependent reflection coefficient predicted by BDM method (pre-defined reflection coefficient = 0.4)

### Reflection as a function of frequency

Even though the reflection coefficient was not preset as frequency dependent in the simulations, both methods produced results showing a variation of the reflection coefficient as a function of frequency as it is shown in Figures 5.22 and 5.23. In the case of the MLM (Figure 5.22), the values tended oscillate around a mean value.

Conversely the BDM results (Figure 5.23) varied quite markedly with frequency but did not oscillate from one frequency bin to another. Despite this, the BDM method produced average reflection coefficient values closer to the simulated coefficient than did the MLM. The average percentage difference is for the MLM +57.51 % and for the BDM +29.37 %.

### The influence of segment length on the directional analysis results

As discussed in section 5.3 of this chapter, the influence of the segment length of the FFT on the directional analysis results was expected to be significant. This was tested by comparing the directional results obtained using the case 5 spectral analysis with those

obtained using the case 3 spectral analysis (in which the segment length was reduced from 512 points to 128 points hence increasing the L/S ratio (see Table 5.3)). The numerically simulated data enabled the quantification of the difference in accuracy of estimates when smoothing is applied. The percentage error between estimates and target values obtained by the BDM and the MLM method for incident significant wave height, direction, directional spreading and reflection coefficient have been calculated. This is illustrated in Table 5.4 with values of *rms* for 7 selected files.

#### *Significant wave height*

For the simulated data without reflection, the wave height estimates are higher for case 3 than for case 5. The predicted significant wave height for the wave period of  $T=8$  sec and directional spreading of  $s=25$  differ less from the target values for case 3 than for case 5 when the BDM was used (Figure 5.15). The MLM estimates for case 5 and case 3 are only slightly different ( $rms=0.046$  and  $0.047$ ).

#### *Direction*

For the simulated data without reflection, the differences between estimated and target values decrease in case 3 for both methods<sup>15</sup>. From Figure 5.17 it can be seen that direction estimates improved for case 3 of data simulated with reflection for the S direction when the MLM was used. It seems that the min and max. differences are smaller but the average error is usually higher for case 3. Generally the BDM estimates have been improved with increasing smoothing and also when all 6 transducers were taken in account.

#### *Directional spreading*

For simulated data without reflection, the directional spreading increases for all directions, for case 3, when the MLM was used. In case 3 when the BDM was used the reduction in directional spreading has been observed for all directions. The same was observed for the data simulated in the reflection. The BDM estimates are closer to the target directional spreading because the previously unresolved frequency components are overcome by smoothing. The percentage differences for directional spreading for the data simulated with reflection included are given in Figure 5.19 and in Table 5.4.

---

<sup>15</sup> Except for the BDM estimates from SW

## Reflection

The reflection coefficient, in case 3, increased when the MLM was used and decreased when the BDM was used to analyse the simulated data without reflection. The difference between reflection coefficient estimates and target values for the simulated data with reflection obtained by both methods decreased in case 3. Generally the difference decreased with increased smoothing (*rms* decreases from 0.071 to 0.070 for case of the MLM and from 0.043 to 0.036 for the BDM).

## Summary

In Table 5.5 the method with the lowest error is shown for each set of test parameters. Overall the BDM (B) gives closer estimates of incident wave height and directional spreading and the MLM (M) gives more accurate main directions. The MLM gives the best estimates for all parameters for cases without reflection. For all parameters and cases the percentage error and root mean square errors are calculated and given in Table 5.4.

	<i>wave height</i>		<i>direction</i>		<i>directional spreading</i>		<i>reflection</i>	
	<i>percentage of difference</i>							
	MLM	BDM	MLM	BDM	MLM	BDM	MLM	BDM
<i>case 5 (cor.)</i>	1.419	1.315	0.992	1.157	8.689	9.982	9.269	105.059
							9.238	6.359
	<i>root mean square</i>							
<i>case 5 (cor.)</i>	0.015	0.014	0.726	0.794	1.643	1.743	0.026	0.365
							0.026	0.019
	<i>root mean square for 7 selected files</i>							
<i>case 5 (cor.)</i>	0.046	0.044	1.496	2.386	4.964	6.079	0.073	1.713
<i>case 3 (cor.)</i>	0.047	0.039	1.420	1.662	5.281	3.307	0.071	0.043
							0.070	0.045
							0.070	0.036

**Table 5.4** Percentage difference and root mean square values where (cor.) means corrected values – the frequencies which were not resolvable were not taken in account ( $K_r$  greater than 1.0)

The same trend, the improvement of BDM results for case 3, can be observed from Table 5.4 and Table 5.5. The percentage difference values show that the MLM and BDM estimates are only a fraction of a percentage different in most of the cases. The largest difference of 3% is observed in reflection prediction. The directional estimates obtained by both methods differ by less than 10% from the target values. Wave height and direction are

predicted with only 1-2% difference. The results depend on direction of wave approach, which is related to the array shape and orientation. For some of the simulated data the BDM estimates are closer to the target values and for the others the MLM estimates are more accurate. The BDM predicts more accurate wave height, even though the MLM estimates are very similar. The BDM method predicts better direction and directional spreading.

Kr		Hi			Di			Si		
		case 5			case 5			case 5		
s=25	T=8	-100	-90	-65	-100	-90	-65	-100	-90	-65
	0	M	M	M	B	M	M	M	M	M
	0.3	B	B	B	M	M	B	B	B	B
	0.4	B	B	B	B	M	B	B	B	B
	0.6	M	M	B	M	B	M	M	M	M
s=10	T=8									
	0.2	B	M	B	M	M	M	B	B	B
	0.3	B	M	B	M	M	M	B	B	B
	0.4	B	M	B	B	B	M	B	M	B
s=10	T=4									
	0.2	B	B	M	B	B	B	B	B	M
	0.3	B	B	M	B	B	M	B	B	M
	0.4	B	M	M	B	B	M	B	B	M
		case3			case3			case3		
s=25	T=8	-100	-90	-65	-100	-90	-65	-100	-90	-65
	0									
	0.3	B	B	B	B	M	B	B	B	B
	0.4		B	B		M	M		B	B
	0.6		B	M		M	B		B	B

**Table 5.5** The method with the closest estimates to the target values<sup>16</sup>

Additionally it can be seen from Table 5.4 that overall the accuracy of the estimates further improves with reducing segment length (case 3). However, this is more significant for the BDM than the MLM results.

### 5.5 Directional analysis of field data

In this section, the same analysis is undertaken on the field data. The difference between directional estimates of two methods, BDM and MLM, is calculated and related to the BDM/MLM difference for simulated data in order to find out the most appropriate

<sup>16</sup> Where Hi = incident significant wave height, Di = incident main direction, Si = incident directional spreading, s=directional spreading, Kr=reflection coefficient

estimates for the numerical model validation.

### 5.5.1 Offshore data

#### Data selection

Forty-two data sets were selected. These data sets were classified into three groups (as in section 5.3) by referring to frequency shape, narrow frequency spectra<sup>17</sup>, bimodal spectra and broad frequency spectra. The main direction for the selected data was from the south (almost normal incidence to the breakwaters) or slightly south-west with only five data sets having a main direction from the south east. Prior to the directional analysis, spectral analysis was performed in the same way as was carried out on the numerically simulated data described in section 5.4. All the data sets were analysed using the case 5 spectral analysis and 18 of these were re-analysed using the case 3 spectral analysis.

#### Results for incident significant wave height

Incident significant wave heights, normalised by the MLM estimates are shown in Figure 5.24 for both case 3 and case 5 spectral analysis. The BDM estimates are generally higher than estimates obtained using MLM. The case 3 spectral analysis increases the significant wave height. Table 5.6 summarises the percentage differences between the BDM and MLM estimates.

<i>BDM/MLM</i>	<i>overall</i>		<i>T &lt; 6 sec</i>		<i>T &gt; 6 sec</i>	
	<i>case 5</i>	<i>case 3</i>	<i>case 5</i>	<i>case 3</i>	<i>case 5</i>	<i>case 3</i>
<i>percentage</i>						
min	-9.193		-5.362		-9.193	
max.	28.066		20.293		28.066	
abs min	0.270		0.270		1.263	
average	7.270		2.540		10.495	
	<i>18 selected data files</i>					
min	-9.193	-18.612	-4.954	-1.191	-9.193	-18.612
max.	22.684	20.255	4.669	11.017	22.685	20.255
abs min	0.27	0.11	0.27	0.11	1.263	1.159
average	3.837	5.792	1.804	5.446	5.464	6.069

**Table 5.6** Percentage difference between BDM and MLM significant wave height estimates

<sup>17</sup> Narrow frequency spectrum stands for spectrum when energy is accumulated around lower frequencies (swell type). However, there is always a presence of some energy for higher frequencies (wind waves).

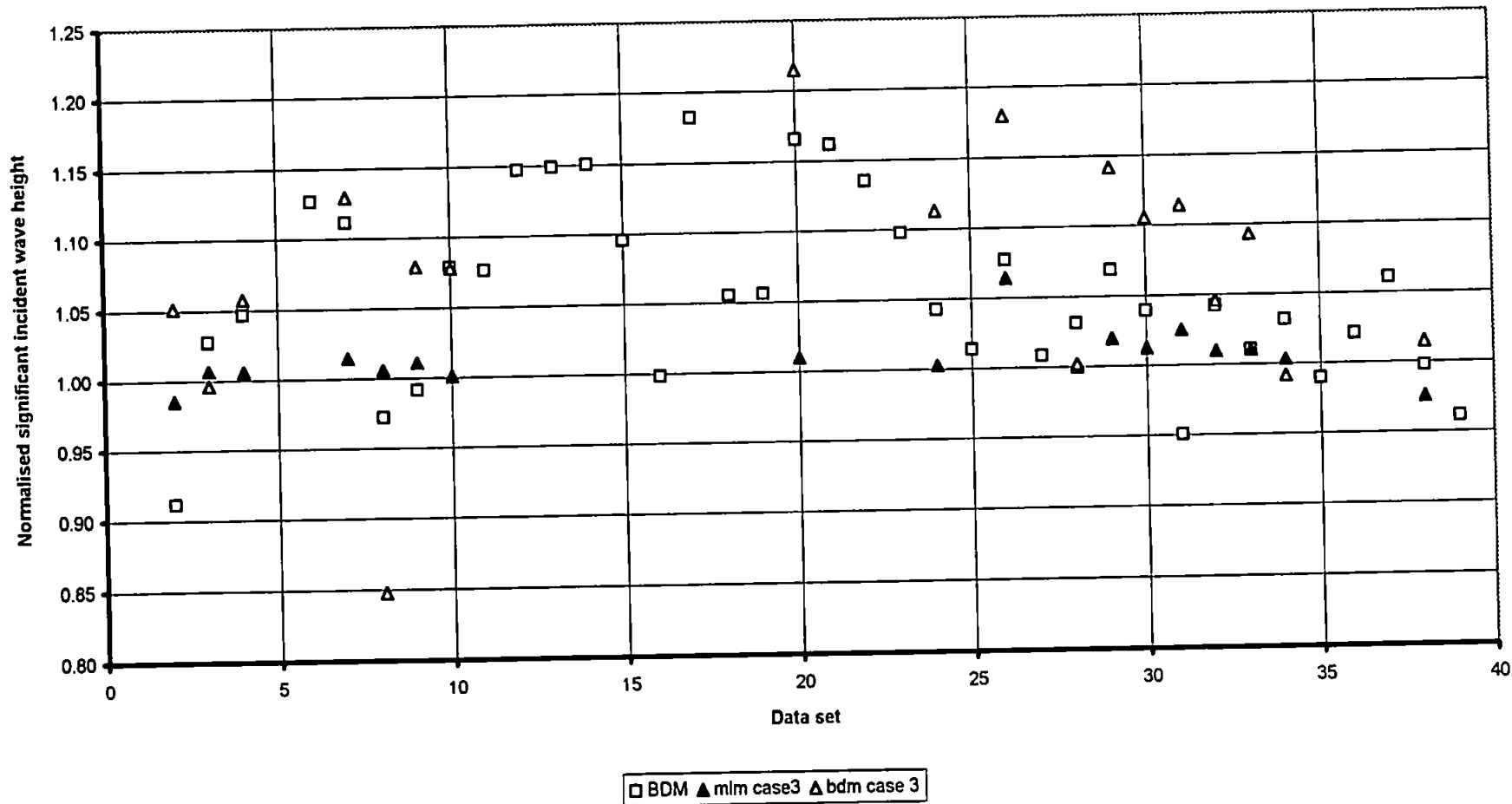


Figure 5.24 BDM and MLM estimates of significant wave height for case 5 and case 3 normalised to the MLM estimates the case 5.



These results show the same trends as was found from the numerically simulated data. However, the percentage difference between the BDM and MLM are larger than for the simulated data. The same was found for re-selected data with spectral and directional distribution similar to the simulated data. The larger differences are observed for a peak period higher than 6s (10.5%) and for waves approaching from the South. The average difference is 7.27%. The maximum difference is 28.07% and the minimum difference is 2.54% for peak wave periods  $T$  less than 6s.

### Results for main direction

Figure 5.25 shows the predicted main incident directions. Both methods predicted almost the same direction. The direction interval for analysis was  $12^\circ$  which could be considered as a tolerable difference between results obtained by the two methods. There are four cases where the differences are larger than  $12^\circ$ . A reason for such disagreement is related to the unstable MLM results when energy is distributed almost uniformly over all directions.

The percentage difference between BDM and MLM is summarised in Table 5.7. The percentage difference between the BDM and MLM is again larger than for the simulated data. The larger differences were observed for the normal (South) direction and for the peak wave period less than 6 s. The average percentage is almost the same for case 5 and case 3 spectral analysis as was found using the numerically simulated data. The average difference is 3.76% and the maximum difference is 18.2%. Overall average percentage difference is less than 1% for case 3.

<i>BDM/MLM</i>	<i>overall</i>		<i>T &lt; 6 sec</i>		<i>T &gt; 6 sec</i>	
	<i>case 5</i>	<i>case 3</i>	<i>case 5</i>	<i>case 3</i>	<i>case 5</i>	<i>case 3</i>
<i>percentage</i>						
min	-9.186		-9.186		-3.565	
max.	18.202		13.686		18.20	
abs min	0.152		0.878		0.152	
average	3.764		2.858		4.382	
	<i>18 selected data files</i>					
min	-1.723	-9.312	-1.723	-9.312	-0.630	-4.447
max.	10.733	6.364	10.733	2.88	7.811	6.365
abs min	0.152	0.236	0.878	0.236	0.152	0.480
average	2.421	-0.405	3.109	-3.329	1.870	1.933

**Table 5.7** Percentage difference between BDM and MLM direction estimates

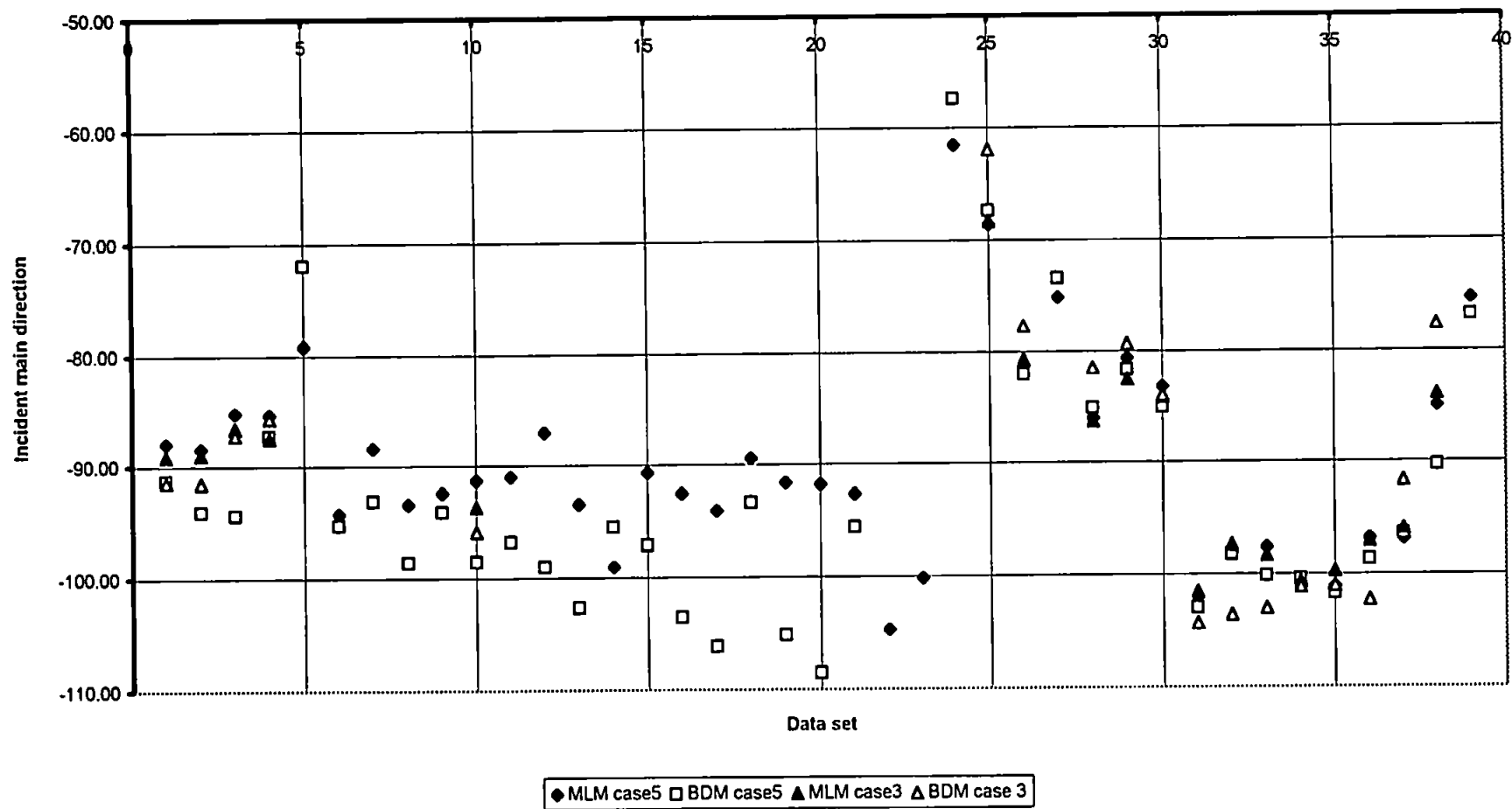


Figure 5.25 BDM and MLM estimates of directions for case 5 and case 3

## Results for directional spreading

The largest difference between the BDM and MLM was found for directional spreading. The BDM generally predicts a narrower directional distribution than the MLM thus the maximum difference was -35%. The average difference is -16%. The difference increases with smoothing (case 3) as shown in Table 5.8.

<i>BDM/MLM</i>	<i>overall</i>		<i>T &lt; 6 sec</i>		<i>T &gt; 6 sec</i>	
	<i>case 5</i>	<i>case 3</i>	<i>case 5</i>	<i>case 3</i>	<i>case 5</i>	<i>case 3</i>
<i>percentage</i>						
min	-35.628		-22.887		-35.628	
max.	13.424		13.424		-8.122	
abs min	0.423		0.423		8.122	
average	-16.418		-9.184		-21.350	
	<i>18 selected data files</i>					
min	-26.431	-39.367	-22.887	-26.675	-26.431	-39.367
max.	13.424	-15.002	13.424	-15.002	-8.122	-21.484
abs min	5.211	15.002	5.211	15.002	8.122	21.484
average	-13.380	-26.790	-10.177	-22.566	-15.943	-30.169

**Table 5.8** Percentage difference between BDM and MLM directional spreading estimates

The largest difference is observed for case 3 when the MLM constantly produces a larger directional spread as was found for the simulated data. This is evident from Figure 5.26 where directional distributions for case 3 and 5 for both methods are given.

<i>BDM/MLM</i>	<i>overall</i>		<i>T &lt; 6 sec</i>		<i>T &gt; 6 sec</i>	
	<i>case 5</i>	<i>case 3</i>	<i>case 5</i>	<i>case 3</i>	<i>case 5</i>	<i>case 3</i>
<i>percentage</i>						
min	-61.569		-52.347		-61.569	
max.	22.033		22.033		-25.009	
abs min	4.163		4.163		25.009	
average	-35.087		-18.461		-46.422	
	<i>18 selected data files</i>					
min	-55.107	-75.225	-52.347	-74.667	-55.107	-75.225
max.	22.033	-38.079	22.033	-44.366	-25.009	-38.079
abs min	8.506	38.079	8.506	44.365	25.009	38.079
average	-35.051	-59.893	-27.935	-60.178	-40.743	-59.666

**Table 5.9** Percentage difference between the BDM and the MLM reflection coefficient estimates<sup>18</sup>.

<sup>18</sup> This is for case when reflection coefficient is corrected.

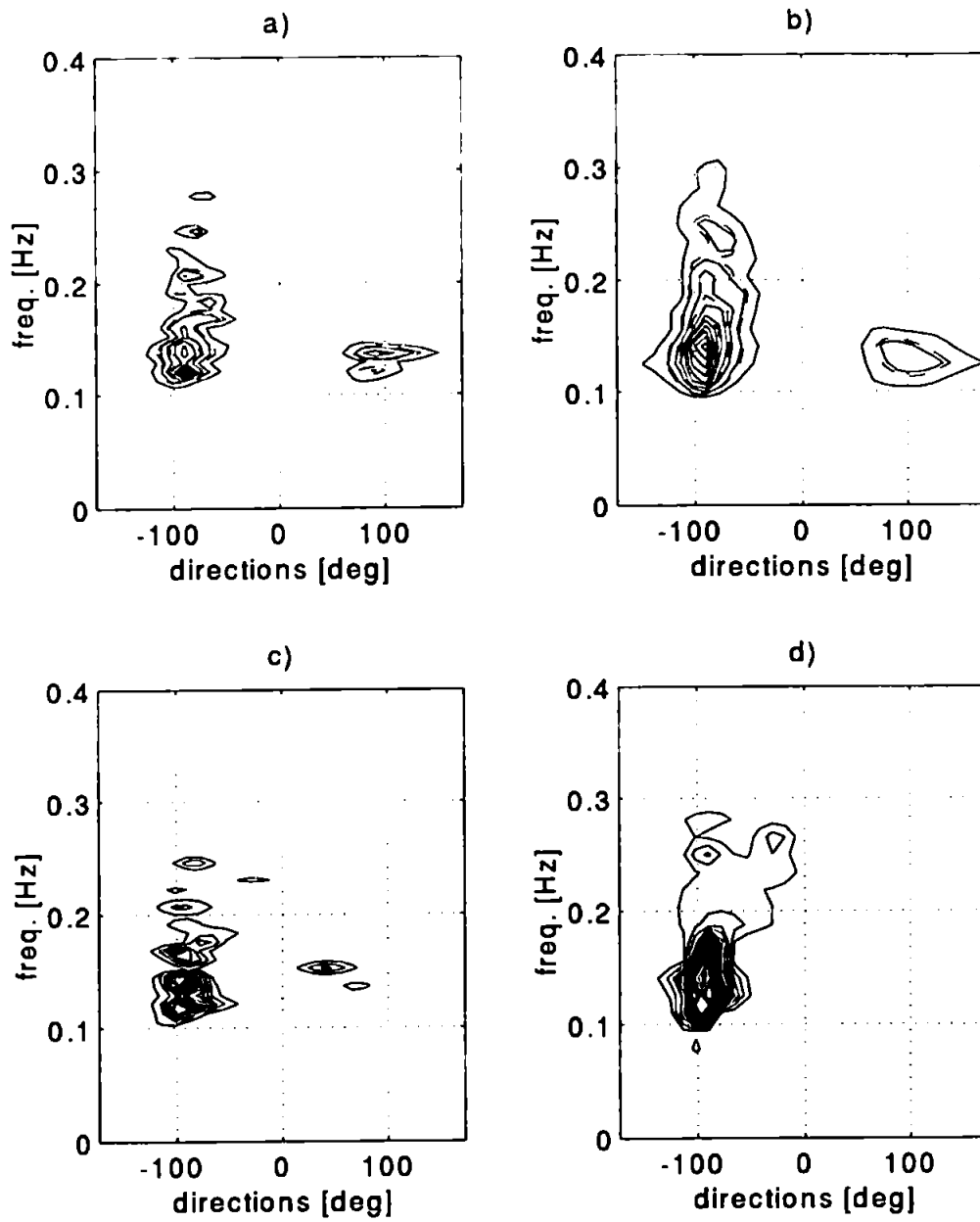


**Figure 5.26** The MLM and BDM directional distribution; a) MLM case 5; b) MLM case 3; c) BDM case 5; d) BDM case 3; (— 5% ; — 10-100% with an interval of 10%)

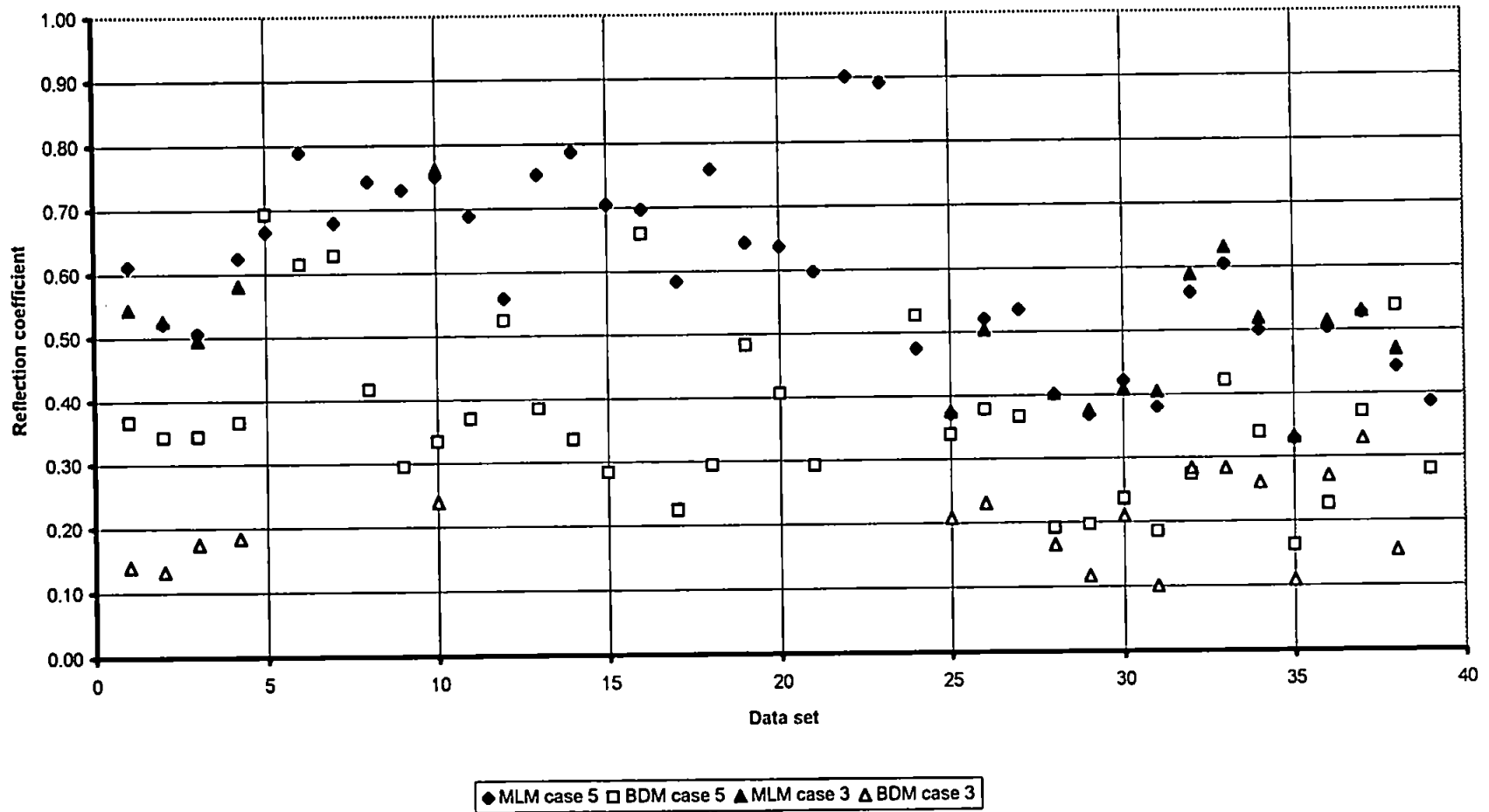


Figure 5.27 BDM and MLM estimates of reflection coefficient for case 5 and case 3

## Results for reflection coefficient

Reflection coefficient estimates are shown in Figure 5.27. The MLM estimates are generally higher than the estimates obtained using the BDM and using the case 3 spectral analysis reduces the reflection coefficients.

These results show the same trends as was found from the numerically simulated data but the differences are again higher. This is also illustrated in Table 5.9. The highest differences are observed for wave periods greater than 6 sec. The difference between the estimates of the two methods also increases for the case 3 spectral analysis. The average difference is -35% and the maximum -61.56%. (The differences increase for case 3).

An example of the frequency dependent reflection coefficient is given in Figure 5.28. The MLM estimates are higher for the lower frequencies, but also higher than expected for higher frequencies where a certain amount of energy was expected to be dissipated in breaking as was already mentioned in section 5.3. In the case of the BDM, the reflection varies quite strongly with frequency. The same was observed for case 5 and case 3.

### 5.5.2 Inshore field data

Forty-two data sets were selected measured at the same time as the offshore data. These wave measured data were collected inshore of the breakwaters (Figure 3.2) using the IWCM and therefore the only wave reflections present were those from the beach face. This is a very interesting case to study as the nature of the reflection is more complex than from a structure. The existing spectral analysis of the data was considered. As shown in Table 5.10, the value of  $L/S$  has been estimated in the interval 0.54 - 1.27<sup>19</sup>. The MLM and BDM directional analysis were performed with these data. The starting value of hyperparameter  $u$  for the BDM method was originally set to 20, as with the offshore and the simulated data. It was found that the method failed to produce results for some frequencies, therefore the value of hyperparameter  $u$  was changed to 2.

---

<sup>19</sup> As data were recorded here for a longer period than offshore the value of  $S$  is larger than for the offshore data but the value of  $L/S$  has been preserved as for the case 5 spectral analysis offshore.

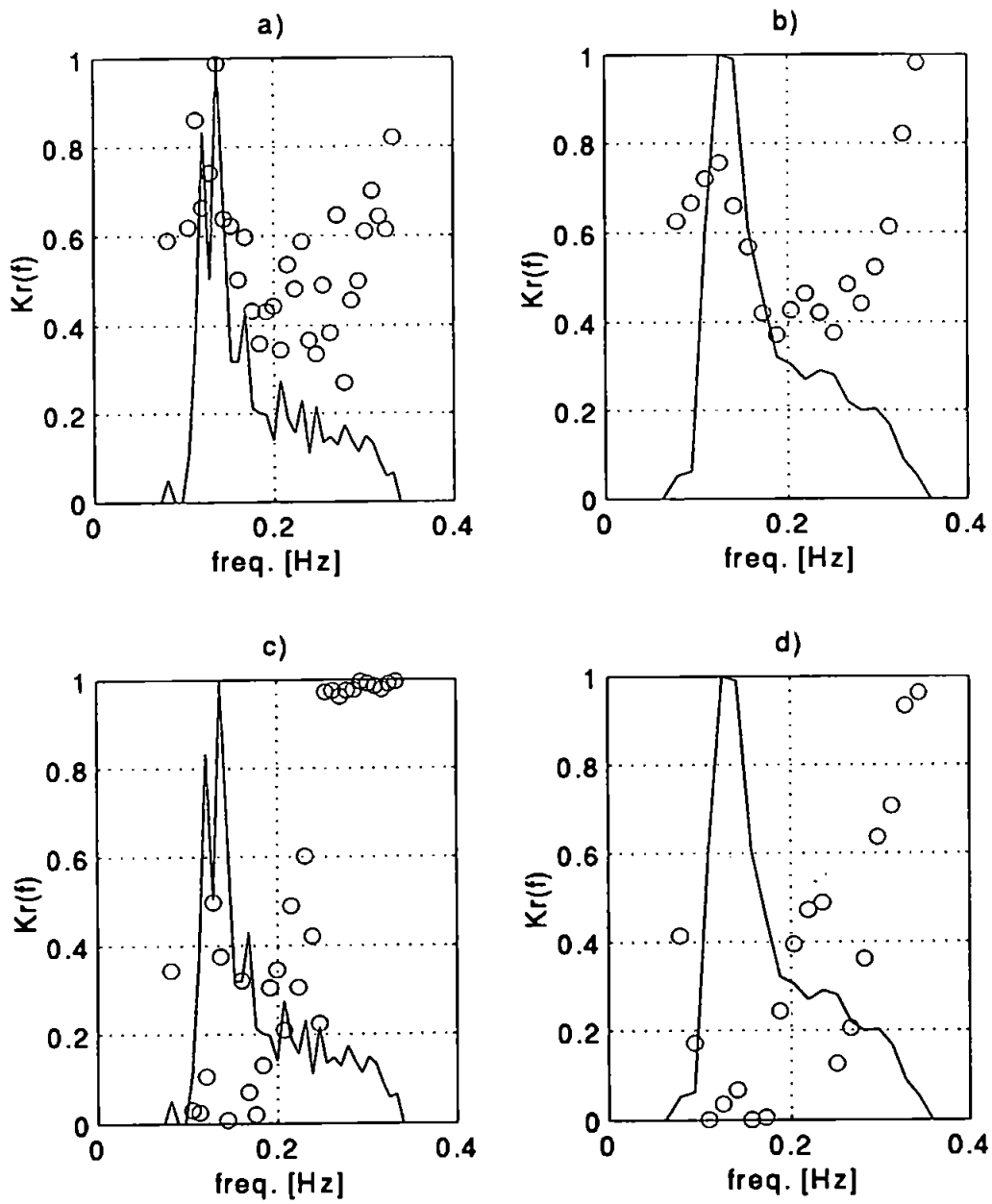


**Figure 5.28** The MLM and BDM frequency dependent reflection coefficient estimates and frequency spectrum normalised to the peak spectral energy; a) MLM case 5; b) MLM case 3; c) BDM case 5; d) BDM case 3

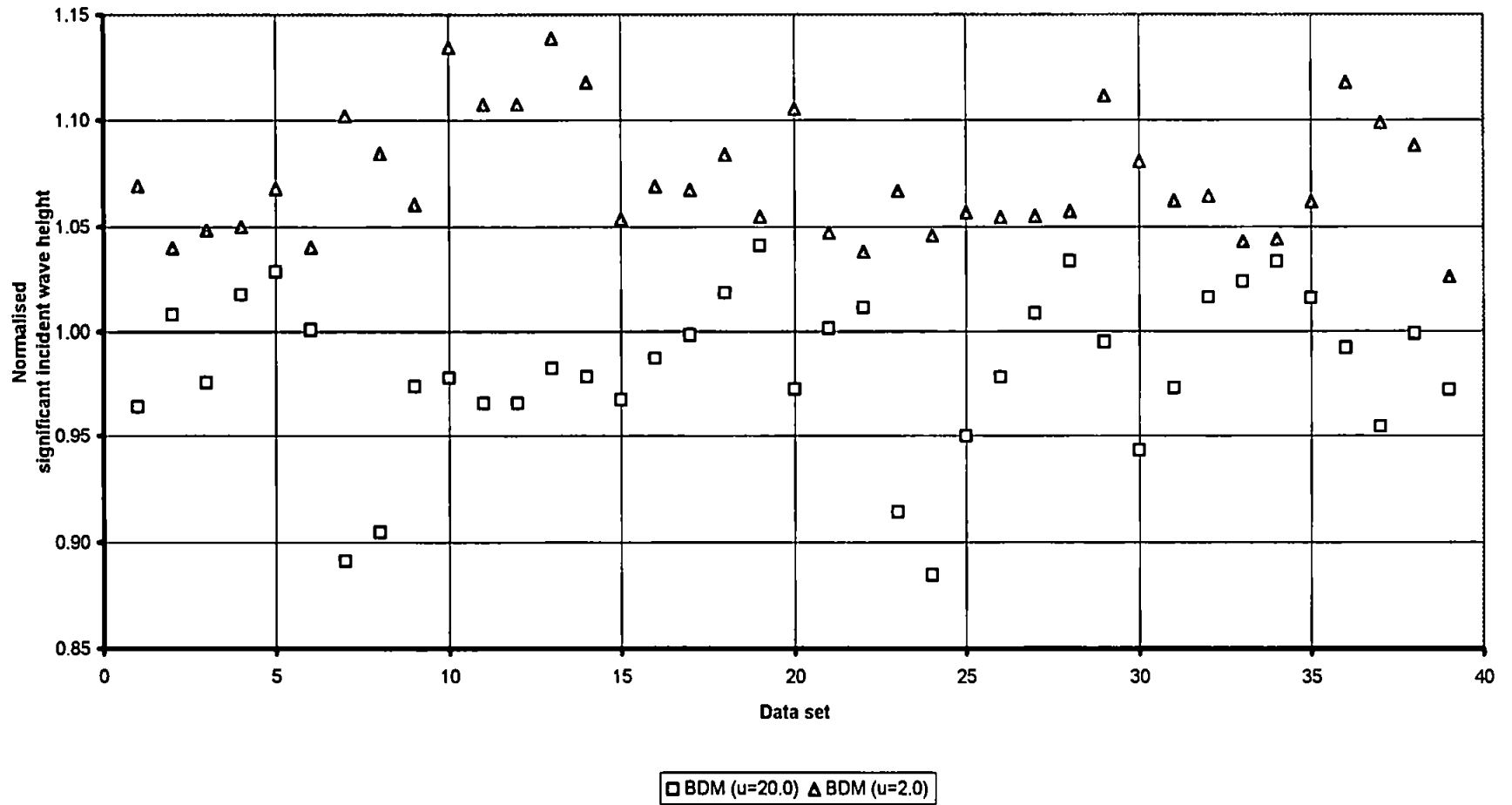
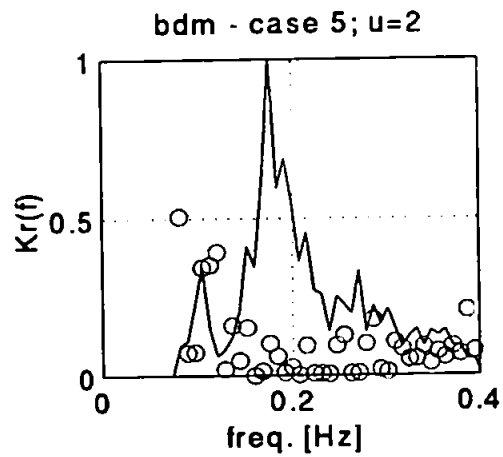
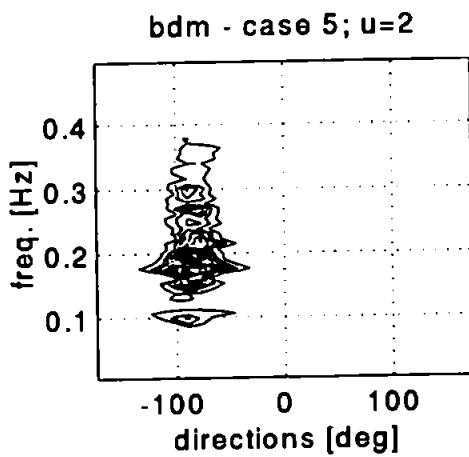
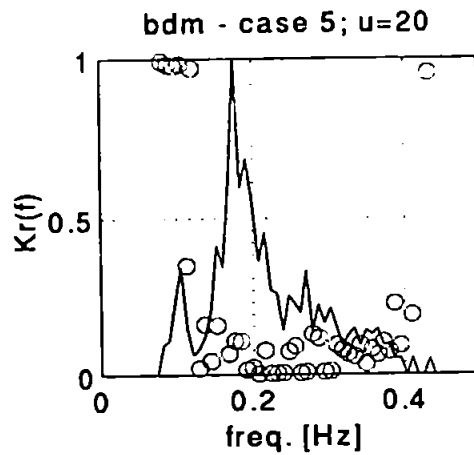
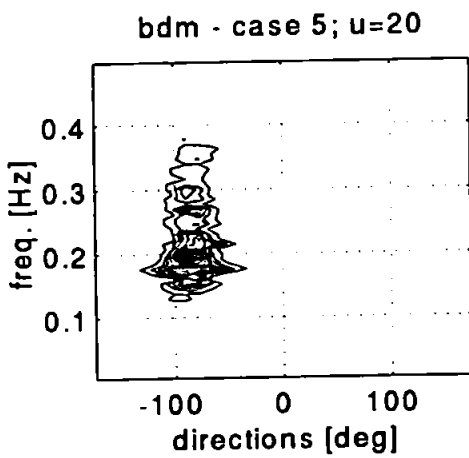
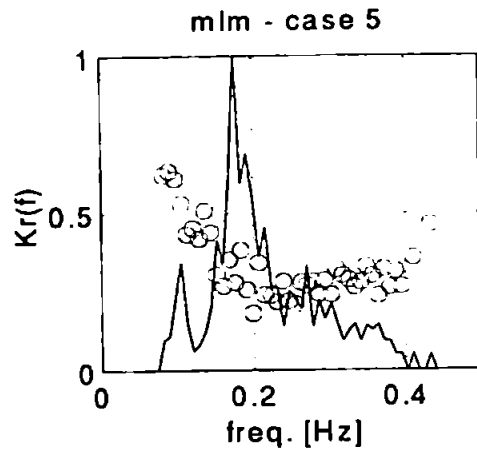
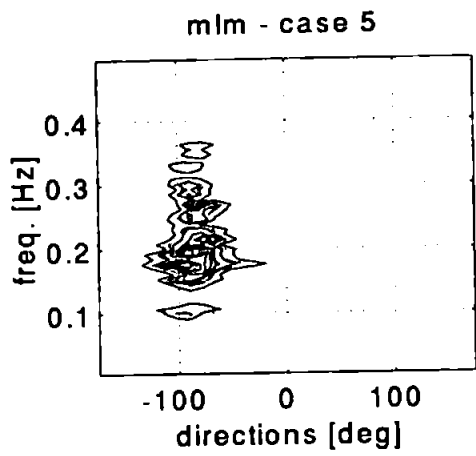


Figure 5.29 BDM estimates of significant wave height normalised to the MLM estimates (inshore field data)





**Figure 5.30** The MLM and BDM directional distribution for inshore data ( — 5%; — 10-100% with an interval of 10%)

**Figure 5.31** The MLM and BDM frequency dependent reflection coefficient estimates for inshore data

<i>Case No</i>	<i>S (sec)</i>	<i>smoothed frequ. bins</i>	<i>Limits Lower f</i>	<i>of L/S Highest f</i>	<i>df</i>	<i>Degrees of freedom</i>	<i>95% confidence limits</i>
5	256	2	0.54	1.27	0.0078	28	0.63-1.8

**Table 5.10** L/S values for the inshore field data

### Results for incident significant wave height

Significant wave height estimates normalised by the MLM are shown in Figure 5.29. Again, the estimates obtained using the MLM are generally lower than those obtained by the BDM. The percentage difference between the BDM and the MLM is given in Table 5.11. They are similar to those for the offshore field data. The maximum difference is 23.71% and the average difference 9.33%.

### Results for the main directions

The agreement between the BDM and the MLM direction estimates is excellent. The maximum difference between predictions obtained by the two different methods was 6° whereas the average difference was between 0° and 2°. The percentage difference between the BDM and the MLM is given in Table 5.11. The maximum and minimum values are smaller than in the case of offshore data and the average difference is only -1.81 % . The maximum difference is -7.65% compared to 18.2 % for the offshore data.

### Results for the directional spreading

The difference between the BDM and the MLM directional spreading estimates is also given in Table 5.11. The values are very similar to the values obtained in the case of the offshore data sets. However, the differences are not consistent. The BDM does not produce a narrower directional spread than the MLM for all inshore field data. The maximum difference is -35% as for offshore data. When the BDM, with a starting value of hyperparameter  $u=2$  was applied, an almost identical directional distribution was obtained as for the MLM. This is illustrated in Figure 5.30.

### Results for reflection coefficient

The reflection coefficients derived using the MLM method have higher values than those

estimated by the BDM. The coefficients derived from the MLM results are in the range from 0.3 to 0.75 whereas the coefficients derived from the BDM results are in the range from 0.08 to 0.55.

A summary of the percentage differences is given in Table 5.11. The average differences when the BDM with a starting value of hyperparameter  $u=20$  was used are very similar to the differences for the offshore data. However, when the hyperparameter was changed to  $u=2.0$ , the most noticeable difference occurred in the estimation of the reflection coefficient. The maximum difference is -74% and the average difference is -54%.

Figure 5.31 shows the frequency dependent reflection coefficients. The values of reflection coefficient oscillate around a mean value in case of the MLM as it was observed for the simulated data. The values of the reflection coefficient in case of the BDM are lower for  $u=2.0$  than for  $u=20.0$ . These estimates vary randomly with frequency and seem to be unreliable.

<i>BDM/MLM percentage</i>	<i>wave height</i>		<i>direction</i>		<i>directional spreading</i>		<i>reflection coefficient</i>	
	<i>u=2.0</i>	<i>u=20.0</i>	<i>u=2.0</i>	<i>u=20.0</i>	<i>u=2.0</i>	<i>u=20.0</i>	<i>u=2.0</i>	<i>u=20.0</i>
min	1.04	-11.56	-7.65	-6.41	-35.36	-24.24	-74.22	-57.88
max.	23.71	4.07	2.13	7.34	15.02	38.46	-24.73	72.90
abs min	1.04	0.08	0.03	0.26	0.34	0.02	24.73	0.01
average	9.33	-1.75	-1.81	0.57	-13.10	4.87	-53.79	-3.49

**Table 5.11** Percentage of differences between BDM and MLM parameter for the inshore data

### *Summary*

The BDM and MLM estimates for field data differ more than their estimates for simulated data. The same trend was observed when increased smoothing was applied. However, smoothing had more influence on the BDM than on MLM results as was established in section 5.3. The BDM method is sensitive on the initial value of hyperparameter  $u$ .

### **5.6 Influence of currents**

One of the parameters which is not taken in account when the numerical data were generated is the influence of currents. Even though, the currents have not been measured, it is worth checking its influence on directional estimates before the final conclusions are made.

Nakagawa *et al* (1996) investigated the influence of currents on the estimation of directional spectra finding that these could be significant. The current influence can be accounted for by suitable modifications to the wave dispersion equation.

When the current is present, the dispersion relation becomes

$$(\omega - U_c k_c \cos \theta_r)^2 = g k_c \tanh k_c \quad (5.6)$$

where  $U_c$  is the current speed, and  $\theta_r$  is relative angle between current and wave propagation direction. This relationship is valid for wave propagation over a uniform current in space and time. Thus, the wave number also depends on the direction and magnitude of the currents.

In general, there is no unique solution to equation 5.6. A discussion of the full solution of the dispersion relationship for waves on uniform current is provided by Peregrine (1976) and also by Hedges (1987). There are four different solutions

1. When the current is positive
2. When is no current or when the current is perpendicular to the direction of wave propagation ( $k_c=k_0$ ).
3. When  $U_c \cos \theta_r$  is just equal and opposite (left side of equation is 0) to the wave energy propagation velocity. The wave cannot propagate upstream and if they were generated on still water they will break. Or the waves are propagating upstream and the wave group as a whole is being swept downstream ( $U_c \cos \theta_r < c_g$ ).
4. When  $U_c \cos \theta_r$  greater than  $c$ , in this condition not only is the wave group swept downstream, but also all individual waves.

Usually, the waves of engineering interest have group velocities which are greater than any current velocities. Thus only cases 1 and 2 will be further considered.

The influence of the current on the wave number was investigated for the conditions related to the field data. Assuming water depth of 7m, and a current magnitude<sup>20</sup> of 1 m/s, the ratio of  $k_c/k_0$  as a function of the relative angle was calculated and plotted in Figure

---

<sup>20</sup> The tidal currents do not exceed 0.7 m/s in Elmer.

5.32. For adverse currents ( $-180^\circ$ ), the ratio is larger than 1, thus the wave number with currents included is larger than the wave number calculated without currents taken in account. There is a larger influence for the smaller wave periods, therefore in case of the wave period of 2 s, the current speed exceeds the wave celerity for relative angles larger than  $120^\circ$  or smaller than  $-120^\circ$ . It was observed that there is no positive solution for the dispersion relation given in equation 5.6 for smaller wave periods and current speed larger than 1 m/s at this depth<sup>21</sup>. The cut frequency was 0.5 Hz for all analysis, thus the smallest considered wave period is 2s.

Figure 5.33, shows the ratio of  $k_c/k_0$  against relative angle, for a current of smaller magnitude (0.5 m/s) in the same water depth. The ratio between the two wave numbers becomes smaller with the reduction of the current speed. There is again a significant difference for the small period waves.

Further, the influence of the current magnitude on wave number for the same water depth was investigated which is illustrated in Figure 5.34. The wave number with currents included becomes larger than the wave number with no current effect included ( $k_c/k_0$  greater than 1) in the case of an adverse current. The ratio  $k_c/k_0$  is smaller than 1 in case of a following current. The current speed exceeds the wave celerity in case of an adverse current speed of -0.5 m/s for a wave period of 2 s, and current speed of -1 m/s for a wave period of 4 s. The influence of current speed and direction is larger for smaller wave periods.

Since the wave number is modified in the presence of currents, the pressure transfer function needs to be modified as well. The transfer function for surface elevation from hydrodynamic pressure is expressed by following equation (see e.g. Nakagawa *et al* (1996)):

$$T_o(f, \theta) = \frac{1}{\rho g} \frac{\cosh k_o h}{\cosh k_o (h+z)} \quad (5.7)$$

in the case when no current is present or taken in account.

---

<sup>21</sup> When the smaller period waves propagate over the jet, they become steeper until they finally break.

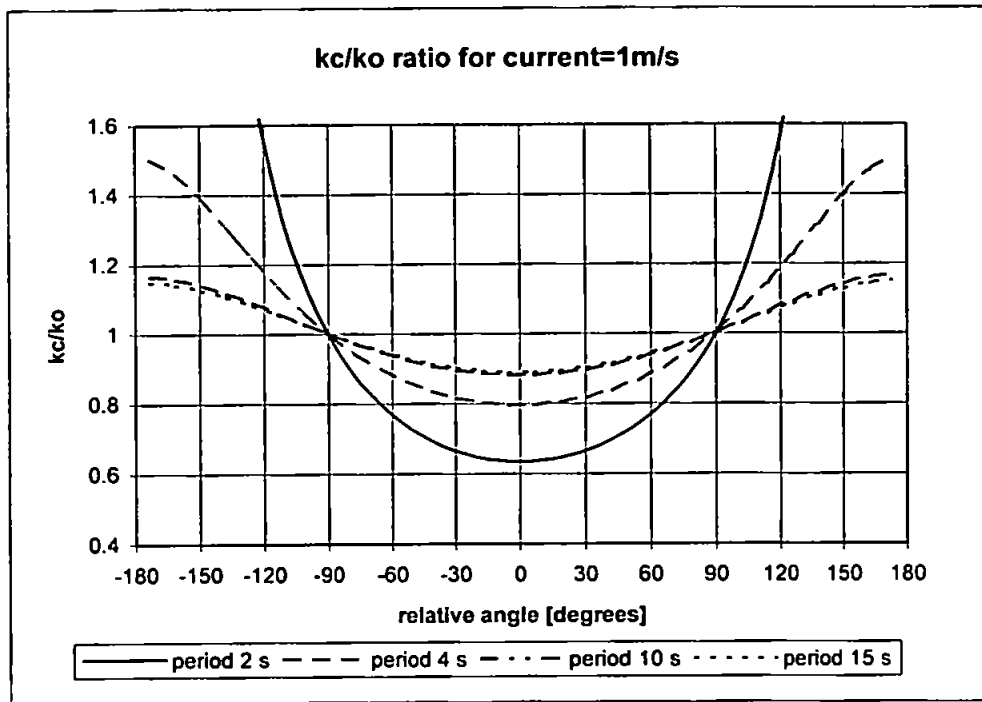


**Figure 5.32** The ratio of wave number with currents included and wave number without currents included versus relative angle for a current speed of 1 m/s in a water depth of 7 m

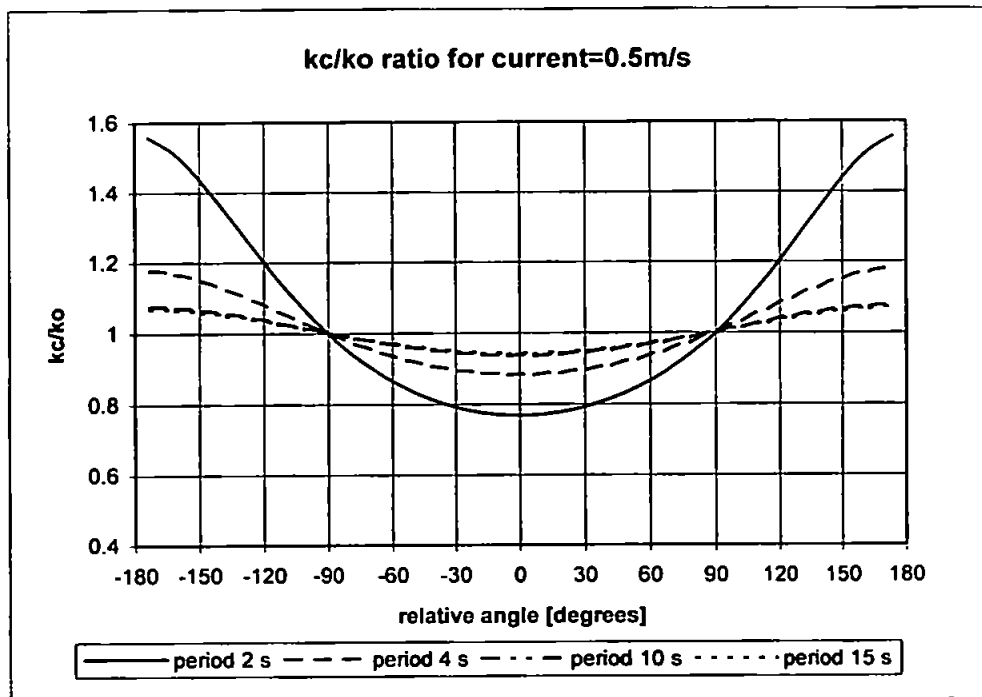


**Figure 5.33** The ratio of wave number with currents included and wave number without currents included versus relative angle for a current speed of 0.5 m/s in a water depth of 7 m

However, this expression becomes (see e.g. Nakagawa *et al* (1996)):

$$T_c(f, \theta) = \frac{1}{\rho g} \frac{\cosh k_c h}{\cosh k_c (h+z)} \quad (5.8)$$

in the case when a uniform current is present.

The ratio of the two transfer functions with and without currents included ( $T_c/T_0$ ), in depth of 7 m is given in Figure 5.35. The ratio was calculated for adverse and following currents of 0.5 m/s and for wave periods of 2, 4, 10 and 15 s. The ratio between two transfer function is very close to 1 (max. 1.02 and min 0.98) for larger wave periods. However, the ratio,  $H_c/H_0$ , increases to 5 for following currents and wave period of 2 s. The transfer function with included currents effect becomes almost zero in case of the adverse current and wave period of 2 s. The ratio increases towards the sea bed, therefore the current effect has an influence on the data measured on the sea bed.

This analysis shows that the influence of currents on wave number and on pressure transfer function is significant in case of smaller period waves (less than 4 s) for adverse and following currents. Therefore, it is necessary to use a modified transfer function and to include the modified dispersion relationship into the directional analysis in such conditions.

### Field data

At the chosen field site, the main wave directions are largely normal to the direction of the tidal currents. Hence, the wavelength and pressure attenuation factors are largely unaffected for the main direction. However, due to the directional spreading, effects will exist for wave angles other than the main direction.

At the chosen field site, tidal currents rarely exceed 0.7 m/s on a spring tide and the measurement depth at the offshore location rarely exceeds 8m. Based on these conditions, the effects of tidal currents were calculated. Some of the derived directional spectra were re-analysed assuming the presence of a 0.5 m/s current orthogonal to the main direction (or crossing) and parallel with the main direction (or following). Three different data sets as representative of a wide range of field data measured offshore were chosen. The first set has a narrow frequency spread ( peak frequency around 0.1 Hz), the second set has a broad energy over frequency distribution and the third case was bimodal (swell and wind waves).

Figure 5.36 show directional distribution for the narrow and Figure 5.37 for broad and bimodal frequency spectra respectively. There is only a slight difference between the directional distribution between the case with no current taken into account and the case with a crossing current taken into account for all three data sets. The difference in directional distribution becomes more pronounced between the case with no current taken into account and the case with a following current taken into account. The difference is present around peak frequencies, particularly for the bimodal data set.

Figure 5.38 shows the sum of energy over all frequencies against directions for cases without and with crossing or following currents taken in account for the chosen data sets. There is very small difference in directional distribution between crossing currents taken in account and without crossing currents taken in account. However, the difference can be seen when the following current is taken in account. The peak direction contains less energy and directional spreading is larger. In case of a bimodal sea, the second peak become more distinguished when a following current is taken in account.

The statistical parameters main direction, directional spreading, incident wave height and reflection coefficient differ only slightly between the case with no current and crossing current taken in account ( the ratio is max. 1.04 and min 0.96). The main direction remains the same and the directional spreading increases when a following current is taken in account.

The influence of currents on directional analysis estimates is introduced by using the modified dispersion relationship. Thus the wave number and thus its relationship to array size is changed. The error in wave number estimation can introduce directional ambiguities into the directional distribution and influence the values of the statistical parameters. The results presented in Figures 5.36 - 5.38 show very small difference between cases with no currents and cases with currents included. There was no significant difference between results with and without a crossing current being taken in account.

Additionally, given that the actual currents were not measured, any corrections introduced to account for them would have to be based on astronomical predictions using chart data. Such estimates would not be very accurate and the results might not be improved.



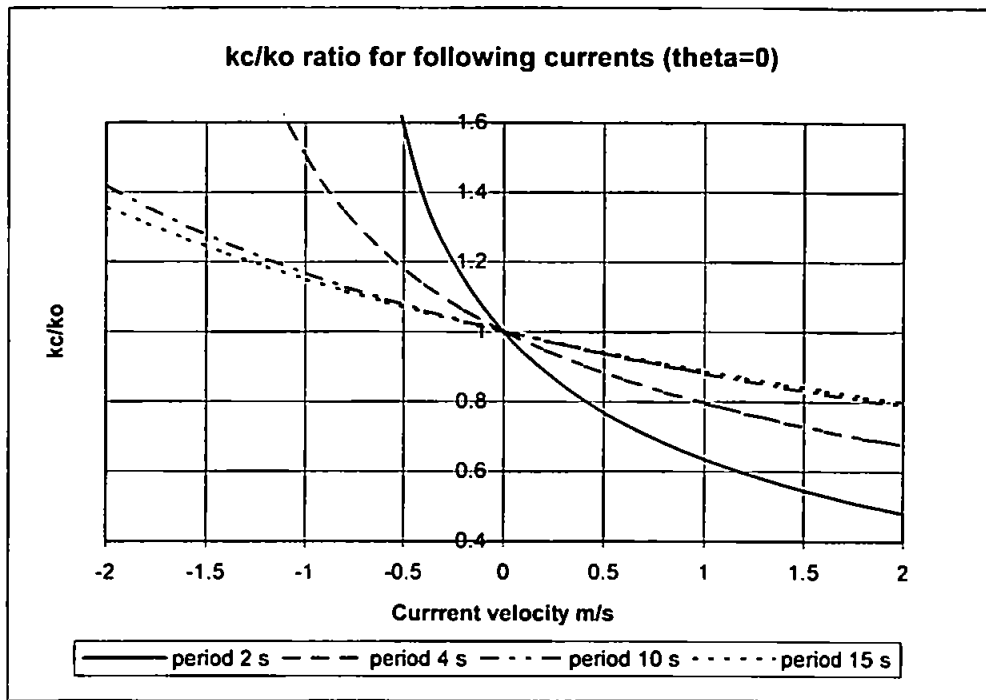


**Figure 5.34** The ratio of wave number with currents included and wave number without currents included versus current speed for relative angle of  $0^\circ$  in the water depth of 7 m

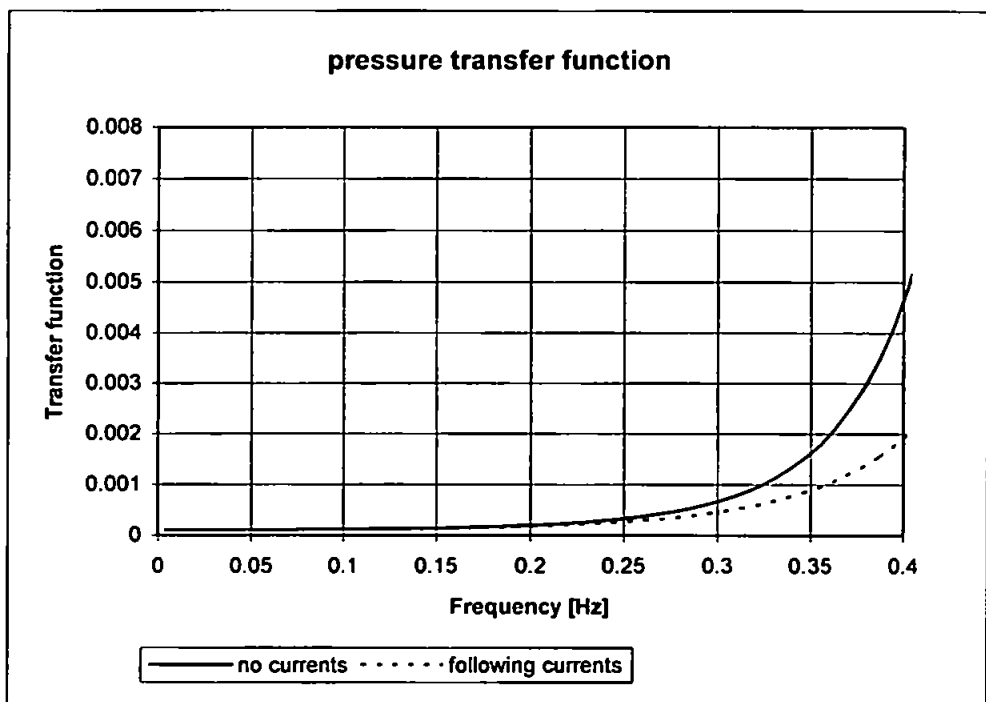


**Figure 5.35** The ratio of pressure transfer function with currents included and pressure transfer function without currents included versus relative frequency in a water depth of 7 m and  $u=0.5$  m/s

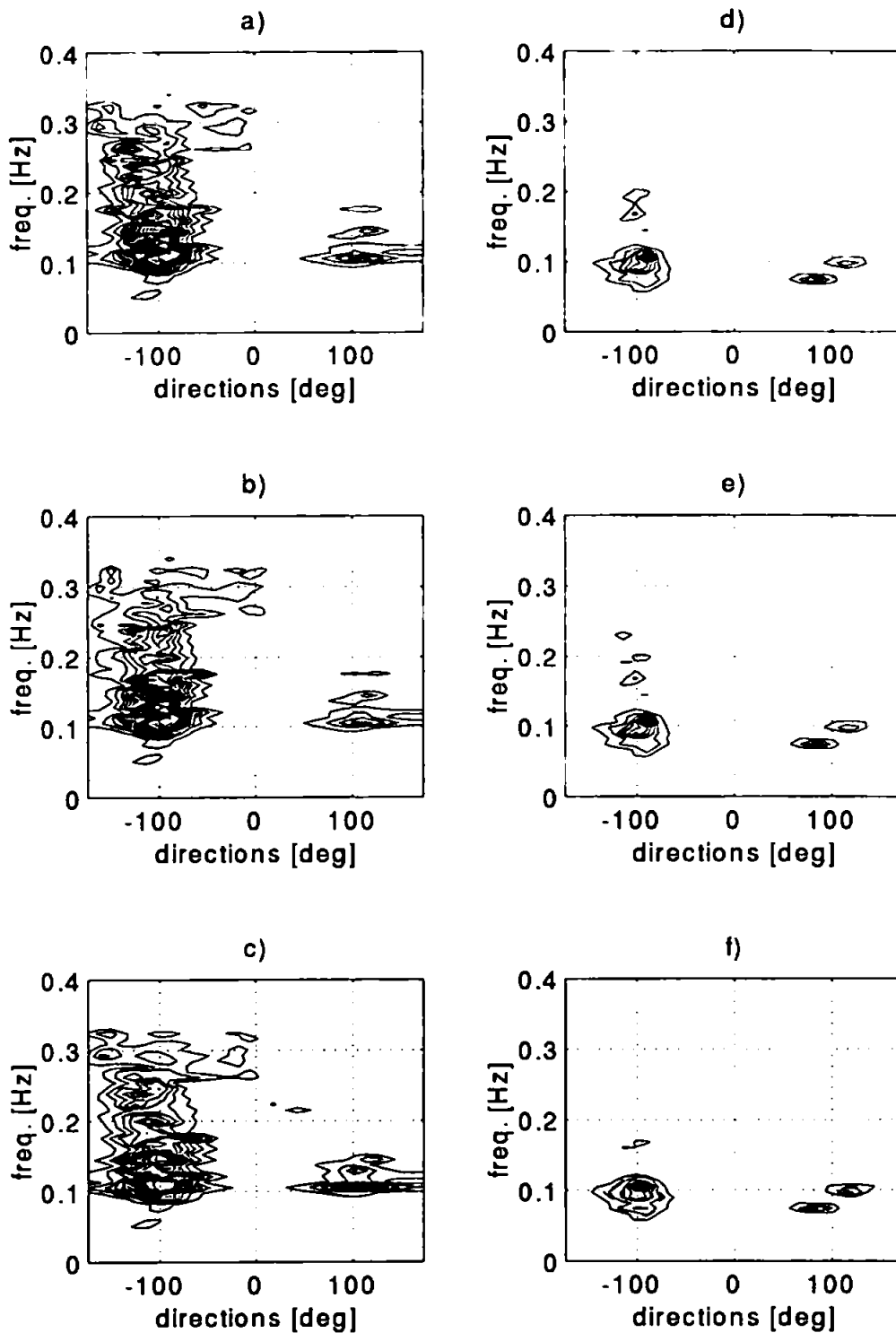


**Figure 5.36** The MLM directional distribution for offshore data combined swell and wind frequency spectrum: a) with no currents, b) currents - speed 0.5 m/s (crossing currents), c) currents - speed 0.5 m/s (following currents) and narrow frequency spectrum: d) no currents, e) currents - speed 0.5 m/s (crossing currents), f) currents - speed 0.5 m/s (following currents); ( - 5% ; - 10-100% with an interval of 10%)

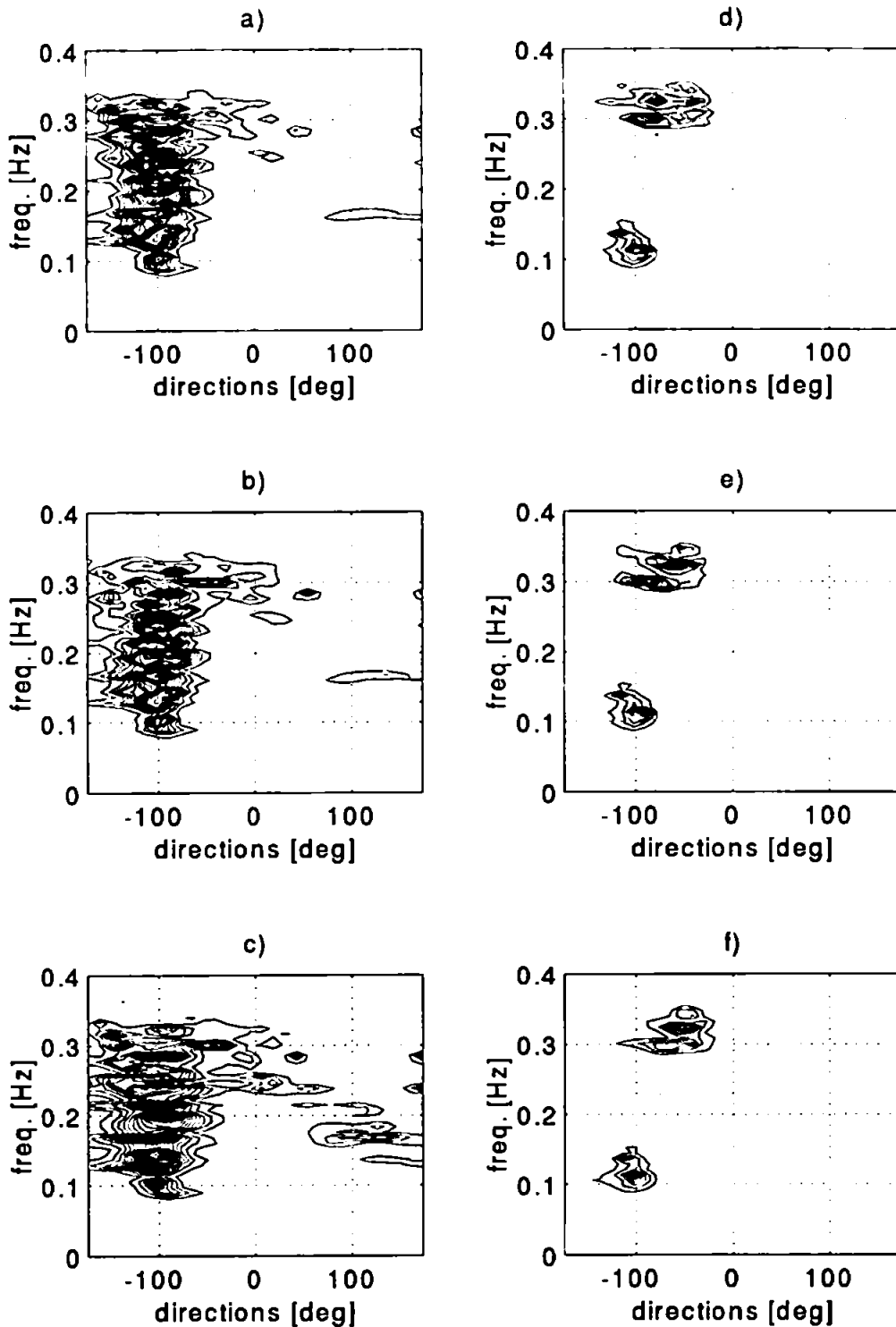


**Figure 5.37** The MLM directional distribution for offshore data broad frequency spectrum: a) with no currents, b) currents - speed 0.5 m/s (crossing currents), c) currents - 0.5 m/s (following currents) and bimodal frequency spectrum: d) with no currents, e) currents - speed 0.5 m/s (crossing currents), f) currents - 0.5 m/s (following currents); ( - - 5% ; — 10-100% with an interval of 10%)

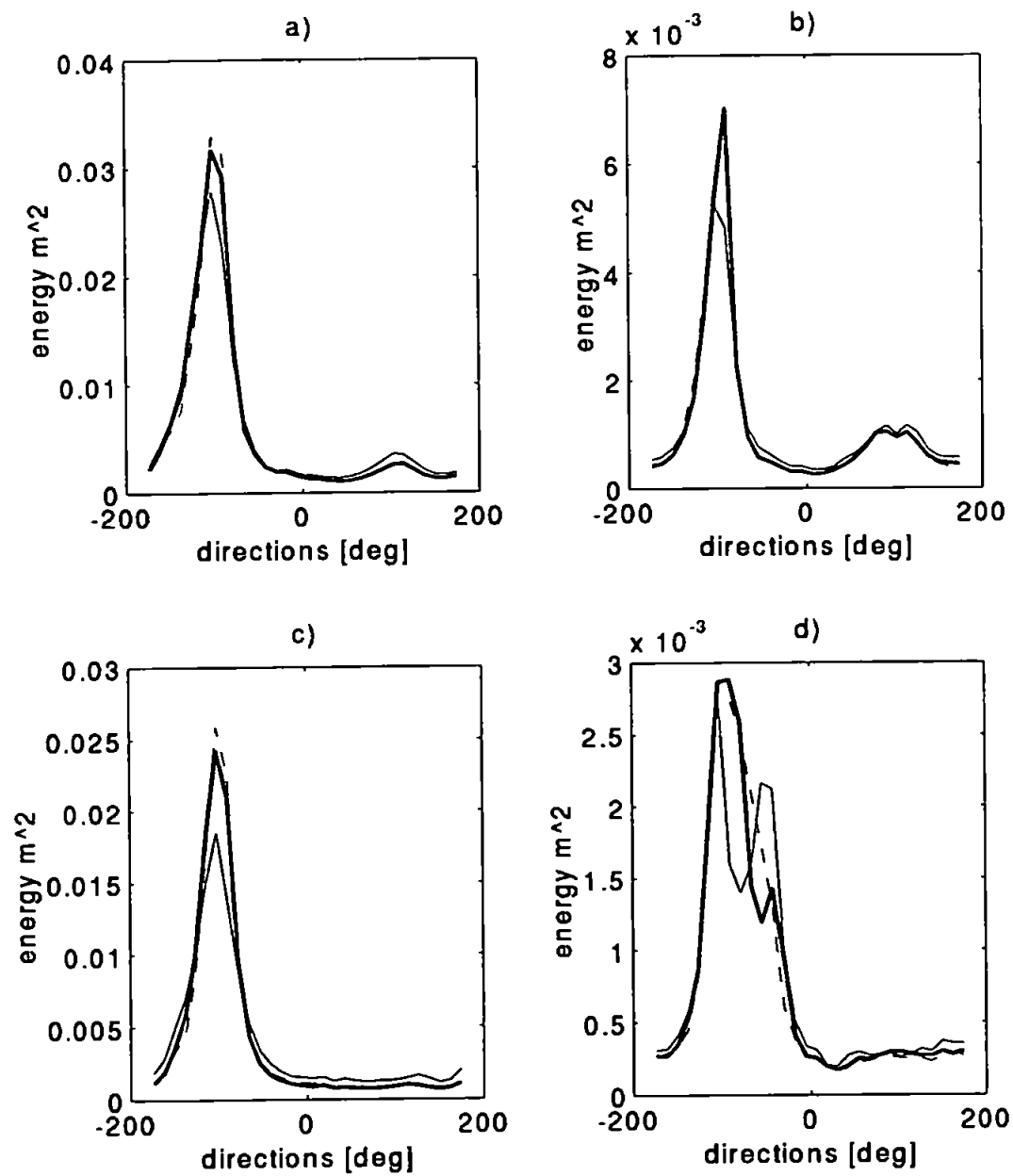


**Figure 5.38** The sum of energy over all frequencies for cases given in Figures 5.36 and 5.37: a) combined swell and wind frequency spectrum, b) narrow frequency spectrum, c) broad spectrum and d) bimodal frequency spectrum); with no currents —, currents - speed 0.5 m/s (crossing currents) ---; currents - speed 0.5 m/s (following currents) -

## **5.7 Summary, discussion and conclusion**

### **Summary on theoretical framework for phase-locked and non-phase-locked methods**

The concept of applicability of the MLM and the MMLM methods regarding  $L/S$  proposed by Huntley and Davidson (1998) was confirmed for the NPL region ( $L/S$  greater than 0.5). The MMLM method applied in the far field ( $L/S$  greater than 0.5) tend to produce spurious peaks. With increasing  $L/S$ , the directional spread increases, and several spurious peaks can be detected. This was in good agreement with the concept that the MMLM method is applicable for wider frequencies range when  $L/S$  less than 0.1. As it was expected the MLM was successfully applied in the zone of its full applicability.

It was demonstrated that the MLM method can detect reflection. The frequency-averaged reflection coefficient calculated from the MLM results varied with the amount of smoothing (increasing  $L/S$ ). However, increasing  $L/S$  has not significantly influenced the energy-weighted reflection coefficient. Incident wave height estimates were generally increasing with increasing  $L/S$ , however this was not the case for energy-weighted incident wave height. Increased smoothing increases directional spreading and alters the main direction estimates.

### **Summary on the numerical simulations**

The directional analysis of the numerical data sets demonstrated that the results obtained were sensitive to the value of predetermined reflection coefficient. Larger discrepancies occurred between the values obtained and expected as the input values of reflection coefficient increased. The results were also influenced by the direction of incoming waves. The best agreement between predicted and target values were from the Southwest direction. The peak period and directional spread also influenced the results. The best agreement was obtained for a peak period of 8s and a directional spread of  $s=10$ . The different combinations of the controlling parameters had different influences on the BDM and the MLM. The results were not sensitive to the frequency distribution.

Increasing  $L/S$  improved the BDM estimates. However the wave height, direction and reflection coefficient estimates only slightly improved for the cases when the MLM method was used. The directional spread estimate increases with increasing  $L/S$  parameter in the case of the MLM. The BDM estimates improved when the data simulated at six positions

were taken in account. This does not seem to have an influence on the MLM estimates. The differences in wave height estimates obtained by the BDM and the MLM are only -2% to 4%. The direction estimates difference is also small from -1% to 9 % and differences in spreading estimates are up to 30%.

### **Summary on the field data**

The differences between the BDM and MLM for field data are larger than in the case of the simulated data. This is not surprising knowing that it is only possible to generate a limited length of time series containing a limited number of frequencies and directions and that the reflection from the breakwaters was simulated as being frequency independent. This is not the case for the field data where the reflection coefficient is frequency dependent. The difference between wave height estimates increased to 3.8% - 5.7% particularly for the waves with peak period greater than 6s. The predicted main directions using the BDM and MLM differed only by a maximum of 6°.

In general the differences between the BDM and the MLM estimates inshore are similar to the differences between the BDM and the MLM estimates offshore even though the values are slightly smaller. The analysis of the field data sets measured inshore showed that both methods predicted reflection from the beach in the lee of the breakwater. The MLM predicts higher reflection than the BDM.

The BDM gave more stable results when more smoothing was introduced in the spectral analysis (larger L/S). Thus, consequently the difference in estimates between the two methods increased. However the BDM stability and accuracy depends on the chosen starting value of the hyperparameter  $u$ . The BDM with starting value of the hyperparameter  $u=20$  fails to give estimates for "noisy" higher frequencies for inshore field data. The BDM with starting value of the hyperparameter  $u=2.0$  (case 3 inshore field data) deals with the "noise" better and accumulates the energy around the peaks in the incident and reflected area.

The largest differences between the two methods were observed for the case when the main energy is accumulated around lower frequencies with a certain amount of energy spread over all higher frequencies. One of the reasons is the array size and shape. From the 3D directional plots it can be seen that both methods have a problem in resolving the frequencies lower than 0.08/0.1. This is related to the array size which will be addressed in

the next section. The other possible reason can be a presence of currents which are not taken in account. The transfer function from pressure to surface elevation with included currents would also affect the directional analysis. However, the currents at Elmer are relatively small (less than 0.7 m/s) and the sensitivity tests showed that their influence on directional distribution is not significant.

### Discussion

It was observed that accuracy of directional estimates for the simulated and field data depend on wave direction. This indicates possible influence of the array shape and size as directional estimates are not only a function of the cross-spectral estimates but also the relative distance between sensors. Only the influence of spectral analysis was tested in the previous section.

The accuracy of the estimate depends on the instrumentation capabilities, position and spatial distribution of the instruments units, and on the spectral and directional analysis. Young (1994) and Chadwick *et al* (1995a) previously investigated the accuracy of the MLM method depending on the number of sensors and their position. With increasing number of sensors the accuracy of the estimates increases. It was also found that the peak of the directional spreading distribution increases with the number of sensors. Also the accuracy is higher for an irregularly rather than regularly spaced sensors.

Young (1994) also pointed out that the critical parameter in the design of the spatial array is the so called co-array, on the basis of co-array lags given by the equation:

$$\xi_{mn} = k(x_n - x_m) / k \quad (5.9)$$

For an optimum array the co-array should have lags evenly and densely distributed in spacing and direction. If there are  $N$  sensors at positions  $(x_n, y_n)$ , then there are  $N^2$  pairs of sensors, with relative positions  $(X_{mn}, Y_{mn})$  where  $X_{mn} = x_n - x_m$  and  $Y_{mn} = y_n - y_m$ ,  $m=1,2,\dots,N$  and  $n=1,2,\dots,N$ . It is possible to calculate the cross-spectrum only for these  $N^2$  shifts, however only  $N(N-1)+1$  values are independent.

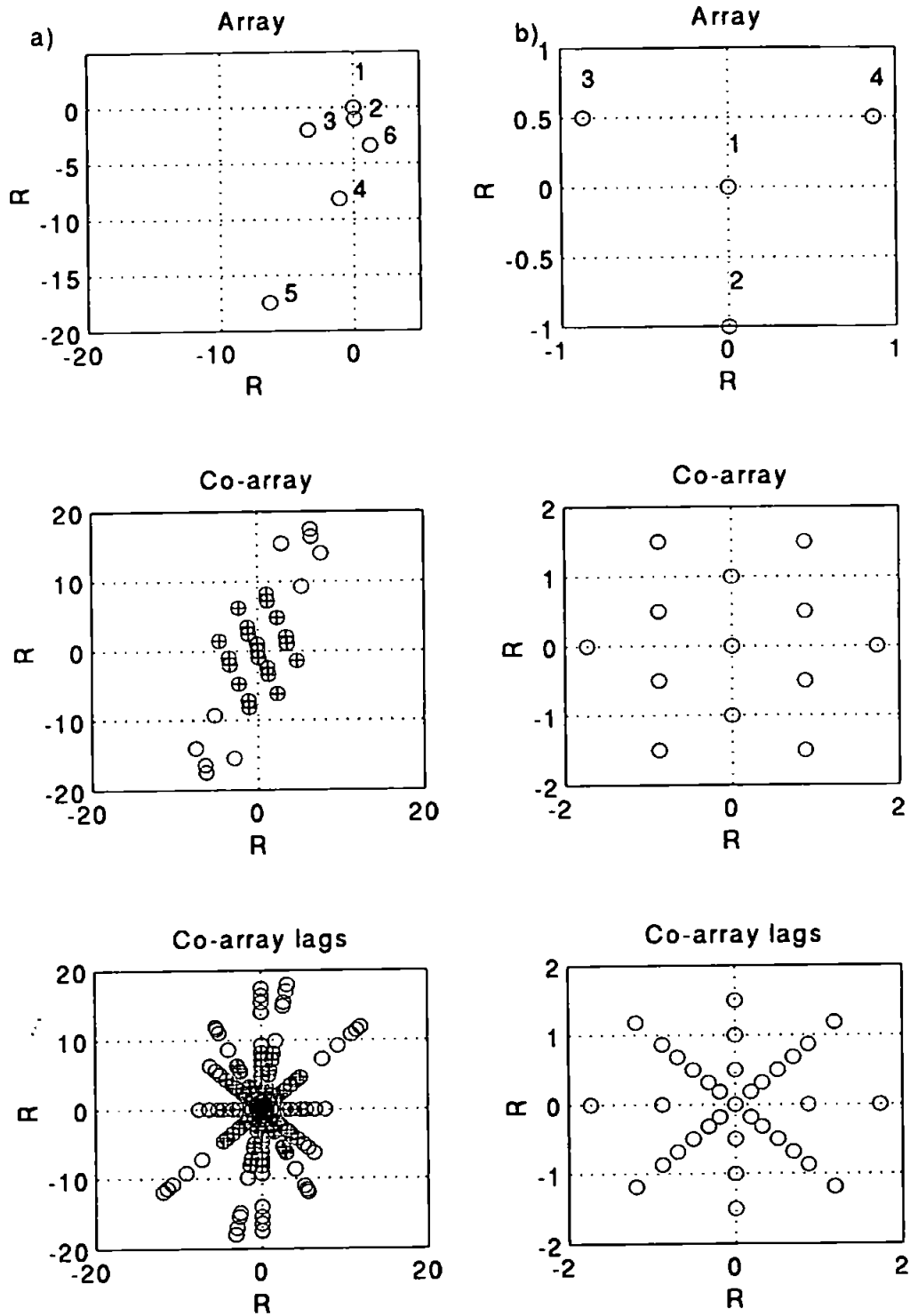


**Figure 5.39** Array layout and corresponding co-array and co-array lags: a) offshore, b) inshore; where  $R=3$  m



In our case, there was a limited number of measurement points of only five sensors offshore (the most seaward transducer (5) did not work continuously) and four sensors inshore (see Figures 3.2 and 5.39). The co-array and co-array lags for the offshore array (see Figure 5.39) indicates that space lags are not densely and evenly distributed over all directions which can cause larger directional spreading for some frequencies and directions. The array orientation is towards the SW therefore the estimates from SW are more accurate. This explains why the results from this direction were more accurate.

The co-array and co-array lags for inshore array are given in Figure 5.39. The co-array lags are more evenly distributed (except for directions  $-135^\circ$  and  $-45^\circ$ ). The error in spatial distribution is highest for  $L/R=1$  (thus  $L = 3\text{m}$  in this case) when spatial aliasing occurs. It reduces for higher values of  $L/R$  and then again increases for  $L/R$  greater than 100 (thus  $L = 300\text{m}$  in this case) (Young (1994)).

It was observed that for certain frequencies (frequencies of 0.141, 0.156 Hz) the amount of reflected energy is higher than in adjacent frequencies for offshore field data. From directional distribution plots (e.g. Figure 5.5), directional ambiguities were observed for combinations of these frequencies and directions (frequencies of 0.141, 0.156 Hz and directions of  $-102$ ,  $-90$ ,  $-78$  degrees). For those frequencies, for particular directions the distance between two transducers is around half the wave length. The method can not distinguish the waves travelling in positive or negative directions relative to the reflected structures in these circumstances. The reflection coefficients were also higher for the lower frequencies (frequencies 0.05-0.06). In this case the array size is small comparing to the wave length and those frequencies can not be resolved accurately. The same implies inshore thus a much larger array would be required in order to resolve infragravity frequencies. Also, the resolution is poor for higher frequencies (higher than 0.2) when the wave length is small in comparison with the array distances.

## **Conclusion**

It was proved that the MMLM method is not applicable for a partially reflected sea in the region of non-phase locked methods when  $L/S$  ratio is greater than 0.5. Both methods, the MLM and the BDM, succeed in producing estimates in an environment outside their domain of application where non-linear processes and reflection are present. With regard to the directional analysis method, it was found that both methods can successfully estimate incident and reflected wave fields in the far field where  $L/S$  greater than 0.5.

The small differences could indicate that both methods produced good results, or conversely that both methods failed to produce the correct result. Directional spread will tend to decrease the phase locking and thus also improve BDM and MLM performance. However the directional spread was quite narrow which in combination with high reflection may introduce the instability into both methods. All this could influence the directional distribution and produce the differences in results. However, both methods do not estimate accurate reflection coefficients at the measured position. Therefore the reflection coefficient for the numerical model boundaries needs to be estimated from the data measured in the vicinity of the structure.

The L/S ratio needs to be greater than 0.5 and the same recommendation as for spectral analysis can be given that the L/S ratio which increases confidence levels and preserve frequency resolution should be used. However, it becomes apparent that accuracy of the estimates is not only a function of the spectral analysis but also of the array shape and size. The array of measuring devices needs to be designed carefully. The increased number of sensors and irregular spacing can improve directional resolutions. Additionally the new concept of optimum L/S ratio and simulated data can be used to design the array size and shape to use one of methods optimally.

The BDM method produced more accurate parameter estimates of wave height for simulated data, but there is still room for improvement. However, the MLM estimates do not differ more than 2% from BDM estimates. The BDM method is sensitive to choice of starting value of hyperparameter  $u$  and results can vary depending on this parameter. Thus it is still more difficult to implement the BDM than MLM method. Taking in account these problems and that the differences for the directional analysis estimates between the MLM and BDM are not large, the MLM method results will be used for the numerical model validation. The errors in parameter estimates need to be taken into account.

# Chapter 6

## Validation of the Mild Slope Evolution Equation Computational Model

*Zippy: "Nature doesn't have a GRID SYSTEM does it Griffy?"*

*Griffy: "No, Zip... Nature's organisation is strictly NON-LINEAR!"  
Things FLOW & MINGLE rather than LINE UP or INTERSECT."*

*Zippy: "Are you trying to tell me LATITUDE and LONGITUDE aren't real?"  
And "Arizona" is just a concept?"*

*Griffy: "Arizona is just a concept, Zippy! We NAME things in order to CONTROL them, but  
is all an illusion!"*

*Zippy: "I knew there was no such thing as MINNEAPOLIS!"*

By Bill Griffith

### 6.1 Introduction

The work presented in this chapter is a continuation of the validation of Li's (1994 b) MSE model by the author of this thesis. The earlier work was undertaken once the field measurements at Elmer and data processing were completed. Li's model (Li, 1994 b) was validated using this field data. The results of this early validation work (Ilic and Chadwick (1995) were presented at the Coastal Dynamics '95 Conference by the author of this thesis and are given in Appendix G. Here, a brief summary of this work is given to provide a context for the subsequent work that forms the main focus of this chapter.

About 70 data sets, all measured synchronously offshore and inshore during high tide and with significant wave height greater than 0.5 m, were chosen from the database for use in the model validation. A computational area of 2000m alongshore and 850m cross-shore covered the complete scheme of eight breakwaters and wave measurement positions offshore and inshore. The beach changes were included in four different bathymetries for model evaluation. The known incident wave field was specified and the reflective waves were allowed to propagate out of the field at the offshore boundaries. Shoreward and lateral boundaries were applied to the outgoing and reflected waves. Only, reflection from the breakwaters was taken into account at this instance.

First, the offshore measured directional spectra were presented by the peak frequency, the main (principal) wave direction and significant wave height for the monochromatic modelling. Disagreement of 33-46% was found between measured and computed wave heights in the bay. The largest disagreement was in the lee of the breakwater where the wave heights were underpredicted. Wave heights were overpredicted in the gap between breakwaters. The influence of spectrum shape and frequency distribution on the results was investigated and no relationship was found. The greatest influence was caused by the lack of transmitted energy by radiation in the lee of the breakwater. This was proved in the second part of the validation when directional modelling was considered.

The next step was to simulate directional waves assuming the validity of linear superposition as a method for the description of random waves. The energetically equalised discretisation method was chosen to discretise (see section 6.3.2 or Appendix G) the measured directional spectra. Three data sets with wave height greater than 1 m and small offshore measured reflection energy (reflection coefficient in range from 0.15 to 0.2) were selected for this purpose. Two series of tests were performed. Directional spectra were represented by 64 monochromatic waves for each frequency interval and with only one main direction in the first test. In the second test, the directional spectra were replaced by 28 monochromatic waves for 7 frequency and 4 directional intervals. The computed energy was greater than measured energy inshore for the first test. The measured and calculated energies for each frequency summed over all directions were found to be in very good agreement except for low and high frequency for the second test. However, the calculated energy summed over all frequencies for each direction differed from the measured one. Overall the agreement between calculated and measured wave height improved and the difference was between 8-12%.

Agreement between measured and predicted wave height depends on the accuracy of data used for the model validation and on the accuracy, capabilities and limitations of the numerical model. The accuracy of the data was analysed in a previous chapter (Chapter 5 ). In this chapter the accuracy of the numerical solution is investigated. The model is linear and does not take in account wave breaking, bed friction and wave current interaction. It does include reflective boundaries but not wave transmission through the structures. In further work presented in this chapter, the sensitivity of the model on reflection and transmission will be investigated. Also, the effect of non-linearities on the solution will be stressed.

The model was developed for regular waves but it was shown in the early stage of validation that it can be used for random waves. However, in such a complex environment around the structures, it was difficult to determine the importance of directional modelling. Therefore, laboratory measurements of random wave diffraction were chosen to validate the model for the case of pure diffraction.

Next, in this chapter, in section 6.2, theoretical investigations of the model stability, accuracy and convergence are considered . The prediction of diffraction coefficients around semi-infinite breakwater on a flat bed is validated using laboratory data in section 6.3. The validation of the model using field data with emphasis on directional modelling is given in section 6.4. The sensitivity test results are discussed in section 6.4.3. Section 6.5 summarises conclusions from all sections.

## 6.2 The Computational model

### 6.2.1 Governing equation based on the velocity potential

Li (1994) derived a model with a time-dependent evolution equation from the transient form of the “mild slope equation”, given by the equation:

$$-\frac{2\omega i}{cc_g} \frac{\partial \varphi}{\partial t} = \nabla^2 \varphi + k_c^2 \varphi \quad (6.1)$$

where:  $\omega$  = wave angular frequency,  $\varphi = \Psi(c c_g)^{1/2}$  and  $\phi(x,y,t) = \Psi(x,y,t^*) e^{-i\omega t}$

Harmonic time is excluded to achieve fast convergence. The model is capable of dealing with refraction, diffraction and reflection, overcoming the main disadvantage of some previous

models based on the mild slope equation (see Chapter 2)<sup>1</sup>. The derivation of the “mild slope equation” and Li’s model is given in Appendix A.

### *Boundary conditions*

The boundary conditions are the same as for the elliptic equation. This makes it easier to solve than hyperbolic models based on the transient form of the equation. The offshore boundary is specified with the following equation:

$$\frac{\partial \varphi}{\partial x} = ik(\varphi_i - \varphi_r) = ik(\varphi_i - (\varphi - \varphi_i)) \quad (6.2)$$

Where  $\varphi_i$  is the incident wave and  $x$  is the direction of incident wave. Thus the incident wave field is known, and reflected waves propagate out of the field.

Shoreward and lateral boundaries are applied to the outgoing and reflected waves. They are given with the following equation

$$\frac{\partial \varphi}{\partial n} - ik\gamma\varphi = 0 \quad (6.3)$$

Where  $n$  is the direction normal to the boundary, and  $\gamma$  is related to the complex reflection coefficient,  $\gamma = 1 - r$ . The value of  $\gamma$  varies with the type of the boundary and may have to be determined empirically.

Behrendt (1985) showed that this condition has a sufficient accuracy for near-normal incidence waves, but the accuracy decreases with the wave’s obliqueness. Dingemans (1997) based on Kostense’s (1986) approach related the complex reflection coefficient,  $r$ , to the physical real reflection coefficient  $R$  with following expression

$$r = 1 + \frac{Re^{i\vartheta} - 1}{Re^{i\vartheta} + 1} \cos \theta \quad (6.4)$$

There is an obvious dependence of,  $r$ , on the angle of incidence,  $\theta$ . The phase shift,  $\vartheta$ , is difficult to determine. It is expected not to be large. The dependence on  $\vartheta$  is therefore generally ignored.

---

<sup>1</sup> One of the main disadvantages of the fast parabolic models was their inability to take into account rapid changes such as reflection.

## 6.2.2 Numerical solution, accuracy and stability

The numerical scheme which is used for the numerical solution is the unconditionally stable Alternating Direction Implicit Scheme (ADI) (e.g. Peaceman and Rachford, 1955). The numerical scheme of the ADI for equation 6.1 after Li (1994b) is

$$f_{p,q} \frac{\varphi_{p,q}^{n+1/2} - \varphi_{p,q}^n}{1/2\Delta t} i = \delta_x^2 \varphi_{p,q}^{n+1/2} + \frac{1}{2} (k_c^2)_{p,q} \varphi_{p,q}^{n+1/2} + \delta_y^2 \varphi_{p,q}^n + \frac{1}{2} (k_c^2)_{p,q} \varphi_{p,q}^n \quad (6.5)$$

$$f_{p,q} \frac{\varphi_{p,q}^{n+1} - \varphi_{p,q}^{n+1/2}}{1/2\Delta t} i = \delta_x^2 \varphi_{p,q}^{n+1/2} + \frac{1}{2} (k_c^2)_{p,q} \varphi_{p,q}^{n+1/2} + \delta_y^2 \varphi_{p,q}^{n+1} + \frac{1}{2} (k_c^2)_{p,q} \varphi_{p,q}^{n+1} \quad (6.6)$$

Where

$$f_{p,q} = \frac{-2\omega}{(cc_g)_{p,q}} \quad (6.7)$$

$$\delta_x^2 \varphi_{p,q}^n = \frac{\varphi_{p-1,q}^n - 2\varphi_{p,q}^n + \varphi_{p+1,q}^n}{\Delta x^2} \quad (6.8)$$

$$\delta_y^2 \varphi_{p,q}^n = \frac{\varphi_{p,q-1}^n - 2\varphi_{p,q}^n + \varphi_{p,q+1}^n}{\Delta y^2} \quad (6.9)$$

where p,q defines a grid point.

In each direction a tridiagonal algebraic system is generated and it is solved by the Gauss elimination method. Li (1994) showed, using Von Neumann's stability analysis that the numerical scheme is unconditionally stable.

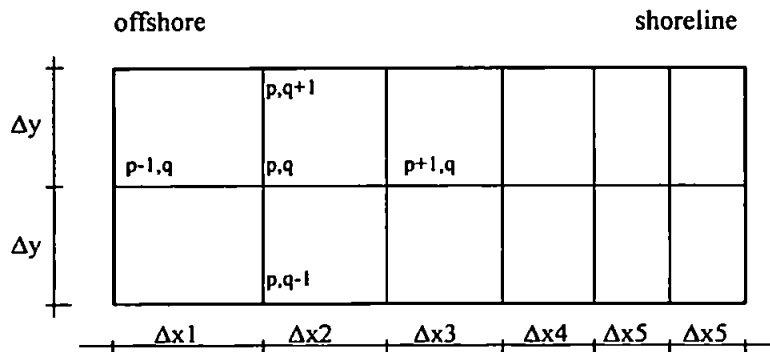


Figure 6.1 The computational domain schematisation where  $\Delta x_2 = v\Delta x_1$ ;  $\Delta x_3 = v\Delta x_2$  etc.

It is desirable to have an adaptive scheme, particularly in the direction of wave propagation. As the wave propagates towards the shore, the wavelength decreases. To describe the wave at least 3 points per wavelength are necessary. Thus, to be able to have reasonably accurate coverage on the shore part of the computational domain, the grid size needs to be relatively small. However, when this is then applied over whole domain, it increases the number of calculation points and consequently the time of calculation.

Here, the possibility of applying a different mesh size and its influence on stability is investigated. Linear analysis by means of Fourier series expansion is performed for the general numerical scheme. A change of grid space  $\Delta x$  to  $\nu \Delta x$  is allowed in the direction of wave propagation and the grid space orthogonal to the direction of propagation,  $\Delta y$ , remains constant. The value of the parameter  $\nu$  is in the interval between 0 and 1. Taking into account the grid points in the area of transition from  $\Delta x$  to  $\nu \Delta x$ , equation 6.5 can be rewritten as follows

$$\begin{aligned} & \varphi_{p-1,q}^{n+1/2} \left( -Cr_x \frac{2}{1+\nu} \right) + \varphi_{p,q}^{n+1/2} \left( -2i + Cr_x \frac{2}{\nu} - G \right) + \varphi_{p+1,q}^{n+1/2} \left( -Cr_x \frac{2}{\nu(1+\nu)} \right) - Cr_y \varphi_{p,q-1}^n - \\ & - (-2i - 2Cr_y + G) \varphi_{p,q}^n - Cr_y \varphi_{p,q+1}^n = 0 \end{aligned} \quad (6.10)$$

And equation 6.6

$$\begin{aligned} & \varphi_{p-1,q}^{n+1/2} \left( -Cr_x \frac{2}{1+\nu} \right) + \varphi_{p,q}^{n+1/2} \left( 2i + Cr_x \frac{2}{\nu} - G \right) + \varphi_{p+1,q}^{n+1/2} \left( -Cr_x \frac{2}{\nu(1+\nu)} \right) - Cr_y \varphi_{p,q-1}^{n+1} + \\ & + (-2i + 2Cr_y - G) \varphi_{p,q}^{n+1} - Cr_y \varphi_{p,q+1}^{n+1} = 0 \end{aligned} \quad (6.11)$$

Where

$$Cr_x = \frac{cc_g}{2\omega} \frac{\Delta t}{\Delta x^2} \quad Cr_y = \frac{cc_g}{2\omega} \frac{\Delta t}{\Delta y^2} \quad G = \frac{1}{2} k_c^2 \frac{\Delta t cc_g}{2\omega}$$

Following the linear stability analysis introduced by von Neumann (see Appendix B), a solution of the finite difference scheme can be written as a Fourier series in complex exponential form for any time level  $n$ , and grid point  $p,q$  in the form



$$\varphi_{p,q}^n = \sum_k \xi_k^n e^{i\alpha p} e^{i\beta q} \quad (6.12)$$

Where  $k$  is a wave component index,  $\xi_k^n$  is the Fourier coefficient for wave number  $k$  at time level  $n$ ,  $m\Delta x = 2\pi/L_x$ ,  $\Delta x = \alpha = 2\pi/N_x$ , where  $N_x$  is the number of grid points per wave length,  $n\Delta y = 2\pi/L_y$ ,  $\Delta y = \beta = 2\pi/N_y$ , where  $N_y$  is the number of grid point per wave length

Initially, the analysis is performed for any individual wave number  $k$ , representing the function

$$\varphi_{p,q}^n = \xi^n e^{i\alpha p} e^{i\beta q} \quad (6.13)$$

Introducing now the amplification factor  $A$  defined as  $\xi^{n+1} = A\xi^n$  and substituting  $A=e^\gamma$ , where  $\gamma=2\pi/\Gamma$ ,  $\xi^n$  can be expressed as  $e^{\gamma n}$ .

Substituting now the function values in the finite difference scheme by Fourier series form (see details in Appendix B), the following is obtained

$$A_1 = \frac{-2i + G - 4Cry \sin^2 \beta/2}{-2i - G + 2Crx\Pi} \quad (6.14)$$

$$A_2 = \frac{-2i + G - 2Crx\Pi}{-2i - G + 4Cry \sin^2 \beta/2} \quad (6.15)$$

Where

$$\Pi = \frac{(1+\nu)(\cos \alpha + i \sin \alpha) - (\cos(\nu\alpha + \alpha) + i \sin(\nu\alpha + \alpha)) - \nu}{\nu(1+\nu)(\cos \alpha + i \sin \alpha)} \quad (6.16)$$

The total amplification factor, which should be  $\leq 1$  for stability is given as:

$$|A| = |A_1 A_2| = \sqrt{\text{Re}^2(A_1 A_2) + \text{Im}^2(A_1 A_2)} = \sqrt{\frac{(C^2 - D^2 - c^2 + d^2)^2 + (2CD - 2cd)^2}{((C+c)^2 + (D+d)^2)^2}} \quad (6.17)$$

where  $C=f(Crx,Cry,G,\text{Re}(\Pi))$ ;  $D= f(Crx,Cry,G,\text{Re}(\Pi))$ ;  $c=f(Crx,\text{Im}(\Pi))$  and  $d=f(Crx,Cry,\text{Im}(\Pi))$

From equation 6.17, the following can be concluded. The amplification factor is equal to 1

when  $c=d=0$ . Thus the scheme is unconditionally stable. This implies that the imaginary part of expression  $\Pi$  is equal to 0, and the real part of expression  $\Pi$  becomes  $2\sin^2(\alpha/2)$ . This is obtained for  $\nu = 1$ .

Closer inspection of the amplification factor shows that the scheme is unconditionally stable only when  $\nu = 1$ . This means that the change of grid size in the direction of propagation will influence the stability of the solution. Therefore it is not advisable to change a grid size during the computation. Nevertheless, the computation can first be performed on the coarser grid and then repeated for the restricted area on a finer grid. From the amplification factor it can be concluded that  $\Delta y$  does not need to have the same value as  $\Delta x$ . Thus  $\Delta y$  can be taken larger than  $\Delta x$ , which is beneficial for the computation over the beach with parallel contours<sup>2</sup>.

### Consistency analysis

Next the consistency of the numerical solution with the differential equation was checked by the author. The consistency analysis is performed by the author of this thesis in such a way that each of the unknowns in the finite difference approximation is replaced by its Taylor's series expansion (see e.g. Abbott (1979) or Abbott and Basco (1990)). Taylor's series is a fundamental tool of numerical methods providing a translation between discrete and continuum description of phenomena. It also provides the efficiency of the translation. The difference between the continuum differential equation and the discrete difference approximation is called the truncation error. The truncation error for equations 6.5 and 6.6, as a result of consistency analysis is given in Appendix C

$$TE = \frac{2\omega}{cc_g} \left[ \frac{1}{8} G \Delta t \frac{\partial^2 \varphi}{\partial t^2} + \frac{1}{24} i \Delta t^2 \frac{\partial^3 \varphi}{\partial t^3} + \frac{1}{12} Cr_x \frac{\Delta x^4}{\Delta t} \frac{\partial^4 \varphi}{\partial t^4} + \frac{1}{12} Cr_y \frac{\Delta y^4}{\Delta t} \frac{\partial^4 \varphi}{\partial t^4} \right] + \dots + h.o.t. \quad (6.18)$$

It is obvious that the scheme is consistent with partial differential equation because the original partial differential equation will be recovered with shrinking of  $\Delta x$ ,  $\Delta y$  and  $\Delta t$ . The scheme is second order accurate<sup>3</sup>. However, consistency gives only a relation between equations. The convergence relation between equations when  $\Delta x$ ,  $\Delta y$  and  $\Delta t \rightarrow 0$  can be further studied. This is not pursued here but therefore it is enough to know that the truncation

<sup>2</sup> Li (personal communication) has started to implement the model with different  $\Delta x$  and  $\Delta y$ .

<sup>3</sup> The scheme is of second order because the derivatives in the truncation error are multiplied by  $\Delta x$ ,  $\Delta y$  and  $\Delta t$  to the power of two and higher.

error disappears when  $\Delta x$ ,  $\Delta y$  and  $\Delta t \rightarrow 0$ .

The oscillations around the main solution and dispersive waves are usually introduced by the presence of third and odd order space derivatives in the truncation error. However, this is not the case here. Therefore, some other effects cause the observed oscillations around the solution. The oscillations might be caused by interaction between the second order scheme used in computational domain and the first order scheme used for the boundaries. The computation begins with a cold start from known initial offshore boundaries. Thus it actually becomes the propagation of a steep front, which is one of the most severe tests for the numerical scheme accuracy. Many even higher order schemes used for such computations suffer from wiggles, which are spread over the computational domain. Furthermore, some other MSE models, which are solved with different numerical methods, suffer from the same effect<sup>4</sup>. This might be one reason for the presence of the oscillations. And the other possible reason is that the shoreline (or possibly offshore) boundaries are not properly defined. In the next section the influence of oscillations is investigated further.

### 6.2.3 Model convergence

The time variable in the model is considered as an iterative parameter without physical meaning and only influences the convergent speed of the model. As the stability analysis showed, the stability of the solution does not depend on the size of the time step. However, the accuracy, as has been shown in consistency analysis, depends on the chosen size of time step. The scheme will be more accurate when a smaller time step is chosen. However, the convergence time depends on the time step size. Thus the small time step chosen will increase the time to achieve convergence.

To find an optimum time step size, one needs to trade between the time of computation and accuracy. Li (1994b) has already acknowledged the problem associated with the determination of the optimal time step in his original work. A routine is built into Li's numerical model, which calculates the minimum required number of steps as a function of the domain length, phase celerity and chosen time step. Thus the choice of the time step is left free.

---

<sup>4</sup> See the MSE model results in Nicholson et al (1997). The same is observed for the time dependent MSE model from personal communication with Michael Brorsen.

<i>Test</i>	<i>Wave period</i> <i>T [s]</i>	<i>Time step</i> <i>Δt [s]</i>	<i>T/Δt</i>	<i>Wave length L</i> <i>[m]</i>	<i>L/Δx</i>
Grid size $\Delta x=1.0$ m $R=0.0$ $\theta=0^\circ$					
A 1.1	3.0	0.38	7.89	14.02	14.02
A 1.2	3.0	0.60	4.97	14.02	14.02
A 1.3	3.0	0.75	3.97	14.02	14.02
A 1.4	3.0	1.51	1.99	14.02	14.02
A 1.5	3.0	2.27	1.32	14.02	14.02
A 2.1	4.5	0.32	14.06	29.20	29.20
A 2.2	4.5	0.63	7.14	29.20	29.20
A 2.3	4.5	0.74	6.09	29.20	29.20
A 2.4	4.5	1.48	3.05	29.20	29.20
A 2.5	4.5	2.22	2.03	29.20	29.20
A 3.1	6.0	0.41	14.78	44.26	44.26
A 3.2	6.0	0.61	9.84	44.26	44.26
A 3.3	6.0	0.76	7.86	44.26	44.26
A 3.4	6.0	1.53	3.92	44.26	44.26
A 3.5	6.0	2.24	2.68	44.26	44.26
A 4.1	9.0	0.39	23.02	72.38	72.38
A 4.2	9.0	0.61	14.73	72.38	72.38
A 4.3	9.0	0.73	12.26	72.38	72.38
A 4.4	9.0	1.52	5.94	72.38	72.38
A 4.5	9.0	2.20	4.09	72.38	72.38
A 5.1	12.0	0.39	30.53	99.32	99.32
A 5.2	12.0	0.61	19.80	99.32	99.32
A 5.3	12.0	0.75	15.91	99.32	99.32
A 5.4	12.0	1.51	7.96	99.32	99.32
A 5.5	12.0	2.29	5.23	99.32	99.32

**Table 6.1** Summary of tested conditions for flat bed

During the preliminary validation of the model using field data (Ilic and Chadwick, 1995) and the validation of the model using the laboratory data (see next section), it was observed that the minimum number of time steps obtained by this expression is not always enough to obtain a stationary solution. It was also found that the magnitude of oscillations around the main solution decreases with increasing number of time steps used. When the solution gets closer to the steady state, the magnitude of the oscillations begins to change more slowly.

This initiated further investigations of the convergence criteria. A series of tests on a flat and sloping bed were undertaken. Different time periods, size of time steps and number of steps were used in order to find the required number of time steps for model convergence or some other convergence criteria to take effect.

Firstly the tests were performed for a flat bed. The size of computational domain was 351 x 351 m, and grid size  $\Delta x = \Delta y = 1.0$  m. The water depth was 7.5 m which created deep water

or intermediate water conditions for the chosen wave periods<sup>5</sup>. The wave periods varied from 3 – 12 s and the wave height was 1.0 m. Table 6.1 summarises the tests performed and the chosen parameters for the flat bed tests.

For each test and each time step the wave heights at the central profile were saved and compared. Also, residuals defined as

$$\varepsilon = \frac{\sqrt{\sum_p \sum_q ABS(\varphi_{p,q}^n - \varphi_{p,q}^{n-1})^2}}{\sum_p \sum_q ABS(\varphi_{p,q}^n)} \quad (6.19)$$

were stored after each time step for each test. Once the calculation was completed, the numerical model predictions were compared to exact solutions and the standard deviation was calculated for each solution.

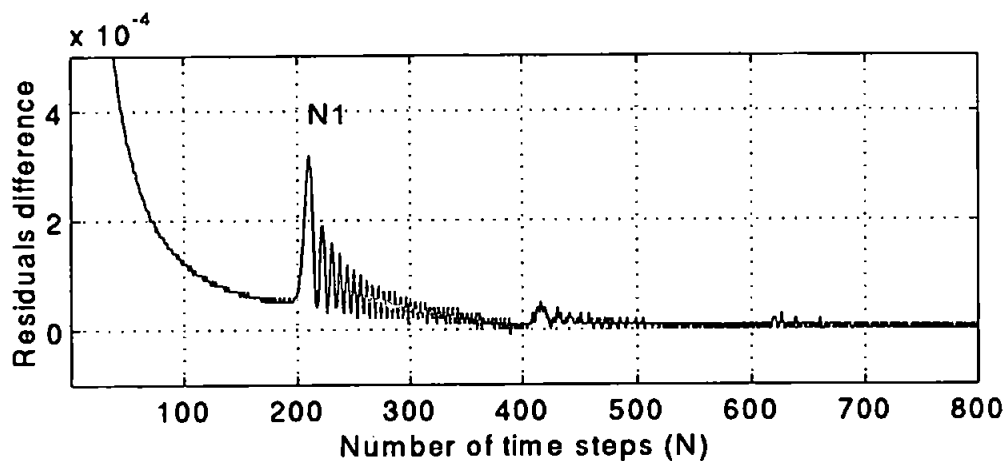


**Figure 6.2** The residuals difference versus the number of time steps for the conditions of the flat bed

The following was observed

- for the same  $L/\Delta x$ , variance of the solution is a function of  $T/\Delta t$  and the number of time steps.

<sup>5</sup> For 3 s wave period  $D/L > 0.5$  which means deep water and for other wave periods  $0.05 < D/L < 0.5$  which means intermediate water.

- when  $L/\Delta x$  increases, the variance decreases<sup>6</sup>.

Some of the models (e.g. Larsen and Madsen MSE model (1987)) have convergence criteria based on minimum error. Hence, the values of the residuals at the end of the calculation were checked. Their values vary depending on  $L/\Delta x$  and  $T/\Delta t$  and they increase with increasing<sup>7</sup>  $L/\Delta x$  and decreasing  $T/\Delta t$ . For different  $L/\Delta x$  and  $T/\Delta t$ , but for the same residual value, the standard deviation will be different. Thus, it was difficult to find a unique formulation, which connects those parameters.

In Figure 6.2 the differences between two subsequent values of residuals for each time step are plotted. The function monotonically converges to a particular value with the exception of a few sudden jumps. The same pattern was observed for all tests. These sudden jumps occur for the time step when the computation over the whole domain is completed (the time step  $N1$ ). As the solution iterates until it converges to the steady state solution, the residuals decrease to zero oscillating.

The possibility of relating the residual difference to chosen  $L/\Delta x$ ;  $T/\Delta t$  and number of time steps was further tested. This time, a sloping bathymetry (slope 1/50) was used for computation<sup>8</sup>. The computational domain was again 351 x 351 m. Three grid sizes were chosen  $\Delta x = \Delta y = 1.0$  m; 2.0 m; 5.0 m. The time period varied from 3 –12 sec. Additionally, tests with oblique waves and reflective boundaries were performed. The parameters are given in Table 6.2 a,b,c.

Again, wave heights for the central cross-section and residuals for each time step were calculated and stored. The standard deviation was calculated for each solution comparing the computational results with analytical results for shoaling waves. It was not possible to relate the number of required time steps to the standard deviation of the solution, or  $L/\Delta x$  and  $T/\Delta t$  parameters. Therefore, the residuals difference is calculated and the standard deviation for it. In Figure 6.3, the residual difference versus number of time steps is plotted. The same features as for the flat bed are observed. The change of residuals is almost a monotonic function except for a few jumps. They occur later than in the case of the flat bed<sup>9</sup>.

<sup>6</sup> The exception from this rule might be related again to the number of time steps.

<sup>7</sup> The same was observed when  $L$  was constant and  $\Delta x$  was changed and when  $L$  was changed and  $\Delta x$  was constant.

<sup>8</sup> The reason for this choice of slope is that it will be easier to relate the results to the Elmer field later on.

<sup>9</sup> One of the reasons is that the phase celerity,  $c$ , is greater in the case of a flat bed than in the case of the sloping beach. Thus the solution propagates more quickly. It should be noted that, in this case the change of  $c_g$  is equal to zero. Thus the expression  $k_c^2 = k_o^2$ , which again speeds up the calculations.

<i>Test</i>	<i>Time period</i> <i>T [s]</i>	<i>Time step</i> <i>Δt [s]</i>	<i>T/Δt</i>	<i>Wave length L</i> <i>[m]</i>	<i>L/Δx</i>
<b>Grid size <math>\Delta x=1.0</math> m <math>R=0.0</math> <math>\theta=0^\circ</math></b>					
B 1.1	3.0	0.30	10	12.68	12.68
B 1.2	3.0	0.60	5	12.68	12.68
B 1.3	3.0	0.75	4	12.68	12.68
B 1.4	3.0	1.50	2	12.68	12.68
B 1.5	3.0	2.25	1.33	12.68	12.68
B 2.1	4.5	0.30	15	21.98	21.98
B 2.2	4.5	0.60	7.5	21.98	21.98
B 2.3	4.5	0.75	6	21.98	21.98
B 2.4	4.5	1.50	3	21.98	21.98
B 2.5	4.5	2.25	2	21.98	21.98
B 3.1	6.0	0.30	20	30.72	30.72
B 3.2	6.0	0.60	10	30.72	30.72
B 3.3	6.0	0.75	8	30.72	30.72
B 3.4	6.0	1.50	4	30.72	30.72
B 3.5	6.0	2.25	2.67	30.72	30.72
B 4.1	9.0	0.30	30	49.09	49.09
B 4.2	9.0	0.60	15	49.09	49.09
B 4.3	9.0	0.75	12	49.09	49.09
B 4.4	9.0	1.50	6	49.09	49.09
B 4.5	9.0	2.25	4	49.09	49.09
B 5.1	12.0	0.30	40	74.65	74.65
B 5.2	12.0	0.60	20	74.65	74.65
B 5.3	12.0	0.75	16	74.65	74.65
B 5.4	12.0	1.50	8	74.65	74.65
B 5.5	12.0	2.25	5.33	74.65	74.65

**Table 6.2 a** The parameters for tests on the sloping bed and grid size  $\Delta x=1.0$  m

<i>Test</i>	<i>Time period</i> <i>T [s]</i>	<i>Time step</i> <i>Δt [s]</i>	<i>T/Δt</i>	<i>Wave length L</i> <i>[m]</i>	<i>L/Δx</i>
<b>Grid size Δx=2.0 m R=0.0 θ =0<sup>0</sup></b>					
C 2.1	4.5	0.30	15	10.99	10.99
C 2.2	4.5	0.60	7.5	10.99	10.99
C 2.3	4.5	0.75	6	10.99	10.99
C 2.4	4.5	1.50	3	10.99	10.99
C 2.5	4.5	2.25	2	10.99	10.99
C 2.6	4.5	0.18	25	10.99	10.99
C 2.7	4.5	0.12	37.5	10.99	10.99
C 3.1	6.0	0.30	20	15.36	15.36
C 3.2	6.0	0.60	10	15.36	15.36
C 3.3	6.0	0.75	8	15.36	15.36
C 3.4	6.0	1.50	4	15.36	15.36
C 3.5	6.0	2.25	2.67	15.36	15.36
C 3.6	6.0	0.20	30	15.36	15.36
C 3.7	6.0	0.15	40	15.36	15.36
C 4.1	9.0	0.30	30	24.55	24.55
C 4.2	9.0	0.60	15	24.55	24.55
C 4.3	9.0	0.75	12	24.55	24.55
C 4.4	9.0	1.50	6	24.55	24.55
C 4.5	9.0	2.25	4	24.55	24.55
C 5.1	12.0	0.30	40	37.32	37.32
C 5.2	12.0	0.60	20	37.32	37.32
C 5.3	12.0	0.75	16	37.32	37.32
C 5.4	12.0	1.50	8	37.32	37.32
C 5.5	12.0	2.25	5.33	37.32	37.32
<b>Grid size Δx=2.0 m R=0.5 θ =0<sup>0</sup></b>					
D 4.1	9.0	0.30	30	24.55	24.55
D 4.2	9.0	0.60	15	24.55	24.55
D 4.3	9.0	0.75	12	24.55	24.55
D 4.4	9.0	1.50	6	24.55	24.55
D 4.5	9.0	2.25	4	24.55	24.55
<b>Grid size Δx=2.0 m R=0.5 θ =20<sup>0</sup></b>					
E 4.1	9.0	0.30	30	24.55	24.55
E 4.2	9.0	0.60	15	24.55	24.55
E 4.3	9.0	0.75	12	24.55	24.55
E 4.4	9.0	1.50	6	24.55	24.55
E 4.5	9.0	2.25	4	24.55	24.55

**Table 6.2 b** The parameters for tests on the sloping bed and grid size Δx=2.0 m



<i>Test</i>	<i>Time period</i> <i>T [s]</i>	<i>Time step</i> <i>Δt [s]</i>	<i>T/Δt</i>	<i>Wave length L</i> <i>[m]</i>	<i>L/Δx</i>
Grid size $\Delta x=5.0$ m $R=0.0$ $\theta=0^0$					
F 3.1	6.0	0.30	20	5.66	5.66
F 3.2	6.0	0.60	10	5.66	5.66
F 3.3	6.0	0.75	8	5.66	5.66
F 3.4	6.0	1.50	4	5.66	5.66
F 3.5	6.0	2.25	2.67	5.66	5.66

**Table 6.2 c** The parameters for tests on the sloping bed and grid size  $\Delta x=5.0$  m

The standard deviation of the residual difference, based on the moving mean, becomes almost constant with increasing number of time steps. Unfortunately, the presence of the oscillations in the residual differences and in standard deviation values disqualified them as criteria for calculation completion. However, it was possible to find the time step when the first jump in residual difference occurs for each case (N1). This time step appeared to be roughly twice the number of time steps (Ns) when the solution reaches the onshore boundary in the middle cross-section<sup>8</sup>. Besides, the required number of time steps for the calculation (N) was determined on the basis that the standard deviation of residual difference becomes constant (small difference between consecutive steps).

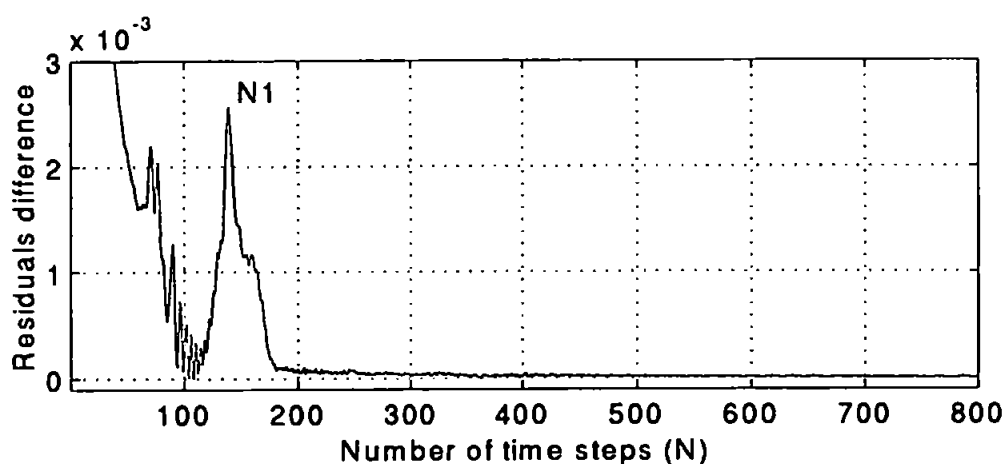


**Figure 6.3** Residuals difference plotted versus number of time steps for sloping bed

<sup>8</sup> The computation starts from the, so called, cold start. All values in the computational domain are set to zero. Only initial conditions at the offshore boundary are known. The solution propagates from offshore to onshore and from left to right boundaries.



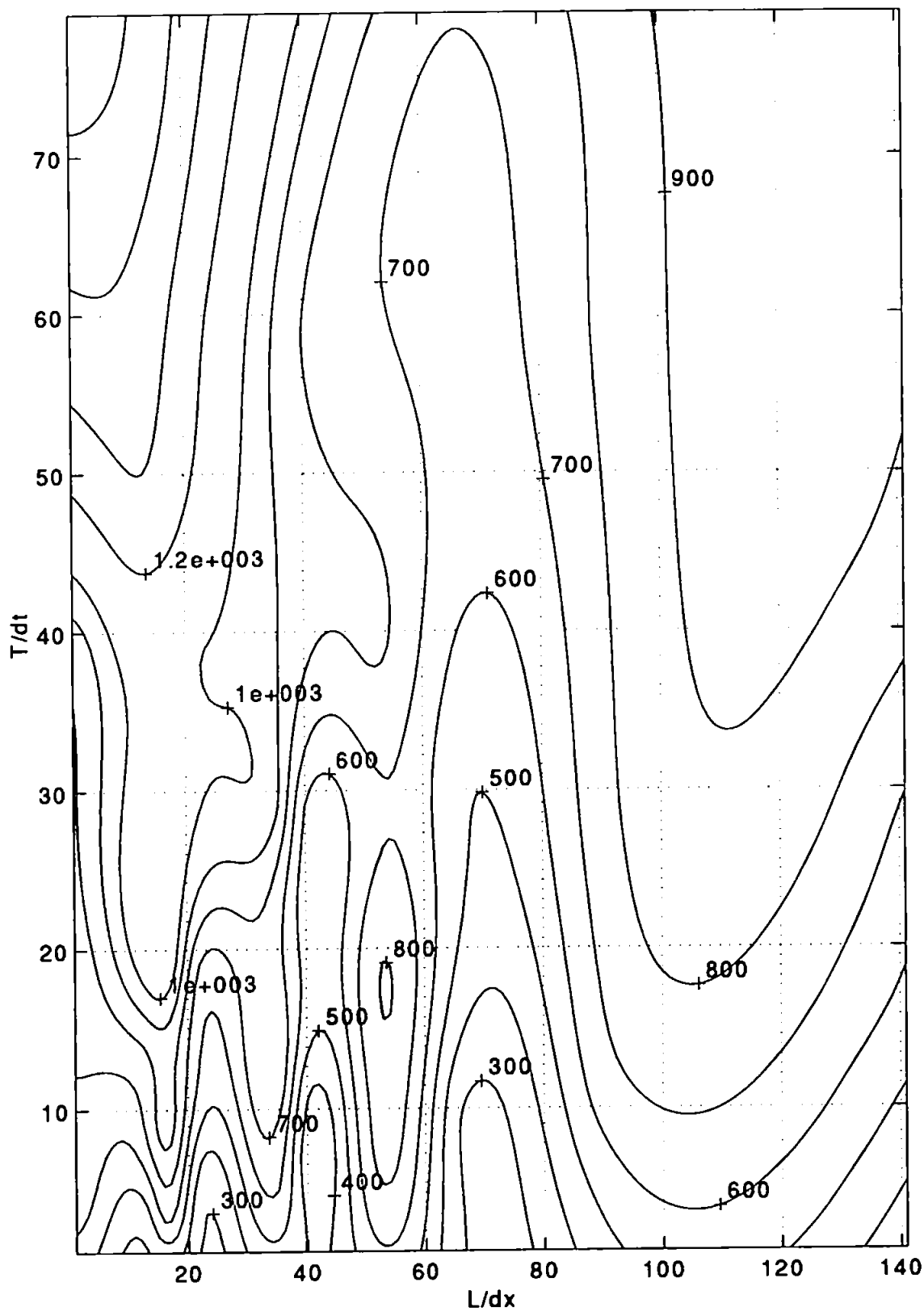


**Figure 6.5** The number of time steps required for the calculation as a function of  $L/\Delta x$  and  $T/\Delta t$ ; — contours for number of steps; every 100 from 0 to 1000 and every 200 from 1000 to 2000

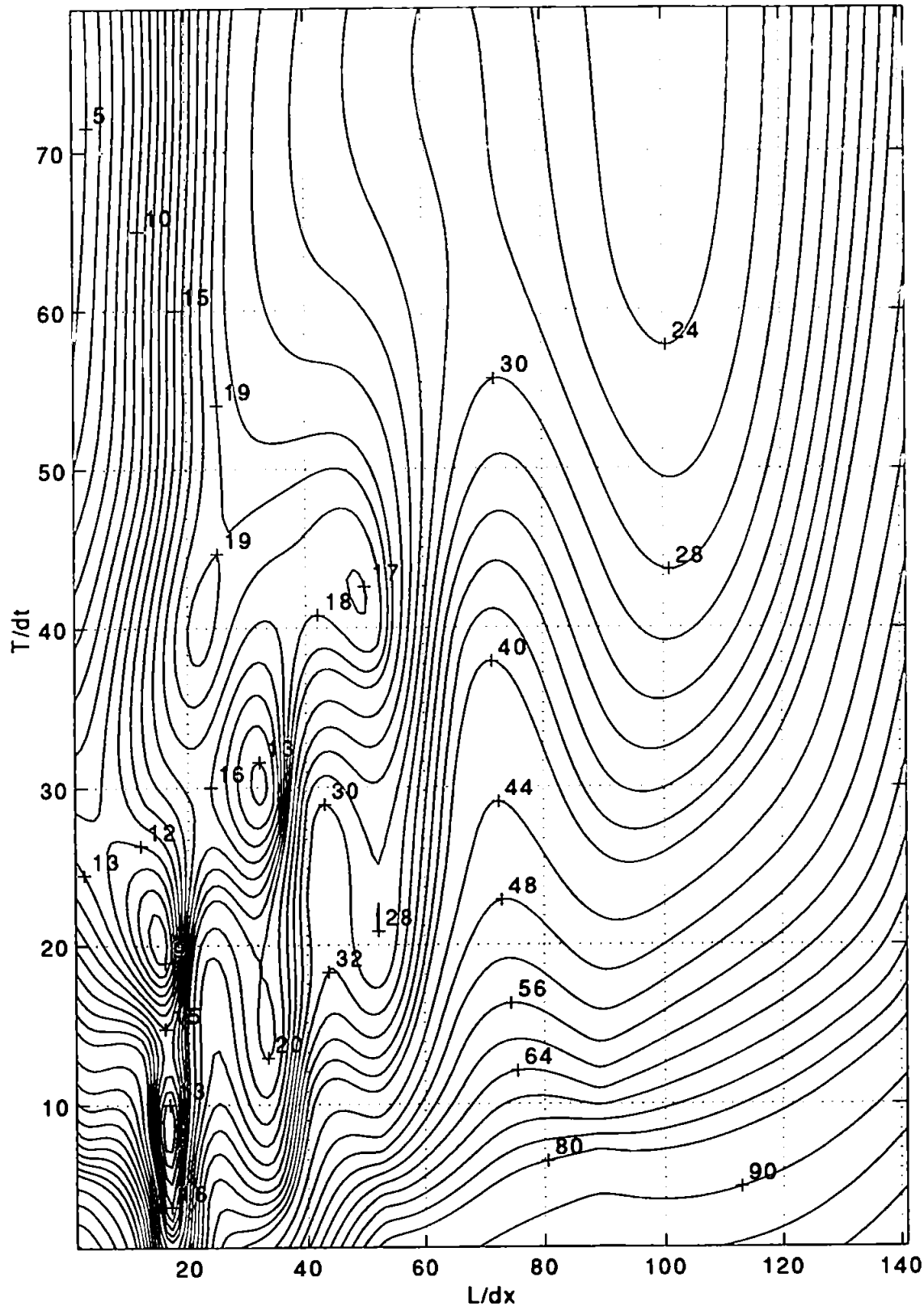


**Figure 6.6**  $N/N_s$  a function of  $L/\Delta x$  and  $T/\Delta t$  (calculated); — contours for  $N/N_s$  every 1 from 0 to 20, every 2 from 20 to 40, every 4 from 40 to 80, every 10 from 80 to 120

This number sometimes coincided with the model calculation of required time steps, but usually was larger. The values of  $N/N_s$  versus  $T/\Delta t$  were plotted for all tests and the relationship on the basis of the best fit between  $N/N_s$  and  $T/\Delta t$  was found. This relationship enabled correct determination of the required number of time steps. Lastly, the values of  $N/N_s$ ,  $N$  and standard deviation are plotted versus  $T/\Delta t$  and  $L/\Delta x$  in Figures 6.4, 6.5 and 6.6 using a linear interpolation routine. These graphs can only be used as a rough guide to choose the required number of time steps for the calculation.

The relationship between these parameters is very complicated as it is illustrated in Figures 6.4, 6.5 and 6.6. It is important to choose the minimum time step with the minimum standard deviation. However, the largest standard deviation plotted on the graph in Figure 6.4 is 0.012, which gives an oscillation amplitude of 0.017 m. Hence the graphs are based on a wave height of 1.0 m. The oscillations, in the worst case, contribute only 2% of the solution.

#### 6.2.4 Dynamic Alternating Direction Implicit (DADI) method

The stability of this scheme does not depend on the time step size, thus a different time step size can be chosen for each time step. The determination of an optimum sequence in the case of the similar equation, for example diffusion equation, is relatively simple (e.g. Abbott and de Leeuw, 1966). The choice becomes more complex in the case of “more dynamic problems” and is a research subject in its own right (e.g. see Basco and Abbott, 1990). Madsen and Larsen (1987) applied the so called Dynamic Alternating Direction Implicit (DADI) method based on work by Doss and Miller (1979) to the completely automatic change of the time step size (iteration parameter)  $\Delta t$ . The method did not only speeded up the computation but also stabilised the numerical solutions.

The method is briefly summarised here. The parabolic equation

$$u_t = (A + B)u - f \quad (6.20)$$

is considered whose steady state ( $t = \infty$ ) solution solves the elliptic equation

$$L(u) \equiv (A + B)u = f \quad (6.21)$$

Equation 6.20 can be discretised in time with time step  $\Delta t$ , applying the ADI method, solving

on odd numbers steps (n+1) implicitly in A and explicitly in B,

$$u^{n+1} - u^n = \Delta t \{ Au^{n+1} + Bu^n - f \} \quad (6.22)$$

reversing the process on even numbered steps (n+2), solving implicitly in B and explicitly in A,

$$u^{n+2} - u^{n+1} = \Delta t \{ Au^{n+2} + Bu^{n+1} - f \} \quad (6.23)$$

The Doss and Miller (1979) approach consists of calculating two double sweeps from time n to time level (n+4) with time step  $\Delta t$ ; then the calculation is repeated from time n to time level (n+4) by a single double sweep with step size  $2\Delta t$ . This time level is defined as (n+4)\* to differentiate the two sets of results. Once both calculations are completed, the following parameter is calculated

$$TP = \|u^{n+4} - u^{n+4*}\| / \|u^{n+4} - u^n\| \quad (6.24)$$

using the  $l_2$  norm, given by following equation:

$$\|u^{n+4} - u^n\| = \sqrt{\sum \sum ABS(u^{n+4} - u^n)^2} \quad (6.25)$$

where double summation represents summation in x and y direction respectively.

Then the time step,  $\Delta t$ , is changed or remains the same depending on the TP value. The strategy they have adopted is as follows: when TP falls in intervals  $(-\infty, .05]$ ,  $(.05, .1]$ ,  $(.1, .3]$ ,  $(.3, .4]$ , or  $(.4, .6]$ , the present calculation and time step are accepted. Time step  $\Delta t$ , for the next calculation, is changed by a factor of 4, 2, 1, 1/2 or 1/4 respectively. When TP falls in the interval  $(.6, \infty)$ , the present computation is rejected and the calculation starts with a new  $\Delta t$  changed by 1/16.

The same method is now tried for Li's (1994 b) model. The parameter TP is calculated as

$$TP = \|\varphi^{n+2} - \varphi^{n+2*}\| / \|\varphi^{n+2} - \varphi^n\| \quad (6.26)$$

using the  $l_2$  norm as in equation 6.25.

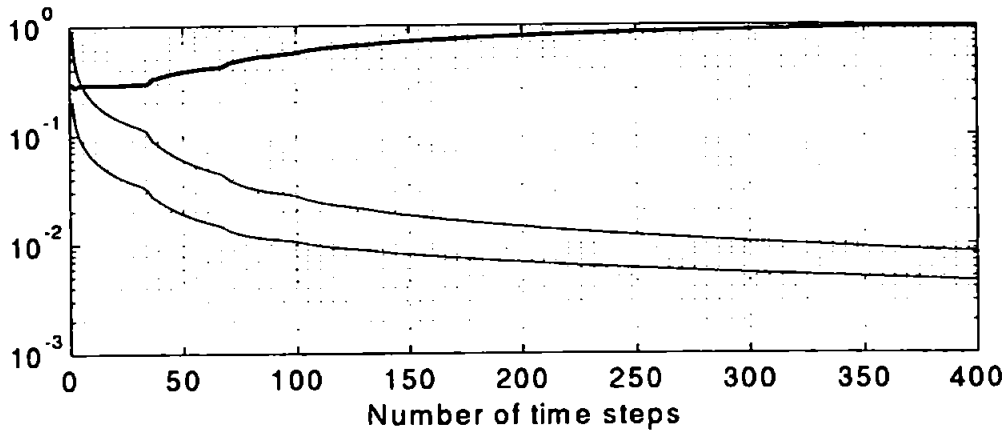


**Figure 6.7** TP values (upper curve), residuals between two time steps ( $2\Delta t$ -middle curve) and residuals between two time steps ( $\Delta t$ -lower curve) as a function of the number of time steps ( $\Delta x = \Delta y = 2.0\text{m}$ ,  $Cr = 1.0$ ,  $T = 6.0\text{s}$ )

The results from tests performed for periods ( $T = 2, 4, 6$  s) with different  $\Delta x$  ( $\Delta x = \Delta y = 1.0, 2.0$  m) and different  $Cr$  (and thus different  $\Delta t$ ) showed that the automatically chosen  $\Delta t$  will decrease as the computation proceeds. Thus a larger number of time steps is needed to complete the computation than when computation is performed with constant  $\Delta t$ . For a smaller time step ( $Cr = 0.5$ ), the TP value is almost constant and is in the range (.1, .3] and there is no change of  $\Delta t$ . If this time step is doubled ( $Cr = 1.0$ ) then TP is greater than .3. For this TP value the time step is automatically reduced and the TP value is again in the range (.1, .3].

Next the change of TP is examined for the constant time step. Figure 6.7 shows the change of TP values versus the number of time steps for  $T = 6.0$  s,  $\Delta x = \Delta y = 2.0\text{m}$ ,  $Cr = 1.0$ . The calculated TP values showed that its value asymptotically reaches a value of 0.96. Sudden changes are observed for the same time step for which the jump in the residual difference occurs. This behaviour was observed for different values of chosen time step.

## 6.3 Validation of the model on laboratory data

Assuming that diffraction is one of the main processes in wave transformation around the structures, the laboratory measurements of Briggs *et al* (1995) were chosen to validate the importance of directional modelling on diffraction prediction.

### 6.3.1 Physical model

Briggs *et al* (1991) conducted physical model tests designed to develop and verify a numerical model for the prediction of diffraction of incident directional wave spectra. The physical model tests and measurements were performed in CERC's directional wave basin (see Figure 6.8). The collected data became widely available for the purpose of verifying wave transformation numerical models particularly those which use the directional modelling approach.

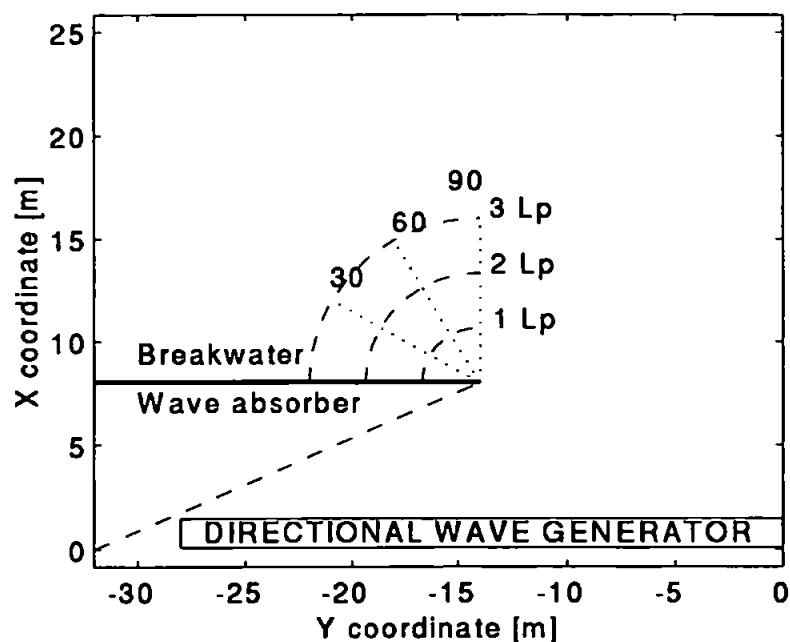


**Figure 6.8** Layout of physical model test. Measurements are taken in the area behind the breakwaters at distances of  $x/L_p = 1 ; 2 ; 3$  from the tip of the breakwater.  $L_p$  is the nominal wavelength for the modelled wave period.

Incident waves were generated using CERC's 27.43 m long directional spectral wave generator. A 0.61 m high by 18.22 m long vertical-faced breakwater was located 8.38 m in front of and parallel to the wave generator, and extended from generator centreline to the



basin side wall. The breakwater was constructed of 1.27 cm thick plywood backed by 2 x 4 lumber, and was therefore a reasonably thin, rigid, vertical structure. Incident and diffracted wave heights were measured using nine parallel-wire resistance type wave sensors mounted on a frame. More details can be found in Briggs *et al* (1995).

One monochromatic and four directional spectral wave conditions were generated. The four directional spectra represent the four combinations of narrow and broad frequency distributions with narrow and broad directional spread. Briggs *et al* (1995) used the TMA shallow water frequency distribution (Bouws *et al* 1985) and the so called wrapped normal directional spreading function (Borgman, 1990) to generate irregular waves in the physical model tests. The wrapped normal directional spreading function is given by the equation:

$$D(f, \theta) = \frac{1}{2\pi} + \frac{1}{\pi} \sum_{l=1}^L \exp\left(-\frac{(l\sigma_m)^2}{2} \cos l(\theta - \theta_m)\right) \quad (6.27)$$

Where  $\theta_m$  is the principal direction and  $\sigma_m$  is a circular standard deviation in radians

$$\theta_m = \theta_0 + \theta_1(f - f_p)$$

$$\sigma_m = \sigma_0 + \sigma_1(f - f_p)$$

In the physical model, both  $\theta_1$  and  $\sigma_1$  were set to zero, which removed the frequency dependence in the directional spreading function.

Waves were normally incident to the semi-infinite breakwater. A summary is given in Table 6.3.

<i>Case</i>	<i>Incident Wave Conditions Description</i>	
M4	Monochromatic	
N1	Broad Frequency Distribution	Narrow Directional Spread
N2	Narrow Frequency Distribution	Narrow Directional Spread
B1	Broad Frequency Distribution	Broad Directional Spread
B2	Narrow Frequency Distribution	Broad Directional Spread

**Table 6.3** Description of laboratory simulated wave conditions

The target incident spectral parameters in the TMA frequency distribution and the wrapped normal directional spreading function are listed in Table 6.4. The values of  $\gamma = 2$  and  $\gamma = 20$  used in the physical model test represent extremes of sea and swell conditions, respectively.

Case	TMA Frequency Distribution				Wrapped Normal	
					Directional	Spreading
	$H_s$	$T_p$	$\alpha$	$\gamma$	Function	Function
	cm	sec			$\theta_m$	$\sigma_m$
					degrees	degrees
M4	7.75	1.3				
N1	7.75	1.3	0.0144	2	0	10
N2	7.75	1.3	0.0044	20	0	10
B1	7.75	1.3	0.0144	2	0	30
B2	7.75	1.3	0.0044	20	0	30

**Table 6.4** Parameters for TMA spectra and directional wrapping function (where  $\alpha$  is Philip's constant and  $\gamma$  is peak enhancement factor)

Diffacted waves were measured at 27 locations in the lee of the breakwater within three nominal wavelengths of the breakwater tip. The frame was positioned on three radial transects from the breakwater tip covering a 60 degrees sector of the shadow zone. Transects were 30, 60, and 90 degrees from the breakwater, as shown in Figure 6.8.

#### Walsh's prediction model

Walsh (1992) developed the numerical model DIRSPDIF to calculate diffraction coefficients for the multidirectional sea in the lee of the breakwater. He compared the model results with the measurements by Briggs and found good agreement (5-20 % difference). It was envisaged by the author, that the comparison of two models (DIRSPDF and MSE) results for random waves is useful for future model applications. The brief description of the Walsh's model is given here. The diffraction coefficients for each spectrum component as a function of frequency and direction for each measured position are first computed, using the diffraction theory for regular waves from the Shore Protection Manual (1984). Next, the diffracted spectrum is calculated. The diffracted frequency spectrum,  $S_{dp}(f,x,y)$ , is predicted by the numerical model using the following expression

$$S_{dp}(f, x, y) = \sum_{j=1}^{37} S_i(f, \theta_j) K_d^2(f, \theta_j, x, y) \Delta\theta \quad (6.28)$$

where

$S_i(f, \theta_j)$  is the discretised incident directional spectrum;  $K_d(f, \theta_j, x, y)$  is frequency dependent

diffraction coefficient;  $\Delta\theta$  is directional bandwidth; x,y are horizontal spatial co-ordinates

The zero moment,  $m_0$ , of each incident, measured and predicted diffracted frequency spectrum was then computed summing up the energy in all frequency bands. Spectral diffraction coefficients  $K_{ds}$  were given as the ratio of diffracted (measured or predicted) and incident zero moment wave height

$$K_{ds} = \frac{H_{mod}}{H_{moi}} \quad (6.29)$$

This approach is similar to the one recommended by Goda (1985).

### 6.3.2 Numerical model tests and results

Assuming the validity of the linear superposition method for describing random waves, they can be simulated applying the numerical wave transformation model to monochromatic wave representatives of the directional spectrum. There are two methods, which can be used to discretise, the spectrum - a constant step method or energetically equalised discretisation. Grassa (1990) specified a few advantages of the latter method. The first advantage is the grouping of wave components around the spectrum peak both in the frequency and the directional domain. The grouping in direction is important because for the large oblique waves the boundary effects are more significant. The second advantage is that each of the equalised components has the same amount of energy and it can contribute equally to the disturbance at a given point. Therefore, fewer components are needed for a description of the directional spectrum. This was also supported by the sensitivity analysis. The results obtained by equalised discrete components converged in a stable way towards the assumed solution and did not improve much for more than 100 components.

Therefore, the energetically equalised discretisation was chosen for the evaluation of the model. The directional wave spectrum is given by  $S(f,\theta) = S(f) G(f,\theta)$  where  $G(f,\theta)$  is a normalised spreading function between given cut-off values,  $(f_{min}, f_{max}), (\theta_{min}, \theta_{max})$  in  $N_f, N_\theta$  components each of which is defined by a corresponding frequency, direction and wave amplitude  $(f_i, \theta_{ij}, a_{ij}, i=1, N_f, j=1, N_\theta)$  where

$$f_i \text{ is given by: } \int_{f_{min}}^{f_i} S(f) df = \left( \frac{m_0}{N_f} \right) (i - 0.5) \quad (6.30)$$

$$\theta_{ij} \text{ is given by: } \int_{\theta_{\min}}^{\theta_{i,j}} G(f, \theta) d\theta = \left( \frac{1}{N_{\theta}} \right) (j - 0.5) \quad (6.31)$$

$$a_{ij} = \sqrt{\frac{2m_0}{N_f N_{\theta}}} \quad (6.32)$$

It should be noted that there are some small differences between these equations and the technique used in practice as the spectral shape is not directly integrable and depends on the frequency and direction increments derived from the spectral and directional analysis.

Firstly, the bathymetry was discretised into 176 x 146 points with equal spacing  $\Delta x = \Delta y = 0.2$  m. Additionally, the same bathymetry was discretised into 351 x 291 points with equal spacing  $\Delta x = \Delta y = 0.1$  m. The water depth was constant at 0.46 m.

However the optimum number of directional and frequency components need to be determined for each case separately. Goda (1985) and Grassa (1990) recommended that a larger number of directional components than frequency components need to be used for cases involving diffraction. Therefore, the number of directions has been varied to test its influence.

It was difficult to resolve the measured directional spread. Therefore, Walsh (1992) used incident directional spectra calculated from measured incident frequency spectra and the calculated<sup>10</sup> directional spreading function. These were also used as an input to the MSE model in preference to measured incident spectra.

The monochromatic wave was represented first with one direction and one wave period. The size of time step varied from test to test (details are given in Table 6.5). The computation was performed for both computational domains. The frequency spectrum, which was derived by Walsh (1992) from measured surface elevations for the monochromatic wave, enabled a computation involving the linear superposition of all frequencies from the wave spectrum (case 6).

---

<sup>10</sup> Calculation was based on the previously mentioned directional distribution (Equ. 6.27).

	<i>Case</i>	<i>Incident Wave Conditions Description</i>
Computational description	<b>M4</b>	<b>Monochromatic</b>
	Mono Case 1	$\Delta t=0.37$ s, $\Delta x=0.2$ m, time steps 200
	Mono Case 2	$\Delta t=0.74$ s, $\Delta x=0.2$ m, time steps 200
	Mono Case 3	$\Delta t=0.18$ s, $\Delta x=0.2$ m, time steps 200
	Mono Case 4	$\Delta t=0.18$ s, $\Delta x=0.2$ m, time steps 800
	Mono Case 5	$\Delta t=0.18$ s, $\Delta x=0.1$ m, time steps 800
Computational description	Mono Case 6	Linear superposition of all frequencies, $\Delta x=0.1$ m, time steps 200
	<b>N1</b>	<b>Broad Frequency Distribution</b> <b>Narrow Directional Spread</b>
	Case 1	One frequency, one direction $\Delta x=0.1$ m, time steps 200
	Case 2	Linear superposition of 8 frequencies and one direction, $\Delta x=0.1$ m, time steps 200, (8 components)
Computational description	Case 3	Linear superposition of 8 frequencies and 8 directions, $\Delta x=0.1$ m, time steps 200, (64 components)
	Case 4	Linear superposition of reduced number of 8 frequencies and 5 directions, $\Delta x=0.1$ m, time steps 200, (40 components)
	<b>N2</b>	<b>Narrow Frequency Distribution</b> <b>Narrow Directional Spread</b>
	Case 1	One frequency, one direction $\Delta x=0.1$ m, time steps 200
Computational description	Case 2	Linear superposition of 4 frequencies and one direction, $\Delta x=0.1$ m, time steps 200, (4 components)
	Case 3	Linear superposition of 4 frequencies and 14 directions, $\Delta x=0.1$ m, time steps 200, (56 components)
	Case 4	Linear superposition of reduced number of 4 frequencies and 5 directions, $\Delta x=0.1$ m, time steps 200, (20 components)
	Computational description	<b>B1</b>
Case 1		One frequency, one direction $\Delta x=0.1$ m, time steps 200
Case 2		Linear superposition of 7 frequencies and one direction, $\Delta x=0.1$ m, time steps 200, (7 components)
Case 3		Linear superposition of 7 frequencies and 21 directions, $\Delta x=0.1$ m, time steps 200, (147 components)
Computational description	Case 4	Linear superposition of reduced number of 7 frequencies and 10 directions, $\Delta x=0.1$ m, time steps 200, (70 components)
	<b>B2</b>	<b>Narrow Frequency Distribution</b> <b>Broad Directional Spread</b>
	Case 1	One frequency, one direction, $\Delta x=0.1$ m, time steps 200
	Case 2	Linear superposition of 4 frequencies and one direction, $\Delta x=0.1$ m, time steps 200, (4 components)
Computational description	Case 3	Linear superposition of 4 frequencies and 21 directions, $\Delta x=0.1$ m, time steps 200, (84 components)
	Case 4	Linear superposition of reduced number of 4 frequencies and 10 directions, $\Delta x=0.1$ m, time steps 200

**Table 6.5** Summary of the tests performed for five different wave conditions generated in the laboratory (M4, N1, N2, B1 and B2)

Four different cases of directional seas were computed in four different ways. Firstly, the spectrum was represented with one direction and one wave period (case 1). A linear superposition of the maximum number of frequencies obtained by equalised discretisation and one main direction was applied next (case 2). The directional modelling or linear superposition of maximum number of frequencies and directions<sup>11</sup> was next carried out (case 3). Finally, directional modelling as the linear superposition of the same number of frequencies and reduced number of directions was used to represent the incident wave spectra (case 4). Table 6.5 summarises the details of the computations performed.

For the spectral and directional runs, firstly the energy over all runs was summed. Wave height was then calculated as

$$H_{mo} = 4\sqrt{m_o} \quad (6.33)$$

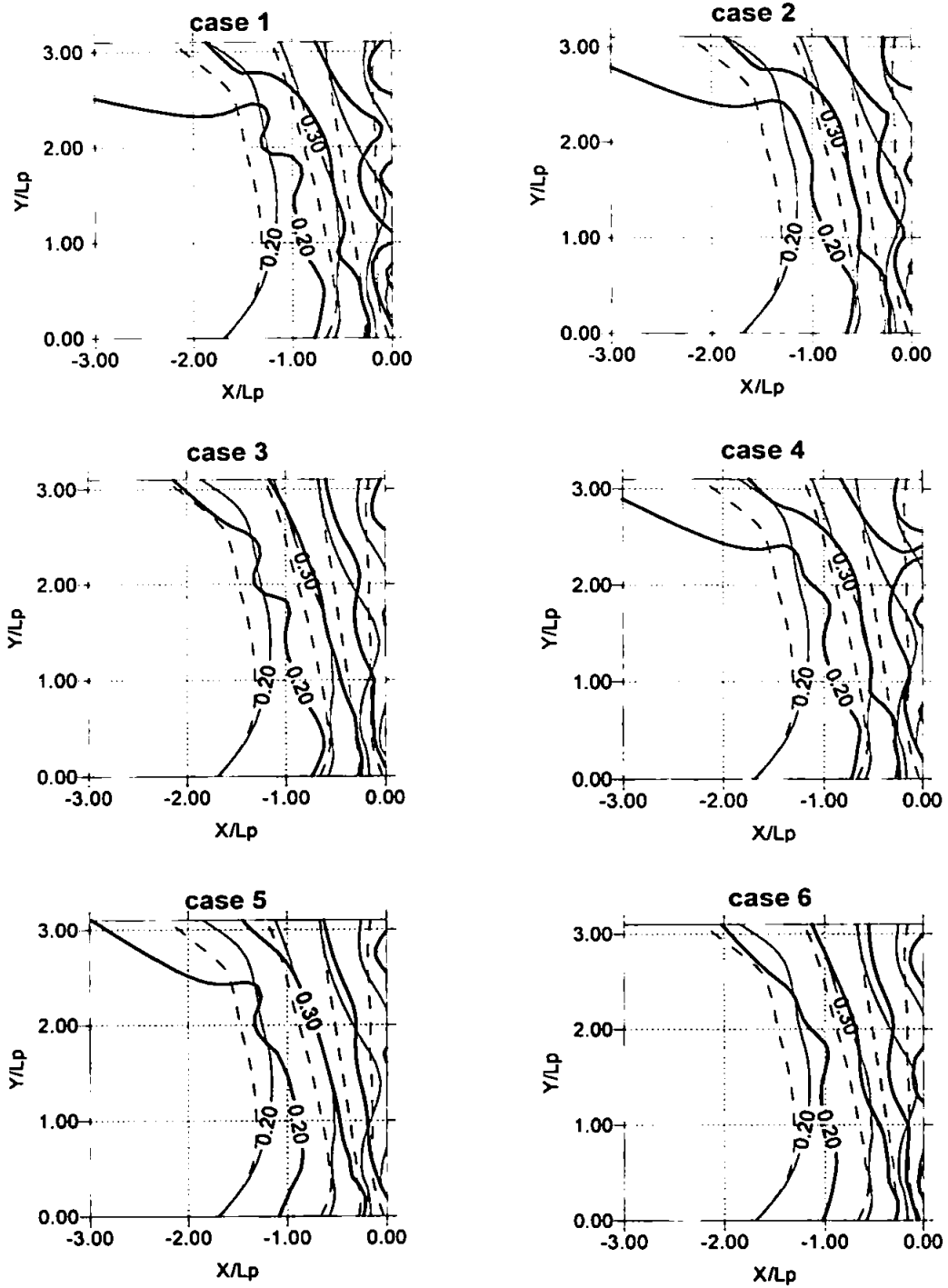
For consistency with the customary presentation of diffraction diagrams and the Walsh (1992) results, the diffraction coefficients were calculated for all MSE computational runs. They were calculated as the ratio of the diffracted wave heights in the measured points in the lee of the breakwater and the incident wave height. The measured spectral diffraction coefficients and the spectral diffraction coefficients predicted by the MSE and DIRSPDF models are shown in Figures 6.9, 6.10, 6.11, 6.12 and 6.13.

Figure 6.9 displays good agreement between measured and calculated diffraction coefficients in the case of the monochromatic wave M4. The MSE predicted coefficients are closer to those measured in the vicinity of the tip of the breakwater than those predicted by DIRSPDF. The best agreement was achieved with the linear superposition of all frequencies and when the bathymetry with the smaller grid size was used (see Figure 6.9 - case 5 and case 6). Also it was observed that better agreement is achieved closer to the tip of the breakwater than in the shadow zone. Therefore, the MSE predictions are closer than the DIRSPDF predictions to the measured ones in the zone near the tip of the breakwater.

For wave condition N1, diffraction coefficients are contoured in Figure 6. 10. The contours predicted by MSE are very close to those measured and they are also close to those predicted by DIRSPDF when directional modelling (case 3) was used (Figure 6.10 - case 3).

---

<sup>11</sup> This number varies depending on a method used for the discretisation and it varies with the given frequency and directional intervals of the measured incident spectrum.



**Figure 6.9** Diffraction coefficients contours for the monochromatic wave, - measured; — predicted by DIRSPDF model; ··· predicted by MSE model. Only the area behind the breakwater is plotted here (contours in 0.1 intervals).

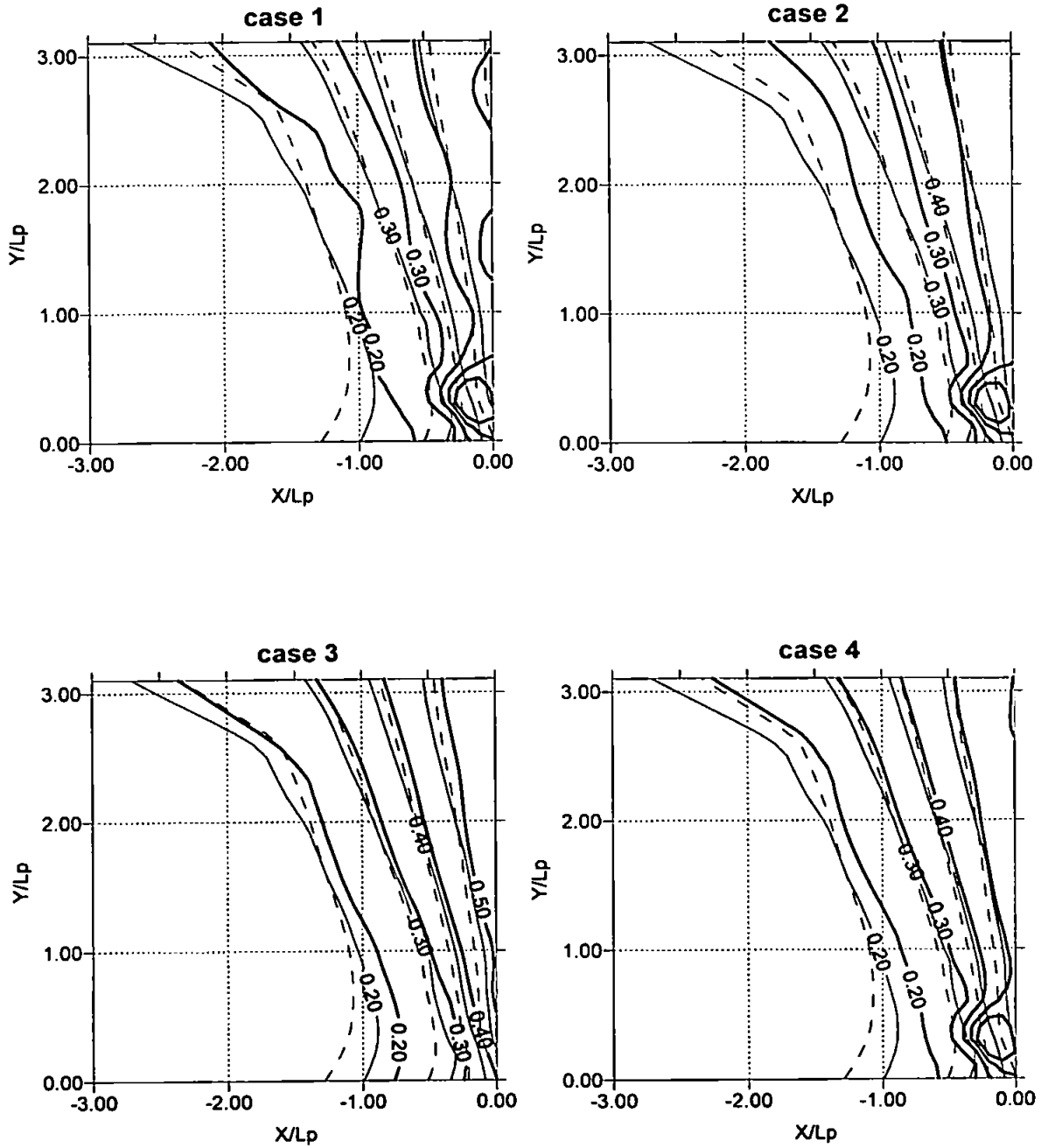


**Figure 6.10** Diffraction coefficients contours for the N1 directional waves, — measured; --- predicted by DIRSPDF model; - predicted by MSE model. Only the area behind the breakwater is plotted here (contours in 0.1 intervals).



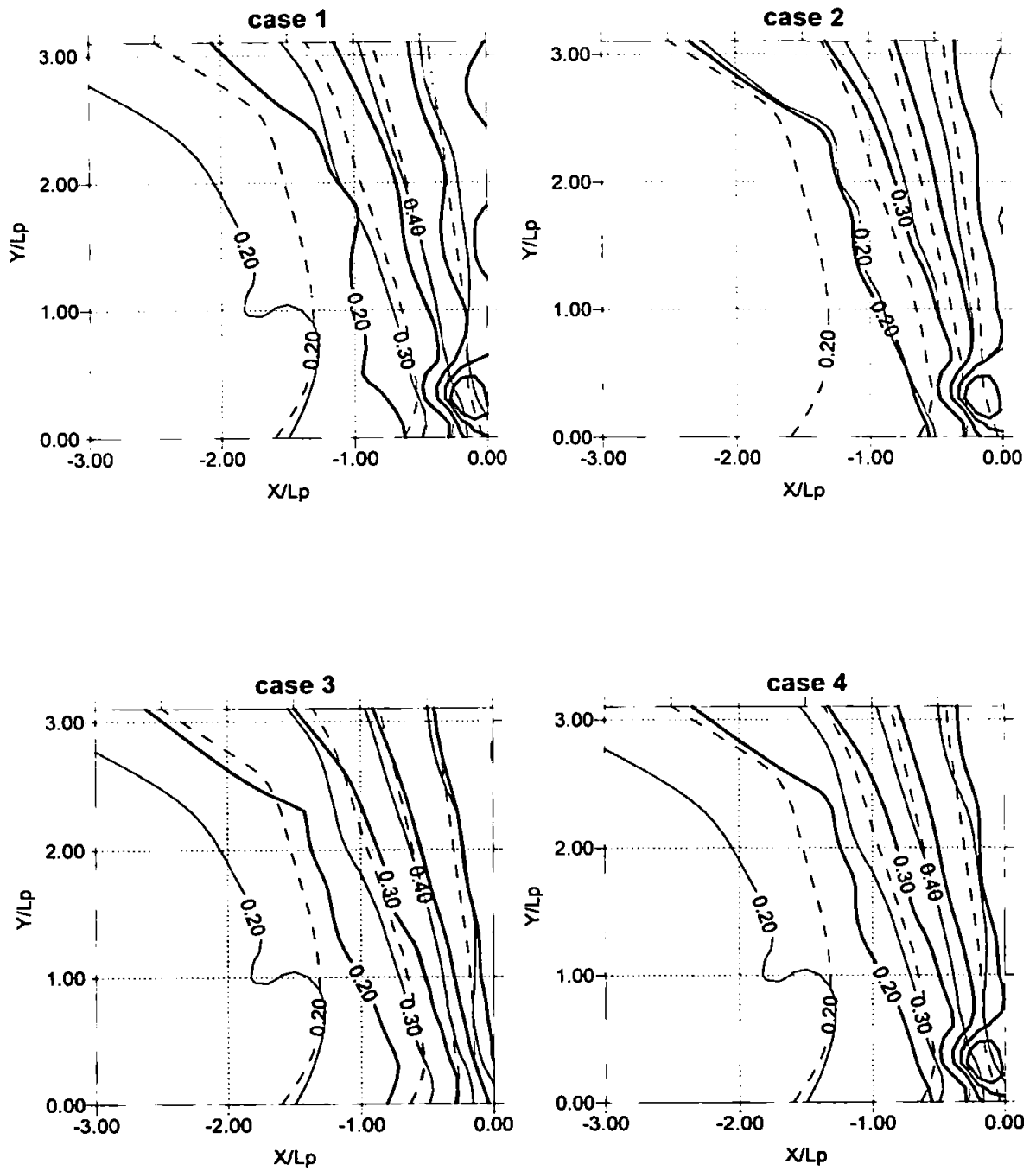


**Figure 6.11** Diffraction coefficients contours for the N2 directional wave, — measured; - - - predicted by DIRSPDF model; - · - predicted by MSE model. Only the area behind the breakwater is plotted here (contours in 0.1 intervals).

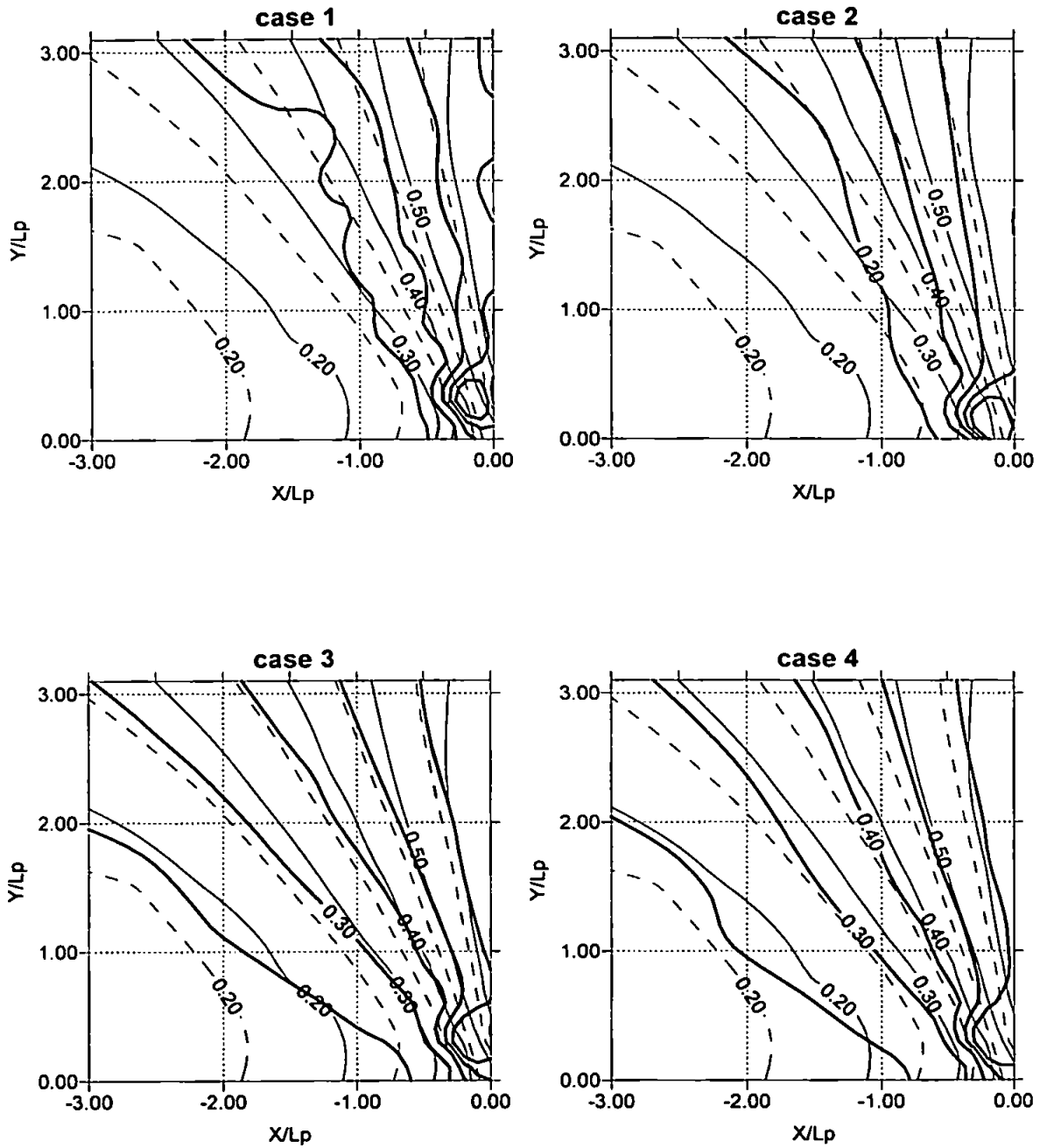


**Figure 6.12** Diffraction coefficients contours for the B1 directional wave, -measured; — predicted by DIRSPDF model; - predicted by MSE model. Only the area behind the breakwater is plotted here (contours in 0.1 intervals).

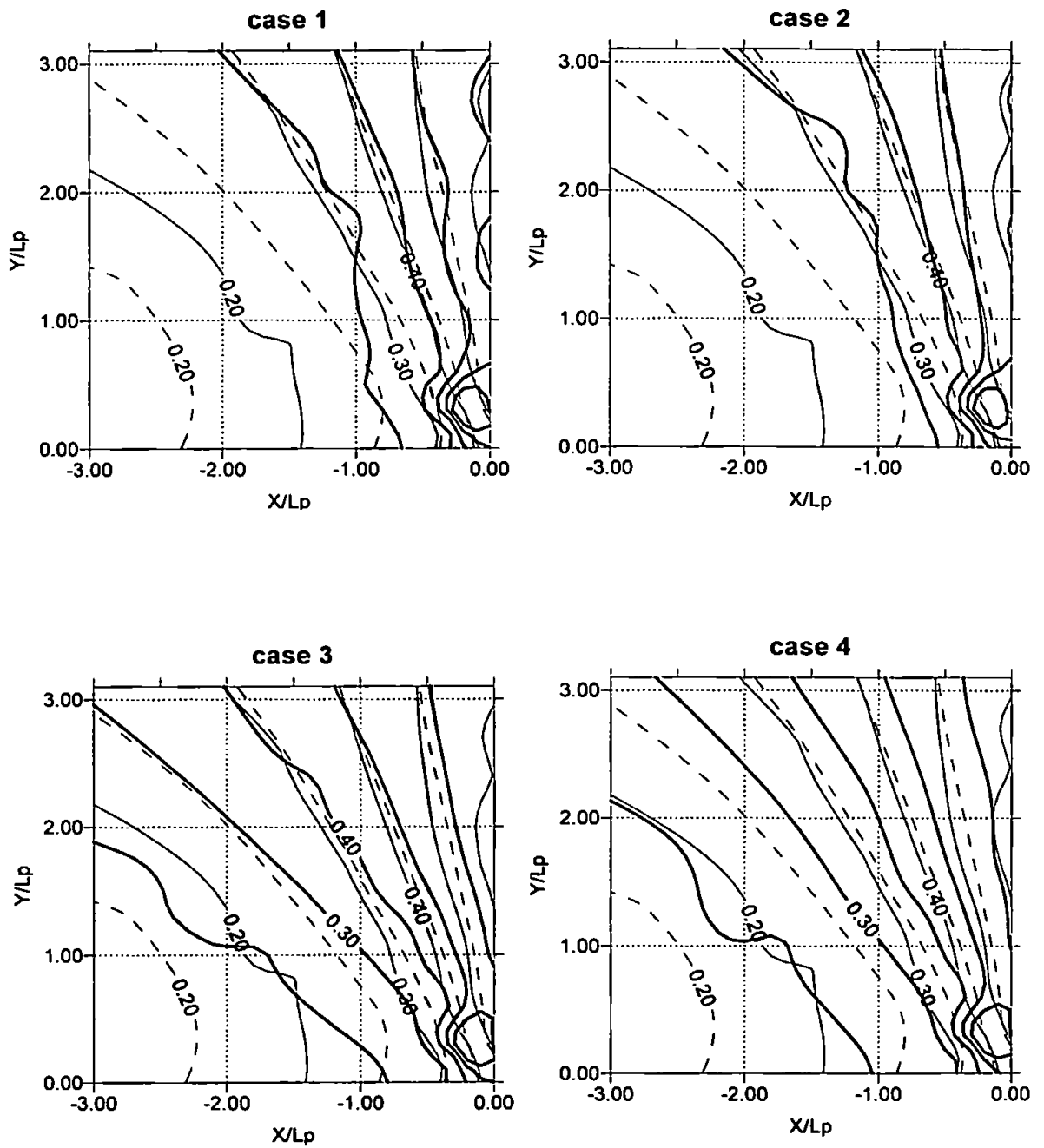


**Figure 6.13** Diffraction coefficients contours for the B2 directional wave, — measured; --- predicted by DIRSPDF model; -·- predicted by MSE model. Only the area behind the breakwater is plotted here (contours in 0.1 intervals).

It is noticeable, that the solution is worse when less frequency and directional components are used for modelling. Thus when only one frequency and one direction was used (case 1), the worst agreement was obtained.

The results for wave condition N2 are given in Figure 6.11. The same trend was perceived as for wave condition N1. Again, the best agreement was obtained when directional modelling (case 3) was used with the larger number of frequency and directional bands. There was an over prediction of the diffraction coefficient immediately behind the tip of the breakwater for the other three cases.

Figure 6.12 shows the diffraction coefficients for the wave condition B1. Once more the best solution was obtained when a larger number of frequency and direction bands were used in computation. The worst agreement was obtained when only one frequency and one direction (case 1) was used. The contours of calculated diffraction coefficients are closer to the measured ones in the entrance area, than in the sheltered area. For all cases, there is an over prediction of the diffraction coefficient immediately behind the tip of the breakwater (measurement point 10). The same features are observed for wave condition B2 in Figure 6.13.

Generally, the model underpredicts the diffraction coefficients for wave condition N1 and N2 for all four different model runs. When directional modelling, mono or all frequencies modelling (cases 1-3) was used for wave condition B1, diffraction coefficients were underpredicted. The reduced frequency and directions run (case 4) overpredicted the diffraction coefficients. When directional and reduced directional modelling (case 3 and 4) were used for wave condition B2, the diffraction coefficients were overpredicted. They were underpredicted when all frequencies and mono runs (case 1 and 2) were performed.

For the monochromatic wave, M4, all runs generally underpredict diffraction coefficients. It is interesting to note that Walsh's numerical model underpredicts diffraction for wave conditions N1, N2 and overpredicts for wave conditions B1, B2, M4. It is not known why the different results were obtained for M4<sup>12</sup>. However, 22 frequency and 37 directional bands (814 components) were used in DIRSPDF to predict directional diffraction coefficients. The number of components, which were used for MSE modelling, is specified

---

<sup>12</sup> However, it is not clear from Walsh's (1992) report whether he took a pure regular wave or the whole frequency spectrum into account.

in Table 6.5, but does not exceed 150 components.

The *rms* difference using the same formulation as Walsh (1992), for easier comparison, was calculated using the following equation

$$rms\ difference = \sqrt{\frac{\sum_{j=1}^N [(K_{dsp})_j - (K_{dsm})_j]^2}{N}} \quad (6.34)$$

where  $K_{dsp}$  is the predicted spectral diffraction coefficient;  $K_{dsm}$  is the measured spectral diffraction coefficient;  $N$  is the number (= 27) of spectral diffraction coefficients computed for each wave condition.

The *rms* values are calculated for all directional wave conditions and all computational wave conditions. The computed *rms* for the MSE and DIRSPDF model results versus measurements are given in Table 6.6.

	<i>MSE</i>						<i>DIRSPDF</i>
	<i>Case 1</i>	<i>Case 2</i>	<i>Case 3</i>	<i>Case 4</i>	<i>Case 5</i>	<i>Case 6</i>	
M4	0.064	0.068	0.055	0.065	0.050	0.051	0.052
<b>All points</b>							
N1	0.133	0.137	0.029	0.137			0.025
N2	0.128	0.133	0.047	0.133			0.029
B1	0.175	0.173	0.111	0.173			0.042
B2	0.144	0.144	0.124	0.144			0.075
<b>Excluding point 10</b>							
N1	0.063	0.067	0.028	0.025			0.023
N2	0.072	0.069	0.046	0.055			0.028
B1	0.134	0.130	0.022	0.025			0.040
B2	0.095	0.094	0.048	0.035			0.074

**Table 6.6** The *rms* values when the MSE and DIRSPDF predictions are compared to the measurements<sup>13</sup>

<sup>13</sup> The results in the lower part of table were calculated excluding predicted values in point 10. This was the point where the results differed the most.

	<i>MSE</i>						<i>DIRSPDF</i>
	<i>Case 1</i>	<i>Case 2</i>	<i>Case 3</i>	<i>Case 4</i>	<i>Case 5</i>	<i>Case 6</i>	
M4	18.95	19.49	16.67	17.93	15.22	14.19	10.87
<b>All points</b>							
N1	19.44	22.69	8.5	14.33			5.89
N2	24.87	24.41	13.37	20.75			7.66
B1	34.94	34.52	9.88	11.18			11.99
B2	28.6	29.26	15.73	13.59			19.72
<b>Excluding point 10</b>							
N1	14.01	17.21	8.42	8.33			5.51
N2	20.72	19.93	13.41	16.22			7.59
B1	30.78	30.27	5.08	6.19			11.81
B2	24.34	24.96	10.75	8.65			19.54

**Table 6.7a** The percentage error difference between MSE and DIRSPDF model predictions and measurements – absolute values (case 1 - mono; case 2 - all frequencies and one direction, case 3 - directional; case 4 - reduced directional)

	<i>MSE</i>						<i>DIRSPDF</i>
	<i>Case 1</i>	<i>Case 2</i>	<i>Case 3</i>	<i>Case 4</i>	<i>Case 5</i>	<i>Case 6</i>	
M4	-5.6	-10.87	-10.49	-9.6	-5.82	-7.07	9.14
<b>All points</b>							
N1	-5.26	-10.45	-8.5	-1.72			2.77
N2	-13.82	-13.70	-12.77	-10.36			-2.47
B1	-24.34	-23.77	6.55	9.38			11.99
B2	-17.71	-18.82	13.96	11.54			19.72
<b>Excluding point 10</b>							
N1	-11.63	-17.21	-8.42	-8.33			2.26
N2	-19.46	-19.93	-12.78	-16.11			-2.93
B1	-30.78	-30.27	1.62	4.32			11.81
B2	-23.74	-24.96	8.9	6.52			19.54

**Table 6.7b** The percentage error difference between MSE and DIRSPDF model predictions and measurements – relative values (case 1 - mono; case 2 - all frequencies and one direction, case 3 - directional; case 4 - reduced directional)

Additionally the percentage difference between model predictions and measurements was calculated for each of those wave conditions and for the DIRSPDF and MSE results. The computed absolute percentage difference values<sup>14</sup> are summarised in Table 6.7a. The

<sup>14</sup> The absolute values of calculated percentage difference for each point are taken, summed and then divided by the number of points.

relative percentage difference values<sup>15</sup> are given in Table 6.7b and they show under- (negative values) and over-prediction (positive values). Comparing the values in both tables, it can be observed that the relative values are smaller than the absolute values for some cases, which means that under- and over-predictions cancelled each other out.

Generally, the best agreement between measured and computed values was for case 3 and case 4, directional and reduced directional modelling, (8-15 %). The largest discrepancy occurred for case 1, when the wave field was represented by the monochromatic wave (14-31%).

When directional modelling was applied, the smallest difference was obtained for wave condition B1 which is a broad frequency and broad directional spectrum<sup>16</sup>. The opposite effects were observed for wave condition N2, the narrow frequency and narrow directional spectrum.

The results given in Tables 6.6 and 6.7 show good agreement between MSE and DIRSPDF predictions. Therefore the reasons for possible discrepancies might be found in the physical experiment and presentations of the measurements. Also, the way in which the input incident spectra were discretised might have caused the difference in results. This may have introduced energy into the portion of spectrum that was not actually generated in the physical model.

Also the 90-degree angle is in the region of high gradients in wave energy as wave energy passes along the crest from the unsheltered to the sheltered region. For incident waves with some degrees of directional spreading, the gradient is smoothed over a wider region. The measured diffraction coefficient along the 90-degree intersect is in the range from 0.5 to 0.6. However the diffraction coefficients in the unsheltered area is equal to 1.0, thus a large gradient is present in that area which is difficult to model (see Figure 6.14). Also there might be some reflection present from the walls of the basin and basin oscillations.

Additionally, the oscillations around the mean solution were observed. Their amplitudes were larger for mono waves than in the case of the directional modelling when the MSE is used. The smaller oscillations in the final directional modelling result may result from linear superposition of the component waves.

---

<sup>15</sup> The relative values of calculated percentage difference for each point are taken, summed and then divided by the number of points.

<sup>16</sup> Also the larger number of components was used in this case.

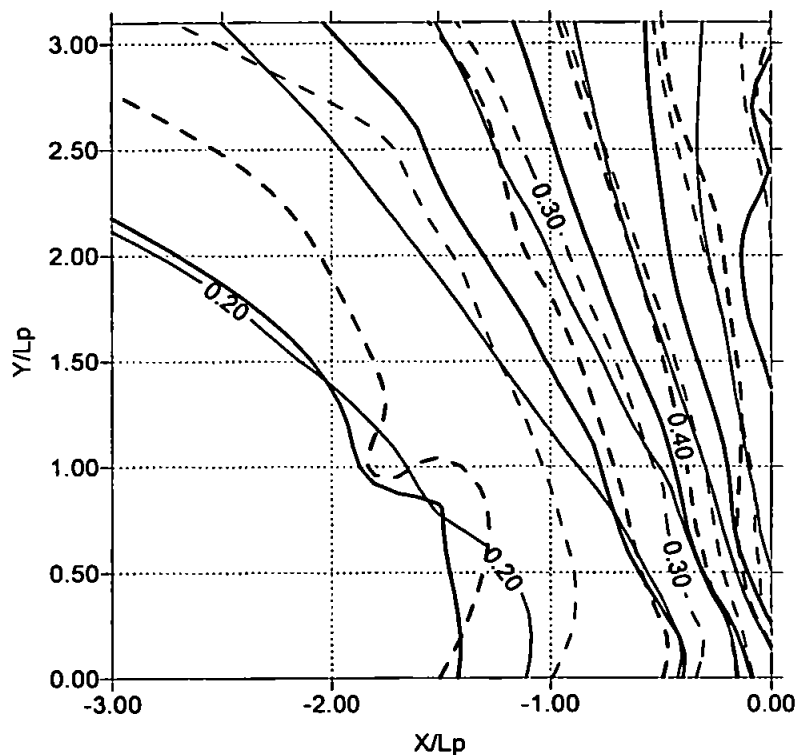


**Figure 6.14** The measured diffraction contours for four directional cases; ---- wave condition N1; - - - - wave condition N2; - wave condition B1; - · - wave condition B2. The area behind the breakwater is only plotted here.

It can be concluded that the model predicts the diffraction coefficient for the directional wave spectra around a semi-infinite breakwater with an accuracy of 5-15%. The accuracy depends on the shape of directional spectra and number of frequencies and directional components taken into account for the calculation. Reducing the number of directions for directional modelling can either slightly improve or worsen the results. The largest difference between predicted and measured values are obtained when only one frequency and one direction are used. It can be concluded that the results depend on the number of increments used, but also how those increments represent the incident spectrum. Taking in account Grassa's (1990) recommendations that the results should not change for more than 100 components and the fact that the smallest difference was obtained for the largest number of components (147), it can be concluded that more directional components need to be taken in account. However this need to be balanced with the hardware capabilities and a length of computational time.



The results also indicate that the directional spreading should be considered in diffraction analysis. From Figure 6.14 it can be seen that the diffraction process is sensitive to the directional spread and to a lesser extent to the frequency spread. Thus in the specific field studies the measured spectra need to be taken in account.

## 6.4 Validation from field data

The transformation of the directional sea around detached breakwaters consists of refraction, diffraction, shoaling, reflection and transmission. In the previous section, it has been shown that the directional modelling can accurately predict diffraction of an irregular sea. Here the validation will be further extended to see how accurately the combination of diffraction and other effects can be predicted.

The emphasis will be given on directional modelling. One of the conclusions of the preliminary validation was that proper reflection coefficients needs to be taken into account. The evaluation of the multidirectional parameters in Chapter 5 has enabled more accurate model inputs. Also, the numerical model has been slightly changed. The reflective boundaries for the oblique waves, similar to ones given with equation 6.7, have been incorporated. An additional improvement is that the number of steps to bring the solution close to the steady state can be determined from the 'rough guides' given in Figures 6.4, 6.5, 6.6. Three data sets used for the preliminary validation of directional modelling are used for the new validation. Additionally three new data sets were chosen to cover the variety of the wave conditions. All data sets were chosen on the basis of criteria given by Ilic and Chadwick (1995) and similar to Dingemans *et al* (1984)

- synchronous wave measurements  $t - 20 \text{ min} \leq t_0 \leq t + 20 \text{ min}$  (91% data are in time interval  $\pm 10 \text{ min}$ )
- wave height  $> 0.5 \text{ m}$
- high tide - to have reasonable depth of water in the area behind breakwaters ( i.e. depth between 2.6 and 3.6 m inshore and between 6.8 and 8.0 offshore )
- small values of the reflection coefficient<sup>17</sup> measured offshore

---

<sup>17</sup> This criteria is not so important after the evaluation of the directional parameters has been done

### 6.4.1 Computational set up

The mild slope bathymetry of the site (except the steeper shingle beach at the shoreline boundary) and the measurements positions are given in Figure 6.15. The offshore depth contours are based on a survey provided from Robert West and Partners (1991). The shoreline bathymetry has been processed from aerial surveys (Axe, 1994).

A computational area of 2000 m (alongshore) x 2000 m (cross-shore) was chosen. A grid spacing of 2 x 2 m was used (401 x 401 points). All of the chosen data were measured in October 1994, thus the bathymetry from the aerial survey in September 1994 was used for all 6 data sets.

The reflection coefficient used for the reflective boundaries at the breakwaters was calculated using following formula

$$Kr = 0.151 R^{0.11} \quad (6.35)$$

where non-dimensional parameter R is given by

$$R = \frac{d_t L_o^2 \tan \beta}{H_i D^2} \quad (6.36)$$

where  $d_t$  is water depth of the toe of the breakwater;  $\tan \beta$  is slope of the breakwater and D is a characteristic diameter of rock armour  $(W50/\rho)^{1/3}$ .

Davidson *et al* (1996) on the basis of the measurements taken in the front of the breakwater 4 derived the formula given in equation 6.36. The reflection coefficient was calculated for each frequency independent of the wave direction.

Unlike the breakwater reflection, the reflection from the beach has not been directly measured. One of the reasons is that those measurements are very difficult. However, the reflection coefficient can be calculated from the equation:

$$Kr^2 = \frac{E_r}{E_i} \quad (6.37)$$

the ratio of the reflective and incident energy based on the MLM estimates from the directional measurements taken in the bay.

The reflection coefficients are quite high (close to 1) for lower frequencies. From numerical tests in Chapter 5 it was found that the reflection coefficients can be overpredicted by 9%. However, there are only a few measurements from shingle beaches which can be used for the verification. Mason *et al* (1997) measured reflection from a shingle beach and found quite high reflection coefficient values for swell conditions. Elgar *et al* (1997) also found a high reflection for swell waves from a steep sand beach.

Therefore, despite its high values the MLM estimates of reflection coefficients were incorporated into the shoreline boundaries.<sup>18</sup> The reflection coefficients were calculated for the same frequency bands, which were taken as representative ones for the directional modelling using equation 6.37. In this way the coefficients were frequency but not directionally dependent.

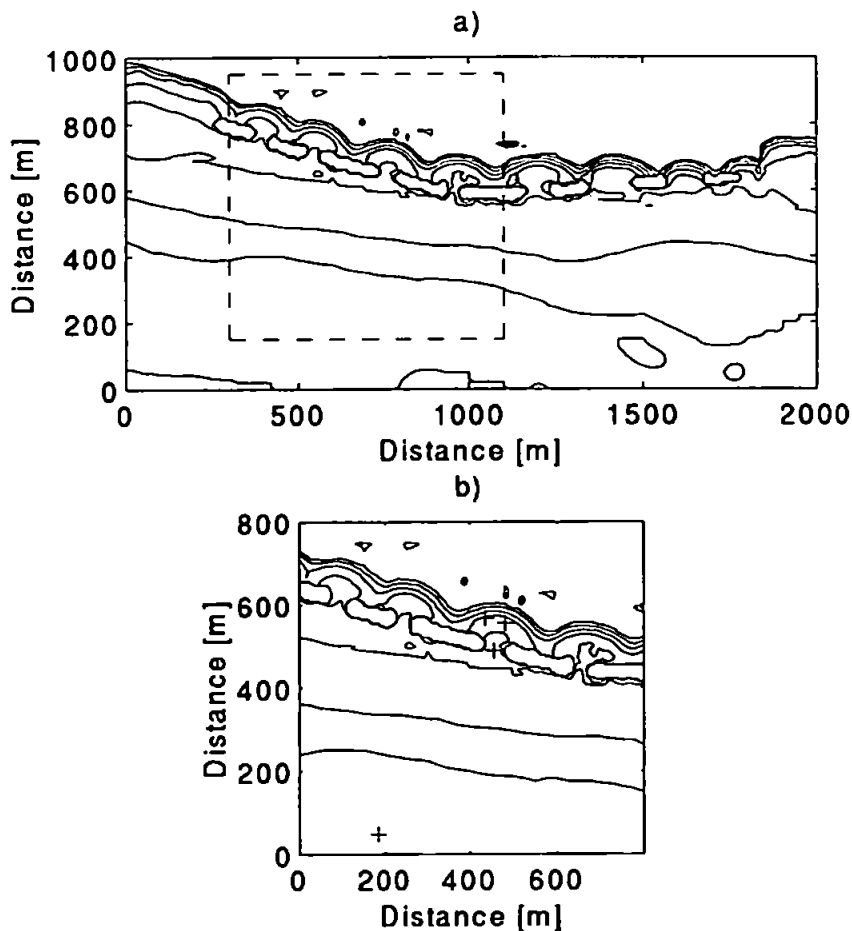


**Figure 6.15** The model bathymetry and measurement positions

<sup>18</sup> During the preliminary validation, the reflective boundaries at the beach were not included

The next parameter which, needs to be chosen is the minimum water depth to be able to give accurate results. The recommendation<sup>19</sup> by Li is to set such water depth for which  $L/\Delta x$  is larger than 6. To preserve the validity of linear theory, the minimum depth was checked using two additional criteria. The first criteria is the breaking criteria, thus the water depth needs to be  $d > H/0.78$ . When directional modelling is implied this becomes irrelevant, as the wave height of each component is very small. However, the waves still break in reality. This problem was addressed by Ozkan and Kirby (1993) (see Chapter 2), but there is still no satisfactory solution. The second criteria is that the Ursell Number<sup>20</sup> is smaller than 1. The Ursell Number is a non-dimensional parameter which gives a quantitative measure of the linearity of the waves (Guza and Thornton, 1980) and is given by the following formula

$$Ur = \frac{H_i}{2d(kd)^2} \quad (6.38)$$

where  $d$  = water depth;  $k$  = wave number. Strong nonlinearities can be expected for  $Ur > 1$ . Thus the water depth chosen on the basis of the second criteria was compared with the water depth chosen on the basis of  $L/\Delta x$  larger than 6. The larger water depth was chosen as the minimum water depth in the model.

Case	Set	$T_p$	$\theta_p$	$R_p$	$T_m$	$\theta_m$	$R_m$	$S$	$H$	WD	DL
wind	64	5.70	-66	0.37	4.20	-68.57	0.32	32.85	1.02	7.31	2.87
Bi modal	65	9.50/ 5.45	-90	0.51/ 0.37	5.04	-81.34	0.36	32.89	0.69	7.32	2.85
wind	69	5.7	-90	0.36	4.50	-80.65	0.33	29.65	1.19	7.57	*2.2 /3.04
swell	72	15.08	-90	0.57	10.26	-98.07	0.48	29.75	0.83	7.43	2.82
swell	73	9.50	-90	0.48	9.50	-97.67	0.48	27.86	0.62	7.46	2.9
wind	75	5.96	-102	0.36	4.84	-	0.33	27.41	1.3	7.31	2.68
						101.18					

**Table 6.8** Summary of offshore wave conditions used as input for model validation – *monochromatic case*

<sup>19</sup> It was found that when  $L/\Delta x$  reduces to only a few points, disturbances from the boundaries propagate back offshore.

<sup>20</sup> The inshore incident wave height was not known *a priori*, therefore the incident wave height was approximated by offshore wave height multiplied by shoaling coefficient

Case	Set	$T_p$	$\theta_p$	$T_m$	$\theta_m$	$R^*$	$S$	$H^{**}$	$WD^{**}$
wind	64	5.70	-78	4.06	-82.29	0.40	31.05	0.55	3.33
								0.60	2.82
								0.93	4.24
Bi modal	65	13.5	-90	6.72	-88.37	0.41*	34.46	0.63	3.33
								0.52	2.81
								0.84	4.22
wind	69	5.7	-90	4.53	-86.71	0.42	28.41	0.88	3.5
								0.80	2.99
								1.30	4.41
swell	72	11.15	-90	7.00	-92.27	0.64	32.49	0.68	3.32
								0.58	2.79
								0.93	4.19
swell	73	12.21	-90	7.63	-91.13	0.66	32.34	0.70	3.35
								0.52	2.82
								0.90	4.22
wind	75	6.58	-90	4.69	-89.70	0.31	28.34	0.93	3.18
								0.56	2.64
								1.14	4.04

**Table 6.9** The summary of inshore wave conditions used for the model validation. The parameters are given for the position shoreward of the gap unless stated otherwise.  $H^{**}$  and  $WD^{**}$  are given for 3 positions, first for the shoreward of the gap, second for the lee of the breakwater and third for the gap<sup>21</sup>.

The number of time steps required to complete the calculation was chosen from the 'rough guide' in Figures 6.4, 6.5, 6.6. The number of time steps per wave period,  $T/\Delta t$ , was set to 8. Thus to reduce the variance of the oscillations, the ratio  $L/\Delta x$ , was between 10–11.

The offshore wave field conditions used for model validation are given in Table 6.8. The wind data sets are characterised by a broad frequency distribution. The bimodal sea has two distinctive peaks - usually swell and wind peaks. Swell conditions are characterised by a narrow frequency band. The following parameters are given in Table 6.8:  $T_p$  is the peak period,  $\theta_p$  is the principal direction,  $R_p$  is the reflection coefficient calculated for  $T_p$ ,  $T_m$  is the mean period,  $\theta_m$  is the mean direction,  $R_m$  is the reflection coefficient calculated for  $T_m$ ,  $S$  is directional spreading,  $H$  is the incident wave height from MLM analysis,  $WD$  is the offshore

<sup>21</sup> \* indicates the case when  $R$  is derived for higher frequencies (for the bimodal sea).

water depth, DL is the limited water depth<sup>22</sup>.

The shoreline reflection coefficient is given together with the other parameters derived from the inshore measurements, taken at the same time, in Table 6.9. The same parameter as in Table 6.8 are specified.

It can be observed from both tables that for wind waves (except set 75 when only a slight change occurred) there is no change in peak period,  $T_p$ , between offshore and inshore wave conditions. However, there is a change in  $T_p$  between offshore and inshore wave conditions for the swell and bimodal sea. The principal wave direction<sup>23</sup> has changed from offshore to inshore for all three types of sea. The wave direction has become close to the normal, unless it was shore normal already (the star array was positioned shoreward of the gap for these measurements).

#### 6.4.2 Tests and results

Three different monochromatic model runs for each data set were performed in the first stage. First, the offshore measured directional spectra were represented by the peak frequency, the principal wave direction and the significant incident wave height. This will be referred to as mono - case 1. Mono - case 1 also included reflection from the breakwater and from the beach. Next, the offshore measured directional spectra were represented by the main frequency, main direction and significant incident wave height. The main direction was calculated using equation 5.1 in Chapter 5. The main frequency was calculated in the same way. This case also included the reflection from the breakwater and the beach and it will be referred to as mono – case 2. Finally, mono – case 1 was repeated without including reflection from the beach. This is called mono – case 3.

The second stage was to simulate directional waves under the assumption of the validity of linear superposition. Thus the measured wave spectrum was represented by a number of monochromatic waves. Tests were then carried out which took into account several frequency intervals (5 – 10) and four to seven directional intervals. This will be referred to as the directional case.

---

<sup>22</sup> \* indicates the case when both frequency are taken in account for DL estimation.

<sup>23</sup> The peak direction in directional distribution of energy.

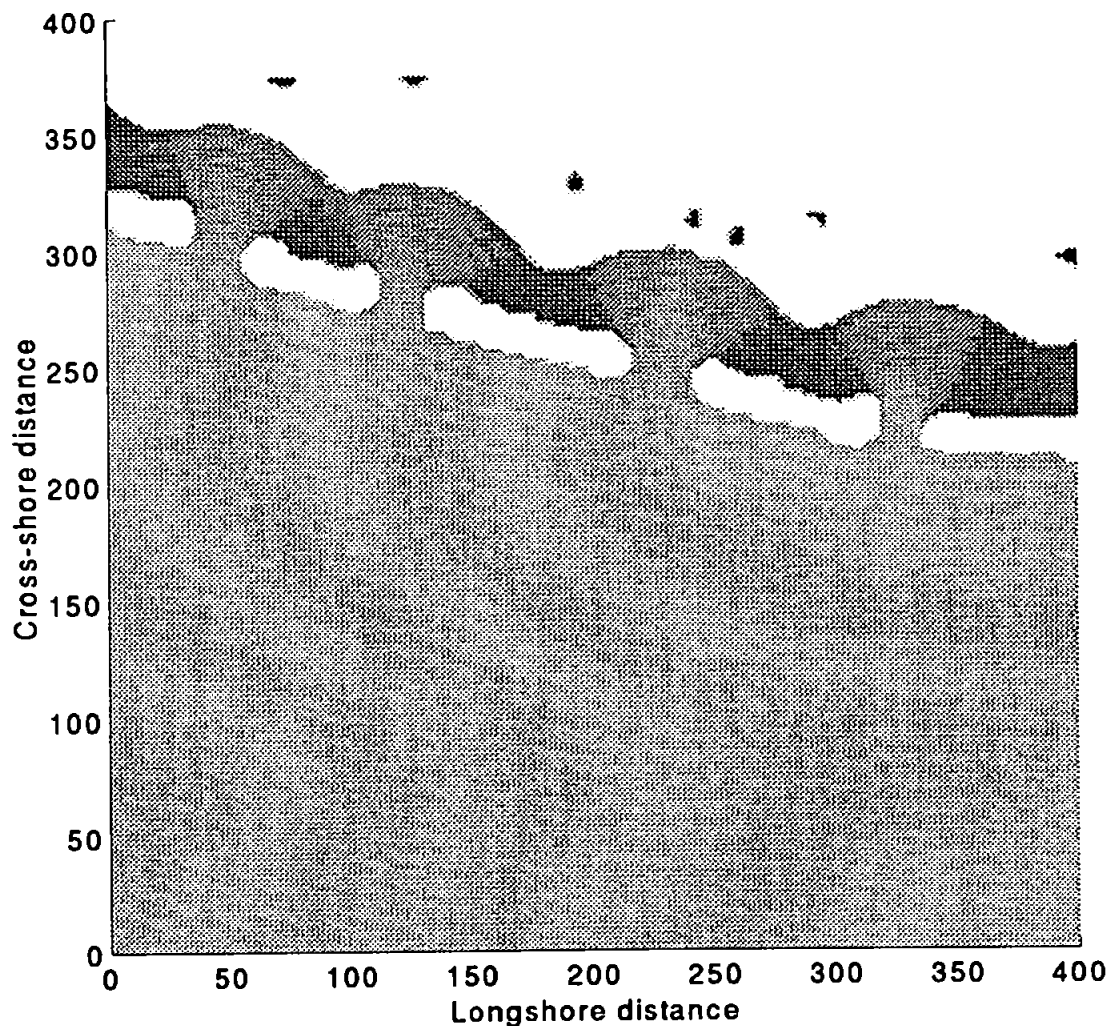


**Figure 6.16** Typical model output (file 64 - directional modelling results)

Typical model output of calculated wave heights is given in Figure 6.16. Standing wave fields can be observed in the front of the breakwaters, as can wave height attenuation behind the breakwaters due to diffraction. The wave penetration through the gap and standing wave field around the shoreline in the gap can also easily be seen. This result looks realistic and convincing. However a detailed comparison between predicted and measured wave height is necessary in order to validate the model.

Figure 6.17 a,b,c show the comparison between measured and calculated wave heights for the three inshore positions where the field measurements are compared with both the monochromatic model results and the directional case. Figure 6.17 a compares model

results and field measurements for the position in the lee of the breakwater. There is quite a high percentage difference (up to 70%) observed for mono cases. A possible reason for the large disagreement between predicted and calculated wave heights is due to the lack of energy transmission by radiation<sup>24</sup>, into the lee of the breakwater, when using the monochromatic wave model. In the position shoreward of the breakwater gap, there is better agreement between measured and calculated wave heights (Figure 6.17b) where the percentage of difference decreases (the difference is below 20% for most cases). In the third position in the breakwater gap (Figure 6.17c), there is an overestimate of the calculated wave heights. Thus the percentage difference increases again. The same trend was observed during the first validation tests.

A quantitative measure of the accuracy of the results has also been made, using a relative root mean square difference between measured values and numerical model predictions for three different positions inshore given by

$$dif_{rms} = \sqrt{\frac{\sum \left( \frac{H_m - H_c}{H_m} \right)^2}{N}} \quad (6.39)$$

where  $H_m$  is a measured wave height,  $H_c$  is the wave height calculated by the numerical model and  $N$  is the number of tests - only six in this case.

The summary of results is given in Table 6.10. The use of the monochromatic wave model to represent real irregular waves with directional spreading confirmed that significant underestimation of wave conditions behind the breakwater occurred.

Position	Relative mean square difference			Error Percentage		
	Case 1	Case 2	Case 3	Case 1	Case 2	Case 3
in the gap	0.41	0.32	0.38	38.15 %	22.50 %	32.99 %
shoreward of the gap	0.30	0.28	0.19	19.39 %	16.18 %	15.20 %
in the lee of breakwater	0.39	0.37	0.40	35.06 %	32.75 %	36.43 %

**Table 6.10** Summary of results for monochromatic case - (case 1 - peak frequency and principal direction with reflection, case 2 - mean frequency and mean direction with reflection, case 3 - same as case 1 without reflection)

<sup>24</sup> When random waves penetrates through the gap, depending on the direction of approach, part of the energy directly radiates and part of the energy diffracts around the breakwater. Each position in the bay is differently related to the approaching wave direction, thus the ratio of the radiated and diffracted energy will be different.



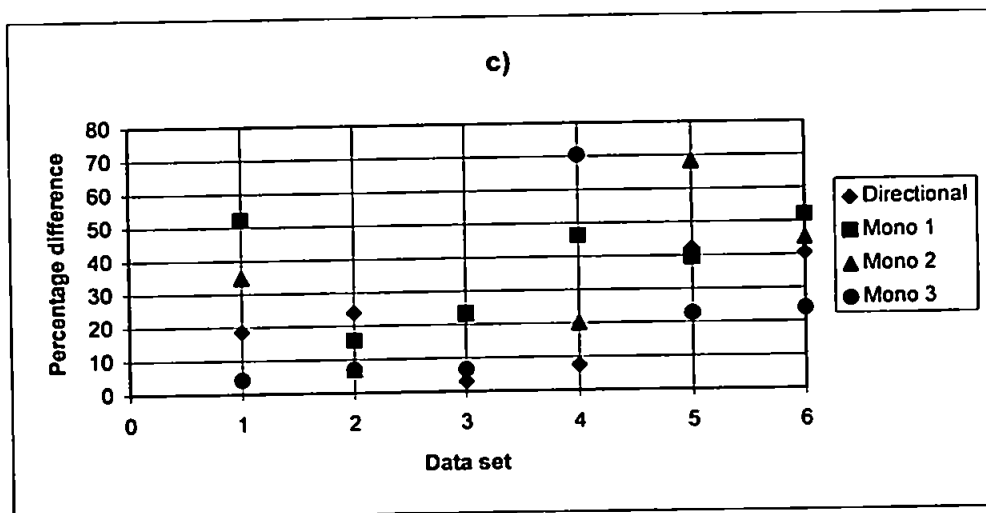
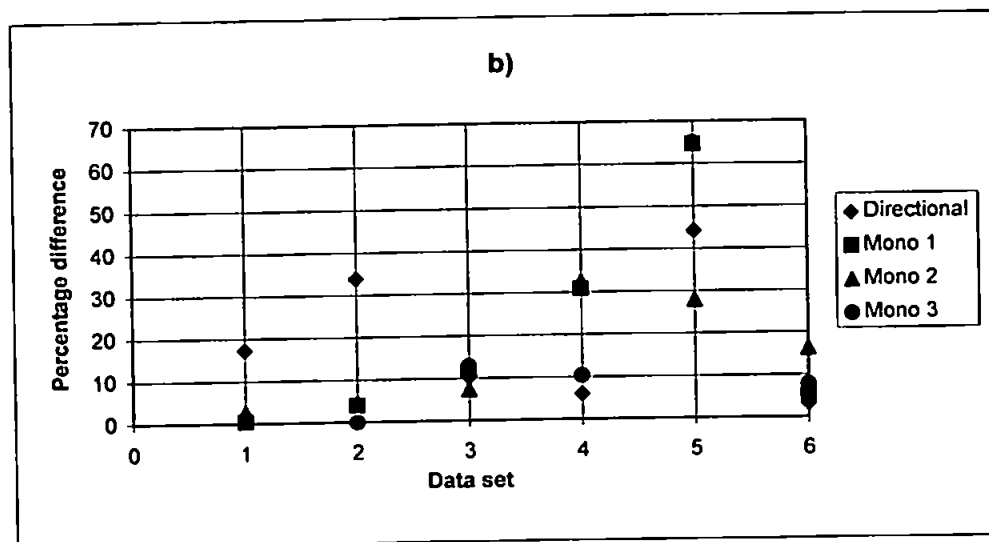
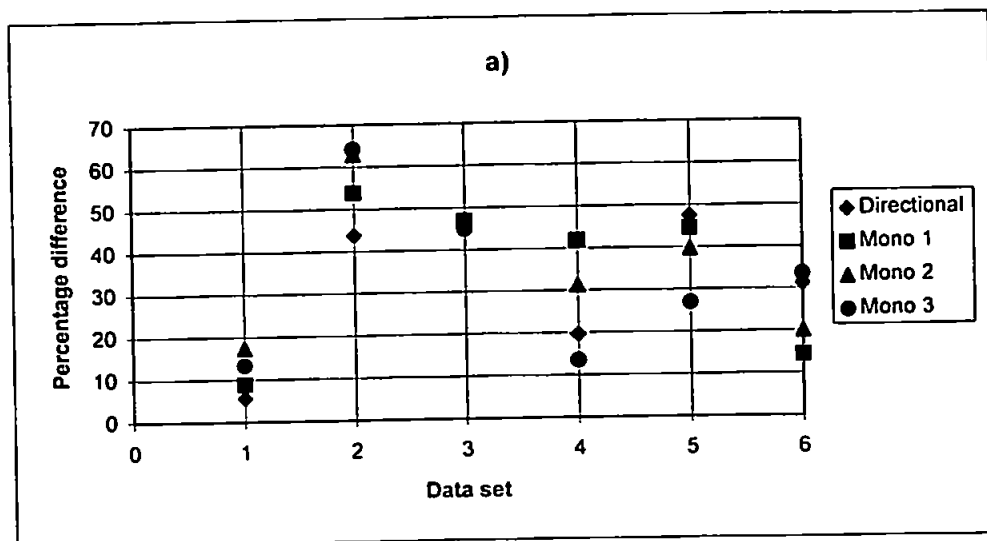
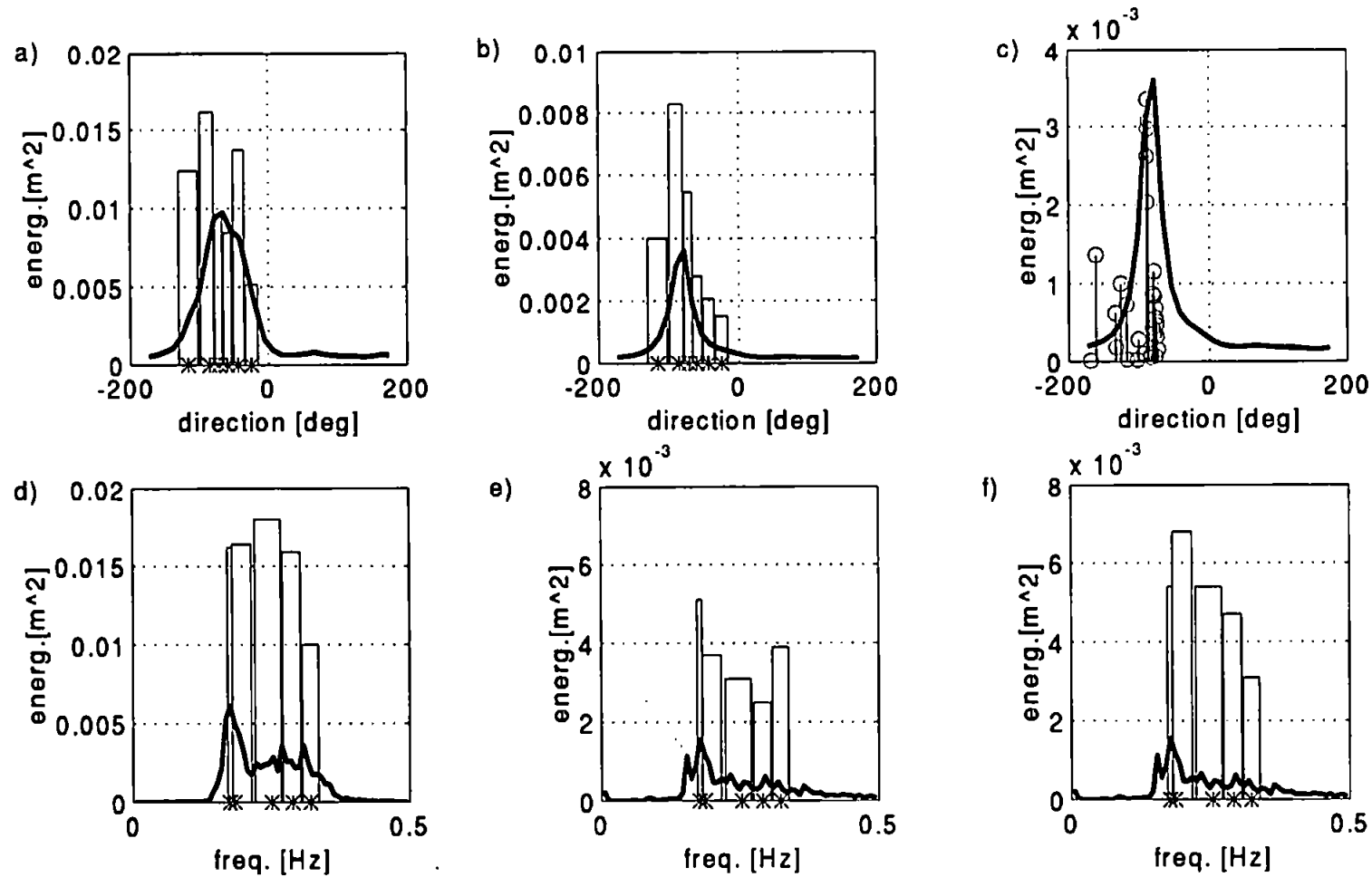
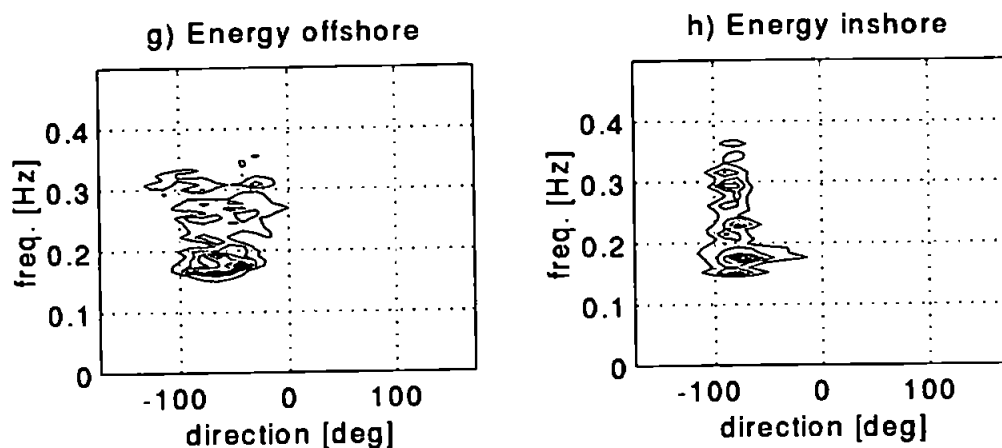


Figure 6.17 The percentage of difference for monochromatic and directional case-(a) lee of breakwater, (b) shoreward of breakwater gap, (c) breakwater gap



**Figure 6.18 a-f** Directional results summary— File 64— a) sum of energy over all frequencies versus direction (line plot) and energy in directional bands chosen for modelling offshore (bar plots); b) sum of energy over all frequencies versus direction (line plot) and energy in directional bands chosen for modelling inshore (bar plots); c) measured inshore (line plot) and model predicted energy versus direction (circles plots); d) sum of energy over all directions versus frequency (line plot) and energy in frequency intervals chosen for modelling offshore (bar plots); e) sum of energy over all directions versus frequency (line plot) and energy in frequency intervals chosen for modelling inshore (bar plot); f) measured inshore (line plot) and model predicted energy versus frequency (bar plot)



**Figure 6.18g-h** Measured directional spectra – g) directional spectrum offshore; h) directional spectrum inshore;

The directional measurements and directional modelling results (for the wind data set 64) are presented in Figure 6.18 a-h. The results for the other wind, bimodal and swell data files are given in Appendix H. The measured and calculated energies for each frequency interval summed over all directions was found to be in very good agreement except for very low and very high frequencies. This possibly explains better results for the case of the wind waves than in the case of swell and bimodal seas. The good agreement for wind data set 64 between model predicted energies and inshore measurements is illustrated in Figure 6.18 e, f. Disagreement for the lower frequencies could be due to an increase of energy in the infragravity band inshore. Disagreement for high frequencies (Figure 6.18 g,h) could be due to the factor of the cut off frequency of 0.35 when the offshore pressure data are transferred to the surface elevations. Therefore, there is no offshore energy above this frequency band. However the inshore data were measured up to 0.5 Hz. Also it was shown in Chapter 5 that directional estimates are less accurate for higher frequencies. Besides, waves of such small wave period can be locally generated and not propagate from offshore which is not included in the model.

A reasonable agreement between measured and predicted directions for the wind data set 64 can be observed in Figure 6.18 c and for the other two wind data sets in Appendix H. Generally, the directional energy distribution predicted by the model does not agree with the measured directional energy distribution. The predicted directions are calculated from the phase information. When the reflective boundaries are included, it is difficult to determine directions accurately because of phase locking.

Good agreement between predicted and measured wave heights was obtained for the wind spectra (broad frequency and directional spectra), wind data sets 64 and 69 (see Appendix H). The measured inshore frequency spectra peaks remain the same as the offshore ones for those two data sets. Underprediction of the wave heights in the lee of the breakwater is larger for data set 69 than data set 64. This can be associated with the angle of wave approach, which is almost normal to the beach for data set 69. In the case of data set 64, the waves are approaching from the SE. Thus the energy in the lee of the breakwater is combined by radiation and diffraction for data set 64 and mostly by diffraction for data set 69. Also, the directional spectrum is narrower for data set 69. Therefore, only 5 directional bands (six for data set 64) were taken for the directional modelling. It was observed from laboratory measurements, in section 6.3, that the energy propagates further into the shadow zone with the broader directional spectrum (Figure 6.14).

Data set 75 presents again wind spectra conditions, with wide frequency spectra and moderately narrow directional spectra. The energy in the measured inshore frequency spectra is reduced over all frequencies except in the infragravity bands. The model predictions in the bay are in very good agreement with the measurements. But the predictions in the lee of the breakwater are underestimated and overestimated in the gap. The possible reason for it could again be the direction of the wave propagation and number of directional bands used for the modelling. The principal direction is from SW, thus even less energy than in the previous two cases is diffracted into the lee of the breakwater where the measurements were taken.

The agreements are not very good in the lee of the breakwater for bimodal spectra, data set 65 (see Appendix H). For swell type waves (or in this case the swell part), significant transmission through the porous breakwater can be expected which is not taken in account. These discrepancies are reduced in the bay and in the gap. From the measured frequency spectra inshore, it is possible to see that the frequency peak has been moved and there is more energy in the lower frequency band than in the same low frequency band offshore. The reasons for this could be strong reflection from the beach, non-linear interactions or the combination of both.

The swell type sea, data set 72 (see Appendix H), has a narrow frequency and moderately broad directional spectrum offshore. The frequency peak inshore has been moved and the energy is significantly reduced in all frequency bands. The directional plot of the measured

inshore spectrum indicates the presence of reflection for the peak frequency. The predicted energy calculated from predicted wave heights are in reasonable agreement at all three positions. There is a slight overprediction of the energy in the lower frequency band. Unfortunately, the predictions for the swell conditions, data set 73 are not so good. This time the model underpredicts energy in lower frequencies. This data set has narrow spectral and directional spread offshore. The peak of the measured frequency spectrum inshore has been moved to a lower frequencies. Also there are no energy reductions evident over the frequencies bands. There is high reflection for the peak frequency. Thus the difference in directional spread and the number of directional bands used probably had an influence on the computational estimates.

The percentage difference between predicted and measured wave heights for the directional case is also given in Figures 6.17 a b c. The predictions and the percentage error vary from case to case. Root mean square differences between measured and predicted results as well as error percentage for the three positions inshore are shown in Table 6.11.

<i>Position</i>	<i>Root mean square difference</i>	<i>Error Percentage</i>
<b>in the gap</b>	0.27	22.62 %
<b>shoreward of the gap</b>	0.24	19.16 %
<b>in the lee of breakwater</b>	0.36	32.23 %

**Table 6.11** Summary of results for directional wave modelling

Contrary to expectations, the results in Table 6.11 and in Figures 6.17 a, b, c are very similar to the results obtained using the mono waves and are also worse than the directional modelling results in the preliminary validation (see Appendix G). However, this time a different number of frequencies and directions were used to represent the offshore directional spectra. Therefore, the band representative frequencies and directions differed from the ones in previous tests. However, a change of number of directions, thus also representative directions, introduced 1-3% difference in error percentage for laboratory conditions. The next important difference is that the reflection from the beach is included in the shoreline boundaries in the new tests. The combination of chosen limited-depth and the reflection at the shoreline introduced differences in wave height prediction. The wave

heights in the lee of the breakwater were further underpredicted and the wave heights in the gap were further overpredicted.

The model predictions were more accurate for wind waves than for swell conditions. This coincides with a broader directional spectra and larger number of directional bands used for modelling and also with smaller reflection from the beach and the absence of non-linear interactions. Here the comparison with only three measurement points is given and therefore the numbers can be misleading. Even though it does not appear that the directional modelling is a more superior technique, the contour plots show much smoother results than in the case of the monochromatic waves ( see Plate 6.1 on the end of the chapter).

### 6.4.3 Discussion

The disagreement between measured and calculated wave heights could have several causes. First, the model is linear and even though the model was used with the data recorded at high water, some non-linearity may be present which Li's model can not reproduce. Wave breaking, bed friction and wave-current interaction are also not taken into account. Transmission through the breakwaters is not included in the model either. However, the most important errors occur in the estimation of the wave heights in the lee of the breakwater using the regular (monochromatic) wave model, or from not using enough directional components. Hence, the model does not reproduce the effects caused by wave direction and directional spread. Because of these lattermost limitations the induced errors are larger in the lee of the breakwater than in the gap or shoreward of the gap. The errors could also be caused by errors introduced by input and boundary values, for example incorrect estimation of the reflection coefficient and limited water depth at the shoreline .

The cross-shore evolution of the sea surface elevation spectrum is dependent upon the refraction, diffraction and shoaling caused by both bathymetry and currents. The spectra also include the effects of reflections from both the breakwater and the beach which cause spatial modulations of the spectrum and the effects of non-linear interactions resulting in exchange of energy between frequency components. There are also the effects of dissipation caused by bathymetry and the breakwaters. Wind generation and bottom friction are considered negligible over the relatively short distance of a few hundred meters. The sensitivity of the model to changes in some of those parameters will be

qualitatively rather than quantitatively assessed.

### Wave-wave interactions

Nonbreaking water waves evolve substantially as they propagate shoreward in shallow water. As the depth decreases, wave amplitudes increase and initially symmetric wave profiles become non-symmetric (Freilich *et al*, 1990). Two effects are seen. Firstly, the waves become sharp crested with broad troughs, thus they become asymmetrical with respect to the horizontal. This is referred to as the skewness or skewed profile. Secondly, close to the breaking point, the wave faces steepen and the wave shapes become asymmetrical with respect to the vertical. This is referred to as the asymmetry or asymmetric profile.

Both linear and non-linear processes act simultaneously to alter the frequency-directional characteristic of shoaling waves. Non-linear interactions between a pair of wave components with frequencies and wave numbers  $(f_1, k_1)$  and  $(f_2, k_2)$  theoretically force secondary waves with the sum and difference frequency and wave number  $(f_3 = f_1 \pm f_2)$  and  $(k_3 = k_1 \pm k_2)$  (super- and subharmonics respectively). Thus, in the frequency domain, nonlinearities may result in significant cross-spectral energy transfer over relatively short distances. In this case the phase relationship between those three waves Fourier components is no longer random, instead there is a phase coherence or fixed phase relation between those triads of frequency.

Elgar and Guza (1986), Doering (1988), Freilich *et al* (1990) and Elgar *et al* (1993) have used bispectral techniques (Appendix I) to elucidate details of non-linear triad interactions in a shoaling wave field. They showed that bicoherence (Hasselmann *et al*, 1963) can be used as a measure of non-linear coupling between modes for shoaling waves. Large bicoherence magnitudes indicate phase coupling between modes at different frequencies and small bicoherences indicate the absence of significant non-linear interactions between the corresponding modes. From bispectrum phase, biphas, a measure for skewness and asymmetry can be derived (see Appendix I).

Freilich *et al* (1990) and Elgar *et al* (1993) extended work studying non-linear effects on directional spectra. They considered non-linear, near-resonant triad interactions. The near resonant triad interactions means that both the frequencies and the vector wave numbers of the interacting waves must sum to (nearly zero):

$$f_1 \pm f_2 \mp f_3 = 0 \quad (6.35)$$

$$k_1 \pm k_2 \mp k_3 = k_\delta \quad (6.36)$$

$$|k_\delta| / |k_{1,2,3}| \ll 1 \quad (6.37)$$

where  $|k_\delta|$  is a mismatch or the difference between the free  $|k_3|$  and the sum  $|k_1 + k_2|$  wave number magnitudes. For example, if bicoherence maximum is due to near-resonant triad interactions then a wave number of the second harmonic ( $f_3=2f_1$ ) must be oriented in nearly the same direction as  $k_1$  and must be nearly  $2k_1$  ( $k_1=|k_1|$ ) in magnitude ( $k_3/2k_1 \sim 1$ ). Interaction between waves propagating in different directions results in a larger wave number mismatch.

The bispectrum for all data sets was calculated using Simmonds' (personal communications) bispectral analysis. The description of the method is given in Appendix I and for more details refer to Doering (1988) and Ozanne (1998).

The bispectrum,  $B(f_1, f_2)$ , will be zero unless there are waves present at frequencies  $f_1$ ,  $f_2$ , and  $f_3$  and there is phase coherence, or a phase relation between the waves at these frequencies. There are non-zero values of the bispectrum detected in almost all measured positions for all data sets. However, offshore bispectrum values are small compared to inshore ones. Several peaks can be detected in the gap, which is evidence for larger wave-wave interactions. For wind data sets 64, 69 and 75 the bispectrum values are smaller than for swell, data files 72 and 73 and for the bimodal case, data file 65. The bispectrum peaks are larger and coincide with the peak frequencies. It was observed that the peak frequency inshore does not coincide with the peak frequency offshore for data files 65 and 73. Also the energy has been moved from one frequency band to another. Therefore further analysis of bispectra results for data files 65 and 73 for offshore and inshore spectra will be given.



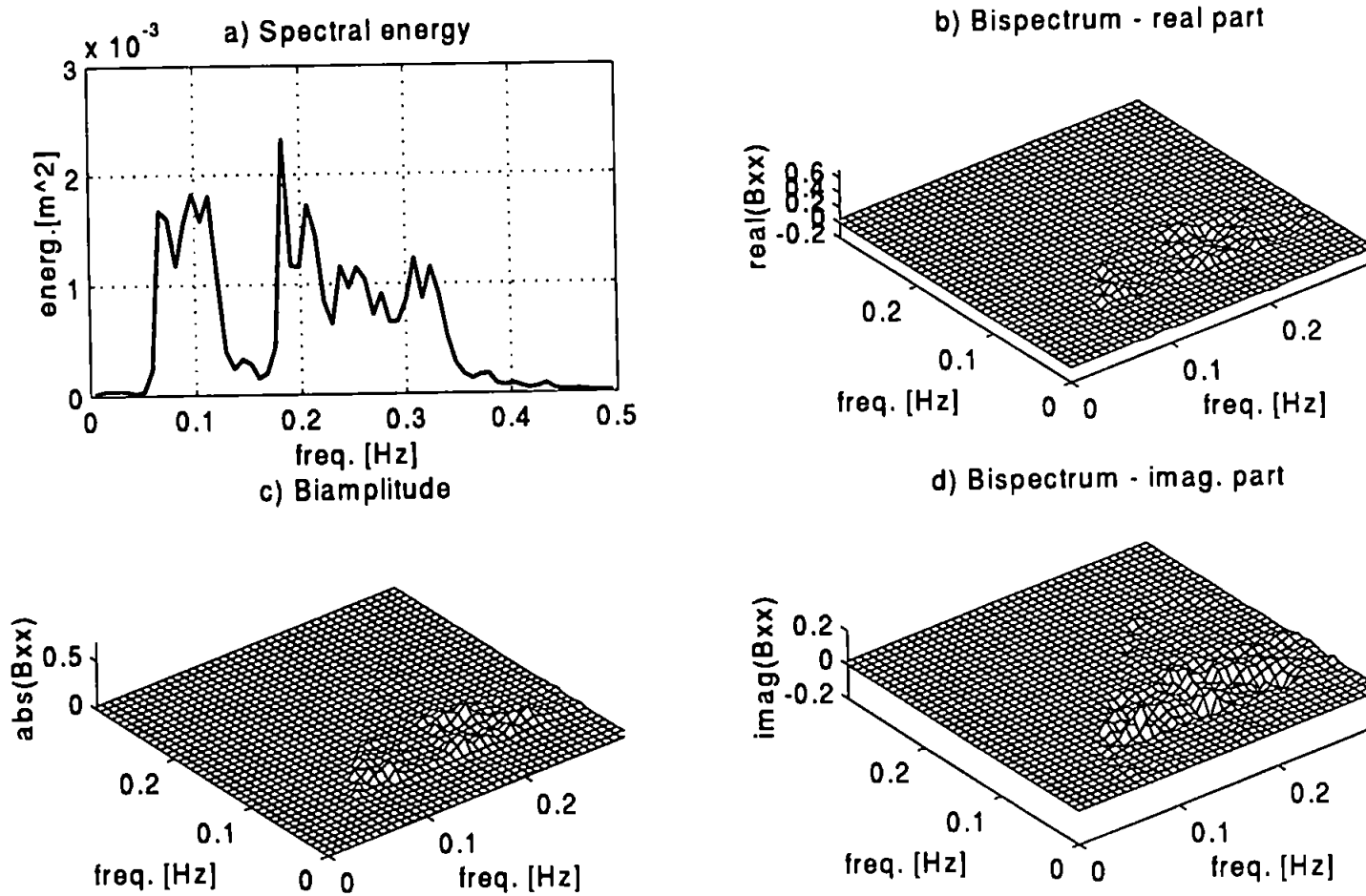


**Figure 6.19** The spectrum, biamplitude, real part of bispectrum for the offshore measured data set 65; a) energy spectrum; b) real part of bispectrum; c) biamplitude; d) imaginary part of bispectrum; ( only the energetic part of spectrum is plotted here)

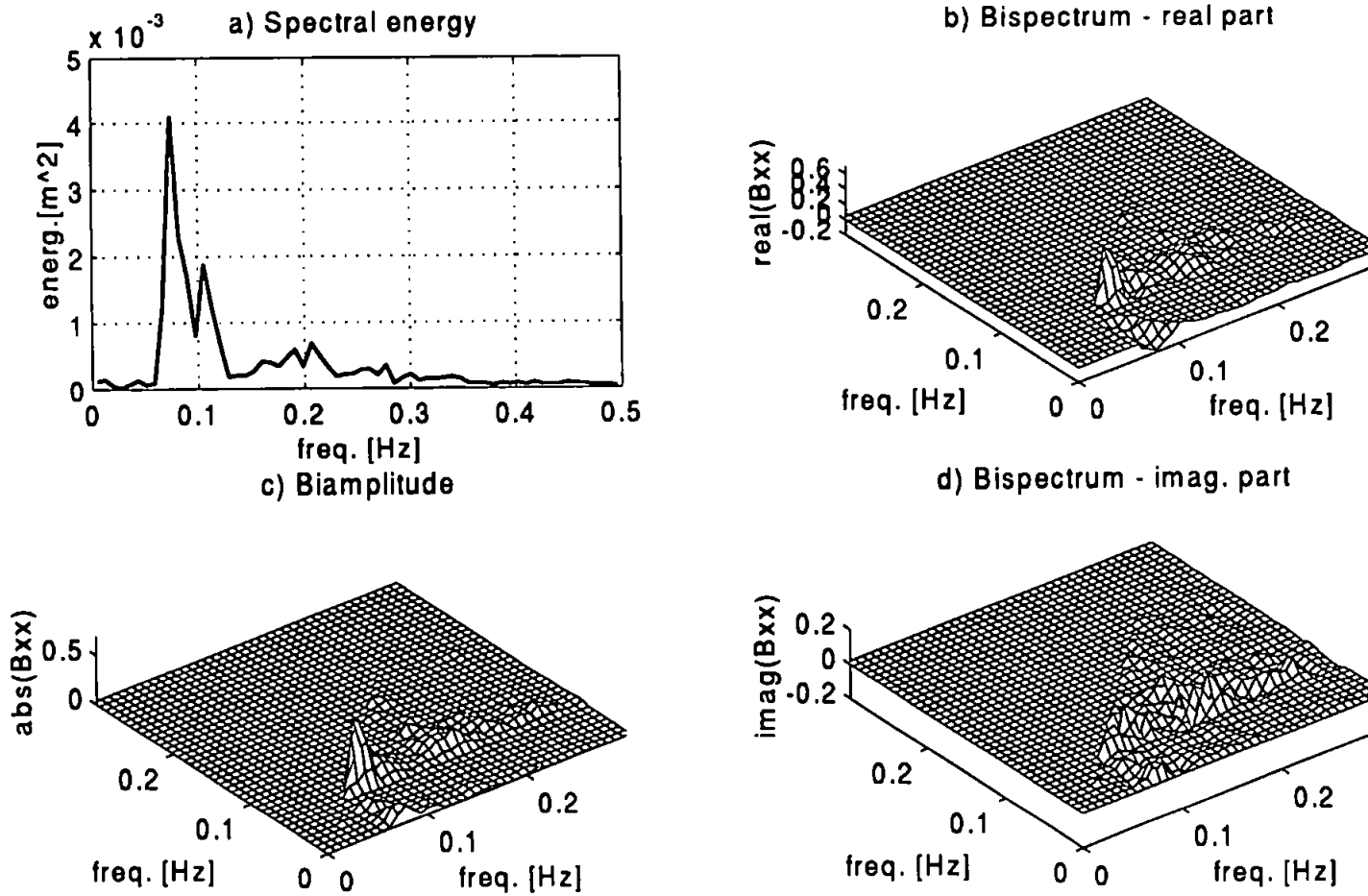


**Figure 6.20** The spectrum, biampplitude, real part of bispectrum for the inshore measured data set 65; a) energy spectrum; b) real part of bispectrum; c) biampplitude; d) imaginary part of bispectrum; ( only the energetic part of bispectrum is plotted here)

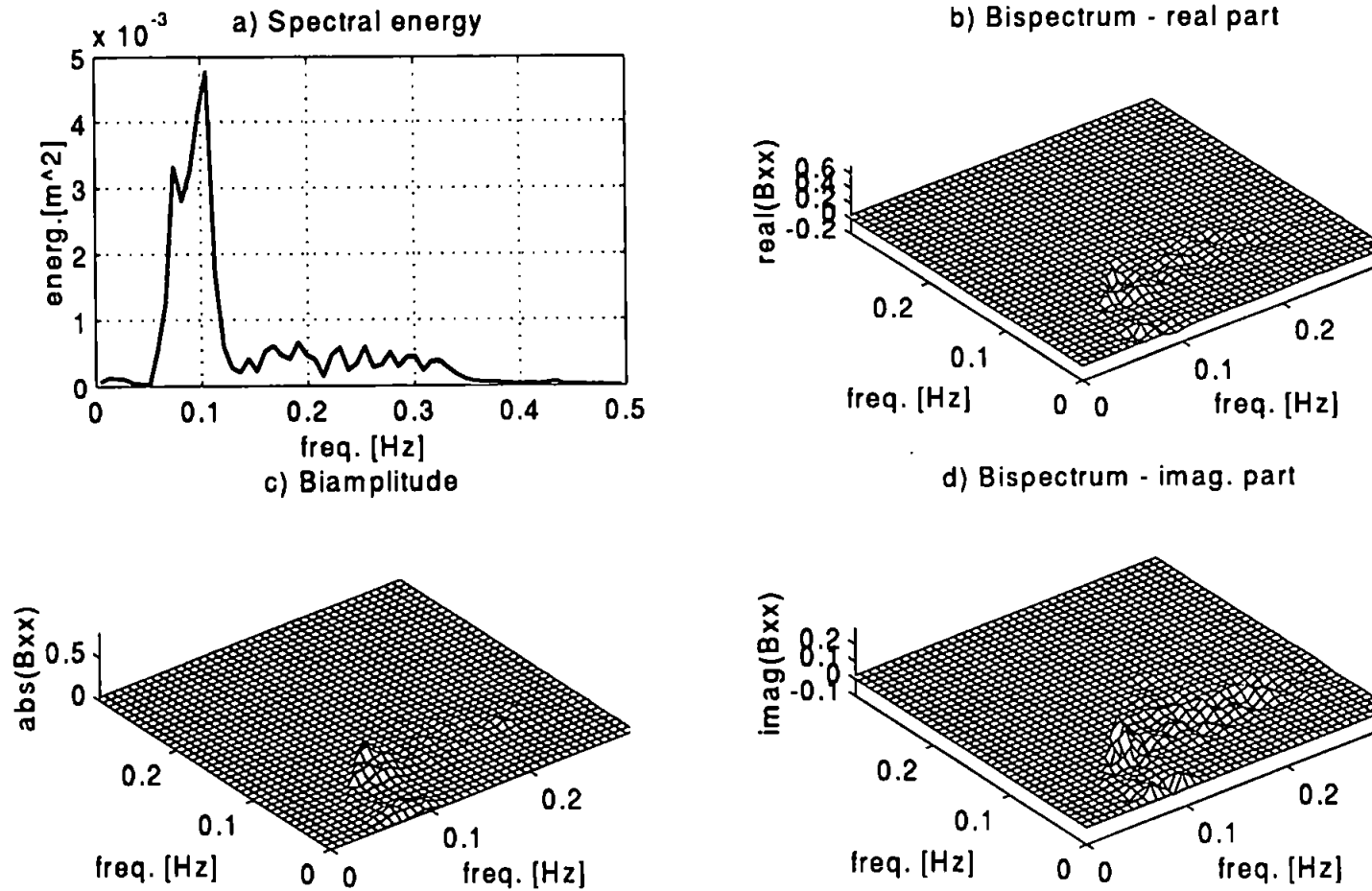


**Figure 6.21** The spectrum, biampplitude, real part of bispectrum for the offshore measured data set 73; a) energy spectrum; b) real part of bispectrum; c) biampplitude; d) imaginary part of bispectrum; ( only the energetic part of bispectrum is plotted here)

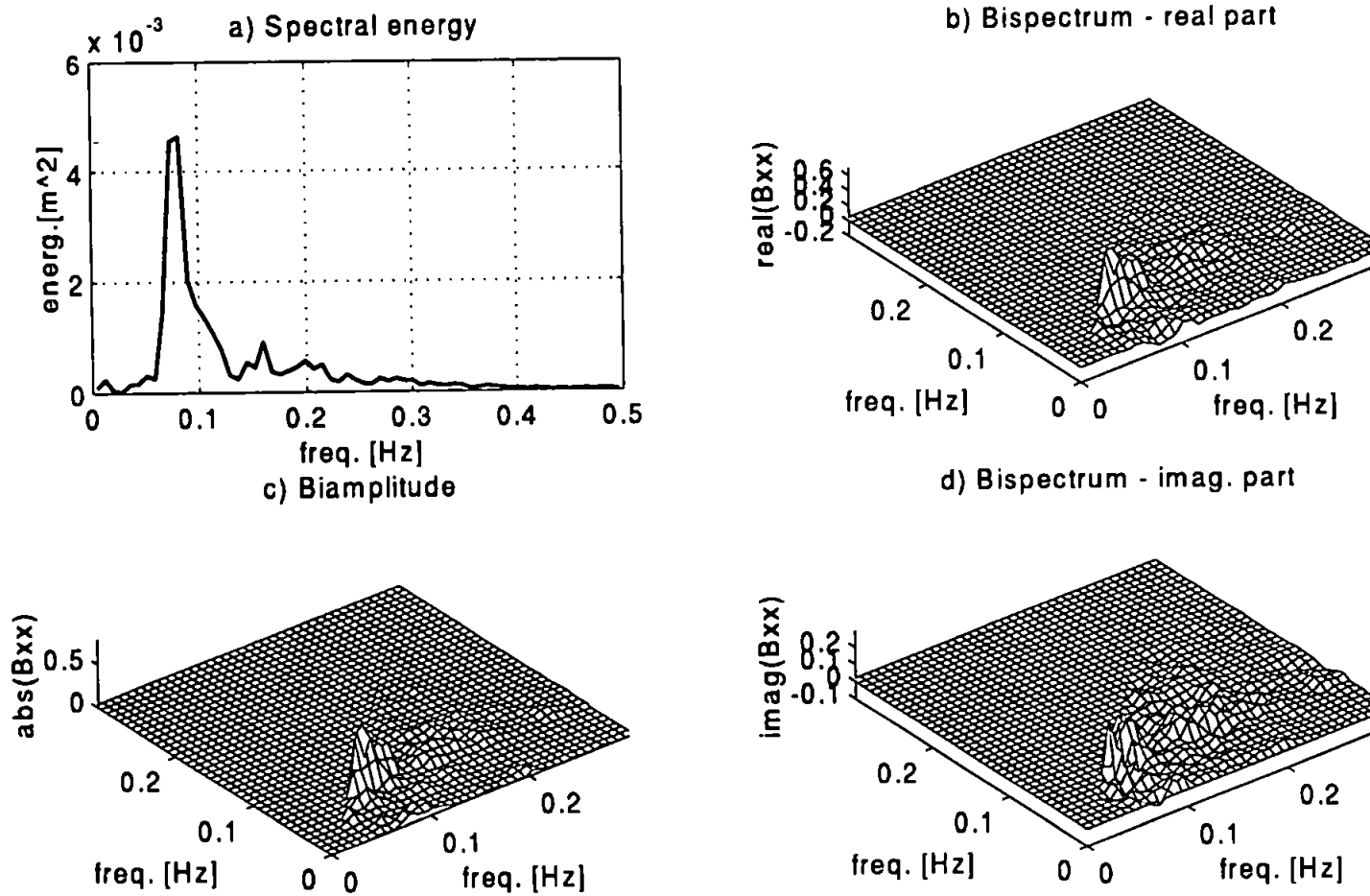


**Figure 6.22** The spectrum, biampplitude, real part of bispectrum for the inshore measured data set 73; a) energy spectrum; b) real part of bispectrum; c) biampplitude; d) imaginary part of bispectrum; ( only the energetic part of bispectrum is plotted here)

Figure 6.19 shows the spectrum, real and imaginary components of the bispectrum and the biamplitude for the offshore measured data set 65. Although the values are small, bispectrum peaks can be detected for frequency band 13 (f1) and frequency band 13 (f2), involving frequency band 26 (f3). This indicates phase coupling between the primary and first harmonic. Peaks can also be detected for frequency band 14 (f1) and frequency band 11 (f2), involving frequency band 23 (f3). This coupling coincides with a secondary peak of the directional spectrum in frequency band 23. The real part and imaginary part of the bispectrum identifies the contribution of triad interaction to skewness and asymmetry, respectively, of the wave train. However, their contributions are very small as can be seen from Figure 6.19.

The spectrum, bispectrum components and biamplitude values for inshore measurements are given in Figure 6.20. Peak energy is now in frequency band 10. There is a bispectrum peak for frequency band 10 (f1) and frequency band 10 (f2) involving frequency band 20 (f3). From the other bispectrum peaks, a coupling between frequency band 10 (f1) and frequency band 11 (f2) involving the frequency band 21 (f3) can be also detected. However, the bispectrum does not show the direction of the energy transfer. Figure 6.20c shows coupling between peak and infragravity frequencies. Physically, this is attributed to an interaction between neighbouring frequencies; the resultant wave group forces a long wave which is then phase-coupled to the gravity waves. The negative values of the skewness arising from phase-coupling between wind-wave frequencies and wind-wave and infragravity frequency can also be detected in Figure 6.20b. The positive values of the imaginary part show a tendency for waves to slope backwards.

Figures 6.21 and 6.22 show the spectra, bispectra components and biamplitudes for data set 73. Because bispectrum values are small, it can be concluded that there is no significant coupling between frequencies offshore. However, several peaks can be observed from the inshore bispectrum. Non-linear self-interactions are present for peak frequency bands 10, 11 and neighbouring frequency band 9, involving frequency bands 20, 22 and 18, respectively. There are also interactions between frequency bands 11 (f1) and 9 (f2) resulting in the frequency band 20 (f3); frequency bands 12 (f1) and 9 (f2) resulting in frequency band 21 (f3) and also frequency bands 10 (f1) and 12 (f2) resulting in the frequency band 22 (f3). However, bands 10 and 11 are the bands with the most energy and therefore the coupling between those frequencies will be most influential. The peaks for the same frequency bands were observed from plots of the real and imaginary part of the

bispectrum in Figure 6.22 b,d. Therefore, these triads also contribute to skewness and asymmetry. Positive asymmetry is related to waves sloping backwards (Figure 6.22 d) which might be associated with reflection. The values of  $k_3/(k_1+k_2)^{25}$  for these triads were somewhat larger than those (~7%) observed by Freilich *et al* (1990), which could indicate the presence of near-resonant triad interactions<sup>26</sup>.

The bispectrum analysis in this case is applied in an environment with high reflection. Also, the number of degrees of freedom was quite small (Elgar and Guza used up to 200) which might influence the bispectral analysis results. Thus, the question remains whether this analysis is applicable in such an environment. More analysis need to be done to determine the validity of this method for flow around breakwaters. Therefore, the bispectral analysis results given here can identify only qualitatively non-linear interactions or the presence of wave – wave interactions. However, this shows that linear modelling is not adequate in such an environment.

## Reflection

The equation 6.35 (Davidson *et al*, 1996) was used to calculate the reflection coefficient at the breakwater boundaries. The sensitivity of the model predicted wave heights in the bay for a change of reflection coefficient was performed.

The sensitivity tests were performed for data set 64 for mono – case 3. First the reflection coefficient at the breakwater obtained by equation 6.35 was decreased to 80 % and then increased to 110 % of the original value. Figures 6.23, 6.24, 6.25 show a very small influence of the change of reflection coefficient on wave heights at the three measured positions as was expected. Indirectly, this proves that the error in reflection coefficient caused by error in incident wave height estimation will not influence the results in the bay.

---

<sup>25</sup> For band 9 self interaction, value of  $k_3/2k_1$  is 1.097; for interaction between band 10 and 12, value  $k_3/(k_1+k_2)$  is 1.1027 and similar for bands 10 and 11. The wave number mismatch is 9.7 % and 10 % respectively.

<sup>26</sup> Elgar *et al* (1997) stated that non-linear interaction between incident and reflected components are far from resonance, and thus do not contribute to non-linear energy exchange.

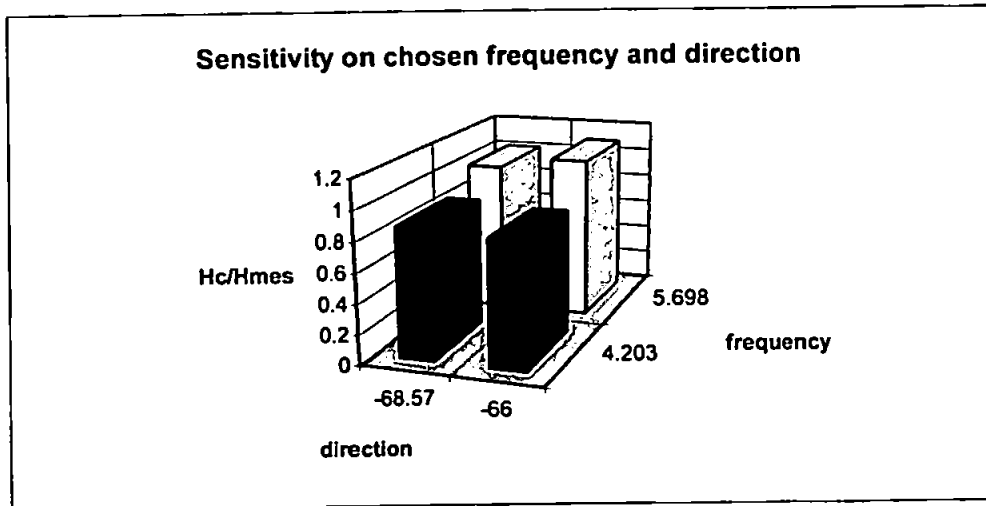
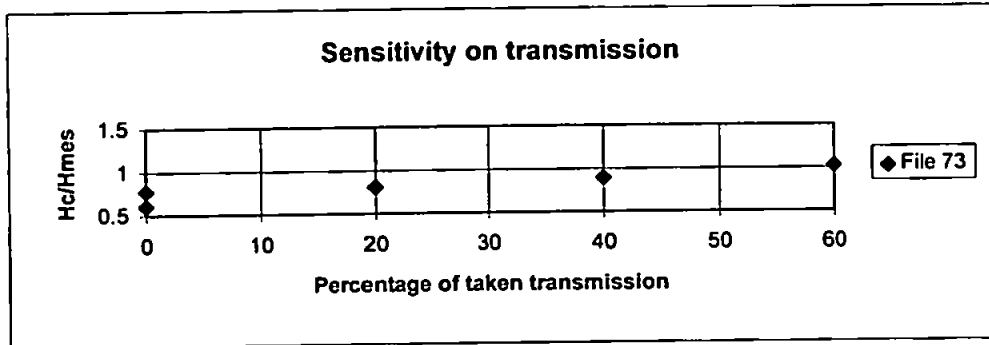
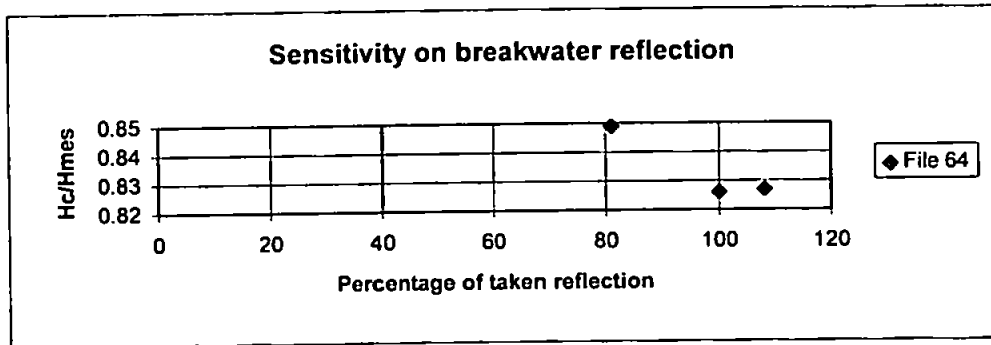
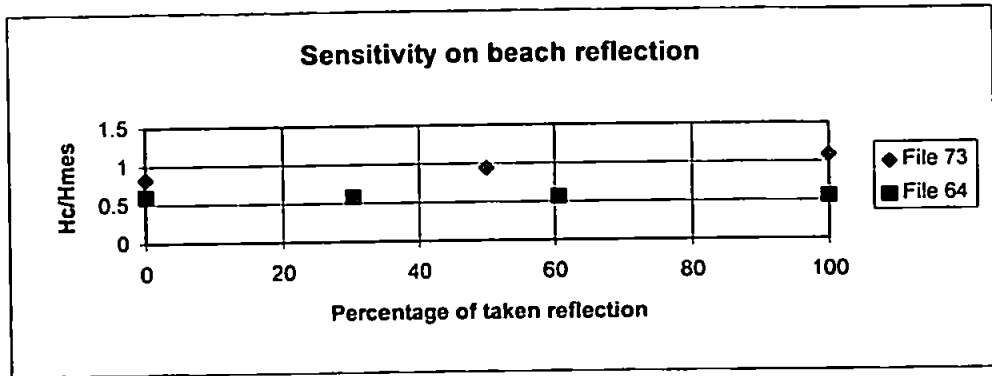


**Figure 6.23** The results of the sensitivity tests for the position in the lee of the breakwater: a) sensitivity on change of beach reflection; b) sensitivity on change of breakwater reflection; c) sensitivity on change of breakwater transmission; d) sensitivity on change of frequency and direction

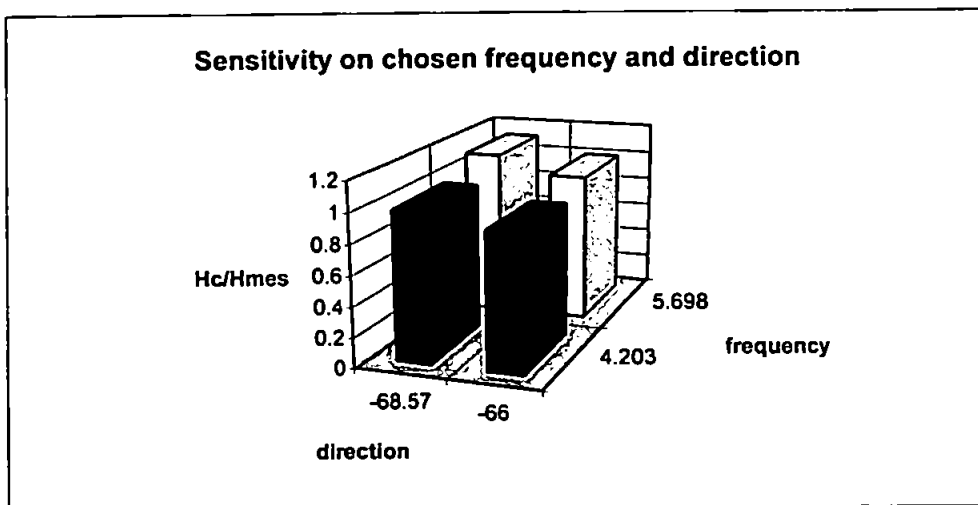
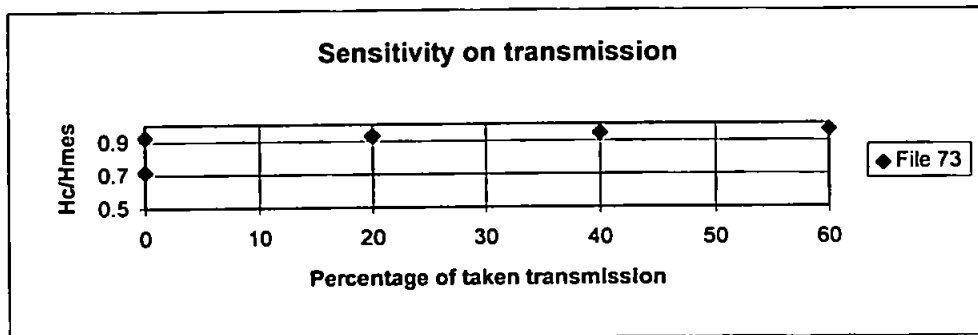
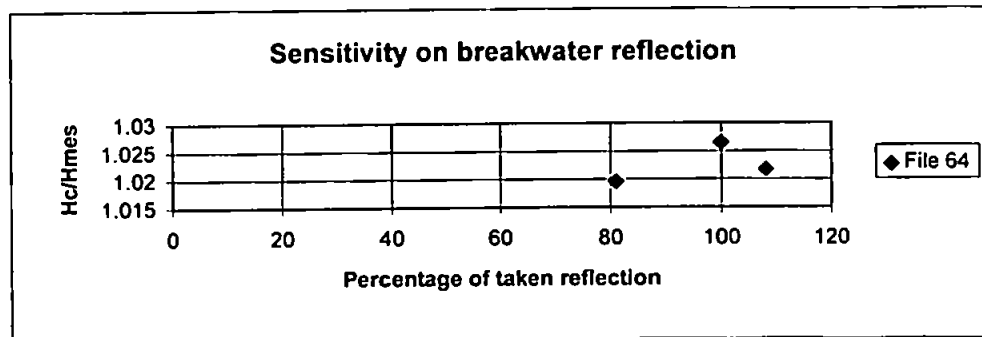
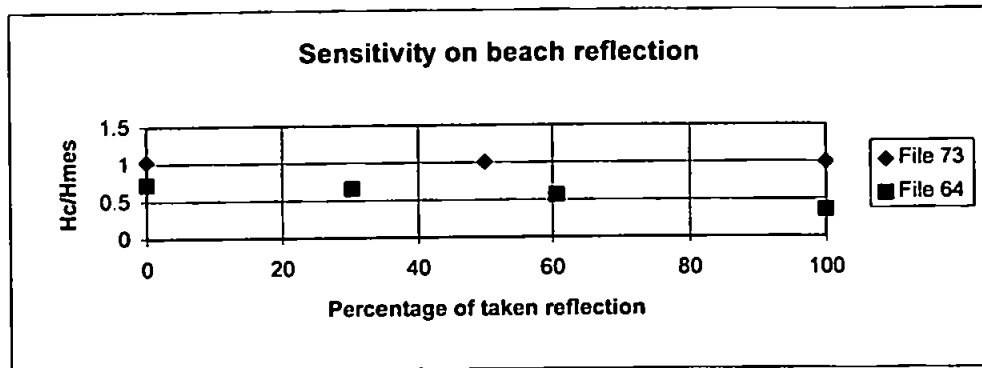


**Figure 6.24** The results of the sensitivity tests for the position shoreward of the gap: a) sensitivity on change of beach reflection; b) sensitivity on change of breakwater reflection; c) sensitivity on change of breakwater transmission; d) sensitivity on change of frequency and direction



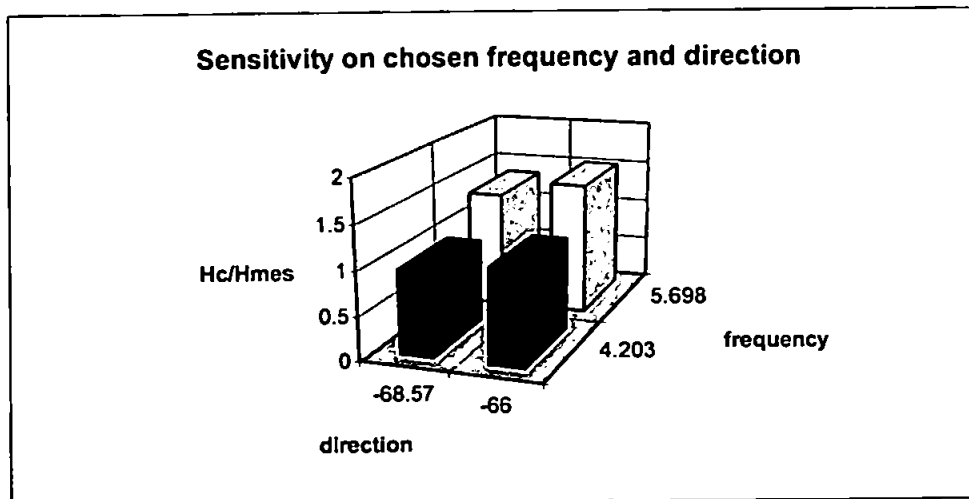
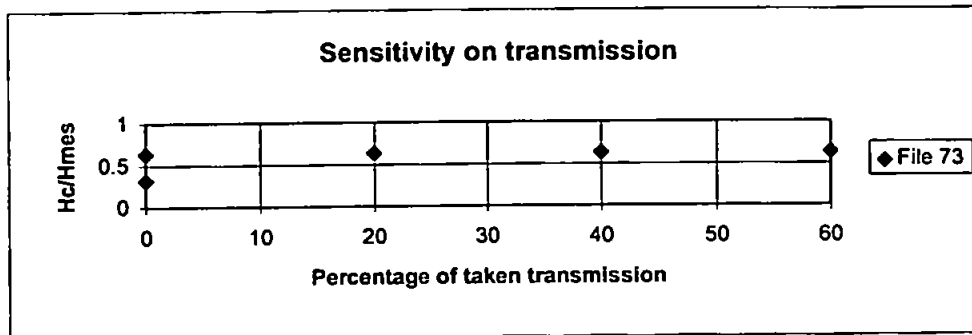
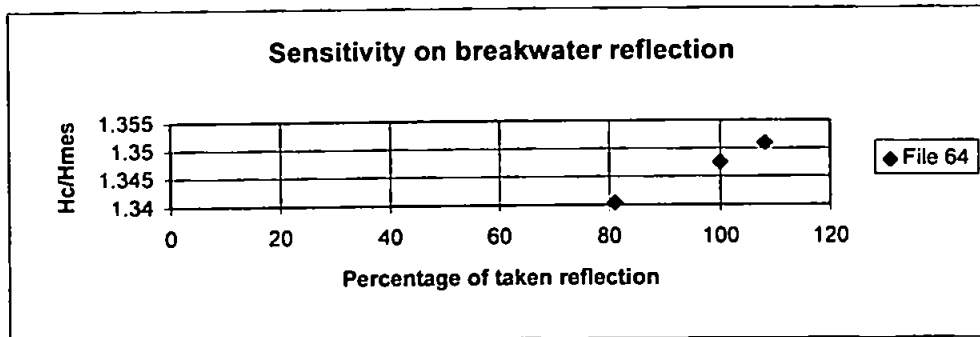
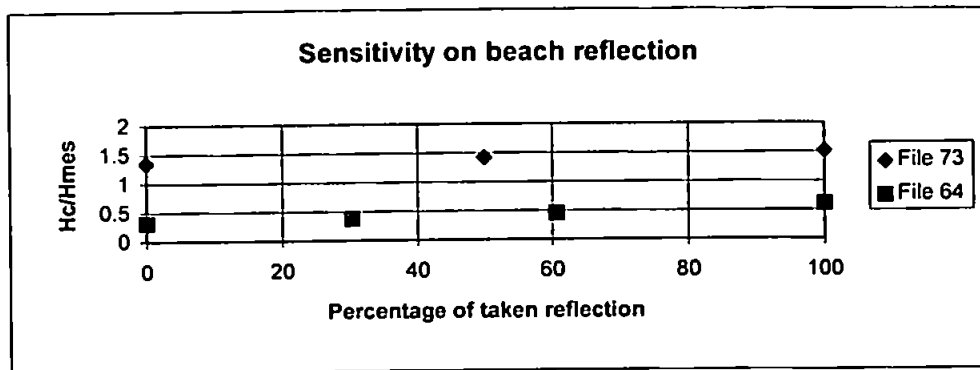


**Figure 6.25** The results of the sensitivity tests for the position in the gap between breakwaters: a) sensitivity on change of beach reflection; b) sensitivity on change of breakwater reflection; c) sensitivity on change of breakwater transmission; d) sensitivity on change of frequency and direction

The value of the beach reflection coefficient is more uncertain. The interference of incident and reflected waves causes partial standing wave patterns with observed swell heights modulated by as much as a factor of 2. Here the value of reflection coefficient at the shoreline boundary was changed from 0 – 100 % of the original value. The tests were performed for data sets 64 and 73. The predicted wave heights are more sensitive to a change of beach reflection. There is more sensitivity in the case of data set 73, which is to be expected because the values were higher. For data set 73, the predicted wave height was decreasing with increasing values of the reflection coefficient. Which might indicate that the measured positions are only in the area of the trough of the standing waves.

### **Transmission**

Transmissive boundaries are not included in the model. Dingemans (1997) suggested incorporating transmissive boundaries including not only a transmission coefficient value but also the phase shift. However, the phase information needs to be known. Simmonds *et al* (1997) presented the results of transmission field measurements. At the moment only the values of the transmission coefficients are available. These values vary from 0.2 to 0.6 for a particular wavelength, dependent on parameters such as wave height, water depth. Simmonds (personal communications) is still working on the parameterisation.

To test the influence of transmission on predicted wave heights, linear superposition was again used. Only the area behind the breakwater was modelled. The input wave height was 20 %, 40 %, 60 % of the offshore incident wave height. The bathymetry was rotated by 16 degrees so that breakwater boundaries were parallel with the grid. Thus, it was possible to use only transmissive wave heights as input. Transmission had only a very small influence on the predicted wave height shoreward of the gap. As expected, the influence is higher in the lee of the breakwater and, for  $T=0.6$ , the predicted and measured wave heights coincided with each other. The influence of transmission is clearly demonstrated in Figure 6.26. Even though this is not a proper way of including transmission in the model, the figure gives an indication of how important transmission is in predicting wave heights behind a porous breakwater.

### **Sensitivity on chosen representative frequencies and directions**

The directional sea can be represented as a regular wave taking either peak frequency and principal direction or main frequency and main direction into account. These tests have

been already performed as monochromatic cases 1 and 2. However, there may be an error in the calculation of those values which could influence the result. Therefore, the sensitivity tests were performed for file 64 with different combinations of the main and principal frequencies and directions. First, the directional waves were presented by the peak frequency and main direction and then by main frequency and principal direction. The results for two previous cases and two new additional tests are given in Figures 6.23, 6.24, 6.25. Different combinations of those input parameters can overpredict or underpredict, depending on the location and the wave conditions at the measured points (0.8 - 1.1 of measured value). It can be concluded that the parameters, frequency and direction, both individually and in combination, have an influence on the final results. A similar result was noticed when the test for file 73 was repeated on the rotated bathymetry for the transmission sensitivity. Figure 6.26a shows contours in the bay for the original layout and Figure 6.20b shows contours for the rotated bathymetry. The wave height predictions are closer to the measured ones in this case.

These performed tests demonstrate the sensitivity of the model to the input parameters. The MLM estimates for the numerical simulated data, in Chapter 5, differed only slightly from the target estimates in the case of direction and wave height (1% and 1.4%). The differences were larger for directional spreading and reflection (8.7 % and 9.3%). Thus the main influences on the results are directional spreading and directional distribution discretisation.

Sensitivity to the number of directional intervals used when directional modelling was applied for field data was not checked. However, the results show that when a larger number of directional intervals was used the wave height predictions were closer to the measured wave heights. Thus, directional modelling seems to work better for broad directional spectra when a larger number of directional increments is chosen. For a narrow directional spectrum, fewer bands, closer to each other, are chosen. Thus, radiation is included only where there is a small number of components. Consequently, the results are similar to cases where monochromatic waves are used.

When reflection is present, standing waves occur. Therefore, the measurement position may be on the crest or in the trough of the wave depending on the chosen frequency, with consequent differences in predicted estimates. The model results are sensitive to the values chosen for reflection from the beach. Thus, the accurate estimation of the reflection

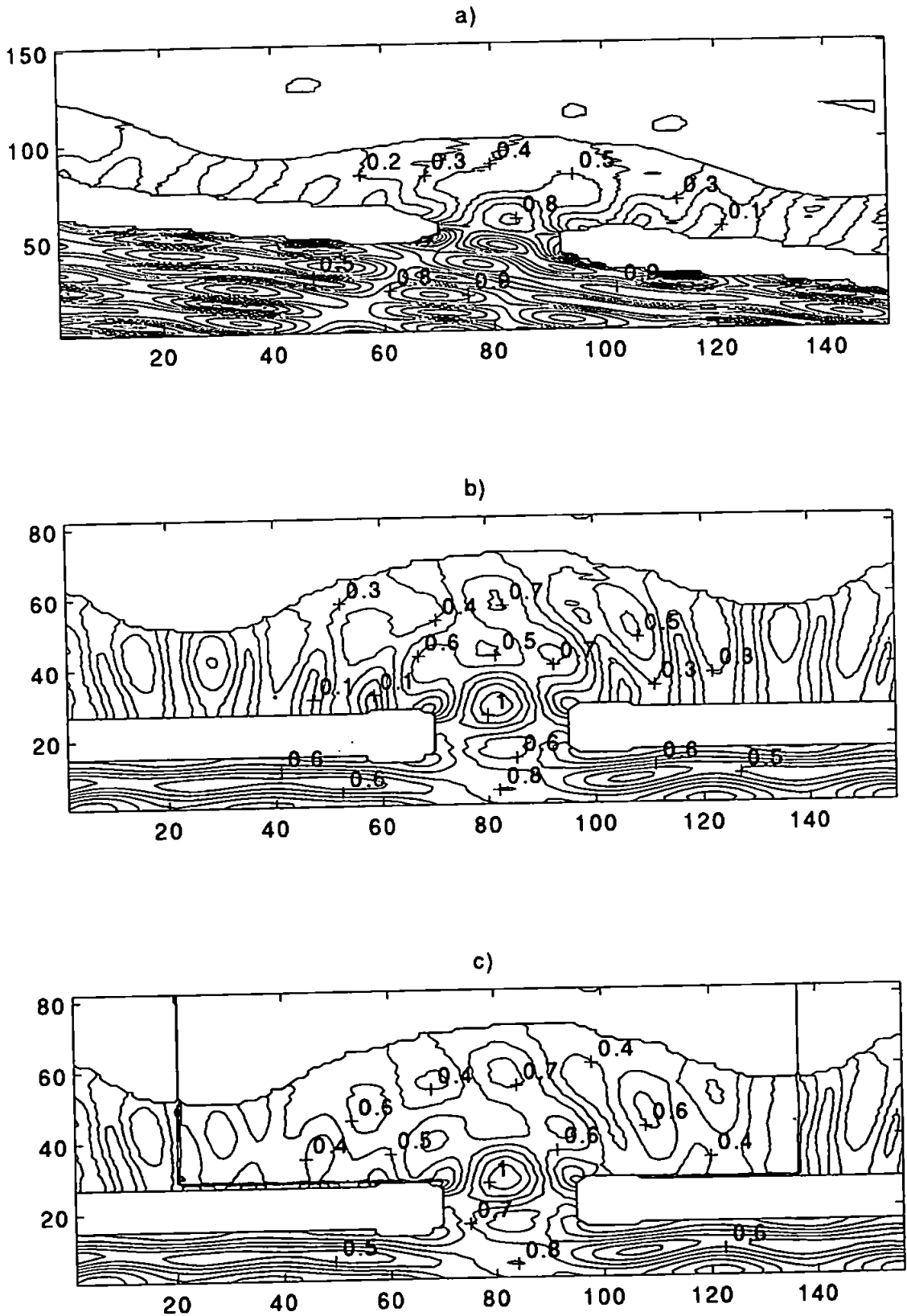


**Figure 6.26** The wave height contours in the bay for file 73: a) original bathymetry with no transmission and no beach reflection taken into account; b) rotated bathymetry with no transmission and no beach reflection taken into account; c) rotated bathymetry with added transmission effect and no beach reflection taken into account (grid points are given on axis, contours are at 0.1 m interval)

coefficient is necessary.

Additionally a few tests were performed with different input wave heights. The relationship between predicted and input wave heights was almost linear as it was expected.

The results will also depend on the chosen analysis technique for the measured data. It was shown in Chapter 5, that the results for directional estimates obtained by the two methods, MLM and BDM, can differ by up to 30% for the field wave height, which can cause larger differences in the numerical model results. This indicates that one needs to take special care when handling input data and interpreting the results. The results will also partly depend on an individual's choice of bathymetry orientation, discretisation technique etc. Thus further work on model optimisation is required.

## 6.5 Conclusions

The theoretical analysis showed that the model would become unstable with progressive decreasing of grid spacing towards the shore. The model is more accurate when  $\Delta x$ ,  $\Delta y$  and  $\Delta t$  are smaller. A 'rough guide' has been given in Figures 6.4, 6.5 and 6.6 for the choice of  $\Delta x$ ,  $\Delta t$  and the number of time steps required to bring the model to nearly steady state.

Li's model predicts the diffraction of directional wave spectra with 5 – 15% accuracy for a semi-infinite breakwater on a flat bed. The predictions were more accurate with broad frequency and directional spectra, for all measurement points except one (10), when directional modelling was applied (5%).

The results from validation using field data show that Li's linear model based on the Mild Slope Equation deals successfully with combined refraction, diffraction and reflection. However it is very important to take directional effects and model constraints into account. For example, when directional modelling was used for the laboratory case, the percentage error was reduced from 19-34% to 8-15%.

The results appear to be similar for monochromatic and directional modelling, in the case of field data when beach reflection was taken into account. Monochromatic wave runs introduce a significant error into wave heights predictions shoreward of the breakwaters in the diffraction region. Therefore it is important to consider random or multidirectional

waves. The percentage error for monochromatic modelling was 19-38% and 19-32% for directional modelling. In Plate 6.1 more spatial variations in wave heights can be observed than in the case with directional modelling. These results are supported by the fact that when beach reflection was not taken in account (Ilic and Chadwick, 1995) the error for the monochromatic modelling was 32-46% and for directional modelling was 8-12%. Therefore directional modelling is recommended.

Using random waves, it appears that directional spread has more influence than frequency spread in determining wave heights in the diffraction zone. This was clearly evident from tests performed with laboratory data. The errors when all frequencies and only one direction was taken into account were 23-34%. Sensitivity tests showed a large influence for transmission on wave heights behind the breakwater. When the transmissive wave height was increased, the predicted and measured wave height in the lee of the breakwater were the same. However, the model does not deal with transmission and this factor should be incorporated. Also, the importance of taking the proper reflection coefficient from the beach needs to be further investigated. Similarly, the influence of wave breaking, bed friction and wave current interactions merit further investigation (see e.g. Yoo *et al* (1984)).

Overall the model predictions are more accurate for the controlled environment of the laboratory than for field conditions where directional modelling accuracy varied from 8-32%. It should not be used for areas where non-linear interactions are present and dominate the other wave transformation processes, such as the surf zone. Where there is significant transmission, the model in this form can be used only for rough estimation of wave height. However, the model can be improved by implementing transmissive boundaries based on transmission measurements.

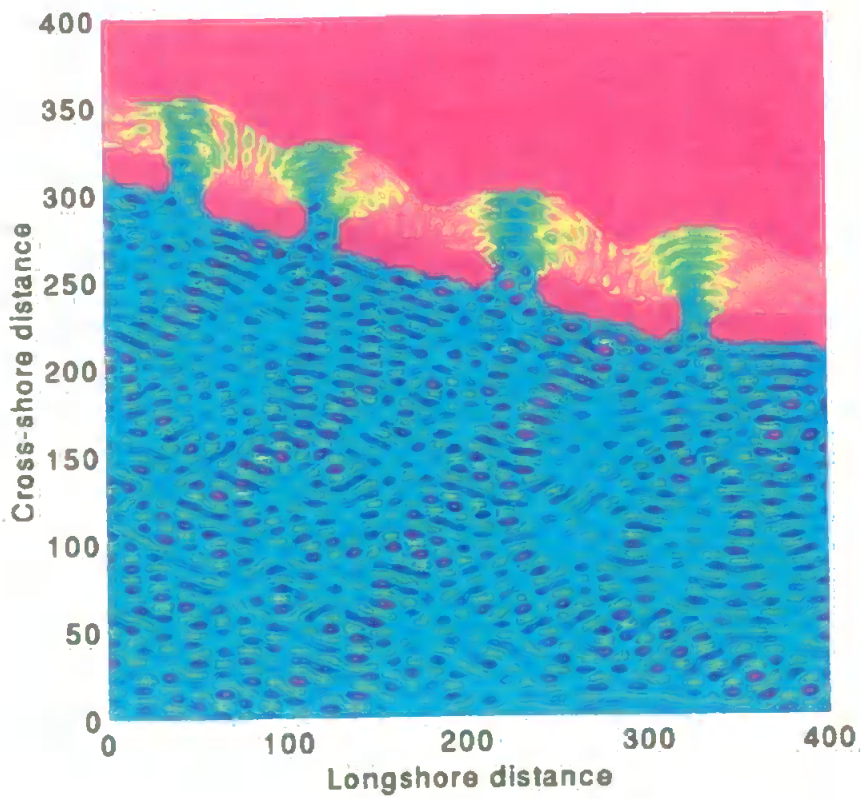
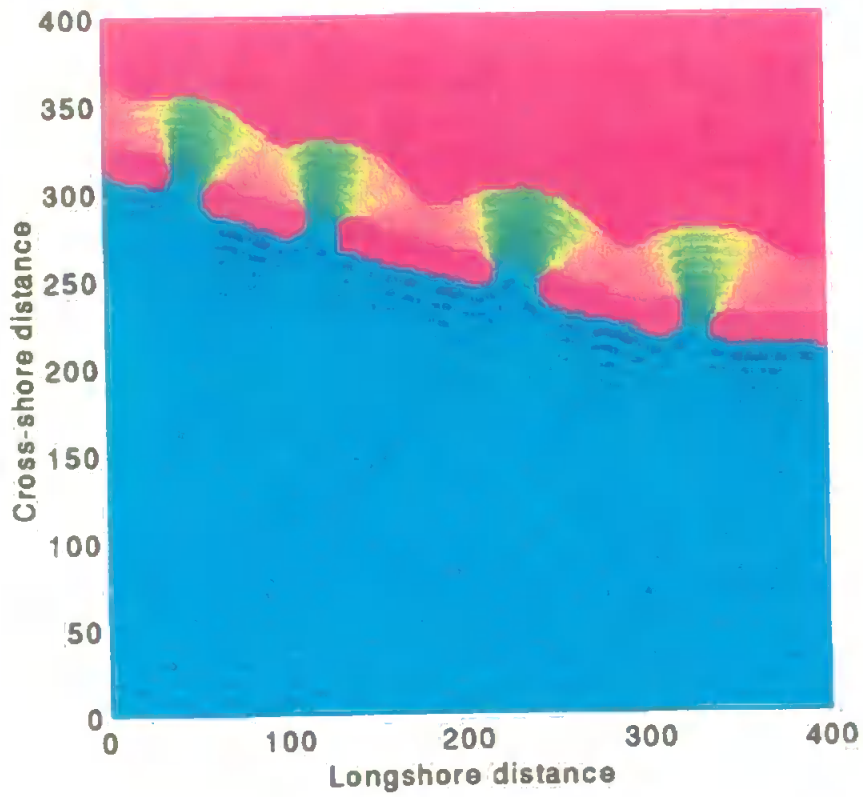


**Plate 6.1** Numerical model results for file 64; directional modelling results above, mono run results below

# Chapter 7

## Summary and Conclusions

*The important thing in science is not so much to obtain new facts as to discover new ways of thinking about them*

*Sir William Lawrence Bragg  
(1890 - 1971)*

### **Field data and spectral analysis**

The directional wave data records for model validation were chosen from 4500 wave records collected in the field campaign at Elmer from September 1993 – January 1995. The data were measured 500m offshore from the detached breakwater scheme and in the bay behind the breakwaters (see Figure 3.2). Together with data collected during the reflection measurements (500 measured records), in the front of the breakwater, they form a database. Special care was taken in the recording of data and analysis to reduce uncertainties of input errors affecting model prediction. The measurements of two different devices, pressure data from WRS and surface elevation from IWCM, were compared in a deployment at Felpham prior to the field campaign. There was no difference in the measurements recorded by the two devices. It was shown that a full comparison is only possible when the same spectral routines are applied to both data sets. These comparisons also showed that measurements of mean sea level were not accurate enough for examination of the spatial



variations in wave set-up.

### **Directional analysis**

It was shown in Chapter 5 that the model predictions depend on the direction and directional spread information. Thus, it is important to use a suitable directional analysis method which accurately predicts direction and directional spread. The applicability of a theoretical framework for phase-locked (PL) and non-phase-locked (NPL) directional analysis methods was first investigated. The MMLM (PL) method (Isobe and Kondo, 1984) used in the analysis of offshore data (far reflected field  $L/S > 0.5$ ) tends to produce spurious peaks. This was in agreement with the theoretical framework (Huntley and Davidson, 1998) based on the time of a wave travelling from the measurement point to the structure and back ( $L$ ) and the length of the FFT segment used for spectral analysis ( $S$ ). Huntley and Davidson (1998) state that the MMLM method is best suited, for a wider frequency range when  $L/S < 0.1$  and the NPL method (e.g. MLM (Capon, 1967)) is more appropriate when  $L/S > 0.5$ .

Therefore, two non-phase-locked methods the MLM and BDM (Hashimoto *et al*, 1988) were chosen to evaluate the accuracy of directional analysis estimates. Both methods were first tested on numerical data sets. The results were dependent on predetermined direction, directional spreading and reflection. The best agreement was achieved for the SW direction, spread  $s=10$  (wind waves), and a smaller amount of reflection. The directional sensitivity can be explained by the orientation of the array and the corresponding co-array. The smaller amount of reflection and larger directional spread which minimises phase interference works in favour of the NPL methods. A predetermined frequency spectrum or wave height did not have any influence on the predicted directional parameters. The accuracy of the BDM results increases with increasing number of transducers and increasing  $L/S$  (more smoothing). The MLM results did not show strong dependence on the number of transducers (5 or 6) and  $L/S$ . Thus  $L/S$  ratio  $> 0.5$ , which does not reduce the spectral frequency resolution can be recommended, for spectral analysis at other sites.

The differences between the BDM and MLM estimates for field data are larger than in the case of the simulated data described in the previous paragraph. One possible reason is that the reflection from the breakwaters for numerical data was simulated as being frequency independent. This is not the case for the field data where the reflection coefficient is

frequency dependent. The small differences could indicate that both methods produced good results, or conversely that both methods failed to produce the correct result. It was also found that both methods can estimate incident and reflected wave fields in the far field where incident and reflected wave are not dominantly phase locked, provided that a suitable choice of the L/S ratio is possible in practice. Directional spread will tend to decrease the phase locking and thus also improve BDM and MLM performance. However, neither method estimates accurately reflection coefficients at the measured position. The presence of currents can change the directional analysis results. However the currents at Elmer were relatively small  $< 0.7$  m/s and orthogonal to the main wave propagation direction. A sensitivity test in Chapter 5 showed that these conditions have only a small influence on the directional estimates.

From the numerical tests, the BDM appears to be more accurate. However, it was found in Chapter 5, that the BDM method was sensitive to the choice of the initial value of the hyperparameter  $u$  and results can vary depending on this parameter. The MLM estimates were very close to the BDM estimates for the numerical data. Also, the method is very easy to implement and the computation of results is faster than is the case for the BDM. Therefore the MLM estimates were chosen for the model validation. However, the MLM reflection coefficient estimates are not accurate and therefore the reflected boundary conditions were obtained from reflection measurements in front of the breakwater. Both methods tend to overpredict directional spread, therefore these inbuilt errors need to be taken into account when considering model results.

Special care needs to be taken in designing the array of measuring devices. The analysis showed that lower frequencies with wavelengths larger than the size of the array and higher frequencies with wavelengths which are small compared to the array spatial lags were not resolvable. An increased number of sensors and irregular spacing can improve directional resolutions. Additionally the new concept of optimum L/S ratio introduced by Huntley and Davidson (1998) can be used with simulated data, in the selection of the optimum directional method and in the design of array size and shape.

### **Validation of the MSE model from experimental data**

The model was first tested in Chapter 6 using laboratory measurements of random directional wave diffraction around a semi-infinite breakwater on a flat bed (Briggs *et al*,

1995). The differences between model results and measurements for five different directional spectra were in the range of 5 – 13 %. The smallest difference was obtained for broad frequency and directional spectra when directional modelling was applied. The largest differences were obtained when diffraction was computed using monochromatic waves as representative of directional random waves. This confirmed the need to use 'directional modelling' for the prediction of wave heights behind the breakwater.

#### **Validation of the MSE from field data**

The wave transformation model was applied to field conditions, and successfully dealt with combined refraction, diffraction and reflection. The representation of the measured random sea by monochromatic wave runs was found to introduce a significant error into wave heights predictions shoreward of the breakwaters in the diffraction region. Therefore it is important to consider directional modelling for irregular wave simulation. The directional spread has more influence than the frequency spread in determining wave heights in the diffraction zone when directional modelling is used.

The discrepancies between measurements and predictions arise due to constraints of the model, numerical errors and the accuracy of the measurement estimates. The largest difference (> 30%) between prediction and measurements was found for field data with non-linear couplings present. The model is linear and therefore its predictions are not accurate for the field where non-linear interactions are present. The influence of wave current interactions, wave breaking or bed friction is not included in the model. However the contribution of this influence to the accuracy of the results is not known at this stage. The model does not incorporate transmissive boundaries. Thus in the area of significant transmission (e.g. behind permeable breakwaters), the model results can be used only as a rough estimate. This can be improved by incorporating proper transmissive boundaries based on field measurements. The model predictions depend not only on the accuracy of the numerical model but also on the reliability of the input and boundary data. Thus the validation results are a function of the model's capabilities and the accuracy of the measured data.

#### **Analysis of the numerical solution**

Numerical accuracy depends on the chosen numerical method (scheme) for the computation of the governing equation and boundaries. The Alternative Direction Implicit

method was used in Li's model for the computation of the main equation. The scheme is unconditionally stable and is second order accurate. Thus, the model is more accurate when  $\Delta x$ ,  $\Delta y$  and  $\Delta t$  are smaller. Use of the flow adaptive scheme, in which the grid size reduces with as wave length decreases, would speed up the computation. However, from the theoretical analysis for the flow adaptive scheme, it has been shown that the model would become unstable with a grid spacing that progressively decreases towards the shore. It was found with the same analysis that the number of grid points in the lateral direction can be smaller than in the main direction which can reduce the computation time for a plane beach. Computation can also be performed by dividing the computational area into subareas with larger (offshore) and smaller (shoreward) grid spacing. In this case the results from the computation on the larger grid offshore become input for the computations on the more refined grid near the shore. The model wave height results were found to oscillate around the mean wave height. The oscillations are most likely caused by inappropriate treatment of the boundaries (physically or numerically) and initial conditions (propagation of steep front). This needs to be investigated further. However, the oscillations can be minimised with a properly chosen  $\Delta x$ ,  $\Delta y$  and  $\Delta t$  and computation time. A way of selecting the required number of time steps to bring the model near steady state with minimum magnitude of oscillation magnitude, is given in Chapter 6.

## **Conclusions**

A large number of wave records have been collected and analysed. They can be used for wave propagation numerical model validation. The collected data cover seasonal changes and therefore together with aerial survey data, they can also be used for the validation of morphological model. With additional measurements of transmission and currents, they form a basis for understanding the complex processes around detached breakwaters.

Both directional analysis methods, BDM and MLM, when tested on simulated data, with narrow and broad directional spread, gave the most accurate results for the data with broad directional spread. At the same time, the wave propagation results were most accurate for wave conditions with broad directional spread in the case of pure diffraction and also in the case of field data. Thus, for most sea conditions in English Channel which are generated by local wind and therefore have broad directional spread, the model will give accurate predictions of wave height on the shore. However, the model requires accurate input parameters. Even though the differences between the model results and measurements

appear to be similar for monochromatic and directional modelling in the field measurement points, directional modelling is recommended. This fact is supported by the results from the validation of the model from laboratory data in Chapter 6.

	<i>Input Error</i>	<i>Output Error</i>		
		Position 1	Position 2	Position 3
Incident Wave Height	2-16%	2-16%	2-16%	2-16%
Reflection from Breakwater	10 - 20%	1 - 2%	~1%	~1%
Reflection from Beach	30%*	2-11%	2-7%	5-7%
Transmission	40%**	12%	1%	-
Direction of propagation	1%	Different Direction		
		3%	8%	11%
Directional Spread	9%	Narrow directional spreading 8% ***		
		Broad directional spreading 5% ***		
Different frequency		7-12%	9-10%	30-45%
Numerical solution		3-5% or for quicker solution 9-11%		

**Table 7.1** The accuracy of the model for the given initial conditions accuracy for three positions; Position 1 - in the lee of the breakwater, Position 2 - shoreward of the gap, Position 3 - in the gap between breakwaters<sup>1</sup>

The accuracy of the model predictions depend on the accuracy of input and boundary data, accuracy of the numerical solution and limitations of the model describing physical processes. On the basis of data analysis, numerical accuracy of the model, testing of the

<sup>1</sup> \*difference between no reflection and reflection taken in account; \*\* difference between no transmission and transmission taken in account; \*\*\* values are taken from validation with laboratory data

model with field and laboratory data and sensitivity tests, the overall accuracy of the model is summarised in Table 7.1. This is valid only if there are no interactions between variables which is usually not the case. Therefore, one needs to take care interpreting these results.

### **Future work**

With the fast development of computing technology, directional modelling started to replace more and more the traditional monochromatic modelling of random seas. So far, the directional modelling results are indicating that it is more important take in account a larger number of directional components than frequency components to represent the measured directional spectra. It would be useful to find the optimum number of directional increments for directional modelling related to the directional spread, providing accurate results without increasing computational time. The MSE model should be extended to incorporate wave current interactions, bed friction and wave breaking. With further development of computing memory and power, it will be possible to perform directional modelling parallelly for each component which will enable incorporation of wave breaking criteria. It is advisable to investigate the implementation of transmissive boundaries and the influence of transmission on the sea state behind the breakwaters, since the tests in Chapter 6 showed the sensitivity of results to the amount of transmission.

However, the validation of the model is not complete unless the wave-induced currents calculated on the basis of the wave transformation model results are validated. This will enable the evaluation of the model for further applications as a module of morphological models. The advantages of Li's model are that it is easy to implement and can be applied for large areas. The disadvantages are that the model is linear and does not take wave interactions in account. Thus, the model results need to be compared with nearly non-linear or non-linear model results to be able to determine the domain of its application for the hydrodynamics and morphological predictions.

The real field conditions are very complex and therefore provide a difficult test for the validation of the numerical model. However, field measurements also suffer from the errors introduced by the measurement equipment or by the data analysis methods. Thus there is still room for improvement in the collection and analysis of field data.

The Plymouth University measurement systems, IWCM and WRS, should be further improved in the future. Both systems need to operate as a single system enabling

synchronised measurements. The array shape and spacing needs to be designed for every site on the basis of the local wave conditions. Simpler methods of deployment should be investigated as these would probably lead to reduced error. The WRS measurement cycle needs to be extended to at least 17 min and the sampling frequency needs to be increased to 4 Hz. It is desirable to use a telemetric system to download the offshore WRS data. Improvements to the directional analysis techniques and their applications for beach reflection prediction should be emphasised in the future.

The sea state around offshore breakwaters is very complex and it is still not possible to include all wave transformations and hydrodynamics in a single wave numerical model. A composite modelling approach integrates the benefits of numerical, physical models and field measurements. Such an approach is currently used for the Elmer breakwater scheme and should provide better understanding of the physical processes. Furthermore, physical laboratory measurements will be used for the numerical model validation and development.

## References

- Abbott, M.B. (1991a). *Hydroinformatics: Informational Technology and the Aquatic Environment*, Ashgate, Aldershot, and Brookfield, USA.
- Abbott, M. B. (1991b). *Numerical Modelling for Coastal and Ocean Engineering*, The handbook of ocean and coastal engineering (Herbich J B ed.), Gulf, Huston.
- Abbott, M.B. and Basco, D.R. (1989). *Computational Fluid Dynamics: An Introduction for Engineers*, Longman, London
- Abbott, M.B. and de Leeuw, E.H. (1966). On the Use of Optimum Time Intervals in Soil Mechanics Problems. *LGM Mededelingen*, Delft, pp 71-83.
- Akaike, H. (1973). Information Theory and an Extension of the Maximum Likelihood Principle, *2<sup>nd</sup> Int. Symp. on Information Thoery*. Petrov and Csaki Eds. Akademiai Kiado, Budapest, pp 267-281.
- Al-Mashouk, M., Reeve, D.E., Li, B. and Fleming, C.A. (1992). ARMADA: An Efficient Spectral Wave Model, *Proc.2<sup>nd</sup> Int. Conf. on Hydraulic and Environmental Modelling of Coastal, Estaurine and River Waters*, (edited by Falconer, R.A., Chandler-Wilde, S.N., Liu, S.Q.), Vol 1, pp 433-445
- Austin, D. J. and Bettes, P. (1982). Longshore Boundary Conditions for Numerical Wave Models, *Int. Jnl. for Num. Methods in Fluids*, Vol 2, pp 263-276.
- Axe, P.G. (1999). Beach Development behind Detached Breakwaters, Phd Thesis, University of Plymouth, submitted
- Axe, P.G., Ilic, S., Chadwick, A.J. (1996). Evaluation of Beach Modelling Techniques Behind Detached Breakwaters, *Proc. of 25th Inter. Conf. on Coastal Engineering*, Orlando 1996, USA, ASCE, pp 2036-2047
- Axe, P. (1994). Elmer Frontage Beach Development - a preliminary report, *Internal Report No SCSE 94-003*, University of Plymouth
- Axe, P.G. and Bird, P.A.D. (1994). Studies at Felpham Beach (West Sussex)- 11<sup>th</sup> February – 24<sup>th</sup> June, 1993, Report to Arund District Council, Report No 94001/C
- Barber, P.C and Davis, C.D. (1985). Offshore Breakwaters – Leasowe Bay, *Proc Instn Civ Engrs*, pt 1, v 78, pp 85-109



- Barnard, T.E. (1969). Analytical studies of techniques for the computation of high-resolution wave number spectra, *Texas Instr. Advanced Array Research Spec. Rep.* No 9
- Behrendt, L. and Jonsson, I. G. (1984). The Physical Basis of the Mild-Slope Wave Equation, *Proceedings 19<sup>th</sup> Coastal Eng. Conf.*, Houston, pp 941-954.
- Benoit, M., Frigaard, P. and Schaffer, H.A. (1997). Analysing Multidirectional Wave Spectra: A Tentative Classification of Available Methods, *IAHR Seminar Multidirectional Waves and Their Interaction with Structures, 27<sup>th</sup> IAHR Congress*, San Francisco, pp 131-158
- Benoit, M. (1993). Extensive Comparison of Directional Wave Analysis Methods from Gauge Array Data, *Proc., 2<sup>nd</sup> Int. Symp. On Wave Measurement and Analysis, Wave '93*, New Orleans, pp 740-754.
- Benoit, M. and Teisson, C. (1994). Laboratory Comparison of Directional Wave Measurement Systems and Analysis Techniques, *Proc. 24<sup>th</sup> Conf. On Coastal Eng.*, Kobe, ASCE, New York, pp 42-56.
- Berkhoff, J. C. W. (1976). Mathematical Models for Simple Harmonic Linear Water Wave Models, Wave Refraction and Diffraction, Phd Thesis, Techn. Univ. of Delft, pp 110
- Berkhoff, J. C. W. (1972). Computation of Combined Refraction-Diffraction, *Proc. 13<sup>th</sup> Coastal Eng. Conf.*, Vancouver, ASCE, Vol.1, pp 471-490.
- Berkhoff, J.C.W., Booij, N. and Radder A.C. (1982). Verification of Numerical Wave Propagation Models for Simple Harmonic Linear Water Waves, *Coastal Engineering*, 6, pp 255-279
- Bettes, P. and Zienkiewicz, O. C. (1977). Diffraction and Refraction of Surface Waves Using Finite and Infinite elements, *Int. J. Num. Meth. Eng.*, II, pp 1271-1290.
- Bird., P.A.D., Davidson, M.A., Bullock, G.N. and Huntley, D.A. (1994). Wave measurements near reflective structures, *Proc. Coast. Dynamics '94*, ASCE, New York, pp 701-711.
- Bird, P. A. D. (1993). Measurements and analysis of sea waves near a reflective structure. Ph.D thesis, University of Plymouth
- Booij, N. (1981). Gravity Waves on Water with Non-uniform Depth and Current, *Report No. 81-1*, Delft University of Technology, Dept. Civil. Eng.
- Borges, J.C.V. (1993). Wave climate & shingle beach response, Ph.D thesis, University of Brighton.

- Borgman, L. E. (1969). Ocean Wave Simulation for Engineering Design, *J. of Waterways, Harbours and Coastal Eng.*, ASCE, Vol 95, No WW4, pp 557-583.
- Borgman, L.E. (1990). Irregular Ocean Waves: Kinematics and Forces, In Ocean Engineering Science The Sea, Vol 9, Part A (Edited by LeMehaute, B., Hanes, D.M.), John Wiley and Sons, New York, 1-1301.
- Bos, K.J., Roelvink, J.A. and Dingemans, M.W. (1997). Modelling the Impact of Detached Breakwaters on the Coast, *Proc. 25<sup>th</sup> Conf. Coastal Eng.*, Orlando, pp 2022-2035.
- Bouws, E., Gunther, H., Rosenthal, W., and Vincent, C. (1985). Similarity of the Wind Wave Spectrum in Finite Depth Water, *J. Geophys. Research*, 90 (C1), pp
- Brandt, A. (1977). Multi-Level Adaptive Solutions to Boundary-Value Problems, *Mathematics of Computation*, Vol 31, No 138, pp 333-390.
- Briggs, M.J., Thompson, E.F. and Vincent, C.L.(1995). Wave Diffraction Around Breakwater, *J. Wtrway.Port.Coast. and Oc. Engrg.*, ASCE, 121(1), pp 23-35.
- Brown, R.M. (1994). Report on Developments to the Inshore Wave Climate Monitor, *Internal Report*, Dept. of Civil Engineering, University of Brighton
- Capon, J., Greenfield, R.J. and Kilmer, R.J. (1967). Multidimensional maximum likelihood processing of a large aperture seismic array, *Proc IEEE*, Vol 55, 129 - 211.
- CERC Technical Report, Engineering Design Guidance for Detached Breakwaters as shoreline stabilisation structures
- Chadwick, A.J., Bird, P.A.D., Ilic, S. and Axe, P.G. (1997). The Elmer Breakwater Study-Final Report for SCOPAC
- Chadwick, A. J., Pope, D. J., Borges, J. and Ilic, S. (1995a). Shoreline Directional Wave Spectra, Pt1: An Investigation of Spectra and Directional Analysis Techniques, *Proc Instn Civ Engrs (Water Maritime and Energy)*, vol 112, issue 3, 198-209.
- Chadwick, A.J., Pope, D.J., Borges, J., Ilic, S. (1995b). Shoreline Directional Wave Spectra. Part 2. Instrumentation and Field Measurements, *Proc Instn Civ Engrs, Water Maritime and Energy*, Vol 112, Issue 3
- Chawla, A., Ozkan-Haller, H.T. and Kirby, J.T. (1998). Spectral Model for Wave Transformation and Breaking over Irregular Bathymetry, *J. Wtrway.Port.Coast. and Oc. Engrg.*, ASCE, Vol 124, No 4, pp 189-198.
- Christensen, M., (1996). Generation and Active Absorption of 2- and 3-Dimensional Linear Water Waves in Physical Models, Ph.D. Thesis, Aalborg University, Denmark

- Copeland, G. J. M. (1985a). A Numerical Model for the Propagation of Short Gravity Waves and the Resulting Circulation Around Nearshore Structures, Ph.D Thesis, University of Liverpool.
- Copeland, G. J. M. (1985b). A Practical Alternative to the "Mild-Slope" Wave Equation, *Coastal Eng.*, 9, pp 125-149.
- Dally, W. R. and Pope, J. (1986). Detached Breakwaters for Shore Protection, *Technical Report CERC-86-1*, US Army Engr. Waterways Experiment Station, Coastal Engrg. Res. Ctr., Vicksburg, Miss.
- Dalrymple, R. A., Kyung, D. S., Kirby, J. T. and Jang, W. C. (1989). Models for Very Wide-Angle Water Waves Diffraction, Part 2, Irregular Bathymetry, *J. Fluid Mech.*, Vol 201, pp 299-322.
- Dalrymple, R. A. and Kirby, J. T. (1988). Models for Very Wide-Angle Water Waves and Wave Diffraction, *J. Fluid Mech.*, Vol 192, pp 33-50.
- Dalrymple, R.A., Kirby, J.T. and Seli, D.J. (1986). Wave Trapping by Breakwaters, *Proc. 20<sup>th</sup> Conf. Coastal Eng.*, pp 1820-1830.
- Dalrymple, R. A., Kirby, J. T. and Hwang, P. A. (1984). Wave Diffraction Due to Areas of Energy Dissipation, *ASCE, Port and Harbours*, Feb/Mar, pp 66-79.
- Darras, M. (1987). IAHR List of Sea State Parameters: A Presentation, *Proc IAHR, Wave analysis and generation in laboratory basins, XXII Congress*, Lausanne, Switzerland, pp
- Davidson, M.A., Huntley, D.A. and Bird, P.A.D. (1998). A Practical Method for the Estimation of Directional Wave Spectra in Reflective Wave Fields, *Coastal Engineering*, Vol 3, No 2-3, pp 91-117.
- Davidson, M.A., Bird, P.A.D., Bullock, G.N., Huntley, D.A. (1996). A New Dimensional Number for the Analysis of Wave Reflection from Rubble Mound Breakwaters, *Coastal Engineering* 29, pp 93-120.
- Davidson, M.A. (1993). Optimal Spectral Analysis Procedures for Wave Records, *Research Report No. SCSE 93-002*, School of Civil and Structural Engineering, University of Plymouth, UK
- Davidson, M.A. (1992). Implementation of Linear Wave Theory in the Frequency Domain for the Conversion of Sea Bed Pressure to Surface Elevation, *Research Report No. SCSE 92-008*, School of Civil and Structural Engineering, University of Plymouth, Plymouth, UK
- Davies, R. E. and Regier, L. A. (1977). Methods for estimation of directional wave spectra

- from multi-element arrays, *J. Mar. Res.* Vol 35, pp 453-477
- Dingemans, M. W. (1997). Water Wave Propagation over Uneven Bottoms, Part 1 - Linear Wave Propagation, Advanced Series on Ocean Engineering, Vol 13, Ed Liu P L F, World Scientific, London
- Dingemans, M. W. (1985). Surface Wave Propagation over an Uneven Bottom; Evaluation of Two-Dimensional Horizontal Wave Propagation Models, *Report W 301*, Delft Hydraulics, part 5, 117 pp.
- Dingemans, M. W., Stive, M. J. F., Kuik, A. J., Radder, A. C. and Booij, N. (1984). Field and Laboratory Verification of the Wave Propagation Model CREDIZ, *Proc. 19th Int. Conf. on Coastal Engr., Houston*, pp. 1178-1191
- Dodd, N. (1988). Parabolic Approximations in Water Wave Refraction and Diffraction, Ph.D. Thesis, University of Bristol, School of Mathematics
- Dodd, N. and Brampton, A. H. (1995). Wave Transformation Models: A Project Definition Study, *Report SR 400*, HR Wallingford
- Doering, J.C. (1988). Wave-Wave Interaction in the Nearshore, Phd Thesis, Dalhousie University
- Dong, P. and Al-Mashouk, M. (1989). Comparison of Transient and Steady State Wave Models for Harbour Resonance, *Proc. Int. Conf. on Hydraulic and Environmental Modelling of Coastal, Estuarine and River Waters*, (edited by Falconer, R.A., Goodwin, P., Matthew, R.G.S.), Vol 1, pp 233-244.
- Doss, S. and Miller, K. (1979). Dynamic ADI Methods for Elliptic Equations. *J. Num. Analysis* SIAM 16, pp 836-837
- Ebersole, B. A. (1985). Refraction-Diffraction Model for Linear Water Waves, *J. Waterway Port Coastal Ocean Eng.*, ASCE, 111, pp 939-953.
- Eckart, C. (1952). The propagation of gravity waves from deep to shallow water, *National Bureau of standards, Circular 20*, pp 165 - 173
- Elgar, S., Guza, R.T., Raubenheimer B., Herbers, T.H.C. and Gallagher, E. (1997). Spectral evolution of shoaling and breaking waves on a barred beach, *Journal of Geophysical Research*, 102, C7, pp 15797-15805.
- Elgar, S., Guza, R.T. and Freilich, M.H. (1993). Observations of Non-linear Interactions in Directionally Spread Shoaling Surface Gravity Waves, *J. Geophysical Research*, 98/C11, pp 20299-20305.
- Elgar, S. and Guza, R.T. (1985). Observations of bispectra of shoaling surface gravity waves, *J. Fluid Mech.*, 161, pp 425-448.

- Freilich, M.H., Guza, R.T. and Elgar, S. (1990). Observation of Nonlinear Effects in Directional Spectra of Shoaling Gravity Waves, *J. Geophysical Research*, 95/C6, pp 9645-9656.
- Frigaard, P., Helm-Petersen, J., Klopman, G., Stansberg, C.T., Benoit, M., Briggs, M.J., Miles, M., Santas, J., Schaffer, H.A. and Hawkes, P.J. (1997). IAHR List of Sea State Parameters – An Update for Multidirectional Waves, *IAHR Seminar Multidirectional Waves and their Interaction with Structures, 27<sup>th</sup> IAHR Congress*, San Francisco, pp 15-24.
- Galofre, J. and Montoya, F.J. (1999). Coastal Structures Applied to Shoreline Stabilisation: Taragona Zone Case Study, *Conference Proceedings Coastal Structures '99*, to appear
- Girolamo, de P. (1995). Computation of Sea-Wave Direction of Propagation of Random Waves, *J. Waterway, Port, Coast. and Oc. Engrg.*, ASCE, Vol 121, No 4, pp 203-209
- Goda, Y. (1998). An Overview of Coastal Engineering with Emphasis on Random Wave Approach, *Coastal Engineering Journal*, Vol. 40, No 1, pp 1-21
- Goda, Y. (1985). Random Seas and Design of Maritime Structures, University of Tokyo Press, Tokyo, Japan
- Goda, Y., Takayama, T., and Suzuki, Y. (1978). Diffraction Diagrams for Directional Random Waves, *Proc. 16<sup>th</sup> Int. Conf. On Coastal Engrg.*, Hamburg, ASCE, pp 628-650.
- Goda, Y. and Suzuki, Y. (1976). Estimation of Incident and Reflected Waves in Random Wave Experiments, *Proc. 15th Conf. on Coastal Eng.*, ASCE, New York, pp 828 – 865.
- Gourlay, M.R. (1974). Wave Set-Up and Wave Generated Currents in the Lee of a Breakwater or Headland, *Proc. 14<sup>th</sup> Conf. on Coastal Eng.*, ASCE, pp 1976-1995.
- Grassa, J.M. (1990). Directional Random Waves Propagation on Beaches, *Proc. 22<sup>nd</sup> Conf. on Coastal Eng.*, Delft, pp 798-811.
- Guza, R.T. and Thornton, E.B. (1980). Local and shoaled comparisons of sea surface elevations, pressures and velocities, *Journal of Geophysical Research*, Vol. 85, No. 3, 1524-1530.
- Hanson, H. and Kraus, N. C. (1991). Numerical Simulation of Shoreline Change at Lorain, Ohio, *Journal of Waterw., Port, Coast. and Ocean Eng.*, Vol 117, No 1, pp 1-17
- Hanson, H. and Kraus, N.C. (1990). Shoreline Response to a Single Transmissive Detached Breakwater, *Proc. 22<sup>nd</sup> Conf. Coastal Eng.*, Delft, pp 2034-2046.

- Hanson, H. (1989). GENESIS – A generalised shoreline change numerical model, *J. Coast. Res.*, 5(1), pp 1-27.
- Hanson, H., Kraus, N. C. and Nakashima, L. D. (1989). Shoreline Change behind Transmissive Detached Breakwaters, *Costal Zone '89*, ASCE, pp 568-583.
- Harris, F.J. (1988). On the Use of Windows for Harmonic Analysis with the Discrete Fourier Transform, *Proceedings of the IEEE*, Vol. 66, No. 1, pp 51-83
- Hashimoto, N., Nagai, T., Asai, T. (1994). Extension of Maximum Entropy Principle Method for Directional Wave Spectrum Estimation, *Proc. 24<sup>th</sup> Int. Conf. on Coastal Eng.*, Kobe, ASCE, pp 232-246.
- Hashimoto, N. and Kobune, K. (1988). Directional Spectrum Estimation from a Bayesian Approach, *Proc. 21<sup>st</sup> Conf. Coastal Eng.*, Malaga, pp 62-76.
- Hashimoto, N. and Kobune, K. (1987). Estimation of Directional Spectrum from a Bayesian Approach in Incident and Reflected Wave Field, *Rep. Of Port and Harbour Research Inst.*, Vol 26., No 4, pp 3-33
- Hashimoto, N., Kobune, K. and Kameyama, Y. (1987). Estimation of Directional Spectrum Using the Bayesian Approach and its Application to Field Data Analysis, *Rep. Of Port and Harbour Research Inst.*, Vol 26.
- Hasselmann, K., Munk W. and MacDonald, G. (1963). Bispectra of Ocean Waves. In Time series analysis (edited by M. Rosenblatt), Wiley, New York, pp 125-139.
- Hedges, T.S., Tickell, R.G. and Akrigg, J. (1993). Interaction of Short-Crested Random Waves and Large-Scale Currents, *Coastal Engineering*, 19, pp 207-221.
- Hedges, T.S. and Lee, B.W. (1992). The Equivalent Uniform Current in Wave-Current Computations, *Coastal Engineering*, 16, pp 301-311
- Hedges, T.S. (1987). Combinations of Waves and Currents: and Introduction, *Proc. Instn. Civ. Engrs.*, Part 1, 1987, 82, pp 567-585.
- Hedges, T. S. (1976). An Empirical Modification to Linear Wave Theory, *Proc. Instn. Civil Engineers*, Part 2, Vol 61, pp 575-579.
- Helm-Petersen, J. and Brorsen, M. (1997). Wave Disturbance in Harbours – the Importance of a Correct Modelling of Wave Reflection, *Proc. IAHR Seminar on Multidirectional Waves and their Interaction with Structures*, 27<sup>th</sup> IAHR Congress, San Francisco, pp 385-398
- Helm-Petersen, J., (1995). Performance Analysis of the BDM Method Applied to Reflected Shortcrested Waves, *Internal Note*, Hydraulics and Coastal Engineering Laboratory, Aalborg University

- Helm-Petersen, J. (1994). The BDM Method, *Internal Note*, Hydraulics and Coastal Engineering Laboratory, Aalborg University
- Holland, B. and Coughlan, P. (1993). The Elmer Coastal Defence Scheme, *Proceedings of MAFF Conference on River and Coastal Engineering*, Keele, UK, pp
- Houston, J. R. (1981). Combined Refraction and Diffraction of Short Waves Using Finite Element Method, *Applied Ocean Res.*, Vol 3, No 4, pp 163-170.
- HR Wallingford (1994). Wave Conditions Along the Arun Coastline: A Guide for Contractors, Prepared by HR Wallingford for Arun District Council, *Report EX 3026*, HR Wallingford
- HR Wallingford (1992). Elmer 3D Physical Model Study, *Report No EX 2529*, HR Wallingford
- HR Wallingford (1986). Wave Recording at Littlehampton 1985-1986, *Report No EX 1462*, HR Wallingford
- Huntley, D.A. and Davidson, M.A. (1998). Estimation of Directional Waves near a Reflector, *J. Wtrway.Port.Coast. and Oc. Engrg.*, ASCE, Vol 124, No 6, pp 1- 8
- Huntley, D.A., Simmonds, D.J. and Davidson, M.A. (1995). Estimation of Frequency Dependent Reflection Coefficients Using Current and Elevation Sensors, *Proceedings Coastal Dynamcis 95*, Gdansk, ASCE, pp 57-68.
- Hurdle, D. P., Kostense, J. K. and Van den Bosch, P. (1989). Mild-Slope Model for the Wave Behaviour in and Around Harbours and Coastal Structures in Areas of Variable Depth and Flow Conditions, *In Advances in Water Modelling and Measurement*, pp 307-324.
- Ilic, S., Chadwick, A.J. (1995). Evaluation and Validation of the Mild Slope Evolution Equation Model Using Field Data, *Proc. Conf. Coastal Dynamics '95*, Gdainsk, Poland, ASCE, pp 149-160
- Ilic, S. (1994). The Role of Offshore Breakwaters in Coastal Defence - Comparison of the Two Measurement Systems, *Internal Report No SCSE-94-002*, University of Plymouth
- Ilic, S. (1993). Spectral Analysis of Data, *Internal Research Report No 001/93*, Department of Civil Engineering, University of Brighton, Brighton, UK
- Isobe, M. (1987). A Parabolic Model for Transformation of Irregular Waves due to Refraction, Diffraction and Breaking, *Coastal Engineering in Japan*, Tokyo, Vol 30, pp 33-47.
- Isobe, M. and Kondo, K. (1984). Method for estimating directional wave spectrum in

- incident and reflected wave field, *Proc 19th Coastal Eng Conf*, Houston, pp 467-483.
- Izumiya, T. (1990). Extension of Mild Slope Equation For Waves Propagating Over a Permeable Submerged Breakwater, *Proc. 22<sup>nd</sup> Conf. Coastal Eng.*, Delft, pp 306-315.
- Jenkins, G.M. and Watts, D.G. (1968). *Spectral Analysis and its Applications*, Holden - Day, San Francisco, USA
- Johnson, H., Broker, I. and Zyserman, J. A. (1994). Identification of some relevant processes in coastal morphological modelling, *Proc. 24th Int Conf on Coastal Engineering*, pp 2871-2885
- Jonsson, I. G. (1979). The General Wave Equation and the Refraction Approximation, *Progress Report 49*, ISVA, Tech. Univ. of Denmark, pp 11-20.
- Jonsson, I. G. (1981). Booij's Current Wave-Equation and the Ray Approximation, *Progress Report 54*, ISVA, Tech. Univ. of Denmark, pp. 7-20.
- Kim, H. (1992). Three-Dimensional Sediment Transport Model, Phd. Thesis, Dept. of Civil Engineering, University of Liverpool
- Kim, T., Lin, L., Wang H. (1994). Application of the Maximum Entropy Method to the Real Sea Data, *Proc. 24<sup>th</sup> Int. Conf. on Coastal Eng.*, Kobe, ASCE, pp 340-355.
- Kim, Y.C. and Powers, E.J. (1979). Digital bispectra analysis and its application to nonlinear wave interactions, *IEEE Trans. Plasma Science*, 1, 120-131.
- Kinsman, B. (1965). *Wind Waves, their Generation and Propagation on the Ocean Surface*, Prentice-Hall, Inc., Englewood Cliffs, 676 pp.
- Kirby, J. T., Lee, C. and Rasmussen, C. (1992). Time-Dependent Solutions of the Mild Slope Equation, *Proc. 23<sup>th</sup> Int. Conf. on Coastal Engineering*, Delft, Vol 1, pp 391-404.
- Kirby, J. T. (1986a), A General Wave Equation for Waves over Rippled Beds, *J. Fluid Mechanics*, 162, pp 171-186.
- Kirby, J. T. (1986b). Higher-Order Approximations in the Parabolic Equation Method for Water Waves, *Jour. of Geoph. Res.*, Vol 91, No C1, pp 933-952.
- Kirby, J. T. and Dalrymple, R. A. (1986), An Approximate Model for Nonlinear Dispersion in Monochromatic Wave Propagation Models, *Coastal Eng.*, 9, pp 545-561.
- Kirby, J. T. (1984). A Note on Linear Surface Wave-Current Interaction Over Slowly Varying Topography, *J. Geophys. Res.*, 89(C1), pp 745-747.



- Kirby, J.T. and Dalrymple, R.A. (1984). Verification of a Parabolic Equation for Propagation of Weakly-Non-linear Waves, *Coastal Engineering*, 8, pp 219-232.
- Kobune, K. and Hashimoto, N. (1986). Estimation of Directional Spectra from the Maximum Entropy Principle, *Proc. 5<sup>th</sup> Int. Offshore Mechanics and Arctic Engineering Symp.* Tokyo, Japan, Vol 1, pp 80-85
- Kostense, J. K., Meijer, K. L., Dingemans, M. W., Mynet, A. E and Van den Bosch, P. (1986). Wave Energy Dissipation in Arbitrarily Shaped Harbours of Variable Depth, *Proc. 20th Int. Conf. on Coastal Engineering*, Taipei, Vol 3, pp 2002-2016.
- Kraus, N. C. and Harikai, S. (1983). Numerical Model of the Shoreline Change at Oarai Beach, *Coastal Eng.*, 7, pp 1-28.
- Li, B. (1997). Parabolic Model for Water Waves, *J. Waterway, Port, Coast. and Oc. Engrg.*, ASCE, 123(4), pp 192-200.
- Li, B. (1994a). A Generalized Conjugate Gradient Model for the Mild Slope Equation, *Coastal Eng.*, 23, pp 215-225.
- Li, B. (1994b). An Evolution Equation for Water Waves, *Coastal Eng.*, 23, pp 227-242.
- Li, B., Reeve, D. E. and Fleming, C. A. (1993). Numerical Solution of the Elliptic Mild-Slope Equation for Irregular Wave Propagation, *Coastal Eng.*, 20, pp 85-100.
- Li, B. and Anastasiou, K. (1992). Efficient Elliptic Solvers for the Mild-Slope Equation Using the Multigrid Technique, *Coastal Eng.*, 16, pp 245-266.
- Liberatore, G. (1990). Detached Breakwaters and Their Use in Italy, *Proceedings of the short course on design and reliability of coastal structures*, Venice, Scuola di S. Giovanni Evangelista, 1-3 October 1992
- Liu, P. L. F. (1990) Wave Transformation. In the Sea, Ocean Engineering Science, Vol. 9A, Eds. B. LeMehaute and D M Hanes, pp 27-63, J Willey and Sons, New York
- Liu, P. L. F. and Tsay, T. K. (1983). On Weak Reflection of Water Waves, *J. Fluid Mech.*, Vol 131, pp 59-71.
- Lozano, C. and Meyer, R. E. (1976). Leakage and Response of Waves Trapped by Round Islands, *Phys. Fluid*, 19(8), pp 1075-1088.
- Lygre, A. and Krogstad, H.E. (1986). Maximum Entropy Estimation of the Directional Distribution in Ocean Wave Spectra, *J. Phys. Oceanogr.*, Vol 16, pp 2052-2060.
- Madsen, P. and Larsen, J. (1987). An Efficient Finite-Difference Approach to the Mild-Slope Equation, *Coastal Eng.*, 11, pp 329-351.
- MAFF, (1994). Coastal Defence and the Environment, a guide to good practice, Report PB 1191, 156p

- Mason, T., Voulgaris, G., Simmonds, D.J. and Collins, M.B. (1997). Hydrodynamics and Sediment Transport on Composite (Mixed Sand/Shingle) and Sand Beaches: A Comparison, *Proc. Conf. Coastal Dynamics '97*, Plymouth, UK, ASCE, pp
- Massel, S. R. (1993). Extended Refraction - Diffraction Equation for Surface Waves, *Coastal Eng.* 19 (1/2), pp. 97-126.
- MacDonald, N.J. (1998). Numerical Modelling of Non-Linear Wave-Induced Nearshore Circulations, Phd Thesis, Dept. of Civil Engineering, University of Liverpool
- McDowell, D. M. (1988). The Interface Between Estuaries and Seas, Development in hydraulic engineering V, (Novak P ed.), Elsevier, Amsterdam, pp 139-194.
- Mitsuyasu, H., Tasai, F., Suhara, T., Mizuno S., Ohkuso M., Honda, T. and Rikishi, K. (1975). Observations of the Directional Spectrum of Ocean Waves using a Cloverleaf Buoy, *J. Phys. Oceanogr.*, Vol 5, No 2, pp 750-760.
- Mobarek, I.E. and Wiegel, R.L. (1966). Diffraction of Wind Generated Water Waves, *Proc. 10<sup>th</sup> Conf. Coastal Eng.*, Tokyo, Japan, pp
- Nakagawa, Y., Tsuruya, H., and Hashimoto, N., (1996). The Effects of Currents on Estimations of Directional Wave Spectra, *Proc. 25<sup>th</sup> Coastal Eng. Conf.*, ASCE, pp 30-42
- Neumann, G. (1953). On Ocean Wave Spectra and a New Method of Forecasting Wind Generated Sea, *US Army Corps of Engrs., Beach Erosion Board Tech. Memo.*, No 43, pp 42
- Nicholson, J., Broker, I., Roelvink, J.A., Price, D., Tanguy, J.M. and Moreno, L. (1997). Intercomparison of coastal area morphodynamic models, *Coastal Engineering*, 31, pp 97-123.
- Nir, Y. (1982). Offshore Artificial Structures and Their Influence on the Israel and Sinai Mediterranean Beaches, *Proc. 18th Int. Conf. Coast. Engr.*, ASCE, 1837-1857
- Nwogu, O.U., Mansard, E.P.D., Miles, M.D. and Isaacson, M. (1987). Estimation of directional wave spectra by the maximum entropy method, *Proc IAHR , Wave analysis and generation in laboratory basins, XXII Congress*, Lausanne, Sept 198, pp.
- O'Connor, B.A., Sayers, P.B. and MacDonald N.J. (1995). Combined Refraction-Diffraction Wave-Current Interaction over a Complex Nearshore Bathymetry, *Proc. Conf. Coastal Dynamics '95*, Gdainsk, Poland, ASCE, pp 173-184
- O'Connor, B.A., Kim, H. and Yum, K.D. (1992). Modelling Siltation at Chukpyon Harbour, Korea, *In Computer Modelling of Seas and Coastal Regions*, P. W.

- Partridge (ed.), Computational Mechanics Publications, Southampton, pp 397-410
- O'Connor, B.A., and Yoo, D. (1988). Mean Bed Friction of Combined Wave-Current Flow, *Coastal Engineering*, Vol. 12, 1988, pp 1-21.
- O'Hare, T. J. and Davies, A. G. (1993). A Comparison of Two Models for Surface-Wave Propagation over Rapidly Varying Topography, *Applied Ocean Research*, 15, pp. 1-11.
- O'Reilly, W. C. and Guza, R. T. (1991). Comparison of Spectral Refraction and Refraction - Diffraction Wave Models, *J. Waterw. Port. Coast. Ocean Eng.*, ASCE, 117, pp 199-215.
- Oltman-Shay, J. and Guza, R.T. (1984). A Data-Adaptive Ocean Wave Directional Spectrum Estimator for Pitch-Roll Type Measurements, *J. Phys. Oceanogr.*, Vol 14, pp 1800-1810
- Ozanne, F. (1998). Performance of a Boussinesq model for Shoaling and Breaking Waves, Phd Thesis, University of Plymouth
- Ozkan, H.T., and Kirby, J.T. (1993). Evolution of Breaking Directional Spectral Waves in the Nearshore Zone, *Proc., 2<sup>nd</sup> Int. Symp. On Wave Measurement and Analysis, Wave '93*, New Orleans, pp 849 -863.
- Panchang, V. G., Cushman-Roisin, B. and Pearce, B. R. (1988). Combined Refraction-Diffraction of Short Waves in Large Coastal Regions, *Coastal Eng.*, 12, pp 133-156.
- Panchang, V. G., Pearce, B. R., Ge Wei and Cushman-Roisin, B. (1991). Solution of the Mild-Slope Wave Problem by Iteration, *Appl. Ocean Res.*, 13(4), pp 187-199.
- Panchang, V.G., Ge, W., Pearce, B.R. and Briggs, M.J. (1990). Numerical Simulation of irregular wave propagation over a shoal, *J. Waterway, Port. Coast. and Oc. Engrg.*, ASCE, 116(3), pp 324-340.
- Panicker, N.N. and Borgman, L.E. (1970). Directional Spectra from Wave Gage Arrays, *Proc. 12<sup>th</sup> Int. Conf. Coastal Eng.*, Washington, ASCE, pp 117-136.
- Panicker, N.N. and Borgman, L.E. (1974). Enhancement of Directional Wave Spectrum Estimates, *Proc. 14<sup>th</sup> Int. Conf. Coastal Eng.*, Copenhagen, ASCE, pp 258-279.
- Pawka, S.S. (1983). Island shadows in wave directional spectra, *J. Geophysical Res.*, Vol 88, No C4, 2579 - 2591.
- Peaceman, D. and Rachford, H. (1955). The Numerical Solution of Parabolic and Elliptic Differential Equations, *Journal Soc Indust Appl Math*, Vol. 3, pp 28-41
- Pechon, P. and Teisson, C. (1996). Numerical Modelling of Bed Evolution Behind a

- Detached Breakwater, *Proc. 25<sup>th</sup> Conf. Coastal Eng.*, Orlando, pp 2050-2061
- Peregrine, D.H. (1976). Interaction of Water Waves and Currents, *Adv. Appl. Mech.*, 1976, 16, pp 9-117.
- Pope, J. and Rowen, D. D. (1983). Breakwaters for Beach Protection at Lorain, Ohio, *Proc. Coastal Structures '83*, ASCE, pp 753 - 768
- Pos, J.D. and Kilner, F.A. (1987). Breakwater Gap Wave Diffraction: An Experimental and Numerical Study, *J. Waterway, Port, Coast. and Oc. Engrg.*, ASCE, 113(1), pp 1-21.
- Press, W.H., Flannery, B.P., Teukolsky, S.A. and Vetterling W.T., (1986). Fourier transform, spectral methods, *In Numerical Recipes*, Camb. Univ. Press, 818pp
- Prislin, I., Zhang J., Johnson P. (1996). Deterministic decomposition of Irregular Short-Crested Surface Gravity Waves, *Proc. 6<sup>th</sup> Int. Offshore and Polar Engrg. Conf.*, Vol III, pp 57-64.
- Radder, A. C. (1979). On the Parabolic Equation Method for Water Wave Propagation, *J. Fluid Mech.*, 95(1), pp 159-176.
- Robert West and Partners, (1991). Arun District Council and National Rivers Authority Joint Coastal Defence Study
- Rodriguez-Iturbe, I., Nordin, C.F. (1969). Some Applications of Cross-Spectral Analysis in Hydrology: Rainfall and Run-off, *Water Resources Res.*, 5(3), pp 608 - 621.
- Rojanakamthorn, S., Isobe, M. and Watanabe, A. (1990). Modelling of Wave Transformation on Submerged Breakwater, *Proc. 22nd Coast. Eng. Conf.*, Delft, pp 1060-1073.
- Sand, S.E. and Mynett, A. E. (1987). Directional wave generation and analysis, *Proc IAHR, Wave analysis and generation in laboratory basins, XXII Congress*, Lausanne, Sept 1987.
- Sand, S. E. (1985). Stochastic processes: Practical Computation of Spectra, *Internal Report*, Technical University Lingby, Denmark
- Sand, S.E., Kirkegaard, J., Larsen, J. and Rodenhuis, G.S. (1983). Numerical and Physical Modelling of Directional Diffraction of Waves, *Int Conf Coast Port Engrg in Developing Countries*, IAHR, Delft, Vol. 11, pp 1290-1303
- Sawaragi, T. (1992). Detached Breakwaters, *Proceedings of the short course on design and reliability of coastal structures*, Venice, Scuola di S. Giovanni Evangelista, 1-3 October 1992, pp
- Shaffer, H.A. and Hyllested, P. (1994). Analysis of Multidirectional Waves Using Deterministic Decomposition, *Proc. Int. Symp. - Waves - Physical and Numerical*

*Modelling*, Vancouver, pp

- Simm, J.D., Brampton, A.H., Beech, N.W., Brooke, J.S. (editors). (1996). Beach Management Manual, Report 153, Construction Industry Research and Information Association
- Simmonds, D.J., Chadwick, A.J., Bird, P.A.D. and Pope, D.J. (1997). Field Measurements of Wave Transmission through a Rubble Mound Breakwater, *Proc. Conf. Coastal Dynamics '97*, Plymouth, UK, ASCE, pp
- Smallman, J.V. and Tozer, N.P. (1990). A Comparison of the Performance of Three Mathematical Models of Wave Disturbance in Harbour Approaches, *Proc. 22<sup>nd</sup> Conf. Coastal Eng.*, Delft, pp 597-610.
- Smith, R. and Sprinks, T. (1975). Scattering of Surface Waves by a Conical Island, *J. Fluid Mech.*, 72, pp 373-384.
- Teisson, C. and Benoit, M. (1994). Laboratory Measurement of Oblique Irregular Wave Reflection on Rubble-Mound Breakwaters, *Proc. 24<sup>th</sup> Conf. On Coastal Eng.*, Kobe, ASCE, New York, pp 42-56.
- Toyoshima, O. (1982). Variation in Foreshore Due to Detached Brekwaters, *Proc. 18th Costal Eng. Conf.*, ASCE, pp 1873-1892
- Toyoshima, O. (1976). Seabed Changes due to Detached Breakwaters, *Proc. 15th Coastal Eng. Conf.*, Vol. 1, pp 365-383.
- Tsay, T.K. and Liu, P.L.F. (1982). Numerical Solution of Water-Wave Refraction and Diffraction Problems in the Parabolic Approximation, *Journal of Geophysical Research*, Vol 87, No C10, pp 7932-7940.
- Vincent, C.L. and Briggs, M.J. (1989). Refraction – Diffraction of Irregular Waves Over a Mound, *J. Wtrway. Port. Coast. and Oc. Engrg.*, ASCE, 115 (2), pp 269-284.
- Walsh, T.M. (1992). Diffraction of Directional Wave Spectra Around a Semi-Infinite Breakwater, U.S, Army Engineer Watrways Experiment station, Report CERC-92-5
- Welch, P.D. (1967). The Use of Fast Fourier Transform for the Estimation of Power Spectra: A method based on time averaging over short, modified periodograms. *IEEE Trans. Audio and Electroacoust.*, Vol. AU-15, pp. 70-73.
- Willmott, C.J. (1981). On the Validation of Models, *Phys. Geog.*, 2, pp 184-194.
- Yoo, D., O'Connor, B.A. and McDowell, D.M. (1989). Mathematical Models of Wave Climate for Port Design, *Proc Instn Civ Engrs, Part I*, Vol. 86, pp 513-530.
- Yoo, D. and O'Connor, B.A. (1988a). The Diffraction of Waves in Caustics, *J. Wtrway. Port. Coast. and Oc. Engrg.*, ASCE, 114 (6), pp 715-731.

- Yoo, D., O'Connor, B.A. and Hedges, T.S. (1988b). Numerical Modelling of Waves in an Estuary, *Proc 5<sup>th</sup> Congress of Asian and Pacific Regional Division of IAHR*, Seoul, South Korea, IAHR, pp 1-13.
- Yoo, D. and O'Connor, B.A. (1986a). Ray Model for Caustic Gravity Waves, *Proc 6<sup>th</sup> Congress of Asian and Pacific Regional Division of IAHR*, Kyoto, Japan, IAHR, pp 65-72.
- Yoo, D. and O'Connor, B.A. (1986b). Mathematical Modelling of Wave-Induced Nearshore Circulations, *Proc. of 20<sup>th</sup> Inter. Conf. on Coastal Engineering*, Taipei, Taiwan, 1986, ASCE, pp 1667-1682.
- Young, I.R., (1994). On the Measurement of Directional Wave Spectra, *Applied Ocean Research*, 16, pp 283-294.
- Zyserman, J.A., Broker, I., Johnson, H.K., Mangor, K. and Jorgensen, K., (1998). On the Design of Shore-Parallel Breakwaters, *Proc. of 26<sup>th</sup> Inter. Conf. on Coastal Engineering*, Copenhagen 1998, ASCE, pp 1693-1705

## **APPENDICES**

# APPENDIX A

## Derivation of the Mild Slope Equation

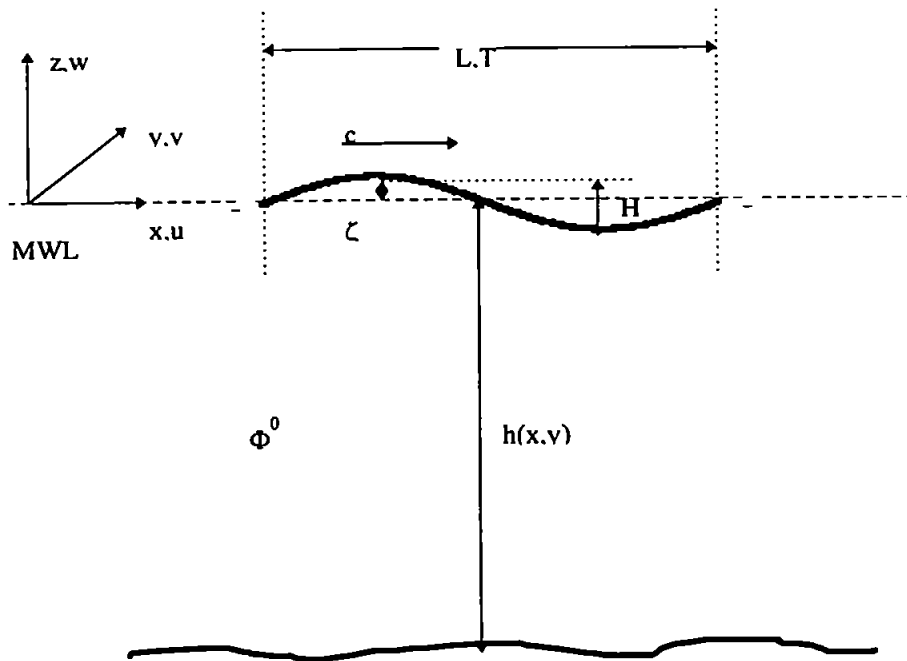


**Figure A.1** Definition scheme for the Mild Slope Equation derivation

Restrictions which are taken in account for the derivation of the Mild Slope Equation (MSE) (see e.g. Dingemans, 1997)

- ideal fluid
- waves of small amplitude



- irrotational flow  $\Rightarrow$  it is possible to use a velocity potential to describe velocities  $\mathbf{v}=(u,v,w)$  of the fluid by  $\mathbf{v} = \nabla\Phi^0$

$$(A.1)$$

- incompressible and homogeneous fluid

- gravity force field

In this case continuity equation (conservation of mass) is given by

$$\text{div } \mathbf{v} = 0 \tag{A.2}$$

which gives Laplace's equation

$$\frac{\partial^2 \Phi^0}{\partial x^2} + \frac{\partial^2 \Phi^0}{\partial y^2} + \frac{\partial^2 \Phi^0}{\partial z^2} = 0 \tag{A.3}$$

Boundary conditions are taken from linear theory. At the free surface when  $z=0$

$$\zeta = -\frac{1}{g} \frac{\partial \Phi^0}{\partial t} \tag{A.4}$$

and at the bottom which is rigid and impermeable when  $z=-h(x,y)$

$$\Phi_x^0 h_x + \Phi_y^0 h_y + \Phi_z^0 h_z = 0 \tag{A.5}$$

The first two terms on the left side of the equation (A.5) are neglected for the mild slope.

For constant depth and waves of constant form the following expressions are valid

$$\Phi^0 = -\frac{Hg}{2\omega} \frac{\cosh k(z+h)}{\cosh kh} \sin(\omega t - kx) \tag{A.6}$$

$$c_g = \frac{1}{2} c \left( 1 + \frac{2kh}{\sin 2kh} \right) \tag{A.7}$$

In an area of varying depth, assuming zero pressure at the surface, the vertical structure of wave motion can be given by a function  $f(z,h)$ , where the dependence of the horizontal coordinates  $(x,y)$  is only weak through  $h(x)$ . A velocity potential can then be written in the form:

$$\Phi^0(x, z, t) = \phi(x, t)f(z, h) \quad (\text{A.8})$$

For the derivation of the MSE, a variational principle is used. The Hamiltonian, which is the total energy (potential + kinetic) constitutes the variational principle when it is expressed in terms of the free surface elevation  $\zeta$ , and the value of the velocity potential at the free surface

$$\phi^1(x, t) = \Phi^0\{x, \zeta(x, t), t\} \quad (\text{A.9})$$

As shown by Zakharov (1968); Broer (1974); Miles (1977), a Hamiltonian is given by

$$\mathbf{H} = \iint dx dy H = \iint dx dy (V + T) \quad (\text{A.10})$$

and a variational derivative

$$\delta\mathbf{H} = \delta \int dx H = \delta \int dx (V + T) = 0 \quad (\text{A.11})$$

where V and T are potential and kinetic energy respectively, given by

$$V = \frac{1}{2} \rho g \zeta^2 \quad (\text{A.12})$$

$$T = \frac{1}{2} \rho \int_{-h(x)}^{\zeta(x,t)} dz \left[ (\nabla\Phi^0)^2 + \left( \frac{\partial\Phi^0}{\partial z} \right)^2 \right] \quad (\text{A.13})$$

To ensure finites of  $\mathbf{H}$ ,  $\Phi^0$  and  $\zeta$  and their derivatives go to zero fast enough for  $|x| \rightarrow \infty$ . The evolution equation for the surface elevation,  $\zeta(x,t)$  and the velocity potential at the free surface

$$\phi^1(x, t) = \Phi^0[x, \zeta(x, t), t] \quad (\text{A.14})$$

are given by Hamilton's canonical equations. (The derivation has been proved by Dingemans (1997))

$$\rho \frac{\partial\zeta}{\partial t} = \frac{\delta\mathbf{H}}{\delta\phi^1} \quad (\text{A.15})$$

and

$$\rho \frac{\partial \phi^1}{\partial t} = - \frac{\delta H}{\delta \zeta} \quad (\text{A.16})$$

Also it was shown that potential at the free surface is

$$\phi^1(x, t) = \phi(x, t) - \zeta \frac{\partial}{\partial x} \left( h \frac{\partial \phi}{\partial x} \right) - \frac{1}{2} \zeta^2 \frac{\partial^2 \phi}{\partial x^2} + \dots \quad (\text{A.17})$$

For linear wave motion it is sufficient to include  $\phi^1 = \phi$ , and the canonical equation becomes

$$\rho \frac{\partial \phi}{\partial t} = - \frac{\delta H}{\delta \zeta} \quad (\text{A.18})$$

These two equations (A.15) and (A.16) give the boundary conditions at the free surface written in terms of  $\zeta$  and  $\phi$ . Taking  $\Phi^0(x, z, t) = \phi(x, t) f(z, h)$ , where  $f(z, h)$  is a function of horizontal space  $x$  through  $h(x)$  and  $k(x)$

$$\nabla \Phi^0 = f \nabla \phi + \phi \nabla f \quad (\text{A.19})$$

The kinetic energy is

$$T = \frac{1}{2} \rho \int_{-h}^{\zeta} dz \left[ (\nabla \phi)^2 f^2(z, h) + \phi^2 \left( \frac{df}{dz} \right)^2 + 2f\phi \nabla \phi + \phi^2 (\nabla f)^2 \right] \quad (\text{A.20})$$

The common assumption for the mild slope equation is used, thus all expression with  $\nabla f$  are neglected and expression for  $T$  becomes

$$T = \frac{1}{2} \rho \int_{-h}^{\zeta} dz \left[ (\nabla \phi)^2 f^2(z, h) + \phi^2 \left( \frac{df}{dz} \right)^2 \right] \quad (\text{A.21})$$

Assuming that for linear wave motion, kinetic energy is at most a quadratic function of the unknowns (i.e.  $\zeta$  and  $\phi$ ), it results in the approximation of the upper limit integration  $z=0$  instead of  $z=\zeta$

$$T = \frac{1}{2} \rho \int_{-h}^0 dz \left[ (\nabla \phi)^2 f^2(z, h) + \phi^2 \left( \frac{df}{dz} \right)^2 \right] \quad (\text{A.22})$$

Introduction of the following expressions

$$F = \int_{-h}^0 dz f^2 \quad G = \int_{-h}^0 dz \left( \frac{df}{dz} \right)^2 \quad (\text{A.23})$$

yields the following equation for T

$$T = \frac{1}{2} \rho \left[ F(\nabla \phi)^2 + G\phi^2 \right] \quad (\text{A.24})$$

Hamiltonian density is then defined by the equation:

$$H = \frac{1}{2} \rho \left[ F(\nabla \phi)^2 + G\phi^2 + g\zeta^2 \right] \quad (\text{A.25})$$

which is valid for linear waves with the effects of the bottom slope,  $\nabla h$ , on the total energy have been ignored.

Canonical equations (A.15) and (A.16) become

$$\frac{\partial \zeta}{\partial t} = G\phi - \nabla(F\nabla\phi) \quad (\text{A.26})$$

$$\frac{\partial \phi}{\partial t} = -g\zeta \quad (\text{A.27})$$

and coupling them by eliminating  $\zeta$  results in

$$\frac{\partial^2 \phi}{\partial t^2} - \nabla(gF(\nabla\phi) + gG\phi) = 0 \quad (\text{A.28})$$

which is a form of the time dependent MSE.

Assuming that vertical structure, which is valid for linear waves on horizontal bottom is given as

$$f(z, h) = \frac{\cosh[k(z+h)]}{\cosh kh} \quad (\text{A.29})$$

and is valid at least locally for the uneven bottom case, yields

$$F = \frac{cc_g}{g} \quad (\text{A.30})$$

$$G = \frac{\omega^2 - k^2 cc_g}{g} \quad (\text{A.31})$$

Using these expressions, equations (A.26) and (A.27) become

$$g \frac{\partial \zeta}{\partial t} = (\omega^2 - k^2 cc_g) \phi - \nabla(cc_g \nabla \phi) \quad (\text{A.32})$$

$$\frac{\partial \phi}{\partial t} = -g \zeta \quad (\text{A.33})$$

Coupling them together by eliminating  $\zeta$ , the time dependent MSE is obtained

$$-\frac{\partial^2 \phi}{\partial t^2} + \nabla(cc_g \nabla \phi) - (\omega^2 - k^2 cc_g) \phi = 0 \quad (\text{A.34})$$

eliminating  $\phi$ , the following expression is obtained:

$$-\frac{\partial^2 \zeta}{\partial t^2} + \nabla(cc_g \nabla \zeta) - (\omega^2 - k^2 cc_g) \zeta = 0 \quad (\text{A.35})$$

The original Mild Slope Equation derived by Berkhoff (1972) can be recovered from equation (A.34) for purely harmonic motion:

$$\phi(x, t) = \text{Re} \{ \Phi(x) e^{-i\omega t} \} \quad (\text{A.36})$$

as

$$\nabla(cc_g \nabla \Phi) + k^2 cc_g \Phi = 0 \quad (\text{A.37})$$

Li (1994b) introduced the slow co-ordinate for the time variable  $t^* = \epsilon t$

$$\Phi(x, y, t) = \psi(x, y, t^*) e^{-i\omega t} \quad (\text{A.38})$$

Substituting into equation (A.34) yields

$$\frac{\partial^2 \psi}{\partial t^2} \varepsilon^2 - 2\omega i \frac{\partial \psi}{\partial t} \varepsilon - \nabla(cc_g \nabla \psi) - (k^2 cc_g) \psi = 0 \quad (\text{A.39})$$

noting

$$\frac{\partial}{\partial t} = \varepsilon \frac{\partial}{\partial t^*} \quad \text{and} \quad \frac{\partial^2}{\partial t^2} = \varepsilon^2 \frac{\partial^2}{\partial t^{*2}} \quad (\text{A.40})$$

yields

$$\frac{\partial^2 \psi}{\partial t^{*2}} - 2\omega i \frac{\partial \psi}{\partial t^*} - \nabla(cc_g \nabla \psi) - (k^2 cc_g) \psi = 0 \quad (\text{A.41})$$

The second order small terms are ignored, thus equation (A.41) becomes

$$-2\omega i \frac{\partial \psi}{\partial t^*} = \nabla(cc_g \nabla \psi) + (k^2 cc_g) \psi \quad (\text{A.42})$$

Using the transformation introduced by Radder (1979)

$$\psi = \frac{\varphi}{\sqrt{cc_g}} \quad (\text{A.43})$$

equation (A.42) can be rewritten as so called time evolution equation (Li, 1994b)

$$-2\omega i \frac{\partial \varphi}{\partial t^*} = \nabla^2 \varphi + k_c^2 \varphi \quad (\text{A.44})$$

where

$$k_c^2 = k^2 - \frac{\nabla^2 \sqrt{cc_g}}{\sqrt{cc_g}} \quad (\text{A.45})$$

## APPENDIX B

### Linear stability analysis

An evolution equation based on Mild Slope Equation (Li, 1994b) is given by

$$-\frac{2\omega i}{cc_g} \frac{\partial \varphi}{\partial t} = \nabla^2 \varphi + k_c^2 \varphi \quad (\text{B.1})$$

and it can be written in finite difference form using Alternating Direction Implicit Scheme as

$$f_{p,q} \frac{\varphi_{p,q}^{n+1/2} - \varphi_{p,q}^n}{1/2\Delta t} i = \delta_x^2 \varphi_{p,q}^{n+1/2} + \frac{1}{2} (k_c^2)_{p,q} \varphi_{p,q}^{n+1/2} + \delta_y^2 \varphi_{p,q}^n + \frac{1}{2} (k_c^2)_{p,q} \varphi_{p,q}^n \quad (\text{B.2})$$

$$f_{p,q} \frac{\varphi_{p,q}^{n+1} - \varphi_{p,q}^{n+1/2}}{1/2\Delta t} i = \delta_x^2 \varphi_{p,q}^{n+1/2} + \frac{1}{2} (k_c^2)_{p,q} \varphi_{p,q}^{n+1/2} + \delta_y^2 \varphi_{p,q}^{n+1} + \frac{1}{2} (k_c^2)_{p,q} \varphi_{p,q}^{n+1} \quad (\text{B.3})$$

where

$$f_{p,q} = \frac{-2\omega}{(cc_g)_{p,q}} \quad (\text{B.4})$$

$$\delta_x^2 \varphi_{p,q}^n = \frac{\varphi_{p-1,q}^n - 2\varphi_{p,q}^n + \varphi_{p+1,q}^n}{\Delta x^2} \quad (\text{B.5})$$

$$\delta_y^2 \varphi_{p,q}^n = \frac{\varphi_{p,q-1}^n - 2\varphi_{p,q}^n + \varphi_{p,q+1}^n}{\Delta y^2} \quad (\text{B.6})$$

These equations are applied over the complete computational domain when  $\Delta x$  is constant. Li (1994b) showed that in this case the scheme is unconditionally stable. Here the possibility of applying a flow adaptive scheme and its stability will be investigated. The grid size,  $\Delta x$ , decreases accordingly to the wavelength reduction from offshore to the shore as it is schematised in Figure B.1.

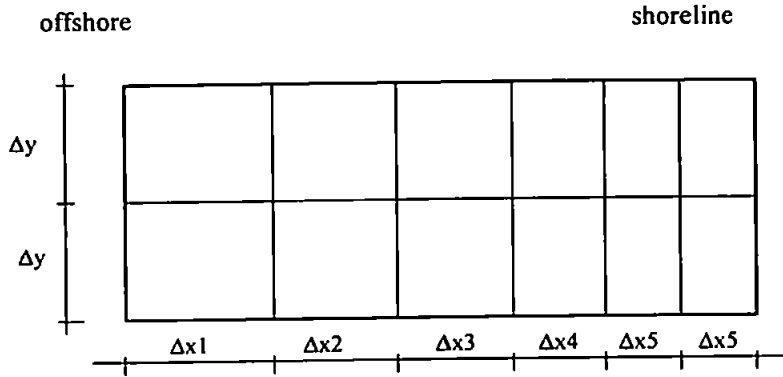


**Figure B.1** The computational domain schematisation where  $\Delta x_2 = \nu \Delta x_1$ ,  $\Delta x_3 = \nu \Delta x_2$ ,  $\Delta x_4 = \nu \Delta x_3$ ,  $\Delta x_5 = \nu \Delta x_4$  etc.

A change of grid space  $\Delta x$  to  $\nu \Delta x$  is allowed in the direction of wave propagation but the grid space orthogonal to the direction of propagation  $\Delta y$  remains constant. The value of the parameter  $\nu$  is in the interval between 0 and 1. Taking into account the grid points in the area of transition from  $\Delta x$  to  $\nu \Delta x$ , equation (B.5) can be rewritten as follows

$$\delta_x^2 \varphi_{p,q}^n = \frac{\nu \varphi_{p-1,q}^n - (1 + \nu) \varphi_{p,q}^n + \varphi_{p+1,q}^n}{\Delta x^2 \left( \nu + \frac{1 + \nu}{2} \right)} \quad (\text{B.7})$$

Substitution of expressions (B.7) into (B.2) and (B.3); multiplication by  $\Delta t$  and definition of following expressions

$$Crx = \frac{cc_g}{2\omega} \frac{\Delta t}{\Delta x^2} \quad Cry = \frac{cc_g}{2\omega} \frac{\Delta t}{\Delta y^2} \quad G = \frac{1}{2} k_c^2 \frac{\Delta t cc_g}{2\omega} \quad (\text{B.8})$$

yields following equations

$$\varphi_{p-1,q}^{n+1/2} \left( -Crx \frac{2}{1 + \nu} \right) + \varphi_{p,q}^{n+1/2} \left( -2i + Crx \frac{2}{\nu} - G \right) + \varphi_{p+1,q}^{n+1/2} \left( -Crx \frac{2}{\nu(1 + \nu)} \right) - Cry \varphi_{p,q-1}^n - (-2i - 2Cry + G) \varphi_{p,q}^n - Cry \varphi_{p,q+1}^n = 0$$



(B.9)

$$\begin{aligned} & \varphi_{p-1,q}^{n+1/2} \left( -Crx \frac{2}{1+\nu} \right) + \varphi_{p,q}^{n+1/2} \left( 2i + Crx \frac{2}{\nu} - G \right) + \varphi_{p+1,q}^{n+1/2} \left( -Crx \frac{2}{\nu(1+\nu)} \right) - Cry \varphi_{p,q-1}^{n+1} + \\ & + (-2i + 2Cry - G) \varphi_{p,q}^{n+1} - Cry \varphi_{p,q+1}^{n+1} = 0 \end{aligned}$$

(B.10)

Following the analysis introduced by von Neumann, it is supposed that a solution of the finite difference scheme can be written as a Fourier series in complex exponential form for any time level  $n$ , and grid point  $p, q$  in the form

$$\varphi_{p,q}^n = \sum_k \xi_k^n e^{i\alpha p} e^{i\beta q} \quad k = 1, 2, 3, \dots \quad (B.11)$$

The linear stability analysis method determines how each individual Fourier coefficient behaves (grows, decays or stays constant) in time for any wave number  $k$ . Initially the analysis is performed for any individual wave number  $k$ , representing the function

$$\varphi_{p,q}^n = \xi^n e^{i\alpha p} e^{i\beta q} \quad (B.12)$$

Introducing now the amplification factor  $A$  defined as  $\xi^{n+1} = A\xi^n$  and substituting  $A=e^\gamma$  then  $\xi^n$  can be expressed as  $e^m$ .

At each time step and for any wave number  $k$ , the Fourier coefficient is multiplied by the factor  $A_k$ , which is called the amplification factor. For stable finite difference schemes, the Fourier coefficient,  $\xi_k$ , should not grow without bound, so that  $|A_k| \leq 1$  should be valid for stability.

Substituting now the function values in finite-difference scheme by Fourier series form, given in general form as

$$\varphi_{p,q}^n = e^m e^{i\alpha p} e^{i\beta q} \quad (B.13)$$

The equations (B.8) and (B.9) read as

$$\begin{aligned}
& e^{\gamma(n+1/2)} e^{i\alpha(p-1)} e^{i\beta q} \left( -Cr x \frac{2}{1+\nu} \right) + e^{\gamma(n+1/2)} e^{i\alpha p} e^{i\beta q} \left( -2i + Cr x \frac{2}{\nu} - G \right) + \\
& + e^{\gamma(n+1/2)} e^{i\alpha(p+\nu)} e^{i\beta q} \left( -Cr x \frac{2}{\nu(1+\nu)} \right) - Cry e^m e^{i\alpha p} e^{i\beta(q-1)} - (-2i - 2Cry + G) e^m e^{i\beta} e^{i\beta q} - \\
& - Cry e^m e^{i\alpha p} e^{i\beta(q+1)} = 0
\end{aligned} \tag{B.14}$$

and

$$\begin{aligned}
& e^{\gamma(n+1/2)} e^{i\alpha(p-1)} e^{i\beta q} \left( -Cr x \frac{2}{1+\nu} \right) + e^{\gamma(n+1/2)} e^{i\alpha p} e^{i\beta q} \left( 2i + Cr x \frac{2}{\nu} - G \right) + \\
& + e^{\gamma(n+1/2)} e^{i\alpha(p+\nu)} e^{i\beta q} \left( -Cr x \frac{2}{\nu(1+\nu)} \right) - Cry e^{\gamma(n+1)} e^{i\alpha p} e^{i\beta(q-1)} + \\
& + (-2i + 2Cry - G) e^{\gamma(n+1)} e^{i\alpha p} e^{i\beta q} - -Cry e^{\gamma(n+1)} e^{i\alpha p} e^{i\beta(q+1)} = 0
\end{aligned} \tag{B.15}$$

Division of the equation (B.14) by  $e^m e^{i\alpha(p-1)} e^{i\beta(q+1)}$  and substituting  $A_1=e^{\gamma/2}$ , yields

$$A_1 = \frac{(-2i - 2Cry + G) + Cry e^{i\beta} + Cry e^{-i\beta}}{(-2i + Cr x \frac{2}{\nu} - G) - Cr x \frac{2}{\nu(1+\nu)} e^{i\alpha\nu} - Cr x \frac{2}{1+\nu} e^{-i\alpha}} \tag{B.16}$$

or rewritten

$$A_1 = \frac{-2i + G - 4Cry \sin^2\left(\frac{\beta}{2}\right)}{-2i - G + 2Cr x \left( \frac{(1+\nu)(\cos\alpha + i\sin\alpha) - (\cos(\nu\alpha + \alpha) + i\sin(\nu\alpha + \alpha)) - \nu}{\nu(1+\nu)(\cos\alpha + i\sin\alpha)} \right)} \tag{B.17}$$

In the case when  $\nu=1$ , the equation (B.17) reduces to the form:

$$A_1 = \frac{-2i + G - 4Cry \sin^2\left(\frac{\beta}{2}\right)}{-2i - G + 4Cr x \sin^2\left(\frac{\alpha}{2}\right)} \tag{B.18}$$

which was given by Li (1994b).

Division of equation (B15) by  $e^{\gamma(n+1/2)} e^{i\alpha(p-1)} e^{i\beta(q+1)}$  and substitution of  $A_2=e^{\gamma/2}$ , yields

$$A_2 = \frac{(-2i - Crx \frac{2}{\nu} + G) + Crx \frac{2}{\nu(1+\nu)} e^{i\alpha\nu} + Crx \frac{2}{1+\nu} e^{-i\alpha}}{(-2i + 2Cry - G) - Crye^{i\beta} - Crye^{-i\beta}} \quad (\text{B.19})$$

or rewritten

$$A_2 = \frac{-2i + G - 2Crx \left( \frac{(1+\nu)(\cos \alpha + i \sin \alpha) - (\cos(\nu\alpha + \alpha) + i \sin(\nu\alpha + \alpha)) - \nu}{\nu(1+\nu)(\cos \alpha + i \sin \alpha)} \right)}{-2i - G + 4Cry \sin^2 \left( \frac{\beta}{2} \right)} \quad (\text{B.20})$$

In the case when  $\nu=1$ , the equation (B.20) reduces to the form:

$$A_2 = \frac{-2i + G - 4Crx \sin^2 \left( \frac{\alpha}{2} \right)}{-2i - G + 4Cry \sin^2 \left( \frac{\beta}{2} \right)} \quad (\text{B.21})$$

The total amplification factor is then given by the equation:

$$|A| = |A_1 A_2| = \sqrt{\text{Re}^2(A_1 A_2) + \text{Im}^2(A_1 A_2)} \quad (\text{B.22})$$

Substituting following expression

$$\Pi = \frac{(1+\nu)(\cos \alpha + i \sin \alpha) - (\cos(\nu\alpha + \alpha) + i \sin(\nu\alpha + \alpha)) - \nu}{\nu(1+\nu)(\cos \alpha + i \sin \alpha)} \quad (\text{B.23})$$

where the real part is given by the equation

$$\Pi' = \frac{1}{\nu(1+\nu)} \left[ \begin{array}{l} (1+\nu) \cos^2 \alpha - \cos(\nu\alpha + \alpha) \cos \alpha - \nu \cos \alpha + (1+\nu) \sin^2 \alpha - \\ - \sin(\nu\alpha + \alpha) \sin \alpha \end{array} \right] \quad (\text{B.24})$$

and the imaginary part is given by the equation

$$\Pi'' = \frac{1}{\nu(1+\nu)} \left[ -\sin(\nu\alpha + \alpha) + \cos(\nu\alpha + \alpha) \sin \alpha + \nu \sin \alpha \right] \quad (\text{B.25})$$

When  $\nu=1$  then real and imaginary parts become

$$\Pi' = 2 \sin^2\left(\frac{\alpha}{2}\right) \quad (\text{B.26})$$

$$\Pi' = 0 \quad (\text{B.27})$$

The total amplification factor is now given by the equation:

$$|A| = \sqrt{\frac{(C^2 - D^2 - c^2 + d^2)^2 + (2CD - 2cd)^2}{((C + c)^2 + (D + d)^2)^2}} \quad (\text{B.28})$$

where

$$C = -4 + G^2 - 4Cry G \sin^2 \frac{\beta}{2} - 2G Cry \Pi' + 8Crx Cry \sin^2 \frac{\beta}{2} \Pi' \quad (\text{B.29})$$

$$D = -4G + 8Cry \sin^2 \frac{\beta}{2} + 4Crx \Pi' \quad (\text{B.30})$$

$$c = 4Crx \Pi' \quad (\text{B.31})$$

$$d = 2G Crx \Pi' - 8Cry Cry \sin^2 \frac{\beta}{2} \Pi' \quad (\text{B.32})$$

For stable and accurate solutions, the amplification factor needs to be ideally equal to 1. From equations (B.28-B.32), it can be concluded that this is not the case, unless  $c = d = 0$ . When  $\nu = 1$ ,  $c = d = 0$  and amplification factor becomes equal to 1 what was previously proved by Li (1994b). From these equations, it can be also concluded that when  $\nu = 1$ ,  $\Delta y$  does not need to be equal to  $\Delta x$  for a stable solution.

## APPENDIX C

### Truncation error analysis

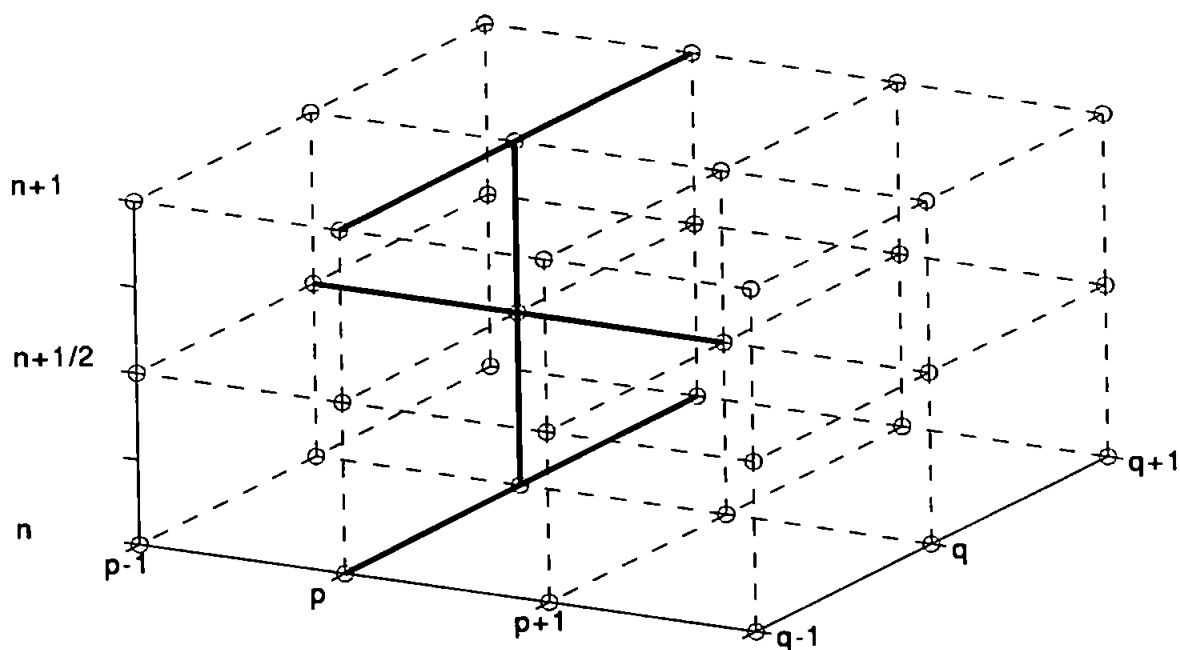


**Figure C.1** The ADI scheme used by Li (1994b)

An evolution equation based on the Mild Slope Equation (Li, 1994b) is given by

$$-\frac{2\omega i}{cc_g} \frac{\partial \varphi}{\partial t} = \nabla^2 \varphi + k_c^2 \varphi \tag{C.1}$$

can be written in finite difference form using Alternating Direction Implicit Scheme as it is shown in Appendix B, equations (B.9) and (B.10), taking  $\nu=1$

$$\begin{aligned} &\varphi_{p-1,q}^{n+1/2}(-Cr_x) + \varphi_{p,q}^{n+1/2}(-2i + 2Cr_x - G) + \varphi_{p,q+1}^{n+1/2}(-Cr_x) - Cr_y \varphi_{p,q-1}^n - \\ &-(-2i + 2Cr_y + G)\varphi_{p,q}^n - Cr_y \varphi_{p,q+1}^n = 0 \end{aligned} \tag{C.2}$$

$$\begin{aligned} & \varphi_{p-1,q}^{n+1/2}(-Cr_x) - \varphi_{p,q}^{n+1/2}(2i + 2Cr_x - G) - \varphi_{p,q+1}^{n+1/2}(-Cr_x) - Cry\varphi_{p,q-1}^{n+1} + \\ & + (-2i + 2Cry - G)\varphi_{p,q}^{n+1} - Cry\varphi_{p,q+1}^{n+1} = 0 \end{aligned} \quad (C.3)$$

where

$$Cr_x = \frac{cc_g}{2\omega} \frac{\Delta t}{\Delta x^2} \quad Cry = \frac{cc_g}{2\omega} \frac{\Delta t}{\Delta y^2} \quad G = \frac{1}{2} k_c \frac{\Delta t cc_g}{2\omega} \quad (C.4)$$

The sum of equations (C.2) and (C.3) can be written as

$$\begin{aligned} & 2a\varphi_{p-1,q}^{n+1/2} + 2b\varphi_{p,q}^{n+1/2} + 2a\varphi_{p+1,q}^{n+1/2} + c\varphi_{p,q-1}^n + (2i + d)\varphi_{p,q}^n + c\varphi_{p,q+1}^n + c\varphi_{p,q-1}^{n+1} + \\ & + (-2i + d)\varphi_{p,q}^{n+1} + c\varphi_{p,q+1}^{n+1} = 0 \end{aligned} \quad (C.5)$$

where coefficients a,b,c,d are defined as

$$\begin{aligned} a &= -Cr_x \\ b &= 2Cr_x - G \\ c &= -Cry \\ d &= 2Cry - G \end{aligned} \quad (C.6)$$

The truncation error analysis will be made through a Taylor's series expansion around the central point  $[p\Delta x, q\Delta y, (n+1/2)\Delta t]$  following the formulation of Taylor's series for functions of three independent variables as it is given in equation (C.8). The derivatives in all further derivations will be noted as

$$\begin{aligned} \varphi_x &= \frac{\partial \varphi}{\partial x} \quad \varphi_y = \frac{\partial \varphi}{\partial y} \quad \varphi_t = \frac{\partial \varphi}{\partial t} \\ \phi_{xx} &= \frac{\partial^2 \varphi}{\partial x^2} \quad \phi_{yy} = \frac{\partial^2 \varphi}{\partial y^2} \quad \phi_{tt} = \frac{\partial^2 \varphi}{\partial t^2} \\ \phi_{xy} &= \frac{\partial^2 \varphi}{\partial x \partial y} \quad \phi_{xt} = \frac{\partial^2 \varphi}{\partial x \partial t} \quad \phi_{yt} = \frac{\partial^2 \varphi}{\partial y \partial t} \\ & \text{etc.} \end{aligned} \quad (C.7)$$

$$\begin{aligned}
\varphi(x + \alpha, y + \beta, t + \gamma) = & \varphi + \frac{1}{1!}(\alpha\varphi_x + \beta\varphi_y + \gamma\varphi_t) + \\
& + \frac{1}{2!}(\alpha^2\varphi_{xx} + \beta^2\varphi_{yy} + \gamma^2\varphi_{tt} + 2\alpha\beta\varphi_{xy} + 2\alpha\gamma\varphi_{xt} + 2\beta\gamma\varphi_{yt}) + \\
& + \frac{1}{3!} \left( \begin{aligned} & \alpha^3\varphi_{xxx} + \beta^3\varphi_{yyy} + \gamma^3\varphi_{ttt} + 3\alpha^2\beta\varphi_{xxy} + 3\alpha^2\gamma\varphi_{xtt} + \\ & + 3\beta^2\gamma\varphi_{yyt} + 3\alpha\beta^2\varphi_{xyy} + 3\alpha\gamma^2\varphi_{xtt} + 3\beta\gamma^2\varphi_{ytt} + \\ & + 6\alpha\beta\gamma\varphi_{xyt} \end{aligned} \right) + \\
& + \frac{1}{4!} \left( \begin{aligned} & \alpha^4\varphi_{xxxx} + \beta^4\varphi_{yyyy} + \gamma^4\varphi_{tttt} + 4\alpha^3\beta\varphi_{xxx} + 4\alpha^3\gamma\varphi_{xxt} + \\ & + 4\alpha\beta^3\varphi_{xyy} + 4\beta^3\gamma\varphi_{yyt} + 4\alpha\gamma^3\varphi_{xtt} + 4\beta\gamma^3\varphi_{ytt} + \\ & + 6\alpha^2\beta^2\varphi_{xxy} + 6\alpha^2\gamma^2\varphi_{xxt} + 6\beta^2\gamma^2\varphi_{yyt} + \\ & + 12\alpha^2\beta\gamma\varphi_{xyt} + 12\alpha\beta^2\gamma\varphi_{xyt} + 12\alpha\beta\gamma^2\varphi_{xyt} \end{aligned} \right) + \\
& + h. o. t.
\end{aligned}
\tag{C.8}$$

where  $\varphi$  and all partial derivatives are taken at point  $(x, y, t)$ .

Taylor series expansion will be provided around the central point with values of  $\alpha$ ,  $\beta$  and  $\gamma$  as shown in Table (C.1).

Point	$\alpha$	$\beta$	$\gamma$
p-1,q,n+1/2	$-\Delta x$	0	0
p,q,n+1/2	0	0	0
p+1,q,n+1/2	$\Delta x$	0	0
p,q-1,n	0	$-\Delta y$	$-\Delta t/2$
p,q,n	0	0	$-\Delta t/2$
p,q+1,n	0	$\Delta y$	$-\Delta t/2$
p,q-1,n+1	0	$-\Delta y$	$\Delta t/2$
p,q,n+1	0	0	$\Delta t/2$
p,q+1,n+1	0	$\Delta y$	$\Delta t/2$

**Table C.1** Steps in the Taylor's series expansion

In a first step the terms of the various orders will be collected separately, giving

## ZERO ORDER

$$(4a + 2b + 4c + (2i + d) + (-2i + d))\varphi_{\rho\Delta x, q\Delta y}^{(n+1/2)\Delta t} = -4G\varphi_{\rho\Delta x, q\Delta y}^{(n+1/2)\Delta t} = -\frac{k_c^2 cc_g}{\omega} \Delta t \varphi_{\rho\Delta x, q\Delta y}^{(n+1/2)\Delta t} \quad (\text{C.9})$$

## FIRST ORDER

$$\begin{aligned} & (-2a + 2a)\Delta x \varphi_x + (-c + c - c + c)\Delta y \varphi_y + \left( \frac{-c}{2} - \frac{c}{2} + \frac{c}{2} + \frac{c}{2} - d + d - i - i \right) \Delta t \varphi_t = \\ & = -2i\Delta t \varphi_t, \end{aligned} \quad (\text{C.10})$$

## SECOND ORDER

$$\begin{aligned} & \frac{1}{2} \left[ (2a + 2a)\Delta x^2 \varphi_{xx} + (c + c + c + c)\Delta y^2 \varphi_{yy} + \left( \frac{c}{4} + \frac{c}{4} + \frac{c}{4} + \frac{c}{4} + \frac{d}{4} + \frac{d}{4} + \frac{i}{2} - \frac{i}{2} \right) \Delta t^2 \varphi_{tt} \right] = \\ & = -2Cr_x \Delta x^2 \varphi_{xx} - 2Cr_y \Delta y^2 \varphi_{yy} - \frac{G}{4} \Delta t^2 \varphi_{tt} = -\frac{cc_g}{\omega} \Delta t \varphi_{xx} - \frac{cc_g}{\omega} \Delta t \varphi_{yy} - \frac{G}{4} \Delta t^2 \varphi_{tt} \end{aligned} \quad (\text{C.11})$$

## THIRD ORDER

$$\begin{aligned} & \left[ (-2a + 2a)\Delta x^3 \varphi_{xxx} + (-c + c - c + c)\Delta y^3 \varphi_{yyy} + \right. \\ & \frac{1}{6} \left[ \left( -\frac{c}{8} - \frac{c}{8} + \frac{c}{8} + \frac{c}{8} - \frac{d}{8} + \frac{d}{8} - \frac{i}{4} - \frac{i}{4} \right) \Delta t^3 \varphi_{ttt} + \left( -\frac{3c}{2} - \frac{3c}{2} + \frac{3c}{2} + \frac{3c}{2} \right) \Delta y^2 \Delta t \varphi_{yyt} \varphi_t + \right. \\ & \left. \left. + \left( -\frac{3c}{4} + \frac{3c}{4} - \frac{3c}{4} + \frac{3c}{4} \right) \Delta y \Delta t^2 \varphi_{yt} \varphi_t \right] = \\ & = -\frac{1}{12} i \Delta t^3 \varphi_{ttt} \end{aligned} \quad (\text{C.12})$$



#### FOURTH ORDER

$$\begin{aligned}
 & \left[ \begin{aligned}
 & (2a + 2a)\Delta x^4 \varphi_{xxxx} + (c + c + c + c)\Delta y^4 \varphi_{yyyy} + \\
 & \frac{1}{24} \left( \frac{c}{16} + \frac{c}{16} + \frac{c}{16} + \frac{c}{16} + \frac{d}{16} + \frac{d}{16} + \frac{i}{8} - \frac{i}{8} \right) \Delta t^4 \varphi_{tttt} + (2c - 2c - 2c + 2c)\Delta y^3 \Delta t \varphi_{yyy} \varphi_t + \\
 & \left( \frac{c}{2} - \frac{c}{2} - \frac{c}{2} + \frac{c}{2} \right) \Delta y \Delta t^3 \varphi_y \varphi_{ttt} + \left( \frac{3}{2}c + \frac{3}{2}c + \frac{3}{2}c + \frac{3}{2}c \right) \Delta y^2 \Delta t^2 \varphi_{yy} \varphi_{tt}
 \end{aligned} \right] = \\
 & = \frac{1}{24} \left[ -4Cr_x \Delta x^4 \varphi_{xxxx} - 4Cry \Delta y^4 \varphi_{yyyy} - \frac{1}{8} G \Delta t^4 \varphi_{tttt} - 6Cry \Delta y^2 \Delta t^2 \varphi_{yy} \varphi_{tt} \right]
 \end{aligned}
 \tag{C.13}$$

Collecting all zero, first, second, third and fourth order terms and neglecting higher order terms (h.o.t) gives, after multiplication by  $\Delta t \omega / cc_g$

$$\begin{aligned}
 -\frac{2\alpha i}{cc_g} \varphi_t - \varphi_{xx} - \varphi_{yy} - k_c^2 \varphi = \frac{2\omega}{cc_g} \left[ \begin{aligned}
 & \frac{1}{8} G \Delta t \varphi_{tt} + \frac{1}{24} i \Delta t^2 \varphi_{ttt} + \frac{1}{12} Cr_x \left( \frac{\Delta x}{\Delta t} \right)^4 \Delta t^3 \varphi_{xxxx} + \\
 & + \frac{1}{12} Cry \left( \frac{\Delta y}{\Delta t} \right)^4 \Delta t^3 \varphi_{yyyy} + \frac{1}{384} \Delta t^3 \varphi_{ttt} + \\
 & + \frac{1}{8} Cry \Delta y^2 \Delta t \varphi_{yy} \varphi_{tt}
 \end{aligned} \right] + h.o.t.
 \end{aligned}
 \tag{C.14}$$

The truncation error is the expression on the right side of the equation.

## APPENDIX D

### Theory of Spectral Analysis Summarised

Here, a summary of spectral analysis theory is given. For a more detailed theoretical appraisal of the Fourier Transform and its applications, the reader is referred to Jenkins and Watts (1968) for example.

#### D.1 General

A Fourier series of a periodic function with period T can be written

$$\eta(t) = \sum_{n=0}^{\infty} c_n \cos(2\pi f_n t + \vartheta_n) \quad (\text{D.1})$$

where

$c_n$  - amplitude or height of oscillation

$\vartheta_n$  - phase angle or phase shift

$f_n$  - particular frequency  $\omega_0$  - angular frequency

$$\omega_0 = 2\pi f_0 \quad f_0 = \frac{2\pi}{\omega_0} \quad \text{or} \quad \omega_0 = \frac{2\pi}{T}$$

Let us consider one particular sinusoidal function expressed generally as:

$$\eta(t) = c_1 \cos(\omega_0 t + \vartheta_1) \quad (\text{D.2})$$

Equation (D.2) can be rewritten

$$\eta(t) = c_1 [\cos(\omega_0 t) \cos \vartheta_1 - \sin(\omega_0 t) \sin \vartheta_1] \quad (\text{D.3})$$

or

$$\eta(t) = A_1 \cos(\omega_0 t) + B_1 \sin(\omega_0 t) \quad (\text{D.4})$$

where

$$A_1 = c_1 \cos \vartheta_1 \qquad B_1 = -c_1 \sin \vartheta_1 \qquad \text{(D.5)}$$

this yields

$$\theta_1 = \arctan\left(-\frac{B_1}{A_1}\right) \qquad \text{(D.6)}$$

and

$$c_1 = \sqrt{A_1^2 + B_1^2} \qquad \text{(D.7)}$$

or in general:

$$A_n = c_n \cos \vartheta_n \qquad B_n = -c_n \sin \vartheta_n \qquad \text{(D.8)}$$

$$\theta_n = \arctan\left(-\frac{B_n}{A_n}\right) \qquad \text{(D.9)}$$

and

$$c_n = \sqrt{A_n^2 + B_n^2} \qquad \text{(D.10)}$$

The function expressed (i.e. in time domain) could be plotted versus time or versus frequency where  $f = \frac{1}{T}$ .

When plotted in the time domain a curve of wave excursion results. In the frequency domain the equivalent is a line spectra.

## D.2 Fourier Transform

The Fourier integral is the primary tool for the Fourier transform, for analysing aperiodic wave forms. It can be derived from the exponential form of the Fourier series.

$$f(t) = \sum_{k=-\infty}^{\infty} \tilde{c}_k e^{ik\omega_0 t} \qquad \text{(D.11)}$$

where  $f(t)$  represents any periodic function in time domain and

$$\tilde{c}_k = \frac{1}{T} \int_{-T/2}^{T/2} f(t) e^{-ik\omega_0 t} dt \quad (\text{D.12})$$

where  $\omega_0 = 2\pi/T$  and  $k = 0, 1, 2, \dots$

The transition from periodic to a non periodic function can be effected by allowing the period to approach infinity, so the function never repeats itself and becomes aperiodic.

$$f(t) = \frac{1}{2\pi} \int_{-\infty}^{\infty} F(i\omega_0) e^{i\omega_0 t} d\omega_0 \quad (\text{D.13})$$

and the Fourier coefficient becomes a continuous function.

$$F(i\omega_0) = \int_{-\infty}^{\infty} f(t) e^{-i\omega_0 t} dt \quad (\text{D.14})$$

The function  $F(i\omega_0)$  given by expression (D.14) is called the Fourier integral of  $f(t)$ .

The major difference between the Fourier series and the Fourier transform is that the Fourier series converts a continuous, periodic time-domain function to frequency-domain magnitudes at discrete frequencies, and the Fourier transform converts a continuous time-domain to a continuous frequency-domain function.

### D.3 Discrete Fourier Transform (DFT)

Assuming that the wave profiles are given a sequential form of  $N$  data points  $n(\Delta t)$ ,  $n(2\Delta t)$ , .....  $n(N\Delta t)$  sampled at a constant interval  $\Delta t$ , where  $T = N \cdot \Delta t$ , a continuous Fourier series can be written as

$$\begin{aligned} \eta(t) &= A_0 \cos(0 \cdot \omega_0 t) + B_0 \cdot \sin(0 \cdot \omega_0 t) \\ &+ A_1 \cos(\omega_0 t) + B_1 \cdot \sin(\omega_0 t) \\ &+ A_2 \cos(2\omega_0 t) + B_2 \cdot \sin(2\omega_0 t) \end{aligned} \quad (\text{D.15})$$

or

$$\eta(t) = A_0 + \sum_{n=1}^{N-1} [A_n \cos(n\omega_0 t) + B_n \sin(n\omega_0 t)] \quad (\text{D.16})$$

where  $\omega_0 = 2\pi f_0$

With a few transformations, the coefficients can be calculated by the following expressions:

$$A_n = \frac{2}{T} \int_0^T \eta(t) \cos(n\omega_0 t) dt \quad (\text{D.17})$$

and

$$B_n = \frac{2}{T} \int_0^T \eta(t) \sin(n\omega_0 t) dt \quad \text{for } n = 1, 2, \dots, N \quad (\text{D.18})$$

Considering that the function was sampled at regular time intervals,  $\Delta t$  and  $T = N \cdot \Delta t$ , the above integrals (D.17) and (D.18) can be replaced by summations.

$$A_n = \frac{2}{N\Delta t} \sum_{k=0}^{N-1} \eta_k \cos(n\omega_0 k\Delta t) \Delta t \quad (\text{D.19})$$

$$B_n = \frac{2}{N\Delta t} \sum_{k=0}^{N-1} \eta_k \sin(n\omega_0 k\Delta t) \Delta t \quad (\text{D.20})$$

$$A_n = \frac{2}{N} \sum_{k=0}^{N-1} \eta_k \cos\left(\frac{nk}{N} 2\pi\right) \quad n = 0 \dots\dots\dots N - 1 \quad (\text{D.21})$$

$$B_n = \frac{2}{N} \sum_{k=0}^{N-1} \eta_k \sin\left(\frac{nk}{N} 2\pi\right) \quad n = 0 \dots\dots\dots N - 1 \quad (\text{D.22})$$

It can be seen that

$$B_0 = 0 \quad (\text{D.23})$$

$$A_0 = \frac{2}{N} \sum_{k=0}^{N-1} \eta_k \quad (\text{D.24})$$

(Note for wave excursion  $A_0$  becomes 0)

When  $n(t)$  taken at time  $t_k$ , a Discrete Fourier Transform can be written as:

$$D_n = \sum_{k=0}^{N-1} \eta_k e^{-ink\omega_0} \quad \text{for } n = 0 \text{ to } N - 1 \quad (\text{D.25})$$

and the inverse Fourier Transform as:

$$\eta_k = \frac{1}{N} \sum_{n=0}^{N-1} D_n e^{ink\omega_0} \quad \text{for } k = 0 \text{ to } N - 1 \quad (\text{D.26})$$

where  $\omega_0 = \frac{2\pi}{N}$

Equations (D.25) and (D.26) represent the discrete analog of the equations (D.13) and D.14), respectively.

#### D.4 The Fast Fourier Transform (FFT)

The so called Fast Fourier Transform is a faster method of calculating the Discrete Fourier Transform and it exploits the periodicity and symmetry of trigonometric functions to reduce the number of operations from  $N^2$  to  $N \log_2 N$ . The idea behind it is to decompose a DFT of length  $N$  into successively smaller DFT's.

The equation (D.25) can be expressed as

$$D_n = \sum_{k=0}^{N-1} \eta_k W^{nk} \quad (\text{D.27})$$

where  $W = e^{-i\left(\frac{2\pi}{N}\right)}$

Dividing the sample into two, equation (D.27) in terms of the first and last  $N/2$  points becomes:

$$D_n = \sum_{k=0}^{\frac{N}{2}-1} \eta_k e^{-ink\frac{2\pi}{N}} + \sum_{k=\frac{N}{2}}^{N-1} \eta_k e^{-ink\frac{2\pi}{N}} \quad (\text{D.28})$$

rearranged:

$$D_n = \sum_{k=0}^{\frac{N}{2}-1} \eta_k e^{-ink\frac{2\pi}{N}} + \sum_{k=0}^{\frac{N}{2}-1} \eta_{k+\frac{N}{2}} e^{-in\left(k+\frac{N}{2}\right)\frac{2\pi}{N}} \quad (\text{D.29})$$

or

$$D_n = \sum_{k=0}^{\frac{N}{2}-1} \left( \eta_k + e^{-im\pi} \eta_{k+\frac{N}{2}} \right) e^{-ink\frac{2\pi}{N}} \quad (\text{D.30})$$

Recognising that  $e^{-in\pi} = (-1)^n$ , for even points is equal to 1, and for odd points is equal to -1. The equation (2.30) can be separated according to even values and odd values of n.

For even values

$$F_{2n} = \sum_{k=0}^{\frac{N}{2}-1} \left( \eta_k + \eta_{k+\frac{N}{2}} \right) e^{-ink\frac{2\pi}{N}} \quad (\text{D.31})$$

or

$$F_{2n} = \sum_{k=0}^{\frac{N}{2}-1} \left( \eta_k + \eta_{k+\frac{N}{2}} \right) W^{2kn} \quad (\text{D.32})$$

And for odd values

$$F_{2n+1} = \sum_{k=0}^{\frac{N}{2}-1} \left( \eta_k - \eta_{k+\frac{N}{2}} \right) e^{-ik\frac{2\pi}{N}} e^{-ink\frac{2\pi}{N}} \quad (\text{D.33})$$

$$F_{2n+1} = \sum_{k=0}^{\frac{N}{2}-1} \left( \eta_k - \eta_{k+\frac{N}{2}} \right) W^k W^{2kn} \quad (\text{D.34})$$

These even and odd expressions can be interpreted as being equal to the transforms of the N/2 - length sequences

$$g_n = \eta_k + \eta_{k+\frac{N}{2}} \quad (\text{D.35})$$

$$h_n = \left( \eta_k - \eta_{k+\frac{N}{2}} \right) W^k \quad \text{for } k=0, \dots, N/2 - 1 \quad (\text{D.36})$$

It follows that

$$D_{2n} = g_n \tag{D.37}$$

$$D_{2n+1} = h_n \quad \text{for } n=0, \dots, N/2 - 1 \tag{D.38}$$

The DFT is computed by first forming the sequence  $g_n$  and  $h_n$  and then computing the  $N/2$  DFT's to obtain the even and odd-numbered transformations.

### 2.5. The Frequency Spectrum

The periodic function  $\eta(t)$  can be presented in the frequency domain as a frequency spectrum when  $D_n$  versus  $f$  is plotted. Plotting  $|D_n|$  versus  $f$ , a two sided frequency spectrum is obtained. Considering that  $N$  time sample values are real numbers then only  $N/2$  frequency components values are complex numbers, the other  $N/2$  are their conjugates. Because the modulus of a conjugate is equal to the modulus of the complex number, the two sided frequency spectrum is obtained.

The value of the frequency over which the spectrum is folded is called the folding frequency or the Nyquist frequency. The frequency spectrum up to the Nyquist frequency is proportional to the sea energy per unit area.

Equation (D.25) can be rewritten, using Euler's identity

$$e^{\pm i\alpha} = \cos \alpha \pm i \sin \alpha \tag{D.39}$$

$$D_n = \frac{1}{N} \sum_{k=0}^{N-1} \left[ \eta_k \cos\left(k_n \frac{2\pi}{N}\right) - i\eta_k \sin\left(k_n \frac{2\pi}{N}\right) \right] \tag{D.40}$$

Comparing with equations (D.21) and (D.22)

$$|D_n| = \frac{\sqrt{A_n^2 + B_n^2}}{2} = \frac{c_n}{2} \tag{D.41}$$

Dividing  $c_n^2/2$  by  $\Delta f$  (chosen frequency interval), the new function is obtained which represents the energy density function.



## APPENDIX E

### Cross-spectral analysis theory summarised

Cross-spectral analysis determines the relationship between two data series in the frequency domain by evaluating the contribution of specific frequencies in both series to the total cross-covariance. The computation technique used for the crossspectra is essentially identical to that used for power spectra (e.g. Ilic, 1993). For more details, the reader is referred to Jenkins and Watts (1968), for example.

The cross-correlation function between two stationary processes  $x(t)$  and  $y(t)$  is estimated according to the formula

$$\rho_{x,y}(s) = \frac{\Xi_{xy}(s)}{\sqrt{\Xi_{xx}(0)\Xi_{yy}(0)}} \quad (\text{E.1})$$

where  $\rho_{xy}(s) \neq \rho_{yx}(s)$  and

where  $\Xi_{xy}(s)$  is the cross-covariance function

$$\Xi_{xy}(s) = \lim_{T \rightarrow \infty} \frac{1}{2T} \int_{-T}^T x(t)y(t-s)dt \quad (\text{E.2})$$

and  $x(t)$  and  $y(t)$  represent sample functions of the processes  $x(t)$  and  $y(t)$ .

The cross spectrum is defined as the Fourier transform of the cross-covariance function

$$P_{xy}(f_n) = \frac{1}{\pi} \int_{-\infty}^{\infty} \Xi_{xy}(s) e^{-if_n s} ds \quad (\text{E.3})$$

Or using the FFT

$$P_{xy}(f_n) = P_x(f_n)P_y^*(f_n) \quad (\text{E.4})$$

where  $P_x$  and  $P_y$  represent the FFT's of the two time series. The asterisk denotes the complex

conjugate (note that  $P_x$  and  $P_y$  are autospectra ).

Being a complex quantity  $P_{xy}(f_n)$  can be written as

$$P_{xy}(f_n) = co_{xy}(f_n) + iq_{xy}(f_n) \quad (\text{E.5})$$

where  $co(f_n)$  is the co-spectrum ( a measure of the in-phase covariance), and  $q(f_n)$  is the quadrature spectrum ( a measure of the out of phase covariance).

This can be written as

$$\begin{aligned} co(f_n) &= Re_x Re_y + Im_x Im_y \\ iq(f_n) &= i(Im_x Re_y - Re_x Im_y) \end{aligned} \quad (\text{E.6})$$

The co - spectrum measures the contribution of oscillations of different frequencies to the total crossvariance of lag zero between two time series. The quadrature spectrum measures the contribution of the different harmonics to the total cross-covariance between the series when all the harmonics of the series  $x(t)$  are delayed by a quarter period but the series  $y(t)$  remains unchanged (Rodriguez, 1969).

From Cramer's spectral representation, any stationary series can be considered as a sum of components of frequency bands, each component being statistically independent of the others (Cramer, 1940,1942 in Rodriguez, 1969). The theory of stationary processes tell us that not only is the component with centre  $f_{ni}$  independent of all the other components of the variable, but it is independent of all components of another variable except the component centred on  $f_{ni}$  (Granger & Hatanaka, 1964 in Rodriguez, 1969).

Considering the process  $y(t)$  as the output of the system an important relation holds between  $P_{xx}(f_n)$ ,  $P_{yy}(f_n)$  and the frequency response function of the system,  $R(f_n)$ , defined as the Fourier transform of the unit impulse response function. This relation is

$$P_{yy}(f_n) = |R(f_n)|^2 P_{xx}(f_n) \quad (\text{E.7})$$

For linear systems, it holds true that

$$S_{xy}(f_n) = H(f_n) S_{xx}(f_n) \quad (\text{E.8})$$

Because  $P_{xx}(f_n)$  is positive, it follows that

$$|P_{xy}(f_n)| = P_{xx}(f_n) |R(f_n)| \quad (\text{E.9})$$

and  $|R(f_n)|$  is usually called gain function or transfer function

$$|R(f_n)| = \frac{|P_{xy}(f_n)|}{P_{xx}(f_n)} \quad (\text{E.10})$$

or as used for analysis

$$|R(f_n)| = \frac{|P_{xy}(f_n)|}{P_{yy}(f_n)} \quad (\text{E.11})$$

Thus from previous relations

$$R(f_n) = \frac{P_{xy}(f_n)}{|P_{xx}(f_n)|} \quad (\text{E.12})$$

The transfer function is related to the cross-spectrum and one of the auto-spectra which does not give the complete information.

A direct measure of the square of amplitude correlation at frequency  $f_n$  is given by the coherence function

$$r_{xy}^2(f_n) = \frac{c_{xy}^2(f_n) + q_{xy}^2(f_n)}{P_{xx}(f_n) + P_{yy}(f_n)} \quad (\text{E.13})$$

or

$$\overline{r_{xy}^2}(f_n) = \frac{|\overline{P_{xy}(f_n)}|^2}{\overline{P_x(f_n)} \overline{P_y(f_n)}} \quad (\text{E.14})$$

where  $0 \leq \overline{r^2}(f_n) \leq 1$ , and the overbar ( $\overline{\quad}$ ) means smoothed and windowed spectrum to suppress leakage

If  $\overline{r_{xy}}(f_n) = 1$ , there is perfect coherence at the discrete frequency  $f_n$ . If  $\overline{r_{xy}}(f_n) = 0$ , there is no coherence. The absence of coherence does not indicate that records are independent, it merely states that there exists no linear relation between them (Rodriguez, 1969).

Even if amplitudes are fully correlated, it is possible that the corresponding frequency

components will have different phases. The phase lag at each frequency is given by

$$\bar{\vartheta}_{xy}(f_n) = \tan^{-1} \left[ \frac{\bar{q}(f_n)}{c(f_n)} \right] \quad (\text{E.15})$$

If  $0 < \bar{\vartheta} < \Pi$  then the  $x(t)$  record leads the  $y(t)$ , if  $-\Pi < \bar{\vartheta} < 0$  then the  $x(t)$  record lags the  $y(t)$  record.

Confidence limits for coherence and phase spectra are functions of the number of degree of freedom (d.o.f. =  $\nu(n)$ ) of the smoothed cross-spectrum. D.o.f. is equal to  $2pl$  where  $p$  is the number of ensemble averaging and  $l$  is the number of frequency points for frequency smoothing.

Jenkins and Watts (1968) showed that the observed smoothed coherence

$\bar{K}_{xy}$  ( $\bar{K}_{xy} = \sqrt{\bar{r}_{xy}^2}$ ) is related to normally distributed, random variable  $\bar{Y}_{xy}$  such that;

$$\bar{Y}_{xy}(f) = \operatorname{arctanh} |\bar{K}_{xy}(f)| = \frac{1}{2} \ln \left\{ \frac{1 + |\bar{K}_{xy}(f)|}{1 - |\bar{K}_{xy}(f)|} \right\} \quad (\text{E.16})$$

The distribution of this random variable with independent variance can be approximate with the Normal distribution. Tables exist for unit normal distribution functions. The  $100(1-\alpha)\%$ , confidence interval limits on  $\bar{Y}_{xy}(f)$  are given by

$$\bar{Y}_{xy}(f) \pm \eta \left(1 - \frac{\alpha}{2}\right) \sqrt{\frac{1}{\nu}} \quad (\text{E.17})$$

where  $\nu$  presents the number of degrees of freedom.

Such limits can be transformed back to the original scale using the inverse of equation (E.16). Calculation of the phase confidence limits is still very poorly known. Jenkins and Watts (1968), suggested a method of calculation and produced a graph for 95% confidence intervals as a function of degrees of freedom and coherence. This graph was used in further analysis.

## APPENDIX F

### Generation of synthetic wave data

There are several existing numerical synthesis model classification. According to Borgman (1969), there are two basic methods to generate synthetic wave data:

-wave superposition and

-linear filters.

Wave superposition methods can be either single or double summation models. The numerical simulation of random sea waves with a double summation model is well described in Goda (1985). One of the earliest double summation model was given by Borgman (1969)

$$\eta(x, y, t) = \sum_{i=1}^I \sum_{j=1}^J a_{ij} \cos(\omega_{ij}t - k_i x \cos \theta_{ij} - k_j y \sin \theta_{ij} + \vartheta_{ij}) \quad (\text{F.1})$$

where

the amplitude  $a_{ij}$  are determined by

$$a_{ij} = \sqrt{2S_{\eta}(f_i, \theta_j) \Delta \theta \Delta f} = \sqrt{2S_{\eta}(f) G(f_i, \theta_j) \Delta \theta \Delta f} \quad (\text{F.2})$$

$S_{\eta}$  = spectral density

$\vartheta_{ij}$  = phase angles which are randomly selected from a uniform distribution  
 $U(0, \pi)$

The double summation is carried out for I frequencies, each of which has J directional components. Sand and Mynett (1987) described the implication of limited number of frequencies on the simulation results using a double summation model. An incoming and reflected wave at the same frequency will create a phase locked pattern. The resulting spectrum will depend on the selected phase angle. To avoid this effect, it is important not to add up the components with different directions at the same frequency. The alternative is a single summation model (e.g. Sand and Mynett, 1987), that is:

$$\eta(x, y, t) = \sum_{i=1}^I a_{ij} \cos(\omega_i t - k_i x \cos \theta_{ij} - k_j y \sin \theta_{ij}) + b_{ij} \sin(\omega_{ij} t - k_i x \cos \theta_{ij} - k_j y \sin \theta_{ij}) \quad (\text{F.3})$$

The amplitudes are chosen as

$$a_{ij}^2 + b_{ij}^2 = 2S_\eta(f)\Delta t \quad (\text{F.4})$$

Only one direction of propagation is chosen at each frequency. It also takes a small band of frequencies to describe a whole directional distribution.

Simulation by linear filtering is based on determination of the digital filter values. Digital filters are designed to be applied to an initial sequence on number to produce a new sequence with the desired properties. White noise is very convenient for simulation of the initial sequence. This is the random input which has spectral density of unity. It remains to determine the digital filter to simulate sea surface elevation which has determined spectral density. Borgman (1969) presented surface elevation simulation in the time domain using a non-recursive linear digital filter. Christensen (1996) extended the time domain method for numerical unidirectional wave generation to multidirectional wave conditions. Applying a non-recursive linear digital filter signal at any position  $y$  can be determined (Christensen, 1996) as follows:

$$X(y, n\Delta t) = \sum_{j=1}^J \sum_{i=1}^I h_i^j \alpha_{n-i}^j, \dots n = 1 \dots N \quad (\text{F.5})$$

where the desired gain  $D$  and phase  $\phi$  of the filter operator  $h$  are given by the equation:

$$|D^j(\omega)| = \sqrt{\frac{\pi}{\Delta t}} \frac{1}{K_f(\omega_j, \theta_j)} \sqrt{S_\eta(\omega_j, \theta_j) \Delta \theta} \quad (\text{F.6})$$

where

$$K_f = \frac{2 \sinh^2 kd}{\sin kd \cosh kd + kd} \quad (\text{F.7})$$

$$\begin{aligned}\phi^j(\omega) &= -ky \sin \theta_j \\ \theta_j &= (j-1)\Delta\theta + \theta_{\min}\end{aligned}\tag{F.8}$$

and  $\alpha^j$  represents a sequence of independent standard normal distributed random numbers  $\alpha_n^j: \mathcal{N}(0,1)$ .

The surface elevation in the combined wave field with present reflection can be written as follows

$$\begin{aligned}\eta(x,y,t) &= \sum_{i=1}^I \sum_{j=1}^J a_{ij} \cos(k_i x \cos \theta_j + k_i y \sin \theta_j - \omega_i t + \mathcal{G}_{ij}) + \\ &\quad \sum_{i=1}^I \sum_{j=1}^J K r_i a_{ij} \cos(k_i x (-\cos \theta_j) + k_i y \sin \theta_j - \omega_i t + \mathcal{G}_{ij})\end{aligned}\tag{F.9}$$

therefore the previously mentioned Christensen (1996) model was adapted by Helm-Petersen (private communication) for the reflected sea.

To determine the parameters in the equations (F.2, F.4) and (F.6) the directional spectrum  $S_\eta(f,\theta)$  should be known, where

$$S_\eta(f,\theta) = S(f)G(f,\theta)\tag{F.10}$$

The frequency spectrum  $S(f)$ , of fully developed wind waves can be approximated by one of the following formulae (see e.g. Goda, 1985)

*Pierson Moskowitz*

$$S(f) = \frac{0.0004988}{f^5} e^{-\left[1.25\left(\frac{f_p}{f}\right)^4\right]}\tag{F.11}$$

where

$$f_p = T_p^{-1}$$

or *Jonswap* based on the observations on North Sea (see e.g. Goda, 1985)

$$S(f) = \frac{aH_s^2 f_p^4}{f^5} e^{-\left[1.25\left(\frac{f_p}{f}\right)^4\right]} \gamma e^{-\left[\frac{(f-f_p)^2}{2\sigma^2 f_p^2}\right]} \quad (\text{F.12})$$

where

$$a = \frac{0.0624}{\left[0.230 + 0.0336\gamma - \frac{0.185}{1.9 + \gamma}\right]} \quad (\text{F.13})$$

$$\begin{aligned} \sigma &= 0.07 \quad \text{for } f \leq f_p \\ \sigma &= 0.09 \quad \text{for } f > f_p \end{aligned} \quad (\text{F.14})$$

and  $f_p = T_p^{-1}$ ;  $\gamma = 1.7$  (mean 3.3)

And directional spreading function,  $G(f, \theta)$  is for example determined by *Mitsuyasu* model (*Mitsuyasu et al*, 1975 or see e.g. *Goda*, 1985)

$$G(f, \theta) = G_0 \cos^{2s} \left( \frac{\theta}{2} \right) \quad (\text{F.15})$$

where

$$G_0 = \frac{1}{\pi} 2^{2s-1} \frac{\Gamma^2(s+1)}{\Gamma(2s+1)} \quad (\text{F.16})$$

$s=10$  correspond to wind waves

$s=25$  correspond to swell with short decay distance

$s=75$  correspond to swell with long decay distance



## **APPENDIX G**

### **Evaluation and Validation of the Mild Slope Evolution Equation Model Using Field Data**

A copy of the paper printed out in *Proceedings Coastal Dynamics '95*, Gdansk 1995,  
ASCE, New York, 1996, pp 149 - 160

# **Evaluation and Validation of the Mild Slope Evolution Equation Model Using Field Data**

Suzana Ilić and Andrew Chadwick<sup>1</sup>

## **Abstract**

This paper describes the application of a new version of the mild slope equation to a detached offshore breakwater scheme. Details of the computational model are briefly described with aspects of its capabilities. The field site at Elmer, Brighton, UK is then described. The field measurements, analysis and data selection for model evaluation are summarised with particular attention focussed on the spectral and directional results. Monochromatic and directional model runs are described. Results from the model are compared to the comprehensive recorded field data from which a preliminary evaluation of its performance is made.

## **Introduction**

The evolution of the shoreline behind offshore detached breakwaters is principally determined by wave diffraction. However, wave transmission through permeable breakwaters has also been suggested by Hanson et al (1989,1990) to have a strong influence in determining the shoreline changes. One way to predict the resultant morphology requires known wave conditions around the breakwaters. These wave conditions can be predicted using a Refraction - Diffraction Model (preferably including wave transmission) with a known offshore wave field. Such predictive models have been developed but remain largely untested against comprehensive field data sets. Field measurements, at a site at Elmer - UK, recently completed by the Universities of Brighton and Plymouth as reported by Chadwick et al (1994), provide the opportunity to evaluate and validate such computational models.

<sup>1</sup> Research Assistant and Reader, School of Civil and Structural Engineering, University of Plymouth, Palace Court, Plymouth PL1 2DE, UK

## Computational model

Berkhoff (1972) developed a combined refraction-diffraction model based on the so called 'mild slope equation', given by

$$\nabla(cc_g \nabla \Phi) + cc_g k^2 \Phi = 0$$

where

$c$  = phase celerity,  $c_g$  = group celerity,  $k$  = wave number,  $\Phi$  = complex wave potential function

It can model refraction, diffraction and reflection. By introducing the effects of wave breaking it can be used over the whole coastal zone. Such models have largely replaced refraction models for more restricted areas, although they must be applied with care due to assumptions made in their derivation. The 'mild slope equation' is an elliptic differential equation. Very often the elliptic equation is slightly modified in order to speed convergence and execution time. Li (1994) derived a model with a time-dependent evolution equation based on the original mild slope equation given by

$$-\frac{2\omega i}{cc_g} \frac{\partial \Phi}{\partial t} = \nabla^2 \Phi + k_c^2 \Phi$$

where

$\omega$  = wave angular frequency,  $\phi = \Psi(c c_g)^{1/2}$  and  $\Phi(x,y,t) = \Psi(x,y,\bar{t}) e^{-i\omega t}$

Harmonic time is excluded to achieve fast convergence. The model is capable of dealing with refraction, diffraction and reflection, overcoming the main disadvantage of some previous models based on the mild slope equation. The boundary conditions are the same as for the elliptic equation, making this model easier to solve than hyperbolic models. The offshore boundary is specified as the known incident wave field, and reflected waves propagate out of the field. Shoreward and lateral boundaries are applied to the outgoing and reflected waves, where the reflection coefficient is taken in account, and varies with the type of boundary and may have to be determined empirically. The numerical scheme which is used is the unconditionally stable Alternating Direction Implicit Scheme.

A series of preliminary tests using Li's model has been undertaken for the Elmer scheme in which the model boundary conditions were taken from offshore field measurements, and the model predictions compared with both inshore and shoreline measurements.

## Field measurements

Field measurements were taken at Elmer near Brighton, Sussex, UK where a

scheme of eight offshore breakwaters were constructed in Summer 1993 ( see Figure 1). Their role is to maintain the renourished beach which protects the hinterland from flooding. The beach behind the breakwaters lies on a wave cut platform of Upper Cretaceous chalk with a gradient of approximately 1 in 50. Above the chalk, a layer of sand ( $D_{50} = 115 \mu\text{m}$ ) forms a low tide terrace, and the upper beach is mainly composed of shingle ( $D_{50} = 11 \text{ mm}$ ). The area is macro-tidal, with a mean range of 5.3 m on spring tides and 2.9 m on neaps.

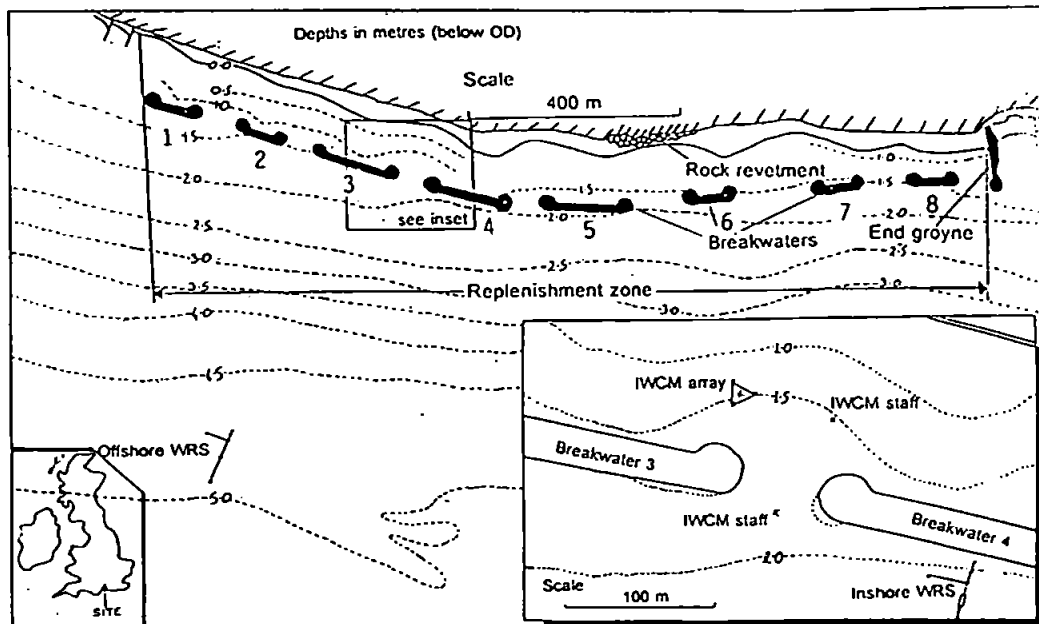


**Figure 1** Site and instrumentation location and siting

Two different types of equipment were deployed for the wave measurements. Their locations are given in Figure 1. An array of six pressure transducers over an area of  $60 \times 16 \text{ m}$  was deployed offshore to measure directional waves approaching the shoreline. Data were collected every 3 hours for 12 minutes with a sampling frequency of 2 Hz. A star array of four surface piercing wave resistance staffs was deployed in the lee of breakwater 3 to give directional information inshore after waves were refracted and diffracted. Two additional independent wave probes were deployed one in the gap between breakwaters 3 and 4 and another one shoreward of the gap. They collected data every 3 hours for 17 minutes with sampling frequency of 4 Hz but were only operational for approximately half the tidal cycle. Additionally an array of 6 pressure transducers was deployed in the front of breakwater 4 to measure reflection for a period of two months in Spring 1994. Wave recorders were deployed from September 1993 until January 1995 and measurements were taken continuously for a year.

## Data selection for model evaluation

All data were processed using the Fast Fourier Transform algorithm in conjunction with a full width Welch window with overlapping subsets of data. Ensemble averaging of the resulting Fourier coefficients was then applied together with spectral smoothing as described by Chadwick et al (1995 a,b). Assuming that offshore incident and reflected waves were not phase locked, the Maximum Likelihood Method (MLM) was used for directional analysis at both the offshore and inshore locations. Figure 2 shows the directional energy recorded offshore and inshore for a particular event in April. Here the modification of directional spectra from offshore to inshore is evident. The broad spectrum containing reflection offshore becomes a narrow spectrum inshore with a very small amount of reflection.

a) Directional wave spectrum offshore on 9/04/1994 23h 20min      b) Directional wave spectrum inshore on 9/04/1994 23h 20min

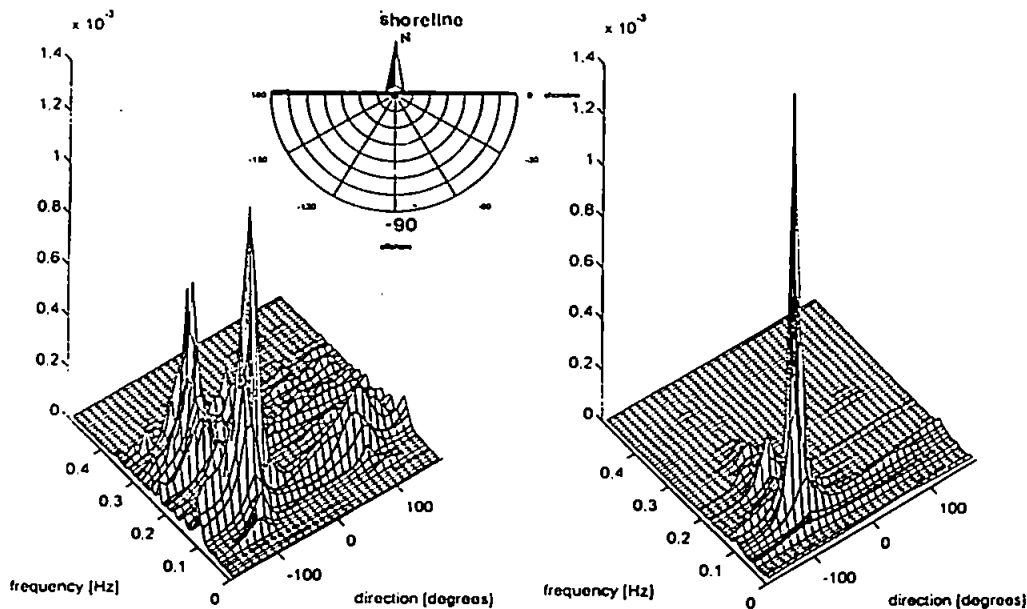


**Figure 2** Example spectral and directional analysis result (a) offshore, (b) inshore

The following criteria were applied to choose the data for the model evaluation (similar to Dingemans et al 1984)

- synchronous wave measurements  $t - 20 \text{ min} \leq t_0 \leq t + 20 \text{ min}$  (91% data are in time interval  $\pm 10 \text{ min}$ )
- wave height  $> 0.5 \text{ m}$
- high tide - to have reasonable depth of water in the area behind breakwaters (ie depth between 2.6 and 3.6 m inshore and between 6.8 and 8.0 offshore)

- small values of offshore reflection coefficient (It should also be noted that the MLM was found to be incapable of completely resolving all of the offshore wave energy into incident and reflected components for some of the field data sets. This presented considerable difficulties in determining the true incident offshore wave field boundary condition for the model.)

About 70 data sets were chosen based on the above criteria. The frequency spectra were then classified as follows

- monochromatic (narrow frequency band)
- bimodal (with two distinguished peaks - usually swell and wind peaks)
- wide frequency spread (broad frequency distribution - wind spectra)

### Computational area

A computational area of 2000 m (alongshore) x 850 m (crossshore) was chosen. A grid spacing of 5 x 5 m was used which gives 401 x 171 points. Additionally a grid spacing of 2 x 2 m was also used for a more restricted area (401 x 401 points). The beach changes behind breakwaters were surveyed by aerial photography and processed every 3 months (Axe, 1995). Offshore bathymetry is very stable, but the beach changes are included in four different bathymetries for model evaluation.

### Results

Typical model output with wave height contours is shown in Figure 3. Standing wave fields could be observed in the front of the breakwaters as could the wave height attenuation behind the breakwaters due to diffraction.

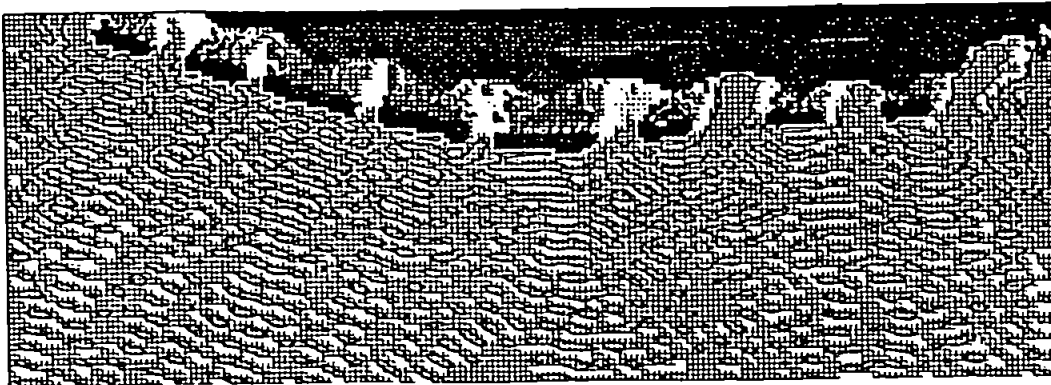


**Figure 3** Typical model output

Figure 4 a,b,c show the comparison between measured and calculated wave heights for the three inshore positions where the field measurements are compared with monochromatic model results. Each of the offshore measured directional spectra are represented in the monochromatic model by the peak frequency, the main wave direction and significant incident wave height. Figure 4a compares model results and

field measurements for the position in the lee of the breakwater. There are several discrepancies. A possible reason for the large disagreement between predicted and calculated wave heights is due to the lack of energy transmission by radiation, into the lee of the breakwater, when using the monochromatic wave model. In the position shoreward of the breakwater gap, there is better agreement between measured and calculated wave heights (Figure 4b). In the third position in the breakwater gap (Figure 4c), there is a small overestimate of the calculated wave heights.

The influence of the spectrum shape and frequency distribution on the results were then investigated. So far no relation has been observed. It could be expected that the errors in results depend on frequency ( because the value of the reflection coefficient is related to the frequency), and some further investigations need to be carried out. A quantitative measure of the accuracy of the results has also been made, using a relative root mean square difference between measured values and numerical model predictions for three different positions inshore given by

$$dif_{rms} = \sqrt{\frac{\sum \left( \frac{H_m - H_c}{H_m} \right)^2}{N}}$$

where:

$H_m$  = measured wave height,  $H_c$  = calculated wave height by numerical model,  
 $N$  = number of tests

The summary of results is given in Table 1

**Table 1** Summary of results for monochromatic case

Position	Relative mean square difference	Error Percentage
in the gap	0.32	32.69 %
shoreward of the gap	0.52	40.49 %
in the lee of breakwater	0.54	46.50 %

The monochromatic model was also used to predict wave heights in front of breakwater 4 and compared with the measurements of Davidson and Bird (in press). The reflection coefficient for this case was 0.4 evaluated from the measurements. The calculated and measured wave heights were compared and the relative mean square difference was only 0.0669 which shows very good agreement and the capability of the model to predict accurately the wave height in the front of the structures in a regime of strong reflection.

The use of the monochromatic wave model to represent real irregular waves with directional spreading confirmed that significant underestimation of wave conditions behind the breakwater occurred. This has also been found by Goda (1978,1985), Grassa (1990), Vincent and Briggs (1989), Briggs et al (1995).

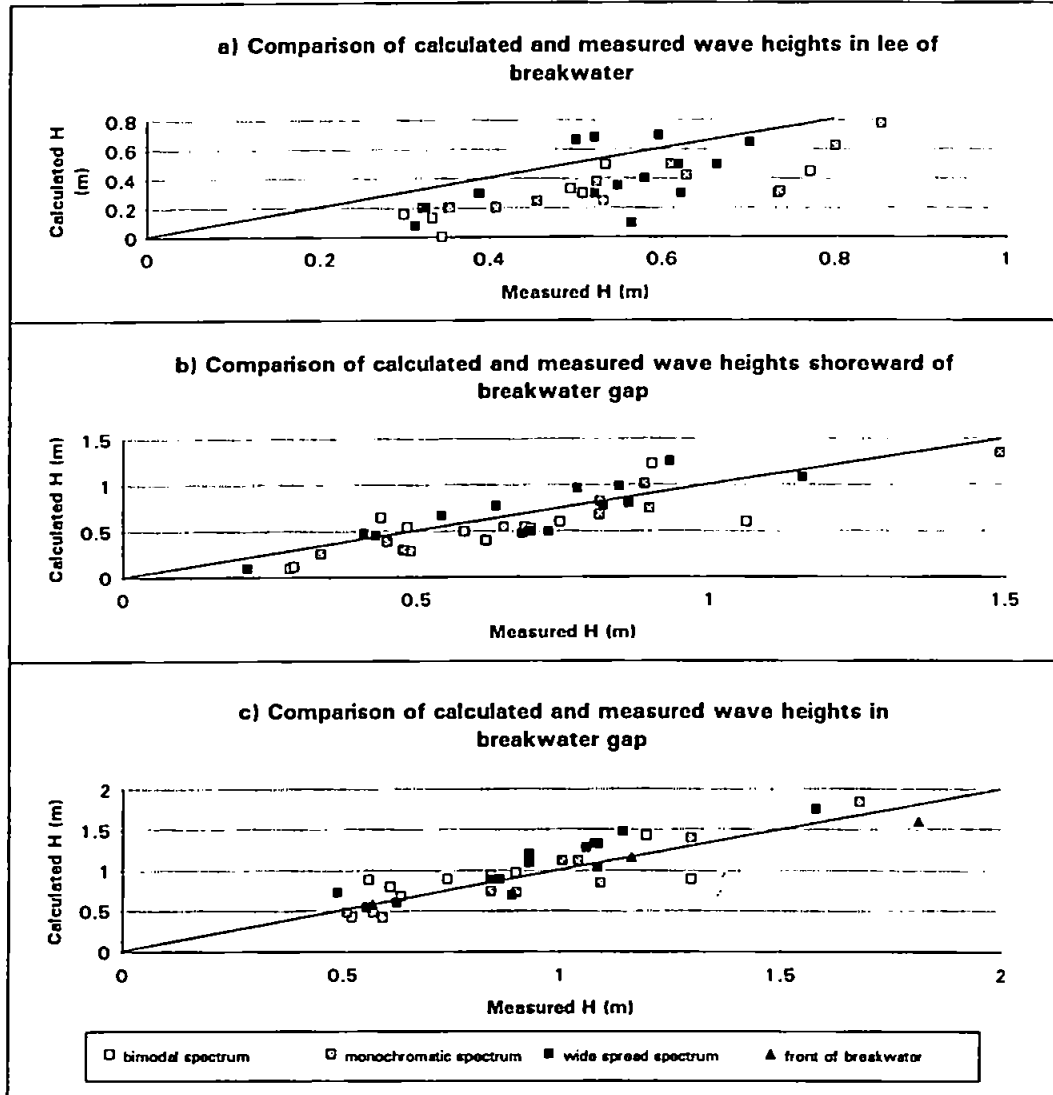


**Figure 4** Comparison of calculated and measured wave heights for monochromatic case-(a) lee of breakwater, (b) shoreward of breakwater gap, (c) breakwater gap

### Directional modelling

The next step was to simulate directional waves under the assumption of the validity of linear superposition as a method for the description of irregular waves. Thus the measured wave spectrum could be represented by a number of monochromatic waves. There are two methods which can be used to discretise the spectrum - a



constant step method or energetically equalized discretisation. The latter one was chosen for the evaluation of the model. The directional wave spectrum is given by  $S(f, \theta) = S(f) G(f, \theta)$  where  $G(f, \theta)$  is a normalized spreading function between given cut-off values,  $(f_{\min}, f_{\max}), (\theta_{\min}, \theta_{\max})$  in  $N_f, N_\theta$  components each of which is defined by a corresponding frequency, direction and wave amplitude  $(f_i, \theta_{ij}, a_{ij}, i=1, N_f, j=1, N_\theta)$  where

$$f_i \text{ given by: } \int_{f_{\min}}^{f_i} S(f) df = \left(\frac{m_0}{N_f}\right)(i-0.5)$$

$$\theta_{ij} \text{ given by: } \int_{\theta_{\min}}^{\theta_{ij}} G(f, \theta) d\theta = \left(\frac{1}{N_\theta}\right)(j-0.5)$$

$$a_{ij} = \sqrt{\frac{2m_0}{N_f N_\theta}}$$

It should be noted that there are some small differences between these equations and the technique used in practice as the spectral shape is not directly integrable and depends on the frequency and direction increments derived from the spectral analysis. The advantages of this method are described by Grassa (1990).

## Tests and results

Irregular model tests have been carried out for three data sets measured in October 1994. The incident wave heights were greater than 1 m offshore and the measured averaged reflection coefficient was low (about 0.15 - 0.2). Tests were carried out to investigate the sensitivity to the chosen number of frequency intervals. The directional spectrum was represented by sixty four monochromatic waves for each frequency interval and one main direction (the frequency dependence of the reflection coefficient was also taken in account). It was found that the inshore calculated spectrum had the same shape as the measured spectrum offshore. The calculated inshore energies in each frequency interval were overestimated (see Figure 5a).

Tests were then carried out taking into account only seven frequency intervals but introducing four directional intervals. The measured and calculated energies for each frequency interval summed over all directions were found to be in very good agreement except for very low and very high frequencies (Figure 5b). The energy summed over all frequencies for particular direction intervals is not in such good agreement (Figure 5c). This suggests that insufficient direction intervals were used.

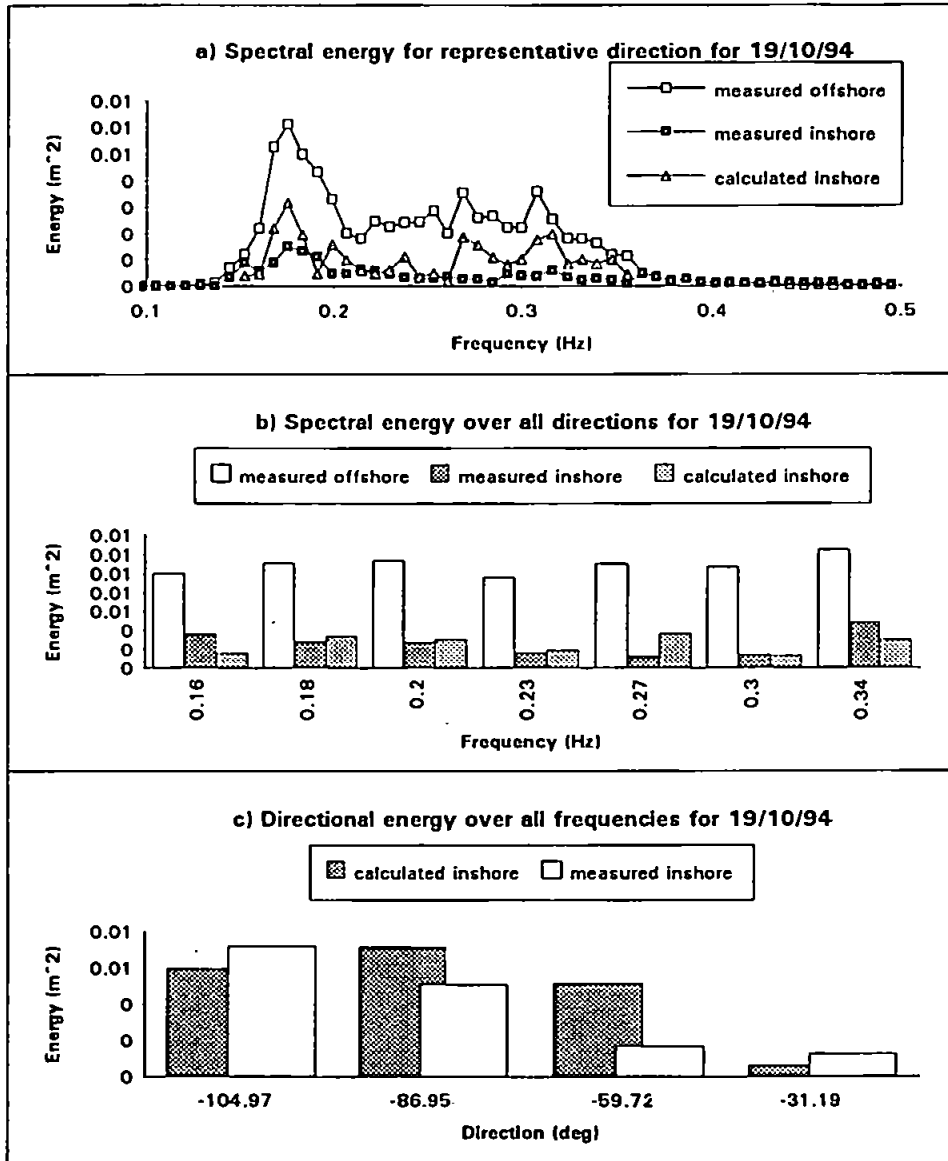


**Figure 5** Directional results summary - (a) spectral energy, (b) spectral energy over all directions, (c) spectral energy over all frequencies

**Table 2** Summary of results for directional irregular wave modelling

Position	Relative mean square difference	Error Percentage
in the gap	0.1044	8.45 %
shoreward of the gap	0.1152	9.7 %
in the lee of breakwater	0.1454	12.24 %

A relative root mean square difference between measured and predicted results for the three positions inshore, are shown in Table 2. The results in Table 1 and Table 2 will be compared when validation is completed.

## Discussion

Figure 6 a,b,c show the summary of all results and tests carried out. The disagreement between measured and calculated wave heights using monochromatic model runs can be clearly seen. This disagreement could be caused by several reasons. First the model is linear and even though the model was used for the larger recorded

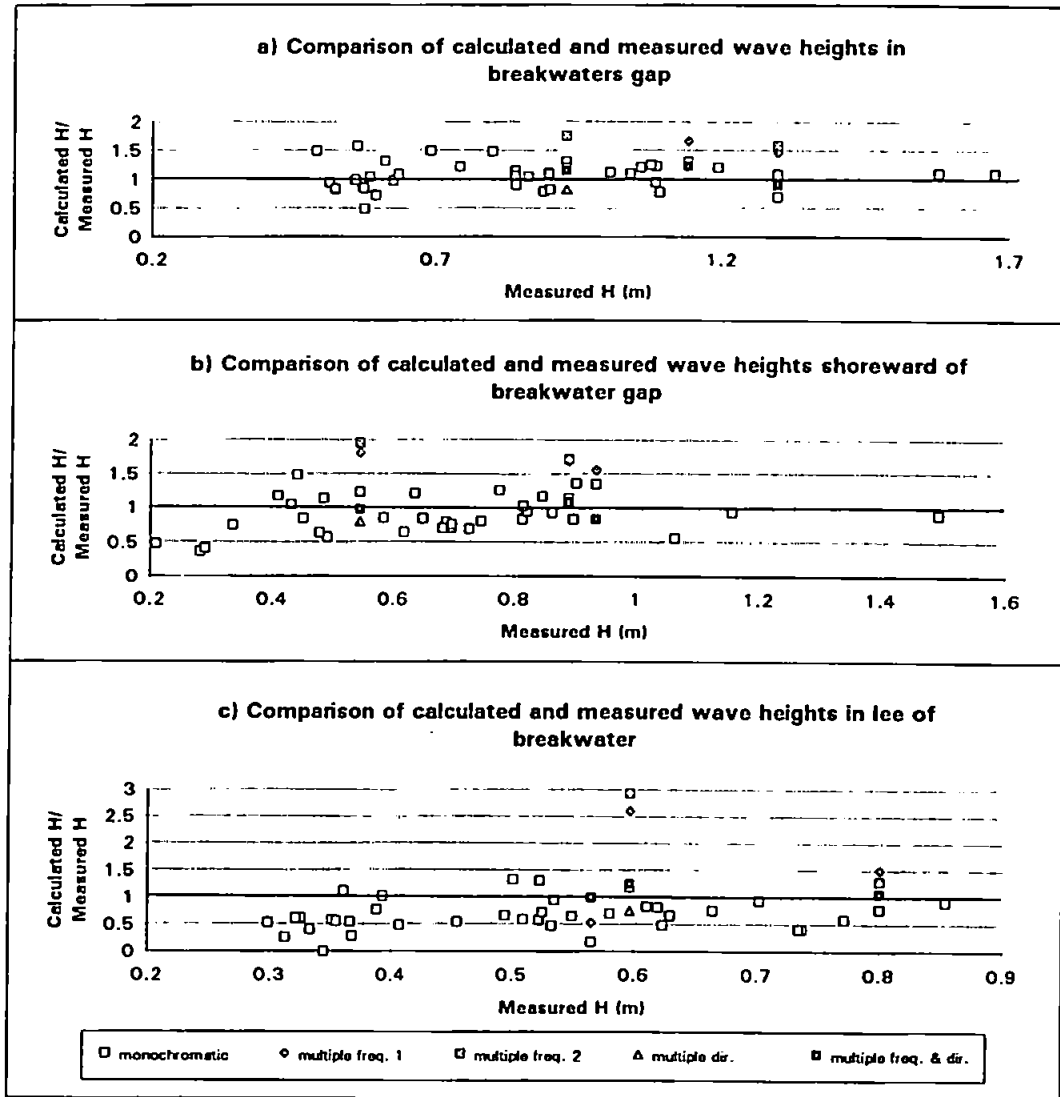


Figure 6 Comparison of calculated and measured wave heights - summary - (a) breakwater gap, (b) shoreward of breakwater gap, (c) lee of breakwater

water depths, some non linearities may be present which can not be modelled by this particular model. Wave breaking, bed friction and wave current interaction are also not taken in account. Transmission is not included in the model either. However, probably the most important errors occur in estimating the wave heights in the lee of the breakwater using the regular (monochromatic) wave model which does not take account of the directional effects. From these reasons the induced errors are larger in the lee of the breakwater than in the gap or shoreward of the gap. The errors could also be caused by incorrect estimation of reflection coefficient. The model is very sensitive to reflection so the proper estimation of the coefficient is necessary. Choosing a non-directional irregular field with a larger number of frequencies did not improve the results. Better agreement was obtained for directional irregular modelling when the effects of directional spread were taken in account. The results also show that a larger number of directional intervals should be chosen to represent the directional sea properly. So far the results show that the linear model based on the Mild Slope Equation can be used to model the sea state around breakwaters but it is very important to take directional effects in account. It is felt that it is necessary to take some more measurements to evaluate transmission and wave currents effects, and this research has now started (Chadwick et al (1995c)).

## **Conclusions**

The wave transformation model successfully deals with combined refraction, diffraction and reflection. Monochromatic wave runs can significantly overpredict or underpredict wave heights shoreward of the breakwaters in the diffraction region. Therefore it is important to consider irregular waves. Using irregular waves, it appears that directional spread has more influence than frequency spread in determining wave heights in the diffraction zone. The importance of taking the proper reflection coefficient needs to be further investigated. The model does not deal with transmission, which may be important in forming the beach behind the breakwaters. This should be implemented in the model. The influence of wave breaking, bed friction and wave current interactions should also be further investigated. The final evaluation of the model will determine its capabilities and limitations with regard to these factors and hence its applicability to design process for coastal works.

## **Acknowledgements**

The financial support of the Science and Engineering Research Council through research grants GR/H74360 GR/J5947 and GR/H2969, Arun District Council and The Standing Conference on Problems Associated with the Coastline is gratefully acknowledged. Thanks also to Prof Chris Fleming and Dr Li Bin of Sir William Halcrow and Partners for their support.

## References

- Axe P.G., 1994, Elmer Frontage Beach Development February 1992 - October 1994, SCSE Internal Report 94-004.
- Berkhoff J.C.W., 1972, Computation of combined refraction-diffraction, *In: Proc. 13th Conf. Coastal Eng.*, Vancouver, ASCE, Vol.1, pp 471-490.
- Briggs M.J., Thompson E.F. and Vincent C.L., 1995, Wave Diffraction Around Breakwater, *J. Wtrway. Port. Coast. and Oc. Engrg.*, ASCE, 121(1), pp 23-35.
- Chadwick A.J., Fleming C.A., Simm J. and Bullock G.N., 1994, Performance Evaluation of Offshore Breakwaters: A Field and Computational Study, *Proc. Conf. Coastal Dynamics '94*, ASCE, Barcelona, pp 950-961
- Chadwick A.J., Pope D.J., Borges J. and Ilic S., 1995a, Shoreline Directional Wave Spectra Part 1: An Investigation of Spectral and Directional Analysis techniques, *Proc Inst Civil Eng, Water Maritime & Energy*, 112(3), pp 198 - 208.
- Chadwick A.J., Pope D.J., Borges J. and Ilic S., 1995b, Shoreline Directional Wave Spectra Part 2: Instrumentation and Field Measurements, *Proc Inst Civil Eng, Water Maritime & Energy*, 112(3), pp 209 - 214.
- Chadwick A.J., Bird P.A.D. and Bullock G.N., 1995c, Analytical and Field Studies of Wave Transformation and Attenuation Processes Around Rock Island Breakwaters, EPSRC, GR/K48594
- Davidson M.A., Bird P.A.D., 1995, Full Scale Measurements of the Reflection Performance of Rock Island Breakwaters of Variable Slope, submitted to *Coastal Engineering*.
- Dingemans M.W., Stive M.J.F., Kuik A.J., Radder A.C. and Booij N., 1984, Field and Laboratory Verification of the Wave Propagation Model Crediz, *Proc. 19th Conf. Coastal Eng.*, Houston, pp 1178-1191.
- Goda Y., Takayama T. and Suzuki Y., 1978, Diffraction Diagram for Directional Random Waves, *Proc. 16th Conf. Coastal Eng.*, ASCE, Hamburg, pp 628-650.
- Goda Y., 1985, Random Seas and Design of Maritime Structures, *University of Tokyo Press*
- Grassa J.M., 1990, Directional Random Waves Propagation on Beaches, *Proc. 22nd Conf. Coastal Eng.*, Delft, pp 798-811.
- Hanson H., Kraus N. C. and Nakashima L. D., 1989, Shoreline Change Behind Transmissive Detached Breakwaters, *Proc. Coastal Zone '89*, ASCE, pp 568-582.
- Hanson H. and Kraus N. C., 1990, Shoreline Response to a Single Transmissive Detached Breakwater, *Proc. 22nd Conf. Coastal Eng.*, Delft, pp 2034-2046.
- Li B, 1994, An Evolution Equation for Water Waves, *Coastal Eng.*, 23, pp 227-242.
- Vincent C.L. and Briggs M.J., 1989, Refraction - Diffraction of Irregular Waves Over a Mound, *J. Wtrway. Port. Coast. and Oc. Engrg.*, ASCE, 115(2), pp 269-284.

## **APPENDIX H**

### **Directional Results Summary**

- Files:**
- 65** - bimodal sea in Figure H.1
  - 69** - wind sea in Figure H.2
  - 72** -swell sea in Figure H.3
  - 73** -swell sea in Figure H.4
  - 75** -wind sea in Figure H.5

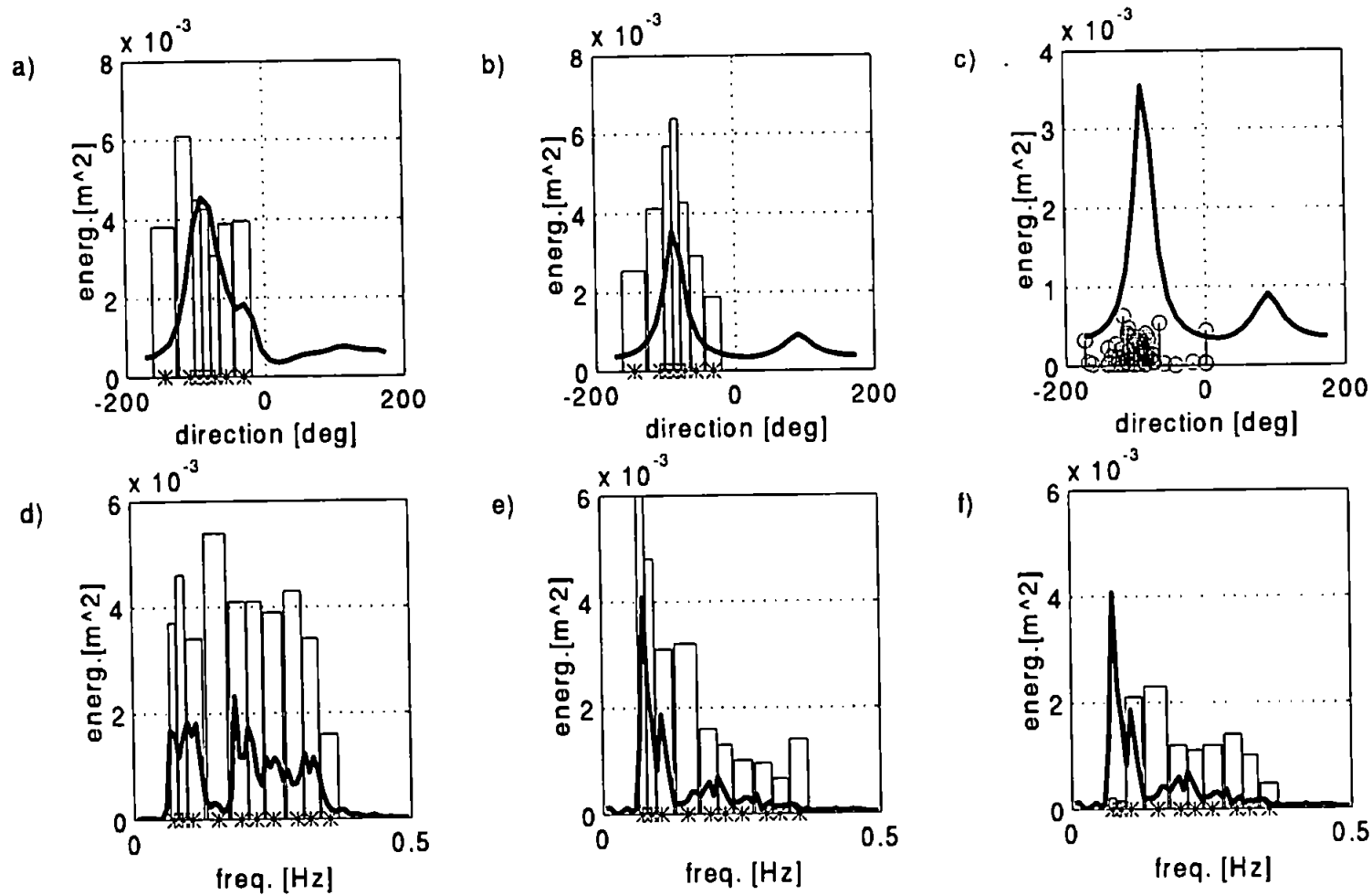


**Figure H.1** Directional results summary – File 65–a) sum of energy over all frequencies versus direction (line plot) and energy in directional bands chosen for modelling offshore (bar plots); b) sum of energy over all frequencies versus direction (line plot) and energy in directional bands chosen for modelling inshore (bar plots); c) measured inshore (line plot) and model predicted energy versus direction (circles plots); d) sum of energy over all directions versus frequency (line plot) and energy in frequency intervals chosen for modelling offshore (bar plots); e) sum of energy over all directions versus frequency (line plot) and energy in frequency intervals chosen for modelling inshore (bar plot); f) measured inshore (line plot) and model predicted energy versus frequency (bar plot)

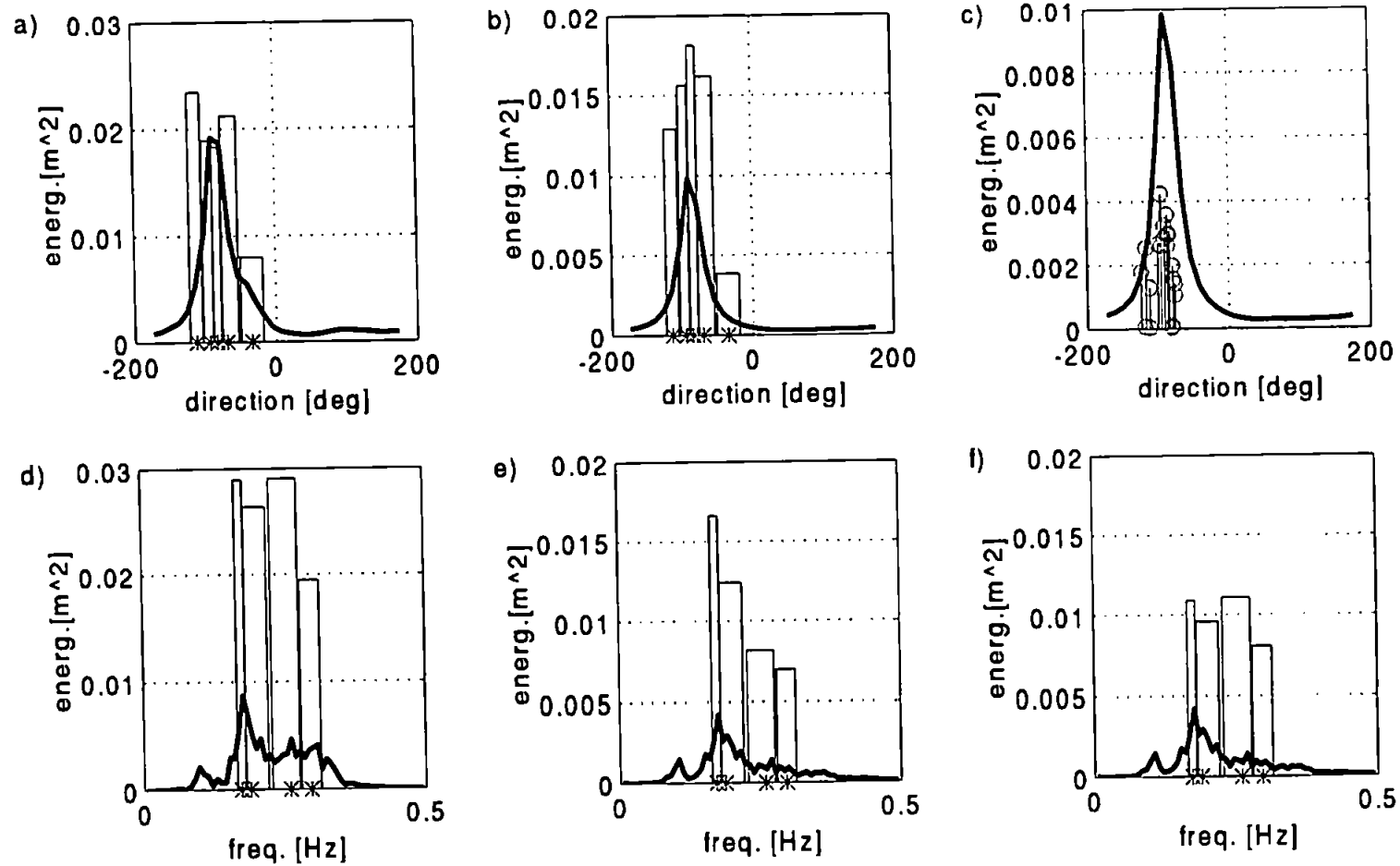


**Figure H.2** Same as for Figure H.1 – Directional results summary – File 69



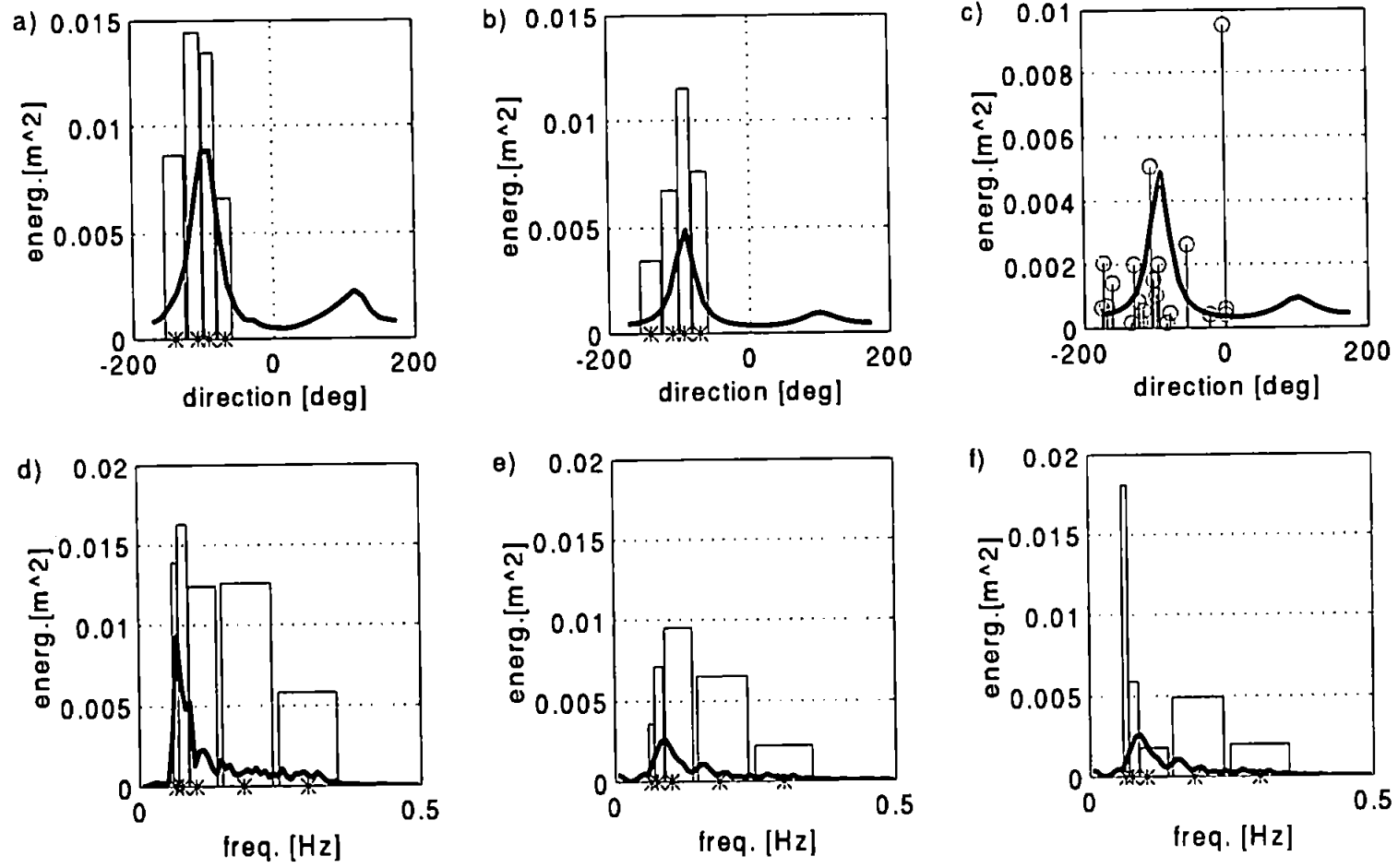


Figure H.3 Same as for Figure H.1 – Directional results summary – File 72

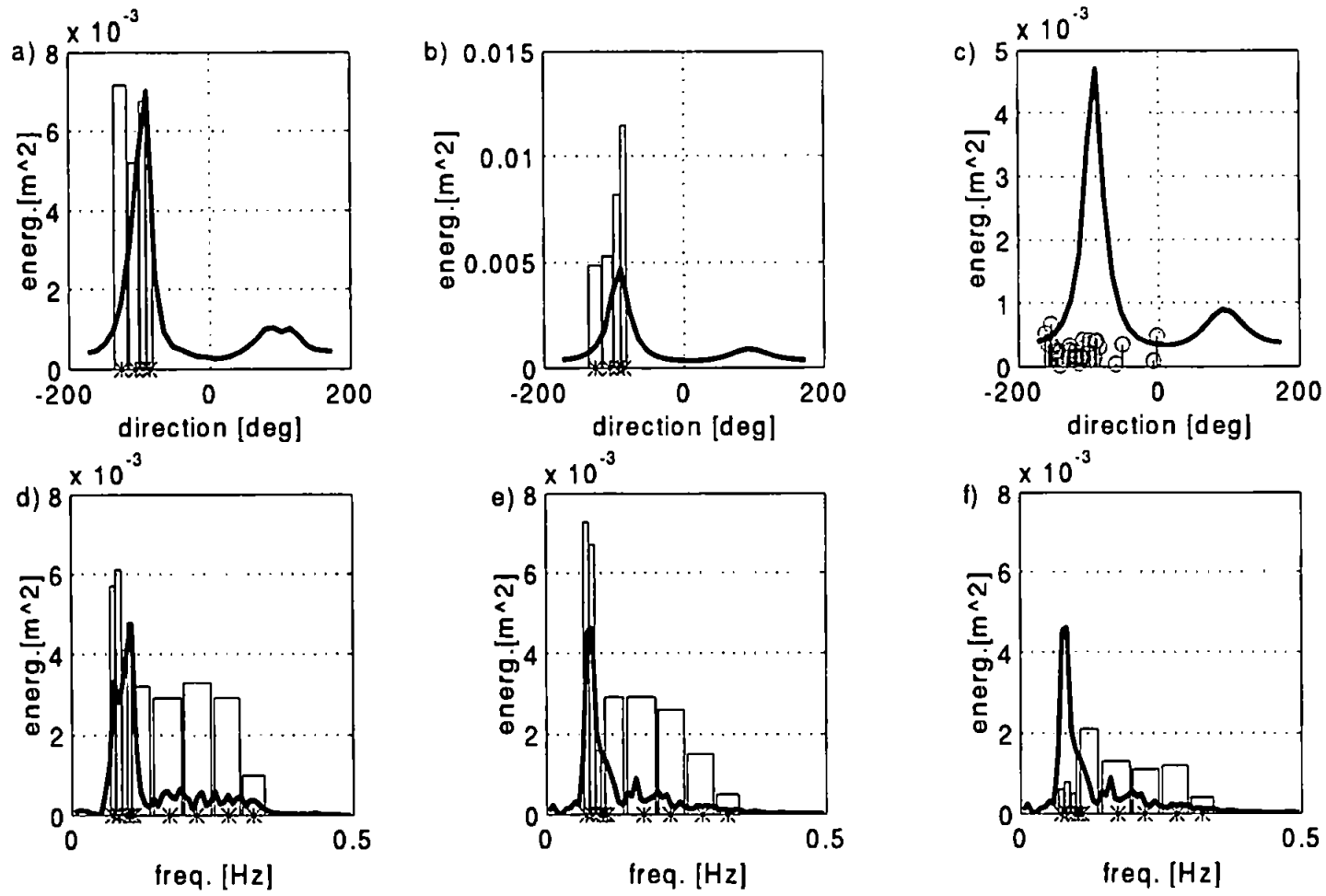
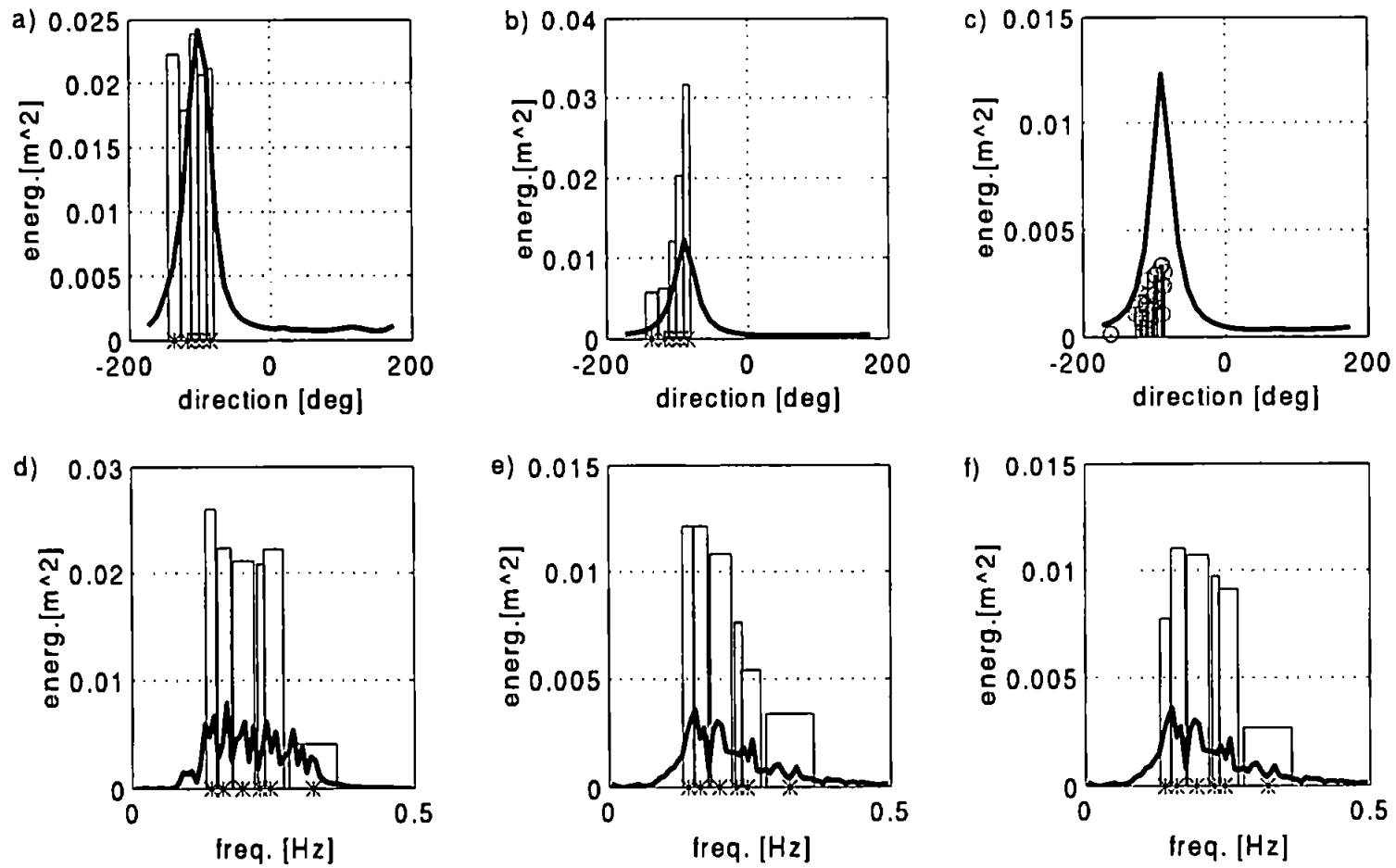


Figure H.4 Same as for Figure H.1 - Directional results summary - File 73



**Figure H.5** Same as for Figure H.1 – Directional results summary – File 75

# APPENDIX I

## Bispectral analysis theory summarised

David Simmonds (personal communications) developed the bispectral analysis software used in this thesis. Bispectral analysis was first carried out by Hasselmann *et al* (1963) to study the non-linear interactions of ocean waves. The bispectrum has been defined as the Fourier transform of the two-dimensional autocorrelation function  $K_{\eta\eta}^{(2)}(\tau_j, \tau_k)$  of a time series  $\eta(t)$

$$B(f_j, f_k) = \frac{1}{(2\pi)^2} \int_{-\infty}^{\infty} \int_{-\infty}^{\infty} K_{\eta\eta}^{(2)}(\tau_j, \tau_k) e^{-i(f_j\tau_j + f_k\tau_k)} d\tau_j d\tau_k \quad (I.1)$$

where

$$K_{\eta\eta}^{(2)} = E[\eta(t)\eta(t + \tau_j)\eta(t + \tau_k)] \quad (I.2)$$

where  $\tau$  is a lag,  $f$  is the frequency,  $E[ ]$  is the expected value, or average, operator.

The bispectrum can also be expressed in terms of Fourier coefficients as:

$$B(f_j, f_k) = E[A_{f_j} A_{f_k} A_{f_j+k}^*] \quad (I.3)$$

where  $A_{f_j}$  is the complex Fourier coefficient of frequency  $f_j$ , and  $*$  denotes the complex conjugate.

The bispectrum is zero if the average triple product of Fourier coefficients is zero. It means that the bispectrum is zero unless there are waves present at the frequencies  $f_j$ ,  $f_k$  and  $f_{j+k}$  or there is a phase coherence, or phase relation, between the waves at these frequencies. If the sum or difference wave  $f_{j+k}$  is generated through an interaction between  $f_j$  and  $f_k$  then a phase coherence will exist and the expected value will be nonzero.

The bispectrum amplitude, biamplitude, is defined as:

$$B(f_j, f_k) = |B(f_j, f_k)| \quad (I.4)$$

The bispectrum phase, biphas, is defined as:

$$\beta(f_j, f_k) = \tan^{-1} \left\{ \frac{\text{Im}[B(f_j, f_k)]}{\text{Re}[B(f_j, f_k)]} \right\} \quad (I.5)$$

where *Re* and *Im* denote the real and imaginary parts respectively. The biamplitude indicates the nature and relative strength of the interactions, and the biphas gives a measure of the relative importance of the real and imaginary parts of the bispectrum.

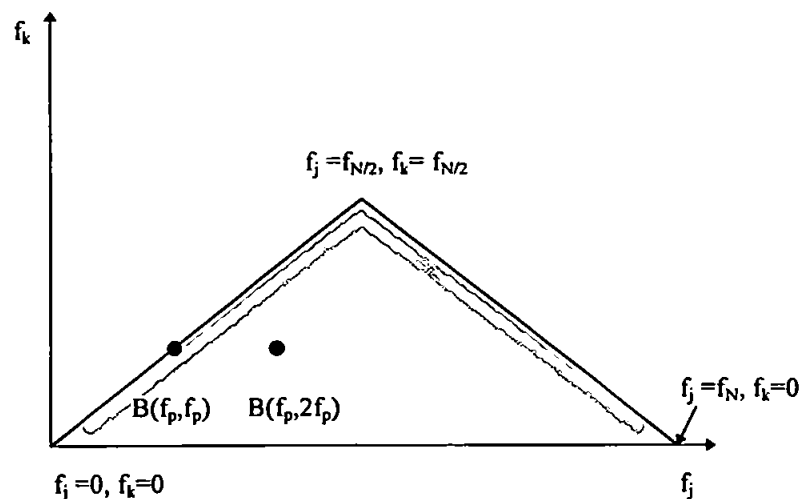


**Figure I.1** Plan view of a unique bifrequency space

Integrating the real part of the bispectrum (Hasselmann *et al*, 1963) yields to the third moment ( $m^3$ ). The skewness is obtained by normalising the integration by the variance to the power of 3/2 (Doering, 1988). Elgar and Guza (1985) related the imaginary part of the bispectrum to a measure of asymmetry of the temporal derivative of time series.

Because of the symmetries, it is enough to evaluate the bispectrum in a bifrequency octant. For a digital time series with Nyquist frequency  $f_N$ , the bispectrum is defined within a triangle in a  $(f_j, f_k)$  - space defined in Figure I.1.

The bispectrum may be expressed in a normalised form defined as the bicoherence spectrum given by Kim and Powers (1979):

$$b(f_j, f_k) = \frac{|B(f_j, f_k)|}{E[|A_{f_j} A_{f_k}|] E[|A_{f_{j+k}}|]} \quad (1.6)$$

**WAVE AND CURRENT INTERACTION IN THE COASTAL ZONE**

by

**KAREN ROSE STAPLETON**

A thesis submitted to the University of Plymouth in  
partial fulfilment for the degree of

**DOCTOR OF PHILOSOPHY**

Institute of Marine Studies  
Faculty of Science

In collaboration with  
the MAST G8M project

September 1996

# LIBRARY STORE

REFERENCE ONLY

<b>UNIVERSITY OF PLYMOUTH</b>	
Item No.	900 200021
Date	- 7 FEB 1997 <sup>S</sup>
Class No.	T 551.47025 TA
Contl. No.	X703413839
<b>LIBRARY SERVICES</b>	

90 0308851 1







Plate 1: Field station in Nieuwpoort, Belgium, showing incoming tide and typical weather conditions.

*This copy of the thesis has been supplied on the condition that anyone who consults it is understood to recognise that its copyright rests with its author and that no quotation from this thesis and no information derived from it may be published without the author's prior written consent.*

## **ABSTRACT**

### **Wave and Current Interaction in the Coastal Zone**

**Karen Rose Stapleton**

This project was set up as part of the MAST G8M project to study wave and current interaction in the field and to compare the results from the field with model estimates.

A history of the study of wave and current interaction is presented including the turbulence modelling and field studies carried out to date.

The field work carried out for this project was performed on a wide, shallow, ridge and runnel beach with a strong tidally driven longshore current. Velocity and pressure data were collected over twelve tidal cycles.

These data were used to estimate shear stresses calculated using three methods; the inertial dissipation method (IDM), the turbulent kinetic energy method (TKE) and the Reynolds stress method, (REY). The results were compared to look for evidence of which method, if any, gave more consistent results under the conditions experienced.

The parameterised wave and current interaction models of Huynh-Thanh and Temperville (1992), Soulsby et al. (1994), Fredsoe (1984) and Grant and Madsen (1979) were compared for a range of waves, currents and bottom roughnesses. The results, when compared, highlighted the need for accurate current velocities and, even more importantly bottom roughnesses.

The models were run for the field conditions and the results were compared with the field estimates of shear stress. The models were run using both observed and modelled estimates of bottom roughnesses. The comparison of field and modelled results showed that the models worked well when the wave to current ratio was small but underestimated the shear stresses when the waves were bigger and steeper. Reasons for this have been investigated and conclusions drawn.

# Contents

<i>List of Figures</i>	iv
<i>List of Tables</i>	viii
<i>List of Plates</i>	x
<i>Acknowledgements</i>	xi
<i>Author's Declaration</i>	xiii
<i>Notation</i>	xiv
1. Introduction and Overview of Thesis	
1.1. Introduction	1
1.2. Aims	1
1.3. Overview of Thesis	2
2. Review of the Literature	
2.1. Wave and Current Interaction: An Introduction.	4
2.2. Bottom Boundary Layers	5
2.3. Turbulence within the Boundary Layer	7
2.3.1. A Brief History of Turbulence	7
2.4. Modelling the Turbulent Boundary Layer	11
2.4.1. Modelling Wave and Current Interaction	14
2.4.2. Parameterisations of Models as determined by the MAST G8M Project	18
2.5. Field Studies	22
2.6. Model of Tidal Currents over the inner shelf, at Nieuwpoort, Belgium, as a large Scale Method to Estimate Bed Stress.	29
2.7. Sediment Transport under Waves and Currents	31
2.8. Conclusions drawn from the Review	32
3. Fieldwork and Data Collection	
3.1. Rationale	33
3.2. Instrumentation	34
3.2.1. Electromagnetic Current Meters	34
3.2.1.1. Filter Characteristics	35

3.2.1.2.	Calibration	37
3.2.1.2.1.	Gains	37
3.2.1.2.2.	Offsets	39
3.2.2.	Pressure Transducers	41
3.2.2.1.	Calibration	41
3.3.	Field Campaign, Nieuwpoort, Belgium	43
3.3.1.	Introduction	43
3.3.2.	Aims of the Field Campaign	46
3.3.3.	Beach Site	46
3.3.4.	Grain Size Analysis	47
3.3.5.	Placement of Equipment	48
3.3.6.	Channel Recognition	54
3.3.7.	Environmental Conditions	56
3.3.7.1.	Weather Conditions	56
3.3.7.2.	Wave Climate	57
3.3.7.3.	Bedforms	57
3.3.8.	Data Quality	57
4.	Data Analysis	
4.1.	Introduction	60
4.2.	Statistical Analysis	60
4.2.1.	Means	61
4.2.2.	Depth Averaged Velocity	63
4.2.3.	Spectral Analysis	64
4.2.3.1.	Significant Wave Statistics	65
4.2.3.2.	Wavenumber	66
4.2.3.3.	Maximum Near Bottom Wave Orbital Velocity and Maximum Orbital Diameter	66
4.2.3.4.	Peak Wave Frequency	67
4.3.	Estimating Bottom Stresses	67
4.3.1.	The Inertial Dissipation Method	67
4.3.2.	The Turbulent Kinetic Energy Method	73
4.3.3.	The Reynolds Stress or Eddy Correlation Method	74
4.4.	Data Selection	75

5.	<b>Results of Fieldwork and Comparison with Other Work</b>	
5.1.	Introduction to the Nomenclature used in the Results	78
5.2.	Estimates of Shear Stress from the Field Data	79
5.2.1.	Station 1	81
5.2.2.	Station 2	82
5.3.	Error Analysis	84
5.4.	Comparison with Other Field Results	87
6.	<b>Inter-comparison of Models and Comparison of Models with Field Results</b>	
6.1.	Inter-comparison of Models	91
6.2.	Estimation of Bottom Roughness	94
6.3.	Estimating Ripple Size	97
6.4.	Comparison of Rippled and Flat Bed Model Results	99
6.5.	Comparison of Model Results with Data from the Field Experiment	101
6.6.	Comparison of Drag Coefficients from the Field Data with the Parameterised Equation	104
6.7.	Discussion	105
7.	<b>Conclusions</b>	
7.1.	Field Campaign and Data	108
7.2.	Shear Stress Estimates	109
7.3.	Modelling of Wave and Current Interaction	109
7.4.	Comparison of model and Field Results	110
7.5.	Future Work	110
	Appendix	112
	References	122

## List of Figures

2.		
2.1.	Diagrammatic illustrations of the boundary layer. (a) For the boundary layer which occupies the whole water depth; (b) for water which is deeper than the boundary layer thickness; bed, logarithmic and outer layers are not to scale.	6
2.2.	Conceptualisation of mixing and momentum transfer (shear stresses) in turbulent boundary layers.	8
2.3.	An example of the curves used in the parameterisation from Soulsby et al. (1993) showing maximum and mean shear stresses calculated from each model.	21
2.4.	Soulsby and Humphery (1989)'s Figure 9 shows the drag coefficient, $C_{100} = \tau_o / \rho U_{100}$ , as a function of wave to current ratio, $\sigma_{\text{wave}} / U_{100}$ .	29
3.		
3.1.	Two types of electromagnetic current meters were used, the annular (left) and the spherical (right).	35
3.2.	Filter characteristics of the EMCM's before, (a) and after, (b), resistors were changed.	36
3.3.	Diagram of tank used in the calibration of both pressure transducers and electromagnetic current meters.	38
3.4.	Calibration results from EMCM B3Y showing line of best fit.	39
3.5.	Diagram showing dimensions of pressure transducer.	41
3.6.	Calibration results from the pressure transducers, PT1 and PT2 are the pressure transducers on Stations 1 and 2 respectively.	42
3.7.	Offsets of pressure transducers measured after the instruments emerged from the water. Nomenclature explained in section 5.1	43

3.8.	Chart of field site taken from chart number 125, Hydrographic Office, North Sea - Belgium, Approaches to Oostende, Scale 1:50 000. The location of the site is indicated.	45
3.9.	Transect of beach at Nieuwpoort, Belgium, showing ridge and runnel features and approximate positions of instrument stations.	46
3.10.	Grain size analysis.	48
3.11.	Arrangement of instruments from 26/02/94, showing positioning of EMCM's and PT's.	53
3.12.	The neap - spring cycle experienced during the field trip.	54
3.13.	Diagrammatic view of data collection system.	56
4.		
4.1.	Mean velocities and wave heights for similar depths over the whole field campaign. The two dotted lines indicate the trends of both mean velocities (avgv) and wave heights (max hsig) as indicated by the legend.	61
4.2.	Mean flows of longshore, cross shore and vertical EMCM's and mean depths for the outer station for the whole field campaign. Nomenclature explained in section 5.1.	62
4.3.	Shows the lag in tidal velocity phase observed during field campaign.	63
4.4.	Spectrum of pressure transducer time series indicating limits of wind wave band and peak period.	70
4.5.	Spectrum of vertical velocity time series showing limits of inertial subrange and the -5/3 roll-off.	71
4.6.	Showing limits of where the inertial subrange might occur and where the current meters can sense turbulence.	72
4.7.	Spectrum of cross shore velocity split into fluctuations due to waves and those due to turbulence.	73
4.8.	Velocity data from a current dominated run.	76
4.9.	Velocity data from a run considered to be wave dominated.	76



4.10.	Velocity data from a data run which was discarded as being unsuitable for further analysis. The large vertical velocities were thought to be due to waves breaking in the vicinity of the instrument array.	77
5.		
5.1.	Spectra from velocity data from longshore components and from estimated time series.	80
5.2.	The results of the three methods used to calculate shear stresses from station 1.	81
5.3.	Results of shear stress estimates from station 2.	82
5.4.	Highlights the similarities between the shear stress estimates made at the two stations.	83
5.5.	Plot of the turbulent kinetic energy method against the Reynolds stress method and the inertial dissipation method, showing the scatter.	84
5.6.	(a) and (b) show the estimates of shear stress with the errors associated with each method in the top left hand corners.	86
5.7.	Drag coefficients from Soulsby and Humphery (1989) and those calculated from Drake and Cacchione (1992).	87
5.8.	Comparison of drag coefficient with those of Drake and Cacchione (1992) and Soulsby and Humphery (1989).	88
5.9.	Showing lines of best fit for each field station.	89
6.		
6.1.	Model results for the four models showing comparison at different wave and current velocities.	92
6.2.	The effect of period on the models is not great, in the Soulsby model it is a little greater.	93
6.3.	The effect of bottom roughness is quite marked.	94
6.4.	After Amos et al. (1995) figure 5, showing a plot of current Shields parameter against wave Shields parameter to estimate when sediment movement occurs. The three lines represent the limits between no sediment movement	95

and ripple formation, this is represented by the heavy solid line; the transition from ripple formation to ripple degradation, the dotted line; and the limit between ripple degradation and sheetflow, the lighter solid line.

- |      |   |     |
|------|---|-----|
| 6.5. | The estimated bottom roughnesses for station 2, the station where a flat bed roughness based on the grain size was used.  | 99  |
| 6.6. | a) and (b) Comparison of the modelled shear stress results for both field stations. The results using the rippled estimates are plotted against those using the observed estimates of bottom roughness. | 100 |
| 6.7. | (a) and (b) Plot of field results with model estimates, the Huynh - Thanh and Temperville (1992) model was chosen as being one of the intermediate models to make this comparison.                      | 102 |
| 6.8. | (a) and (b) Comparison of the HT model results for both rippled and flat bed assumptions with the field stress results.   | 103 |
| 6.9. | Plot of nondimensional wave height against water depth the showing line where the ratio of convective to local inertia equals 10%.  | 107 |

## List of Tables

3.		
3.1.	Comparison of the technical data of two EMCM types, from Valeport technical datasheet.	37
3.2.	EMCM calibration constants, giving the degrees of freedom for the linear best fit.	39
3.3.	Table of offsets in volts taken at the time of calibration at RNEC Manadon, in the laboratory and in the field.	40
3.4.	Technical data for the pressure transducers.	41
3.5.	PT calibration details calculated by the manufacturer and at Manadon.	42
3.6.	Results of grain size analysis, the mean grain size is ~ 200 $\mu$ m.	47
3.7.	Channel identifications.	55
3.8.	Table of instrument heights, observed bed roughness and problems found and overcome.	58
3.9.	Environmental conditions experienced during the field campaign, including observed wave and weather conditions.	59
4.		
5.		
5.1.	Explanation of nomenclature used in presenting the field results.	79
5.2.	The data runs suitable for use in subsequent analysis, tidal cycle 'gp' was not used as white horses were present at the time of data recording.	80
5.3.	The equations of the lines of best fit for the data presented in figure 5.9.	89
6.		
6.1.	A synopsis of the models used in the following analysis.	91
6.2.	Key to figures 6.1 to 6.3, showing line styles and colours for each model and each velocity.	92
6.3.	The equations used to calculate the critical Shields	96

parameters for sheetflow, saltation/suspension and bedload transport for wave alone and current alone cases.

- 6.4. Drag coefficient associated with current alone, from the parameterised equations. 105
- 7.

## List of Plates

- |   |              |
|---|--------------|
| 1. Field station in Nieuwpoort, Belgium, showing incoming tide and typical weather conditions.  | Frontispiece |
| 2. The beach at low tide showing the ridges and runnels, the instrument stations were placed on the ridge between the two runnels seen. The beach was over 450m wide at low tide.   | 44           |
| 3. Station 1 on the landward side of the ridge, showing the placement of electromagnetic current meters and pressure transducers.   | 49           |
| 4. Station 2 was situated in the seaward side of the ridge, 6 optical backscatter sensors were arranged on the post with the electromagnetic current meters and pressure transducer. The difference between the annular and spherical current meters is plainly seen. | 50           |
| 5. The top of the ridge was the point at which the flat bed changed into a rippled bed, this is shown up well in this plate.  | 51           |
| 6. Station 1 before the instrument arrangement was altered, highlighting ripples formed near station.   | 52           |

## Acknowledgements

This study has been completed with the help and support of many people, both scientists and friends whom the author wishes to acknowledge. Professor David A. Huntley has been director of studies for this project, his guidance help and patience are gratefully acknowledged.

The project was funded by the Commission of the European Communities Directorate General for Science, Research and Development under the contract No. MAST 0035-C.

The field work was funded as part of the MAST II Programme by the Commission of the European Union under MAST MAS2-CT92-0024.

I would also like to thank the following:

Professor Phil G.G. Dyke (supervisor) for his keen interest in the progress of this study.

Dr. Dave Simmonds for his help and support both as colleague and friend, both during the field campaigns and daily travelling on the train.

Mrs Pauline Framingham for her help as a computer expert and, more especially as a friend.

The scientists and technicians who gave their time and effort to the field campaign to make it a success.

Paul Chatwin, my 'room mate', who has shared my office and many of my problems.

The coffee club who provided an oasis of relaxation during this study.

I would also like to thank my family, my parents, Frank and Emma Hamlyn, my sisters and brother, and my husband John, without whose help and support I could never have begun this study.

Finally, a big thank you to my children, Nick and Amy, who helped to keep my feet on the ground throughout this whole project.

## Author's Declaration

At no time during the registration for the degree of Doctor of Philosophy has the author been registered for any other University award.

This study has been sponsored in the framework of the Marine Science and Technology Programme (MAST-II) by the Commission of European Communities of the European union, as part of the work done by the G8 Coastal Morphodynamics (G8M) research project.

A programme of advanced study was undertaken, which included a post-graduate course in Sediment Transport in the Coastal Zone and an advanced summer school, see below.

Relevant scientific seminars and conferences were regularly attended at which work was presented; external organisations were visited for consultation purposes, and papers prepared for publications.

### Papers Presented

#### Conference:

"Wave and Current Interaction in the Coastal Zone"  
Stapleton and Huntley.  
UK Oceanography, 1994.

"Wave and Current Interaction on a Sand Spit"  
Stapleton and Huntley, The Marine Studies Group of the  
Geological Society, Shallow Water Sedimentary Processes:  
Transport Fluxes and Budgets, 1994.

"Field measurements in a Tidal River Estuary on the Cantabrian  
Coast, Spain " Huntley et al., Coastal Dynamics, 1994.

#### Journals

"Seabed Stress Determinations using the Inertial Dissipation  
Method and the Turbulent Kinetic Energy Method"  
Earth Surface Processes and Landforms, Technical and  
Software Bulletin, Vol. 20, 807-815 (1995).

#### Courses

1st EU MAST Advanced Summer School  
"Modelling and Prediction of Physical Processes in the Coastal  
Zone and Estuaries", run by the Netherlands Centre for Coastal  
Research.

#### External contacts:

Members of the MAST G8M group.

Signed K.R. Stapleton  
Date 29/01/97



## Notation

$\alpha_i$	One dimensional Kolmogorov constant
$\alpha$	Internal friction angle
$\delta$	Boundary layer thickness.
$\varepsilon$	Dissipation rate
$\varepsilon_T$	Relative importance of surface tension
$\phi$	Angle between instantaneous flow and mean current in the boundary layer; Potential function for Stokes waves.
$\phi_{ii}$	Spectrum, in a given direction
$\gamma$	Angle between mean current flow and direction of wave propagation
$\eta$	Ripple height
$\kappa$	von Karman's constant (taken as 0.4)
$\Lambda$	Length scale
$\lambda$	Ratio of current to wave/current interaction friction velocity; Wavelength of ripple
$\nu$	Kinematic viscosity
$\theta$	Shields parameter
$\rho$	Fluid density, taken as 1025kg/l for seawater
$\sigma$	Absolute wave frequency
$\sigma_w^2$	Variance associated with wind wave band
$\tau_{(0)}$	Shear stress (at the bed)
$\tau_{ij}$	Stress
$\psi'$	Critical Shields parameter
A	Constant
$A_b$	Wave orbital excursion amplitude
a,b,m,n,p,	Fitting Coefficients for parameterisation of models
q	
$a_i, b_i$	Fourier coefficients
$C_D$	Drag coefficient
$C_1$	Empirical Constant
c, w	(Subscript) Denote that the parameter is associated with either currents or waves, or both
d	Diameter of sediment; distance between electrodes

$d_0$	Maximum orbital diameter
$D_{50}$	Mean grain size
$E(k)$	Energy density of velocity spectrum associated with wavelength, $k$
$F_0$	Forcing term
$f$	Frequency
$f'$	Friction factor
$H_s$	Significant wave height
$h$	Water depth
$h'$	Fluctuation amplitude associated with a given wavenumber
$K$	Linear friction coefficient, number of segments each time series is divided into (spectral analysis)
$k$	Kinetic energy, wavenumber
$L$	Typical length scale
$l_{(m)}$	Typical length scale; small vertical displacement, (Prandtl mixing length)
$m$	Number of points in each segment (spectral analysis)
$\bar{m}$	(Subscript) Denotes the mean
$m_{max}$	(Subscript) maximum
$N$	$2*m$
$p$	Pressure
$p_i$	Value of spectrum at $i$ th point
$p(f)$	Frequency spectrum
$\bar{p}(f)$	Spectral estimate
$q$	Mean turbulent kinetic energy
$R_{ij}$	Velocity covariance
$Re_{(c)}$	Reynolds number (critical)
$T$	Wave period
$t$	time
$U$	Typical velocity
$U_i(z)$	Mean velocity at a height $z$ above the bed, in a given direction; No subscript implies mean
$u_b$	maximum near bottom orbital velocity
$u_c$	Component of flow
$u_*$	Friction velocity
$\hat{u}_*$	Friction velocity corrected using modified inertial dissipation method
$u', v', w'$	Fluctuations about the mean
$w_j$	Window function
$w_s$	Settling velocity
$x, y, z,$	Cartesian co-ordinates
$x$	Measure of relative strengths of wave and currents (ranges from 0 to 1)
$Y$	Non dimensional parameter associated with maximum shear stress
$y$	Non dimensional parameter associated with mean shear stress
$z_0$	Physical bottom roughness
$z_{cr}$	Critical height above bottom
$\bar{\bar{\quad}}$ overbar	Time averaging

# Chapter 1

## Introduction and Overview of Thesis

### 1.1 Introduction

Waves and currents give rise to the dominating hydrodynamic forces over the whole of the continental shelf. Their importance has long been recognised but until recently the effect of the interaction between waves and currents has been little studied. The first model to take wave and current interaction into account was developed in 1967, however it was not until the late 1970's that more work was done to model and measure these effects.

The main predicted effects of waves within the bottom boundary layer are the enhanced shear stress felt at the bed and the effect on the flow above the wave boundary layer which is equivalent to an enhanced bottom roughness. The shear stress within the bottom boundary layer is important in the study of sediment transport. As wave and current interaction affects the shear stress felt at the bed, its effects, if not taken into account could result in low estimates when modelling sediment transport or the effects of waves and currents on structures.

### 1.2 Aims

The main aims of this project can be presented in three main categories:

- 1) To collect field data in the nearshore in the presence of waves and a current, to include a range of wave and current conditions.
- 2) To estimate shear stresses from field data using three methods and to establish which, if any, are more suitable for the various conditions experienced during

the field campaign. Also, to identify under which conditions the methods do not work.

- 3) To compare the results of the three methods used to estimate shear stress with models of wave and current interaction and to improve and extend the range of prediction schemes.

### **1.3 Overview of Thesis**

A review of the literature available on waves and currents is presented in chapter 2. A brief history of turbulence modelling and how these models are used is given. As part of the MAST G8M project several wave and current interaction models have been parameterised to make them more readily available to engineers. This parameterisation will be explained in chapter 2. There have been a number of field campaigns carried out where the data collected has been used to investigate wave and current interaction. These campaigns will be described giving an insight into the methods used and results obtained.

In chapter 3 the field campaign carried out for this project is described. The choice of field site, instruments used and problems overcome, anticipated or unexpected, are all presented. The instrument calibration methods are also explained and there is a detailed description of the environmental conditions experienced.

Methods used to analyse the data are shown in chapter 4 and a detailed description of the three methods used to estimate shear stresses is given. The means of some of the data are presented to give an indication of the hydrodynamic conditions encountered.

Chapter 5 presents the results of the shear stress estimates and shows a comparison of these field estimates with shear stress estimates from other field campaigns.

In chapter 6 an inter comparison of the parameterisation of four wave and current interaction models is made for a variety of wave, current and bed roughness conditions. Model results for the conditions experienced during the field campaign are then compared with the estimates made from the field data.

Chapter 7 is a discussion of the implications of the results, conclusions and suggestions for future work.

# Chapter 2

## Review of the Literature

The literature available for wave and current interaction falls into 4 main categories:

- 1) Boundary layer turbulence
- 2) Models which include the effects of wave and current interaction
- 3) Field studies
- 4) Comparisons of 2) and 3).

The hydrodynamic environment within the bottom boundary layer will be described along with the way in which wave and current interaction affects the bottom boundary layer. Models which have been evolved to explain and predict wave and current interaction will be presented and discussed in section 2.4. A description of field experiments set up to explore the nature of wave and current interaction and to compare with model predictions will be given in section 2.5.

### 2.1 Wave and Current Interaction: An Introduction

The coastal zone is dominated by two equally important elements: waves and currents. The waves are usually wind generated, but the currents are generated by a number of factors. These factors include the tides, wind and waves, also density gradients and outflows from rivers. The wave and current interaction acts through a number of mechanisms, (Soulsby et al. (1994)):

- a) refraction of the waves by horizontally sheared currents
- b) modification of the wave kinematics by the (possibly vertically sheared) current
- c) generation by the waves of “mass transport” or “streaming” currents

- d) generation by the waves of radiation stresses giving rise to currents, particularly longshore currents in the surf zone
- e) enhancement of the bottom friction felt by the currents, due to interaction with the wave boundary layer
- f) enhancement of the bed shear stresses and energy dissipation of the waves due to interaction with the current boundary layer.

For this thesis attention will be focused on the mechanisms e) and f), more particularly on e). The reasons for this will be revealed in subsequent sections and chapters. The study will therefore concentrate on the bottom boundary layer.

## 2.2 Bottom Boundary Layer

A general definition for the bottom boundary layer, given by Bowden (1978) is:

“the layer adjacent to the seabed in which flow is affected by the processes at the boundary and in which strong gradients of physical, chemical and biological properties may occur. It is the layer within which exchanges between the water column and sediment takes place.”

Also:

“it may also be said to extend a short distance of the order of centimetres or decimetres downwards into the sediment.”

The velocity of the fluid at the bed is zero and reaches free stream velocity,  $U_{\infty}$ , at the top of the boundary layer providing the water is deep enough. The boundary layer thickness,  $\delta$ , is defined by Soulsby (1983) using the mean velocity such that  $U(\delta) \approx U_{\infty}$ , where  $U(z)$  is the mean velocity at height  $z$ . In shallower water the boundary layer affects the entire water column and hence the boundary layer thickness is the water depth,  $h$ . Figure 2.1 is a diagrammatic view of these boundary layers showing both the boundary layer with free stream velocity above and the boundary layer which occupies the entire water depth. The forces acting on the flow in the boundary are generally defined as force per unit area, i.e. stress. The stress acting perpendicular to the bed is the pressure ( $p$ ) caused by the water mass, the stress acting along the bed, parallel to the boundary layer, is the shear stress ( $\tau$ ). If  $\tau_0$ , the bed shear stress, exceeds a threshold value then sediment may be moved. An interesting effect of this shear stress is its effect on tidal currents which, ultimately, leads to a reduction in the Earth's rotation (Bowden (1978)). Direct

measurements of stress are not easy, in many cases impossible, since instruments to measure stress in situ are either too delicate to be used in the field or are still at the inception stage. Therefore estimates for stress are derived either from velocity profiles or turbulent fluctuations.

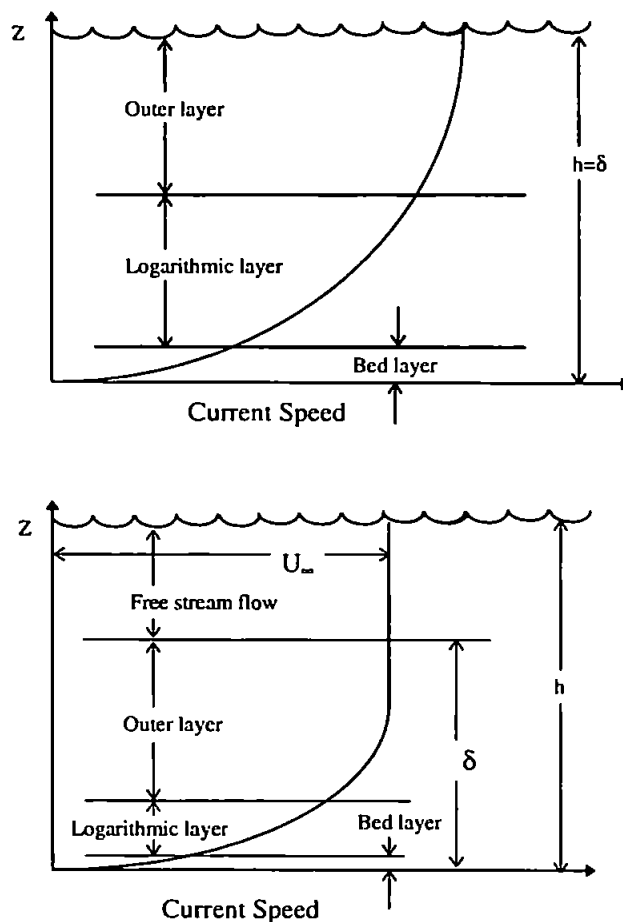


Figure 2.1 Diagrammatic illustrations of the boundary layer. (a) For the boundary layer which occupies the whole water depth; (b) for water which is deeper than the boundary layer thickness; bed, logarithmic and outer layers are not to scale.

The above is a description of a boundary layer in which no effects from waves are felt. On the continental shelf the most common environment is one in which both waves and currents interact. This is especially true during storms when there is enhanced wave activity. Waves of period 5-15s start “feeling” the bottom in about 20 -180m water depth (Grant and Madsen (1979)). The simultaneous presence of current and waves over a hydrodynamically rough bottom results in a non-linear interaction that changes both the flow and the associated bottom stress. By scaling arguments (Soulsby (1983)) it is possible to show that two distinct vertical boundary layers exist for this combined flow.



A wave boundary layer is a layer close to the bed in which the shear stress is dependent on a non-linear combination of both waves and currents and a roughness associated with the physical bottom roughness. The height  $\delta_w = \kappa u_{*w} / \omega$ , where  $\omega$  is the wave frequency, the subscripts w and c indicate waves and currents respectively,  $u_{*w}$  is the friction velocity associated with the wave and current interaction and  $\kappa$  is the von Karman constant, is the limit to which the wave induced turbulence, i.e. the turbulence caused by the presence of the waves, can diffuse and limits the region of wave turbulence to the wave boundary layer. Above this height, the turbulence is associated with current only. However, the flow in the upper layer is considerably affected by the presence of the wave boundary layer. This is due to the highly dissipative turbulent flow in the wave boundary layer extracting energy from the flow above, causing an enhancement of the shear stress in the outer region (Lyne et al. (1990)). This enhanced shear stress is, effectively, equivalent to an enhanced roughness length for the flow in the outer region.

## 2.3 Turbulence within the Boundary Layer

Many flows in nature are turbulent, and it is therefore important to understand the mechanisms at work within such flows. Turbulent flows are unsteady and contain fluctuations that are random in space and time. Fully developed turbulent flows contain a full range of length scales from large eddies which fit within the flow region to the smallest scale possible due to the dissipative process. Turbulence occurs in nature because low viscosity flows become unstable at high Reynolds numbers and cannot be maintained indefinitely as steady laminar flows. The first step from steady to fully turbulent flow, (i.e. transitional flow) is instability to small disturbances.

### 2.3.1 A Brief History of Turbulence

Whilst turbulent motion has been around since the beginning of time, the first serious investigations into the nature of turbulence were not carried out until the latter half of the 19th century (Landahl and Mollo-Christensen (1986)). Osborne Reynolds and Lord Rayleigh were the first to investigate flow instability. The investigations carried out by Reynolds (1883) into pipe flow clearly demonstrated that two modes of flow existed, laminar and turbulent (sinuous, as Reynolds termed it). Reynolds found that a non-dimensional parameter could determine the type of flow that could be sustained. This now famous, and ubiquitous, Reynolds number can be calculated for any flow,

$$Re = \frac{UL}{\nu} \quad 2.1$$

where  $U$  is a typical velocity,  $L$  a typical length scale and  $\nu$  is the kinematic viscosity. The Reynolds number is a ratio of typical acceleration to typical viscous stress gradients. If it is greater than some critical value, for pipe flow 2300, turbulent flow can be sustained, if it is less laminar flow can be sustained. Reynolds (1894) also derived the equations of motion for turbulent mean flow, see section 2.4, which lead to the introduction of the Reynolds stresses, which are parameters with the same dimensions as stress but physically cannot be measured as stresses. The idea behind the Reynolds stresses and turbulent mean flow, that turbulent flow may be treated as laminar flow with different fluid properties, was first proposed by Boussinesq (1877). Boussinesq assumed the turbulent shear stress is proportional to the velocity gradient, just as viscous shear stresses are in laminar flow, but with a different, (generally higher), coefficient of proportionality. The turbulent (or “eddy”) viscosity approximation is commonly used in the modelling of mean flow in turbulent conditions.

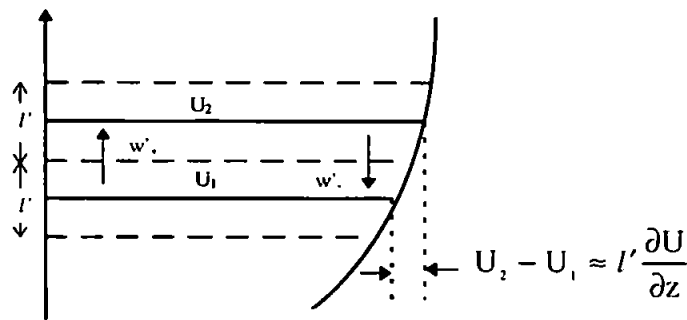


Figure 2.2 Conceptualisation of mixing and momentum transfer (shear stresses) in turbulent boundary layers.

In the 1920's work done by Prandtl and von Karman developed methods of calculations which enable one to obtain approximations to the mean velocity flow field, based on a small number of empirical parameters. The mixing length hypothesis was first used by Taylor (1915) and later employed by Prandtl (1925). This hypothesis utilises the average distance a fluid particle deviates from the mean streamline, see figure 2.2. An approximate expression for the mean momentum transfer by turbulent mixing in terms of the mixing length was set out by Prandtl. He assumed that the mixing length was proportional to the distance from the wall/bed, and thence determined the mean velocity distribution near the wall using one empirical constant. Many more complicated and

different hypotheses of momentum transfer by turbulent fluctuations have been put forward since Prandtl but there is still no practical calculation of the mean flow field based on the Navier-Stokes equations without using some empirical data. This is due to the non-linearity in the dependence of the instantaneous flow field on the mean velocity distribution.

Until Prandtl, the study of hydrodynamics, and hence turbulence, had been split into two parts. Classical hydrodynamics was one part, an elegant mathematical development of the theory of inviscid fluid flow, usually incompressible and irrotational which slipped freely over surfaces but did not generally focus on regions close to boundaries. The other part was hydraulics. This was based on formulae and data sheets developed from experiments and experience. Prandtl brought these two fields of study together establishing a logical basis on which subsequent developments in the field of modern fluid dynamics have been built. This basis is Prandtl's boundary layer theory which he first presented in 1904.

In 1937 Taylor and von Karman gave the following definition:

“Turbulence is an irregular motion which in general makes its appearance in fluids, gaseous or liquid, when they flow past solid surfaces or even when neighboring streams of the same fluid past or over one another”.

Taylor formulated many of the fundamental ideas in the statistical theory of turbulence. He introduced the concept of velocity covariances:

$$R_{ij} = \langle u_i(x)u_j(x + \xi) \rangle \quad 2.2$$

between one velocity component,  $u_i$ , (in Cartesian tensor notation) at a point  $x$  with another component of the flow,  $u_j$ , where  $i$  and  $j$  can be equal or not and the angled brackets,  $\langle \rangle$ , imply averaging. The covariances may be regarded as generalisations of the Reynolds stresses where  $\xi = 0$ . Velocity covariances, equation 2.2, can be thought of as a measure of the energy of eddies whose lengths in the direction of  $\xi$  are greater than the magnitude of  $\xi$ . The integral of the velocity covariances:

$$L_x = \int_0^{\infty} \tilde{R}_{ij}(\xi) d\xi \quad 2.3$$

where  $\tilde{\mathbf{R}}$  is a non-dimensional form of the covariances. Equation 2.3 is used in modelling as a length scale defined in terms of the velocity fluctuations. Taylor also introduced the spectral representation of turbulence.

During the 1940's and 50's developments in the statistical theory of turbulence were made by a group in the USSR, including Kolmogorov, Millionshikov and Obukhov, and in Cambridge where Taylor, Batchelor and Heisenberg were working. Historically, the first length scale used to characterise a turbulent field was the microscale introduced by Taylor (1935) and named after him:

$$\lambda_T^2 = \frac{\int_0^{\infty} E(k) dk}{\int_0^{\infty} k^2 E(k) dk} \quad 2.4$$

where  $E(k)$  is the energy density of the velocity spectrum and  $k$  is the wave number. Another set length scales was developed soon after, the Kolmogorov scale. These are typical length and velocity scales for dissipating eddies and were developed from dimensional analysis:

$$\lambda_K = \left( \frac{v^3}{\epsilon} \right)^{1/4} \quad \text{and} \quad v = (v\epsilon)^{1/4} \quad 2.5$$

where  $\lambda_K$  is the Kolmogorov microscale and  $v$  the velocity scale,  $\epsilon$  is the dissipation rate of the velocity fluctuations.

In more recent times the theory of chaos, (Thompson and Stewart (1986)) has been applied to the inherently non-linearity of fluid flows. This has lead to a highly complex branch of computational fluid dynamics and because of the need for very accurate measurements and the comparative crudity of instruments available for field measurements this will not be considered for this project.

Even with all the advances made in the last century there is still no completely deductive theory for isotropic turbulence, and work still continues.

The random nature of turbulent flows requires statistical methods to describe the flow. This description will be presented in section 2.4.

## 2.4 Modelling the Turbulent Boundary Layer

There is a hierarchy of turbulent boundary layer models. According to Young (1989) the modelling processes can be broadly classified as follows:

(1) Simple applications of the eddy viscosity concept combined with the Prandtl mixing length concept - the so called zero equation models.

(2) The eddy viscosity concept is expressed as the product of a characteristic velocity and length derived from modelled or simplified forms of the transport equations for turbulent quantities, usually the kinetic turbulent energy and dissipation - the so-called one or two equation models.

(3) The additional use of modelled forms of the Reynolds stress transport equation but without the eddy viscosity concept - the so-called Reynolds stress transport models. These forms may be either algebraic or differential.

(4) The time averaged Navier-Stokes Equations are solved for the larger eddies but the small eddies are empirically modelled using a sub-grid scale hypothesis. This is known as the large scale simulation process.

The governing equations associated with modelling of wave and current interaction are, as with fluid flows in general, the Navier-Stokes equations. It is assumed, from dimensional arguments and for all the models described below, that the convective accelerations as well as the Coriolis accelerations are negligible. Also assumed is that the flow is incompressible, i.e. that the term  $\partial\rho/\partial t$  in the continuity equation can be ignored.

This leads to the following equations:

$$\frac{\partial U}{\partial t} = -\frac{1}{\rho} \nabla p + \frac{\partial}{\partial z} \left( \frac{\tau}{\rho} \right) \quad 2.6$$

where  $t$  is the time variable,  $\nabla$  is the vector operator:

$$\nabla = \frac{\partial}{\partial x} \mathbf{i} + \frac{\partial}{\partial z} \mathbf{j} \quad 2.7$$

p is the pressure

$$\mathbf{p} = p + p' \quad 2.8$$

and  $\mathbf{U}$  is the velocity vector

$$\mathbf{U} = \mathbf{u} + \mathbf{u}' \quad 2.9$$

and  $\mathbf{u}^{(i)}$  is the vector

$$\mathbf{u}^{(i)} = (u^{(i)}, w^{(i)}) \quad 2.10$$

The superscript ' indicates the components due to the waves and turbulence (or unsteady component) and the unmarked component is the current (the steady component).  $\tau$  and  $\rho$  are the stress, that is the force per unit area acting parallel to the bed, and density of the water.

These equations, however, are not a closed set as they contain second order products, the Reynolds stresses, within the stress term; the Reynolds stress transport equations contain third order products (as well as other unknown turbulence quantities) and so on. The Reynolds stress transport equations are obtained from the instantaneous Navier Stokes equations, if the equation for  $u$  is multiplied by  $w'$  and  $u'$ . The resulting equation for  $w$  is multiplied by  $u'$ . The resulting equations are then added together and the mass weighted time mean subtracted from the result, this leads to the equation

$$\frac{\partial(\overline{u_i u_j})}{\partial t} = -\frac{\partial(\overline{u_i u_j u_i})}{\partial x_i} + \dots \quad 2.11$$

that is the triple correlations. An infinite set of time-mean equations would be needed to reproduce all the information in the instantaneous Navier-Stokes equations. To close the set of equations the set of equations must be truncated by using experimental data or "inspired guesses" (Bradshaw et al. (1981)).

The simplest closure able to account for the variability of turbulent mixing is the mixing length concept introduced by Prandtl (1925). The mixing length is the average vertical distance (normal to the boundary) travelled by a fluid particle over which its initial momentum (or vorticity, Taylor (1935)) was conserved, but at the end of which it mixed with its surroundings. Physically this means that it must be assumed that the streamwise pressure forces and viscous stresses are comparatively small and hence unimportant, and this may be justified if the eddies are "flat" in the sense that the vertical dimensions are

much smaller than the horizontal. If an element (fluid particle) is displaced vertically a small distance,  $l$ , its apparent perturbation velocity will be :

$$u' = u(z) - u(z+l) \approx -l \frac{\partial u}{\partial z} \quad 2.12$$

Figure 2.2 shows this momentum transfer schematically. By considering the momentum transfer due to the interchange of the two “envelopes” of fluid with streamwise velocities of  $-l \partial u / \partial z$  and  $l \partial u / \partial z$  respectively, Prandtl (1925) reasoned that the  $z$  component could be taken as  $l |\partial u / \partial z|$ . Thus the shear stress

$$\tau_u = -\rho \langle u'w' \rangle \sim \rho \langle l^2 \rangle \frac{\partial u}{\partial z} \left| \frac{\partial u}{\partial z} \right| = \rho l_m^2 \frac{\partial u}{\partial z} \left| \frac{\partial u}{\partial z} \right| \quad 2.13$$

where  $l_m = (\langle l^2 \rangle)^{1/2}$  is the Prandtl mixing length.  $l_m$  may be taken to be proportional to the distance from the boundary, i.e.  $l_m = Az$ . For the constant stress region this gives

$$v \frac{\partial u}{\partial z} + \rho A^2 z^2 \left( \frac{\partial u}{\partial z} \right)^2 = \rho u_*^2 \quad 2.14$$

where  $u_*$  is the friction velocity.

Solving the quadratic equation 2.13 for  $\partial u / \partial z$

$$\frac{\partial u}{\partial z} = -\frac{v}{2A^2 z^2} + \sqrt{\left( \frac{v}{2A^2 z^2} \right)^2 + \frac{u_*^2}{A^2 z^2}} \quad 2.15$$

and using the scaling arguments  $u^* = u/u_*$  and  $z^* = zu_*/v$  yields

$$\frac{\partial u^*}{\partial z^*} = \left[ \frac{1}{2} + \sqrt{\frac{1}{4} + A^2 (z^*)^2} \right]^{-1} \quad 2.16$$

For large  $z^*$  this gives

$$\frac{\partial u^*}{\partial z^*} \approx \frac{1}{Az^*} \quad 2.17$$

Integration of 2.17 yields the logarithmic law of the wall and hence  $A = \kappa$  the von Karman constant taken as  $\sim 0.4$ . This approach for modelling wave and current interaction was taken by Bijker (1967).

The eddy viscosity concept was first introduced by Boussinesq (1877). It assumes that the eddy shear stress  $-\rho\overline{u'w'}$  and the mean rate of stress  $\partial u/\partial z$  are linearly related as in laminar flow :

$$\tau = -\rho\overline{u'w'} = \mu_t \frac{\partial u}{\partial z} = \rho\nu_t \frac{\partial u}{\partial z} \quad 2.18$$

where  $\mu_t$  is the eddy viscosity coefficient, a function of the local flow conditions. Similarly,  $\nu_t$  can be regarded as the eddy kinematic viscosity coefficient. The two coefficients are determined by local flow conditions, and this is generally done by a combination of dimensional reasoning plus the analysis of experimental data leading to useful empirical relations.

A large number of more complicated turbulence models have been proposed since Prandtl's initial work. In his own work, Prandtl (1945) assumed that the eddy viscosity was related to the mean turbulent kinetic energy  $q = 1/2\langle u_i' u_j' \rangle$  as follows:

$$\nu_t = Aq^{1/2} \Lambda \quad 2.19$$

where  $A$  is a constant and  $\Lambda$  is a length scale. This correlation function is known as an integral length scale. Jones and Lauder (1972) proposed a relation of the form

$$\nu_t = \frac{C_1 q^2}{\epsilon} \quad 2.20$$

where  $C_1$  is an empirical constant and  $\epsilon$  is the dissipation rate. To use this relation, one needs in addition a model for the dissipation, as well as the energy equation, suitably modelled. This introduces several more empirical constants and better possibilities to achieve good fits to experimental flows. The model proposed by Jones and Lauder (1972) is the so-called  $k$ - $\epsilon$  model ( $k$  is the kinetic energy), and several versions of this model exist.

#### 2.4.1 Modelling Wave and Current Interaction.

There are many more closure schemes for modelling turbulent flows, including spectral models, Reynolds stress transport models and other models that introduce more and more equations. These models tend to be used more in aerodynamic flows than in hydrodynamic flows.



In the study of the continental shelf boundary layer, particularly wave and current interaction the most often used models are those based on the zero-, one-, or two-equation models, as described above. Before 1977 the only models that had been developed for these flows were simple, linear models for a current in the presence of a wave for both co-directional and perpendicular flows. Both Smith (1977) and Grant and Madsen (1979) developed models to hypothesise the non-linear-interaction mechanism and to treat the flow for the wave and the current in both boundary layer regions simultaneously. Both these models looked at near-bottom flow and used simple time invariant, linearly varying eddy viscosity closures to model the flow while adopting different velocity scales in their closures. The Grant and Madsen model is formulated in such a way as to treat waves and currents at arbitrary angles. A description of a boundary layer using the eddy viscosity hypothesis is given below.

Smith (1977) and Grant and Madsen (1979) were the first to consider non-linear wave and current interaction. They agree on the use of an eddy viscosity which varies linearly with depth but differ on the equation taken for  $u_*$ . Smith assumes that  $u_*$  is the sum of  $u_{*w}$ , a friction velocity associated with the waves, calculated from an oscillatory turbulent boundary layer model, and a steady flow friction velocity  $u_{*c}$ . Above the wave current boundary layer the wave component of the eddy viscosity is taken to be constant. Both the mean and oscillatory flows exhibit modified logarithmic layers, for the mean flow

$$u = \frac{u_{*c}}{\kappa} \left[ \ln \frac{z}{z_0} \right] \quad 2.21$$

in the inner layer and

$$U = \frac{u_{*c}}{\kappa} \ln \left[ \frac{z + \delta_w}{z_1} \right] \quad 2.22$$

where  $z_1 = \delta_w \left( \frac{z_0}{\delta_w} \right)^\lambda$ , in the current boundary layer, where  $\lambda = \frac{u_{*c}}{u_{*w}}$ .

The flow in the wave and current boundary layer is identical to the form for waves only but with the friction velocity replaced with the total wave and current friction velocity.

The effect of the presence of waves is an increase in the bottom shear stress. This effect can be perceived as an apparent increase in the law of the wall derived from equation 2.12 and hence, the lowering of the ratio of  $U$  to  $u_*$  for a given  $z/z_0$ . This effect is significant even for small waves; for example, if  $u_{*w}/u_{*c} = 1/4$  then the boundary shear stress is increased by approximately 56% (Huntley, 1988). This enhanced shear stress is important for sediment transport, particularly as bedload.

Grant and Madsen (1979) use the quadratic stress law for a combination of waves and current conditions to compute appropriate values of friction velocity in the inner and outer layer. They consider the general case in which the wave and steady current directions are at an angle to each other. They argue that since the bed stress and the relative magnitude of wave and mean flows are inter-related in a complex non-linear manner, it is not clear which is the appropriate mean current to use in the quadratic stress law. Therefore, the mean flow and direction in the shear stress law are taken as unknowns. The solution is given in the form of a zero order Kelvin integral.

Bed stress and velocity profiles are computed by an iterative process. Mean flow speed and direction are known for a given reference height and various values of flow speed and direction are tried within the stress equations until the resulting mean flow profile matches this reference flow speed and direction.

As with Smith's model the profile found by Grant and Madsen's model in the outer regions has an apparent bottom roughness much larger than  $z_0$  as the wave amplitude increases relative to the flow. Observations supporting the enhanced bottom roughness in the presence of large waves were quoted by Grant and Madsen (1979) from Forestall et al. (1977) who when using a simple log velocity profile model determined an apparent bottom roughnesses as high as 6m over a mud bottom. The wave heights were up to 7.3m and current speeds greater than  $1.5\text{ms}^{-1}$  in 21m of water during tropical storm Delia in the Gulf of Mexico.

The Grant and Madsen model is claimed to be the better method to use when wave and current interaction is being studied in a wave dominated environment whilst Smith's is more appropriate in current dominated flows, (Wiberg and Smith (1983)).

Christoffessen and Jonsson (1985) presented two eddy viscosity models, which make an analytical model solution possible, to describe the velocity field and shear stress under waves and current motion. The models have the same eddy viscosity in the current boundary layer but different wave boundary layer eddy viscosities. These two eddy viscosities ensure coverage of the whole rough turbulent regime.

A straightforward relationship between instantaneous bed shear stress and the current - wave motion is introduced which avoids the use of the reference velocities and Kelvin integrals used by Grant and Madsen (1979) and allow the analytical solution.

Fredsoe (1984) calculates the mean velocity profile in wave and current motion using a depth integrated momentum equation. Two velocity distributions are assumed inside and outside of the wave boundary layer, both logarithmic, which allows description of the flow for the whole range from pure wave to pure current motion and for any angle. The momentum equation used is:

$$\int_{\frac{1}{30}}^{\delta + \frac{1}{30}} \rho \frac{d}{dt} (u \sin \phi - u_{\delta_w} \sin \gamma) dz = -\tau_s \sin \phi \quad 2.23$$

where  $\phi$  is the angle between the instantaneous flow direction in the boundary layer and the mean current,  $\gamma$  is the angle between the mean current direction and the direction of wave propagation and  $u_{\delta_w}$  is the velocity at the top of the wave boundary layer.

The analogy between wave and current boundary layer flow and planetary layer flow is utilised in the model of Myrhaug and Slaattelid (1990) by using similarity theory. The analogy is well known (Soulsby (1983) and Grant and Madsen (1982)) and is used following the work of Gill (1982). The turbulent current is described using a simple eddy viscosity representation which varies linearly with depth. Comparisons made with the experiments of Kemp and Simons (1982) and Bakker and Van Doorn (1978) gave generally good agreement with model results.

Davies et al. (1988) introduced a fully numerical model based on a two equation - k- $\epsilon$  - turbulence closure model. A feature of this closure scheme is that no assumptions are used other than those used successfully in modelling wave and current boundary layers

separately. This means that this approach works equally well with strong current and weak waves, weak current and strong waves and any intermediate condition. Many of the previous methods were designed with one or other end of the continuum in mind. This model does not have the discontinuities of the earlier models as the boundary layer is not separated into parts associated with waves or currents.

The final model to be discussed here is the model of Huynh-Thanh and Temperville (1992) using another turbulence closure scheme,  $k-l$ , (turbulent kinetic energy - mixing length). In three dimensions Huynh-Thanh and Temperville (1992) investigated the effect of wave and currents on the boundary layer. The fully numerical model was developed in Cartesian co-ordinates to study flat bed wave and current interaction and in orthogonal curvi-linear co-ordinates in order to investigate oscillatory turbulent flow over a rippled bed. Results from the model were compared with those of DuToit and Sleath (1981). The models were shown to work well in predicting both velocity profiles and friction velocities as well as the complex flow properties over rippled beds.

The principal conclusions of these models, for example greatly enhanced apparent bed roughness as “seen” by the outer flow, are qualitatively similar. The results of various model runs for a selection of the models presented, using the parameterised versions (see section 2.4.2) will be shown in chapter 6.

More advanced models of the bottom boundary layer that include the effects of sediment stratification, armouring and bioturbation have been developed. The effects of the Earth’s rotation and stratification effects induced by temperature and salinity gradients in the outer boundary layer have also been included in some models (Grant et al. (1983), Glen and Grant (1987)) and Myrhaug and Slaattelid (1990) but are not included here.

#### **2.4.2 Parameterisation of the Models as done by the MAST G8M Project**

Soulsby et al. (1994) presented results from eight different models in terms of non-dimensional parameters,  $y \equiv \tau_m / (\tau_c + \tau_w)$  and  $Y \equiv \tau_{max} / (\tau_c + \tau_w)$ , where  $\tau_c$  is the bed shear stress produced by the current alone having the same depth averaged speed,  $U_{mean}$ , as for the combined case,  $\tau_w$  is the maximum bed shear stress of a wave alone having the same bottom orbital velocity amplitude,  $u_b$ , as for the combined case,  $\tau_m$  is the mean bed shear stress and  $\tau_{max}$  is the maximum shear stress. These eight models were chosen

by the MAST G8 group as the ones either used by or devised by members of the G6M group. Both analytical and fully numerical models are included. The analytical models include the time invariant, eddy viscosity models of Grant and Madsen (1979) and Christofferson and Jonsson (1985); the analytical mixing length models of Bijker (1967) and van Kestern and Bakker (1984), the momentum defect model of Fredsoe (1984) and the similarity model of Myrhaug and Slaattelid (1990). The fully numerical models of Davies et al. (1988) and Huynh-Thanh and Temperville (1992) were also included, the former a two equation k- $\epsilon$  model and the latter a one equation k-mixing length model.  $Y$  and  $y$  are plotted against  $x$ , where  $x \equiv \tau_c / (\tau_c + \tau_w)$  is a measure of the relative strengths of the current and wave.  $x$  ranges from 0 for wave alone to 1 for current alone conditions. The stresses  $\tau_c$  and  $\tau_w$  are calculated directly from the input variables  $U_{mean}$  and  $u_b$ , using the relationships  $\tau_c = \rho C_d U_{mean}^2$  and  $\tau_w = 0.5 \rho f_w u_b^2$ , where  $C_d$  is the drag coefficient for the current  $U_{mean}$ , on its own,  $f_w$  is the friction factor associated with the orbital velocity  $u_b$ , and  $\rho$  is the water density. The drag coefficient was obtained from the logarithmic profile expression

$$C_d = \left[ \frac{0.4}{\ln\left(\frac{h}{z_0}\right) - 1} \right]^2 \quad 2.24$$

and the wave friction factor was calculated using the explicit formula of Swart (1974)

$$f_w = 0.00251 \exp\left[5.21 \left(\frac{A_b}{k_s}\right)^{-0.19}\right] \quad \text{for } \frac{A_b}{k_s} > 1.57 \quad 2.25$$

$$= 0.3 \quad \text{for } \frac{A_b}{k_s} \leq 1.57$$

In the absence of any non-linear interaction, for waves at an angle of  $\phi$  to the current,  $Y = \left[ x^2 + (1-x)^2 + 2x(1-x)\cos\phi \right]^{1/2}$ , by linear vector addition. For the special case of co-linear waves and currents  $Y = 1$ . Since in the absence of non-linear interaction the mean shear stress equals the stress due to the current for all angles,  $\phi$ ,  $y = x$ .

The other input parameters required for the models are  $z_0/h$ , and  $A_b/z_0$ , where  $z_0$  is the physical bottom roughness,  $h$  is the mean water depth and  $A_b = u_b/\sigma$  is the wave

orbital excursion amplitude, where  $\sigma$  is the absolute wave frequency,  $\sigma = 2\pi/T$ ,  $T$  is the wave period and  $k_b$  is the bottom roughness associated with the grain size.

The models chosen were run for 24 combinations of  $z_0/h$ ,  $A_b/z_0$  and  $\phi$  and enough values of  $x$  to resolve the curves. An example of the results is given in figure 2.3, (Soulsby et al. (1994), figure 7).

All of the above models are computationally expensive and as such are not ideal for using in morphodynamic models. It was decided that simple algebraic expressions would be preferable for this purpose.

The functions chosen give  $y$  and  $Y$  as functions of  $x$ , as defined above, in the forms:

$$y = x \left[ 1 + bx^p(1-x)^q \right] \quad 2.26$$

$$Y = 1 + ax^m(1-x)^n \quad 2.27$$

where  $a$ ,  $m$ ,  $n$ ,  $b$ ,  $p$  and  $q$  are fitting coefficients. These equations are not physically meaningful, in that they have no base in physics and were chosen only because they were suggested by the shape of the result curves from the inter-comparison exercises. Equations 2.26 and 2.27 were fitted by a non-linear least squares technique to the results from each of the models in the inter-comparison. Values for the fitting coefficients were calculated for each model. Comparisons between the parameterised models and the calculated models were made and reasonable agreement was found. In nearly all cases a relative standard error of between 1 and 3% and a maximum relative error of 5 to 10% were found. This accuracy was considered acceptable as the errors are smaller than the differences between the models. These equations and coefficients, it was concluded, give a computationally efficient and acceptably accurate approximation to the maximum and mean shear stresses predicted by the models.

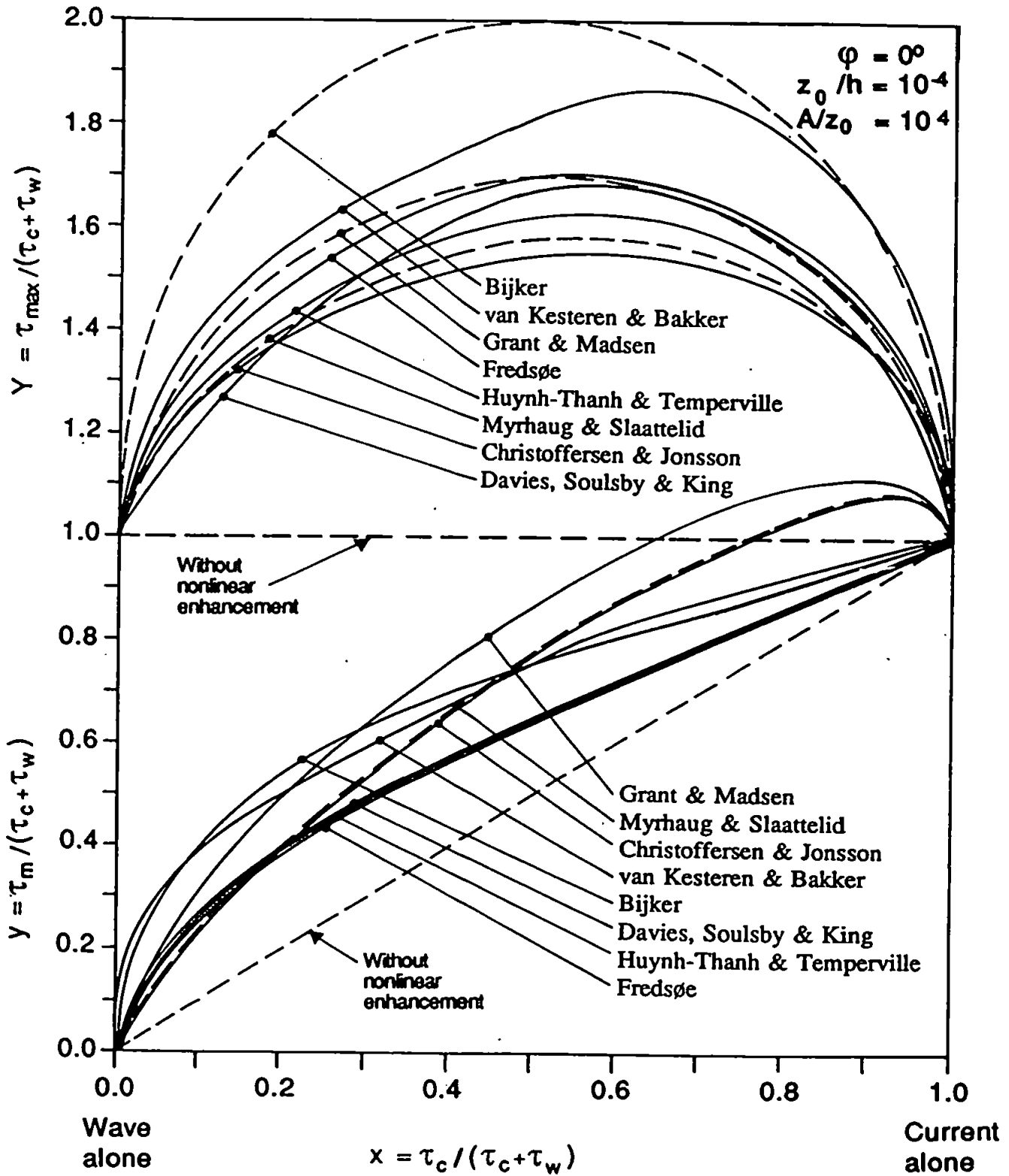


Figure 2.3 An example of the curves used in the parameterisation from Soulsby et al. (1994) showing the maximum and mean shear stresses calculated for each model.

Soulsby et al. (1994) and Simons et al. (1995) used equations 2.26 and 2.27 to produce a parameterised model based on field data. A least squared fit of 131 field estimates of maximum and mean shear stresses was carried out using 2, 3 and 13 coefficients. These coefficients were used in the same way as the parameterised models to then estimate shear stresses from other field data.

## 2.5 Field Studies

With the development of the models suitable for demonstration and prediction of wave and current interaction it became necessary to collect data to test the accuracy of the model predictions.

Cacchione and Drake (1982) collected a set of data during a storm on the Bering Sea shelf. The relatively large and steady currents and high waves generated during the storm made it a satisfactory set of data for testing these models.

The field site was located in Norton Sound, Alaska. The Geoprobe tripod system was situated in approximately 18m of water on a relatively smooth bed of fine grained non-cohesive material with a mean diameter of  $70\mu\text{m}$ , (Cacchione and Drake, 1982). The data set was comprised of measurements of pressure and horizontal components of current velocity measured at four levels above, but within one metre of, the seabed. The data were collected in bursts of 60 seconds every hour at a frequency of 1 Hz. Also at 2m above the bottom values of percent light scattering and light transmission were recorded hourly and subsequently converted to suspended sediment concentration units. Cacchione and Drake analysed their data using the logarithmic profile to estimate bottom stresses and bottom roughness and compared the results with the Grant and Madsen model predictions. They concluded that the large values of apparent bottom roughness,  $z_0$ , indicated by their measured data were not fully explained by the wave and current interaction model.

Wiberg and Smith (1983) did a comparison of field data and theoretical models using some of the data collected by Cacchione and Drake (1982). They used the Grant and Madsen (1979) model and the Smith model with a few alterations: first the total shear stress was found by summing the enhanced boundary shear stresses associated with waves and currents rather than by summing the respective shear velocities. Second, the



model was altered to take into account differences between wave and current directions. Stratification effects resulting from the near bottom suspended sediment were included in the Smith model also. The effect of stable stratification inhibits vertical momentum and mass transfer and hence reduces the shear stress near the bottom.

Wiberg and Smith (1983) suggested that the frame of the Geoprobe station settled or scoured several centimetres into the soft bottom, thereby reducing the distance between the instruments and the bed. This settling/scour could have caused the velocity profiles, determined from the data, to curve relative to the ideal semi-logarithmic profile and to yield physically unrealistic values of the roughness parameter. Also they found that the lowest current meter appeared to be within the wake caused by one of the support legs of the instrument tripod, with the result that the velocity measured at that height was low. This reduction in velocity was corrected for using turbulent wake theory. The velocity profiles were adjusted for the change in distance between the bed and the current meters by decreasing the distance until each profile was straight. The change in height above bottom and current velocity resulted in lower values of the shear (friction) velocity,  $u_*$ , and roughness parameters,  $z_0$ . The Smith and Grant and Madsen Models were able to predict the adjusted profiles well.

Wiberg and Smith (1983) used a density stratification correction incorporated into the Smith model following procedures outlined by Smith and McLean (1977) and Long (1981). The presence of stable stratification inhibits vertical momentum and mass transfer, thereby reducing the shear stress near the bottom. Long (1981) presented a model to estimate the effect of stable density stratification on the vertical diffusion of mass and momentum. Applying this stratification model, however, does create a problem, since the density stratification correction is not time dependent, and the effect of the waves on the suspended sediment was not clear. Wiberg and Smith decided that since the average particle fell at most 1.1 cm per half wave cycle, less than half the wave boundary depth, the error introduced by the neglecting of the time dependence is small and so time dependence was ignored.

They concluded that the results of the model were sufficiently similar that there is no basis upon which to single out one of the models as being superior over the other. Also that

“Estimates of the reduction in vertical diffusion of momentum and mass as a result of near-bottom suspended sediment indicate that no sediment stratification correction is required in this case.”

It was also found that the models provided a better estimate of the measured shear velocity than can be obtained when only the currents are included in the calculations.

The Coastal Ocean Dynamics Experiment - (CODE) - (Allen et al. (1982)) on the Northern Californian continental shelf provided an excellent opportunity to investigate the structure of the bottom stress field on a geomorphologically simple continental shelf. The overall objectives of the CODE experiment were to identify and study important dynamical processes that govern the wind driven motion of coastal waters over the continental shelf. A 4 year research program was initiated to collect high quality data sets of all the relevant physical variables needed to construct accurate kinematic and dynamic descriptions of the response of shelf water to strong wind forcing in the 2-10 day synoptic scale. Two small scaled densely instrumented field experiments each of 4 months were carried out in the spring of 1981 and 1982. Data including wind speed and direction, solar radiation, temperature, surface currents, bottom pressure and near bottom currents, as well as shipboard observations of temperature, conductivity and surface fluxes, and aircraft and satellite derived measurements, were all collected over these periods.

Grant et al. (1983) presented results of the bottom current measurements made as part of the bottom boundary layer and bottom stress component of CODE-1. Geoprobe (Cacchione and Drake, 1982) was deployed in 90m water depth at a midshelf location in the CODE-1 area for up to two months. The tripod measured velocity profiles every two hours along with a set of supporting data variables. These measurements were analysed to give long time series of stress and near bottom flow.

A shorter term experiment was set up, consisting of an array of Woods Hole Oceanographic Institution bottom tripods (WHOI BASS W) deployed for between 3 and 5 days. Three components of velocity were measured at four levels above the seabed to a maximum height of 2m above the seabed, using a repeating sequence of continuous measurements for up to several hours and a shut-off period of approximately an hour. The current meters, acoustic-travel-time meters, measured velocity averaged over a 15cm

diameter sphere. The data were collected at 5 Hz. The bottom boundary layer measurements were analysed for velocity profiles, roughness lengths and shear stress estimates using dissipation and profile techniques. The results of the analyses were compared with predictions made using Grant and Madsen's 1979 model. It was found that roughness length and shear velocity value estimates were much larger than could be explained by physical bottom roughnesses and mean flow alone. Support data on temperature, salinity and variables demonstrated that the observed  $u_*$  and  $z_0$  values cannot be attributed to their influence.

Comparisons between the data estimates and predictions using the combined wave and current model of Grant and Madsen (1979) show good agreement between estimated and predicted  $u_*$  and  $z_0$  values. There was found to be a minor problem with the prediction scheme, involving the estimation of physical bottom roughness over the bioturbated bottom characteristic of the midshelf region. The values had to be estimated empirically which, it was stated, did not affect the validity of the results but did complicate predictions unless photographs or box cores existed. Grant et al. (1983) concluded that the correspondence between the estimates from the dissipation and profile techniques was a good measure of the quality of the data set. They point out that care must be used when interpreting and applying stress values estimated in the field and that the field measurements provide good support for the general importance of wave and current interaction to bottom stress behaviour and boundary layer processes on continental shelves. However, there was some uncertainties about the contribution of bedforms to the large measured stresses (Huntley (1985) and Grant and Williams (1985)). Gust (1985) also pointed out two apparent errors in their use of the dissipation method for estimating bottom stress. The Grant et al. (1983) results were revised and discussed in Huntley (1988).

Huntley and Hazen (1988) describe field measurements made on the Nova Scotia continental shelf in two separate deployments. In July 1984 the tripod was deployed in 25m water depth in Cow Bay, Nova Scotia, the second deployment site was on Sable Island Bank in a depth of 45m in September 1984. The instruments on the tripod consisted of 2 or 3 pairs of electromagnetic current meters (EMCM) deployed orthogonally at different heights, each measuring one horizontal and the vertical component of the flow. Also, an array of heated thermistors was used in one of the

deployments which helped in the determination of the zero flow offset. Other sensors attached to the tripod included a stereo camera, to help with the small scale topographic scales, an optical transmissometer, a digital compass and direction vanes for monitoring mean flow direction.

The paper discussed the estimation of mean flow friction (shear) velocity for the two sites where both mean flow and waves were present. Friction velocities were estimated by the modified dissipation method described by Huntley (1988).

The number of observations discussed was small, covering a restricted range of waves and mean flow conditions. The measured values of the friction velocity were consistently larger than can be readily explained by a boundary layer where mean flow effects alone are important. It was impossible to rule out entirely the possibility that the observations were the result of extremes of bottom roughness, but it is unlikely to have been the case at both sites. It was concluded that it was reasonable to suggest that enhanced bottom stresses were due to the presence of wave motion.

The results were compared with the predictions based on the Grant and Madsen (1979) model. The predictions based on the significant wave velocity were in close agreement with the observations. This agreement was encouraging and suggested that, at least for low energy conditions, the Grant and Madsen model accurately predicted the influence of waves.

Lyne et al. (1990) investigated sediment movement along the U.S. east coast continental shelf and estimated bottom stress using the Grant and Madsen model and near bottom wave and current measurements. They took the position that the shear stress model results were correct and compared these with conventional drag law estimates of shear stress. A long term programme of measurements of bottom pressure fluctuations and currents over the Mid Atlantic Bight continental shelf and the southern flank of the George's Bank was carried out between 1976 and 1984. One of the objectives of the programme was to assess the spatial and temporal variability of bottom stress, and its implications for sediment transport. The instruments were deployed on a bottom mounted tripod system. Time series of current speed and direction were measured, at approximately 1m above the bed, by a Savonius rotor and small vane sensor. Pressure

was measured by a quartz crystal transducer and turbidity was measured by a transmissometer. Time lapse photographs of the seabed were also taken. Samples were taken at a burst rate of 4s for a period of 48s (12 samples) repeated every 3.75 or 7.5 minutes. The tripod was deployed at 4 stations along the U.S. north-eastern continental shelf which spanned a wide range of tidal currents and bottom sediment texture, in water depths varying from 64 to 80m. Sediment varied from coarse ~ 200 $\mu$ m median size with megaripple sand wave field to finer texture sediment with asymmetrical sand ripples a few centimetres in height.

Bottom stress was computed using the Grant and Madsen (1979 and 1982) models but uncertainties in the bottom stress were found to be due to errors in measured waves and bedforms. Lyne et al. (1990) found that the Savonius rotor and vane sensors provided adequate current observations during most of the observation period except when the waves were large and mean currents weak.

Computations of stress and roughness which incorporate moveable bed effects, such as ripple formation and sediment transport, suggest large increases and decreases in effective bed roughness during storms. At one station predicted ripple roughnesses were almost twice as large as those based on observed ripples. Lyne et al. (1990) concluded that the moveable bed effects are a limiting factor in using the models to predict bottom stress and that further field and laboratory studies were needed to refine and validate both fixed and moveable bed models in realistic field conditions. They also concluded that, assuming the model to be right, the bottom shear stress calculated from the corrected wave and current were accurate to within 10-20% except when the bottom wave speed exceeded the current speed. When this occurred stress estimates were considerably larger than predicted, this was attributed to a problem with the sensors and sampling scheme rather than the model.

Data were collected in Marsden Bay on the N.E. coast of England in approximately 24m water depth by Green et al. (1990). Instruments were attached to a tetrapod and included an array of 5 EMCM's, a camera and flash, a transmissometer, an altimeter and a logging processing unit. The current meters measured two orthogonal components of the horizontal flow at 5 elevations above the bottom, from 13cm to 133cm above the bed. Sampling was carried out in bursts of 10 minutes out of every 30 minutes and consisted

of 500 points with a sampling interval of 1.2 seconds. Using a logarithmic profile method they found that the magnitude of the friction velocity inferred by the measured velocity profiles appeared to decrease with the near bed wave energy, which is consistent with wave/current theory. Also, the discrepancy between roughness inferred by the measured velocity profiles above the wave boundary layer and the expected roughness was greatest when the waves were most energetic, as would also be expected with wave and current interaction.

A two layer time invariant eddy viscosity model of the wave/current boundary layer was used to predict the time averaged friction velocity and the predictions compared well with observations with the exceptions that formed two groups. The first group, in which the modelled estimates were underestimates of the observations, comprised observations from the time of peak observed bed stress. Green et al. (1990) suggest that a plausible explanation for this discrepancy is that an evolving ripple field an/or saltating layer was unaccounted for in the predictions. The second group, in which model predictions were over estimates of the observations, comprised observations for times of minimum observed bed stress. These bursts also had the lowest observed roughness Reynolds number, all of which fell below the critical value for transition to fully rough turbulent flow. Since laboratory measurements imply wave and current interaction does not occur within a the smooth turbulent boundary layer, (Green et al. (1990)), the predictions of time averaged velocity were repeated using a smooth turbulent pure current model. The predictions were significantly improved, thus supporting the suggestion that ripples could be forming.

Soulsby and Humphrey (1989) present data collected over an immobile rough bed, a featureless mixture of gravel sand and shell. The measurements were made in October 1986 at a site in the English channel 7.5 km south west of the Isle of Wight. The instruments were mounted on a self-recording frame - STABLE - (Sediment Transport And Boundary Layer Equipment) and consisted of four EMCM's, two of which measured two horizontal components of velocity at heights of 10 and 80 cm and an orthogonal pair mounted at 40 cm to record all three components of the flow. A pressure transducer measured tidal variation but failed to record wave induced pressure fluctuations. Data were collected at 4 Hz for 8.5 minutes with one record made every 3 hours.

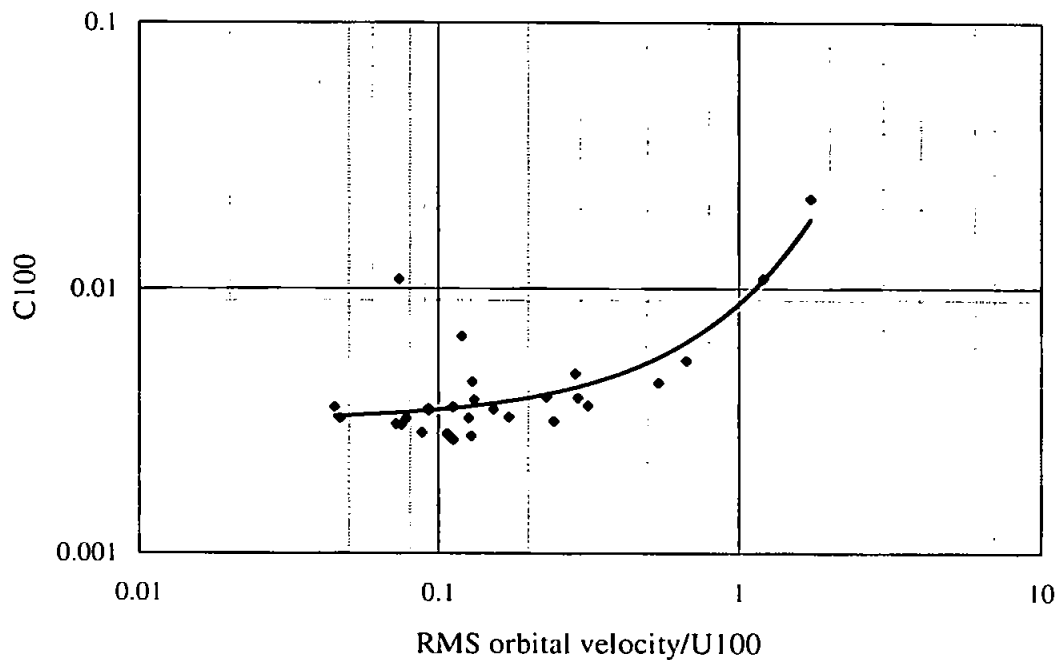


Figure 2.4 Soulsby and Humphrey (1989)'s Figure 9 shows the drag coefficient,  $C_{100} = \tau_o / \rho U_{100}$ , as a function of wave to current ratio,  $\sigma_{wave} / U_{100}$ .

The data collected were used to estimate bottom stresses using three different methods: logarithmic profile, Reynolds stress method (i.e.  $\tau_r = \rho \left( \overline{u'w'^2} + \overline{v'w'^2} \right)^{1/2}$ ) and a new technique of splitting the spectrum into fluctuations due to waves and fluctuations due to turbulence. Soulsby and Humphrey concluded that the three methods of deriving the bed shear stress gave essentially similar values under all wave and current conditions and that the bed shear stress and turbulent kinetic energy increased strongly with the wave:current ratio. Figure 2.4 is a copy of their results, their figure 9, which shows the drag coefficient as a function of the wave to current ratio.

## 2.6 Model of Tidal Currents over the inner shelf, at Nieuwpoort, Belgium, as a Large Scale Method to Estimate Bed stress.

Another method to estimate shear stresses was suggested by O'Connor et al. (1995). This large scale method used the relationship between the tidal elevation and the tidal current to estimate a linear friction coefficient.

Studies at or just offshore from the proposed field site for this project have revealed a difference between tidal flows measured offshore and those measured at the coast. Lanckneus et al. (1994; quoting Van Cauwerberghe (1992)) described the tidal flow "off

Nieuwpoort” as lagging the elevation by about one hour at low tide and between one and two hours at hightide, implying the easterly tidal flow increases in magnitude over high tide. O’Connor et al. (1995) found, in contrast, that beach measurements show a consistent decrease over high tide, with maximum eastward flow as the sensors were covered and a decreasing flow until the instruments emerged. In order to explain this phase shift a simple model of the alongshore tidal flow due to the tidal wave propagating from west to east along the Belgian coast was proposed.

Assume a simple linearised equation for depth-averaged flow, with a linear friction coefficient, such that the alongshore tidal current is dependent only on tidal elevation and water depth, i.e.

$$\frac{\partial v}{\partial t} = -g \frac{\partial \eta}{\partial y} - \frac{Kv}{h} \quad 2.28$$

where  $v$  is the alongshore tidal flow,  $\eta$  is the tidal elevation,  $K$  is the linear friction coefficient, with dimensions of velocity,  $h$  is the water depth, the  $y$  co-ordinate is orientated alongshore, positive to the east, and  $g$  is the acceleration due to gravity.

It is also necessary to assume that the tidal elevation gradient term is independent of the water depth, i.e. has no dependence on cross-shore distance.

Writing:

$$g \frac{\partial \eta}{\partial y} = F_0 e^{i(ky - \sigma t)} \quad 2.29$$

$$v = v_0 e^{i(ky - \sigma t)} \quad 2.30$$

where  $k$  is the tidal wavenumber and the wave propagation is assumed to be in the positive  $y$  direction (eastwards), substituting into equation 2.28 gives:

$$-i\sigma v_0 = -F_0 - \frac{Kv_0}{h} \quad 2.31$$

rearranging gives

$$v_0 = -\frac{\left(\frac{K}{h} + i\sigma\right)F_0}{\left(\left(\frac{K}{h}\right)^2 + \sigma^2\right)} \quad 2.32$$

Since it is only necessary to be concerned with the phase of  $v$  relative to the elevation gradient it is possible to assume that  $F_0$  is real, i.e. that it has a phase of zero. Hence:

$$v_0 = |v_0| e^{i\alpha} \quad 2.33$$



where

$$|v_0| = \frac{F_0}{\left(\left(\frac{K}{h}\right)^2 + \sigma^2\right)^{0.5}} \quad 2.34$$

and

$$q = \tan^{-1}\left(\frac{\sigma h}{K}\right) \quad 2.35$$

Thus as  $K$  tends to zero, when friction can be considered negligible, the phase between the elevation gradient and the current approaches  $\pi/2$ , i.e. the elevation and current are in phase and the tide is just an eastward progressive wave. When the friction dominates,  $q \rightarrow 0$ , the elevation and current are in quadrature, as for a standing wave. This model implies that as the depth decreases towards the shore the tidal wave becomes more like a standing wave with maximum flows occurring inshore earlier than offshore. This prediction agrees with observations made off the Belgian coast (Van Cauwenberghe (1977, 1985 and 1992)), and presents an explanation for the observed flows.

O'Connor et al. (1995) used this model to give a rough estimate of the linear friction coefficient for the beach alongshore currents. By fitting a sinusoid of  $M_2$  period to the data from a tidal cycle using a least squares method they found estimates for the quadratic drag coefficient,  $C_d$ , in the range  $(0.5 - 1.5) \times 10^{-3}$ . They suggest that whilst there is ample room for refinement, the methodology showed promise. This method will not be used to estimate shear stresses, those chosen will be described in detail in chapter 4.

## 2.7 Sediment transport under waves and currents

Wave motion by itself does not produce any net sediment transport. However, the waves are a very effective stirring mechanism (Dyer (1986)), and can create suspension at a much lower equivalent velocity than a steady current. Once in suspension the sediment can be moved by relatively small currents which by themselves would not be able to move the sediment.

When water flows over a bed of loose grains there is a velocity at which the combined lift and drag forces on the top particles are great enough to dislodge the sediment particles. This velocity is known as the critical or threshold velocity. Related to this is the critical or threshold shear stress.

For a high Reynolds number regime the lift and drag coefficients are independent of the grain Reynolds number:

$$Re_* = \frac{u_* d}{\nu} \quad 2.36$$

where  $d$  is the mean sediment grain size. The Shields entrainment function,  $\theta$ , is a dimensionless function which compares the shear stress with the immersed weight of a unit grain thickness layer of the bed:

$$\theta = \frac{\tau}{(\rho_s - \rho)gd} \quad 2.37$$

where  $\rho_s$  is the density of the sediment. Shields produced a threshold curve (see Dyer (1986), p112) relating the grain Reynolds number to the Shields parameter. If the critical Shields parameter is exceeded then sediment transport occurs. This however does not mean that there is no sediment transport below its threshold. Bursting events can occur within the viscous sublayer which may result in the movement of some of the exposed grains.

Sediment transport has been modelled under waves and currents, for example Glen and Grant (1987) using an eddy viscosity closure scheme, but these models have not been used in subsequent chapters and will not be discussed here.

## 2.8 Conclusions drawn from the review

Wave and current interaction has been studied extensively over the last two decades. A wide range of models exist, all predicting the enhanced mean flow bed stress in the presence of waves and currents. Field measurements confirm this enhancement, however, there is still considerable uncertainty about its magnitude. This is especially true for the relatively large wave conditions experienced in the nearshore zone. Hence, the work described in the following chapters will, in some part, remedy this situation.

## **Chapter 3**

### **Fieldwork and Data Collection**

#### **3.1 Rationale**

There has been little work until recently on the effects of wave and current interaction (WCI) in the nearshore zone. In section 2.5 field studies were presented in which the data collected were used to investigate wave and current interaction. All of these studies were carried out in water depths of greater than 20m where wave action was still present, but none were carried out in the intertidal zone. The problems of collecting data in the inter-tidal zone are many: the equipment is only covered for short periods of time on either side of high tide and hence there is only a short time to collect data over each tidal cycle. The surf zone is an intensely dynamic environment and breaking waves can produce enormous forces which are potentially damaging to both the instruments and their rigs, as experience has shown. There is also the problem of sediment movement, not just in the surf zone but when the sea covers the beach area the seawater permeates into the sand and the sand-seawater mixture acts as a liquid. This liquefaction effect is felt for as much as 1m below the seabed, (Huntley, Pers. Comm). To keep the equipment steady it is necessary to have the bottom of the rigs deep enough to minimise the instability caused by the liquefaction of the sediment. These problems were just some which were anticipated; other problems were encountered and overcome and will be described as the situations occur. Most studies carried out have been in environments of co-linear or nearly co-linear waves and currents; but the object of the field campaign was to gain knowledge of WCI in a natural setting and to obtain data of a sufficient quality to make comparisons with turbulence models being developed as part of the MAST G8M project. Another objective was to establish the conditions under which existing methods

for estimating bed shear stresses can be used and to ascertain the predictability of the results. Whilst there are other data sets available it was anticipated that the new data set would expand the breadth of useful data sets by collecting data in the presence of a larger wave to current ratio.

Since wave and current interaction occurs wherever there are waves and a current present, whether in estuaries or on beaches, in shallow or in deep water, it was unnecessary to set up a specific and separate field campaign. This made it possible to collaborate with another project. The data were collected as part of the MAST II CSTAB (Circulation and Sediment Transport Around Banks) project (contract MAS2-CT92-0024). Collaborators on this campaign included Southampton University; University of Liverpool; University of Reading; Birkbeck College, London, University of Lisbon, Portugal and Bordeaux University, France.

To study wave and current interaction in the field, only two things are necessary, waves which affect the entire water column and currents of sufficient velocities to enable the turbulent fluctuations to be perceived by the current meters. This statement will be explained in more detail in chapter 4, (figure 4.6), but briefly, velocities greater than  $15 \text{ cm s}^{-1}$  are required.

## **3.2 Instrumentation**

Three types of instruments were used in the deployment - electromagnetic current meters, pressure transducers and optical backscatter sensors.

### **3.2.1 Electromagnetic Current Meters (EMCM)**

Two types of EMCM's were used, Series 800, 5.5 cm spherical and 17 cm annular, (see figure 3.1), made by Valeport of Dartmouth, Devon. Both types of EMCM's work by the same principle. In the head of each instrument is a coil which sets up a magnetic field. Two pairs of electrodes are arranged around the head so that each electrode is diametrically opposed to its mate and each pair is orthogonal to the other. By Faraday's law of induction when an electrical conductor of a given length passes through a magnetic field of a known strength at a velocity in a direction at right angles to both the magnetic field and its length an electromotive force  $E$  is generated

where  $V$  is the velocity. The length of the electrical conductor for the current meters is the diameter of the sensing volume, given in table 3.1,  $E$  is measured in the field and the constant of proportionality is the calibration gain.

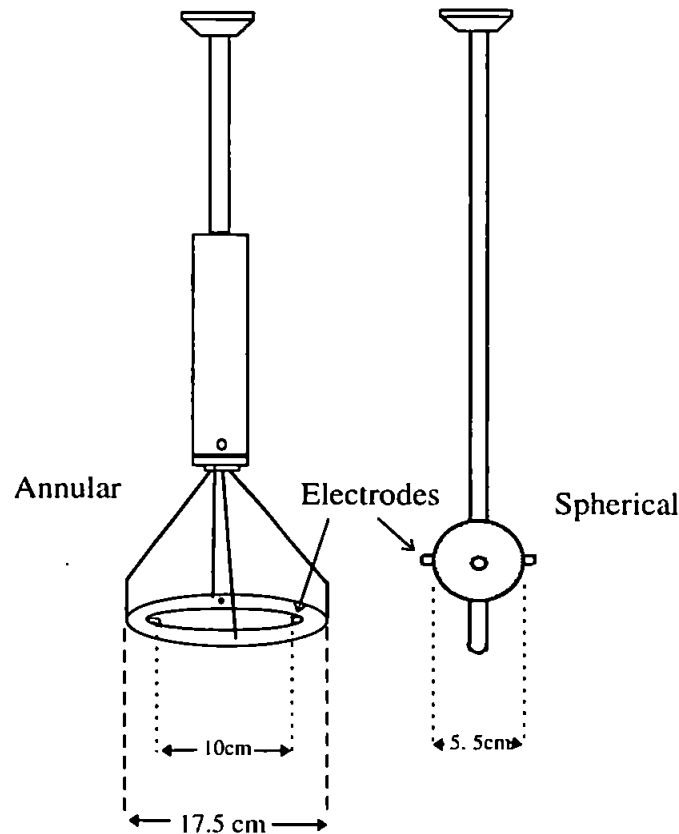


Figure 3.1 Two types of electromagnetic current meters were used, the annular (left) and the spherical (right).

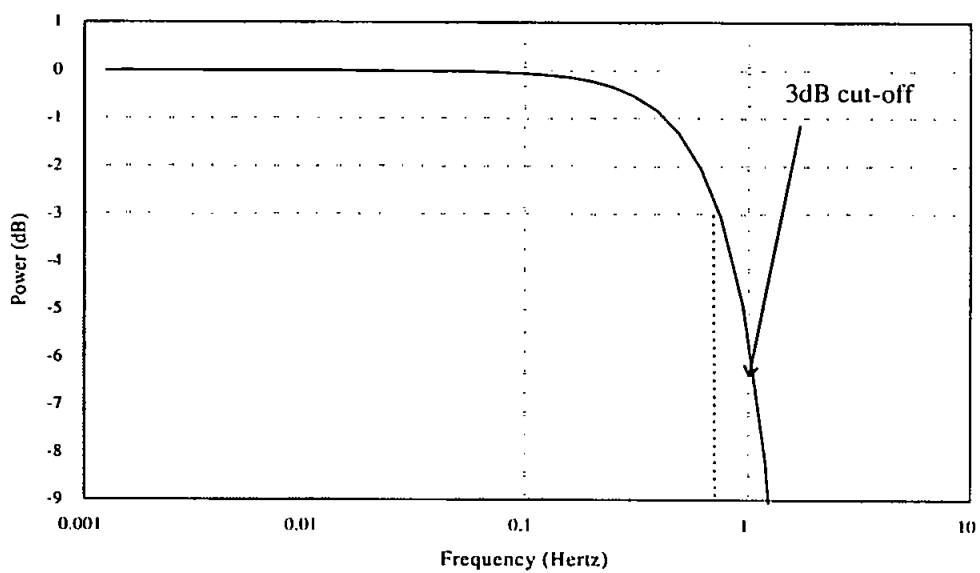
Figure 3.1 shows the two heads of the instruments used. At the top of these heads are stainless steel fixing points which enable the instruments to be attached to the deployment frame. A 3 m cable runs from the top of each meter to a watertight canister containing all the electronic equipment controlling the sensing ability of each instrument. The arrangement of the instruments will be described in more detail in section 3.3.5, and the data logging system will be described in section 3.3.6.

### 3.2.1.1 Filter Characteristics

The EMCM's each have a manufacturer's low-pass filter in the instrument pod attached to the 3 m cable from the pod to the head. The filter insures against aliasing of the signal, which can occur when fluctuations at higher frequencies than the Nyquist frequency, half

the digitisation rate, are interpreted as fluctuations due to lower frequencies. The manufacturers specified that the filters supplied had a cut-off of 1.25 Hz, that is that at 1.25 Hz the signal was at half power, -3dB. To collect data with turbulent fluctuations at a higher frequency than 1.25 Hz the filters had to be changed. This involved changing a number of resistors, (30), in each instrument pod. Because of the intricacy of this operation only two current meters were changed from 1.25 to 4 Hz. Despite this change subsequent analysis of data collected in a previous campaign indicated that the filters were not working in the anticipated way.

(a)



(b)

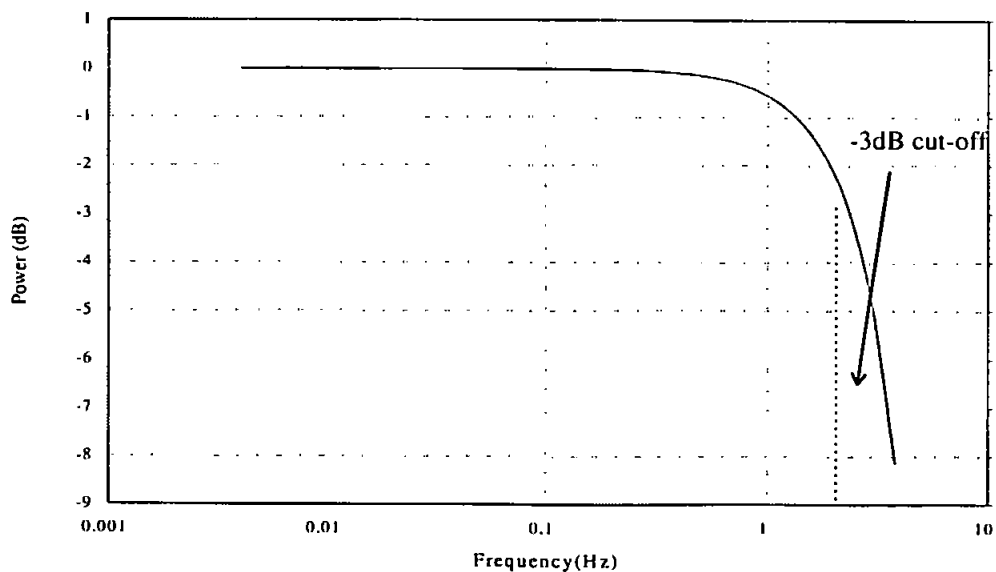


Figure 3.2 Filter characteristics of the EMC's before, (a), and after, (b), resistors were changed.

An examination of the filter description in the manufacturer's manual revealed that the filters had a cut-off of 1.25 Hz. However, there were three of these filters in series within each of the instrument pods. As a result the signal at 1.25 Hz was actually at -9dB after going through the three filters, that is not 1/2 but 1/8 power.

The filters were checked by sending signals of a known frequency and amplitude into the filters and comparing these with the output. The results are shown in figure 3.2. Figure 3.2(a) are the results from the manufacturer's original filters showing a -3dB cut-off at 0.8 Hz and figure 3.2(b) shows the results from the filters that were changed giving a cut-off of 2.4 Hz, which is consistent with a -9dB at 1.25Hz and 4Hz, respectively.

The technical data for the two types of EMCM's is listed in table 3.1 below.

	Spherical 0.055m diameter	Annular 0.17m diameter
Sensing Volumes	3 times sensor head diameter 0.175m diameter sphere	0.1m diameter sphere
Noise	< 0.015 ms <sup>-1</sup> rms	< 0.01ms <sup>-1</sup> rms
Typical errors to linear calibration fit	< 0.02ms <sup>-1</sup>	< 0.002ms <sup>-1</sup>

Table 3.1 Comparison of the technical data of two EMCM types, from Valeport technical data sheet.

### 3.2.1.2 Calibration of the EMCM's

Calibration of the instruments took place both before and after the field campaign.

#### 3.2.1.2.1 Gains

The instruments were calibrated in a large towing tank at the Royal Naval Engineering College (RNEC), Manadon. The tank was 30m long and 5m wide and varied in depth from 2 to 3 m, figure 3.3. A gantry above the tank could be moved down the length of the tank by computer controlled stepper motors at speeds ranging from 5 cms<sup>-1</sup> to 3 ms<sup>-1</sup>. The instruments were suspended from the gantry above the water using the frames which would be used in the field campaign as field stations and submerged to a depth of approximately 0.3 m beneath the water surface. Sensor orientation was accomplished as follows: at the top of each current meter is a notch, denoted as the "y-notch", to indicate

the orientation of the flow meter, that is the nominal positive y axis when the notch is into the flow. The instrument pods were attached to the gantry above the water to insure that they did not drag through the water and interfere with the flow over the instruments. A cable, known as the beach cable ran the length of the tank and was suspended away from the gantry by a pole so as not to impede the movement of the gantry. The complete system to be used in the field, including the data logging system, was used to ensure calibration of the system as it would be used in the field. A more complete description of the data logging system is given in section 3.3.6.

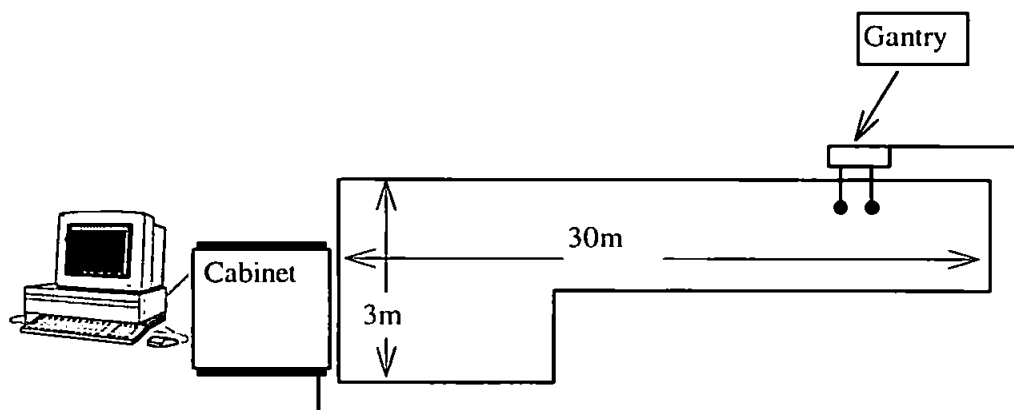


Figure 3.3 Diagram of tank used in calibration of both pressure transducers and electromagnetic current meters.

An initial run of  $2.5 \text{ ms}^{-1}$  was carried out to look for any misalignment of the instruments into the flow. A misalignment would manifest itself as an increase in the voltage recorded for the electrodes normal to the flow, showing that the electrodes were sensing a change in the magnetic field caused by the velocity of the instruments through the water. Sets of data were recorded for velocities ranging from 0 to  $2.5 \text{ ms}^{-1}$ , first with the y notch into the flow then with the y-notch at  $90^\circ$  to the flow. A run of  $3 \text{ ms}^{-1}$  was done for one set of instruments but bubbles of air were observed forming around the instrument head, due to the wake caused by the post connecting the head to the rest of the instrument and so the data had to be discarded.

Data collected from each run were processed and a straight line of best fit for voltage versus towing speed was calculated for each instrument channel. Table 3.2 gives the calibration gains found in the experiment, with the  $r^2$  values and degrees of freedom. Figure 3.4 shows the calibration data from the current meter B3Y, (chosen for having the



lowest  $r^2$  value). Whilst the gains vary considerably between instruments, ranging from 0.99 and 1.35 at the extremes, it is satisfying to note the similarities between each current meter pair.

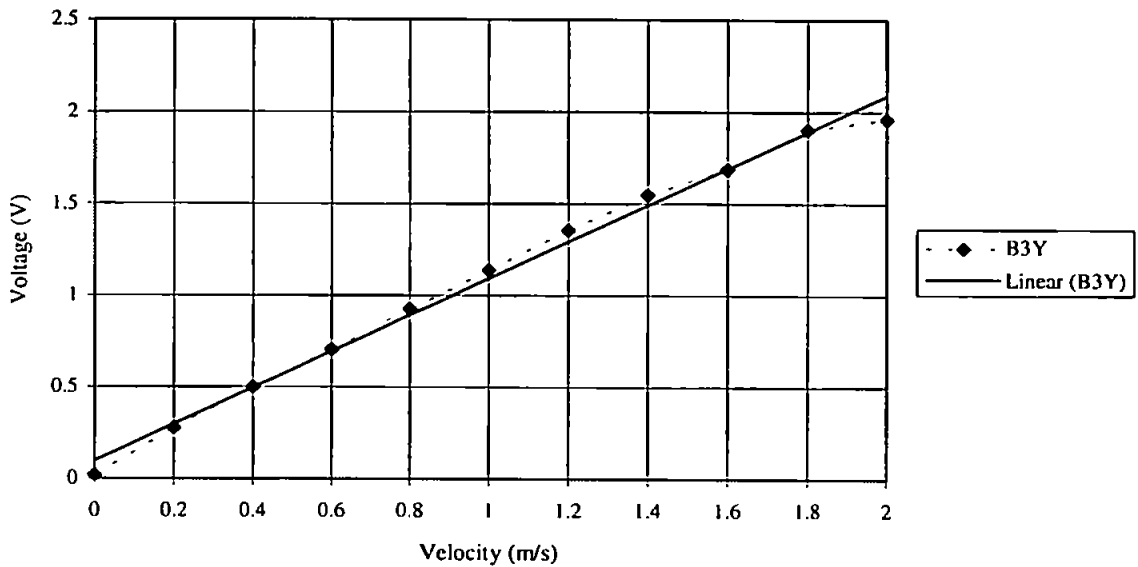


Figure 3.4 Calibration results from EMCM B3Y showing linear line of best fit.

Current Meter	Channel	Gain Volts/(m/s)	$r^2$ For Linear Fit	Degrees of Freedom
A1	X	1.29	0.996	9
	Y	1.30	0.997	10
A2	X	1.02	0.998	9
	Y	1.08	0.992	10
A3	X	1.35	0.999	10
	Y	1.31	0.9995	10
B1	X	0.99	0.995	9
	Y	1.01	0.993	9
B2	X	1.23	0.999	9
	Y	1.21	0.998	9
B3	X	0.99	0.996	9
	Y	0.96	0.992	9

Table 3.2 EMCM calibration constants, giving the degrees of freedom of the linear best fit.

### 3.2.1.2.2 Offsets

It is known that offsets of the EMCM's vary depending on the environment in which the EMCM's are found. For this reason offsets taken in field conditions are used in subsequent analysis. Examples of variation in the offsets are given in table 3.3; the disparity is quite considerable and could lead to a difference in velocity of as much as

50cms<sup>-1</sup> in the worst case. It was suggested, Humphery (Pers. comm.) that the offsets changed when the instruments dried out, however a subsequent field deployment at a shelf edge site, (Chatwin (1996)), where rotor current meters were also deployed, revealed a continuous drift in the offsets over the entire deployment, two weeks, although the instruments were covered for the whole campaign. Consultation with the manufacturers revealed that they were unaware of this problem and details of the observations made were sent to them. The manufacturers suggested that the differences in offsets in the Manadon data were caused by high frequency noise due to the stepper motors used to run the gantry.

Reasons for the drift in the offsets are not completely understood. The EMCM's are very sensitive to changes in the magnetic field surrounding them and electrical interference can cause a significant difference in the zero-offset voltage. Huntley and Hazen (1988) found that the offset variations lead to uncertainties in the mean flow of 2 – 3 cms<sup>-1</sup>. Errors from offsets of the order of tens of centimetres in the field are unlikely to occur as the magnetic field surrounding the instrument station would not be of the same strength as those in the laboratory. Also, an enormous error in offsets such as this would show up when the velocities from the different current meters are compared. It was decided to use the offsets taken in the field to calculate the flows from the time series.

Current Meter	Channel	Offsets Manadon	Laboratory	Belgium
A1	X	0.0563	0.1836	-0.1552
	Y	0.0647	0.0048	-0.0873
A2	X	0.0661	0.0656	-0.0246
	Y	0.2608	0.0053	0.1138
A3	X	-0.2136	0.4668	-0.0544
	Y	-0.0313	0.1063	0.0941
B1	X	0.1329	-0.1093	0.2258
	Y	-0.0572		-0.0708
B2	X	-0.1705	-0.0031	0.0575
	Y	-0.1886	0.0315	0.0201
B3	X	0.0825	0.0855	0.0572
	Y	0.0825	0.1216	0.0224

Table 3.3 Table of offsets in volts taken at the time of calibration at Manadon RNEC, in the laboratory and in the field.

The offsets and gains are used to convert voltage to velocity using a linear equation of the form:  $\text{velocity} = (\text{voltage} - \text{offset})/\text{gain}$ .

### 3.2.2 Pressure Transducers.

The pressure transducers used were Druck PTX 164 pressure sensors manufactured by Druck Limited of Leicester, England, shown schematically in figure 3.5. The sensors are piezo-resistive strain gauges and use high performance silicon diaphragm technology to translate pressure signals to a voltage output. The deformation of the diaphragm causes a change in the resistance of the material which is recorded as a fluctuation in the voltage output. The PTX 164 model is particularly recommended for salt water applications as it is built of titanium in order to be corrosion resistant. The two PT's used in the experiment had the specifications shown in table 3.4.

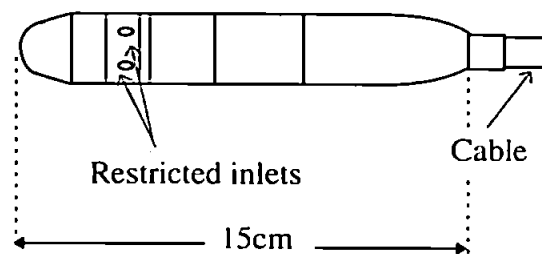


Figure 3.5 Diagram showing dimensions of pressure transducer.

	Red		Blue	
Pressure Range	2 bars absolute		2 bars absolute	
	Input	Output	Input	Output
Low Pressure	200 mbars	5.530 mA	35 mbars	4.275 mA
High Pressure	2000 mbars	20.012 mA	2000 mbars	20.000 mA

Table 3.4 Technical data for the pressure transducers.

#### 3.2.2.1 Calibration

The PT's were calibrated statically in a deep tank at RNEC, Manadon, where each transducer was lowered to a pre-specified depth below the surface of the water. Readings were taken to a depth of 3.5m and lines of best fit of output voltage against depth were

calculated for both PT's. The results of the calibration can be seen in figure 3.6. The  $r^2$  values in table 3.5 show the fit to a straight line to be excellent. The gain and offset convert voltage to meters using a linear equation of the form  $\text{depth} = (\text{voltage} - \text{offset})/\text{gain}$ , as the independent variable for the regression is depth.

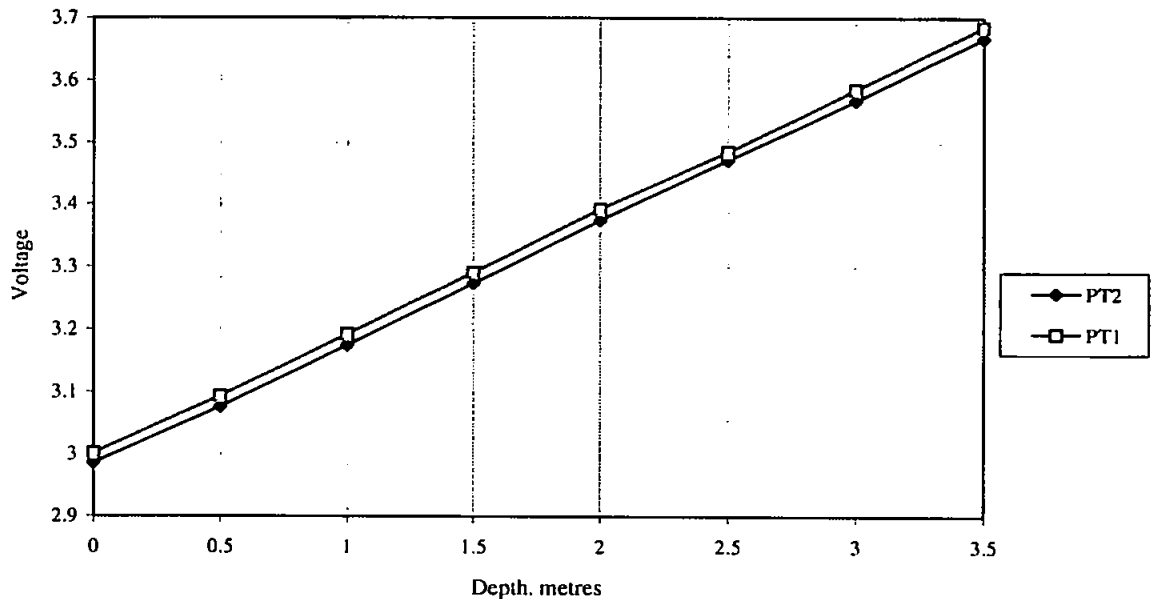


Figure 3.6 Calibration results for the pressure transducers, PT1 and PT2 are the pressure transducers on Station 1 and 2 respectively.

Pressure Transducer	Blue 2		Red 1	
	Manufacturers volts/pascal	Manadon volts/m	Manufacturers volts/pascal	Manadon volts/m
Gain	124.96	4.9	124.29	4.9
Offset	-499.2	4.0	-487.3	3.0

Table 3.5 PT Calibration details calculated by manufacturer and taken at Manadon.

The offsets were measured each day as initial and final data runs, when the equipment was out of the water. Figure 3.7 shows the offsets for the duration of the field campaign. There is some drift in the offsets over the period of the field campaign which could be attributed to change in atmospheric conditions. However, the two pressure transducers do not vary in exactly the same way, as might be expected if the cause of the drift were solely attributable to atmospheric conditions, but the difference between the extremes of the offset estimates results in an error of only 1 cm and affects only the mean water depth, not the wave height.

To check the depths and ensure that there was no attenuation of the signal due to the depth a second method was used to validate the other calibrations. The manufacturer supplied calibrations were used to convert voltage to pressure. To transform these pressure time series to water depth the hydrostatic equation is invoked

$$p - p_0 = \rho g(h - h_0) \quad 3.2$$

where  $p$  is the pressure at depth  $h$ ,  $p_0$  is the pressure at a known depth  $h_0$ ,  $g$  is the acceleration due to gravity, taken as  $9.81 \text{ ms}^{-2}$  and  $\rho$  is the density of sea water taken to be  $1025 \text{ kg/m}^3$ . In this case  $p_0$  is the pressure at the air-sea interface which was taken from data collected at the beginning and/or end of the tidal cycle data runs when the instruments were out of the water,  $h_0$  was also taken as zero.

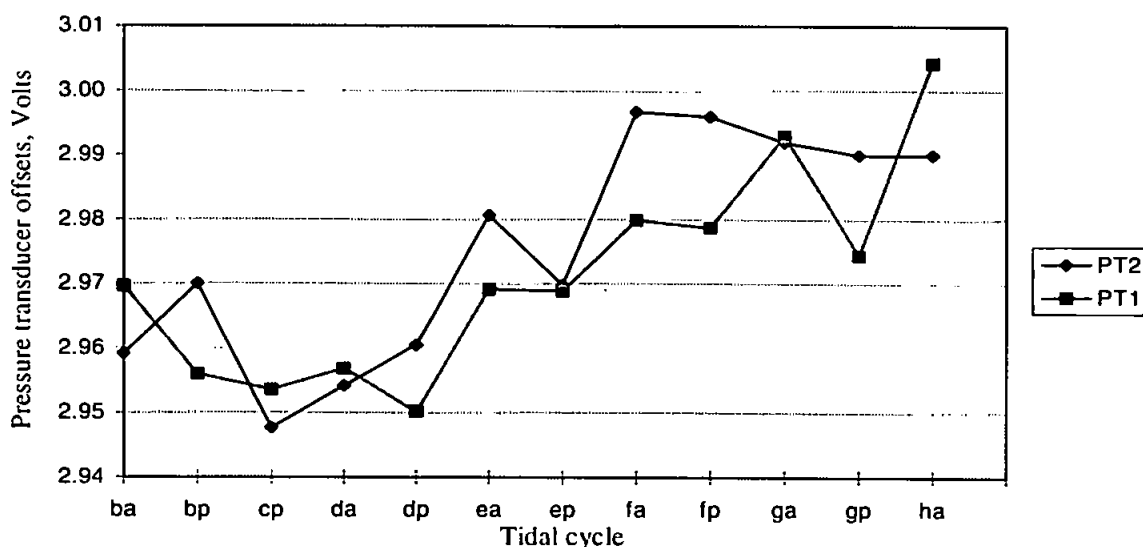


Figure 3.7 Offsets of pressure transducers measured after the instruments emerged from the water. Nomenclature explained in section 5.1.

### 3.3 Field Campaign, Nieuwpoort, Belgium.

#### 3.3.1 Introduction

As mentioned previously, to study wave and current interaction waves and currents are the only necessary factors. For a successful field deployment several other factors must be considered. From the hydrodynamics point of view, a strong current must be present to enable the current meters to register the turbulent fluctuations, see section 4.3. The tidal range, the difference in height between consecutive high and low waters, must be large so that the instruments are well covered by water at high tide. The waves have to be unbroken over the instruments, as the breaking of waves adds turbulence to the water column, which could affect shear stress estimates made using turbulence methods.



Plate 2: The beach at low tide showing ridges and runnels, the instrument stations were placed on the ridge between the two runnels seen. The beach was over 450m wide at low tide.

From a more practical point of view easy access to the field site is important, (although not vital), as much of the equipment is cumbersome. The availability of power is another consideration, although it is possible to use generators to power the equipment.

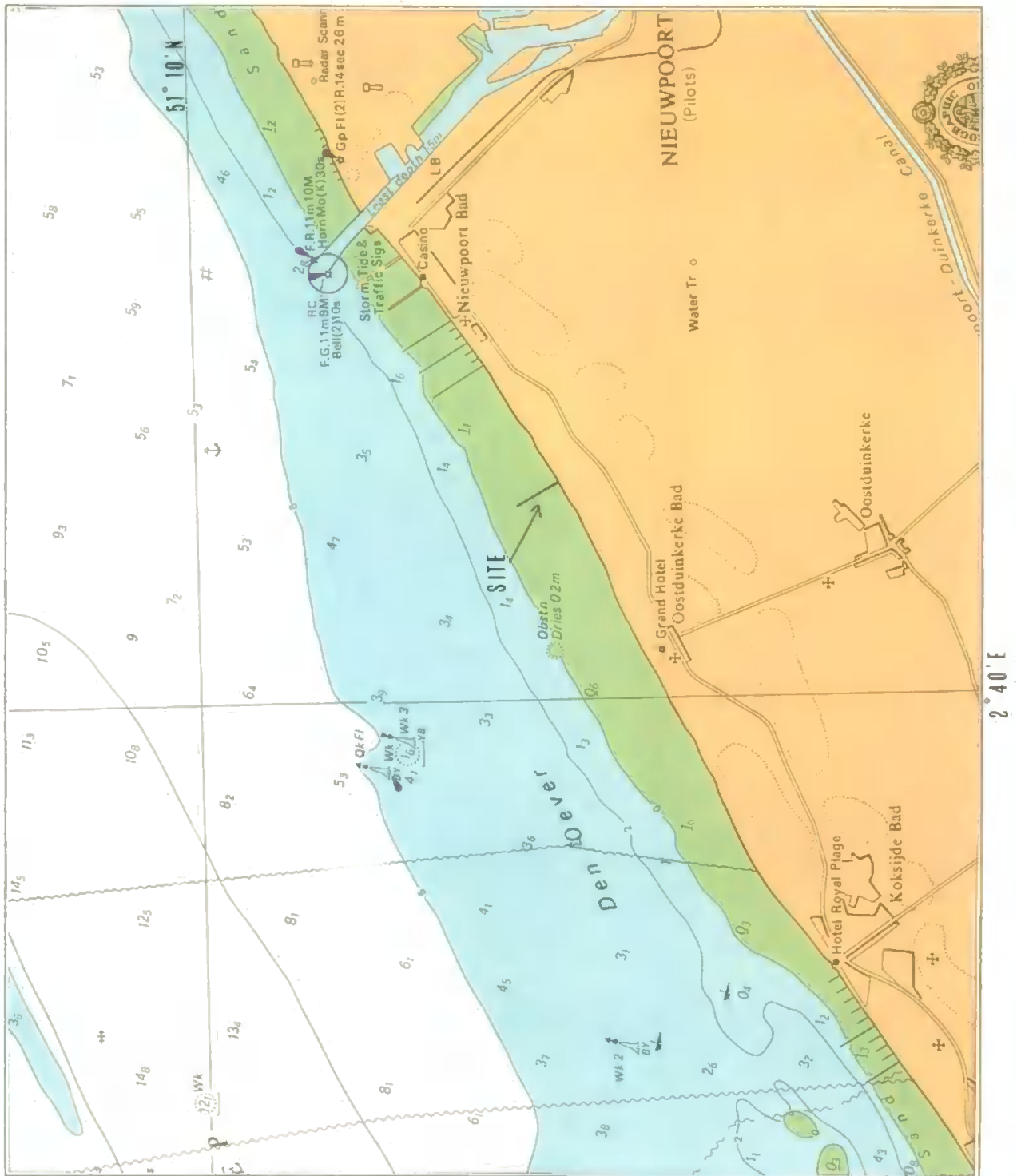


Figure 3.8 Chart of field site taken from chart number 125, Hydrographic Office, North Sea - Belgium, Approaches to Oostende, scale 1:50 000, The location of the site is indicated

The beach, section 3.3.3 below, chosen by the CSTAB project was ideal for our purposes. It was known to have a strong tidally driven longshore current and due to dissipative nature of the beach the waves are rarely large enough to damage or cause movement of the equipment..

### 3.3.2 Aims of the Field Campaign

From the CSTAB standpoint the objective of the field campaign was to provide data on wave current and sediment movements on the Middlekerke beaches during winter storms so as to assess the effects of the offshore banks on the beaches (Technical Annex of MASTII Project CSTAB). From the point of view of this project the aim was to collect data of sufficient quality to make comparisons of shear stress with numerical models of wave and current in order to test whether the models can be used to predict wave and current interaction in this extreme environment.

### 3.3.3 Beach Site

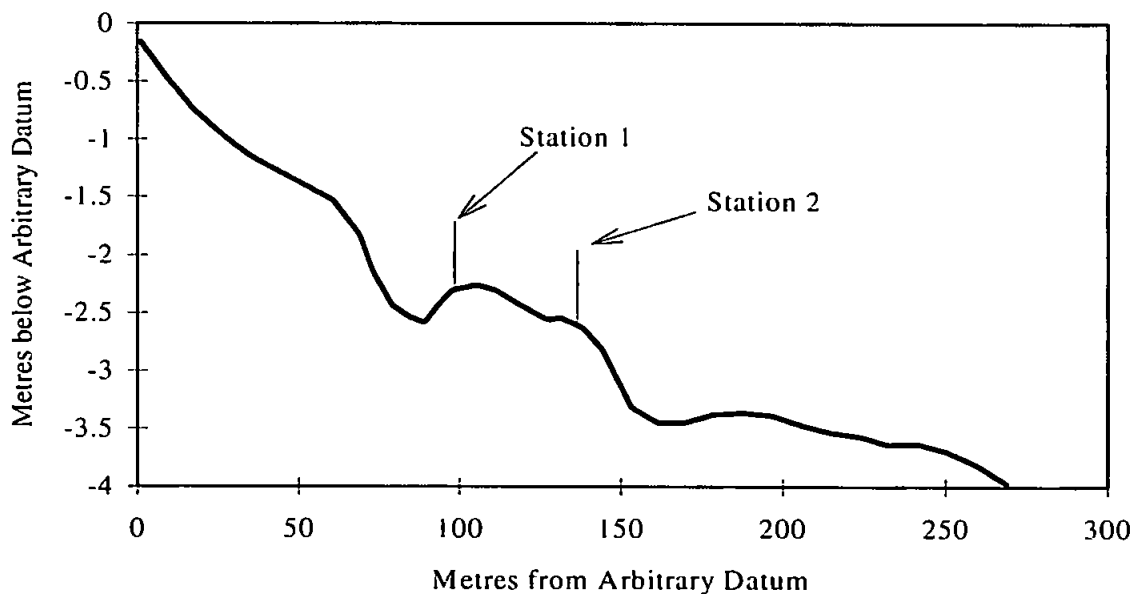


Figure 3.9 Transect of beach at Nieuwpoort, Belgium, showing ridge and runnel features and approximate positions of the instrument stations.

The site, at Nieuwpoort, Belgium, (see figure 3.8) is located at 51°09'N 2°43'E. The chosen site for the caravan, which contained the data logging equipment, was located at the top of the beach on the raised berm, amongst the dunes. Access to power was provided by a local hospital on the landward side of the dunes. Armoured cable ran from an electrical outlet beneath the mortuary across the main entrance to the hospital and



from there over the dunes to the field site. Where possible the cable was buried beneath the sand, but the dunes were a conservation area and the cable was left exposed with warning signs to inform the public of the danger. The beach itself is very wide and dissipative with a short fetch and a tidal range of greater than 5m, plates 1 and 2 show views of the beach. The inter-tidal (springs) zone is greater than 450m. It has ridge and runnel features (see figure 3.9). Most of the runnels did not drain completely even at low spring tide although a new runnel which formed at the top of the beach during the field experiment did drain. Anecdotal evidence, provided by local windsurfers, suggests that this runnel appears after a period of greater wave activity and fills in again during quieter periods.

### 3.3.4 Grain Size Analysis

The beach was made up of sand and shell fragments. Sediment samples were collected at the time of the deployment and were analysed on return from the experiment. The samples were washed and then dried. The dried sand was put through a set of sieves at  $1/2\phi$  intervals ranging from  $3.75\phi$  to  $-0.75\phi$ . The results of the analysis are shown in table 3.6, giving a mean grain size of approximately  $200\mu\text{m}$ , calculated using the Folk and Ward (1957) index for the mean:

Size $\mu\text{m}$	1700	1180	850	600	425	300	212	150	106	75+
Weight grams	4.195	3.722	3.271	3.466	3.206	4.698	15.490	50.945	9.018	0.064

Table 3.6 Results of grain size analysis, the mean grain size is  $\sim 200\mu\text{m}$

$$M = \frac{\phi_{16} + \phi_{50} + \phi_{84}}{3} \quad 3.1$$

where  $\phi_a$  is the phi value at a%

A cumulative percentage chart is given in figure 3.9. The distribution of grain sizes is positively skewed,  $SK = 0.612$ . This was calculated using equation 3.2, below

$$SK = \frac{\phi_{16} + \phi_{84} - 2\phi_{50}}{2(\phi_{84} - \phi_{16})} + \frac{\phi_5 + \phi_{95} - 2\phi_{50}}{2(\phi_{95} - \phi_5)} \quad 3.2$$

Folk and Ward (1957).

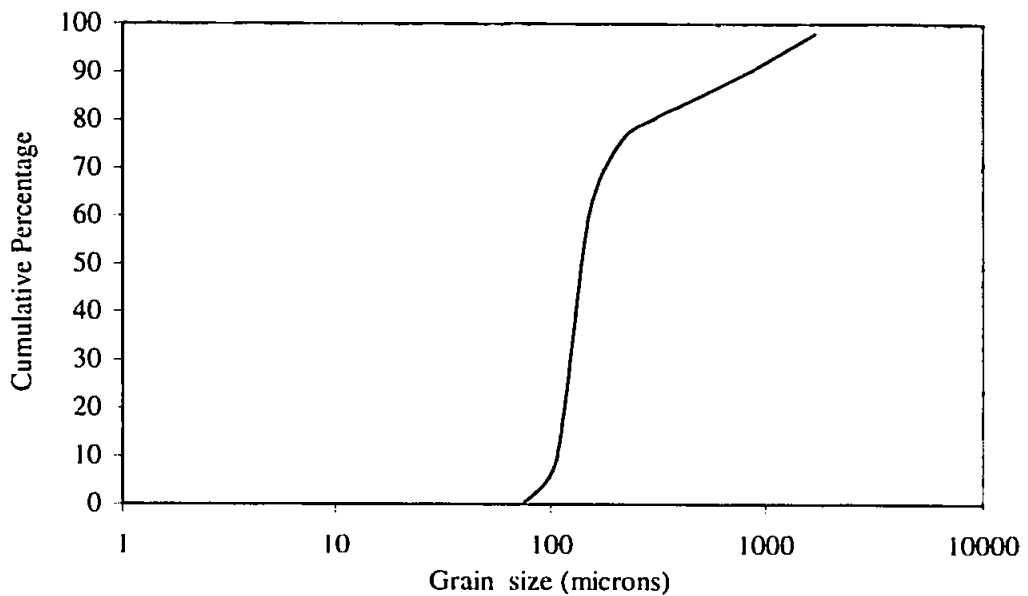


Figure 3.10 Grain size analysis

### 3.3.5 Placement of Equipment

Two instrument stations were placed on the beach. There were three major factors contributing to the precise location chosen for the stations.

- 1) The beach cables were 200m long, the maximum possible length of cable without too great a loss of signal to the data logger.
- 2) Time to rig the stations and place equipment whilst the beach is uncovered. The stations are posts knocked into the beach to sufficient depth to remain solid even during the liquefaction of the upper layers of sand and are braced with guy wires. The instruments have to be connected to the power supply and attached to the posts. All the pods containing the electronics and excess cable heads need to be buried to minimise the disturbance of the flow around the station. It is possible to leave some of the setting up of instruments for the next low water but much of the connecting must be done before the water returns to ensure the equipment remains watertight.
- 3) For the sake of the CSTAB project, a rig on either side of a ridge was required.

Taking all these points into consideration the two stations were deployed on the first ridge, station 1, on the near shore slope about 100m from the top of the beach, and the second, station 2, on the offshore side about 30m farther out, (see figure 3.9). The instrument stations each had a set of three EMCM's and a PT. Station 2 additionally had six OBS's arranged at various heights, see table 3.7. Brackets on the table indicate the following,

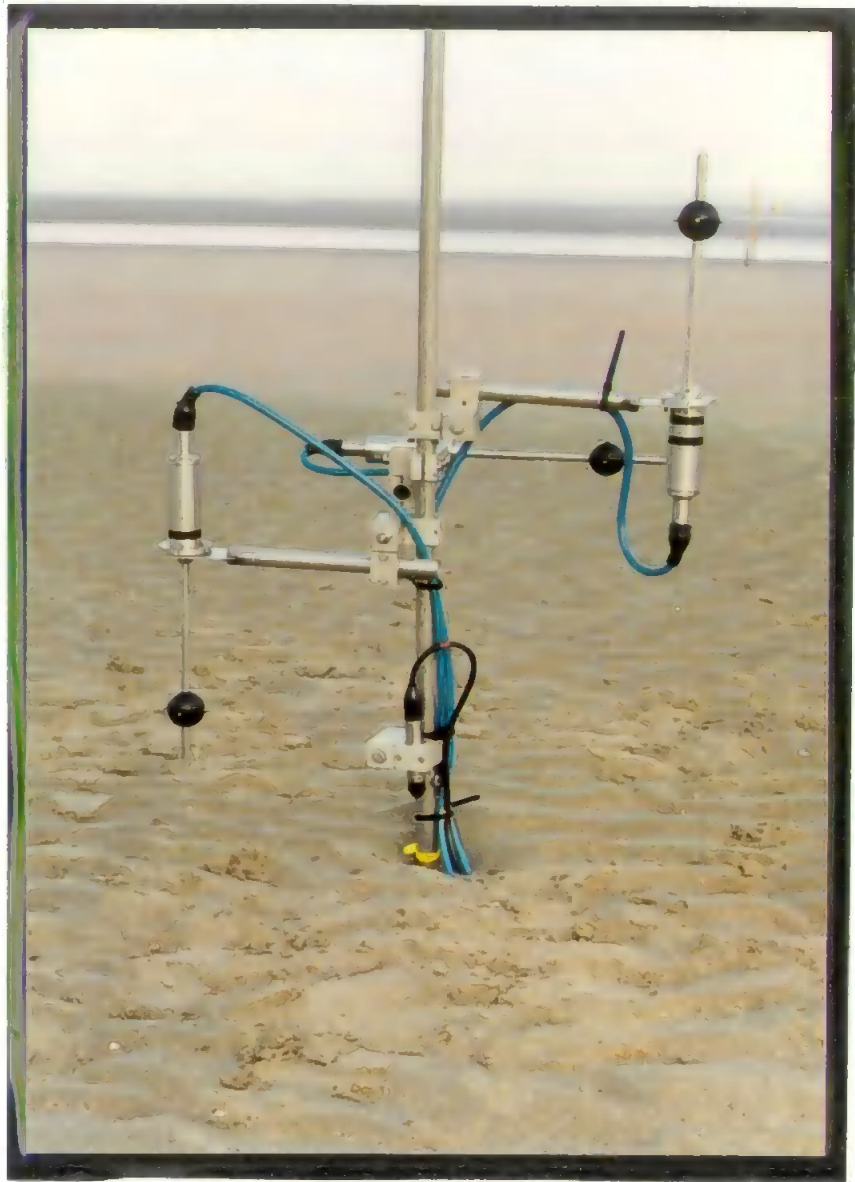


Plate 3: Station 1 on the landward side of the ridge, showing the placement of the electromagnetic current meters and pressure transducers



Plate 4: 'Station 2' was situated on the seaward side of the ridge, 6 optical backscatter sensors were arranged on the post with the electromagnetic current meters and pressure transducer. The difference between the annular and spherical current meters is plainly seen.

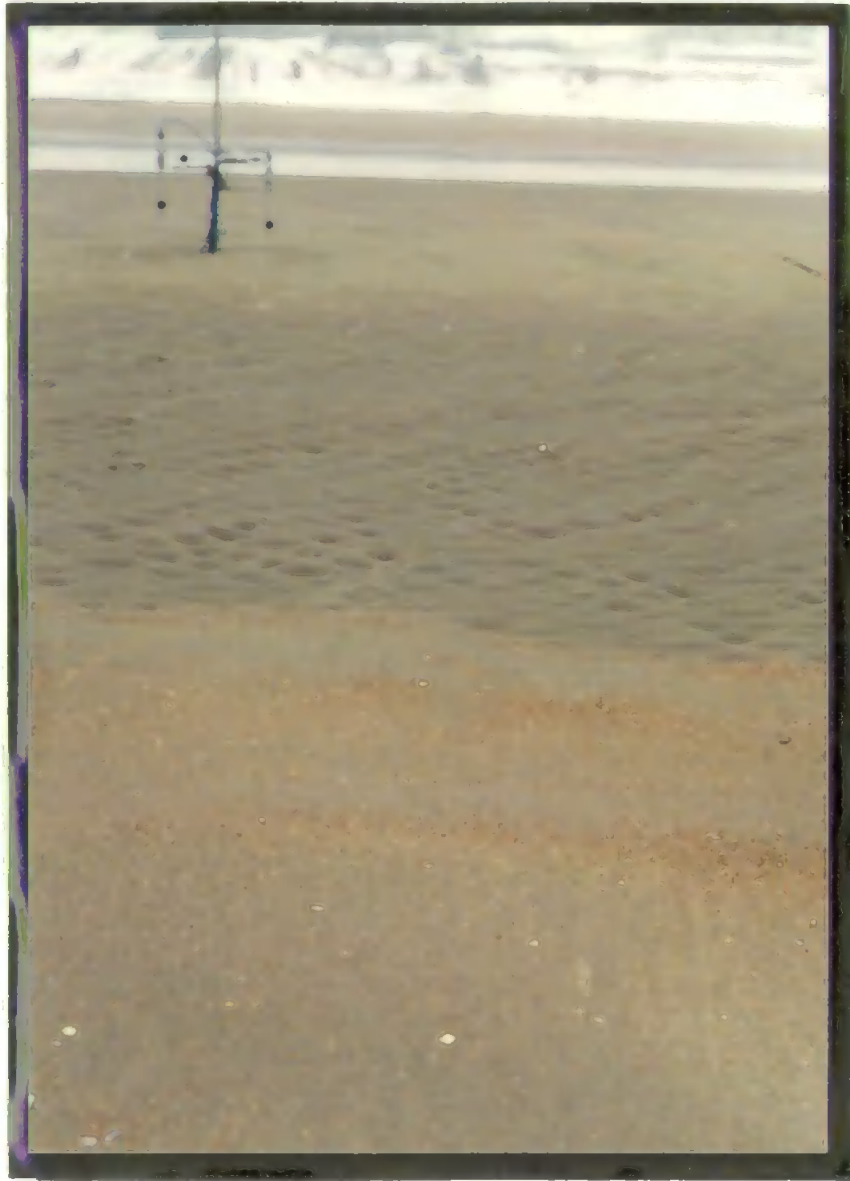


Plate 5: The top of the ridge was the point at which the flat bet changed into a rippled bed, this is shown up well in this plate.



Plate 6: Station 1 before instrument arrangement was altered, highlighting ripples formed around station.

- ⇒ No brackets, first measured heights of the day,
- ⇒ Parentheses ( ) measured after tidal cycle,
- ⇒ Braces { } indicate measurements after manual movement of equipment.

Figure 3.11 shows the arrangement of the instruments after 26/02/94. Plates 3, 4 and 6 show the instrument on the stations and the different arrangements. The instruments were rearranged to enable recording of velocity data at ~1m above the bottom. Instrument heights were altered according to the water level predicted by the Admiralty tide tables. The neap-spring cycle

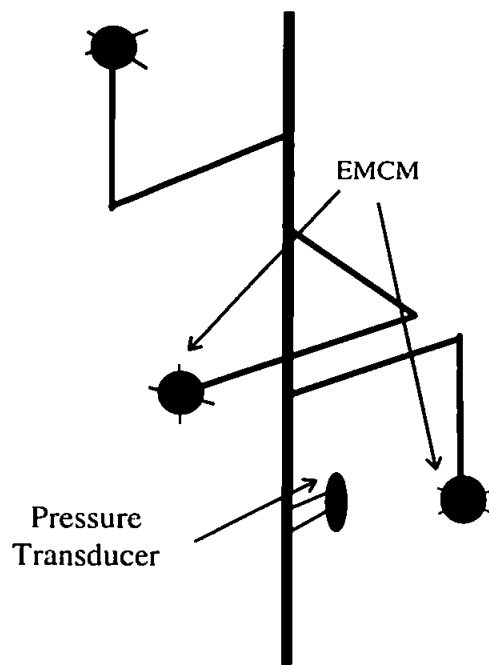


Figure 3.11 Arrangement of instruments from 26.02.94, showing positioning of EMCM's and PT's

experienced during the field trip is shown in figure 3.12. The daily records of instrument heights are given in table 3.7, (at the end of the chapter). As well as manual movements, some of the daily variations in heights are due to sediment erosion and accretion. Surveys of the beach surrounding the field site were carried out at low tide, when daylight and weather permitted, to monitor the movement of sediment on the beach.

From the instrument stations cables ran up the beach and into the field station. A diagrammatic view of the data collection system is shown in figure 3.13. The cables were attached to a cabinet which contains the filters for the OBS's and PT's and power sources for all the instruments. The data from the equipment were then passed through the

Microlink board which samples the data at a pre-specified rate, converting the continuous analogue signal to the discrete digital time series required for further data analysis. The data is in a multiplexed form due to the sampling technique. The Microlink samples from each channel of data coming into the system sequentially and almost instantaneously, at a pre-set sampling frequency. The data sets are then saved onto the computer in this form, all channels for each data run in one file. This can then be demultiplexed at a later date. The software package used to control data collection and store it is High Speed Data Collection (HSDC). Data were collected at either 4 Hz or 8 Hz whilst the equipment was submerged.

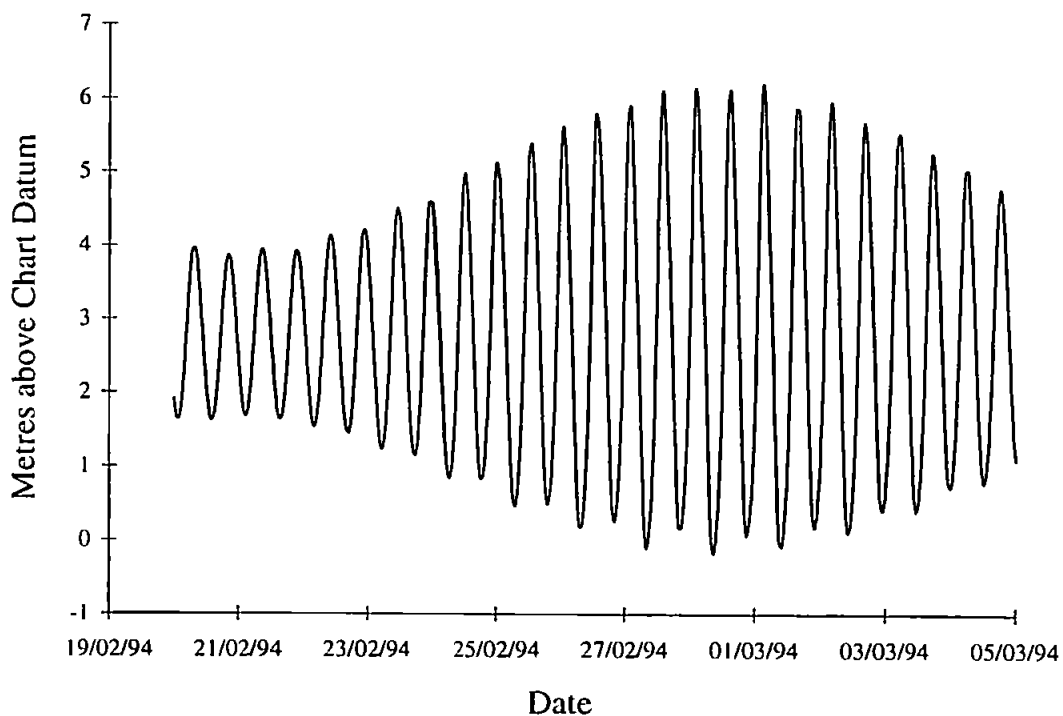


Figure 3.12 The neap-spring cycle experienced during the field trip.

### 3.3.6 Channel Recognition

The cabinet containing the filters, power sources and Microlink board had to be dismantled to fit it into the caravan that was to be used as the field station. The data coming into the Microlink board were from 20 different sources, (12 EMCM, 6 OBS and 2 PT channels). Due to wiring complexities within the cabinet and the uncertainty of the manufacturer's, (Valeport), sensor identifications, particularly that of the polarity of the EMCM's, it was necessary to affirm which data channel was which. This was done in a variety of ways.



- 1) The main way was to view the data coming in and, using experience gained on other field campaigns, identify channels by their appearance. It was possible to distinguish between the three types of data by eye.
- 2) To discover the orientation of instruments and their positions on the stations, the data runs were examined to see in which order the instrument emerged from the sea. Comparison of data channels within each run enabled the orientation of each channel to be identified. Table 3.7 shows the channels and their identification.
- 3) A third way to discover the links was to test the equipment when they were out of the water. The EMCM's and PT's were placed in buckets of water, the changes in the readings were possible to detect, easily in the case of the EMCM's as the signal is saturated when they emerge from the water. The PT's were more difficult but the method described in 2) above worked for the PT's. The OBS's sense particles within 5 cm of the head, so passing something in front of the head can be seen as a change in the signal.

Using these methods described above it was possible to be very confident that the channel designation was correct.

Channel	Instrument		Orientation	
1300	EMCM	B1X	Cross shore	
1301		B1Y	Long shore	
1302		B2X	Long shore	
1303		B2Y	Cross shore	
1304		B3X	Cross shore	
1305		B3Y	Vertical	
1400		A1X	Cross shore	
1401		A1Y	Long shore	
1402		A2X	Long shore	
1403		A2Y	Cross shore	
1404		A3X	Cross shore	
1405		A3Y	Vertical	
1406		OBS	R1	
1407			R2	
1408			R3	
1409	B1			
1410	B2			
1411	B3			
1412	PT	BLUE		
1413		RED		

Table 3.7 Channel Identifications.

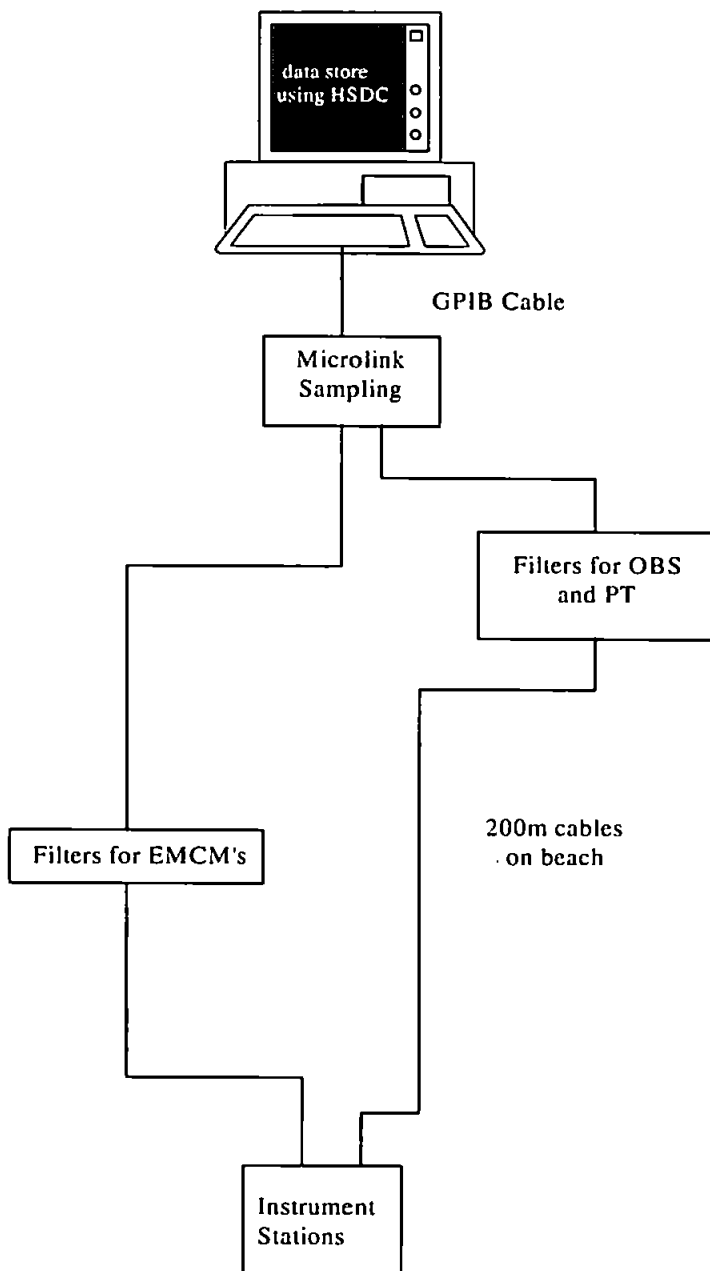


Figure 3.13 Diagrammatic view of the data collection system.

### 3.3.7 Environmental Conditions

#### 3.3.7.1 Weather Conditions

For the first week of the two week field campaign the weather was very cold, with snow and sleet on several days. The seawater in the runnels froze and icicles formed on the instruments and stations. There was little or no wind during this period and visibility was restricted due to fog. The second of the two weeks was milder with rain and drizzle on

most days. Wind speeds, measured with a hand held anemometer, varied from approximately  $1 \text{ ms}^{-1}$  to  $8 \text{ ms}^{-1}$  (about 16 knots), force 4-5 on the Beaufort scale (moderate to fresh breeze).

### **3.3.7.2 Wave Climate**

Large waves were not anticipated because of the wide and shallow nature of the beach. Wave heights experienced varied from 20 cm to 80 cm over the period of the field campaign. Waves were normal to the beach for much of the field campaign, although on 2 March the angle of approach altered to approximately  $30^\circ$ .

### **3.3.7.3 Bedforms**

Ripples were present around station 1 after the tidal flow receded, examples of the ripples formed can be seen in plates 2 and 6. The bed was flat around station 2 after each tidal covering this can be seen in plate 3. The point at which the bed changed from rippled to flat was well marked at the top of the ridge and is shown in plate 5.

For a more detailed day to day description of environmental conditions see table 3.9.

### **3.3.8 Data Quality**

Once initial technical difficulties were overcome the data collected were of sufficient quality to be used for the purpose intended. The OBS's failed to work successfully, reasons for this are unclear and so data from these instruments are not subsequently used. Wave and current conditions varied over the period and promised to make data interesting from the WCI point of view. A description of the data collected is given in table 3.7, and includes details of instrument heights bedforms around the stations and problems encountered over the field campaign.

Table 3.8 Table of instrument heights, observed bed roughnesses and problems found and overcome

Date	Data	Bedforms	Instrument Heights (m)									Comments
			Station 1			Station 2						
				1	2	3		1	2	3		
20/02/94	No data collected-no power		EMCM A	0.15	0.415	0.80	EMCM B	0.15	0.395	0.80	EMCM's appear to be working, some doubt about the OBS's and PT's	
			PT	0.155			OBS R	0.045	.0115	.024		
							OBS B	0.365	.0475	.0955		
							PT	0.15				
21/02/94	No data collectd-need new cable to hospital											
22/02/94	Power connected Channels identified	rippled beds around Stn 1 Flat around Stn 2	EMCM A	0.175	0.29	0.605	EMCM B	0.235	0.49	0.92	Instruments lowered to be well covered by water. Station 1 rock steady. Ch1400 and 01 identical could be a problem.	
			PT	0.22			OBS R	0.06	0.13	0.255		
							OBS B	0.38	0.49	0.97		
							PT	0.05				
23/02/94			EMCM A	0.18	0.30	0.62	EMCM B	0.165	0.31	0.755	Time series from 1400 and 1401 still identical, now convinced a problem.	
			PT	0.10			OBS R	0.065	0.13	0.26		
							OBS B	0.355	0.56	0.985		
							PT	0.065				
24/02/94	N242pm01-12	Washover fans by Stn 2 (flat) Ripples by Stn 1	EMCM A	0.19 (0.18)	0.315 (0.31)	0.62 (0.62)	EMCM B	0.21 (0.205)	0.345 (0.34)	0.79 (0.80)	Problem solved channels 1400 and 1401 - loose connection in cabinet.	
							OBS R	0.10 (0.105)	0.17 (0.175)	0.30 (0.31)		
							OBS B	0.425 (0.425)	0.535 (0.535)	1.015 (1.02)		
			PT	0.06 (0.10)			PT	0.06 (0.10)				
25/02/94	N252am01-10 N252pm01-09	ripples at Stn 1 $\lambda=0.10m, \eta=0.02m$	EMCM A	0.185	0.32	0.635	EMCM B	0.205	0.34	0.80	OBS data does not look good 1409 not working	
			PT	0.115			OBS R	0.105	0.175	0.315		
							OBS B	0.43	0.43	1.02		
							PT	0.10				
26/02/94	N262am01-10 N262pm01-01	Deeply rippled around Stn 1 $\eta=0.025$	EMCM A	0.19 (0.185) (0.195)	0.32 (0.925) (0.935)	0.63 (0.535) (0.54)	EMCM B	0.195 (0.195) (0.20)	0.34 (1.015) (1.015)	0.805 (0.55) (0.55)	Problems with PC N262am01 not collected.	
							OBS R	0.10 (0.105)	0.17 (0.175)	0.305 (0.315)		
							OBS B	0.42 (0.425)	0.535 (0.54)	1.015 (1.02)		
			PT	0.12 (0.13)			PT	0.10 (0.105)				
27/02/94	N272pm01-08		EMCM A	0.155 (0.20)	0.92 (0.92)	0.53 (0.53)	EMCM B	0.205 (0.21)	1.025 (1.025)	0.555 (0.565)		
			PT	0.12 (0.135)			OBS R	0.11 (0.115)	0.18 (0.185)	0.315 (0.32)		
							OBS B	0.43 (0.435)	0.545 (0.55)	1.025 (1.03)		
							PT	0.10 (0.105)				
28/02/94	N282am01-08 N282pm01-11		EMCM A	0.195	0.925	0.535	EMCM B	0.22 (0.13)	1.035 (0.96)	0.57 (0.49)		
			PT	0.13			OBS R	0.12 (0.045)	0.19 (0.12)	0.33 (0.26)		
							OBS B	0.445 (0.37)	0.555 (0.485)	1.035 (0.97)		
							PT	0.11 (0.115)				
01/03/94	N013am01-09 N013pm01-10		EMCM A				EMCM B					
			PT				OBS R					
							OBS B					
							P					
02/03/94	N023am01-10 N023pm01-10		EMCM A	0.20 (0.20)	0.92 (0.965)	0.55 (0.555)	EMCM B	0.145 (0.16)	0.985 (1.00)	0.505 (0.53)		
							OBS R	0.07 (0.09)	0.14 (0.16)	0.27 (0.30)		
							OBS B	0.39 (0.405)	0.505 (0.53)	0.98 (1.01)		
			PT	0.175 (0.15)			PT	0.135 (0.16)				
03/03/94	N033am01-05 N033pm01-08	$\eta=0.02$ $\lambda=0.075$	EMCM A	0.19	0.925	0.525	EMCM B	0.16	1.01	0.53		
							OBS R	0.09	0.16	0.265		
							OBS B	0.41	0.525	1.00		
			PT	0.125			PT	0.155				
04/03/94	N043am01-10	$\eta=0.01$ $\lambda=0.08$	EMCM A	0.18	0.90	0.49	EMCM B	0.175	1.03	0.545		
							OBS R	0.105	0.175	0.28		
							OBS B	0.425	0.54	1.015		
			PT	.012			PT					

Table 3.9 Environmental conditions experienced during field campaign, including observed wave and weather conditions

Date	Weather Conditions	Observed Wave Height	Comments	High Tide
20/02/94	Wind: SW light, cold, watery sunshine.	0.75m	Placement of two stations 1: A set of EMCM red PT 2: B set of EMCM blue PT Red and Blue OBS	07:35 20:20
21/02/94	Snow, very cold		Problems with power connection to hospital	08:50 21:20
22/02/94	Snow, little/no wind Rain later wind increasing		Replaced power cable to hospital Instruments lowered to ensure good covering by water Some erosion around station 2 pods uncovered Accretion of sand on top of snow at high tide mark	10:10 22:30
23/02/94	Snow thawing fresh breeze WSW dropping Later "wet and miserable"		Too wet for survey	11:00 23:30
24/02/94	Snow melted little wind, very foggy. Low pressure approaching from the SW	0.4m growing more regular	New runnel formed at top of beach	11:50
25/02/94	Cold cloudy Winds light NE~2m/s Later cloud clearing wind ~3m/s. Full moon	0.3-0.4m normal to beach	Drop in power noticed for filter power supply during evening run	00:00 12:20
26/02/94	Sunny am wind increasing ~4m/s	0.2m	Changed instrument arrangement	01:00 13:20
27/02/94	Rain, wind 2m/s SSW	0.2-0.3 m up to 0.4m at breakpoint. Three lines of breakers		01:30 14:00
28/02/94	Rain, showers, wind 2m/s s	0.2m	Easterly current	02:20 14:40
01/03/94	Wind 2-3m/s increasing 5m/s NW Rain	0.3m increasing to 0.5m isolated white horses		03:00 15:25
02/03/94	Dry, broken cloud wind 2-3m/s SW increasing 9m/s rain "wet, windy, woeful"	0.3m increasing to 0.5m angle of approach ~30° to the beach		03:45 16:15
03/03/94	"Nasty" Rain 6m/s W Rain increasing 8m/s NW Later cloud breaking blue skies	0.2-0.3m choppy		04:30 16:52
04/03/94	Cold clear wind 2-3m/s	0.5m/s twolines of breakers		05:30 18:00

## **Chapter 4.**

### **Data Analysis**

#### **4.1 Introduction**

Statistical analysis of the data was carried out to quantify the conditions experienced over the period of the field campaign. Means and significant wave heights and velocities were calculated to give an indication of overall conditions and bottom stresses were estimated to be used in comparison with model results. Owing to the extreme hydrodynamic conditions it was anticipated that some of the data would be unsuitable for analysis, perhaps from additional turbulence caused by breaking or spilling waves or conditions too extreme to be recorded accurately by the instruments available.

#### **4.2 Statistical Analysis**

To establish the prevailing hydrodynamic conditions experienced for each time series means, variances and significant wave height and velocities were calculated. Figure 4.1 shows the significant wave height and mean velocity, for the duration of recording the mean velocity was generally long shore, in an easterly direction, for each tidal cycle at a particular water depth. Since all of the data runs shown are outside of the breaker zone the long shore current is assumed to be essentially tidally driven and not due to wave breaking. Over the period of the field campaign a wide variety of conditions was experienced, from current dominated at the beginning of the week to wave dominated conditions in the latter half. The terms wave dominated and current dominated, for this thesis, are defined, for wave dominated as when the near bottom wave orbital velocity is greater than the depth averaged current and current dominated as when the depth

averaged current velocity is greater than the near bottom wave orbital velocity. Figure 4.1 shows clearly that for the first 4 tidal cycles the current is greater than the waves and for the latter part the waves dominate.

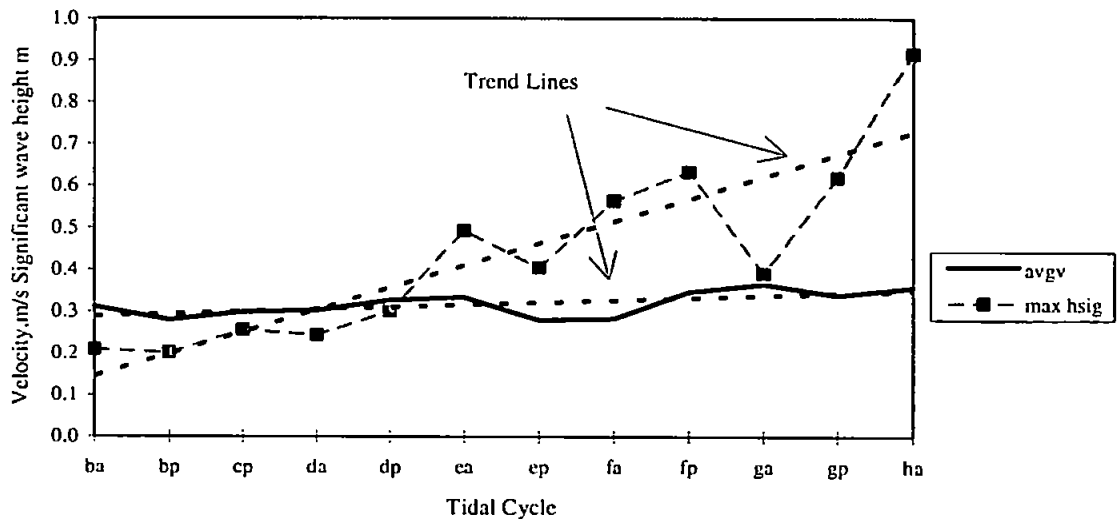


Figure 4.1 Mean velocities and wave heights for similar depths over the whole field campaign. The two dotted lines indicate the trends of both mean velocities (avgv) and significant wave heights (max hsig) as indicated by the legend.

#### 4.2.1 Means

Means of long shore, cross shore and vertical velocity and water depth time series were calculated, by finding the arithmetic mean of the time series of calibrated data. Figure 4.2 shows examples of long shore cross shore and vertical flows and depth over a period of the field experiment.

Arithmetic means were calculated for each time series giving mean flow and depth data for each data run, resulting in a series of points for each tidal cycle. Figure 4.2 shows the mean flows and depths for station 2, the outer station, over the period of the field campaign. The mean long shore flow is always positive, easterly towards Holland, and is at a maximum at the beginning of data collection for each tidal cycle, just before high tide and decreases over the tidal cycle.

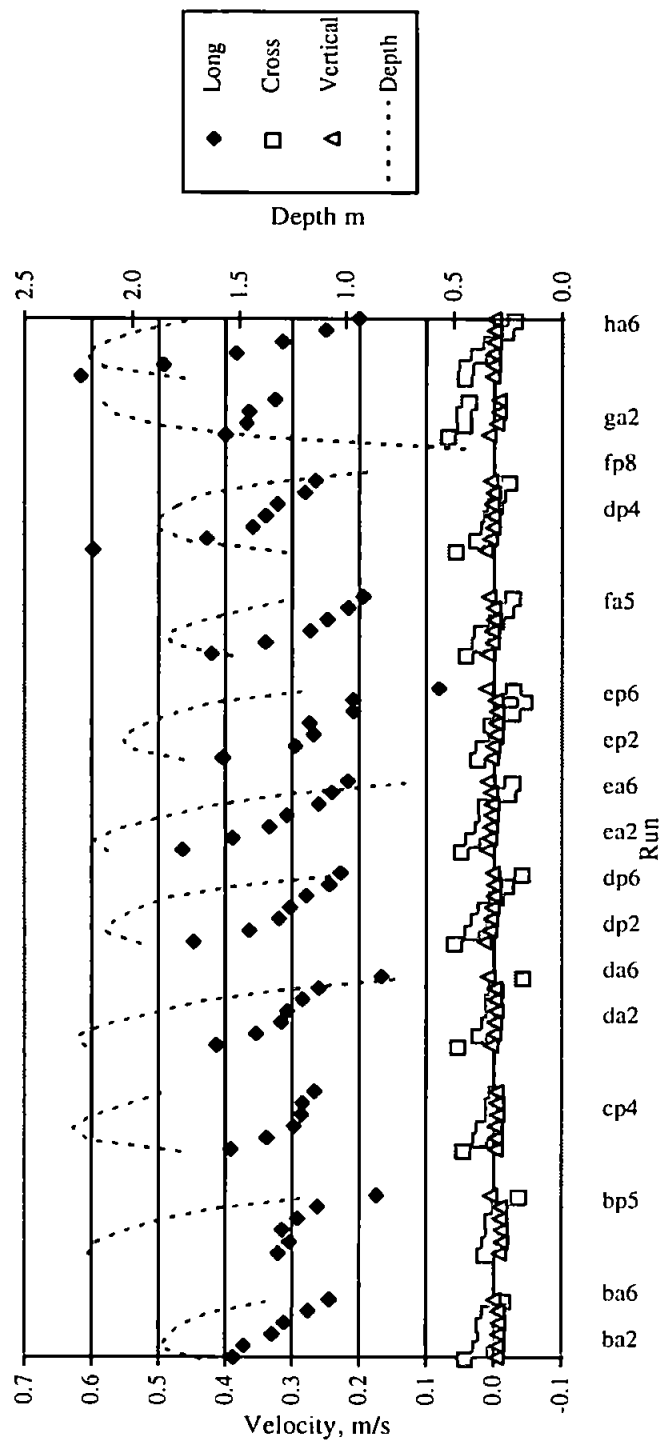


Figure 4.2 Mean flows of long shore cross shore and vertical EMCM's and mean depths for the outer station for the whole field campaign. Nomenclature explained in section 5.1.



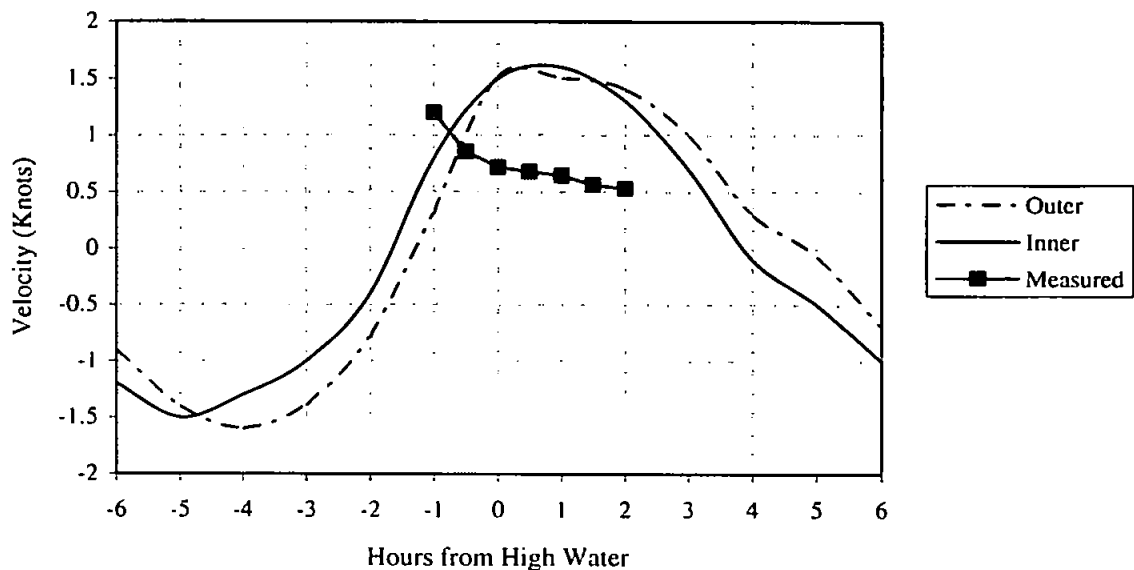


Figure 4.3 Shows lag in tidal velocity phase observed during field campaign.

Comparison of the long shore velocities and depths with predictions from the nearest tidal diamond (Tidal diamond G, Hydrographic Office, North Sea - Belgium, Approaches to Oostende, scale 1:50 000, chart number 125) showed that the lag between tidal along coast velocity and elevation was substantially different to that predicted. Figure 4.3 highlights these differences. O'Connor et al. (1996) suggest a simple model of the alongshore flow which could be employed to illustrate this phase shift, section 2.6. Tidal diamond G is the closest diamond to the field site but it is quite a long way offshore, some 4.5 km and in much deeper water, approximately 13 m. There is another diamond, H, closer to the shore, just over 1 km off, but further west off the coast of France. The difference between high tides at these two diamonds is only a few minutes. Comparing the predictions from these two diamonds shows that the model of O'Connor et al. (1996) predicts qualitatively what occurs. Whilst figure 3.8 does not cover the area of the tidal diamonds, the positions are indicated at the edge of the chart. As the water depth decreases, the phase between the velocity and tidal height changes, with the greatest change in phase occurring between the inner tidal diamond and the measured flow, as the model predicts.

#### 4.2.2 Depth averaged velocity

The depth averaged velocity was required as an input for the parameterised models. To calculate the depth averaged velocity it was assumed that the long shore velocity had a

logarithmic profile and from this assumed profile the depth averaged velocity was interpolated.

### 4.2.3 Spectral Analysis

It is accepted that any function periodic in time can always be expressed as an infinite trigonometric (Fourier) series of the form

$$x(t) = a_0 + \sum_{k=1}^{\infty} \left( a_k \cos\left(\frac{2\pi kt}{T}\right) + b_k \sin\left(\frac{2\pi kt}{T}\right) \right) \quad 4.1$$

where  $a_i$  and  $b_i$  are the Fourier coefficients,  $T$  is the period and  $t$  is the time. The Fourier coefficients can be expressed as integrals:

$$a_0 = \frac{1}{T} \int_{-T/2}^{T/2} x(t) dt \quad 4.3$$

$$a_k = \frac{2}{T} \int_{-T/2}^{T/2} x(t) \cos\left(\frac{2\pi kt}{T}\right) dt, \quad k \geq 1 \quad 4.4$$

$$b_k = \frac{2}{T} \int_{-T/2}^{T/2} x(t) \sin\left(\frac{2\pi kt}{T}\right) dt, \quad k \geq 1 \quad 4.5$$

MATLAB, an analysis software package, was used for the spectral analysis of the data.. A method known historically as the Welch's averaged periodogram was used. Each time series is divided into  $K$  segments, each segment containing  $m$  points (where  $m$  is an integer power of two). Each pair of adjacent segments,  $K-1$  in total, are taken together forming a time series containing  $2m$  points and a window function is applied. The application of the window function involves multiplying the time series of  $2m$  points by a smooth, continuous, symmetrical curve that varies from zero to one and then falls again to zero. The window function chosen was the Hanning window:

$$w_j = \frac{1}{2} \left[ 1 - \cos\left(\frac{2\pi j}{N}\right) \right], \quad N = 2m \quad j = 1 \dots N - 1. \quad 4.6$$

The reason for windowing will be explained later. The fast Fourier transform (FFT) of the data is then calculated for each double segment of 2m data points. The FFT is an algorithm used to compute the discrete Fourier transform efficiently.

All of the estimates are then averaged over each frequency bin. A frequency bin extends from the halfway from the preceding discrete frequency to halfway to the succeeding one. The spectral estimate at the discrete frequency,  $f_k$ , is representative of the spectral estimate for the whole frequency bin. Using this estimator the spectral variance per data point is minimised. It can be shown (Press et al. (1992)) that the Hanning window method reduces the variance by a factor of approximately  $9K/11$ , which is a greater reduction than if the same number of data points are segmented without overlapping, and so increase the confidence level in the peaks within the spectrum.

If no window is applied the analysis is equivalent to applying a square window to the data. When a Fast Fourier Transform (FFT) of the data is calculated the square window introduces substantial components at higher frequencies effectively smearing the power associated with a given frequency bin into the surrounding bins. The application of the window function is to reduce this spectral leakage or side lobe distortion. There are other windows available but the choice of Hanning window was made to reduce the spectral leakage to a minimum within two frequency bins of the central frequency.

#### 4.2.3.1 Significant Wave Statistics

The significant wave height is calculated from the variation in wave height associated with the wind wave band. It is first necessary to correct for the hydrodynamic filter effect. The pressure transducer is situated near to the bottom of the water column. The water between the sensor and the surface acts as a filter, damping the higher wavenumber fluctuations. Corrections for the hydrodynamic filtering effect were done using the following:

$$h' = \frac{p}{\rho g} \left( \frac{\cosh(kh)}{\cosh[k(z+h)]} \right) \quad 4.7$$

where  $h'$  is the fluctuation amplitude associated with the wavenumber,  $k$ ,  $h$  is the mean water depth,  $z$  is the depth of the sensor (negative downwards) and  $k$  is the surface wave number.

From the corrected spectrum of the depth time series the wind wave band is selected, and the area between the limits and under the curve is calculated using the trapezium rule:

$$\text{area} = \left[ \frac{p_0 + p_n}{2} + \sum_{i=1}^{n-1} p_i \right] \Delta k \quad 4.8$$

where  $p_i$  is the value of the spectrum at the  $i$ th point,  $\Delta k$  is the increment wavenumber between each estimation of the spectrum. The corrections were small, less than 10% at the maximum. The area under the curve is the variance associated with the wind wave band,  $\sigma_{\text{wind}}^2$ . The  $H_{\chi}$ , is directly proportional to the variance:

$$H_{\chi} = 4\sigma_{\text{wind rms}} \quad 4.9$$

The significant wave height is proportional to the square root of the total variance of the wind wave band (Guza and Thornton (1980)), assuming that the processes are Gaussian and narrow banded.

#### 4.2.3.2 Wavenumber

The wave number is calculated from the dispersion relation:

$$k^2 c^2 = \omega^2 = gk(1 + \epsilon_{\tau}) \tanh(kh) \quad 4.10$$

(Crapper 1984) where  $\epsilon_{\tau}$  is a parameter giving the relative importance of surface tension to gravity. For this study it was assumed that this parameter could be considered as unimportant and was not included. The wavenumber for a given frequency was calculated using the Newton Raphson method to an accuracy of order  $(10^{-4})$ .

#### 4.2.3.3 Maximum Near Bottom Wave Orbital Velocity and Maximum Orbital Diameter

The maximum near bottom orbital velocity,  $u_b$ , and maximum orbital diameter,  $d_0$ , were calculated using standard linear theory:

$$u_b = \frac{\pi H_s}{T \sinh(kh)} \quad 4.11$$

and

$$d_0 = \frac{H_s}{\sinh(kh)} \quad 4.12$$

where  $T$  is the period of the water waves. Grace (1976) showed that linear wave theory is invalid for breaking waves. The Miche parameter was used to determine when breaking occurred:

$$H_b = 0.78 \frac{H_s}{h} \quad 4.13$$

#### 4.2.3.4 Peak Wave Frequency

The peak wave frequency was obtained from the spectrum of the depth time series, by selecting the most prominent peak of the wind wave band, (see for example figure 4.5).

### 4.3 Estimating Bottom Shear Stresses

Direct measurement of bottom shear stresses in turbulent environments is difficult, if not impossible, in the field. There are several indirect methods for estimating these stresses using current meter data. The three chosen to work with on this data were the inertial dissipation method, the turbulent kinetic energy method and the Reynolds stress method. It was not possible to use the logarithmic layer method as there were only three EMCM's in the vertical array and only two of these were sensing the long shore direction.

#### 4.3.1 The Inertial Dissipation Method

If the wave numbers at which turbulent energy is produced and dissipated are well separated, the region of separation in wavenumber space is known as the inertial sub-range. In this range the flux of energy from low to high wavenumber is equal to the dissipation rate, as there are no sinks or sources of energy within the wavenumbers of the sub-range. The spectrum, in a given direction within this range, is given by

$$\phi_{ii} = \alpha_i \varepsilon^{2/3} k^{-5/3} \quad 4.14$$

where  $k$  is the one dimensional wave number,  $\alpha_i$  is the one dimensional Kolmogorov constant,  $\varepsilon$  is the energy dissipation rate and the subscript  $i$  represents a given direction.

It is necessary to make two assumptions in order to estimate bottom shear stress from the above equation:

1. There is a local balance between production and dissipation of turbulent energy. The production rate of turbulent kinetic energy is given by  $\tau/\rho \frac{\partial u}{\partial z}$  and in the logarithmic layer  $\frac{\partial u}{\partial z} = u_*/\kappa z$ , where  $\tau = \rho u_*^2$  is the stress felt at the bottom,  $u$  is the velocity in the  $x$  direction,  $\rho$  is the density of the water (taken as  $1025 \text{ kg/m}^3$ ),  $\kappa$  is von Karman's constant (taken as 0.4),  $u_*$  is a parameter known as the friction velocity and  $z$  is the height of measurement above the bottom. The parameter friction velocity has the dimensions of velocity but has no physical meaning, in that it is not a velocity and cannot be measured as such.
2. The measurements are made within the constant stress part of the logarithmic boundary layer. Within this part of the boundary layer local stress is equal to the bottom stress.

These assumptions give, after some rearranging,

$$u_* = (\phi_{ii}(k)k^{5/3}/\alpha_i)^{1/2} (\kappa z)^{1/3} \quad 4.15$$

Turbulence measurements are generally in the form of time series and therefore provide spectra as functions of frequency and not wavenumber. The Taylor concept of 'frozen turbulence' is used to convert wave number spectra to velocity spectra,

$$\phi_{ii}(k) = \phi_{ii}(f)\bar{u}/2\pi, \quad 4.16$$

where  $\bar{u}$  = mean velocity in the  $i$  direction and  $f$  = frequency. For this concept to be valid it is necessary that the time scale of a turbulent eddy with wavenumber  $k$  must be much longer than the time taken for the eddy to advect past the point of measurement. For this to be true it is required that

$$k\phi_{ii}(k)/\bar{u}^2 \ll 1 \quad 4.17$$

For an environment with significant oscillatory flows it has been suggested that Taylor's Hypothesis would need to be significantly revised. Huntley (1988), following the theoretical work of Lumley and Terray (1983) suggests that, for isotropic turbulence, horizontal wave velocities much greater than vertical wave velocities, and small values of the waves to mean current ratio, the correction to friction velocity due to the wave advection is approximately

$$\hat{u}_* = (1 - 0.16(u_{rms}/\bar{u})^2)^{\frac{1}{2}} u_* \quad 4.18$$

where  $u_{rms}$  = the root mean square horizontal velocity

The inertial sub-range will only exist in flows where the low wavenumbers (where energy is produced) are well separated from those where energy is dissipated. Tennekes and Lumley (1972) suggest that this will only occur in flows where the turbulent Reynolds number (Re) is greater than some critical Reynolds number ( $Re_c$ ),

$$Re = u_* \kappa z / \nu > Re_c \quad 4.19$$

Estimates for the critical Reynolds number range from 2500-4000 (Huntley, 1988).

Taking a different perspective of equation 4.19, assuming that it is generally valid, it is possible to derive a critical height above which measurements must be made to ensure an inertial sub-range

$$z_{cr} = Re_c \nu / (\kappa u_*). \quad 4.20$$

However, it is also a requirement that the measurements are made within the constant stress part of the logarithmic layer (see assumption 2). It is possible that, in certain circumstances, these two height requirements cannot both be satisfied, i.e. that there is no height at which the instrument is high enough to satisfy the Reynolds number criterion whilst also being within the constant stress layer. If this is found to be true, Huntley (1988) suggests a modification to the inertial dissipation method so that this method may

be used. In the data discussed further here, equation 4.19 is readily achieved and an inertial dissipation range is therefore expected.

In the spectrum, (see figure 4.4), the wind wave band can be seen and is indicated on the diagram. The limits marked on the spectrum, figure 4.5, are the theoretical limits within which the inertial sub-range is expected to occur. These will be explained in more detail in subsequent paragraphs. Within these limits, an approximate  $-5/3$  run-off can be seen as predicted by theory, equation 4.14.

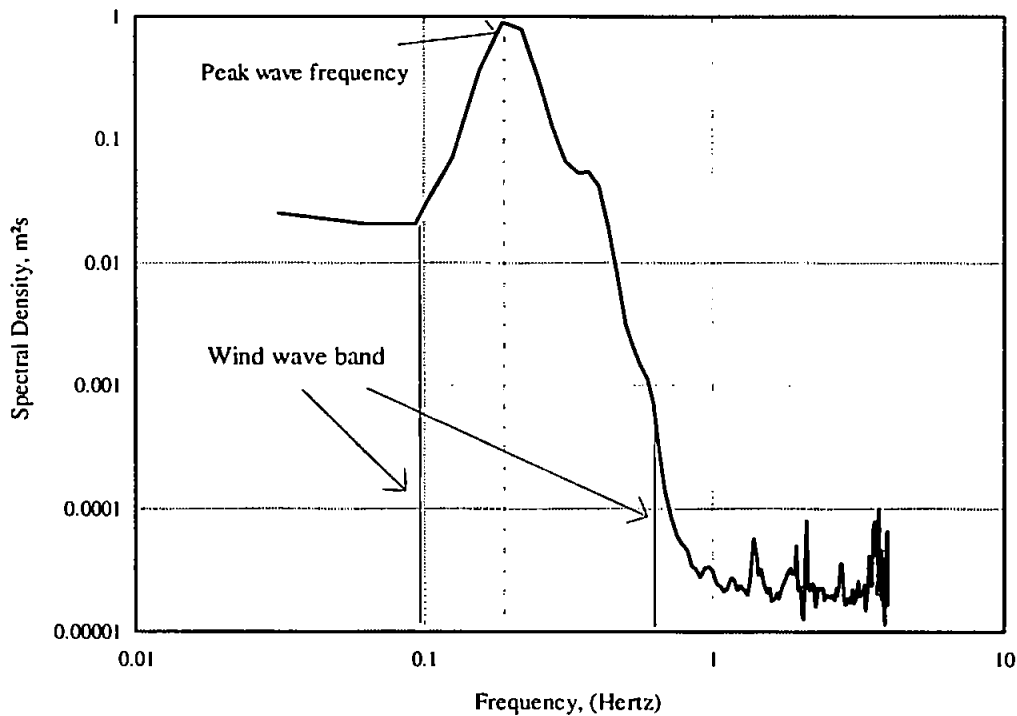


Figure 4.4 Spectrum of pressure transducer time series indicating limits of wind wave band and peak period.

There is a limit to the physical size of the turbulent motions that the current meters can sense. This is due to the physical dimensions of the EMCM. This upper limit for the sub-range is given, (Soulsby, 1983), as

$$k = 2.3/d, \quad 4.21$$

where  $d$  is the distance between the electrodes on the sensing head of the EMCM, 55 mm and 100 mm for the two types of EMCM used in this experiment.



There is also a lower limit to where the  $k^{-5/3}$  roll-off will occur, figure 4.5. This is given by

$$k = 2\pi/z. \quad 4.22$$

For a sensor at height  $z$  above the bed the peak turbulent energy is expected close to  $k = \pi/z$ , but for the assumed value of the Kolmogorov constant to be valid, it has been suggested (Huntley and Hazen (1988)) that wavenumbers greater than twice the expected peak should be used. If effects of wave energy from the surface prevent the confirmation of the turbulent peaks then the lower wavenumber limit can be chosen to be at or larger than the number found from equation 4.22.

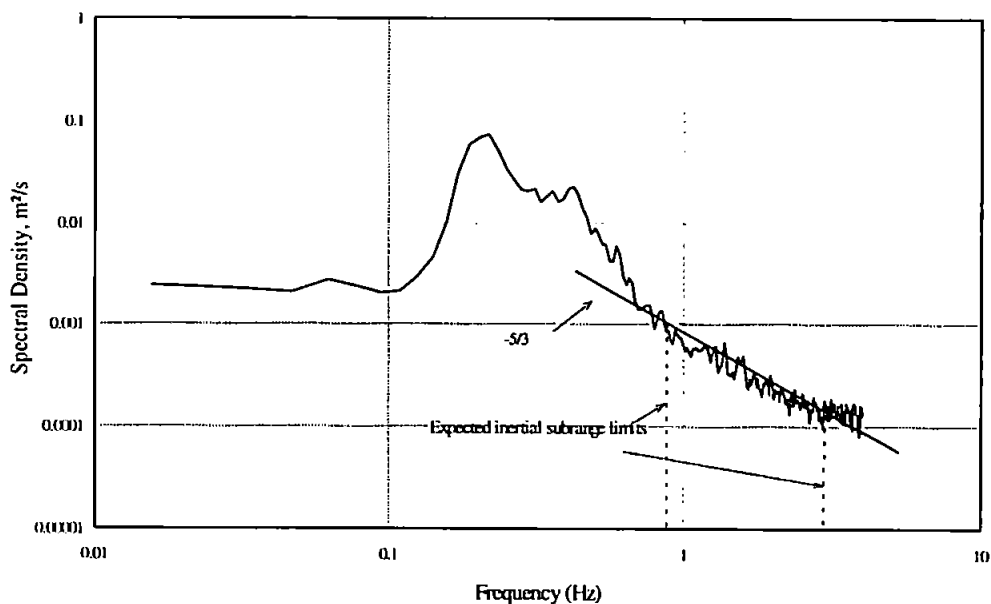


Figure 4.5 Spectrum of vertical velocity time series showing limits on inertial subrange and the  $-5/3$  roll-off

However, since frequency is measured and not wavenumber, it is necessary to convert wavenumber to frequency. This is done using the formula,

$$k = 2\pi f/\bar{u}, \quad 4.23$$

where  $f$  is the frequency. Substituting equation 4.23, into equations 4.21 and 4.22 and rearranging gives two new equations,

$$f = \bar{u}/z, \quad 4.24a$$

and

$$f = 2.3\bar{u}/2\pi d, \quad 4.24b$$

which are linearly dependent on the magnitude of the mean velocity at a given height. These are plotted in figure 4.7 as solid lines.

A very important consideration in measuring turbulence with electromagnetic current meters is the high frequency cut-off filter in the sensor. The current meters in this study contained 9th order Elliptical low pass filters and the -3dB frequency was set at 2.4 Hz. This cut-off and the filter characteristics were verified by laboratory measurement. In figure 4.6 the filter limit is shown as a single frequency boundary at 2.4 Hz (all data in this thesis are collected with this type of filter), and the sharp roll-off of the 9th order filter ensures that spectral amplitudes are not reduced by more than 20% for frequencies below 2 Hz.

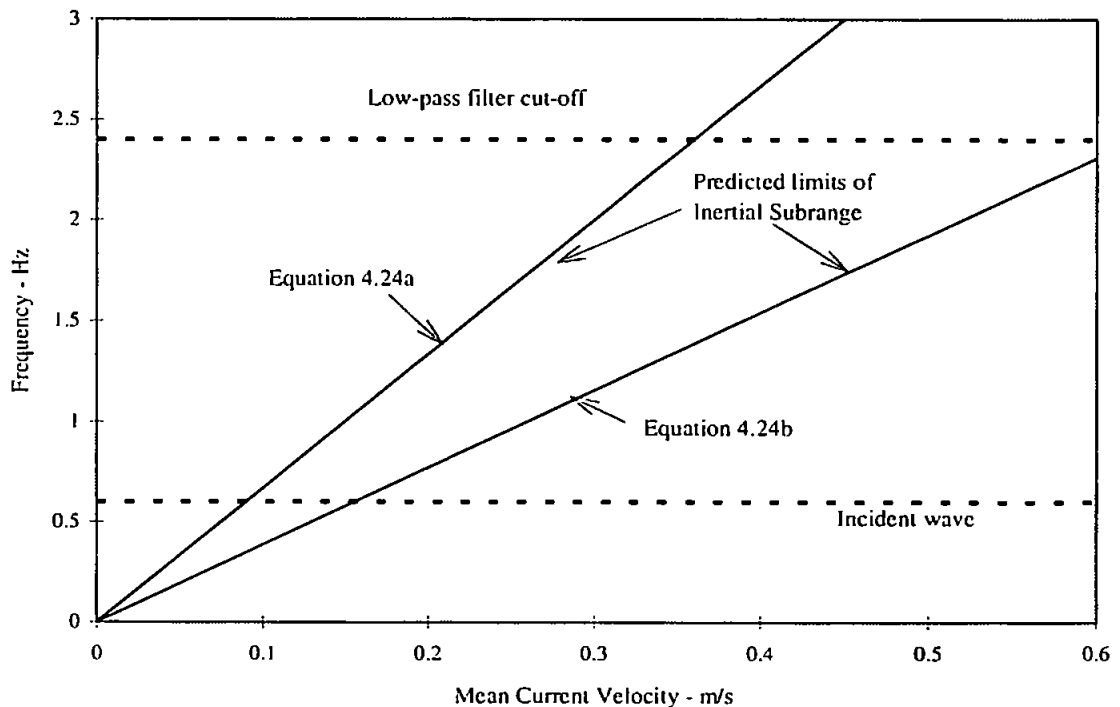


Figure 4.6 Showing limits of where the inertial subrange might occur and where the current meters can sense turbulence.

The lower frequency limit for the turbulence is set by the upper frequency limit of the incident wave band, and will vary with conditions at the time of data collecting. The

lines defining the limits of the inertial sub-range are calculated using the equations 4.24a and b given above.

### 4.3.2 The Turbulent Kinetic Energy Method

Instantaneous velocity, at time  $t$ , in the  $x$  direction for example, can be written as

$$u(t) = \bar{u} + u_w(t) + u_t(t), \quad 4.25$$

where  $\bar{u}$  is the mean (time averaged) velocity and the subscripts  $w$  and  $t$  refer to fluctuations due to waves and turbulence respectively. Since  $u_t(t)$  is, by definition, not correlated with  $u_w(t)$  then it can be seen from the equation that the variance of a time series can be attributed to either waves or turbulence, i.e.  $\overline{u^2} = \overline{u_w^2} + \overline{u_t^2}$  where  $\overline{u^2}$  is the total variance of the time series. There is no hard and fast rule for separating these fluctuations in frequency space but Soulsby and Humphery (1989) suggests it can be done by interpolating across the base of the wave band, as shown in figure 4.7.

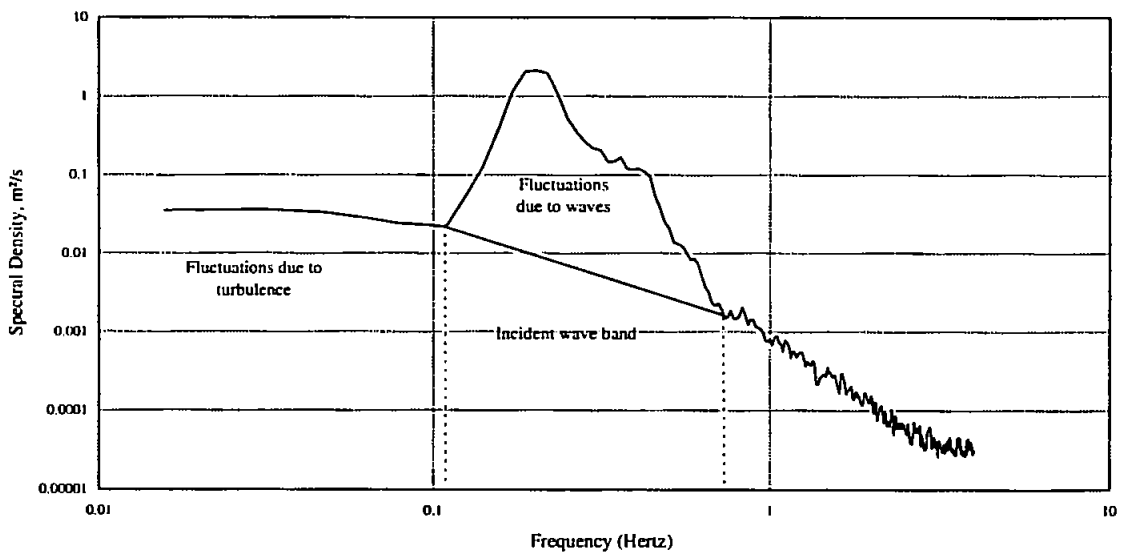


Figure 4.7 Spectrum of cross shore velocity split into fluctuations due to waves and those due to turbulence.

The area above the line is taken to be the wave variance and the area below, the variance due to turbulence. The same procedure can be applied to both the  $u$  and  $v$  components of flow. The vertical component,  $w$ , is assumed uncontaminated by waves and consequently all fluctuations are taken to be due to turbulence. When the velocity measurements are made well above the seabed it is possible that the wave motion will have an effect on the vertical velocity time series and if this is found to be the case, the

fluctuations due to the waves can be removed in the way described above. Removal of the wave energy could also be useful if the alignment of the instruments was not perfect.

The turbulent kinetic energy,  $E$ , is calculated from the definition

$$E = \frac{1}{2} \rho (\overline{u_i^2} + \overline{v_i^2} + \overline{w_i^2}). \quad 4.26$$

From this it is possible to calculate the bed shear stress. In the region close to the bed where energy production equals energy dissipation the bed shear stress is proportional to the turbulent kinetic energy density. Using the constant of proportionality observed in a wide range of flows (Soulsby 1983) the bed shear stress can be calculated

$$\tau = 0.19E. \quad 4.27$$

The value 0.19 is assumed constant under diverse conditions (Soulsby, (1983)).

### 4.3.3 The Reynolds Stress or Eddy Correlation Method.

The Reynolds stresses  $\overline{\rho u'w'}$  and  $\overline{\rho v'w'}$  measure the flux of momentum and hence the stress at the measured height. As with the previous methods it is necessary to assume that all measurements are made within the constant stress layer. The turbulence is assumed anisotropic and the waves are assumed to have no vertical component. This being so the correlation between the vertical and long shore/cross-shore flow is due entirely to the turbulence.

The errors associated with this method due to misalignment of instruments can be very large, as much as 156% per degree of misalignment in wave dominated flow, (Soulsby and Humphery (1989)). Efforts taken during the fieldwork ensure this was kept to a minimum by ensuring that the EMCM's were kept vertical or horizontal (as required) and that all electrodes reading cross shore or long shore were parallel. There is also the problem of establishing where the horizontal plane lies, in that the bottom slope was not horizontal which could affect the way in which the waves move past the sensors. By plotting the horizontal components of the flow against the vertical flow it was possible to establish if it was necessary to rotate the axes. Because of this problem it was decided to look at the long term averages of the horizontal and vertical velocities to look for any trend that might indicate that the sensors were misaligned. For example if the vertical

velocity mean showed some correlation to either or both horizontal components of the flow. Examination of the plots showed that there was no need to rotate the axes.

#### 4.4 Data Selection

All three methods above were used to calculate estimates for the stresses felt at the bottom and hence friction velocity,  $u_*$ . The results of these methods will be given in the next chapter. However, because all of the above methods are based on measurements of turbulence generated from the seabed boundary it was necessary to remove all parts of the data set where turbulence from other sources was introduced into the system. Time series where breaking or spilling waves were present at or near to the equipment stations were removed, also tidal cycle 'gp', see section 5.1, was removed as there were "white horses" present during the entire tidal cycle. The existence of breaking was determined by the Miche parameter, (equation 4.13), and by observations made at the time of data collection.

Figure 4.8 -4.10 give examples of the raw velocity data, given in physical units. Figure 4.8 shows a short burst of data from the first tidal cycle considered for this study to be current dominated. The long shore current, mean  $\approx 40 \text{ cms}^{-1}$ , is greater than the maximum cross shore velocity which is associated with the waves.

The data presented in figure 4.9 are from the final tidal cycle, considered to be wave dominated, the cross shore velocity varies between more than  $\pm 50 \text{ cms}^{-1}$ , and can be seen to be much greater in variance than the long shore velocity.

Figure 4.10 is from tidal cycle 'gp', and are examples of data that were rejected. Whilst the instruments were covered there were waves breaking at or very close to the station. This phenomenon can be seen as a dramatic increase in the vertical velocity as the wave plunges past the station.

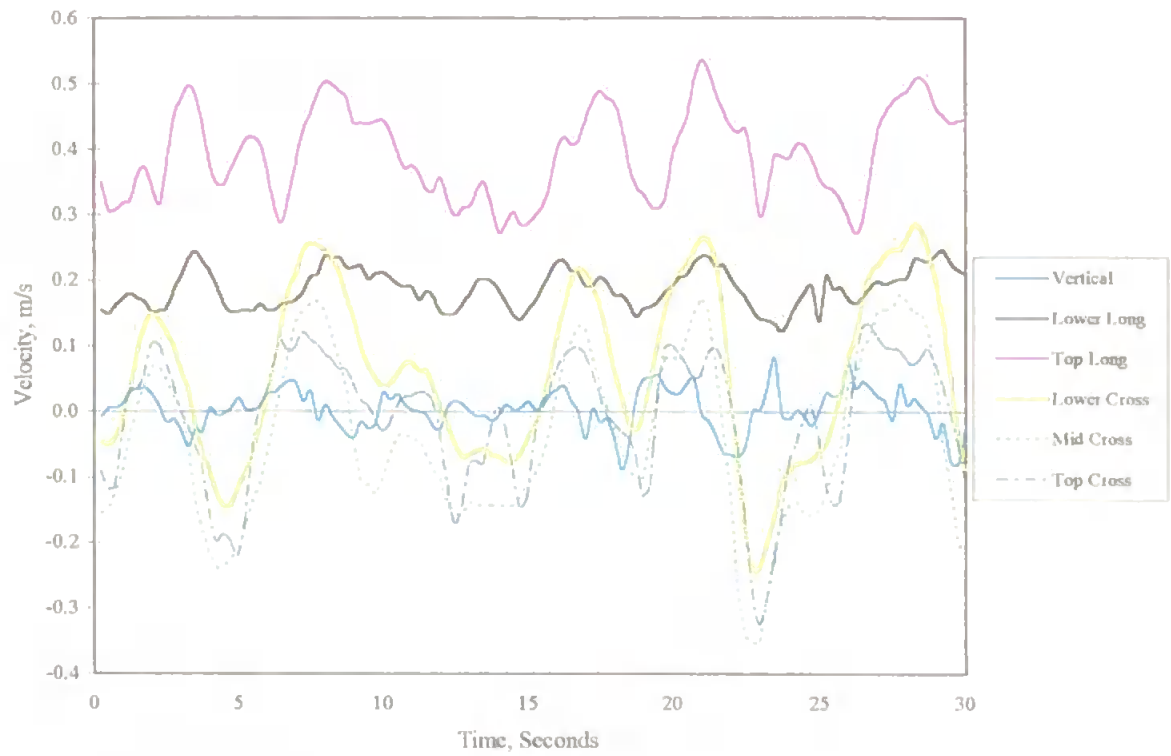


Figure 4.8 Velocity data from a current dominated data run.

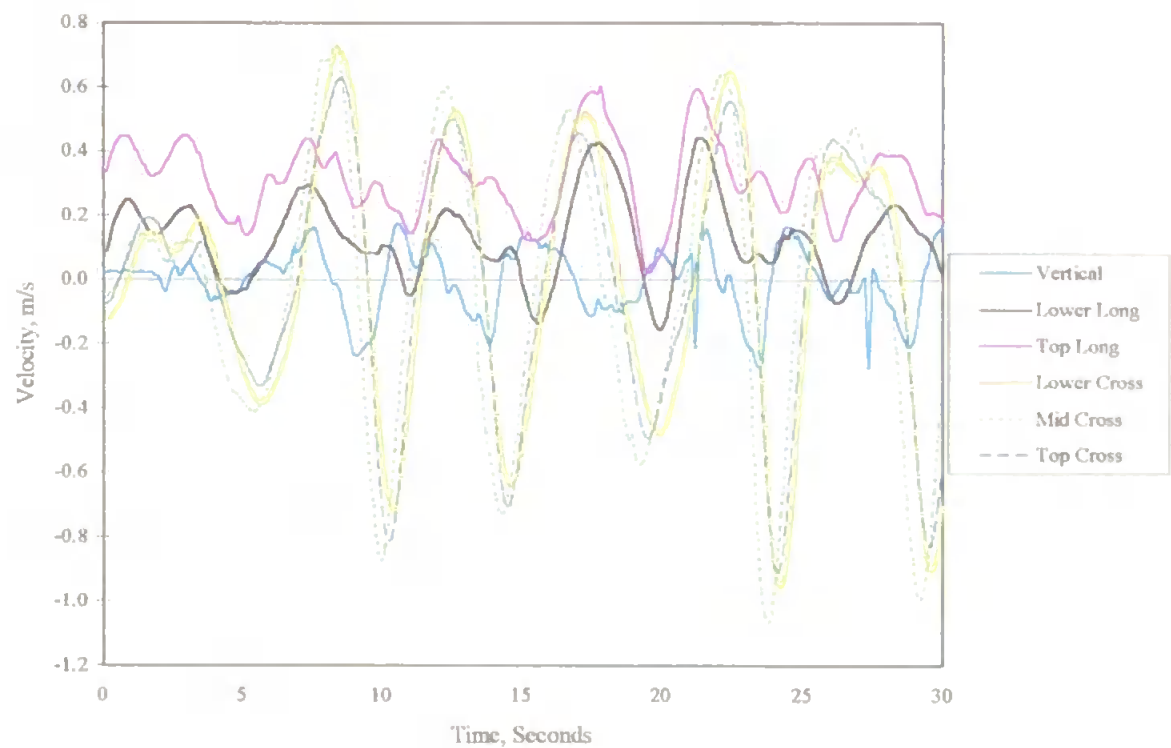


Figure 4.9 Velocity data from a data run considered wave dominated.

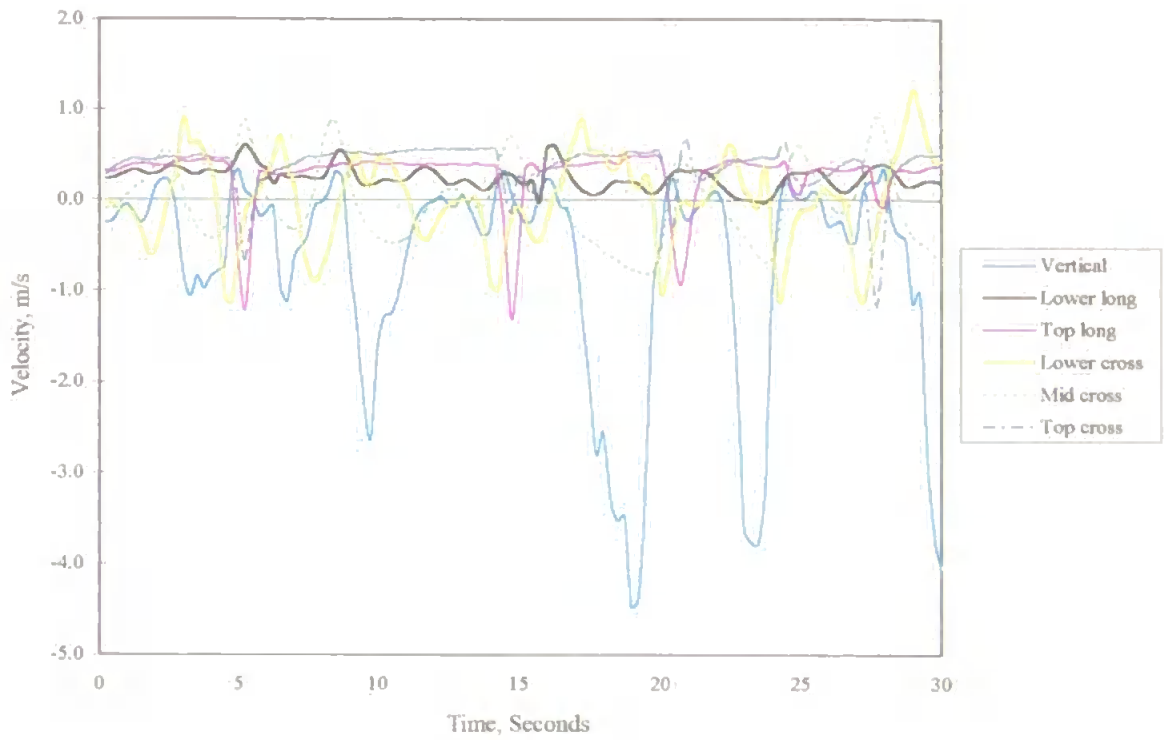


Figure 4.10 Velocity data from a data run which was discarded as being unsuitable for further analysis. The large vertical velocities were thought to be due to waves breaking in the vicinity of the instrument array.

## **Chapter 5**

### **Results of Field Work and Comparison with Other Work**

Data from the field campaign described in chapter 3 were used to estimate shear stresses using the three methods outlined in chapter 4. In the succeeding sections these results, from both instrument stations, will be presented and compared with the results of the field campaigns conducted by Cacchione and Drake, (1992) (CD92), and Soulsby and Humphery, (1989), (SH89); these campaigns are described in detail in section 2.5. Whilst there are other field campaigns, section 2.5, the two used below are the only two with data in tabular form which makes an accurate comparison possible.

#### **5.1 Introduction to the Nomenclature used in the Results**

Table 5.1 below shows the rationale behind the nomenclature used in the description of the results. Each day was first labelled with a letter, from a to h, starting on 25/02/94 and ending on 04/03/94. If data collecting began in the morning the next part of the label was an “a” and, if the collecting began in the afternoon the second letter of the label was a “p”. The next two digits in the labelling system are the run numbers: 01 to 11. Hence, fp03, was collected on 02/03/94 with the data collection in the afternoon and it was the third run in the series.



The first data runs, “aa” and “ap”, collected on 25/02/94 were not used as the instruments were not all covered for most of the tidal cycle and also the instruments had to be rearranged so that the vertical fluctuations could be recorded.

Date	Letter	am/PM	Run Numbers
26/02/94	b	a	01 - 10
		p	01 - 08
27/02/94	c	p	01 - 09
28/02/94	d	a	01 - 08
		p	01 - 11
01/03/94	e	a	01 - 09
		p	01 - 10
02/03.94	f	a	01 - 10
		p	01 - 10
03/03/94	g	a	01 - 05
		p	01 - 11
04/03/94	h	a	01 - 11

Table 5.1 Explanation of the nomenclature used in presenting the field results.

## 5.2 Estimates of Shear Stress from Field Data

Not all data collected were suitable for using in the analysis as data collection started before all instruments were covered and continued after the top instruments were uncovered. The period of data collection included periods of waves breaking on or near the instrument stations which could affect the shear stress estimates made using methods which rely on turbulence. It was necessary to remove all data sets in which it was suspected that either or both of these phenomena occurred. To establish if breaking occurred during the data run the Miche parameter – equation 4.13 – was used. Careful examination of the time series revealed when the instruments were uncovered as the EMCM's record a saturated signal when out of the water. Also, observations made at the time of data collection relating to the waves and water depth proved invaluable. The minimum water depth was found for each time series using MATLAB, a software package, which simply finds the minimum value within a vector. If the minimum depth was below that of the highest instrument then the time series was discarded and not used in the subsequent analysis. Table 5.2 below shows the data runs which were considered suitable to use in the subsequent analysis.

It was not possible to arrange the instruments such that all three components of the flow were read at the same height. This was due to the need to read the cross shore flow at three heights above the bed for the CSTAB project. For the three methods used to calculate the

Date	Tidal Cycle	Time series used in subsequent analysis	
		Station 1	Station 2
26/02/94	ba	02 - 05	02 - 07
	bp	02 - 05	02 - 07
27/02/94	cp	02 - 06	02 - 07
28/02/94	da	01 - 04	01 - 06
	dp	03 - 06	02 - 07
01/03/94	ea	02 - 05	02 - 07
	ep	02 - 05	02 - 07
02/03.94	fa	02 - 05	02 - 07
	fp	03 - 07	02 - 07
03/03/94	ga	02 - 04	02 - 05
	gp	'white horses'	∴ not used
04/03/94	ha	03 - 07	03 - 07

Table 5.2 The data runs suitable for use in subsequent analysis, tidal cycle 'gp' was not used as white horses were present at the time of recording.

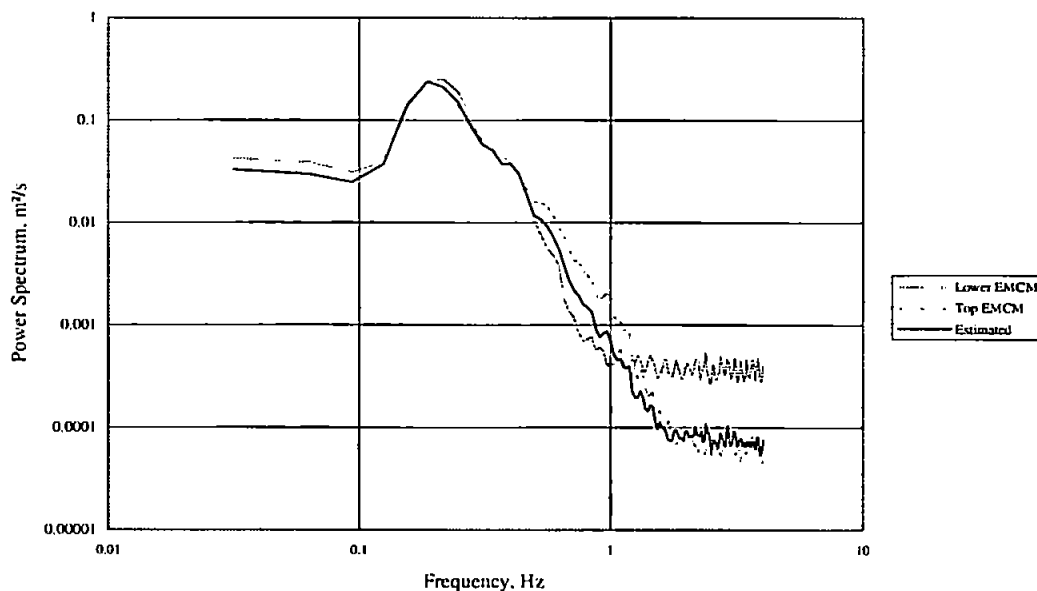


Figure 5.1 Spectra of velocity data from longshore flow components and from estimated time series.

shear stresses at the bottom, it would have been ideal to have all three components of the flow measured at the same height above the bed. This was not feasible, hence the time series for the longshore component of the flow at the mid height was estimated from the other two longshore current meter time series. This was done by assuming a logarithmic

profile and calculating the velocity time series at the height of the mid current meter from the assumed profile. This interpolation might have a smoothing effect on the estimated time series, diminishing the turbulence, and hence slightly lowering the estimates of shear stress. Figure 5.1 shows the spectra of the two measured and one estimated components of the flow, as can be seen, the estimated spectrum does vary slightly, the variance of the estimated time series is  $0.0012 \text{ m}^2$  as compared with  $0.0015 \text{ m}^2$  and  $0.0012 \text{ m}^2$  of the top and lower EMCM's respectively.

### 5.2.1 Station 1

Station 1, the innermost station was positioned on the inshore side of the ridge feature on the beach, as shown in figure 3.9. The instruments were covered by unbroken waves for approximately two hours over each tidal cycle. In the figures of results the small groups of 4 or 5 points represent the results calculated for each data run over a tidal cycle, starting on 26/2/94 and concluding on 4/3/94. Figure 5.2 shows the values of shear stress calculated by the three methods. Results using each method show a general increase in the estimated shear stress from the beginning to the end of the field campaign, with a slight dip in the penultimate tidal cycle, "ga". This dip corresponds exactly with the decrease in the wave conditions experienced during the campaign, shown in figure 4.1.

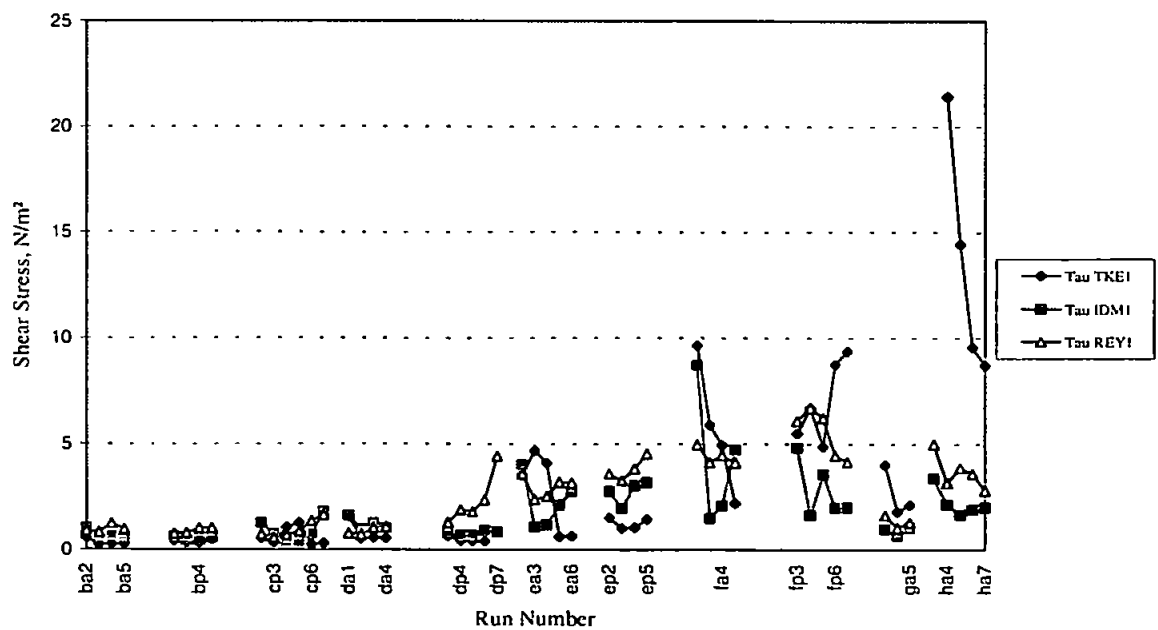


Figure 5.2 The results of the three methods used to calculate shear stresses for station 1

### 5.2.2 Station 2

In Figure 5.3, the results from the outer station are shown, station 2, and very similar trends can be seen in the results. The instruments on the station were covered for between two and a half to three hours. Again there is a dip in tidal cycle “ga” where the significant wave height lessens for the tidal cycle.

Comparisons of the results from the two stations for each of the three methods are shown in figure 5.4 a), b) and c). It is reassuring to note the very similar results under the very similar hydrodynamic conditions experienced by each instrument rig.

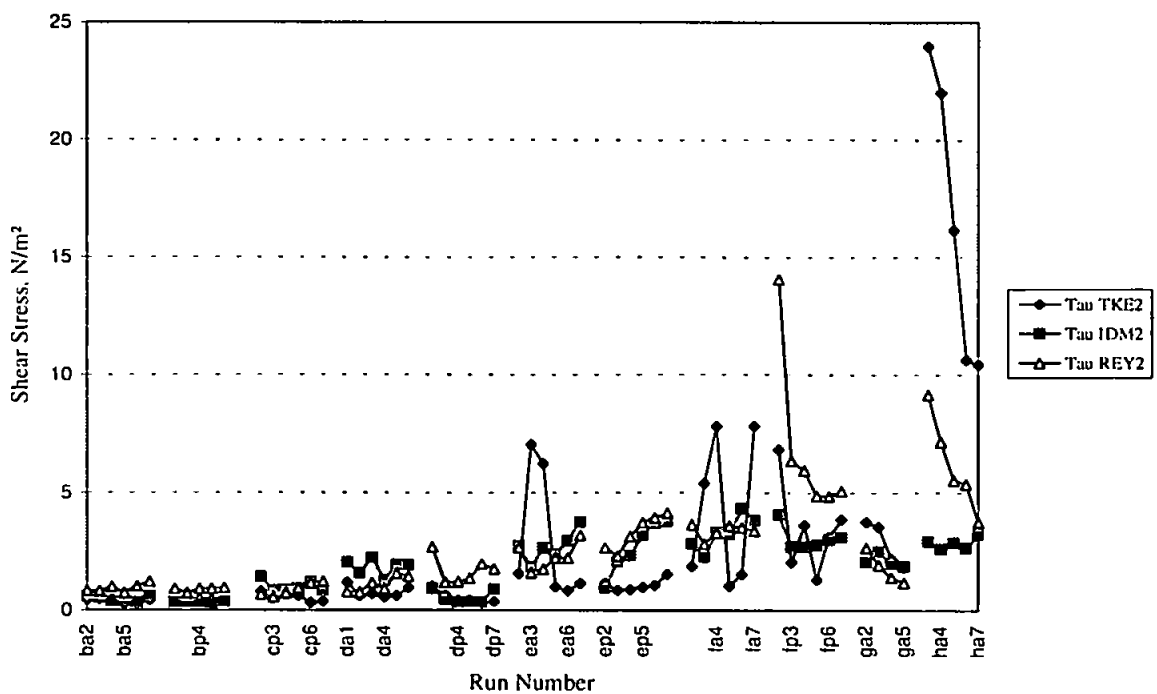
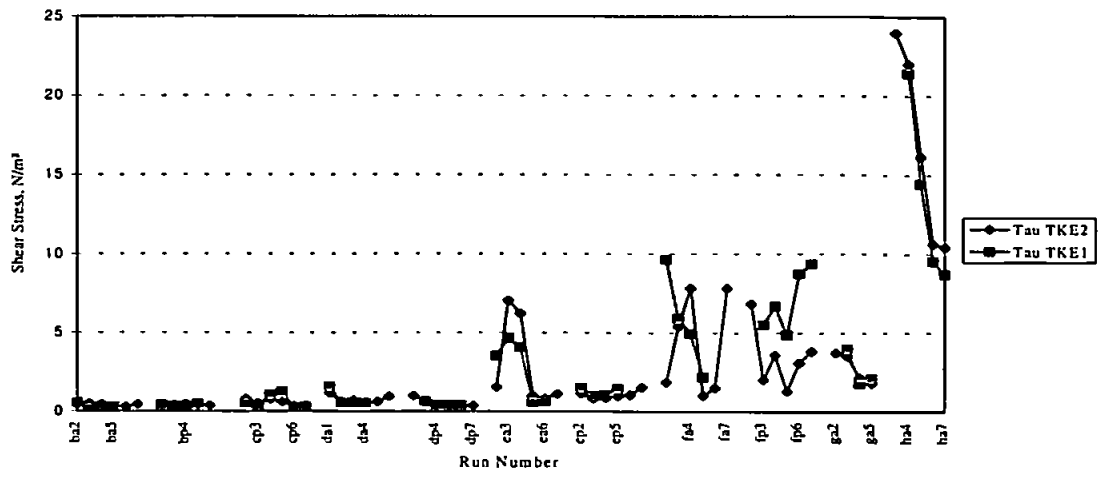


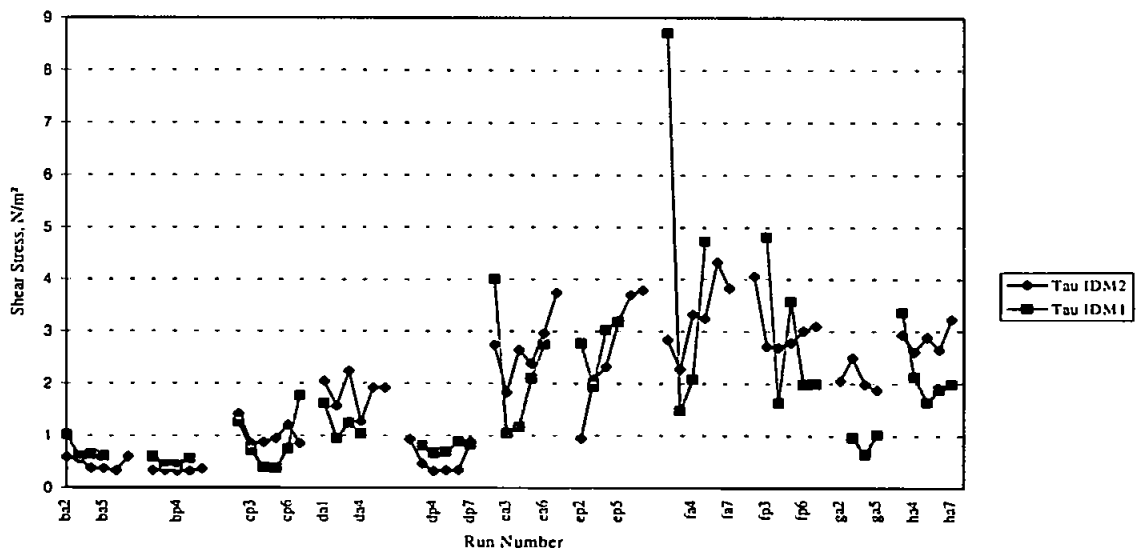
Figure 5.3 Results of shear stress estimates from station 2.

Figure 5.5 shows a plot of the results from station two plotting the turbulent kinetic energy method against the results from the other two methods. It is noticeable from the plot that the TKE method tends to give comparatively larger results than the other methods for the larger shear stresses. There is considerable scatter, but the trends are similar and all results are within an order of magnitude

(a)



(b)



(c)

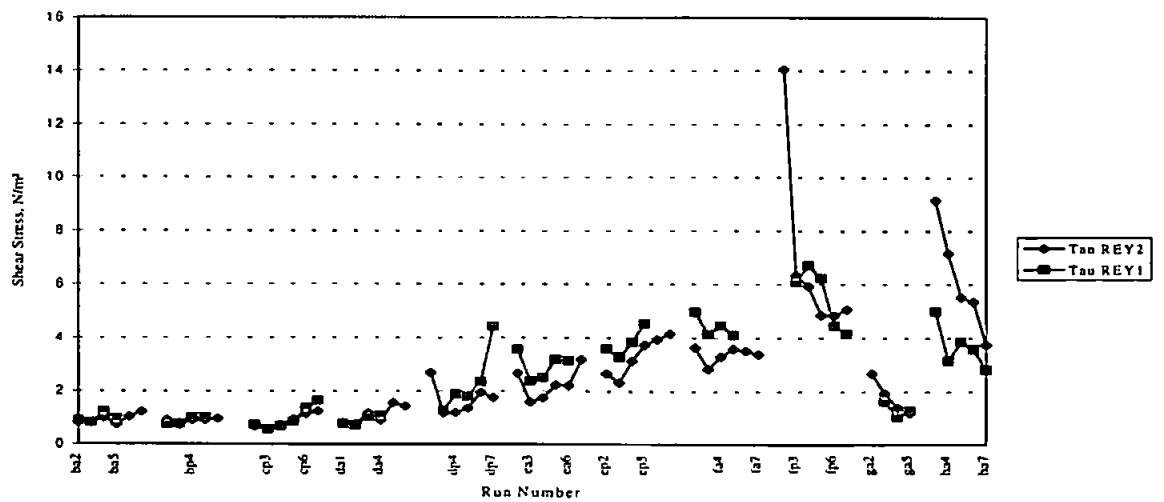


Figure 5.4 Highlights the similarities between the shear stress estimates made at the two stations.

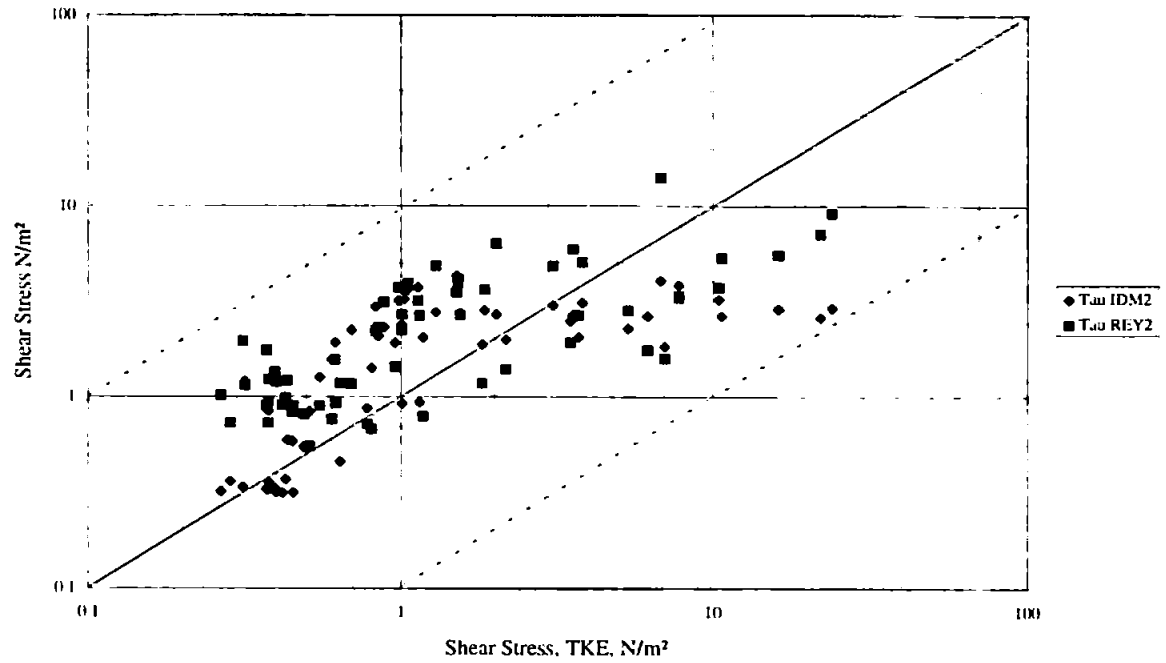


Figure 5.5 Plot of the turbulent kinetic energy method against the Reynolds stress method and the inertial dissipation method, showing the scatter

### 5.3 Error Analysis

Errors in the inertial dissipation method can be calculated from the degrees of freedom of the spectra used in the calculations. The degrees of freedom for this experiment are calculated from:

$$Df = 3.82 * N - 3.24 \quad 5.1$$

(Nuttal (1979)), where N is the number of non-overlapping time series segments used to calculate the spectra. In this case  $Df = 27$ . The confidence intervals are found using:

$$\frac{Df}{\chi_{Df}^2(\alpha/2)} \hat{p}(f) \leq p(f) \leq \frac{Df}{\chi_{Df}^2(1-\alpha/2)} \hat{p}(f) \quad 5.2$$

where  $(1-\alpha)*100$  is the confidence interval required,  $\hat{p}(f)$  is the spectral estimate calculated from the data using the method described in section 4.2 and  $p(f)$  is the true spectrum. From the chi-squared probability distribution, using the degrees of freedom calculated above and choosing a 95% confidence interval the errors associated with the spectra are approximately  $\approx \pm 0.35$ .

Errors for the mean flow are a little more problematical as the mean flow, unlike the turbulent fluctuations, is affected by the choice of offset. The offsets taken in the field

were used to calculate mean flows. Green and McCave (1995) suggests that errors in the mean flow attributable to the current meters are no more than 5%, however because of the doubts in the magnitude of the mean flow a 10% error was allowed. Since only velocities of greater than 20 cms<sup>-1</sup> have been used the 10% margin leads to errors of ± 2 cms<sup>-1</sup> or more, which corresponds to errors experienced by Huntley and Hazen (1988).

For the inertial dissipation method of calculating shear stress, using the errors for the spectra and mean flow, the errors are estimated from equation 4.14 with equation 4.15 substituted into it. This equation becomes:

$$\text{error}(u_s) = \left( (1 \pm 0.35) \times \frac{1}{(1 \pm 0.1)} \right)^{\frac{2}{3}} \quad 5.3$$

Using Maclaurin series expansions, the error for  $u_s$  is given as  $(1 \pm 0.30)$ , hence the error associated with the shear stress is, conservatively, is  $(1 \pm 0.60)$ , i.e. ± 60%.

The turbulent kinetic energy method is based solely on spectral analysis and consequently the errors are  $(1 \pm 0.35)$ , i.e. ± 35% for the shear stress.

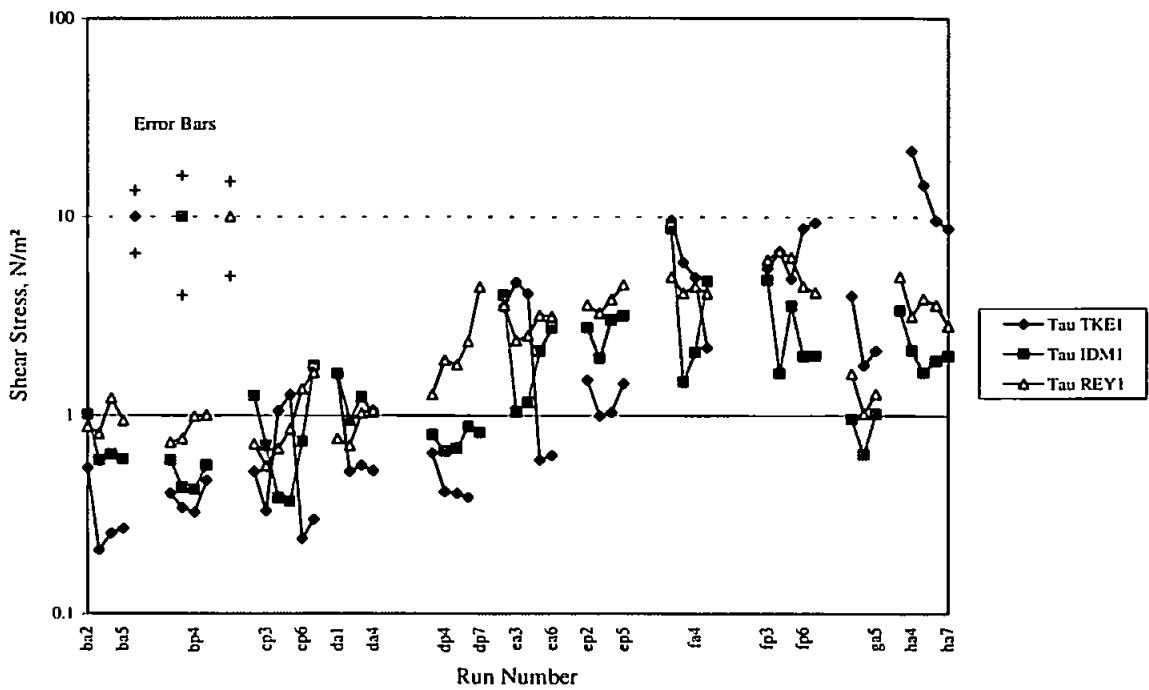
The Reynolds stress method is very sensitive to errors in the alignment to the vertical of the current meters, in very wavy conditions as much as 156% error per degree (Soulsby and Humphery (1989). Huntley (1988) proposes that alignment accuracy of one tenth of a degree is necessary to provide accurate estimates. This degree of accuracy is not possible in the field and cannot be supposed to have been obtained. Assuming an inaccuracy of approximately one half a degree to the vertical in wavy conditions an error of 50% is assumed for the Reynolds stress method. Figure 5.6 a) and b) show the error bounds of each of the methods applied to the results.

The error bars overlap for most of the estimates, but not for all, for example for run number ha3 the error bars for the TKE and REY methods do not overlap. The differences between the methods do not show any systematic changes; none are consistently bigger than any of the others and there is no significant correlation between the differences.

As mentioned before, all of the methods used to calculate the shear stresses are turbulence based and, hence it was decided to take the mean of the three methods to give

just one estimate for the shear stress for comparison in later sections. However, at times, all three methods may be presented.

(a)



(b)

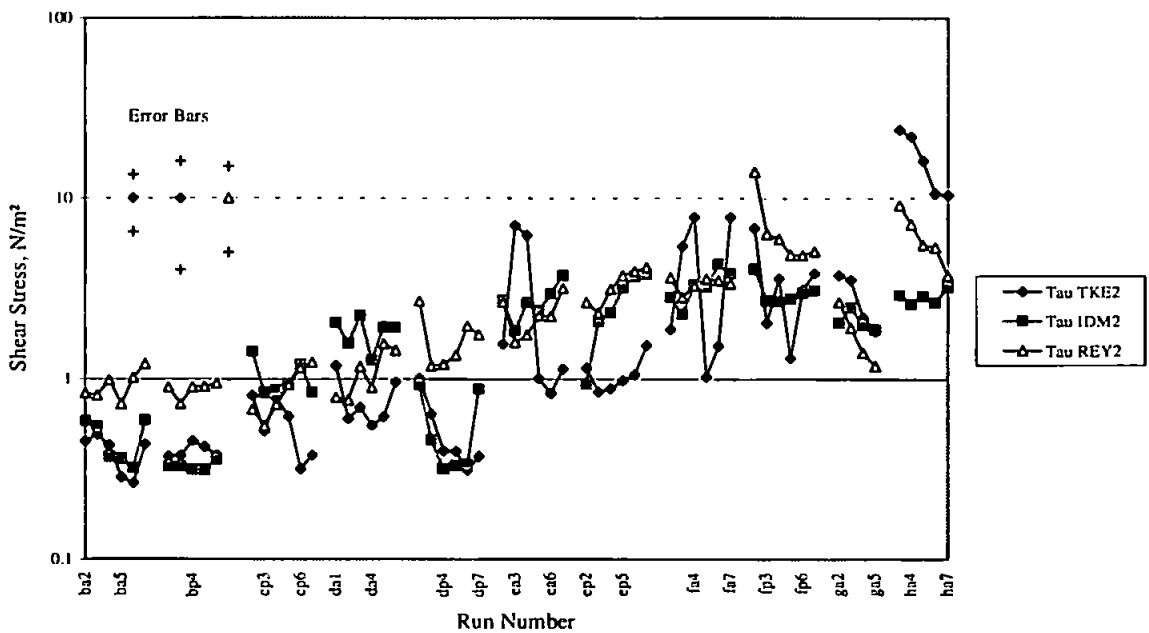


Figure 5.6 (a) and (b) show the estimates of shear stress with the errors associated with each method marked in the top left hand corners.



## 5.4 Comparison with other Field Results

In this section the results from two previous field campaigns are compared with the results presented above. A more detailed description of these field deployments is given in chapter 2. Soulsby and Humphery, (1989, table 1, ) give 30 values of current speed,  $U_{100}$ , orbital wave velocity,  $\sigma_{\text{wave}}$ , and bed shear stress, estimated using the velocity profile method, the Reynolds stress method and the turbulent kinetic energy method. Using the relationship:

$$C_d = \tau_0 / \rho U_{100}^2 \quad 5.4$$

the drag coefficient was calculated as was the wave to current ratio,  $\sigma_{\text{wave}} / U_{100}$ . Similarly, Drake and Cacchione, 1992, present their results in the form of the drag coefficient,  $C_d$ , and  $\sigma_{\text{wave}}$  but give  $U_{18}$ , the velocity at 18 cm above the bed, as the mean current velocity. The values of the shear stress were calculated by the log profile method and values of bottom roughness,  $z_0$ , for the profiles were given in their table 2. For comparison with our results and those of Soulsby and Humphrey we have calculated  $U_{100}$  using the formula below:

$$U_{100} = \frac{u_*}{\kappa} \ln \left( \frac{100}{z_0} \right) \quad 5.5$$

where  $\kappa$  is von Karman's constant, taken as 0.41.

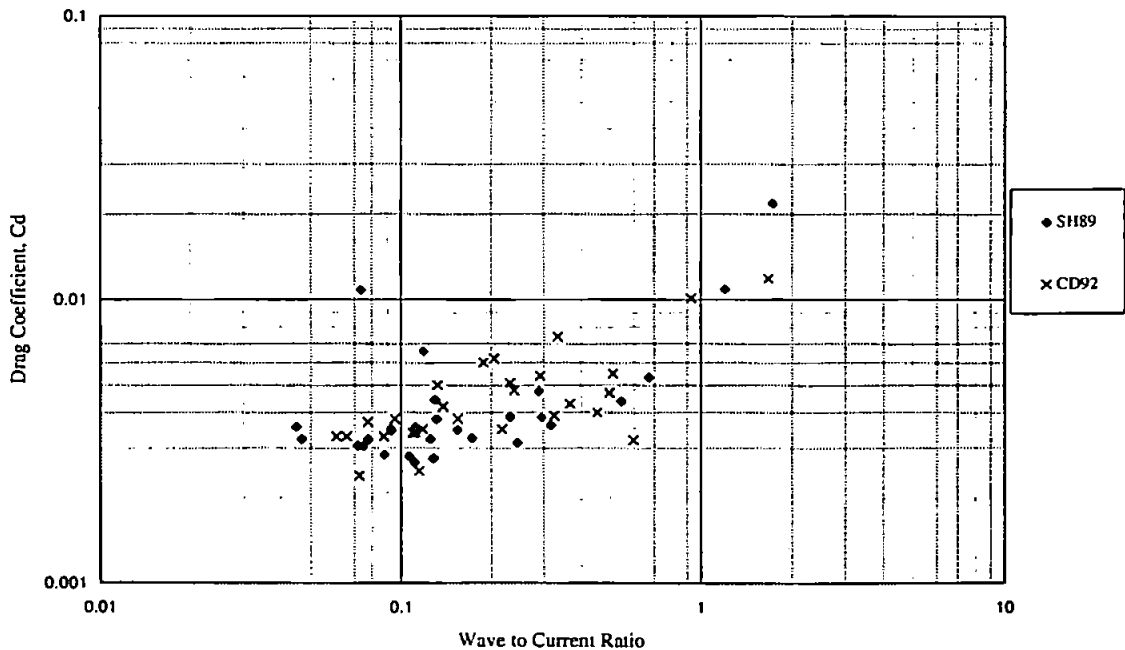


Figure 5.7 Drag coefficients from Soulsby and Humphery (1989) and those calculated from Drake and Cacchione (1982).

A plot of the drag coefficient as a function of the wave to current ratio from both of the field campaigns is shown in figure 5.7. The general trend for the data is an exponential curve which appears to increase rapidly once the wave to current ratio is greater than one. Introducing the drag coefficient, estimated from the data collected in this study, to the plot, figure 5.8 shows that they are consistent with the other field data. The points at the lower end from the study fit in at the upper end of the Soulsby and Humphery data and the data from Drake and Cacchione and intermingle well, and then extend the range of data to greater values of the wave to current ratio in a manner consistent with the line of fit suggested by Soulsby and Humphery.

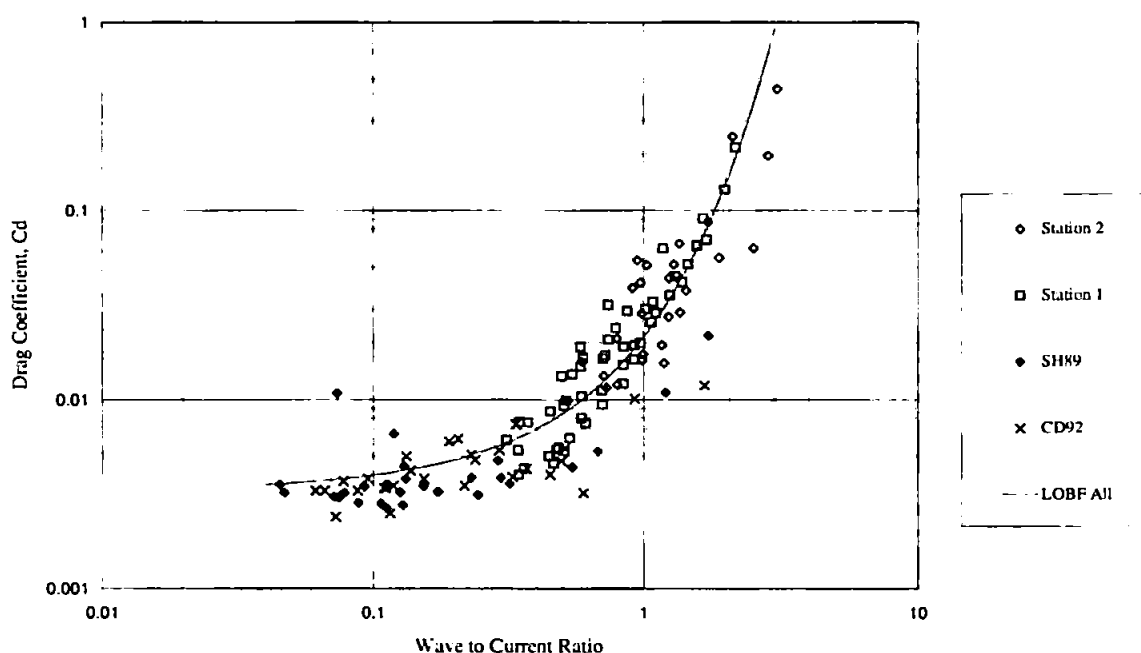


Figure 5.8 Comparison of drag coefficient with those of Cacchione and Drake (1982) and Soulsby and Humphery (1989).

The line shown on the graph is an exponential line of best fit for all of the data points presented. The equation for this line is:

$$C_d = 0.0033e^{1.8741x} \quad 5.6$$

with an  $r^2$  value of 0.8843, where  $x = \sigma_{w,vc}/U_{100}$ . Figure 5.9 is identical to figure 5.8, but the lines of best fit for each individual field site are shown. The two equations for stations 1 and 2 are similar in shape and the two for the other field campaigns show similarity but there is a distinct and large difference between the lines of best fit for this field campaign and the other two. The equations for these lines and for the line of best fit for all points are listed in table 5.3.

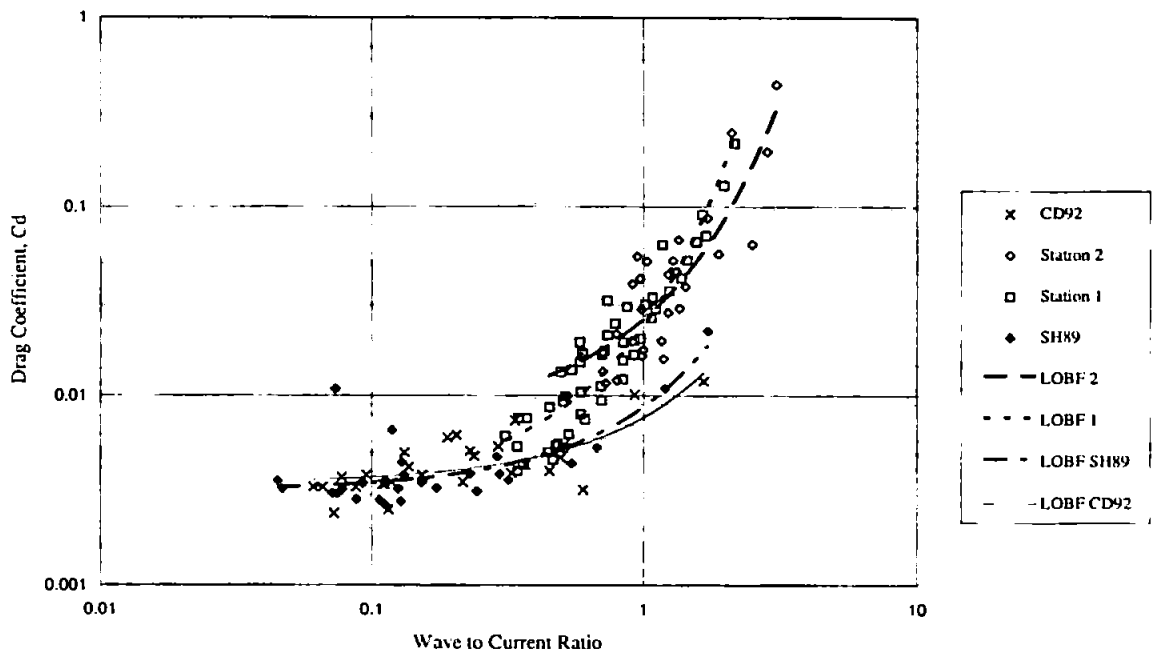


Figure 5.9 Showing lines of best fit for each field station.

Field Site	Equation	R <sup>2</sup> value	Equation
Station 1 (Mean)	$C_d = 0.0031 \exp(2.0038 \sigma_{\text{wave}} / U_{10})$	0.88	5.7
Station 2 (Mean)	$C_d = 0.0039 \exp(1.875 \sigma_{\text{wave}} / U_{10})$	0.84	5.8
SH89	$C_d = 0.0031 \exp(1.0211 \sigma_{\text{wave}} / U_{10})$	0.63	5.9
CD92	$C_d = 0.0034 \exp(0.8057 \sigma_{\text{wave}} / U_{10})$	0.53	5.10
All	$C_d = 0.0033 \exp(1.8741 \sigma_{\text{wave}} / U_{10})$	0.84	5.11

Table 5.3 The equations of the lines of best fit for the data presented in figure 5.9.

There is a remarkable similarity between the constants of the equations in table 5.3 and also a notable change in the exponential; these similarities/differences will be discussed in the next chapter.

The scatter is large, almost an order of magnitude in the extreme, between drag coefficients of similar wave to current ratios. The spread is greater for the higher wave to current ratio but it is still quite large for the lower ratios, with some estimates of a given

ratio 3-4 times larger than others of a similar one. Again, reasons for this scatter will be investigated in the final chapter.

## Chapter 6

# Inter-comparison of Models and Comparison of Models with Field Results

### 6.1 Inter-comparison of Models

The models and their parameterisation chosen for the comparison were described in detail in chapter 2. SANDCALC, a package supplied by H.R. Wallingford, was used to calculate the model results. This package uses the parameterised versions of the models for quick calculation of the model estimates. To compare the models a range of the input parameters was chosen. Wave and current velocities ranging from 0.2 m/s to 1 m/s were chosen. Three values of bottom roughness were chosen. 0.1, 1 and 10 mm; these roughnesses were taken as representative of flat, small ripples and larger ripples to cover the different roughnesses possible. Wave periods of 5s and 10s were taken as representative of conditions experienced and an angle of 90° between the waves and current was chosen for the same reason.

Model	Abbreviations	Modelling techniques
Huynh Thanh and Temperville	HT92	One equation, fully numerical k-l turbulence closure scheme.
Grant and Madsen	GM79	Two layer eddy viscosity, zero equation turbulence closure scheme.
Soulsby13	Soulsby13	Line of best fit of field data, in the same form as parameterised models.
Fredsoe	Fredsoe	Momentum defect assumption.

Table 6.1 A synopsis of the models used in the following analysis.

Table 6.1 gives a brief reminder of the assumptions made in each of the models, for a more in depth description see chapter 2.

Representative results have been chosen to highlight the differences between the models. Table 6.2 below gives the key to all the figures of model results in this section. Figure 6.1 shows the predictions for the four models for bed roughnesses of 1 cm and a period of 10s. As given in table 6.2 each depth averaged velocity is represented by a different colour and each model by a different line style. So, for example, the Fredsoe model for a depth averaged velocity of  $0.4 \text{ ms}^{-1}$  is represented by a solid black line.

Key to figures			
Velocity, (m/s)	Colour	Model	Line Style
0.2	pink	Huynh Thanh and Temperville	-----
0.4	black	Grant and Madsen	- - - -
0.6	green	Soulsby13	---
0.8	red	Fredsoe	————
1.0	bluc		

Table 6.2 Key to figures 6.1 to 6.3, showing line styles and colours for each model and each velocity.

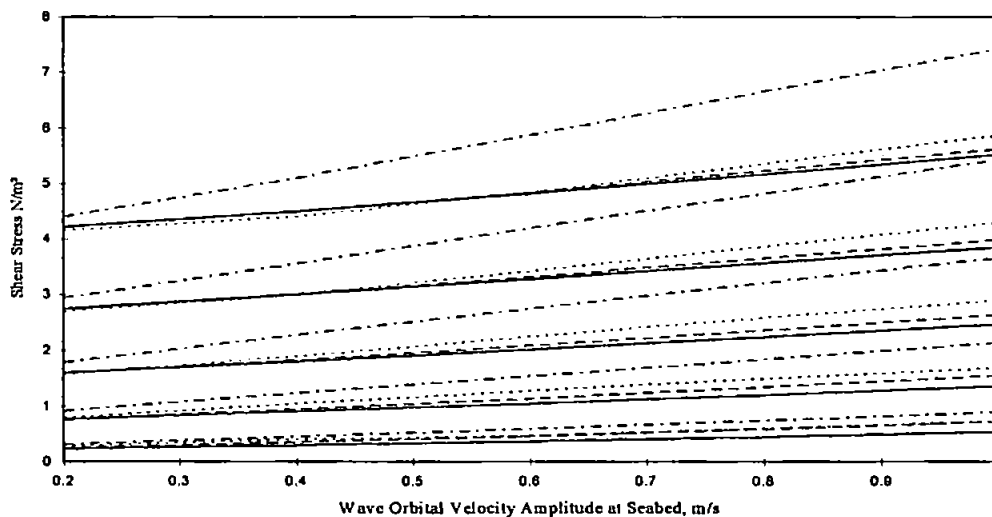


Figure 6.1 Model results for the four models showing comparison at different wave and current velocities.

Overall, the Grant and Madsen, (1979), model gives the largest results over the range whilst the Fredsoe model tends to give the smallest results with the Huynh Thanh and

Temperville (1992) giving very similar results to the Fredsoe model. The Soulsby13 model gives similar results as the HT and Fredsoe models except at the higher roughnesses where the results tend to be larger but not as large as the GM model.

Comparisons between the results for the different wave periods reveals that the period has little effect on the predictions, figure 6.2. The shorter period gives the slightly larger results. As an example, the Soulsby13 model for  $z_o = 1\text{mm}$ , the wave orbital velocity magnitude,  $0.8\text{m/s}$ , and depth average velocity,  $0.6\text{m/s}$ , gives for  $T = 10\text{s}$ ,  $\tau = 2.6 \text{ Nm}^{-2}$ , and for  $T = 5\text{s}$ ,  $\tau = 2.8 \text{ Nm}^{-2}$ . This gives a difference of less than 10%, which is typical for all estimates and all models.

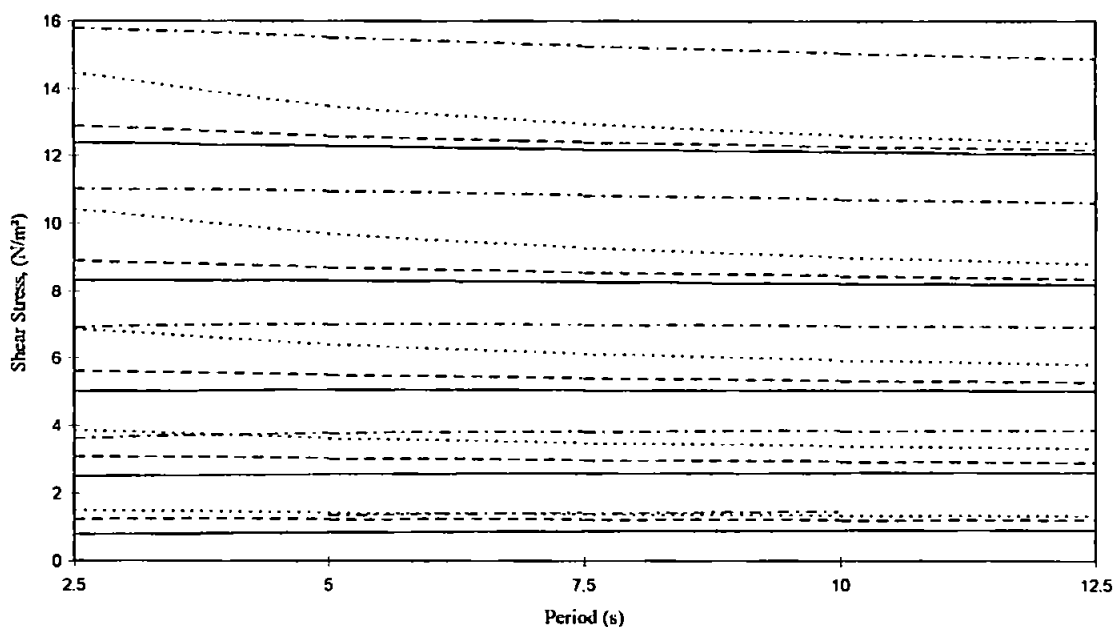


Figure 6.2 The effect of period on the models is not great, in the Soulsby model it is a little greater.

Errors in velocities when working with EMCM's are to be anticipated, as has been described in chapter 5. Looking at figure 6.2 and comparing wave orbital velocities, the changes in the gradients of each of the lines of different colour, shows that errors of as much as  $20 \text{ cm/s}$  in the wave orbital velocity amplitude will give errors in the shear stresses less than 20% in the Grant and Madsen model estimates and less than that for the other models. On the other hand, comparing lines of different colours, errors of similar magnitude in the depth averaged velocity will give much larger errors of reaching nearly 70%, in the most extreme cases.

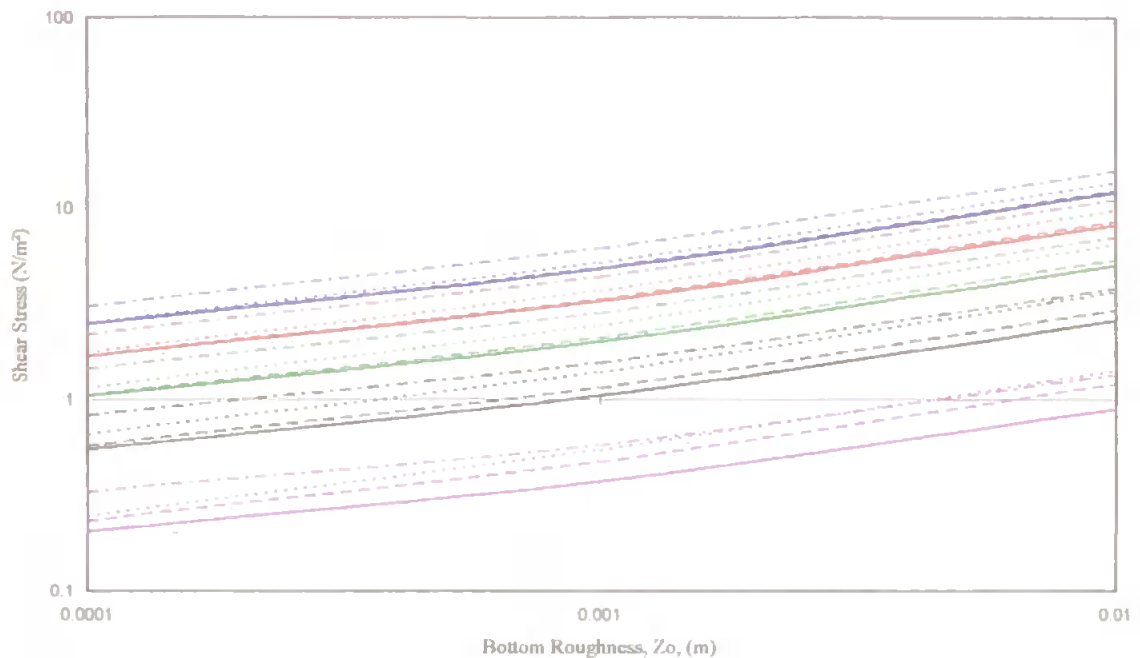


Figure 6.3 The effect of bottom roughness is quite marked.

The other factor which has been looked at is the bottom roughness. Figure 6.3 shows a range of bottom roughnesses from  $10^{-4}$  m to  $10^{-2}$  m. Errors in representing the value of bottom roughness could result in very large errors. If, for example, the bed roughness is estimated from the grain size, say 0.1 mm but the actual roughness is due to the presence of ripples, with an equivalent bottom roughness of the order of 10 cm, there is an error of almost 500% for a depth averaged velocity of  $1.0\text{ms}^{-1}$ . This error could occur if a flat bed assumption is made when ripples are present. In the field study it was not possible to record the bottom roughness during the tidal cycle, observations made at the beginning and end of the tidal cycle and the grain size analysis carried out after the fieldwork are the only evidence available from which to estimate bottom roughness. If the hydrodynamic conditions were such that ripples formed during the tidal cycle and were wiped out as the water receded the flat bed assumption could lead to massive errors in the estimates.

## 6.2 Estimation of Bottom Roughness

The model comparison has highlighted the need for accurate bottom roughness estimates. The only estimates available for this study are the observations made after the tide had receded and the grain size analysis carried out after the experiment. Field records showed that whenever station 2 was uncovered the bed was flat; this, however, gave no indication



bottom roughness estimates could lead to large errors in shear stress predictions. Similarly for station 1, although ripples were observed after the tide had ebbed, this was no real indication of bottom roughnesses throughout the tidal cycle.

It is necessary in the first instance to establish whether the hydrodynamic conditions were such that sediment transport would occur. Ripples form when the bottom shear stress is great enough to overcome the stabilising forces acting on the sediment particles. It might be expected that sediment transport would occur, given the shallow water depth and comparatively large waves and currents. A more detailed description of the processes is available in chapter 2.

In a study on Sable Island Bank, the Scotian Shelf, Canada, Amos et al. (1995) observed ripple formation and erosion in orthogonal or near orthogonal wave and current conditions, described in chapter 2. Amos et al. (1995) in their figure 5 plotted the wave Shields parameter against the current Shields and inserted limits for the thresholds of sheetflow, for saltation/suspension and for traction. The threshold conditions were derived using skin friction only, (Dyer, 1986). In table 6.3 below the equations used to define the limits are listed.

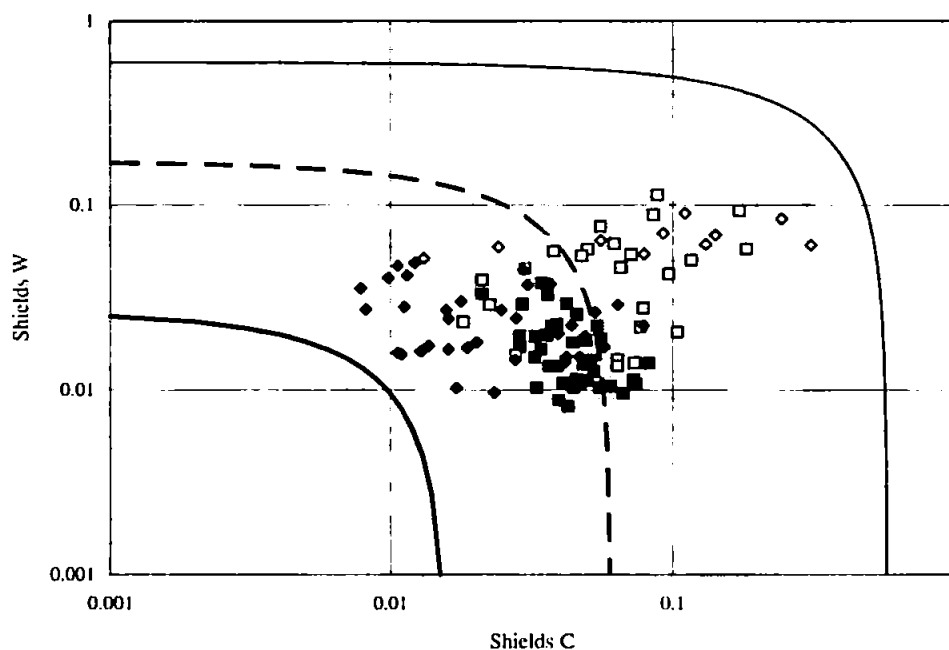


Figure 6.4 After Amos et al. (1995) figure 5, showing a plot of current Shields parameter against wave Shields parameter to estimate when sediment movement occurs. The three lines represent the limits between no sediment movement and ripple formation, this is represented by the heavy solid line; the transition from ripple formation to ripple degradation, the dotted line; and the limit between ripple degradation and sheetflow, the lighter solid line.

Amos et al. (1995) assumed that at very small waves (currents) the Shields parameter for the limits for sediment movement are equivalent to the current (wave) limits expressed in equations in table 6.3. A combined wave against current Shields parameter was then calculated for these limits by interpolating using a straight line between these points. Figure 6.4 shows these limits worked out for the environmental conditions found at the field site. Plotted in figure 6.4 are the current against the wave Shields parameters calculated from the data collected in this study for both station 1 (diamonds) and station 2 (squares). The filled and empty symbols will be explained in the following section. From the diagram it can be seen that sediment transport in some form is occurring at all times during the period of data collection.

Limits for Shields Parameter	Equation	Reference
<b>Wave</b>		
Sheetflow	$\psi'_w = 0.413D_{50}^{-0.4}$	Komar and Miller (1975)
Saltation/suspension	$\psi'_w = 0.5(1 - \pi \eta/\lambda)^2$	Nielsen (1986)
Bedload	$\psi'_w = 0.1f'_w(2A_b/D_{50})^{1/2}$	Komar and Miller (1975)
<b>Current</b>		
Sheetflow	$\psi'_c = C_0 \tan \alpha$	Bagnold (1966)
Saltation/suspension	$\psi'_c = \frac{0.64\rho W_s^2}{\Delta\rho g D_{50}}$	Bagnold (1966)
Bedload	$\psi'_c = \frac{\rho u_*^2}{\Delta\rho g D_{50}}$	Yalin (1977)

Table 6.3 The equations used to calculate the critical Shields parameters for sheetflow saltation/suspension and bedload transport for wave alone and current alone cases.

$A_b$  is the maximum wave orbital amplitude,  $C_0$  is Bagnold's (1966) static volume concentration, taken as 0.65,  $D_{50}$  is the mean grain diameter,  $f'_w$  is the pure wave friction factor,  $W_s$  is the settling velocity,  $\alpha$  is the internal friction angle ( $\tan \alpha = 0.963$  after Allen and Leeder (1980)),  $\eta$  is the ripple height,  $\lambda$ , the ripple wavelength,  $\Delta\rho$  is the relative density and  $\psi'$  is the Shields parameter associated with the skin friction with subscripts c or w for current or waves.

From these results it was decided to use the mean hydrodynamic conditions experienced over each data run to predict a temporally varying bed roughness.

### 6.3 Estimating Ripple Size

Wikramanayake and Madsen, (1990), found, by trial and error, that the form of skin friction Shields parameter,  $\psi'_m$ , providing the best correlation between ripple geometry,  $\eta/\lambda$ , for field data, was

$$Z = \frac{\psi'_m}{S_*} \quad 6.1$$

where  $S_*$  is the sediment-fluid parameter defined below, (equation 6.7) and the subscript  $m$  implies the mean. The equations for the empirical relations for the ripple geometry in the field are:

$$\frac{\eta}{A_b} = \begin{cases} 1.8 \times 10^{-2} Z^{-0.5} & 0.0016 < Z < 0.012 \\ 7.0 \times 10^{-4} Z^{-1.23} & 0.012 < Z < 0.18 \end{cases} \quad 6.2$$

and

$$\frac{\eta}{\lambda} = \begin{cases} 1.5 \times 10^{-1} Z^{-0.009} & 0.0016 < Z < 0.012 \\ 1.05 \times 10^{-2} Z^{-0.65} & 0.012 < Z < 0.18 \end{cases} \quad 6.3$$

where the lowest and highest range of validity indicate the range covered by the experimental data used in Wikramanayake and Madsen, (1990).

Ripple size was estimated for each data run following Madsen (1993), using the prevailing hydrodynamic conditions. Calculations were made employing the following algorithm:

- 1) Calculate wave shear (friction) velocity,  $u'_{*wm}$  (the prime denotes skin friction and the subscripts  $w$  and  $m$  denote wave and maximum respectively). This is done by first calculating the wave (skin) friction factor,  $f'_w$ , and using the equation:

$$u'_{*wm} = \sqrt{0.5 f'_w} u_{bm} \quad 6.4$$

The friction factor associated with the skin friction is calculated using an iterative process. The equation used in this process is:

$$\frac{1}{x^{(n+1)}} = \left( \log_{10} \frac{A_{bm}}{k_n} - 0.17 \right) - \log_{10} \frac{1}{x^{(n)}} + 0.24x^{(n)} \quad 6.5$$

where the superscript denotes the iteration step,  $x = 4\sqrt{f_w'}$ , and the iteration is started with  $x^{(0)} = 0.4$

2) From 1) calculate the skin friction Shields parameter,  $\psi_m'$ .

$$\psi_m' = \frac{\tau_{wm}'}{(s-1)\rho g D} = \frac{\left( u_{*wm}' \right)^2}{(s-1)gD} \quad 6.6$$

where  $s$  is the specific weight of the sediment ( $\rho_s/\rho$ ), and  $D$  is the grain size diameter.

3) Evaluate  $S_*$  as defined in the following equation:

$$S_* = \frac{D}{4\nu} \sqrt{(s-1)gD} \quad 6.7$$

4) Determine the critical Shields Parameter,  $\psi_{cr}$ .

$$\psi_{cr} = 0.1S_*^{-2.7} \text{ for } S_* < 0.8$$

$$\psi_{cr} = 0.06 \text{ for } S_* > 300 \quad 6.8$$

for  $0.8 < S_* < 300$   $\psi_{cr}$  is obtained from figure 6.3

5) If  $\psi_m' < 1/2 \psi_{cr}$ , (for field measurements) there is no sediment motion and hence no ripples. Bed roughness is assumed to be the sediment grain diameter,  $D$ , unless other information is available.

6) If  $\psi_m' > 0.35$ , saltation/suspension or sheet flow is assumed. The bed is eroding or flat and bed roughness is the moveable bed roughness, Smith and McLean (1977).

7) If  $1/2 \psi_{cr} < \psi_m' < 0.35$  the parameter  $Z$ , equation 6.1, is computed.

$\eta$  and  $\lambda$  are calculated from equations 6.2 and 6.3 depending on the value of  $Z$ .

The limits described above are different from the ones used by Amos et al. (1995) as the new limits and Shields parameter take wave and current interaction into account whereas the ones used before are limits which do not.

The algorithm above is a concise outline of the procedure to estimate ripple size and hence bottom roughness from the prevailing hydrodynamic conditions. This was used to calculate bottom roughnesses which were then applied to the models, the results of which are shown below in figure 6.5.

In figure 6.4 the filled squares and diamonds are the results where ripples were predicted to be present and the empty ones are those where the bedforms were predicted to be eroding or eroded. This fits well with the limits suggested by Amos et al. (1995). There are a few exceptions and reasons for this are being investigated.

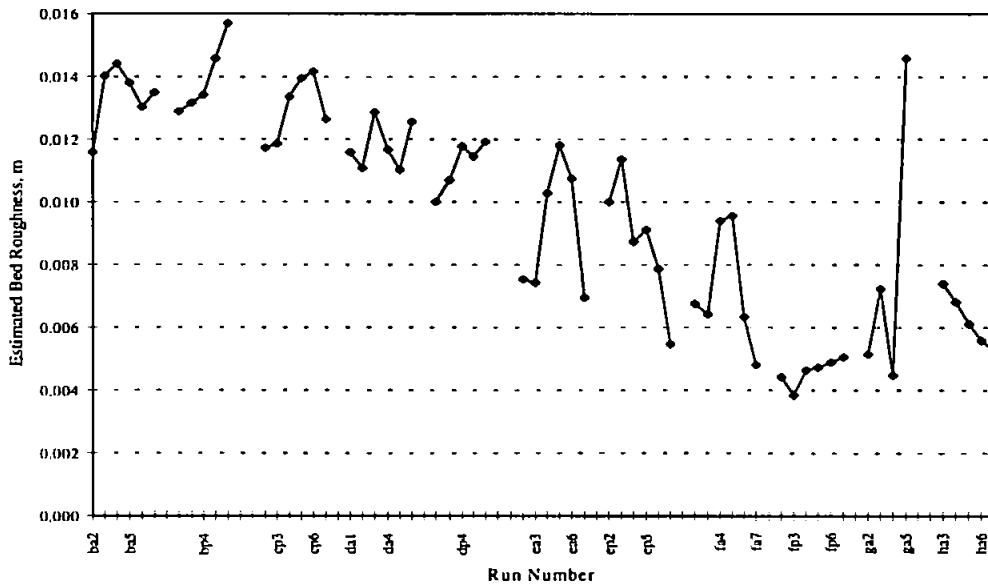


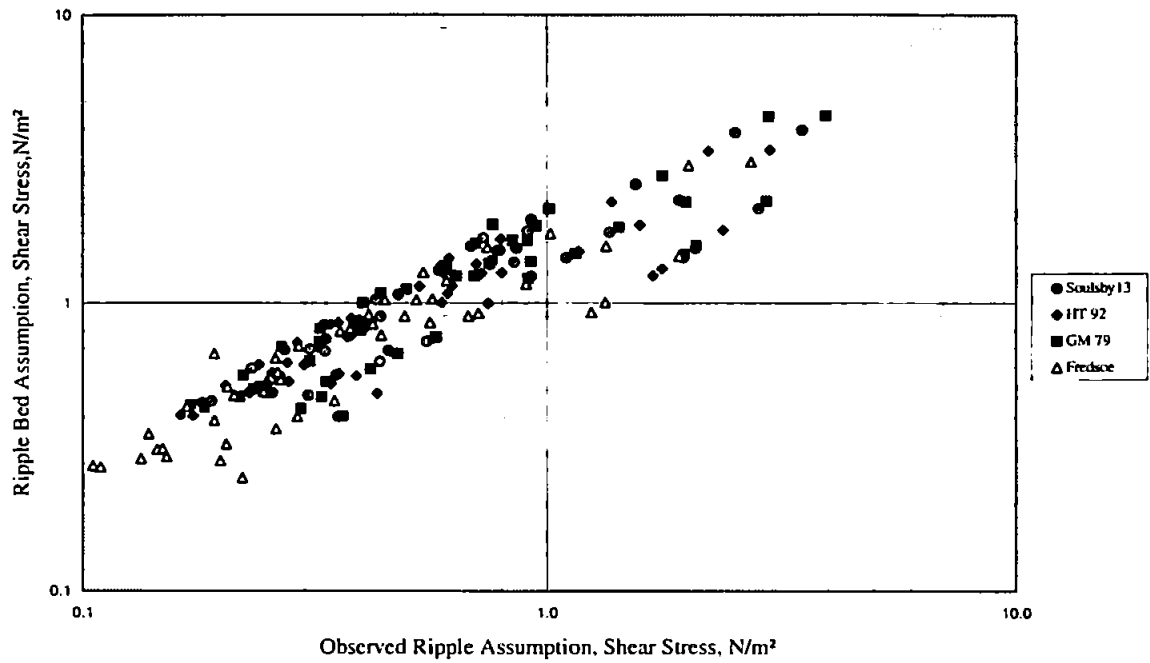
Figure 6.5 The estimated bottom roughnesses for station 2, the station where a flat bed roughness based on the grain size was used.

### 6.4 Comparison of Rippled and Flat Bed Model Results.

The input quantities required for the models were depth averaged current, near bottom orbital velocity, water depth, peak wave period and the bottom roughness length,  $z_0$ . The bottom roughness was calculated in the first instance using the observed bedforms, for the inner station, station 1,

$$z_0 = 27.7/30 \times \eta^2 / \lambda, \tag{6.9}$$

(a)



(b)

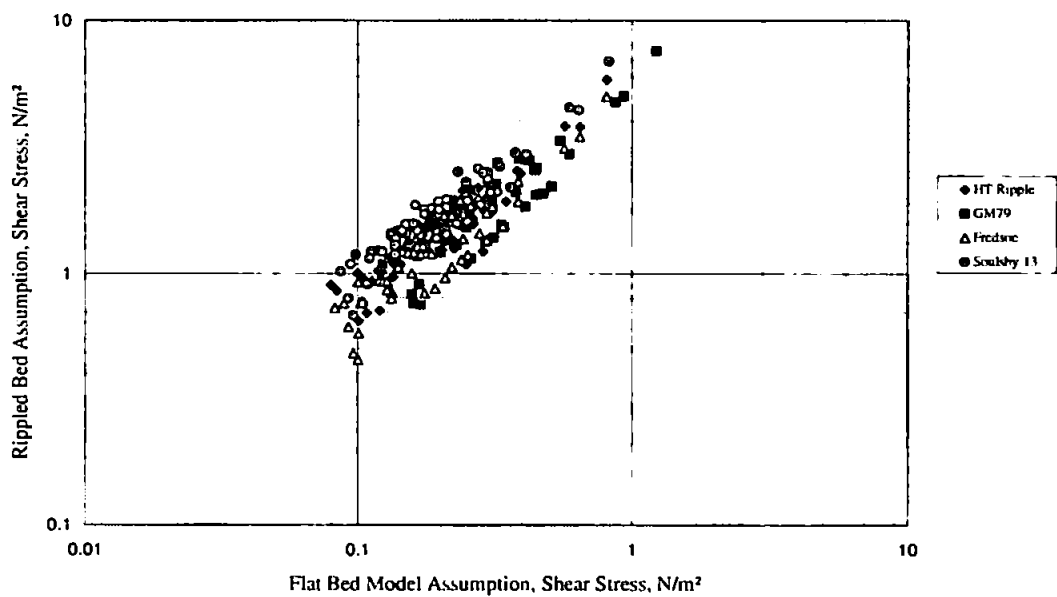


Figure 6.6 (a) and (b) Comparison of the modelled shear stress results for both field stations. The results using the rippled estimates are plotted against those using the observed estimates of bottom roughness.

All the estimates for the bottom roughness were then used in the wave current interaction models with the data collected during the field campaign.

(Grant and Madsen (1982), Madsen (1993)), where  $\eta$  and  $\lambda$  are the ripple height and length respectively.  $\eta$  and  $\lambda$  were recorded during the field campaign, see table 3.7, the table of environmental conditions experienced over the period of the field campaign. For station 2, the outer station, the bed was flat for all observations when the station was uncovered,  $z_o$  was calculated from the mean grain size,  $D_{50}$ ,

$$z_o = D_{50}/30. \quad 6.10$$

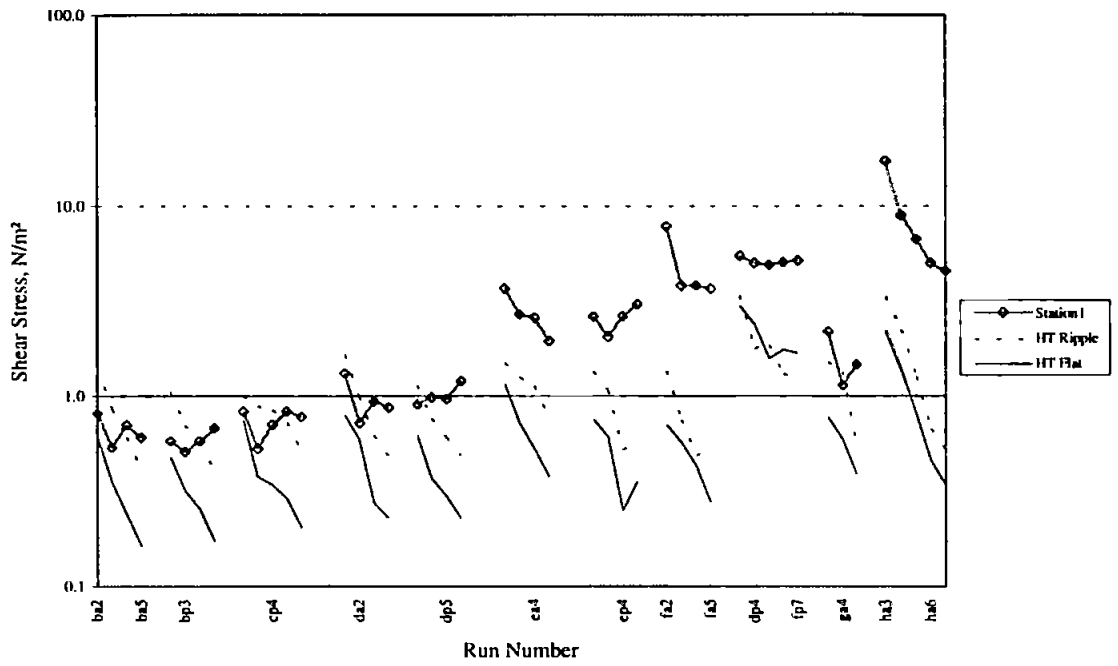
Bed roughnesses were also calculated from the model results predicting ripple size using equation 6.9.

Figure 6.6 a) shows the results of the model runs using the field data collected at station 1 and figure 6.6 b) the results from station 2. The model results using the roughnesses calculated from the ripple and bedload models are plotted as the abscissa and the model estimates using the observed bed roughness as the ordinates. There is very good agreement between models, less than a factor of 2 between the extremes, the Grant and Madsen model gives larger results than the others. This is particularly noticeable in the wave dominated tidal cycles. There are very significant differences between the flat and rippled assumptions up to about 500% in the extreme, figure 6.6 b). The differences between the station 1 estimates is less marked as ripples were observed after the tide had receded. In a few cases, for station 1, the observed bed roughness is greater than the predicted and gives larger shear stresses.

### **6.5 Comparison of Model Results with Data from the Field Experiment.**

Figure 6.7 shows the mean field estimates of shear stress plotted with the model results using the observed ripple size to estimate bed roughness and the modelled ripple size estimates of bottom roughness for station 1. The two sets of model predictions are close to the field estimates for the first five and the penultimate tidal cycles. The other tidal cycles show considerable scatter and do not fit within the range of the model estimates.

(a)



(b)

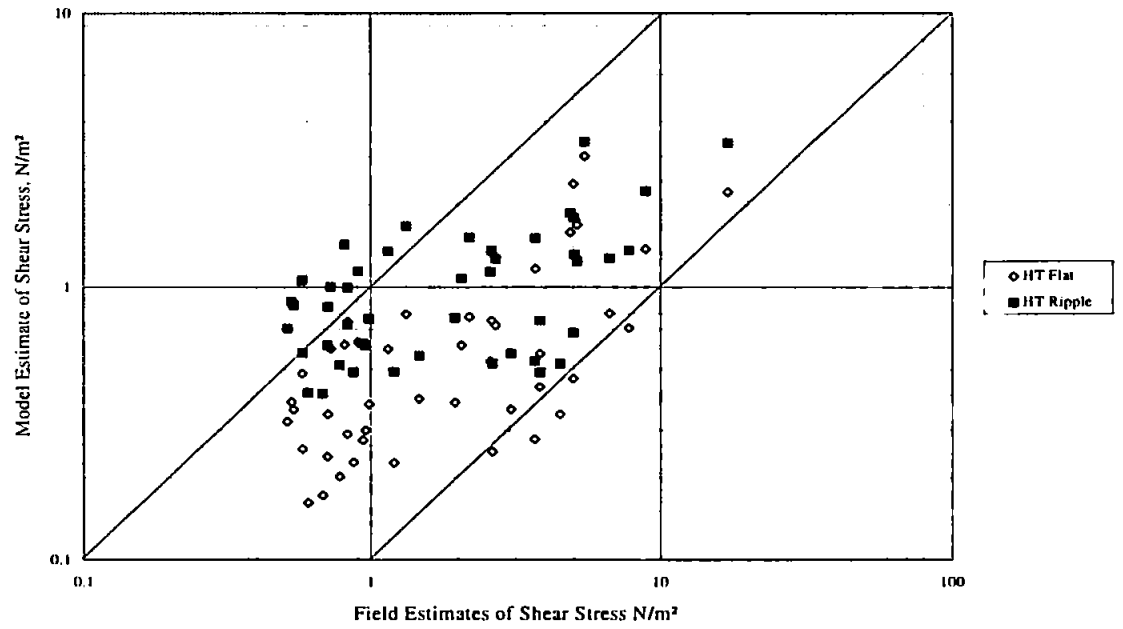
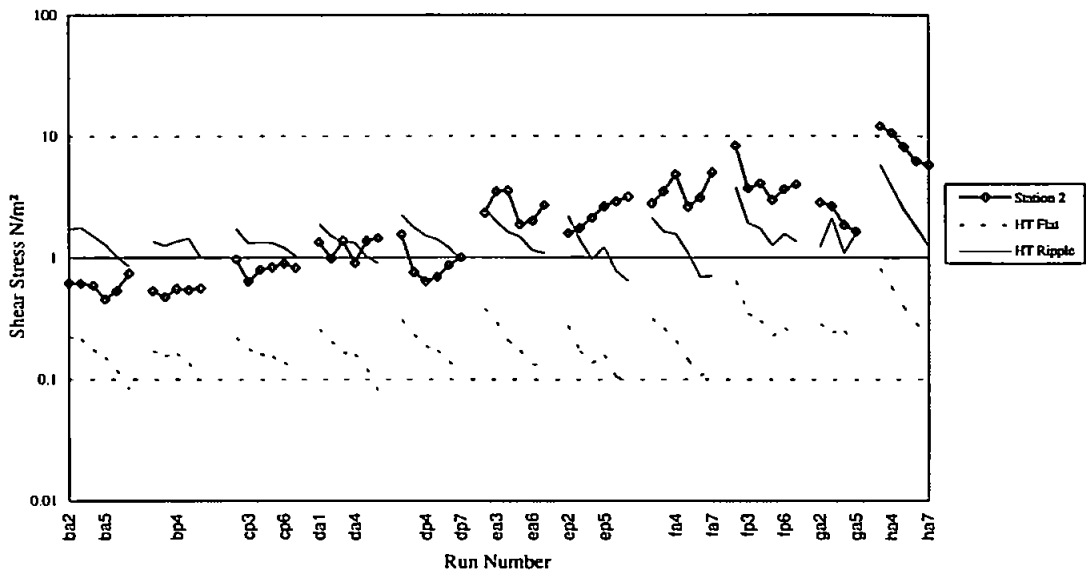


Figure 6.7 (a) and (b) Plot of field results with model estimates from station I, the Huynh-Thanh and Temperville (1992) model was chosen as being one of the intermediate models to make this comparison.



(a)



(b)

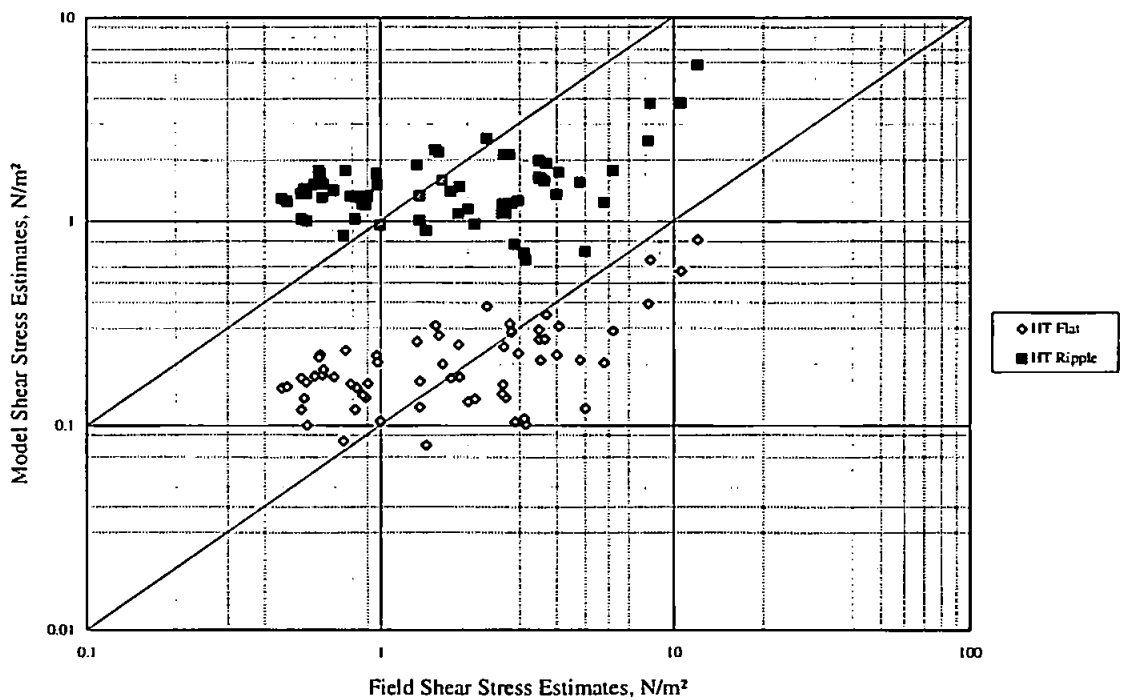


Figure 6.8 Comparison of the HT model results for both rippled and flat bed assumptions with field shear stress results, station 2.

Similarly, figure 6.8 shows the model results plotted with the field results for station 2. Again the results are good for the same tidal cycles as before but field measurements are much larger than the model results for the other tidal cycles. Reasons for this discrepancy will be discussed in the section 6.7.

## 6.6 Comparison of Drag Coefficients from the Field Data with the Parameterised Equation

In section 2.4.1 the parameterisation of the models was introduced. Equation 2.13 was chosen as it had a shape similar to the lines given by the model results. To reiterate, equation 2.13 was of the form:

$$y = x \left[ 1 - bx^p (1-x)^q \right] \quad 6.11$$

where  $y = \frac{\tau_m}{\tau_c + \tau_w}$ , and  $x = \frac{\tau_c}{\tau_c + \tau_w}$ ,  $b$ ,  $p$  and  $q$  are the fitting parameters and depend on which model is being parameterised,  $\tau_c = \rho C_d U_m^2$  and  $\tau_w = 1/2 \rho f_w U_b^2$ .

Introducing the equations for  $y$  and  $x$  into equation 6.11 and after some rearranging the following relationship is found:

$$C_{dwc} = C_d \left[ 1 + b \left( \frac{\tau_w}{\tau_c} \right)^q \left( \frac{1}{1 + \tau_w/\tau_c} \right)^{p+q} \right] \quad 6.12$$

where the subscripts  $c$ ,  $w$  and  $wc$  indicate current, waves or wave and current interaction respectively. In chapter 5, table 5.3 four estimates for  $C_{dwc}$ , as a function of  $U_w/U_m$ , from three different field campaigns. Although these equations are in a different form to 6.12 above and direct comparison is not possible, it is possible to compare the equations in the extreme, where there are no waves, i.e. when  $U_w/U_m = 0$ . In this extreme the drag coefficients are those associated with the current alone and this is equal to the multiplicative constant at the beginning of each equation.

For the equations in table 5.3 taken in order the drag coefficients associated with the current alone are listed below in table 6.4:

Field Site	Current Drag Coefficient
Station 1	0.0031
Station 2	0.0039
CD92	0.0034
SH89	0.0031

Table 6.4 Drag coefficient associated with current alone, from the parameterised equations.

These values are consistent with values found for current alone drag coefficients in previous work carried out by Soulsby (1983), his table 5.4. It is interesting to note that the drag coefficient for station 2 is large and corroborates the hypothesis that ripples may have been formed during the tidal cycle.

## 6.7 Discussion

In the shallow water, as experienced during the field campaign, the waves will almost inevitably be non-linear, but as it has been shown, the models can predict shear stresses quite accurately under certain circumstances. One suggestion is that the mean shear stresses are greater under cnoidal waves than under linear waves.

The circumstances under which the models no longer accurately predict the shear stress was investigated. To establish the form of the waves experienced during the field campaign, a plot of wave height divided by the square of the period against the water depth divided by the square of the period, after Le Méhauté (1976) was made. The plot was turned into a non-dimensional form following Davies (Alan G., lecture notes, UNCW, Bangor) by dividing the ordinate and abscissa by the acceleration due to gravity. Figure 6.9 shows the results of this procedure using the waveheight and water depths measured during the fieldwork. The two dotted lines are the limits of cnoidal waves, the upper limit is the Miche formula (equation 4.13), the breaking criterion. The lower dotted line is the limit between cnoidal and Stokes waves. As anticipated, all of the waves fall into the non-linear region, most are cnoidal, some second or third order Stokes waves.

The potential function for a Stokes wave travelling over a constant depth at a second order approximation is found to be:

$$\phi = \frac{-Hk}{2m} \left( \frac{\cosh m(h+z)}{\sinh mh} \right) \sin(kt - mx) - \frac{3}{8} \left( \frac{H^2}{2} \right) k \frac{\cosh 2m(h+z)}{\sinh^4 mh} \sin(kt - mx) \quad 6.13$$

where  $m = 2\pi/L$ ,  $L$  is the wavelength of the waves,  $k$  is the wavenumber,  $h$  is the water depth and  $H$  the wave height. The term in  $H$  is the solution obtained by taking only the local inertial terms into account, the term in  $H^2$  is the most significant correction due to convective inertia. The ratio of these two inertial terms, the relative importance of the convective inertial term, leads to the Ursell number introduced by Korteweg and de Vries

$$U_R = \frac{\eta_0}{L} \left( \frac{L}{h} \right)^3 \quad 6.14$$

where  $\eta_0$  is the maximum elevation above the still water level.

In very shallow water with long waves the Ursell number can be difficult to use since the interpretation of  $L$ , the wavelength, can be unclear, Le Méhauté (1976). Le Méhauté suggested that  $H/h$  might be a more significant parameter to assess the importance of the non-linear terms. He took the vertical inertial force to be negligible and the only significant term for the convective inertia to be  $\rho u(\partial u/\partial x)$ . It is then possible to calculate the ratio of the amplitude of the convective inertia to the amplitude of the local inertia,  $\rho u \partial u/\partial x / \rho \partial u/\partial t$ , directly. In shallow water  $h/L$  is very small, therefore:

$$u = -\frac{\partial \phi}{\partial x} = -\frac{H}{2} \frac{k}{mh} \cos(mx - kt) \quad 6.15$$

After some manipulation Le Méhauté found:

$$\frac{\rho u \left. \frac{\partial u}{\partial x} \right|_{\max}}{\rho \left. \frac{\partial u}{\partial t} \right|_{\max}} = \frac{H}{2h} \quad 6.16$$

The solid line on figure 6.9 is the line  $H/h = 0.2$ , this line can be interpreted as the line where the convective inertia is 10% of the local inertia. On the diagram, the squares and diamonds represent the results from stations one and two respectively. The solid squares and diamonds are those where the modelled and field estimates of shear stress were judged to be similar, the empty squares and diamonds are those where the field shear

stress estimates were much greater than the model results. It is possible to conclude from this that the models work well for the non-linear waves when the convective inertial terms are small compared with the local inertial term.

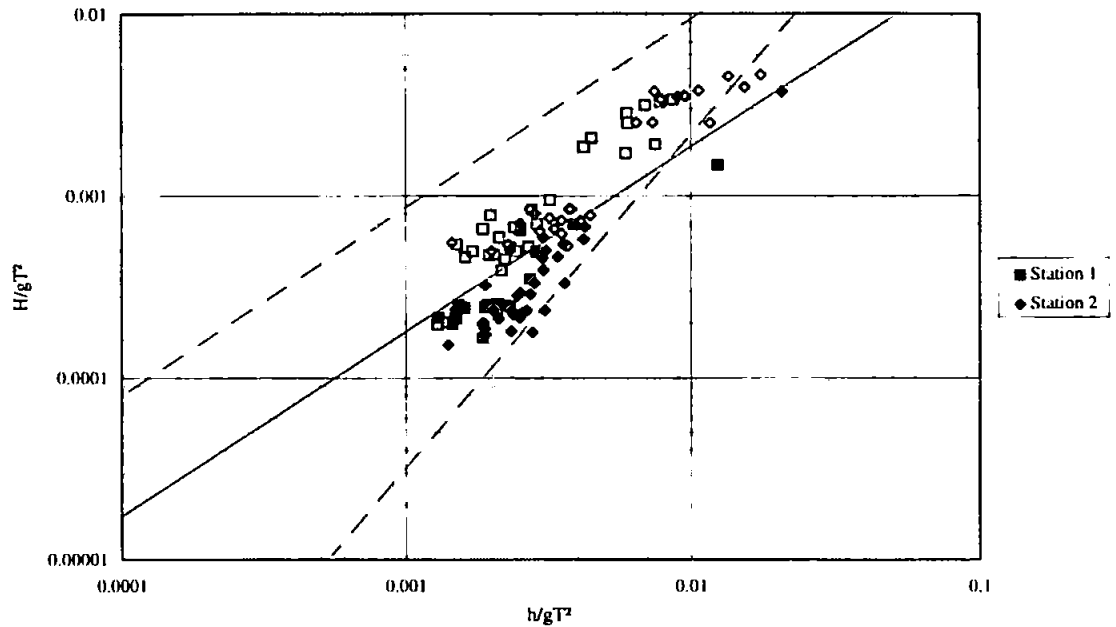


Figure 6.9 Plot of nondimensional wave height against nondimensional water depth showing line of where the ratio of convective inertia to local inertia equals 10%. The two dotted lines show the limits of cnoidal wave theory, the upper being the Miche parameter, the lower the limit between cnoidal and Stokes waves.

# Chapter 7

## Conclusions

The project has been successful overall in fulfilling the aims set out at the beginning. Several problems have been highlighted and some interesting conclusions will be drawn in the subsequent sections. As a result of both problems and conclusions suggestions for future work will be made.

### 7.1 Field Campaign and Data

The field campaign was conducted successfully, with 12 tidal cycles during which data were successfully collected. Conditions were such that the range of wave/current data was good, varying from current to wave dominated conditions over the period of the data collection period. Observations of wave conditions at the time of data collection proved very useful when eliminating data runs during which waves were breaking. In all it was necessary to discard 50% of the data runs mostly owing to data collection after one or more instruments were uncovered. Some, less than 7%, were discarded as there were waves breaking close to the instrument stations.

One problem which arose in the subsequent analysis was the lack of measured bed roughnesses for each data run. This problem was overcome by modelling ripple formation and erosion. More accurate and more frequent observations of bed roughnesses during the tidal cycles would have contributed to the success of the campaign and subsequent data analysis.

## **7.2 Shear Stress Estimates**

Three methods for calculating shear stresses were used, all of which were turbulence based methods, it was not possible to use the logarithmic profile method to estimate shear stresses as only two current meters were reading the longshore velocity profile. Each method was calculated for all runs in which there was no evidence, mathematical or observational, that waves were breaking adding extra turbulence to the water column and thereby, possibly affecting the amount of turbulence measured by the current meters. Comparisons of the three methods revealed that there were no systematic differences with no one method consistently larger or smaller than either of the others. Correlations between the shear stress estimates and other parameters suggest that the scatter, in extremis 500%, cannot be attributed to any of the external parameters. Soulsby and Humphery (1989) found that the greatest scatter between estimates was discovered at the low current speeds, in this case the data cycles where low current speeds were experienced were removed prior to data analysis because of the size of the sensor head and the advection of turbulent eddies past the sensor, the EMCM's cannot sense turbulence at low speeds, see figure 4.6. Reasons for the observed scatter have not therefore been identified.

## **7.3 Modelling of Wave and Current Interaction**

The four parameterised models investigated in this project all showed that an enhanced shear stress would be expected in the presence of waves and currents. The magnitude of the enhancement was different for each model with the Grant and Madsen (1979) model being generally the greatest and the Fredsoe (1984) model giving the smallest stresses. The differences between models even at the extremes was always less than 100%.

A point raised by the comparison was the importance of both current velocity and the bottom roughness. An error in either of these parameters was shown to lead to massive errors in the estimation of the bottom shear stress. A 20% error in current velocity measurement could lead to a 70% error in the estimation of bed stress. If a flat bottom bed roughness is used where ripples are present errors of the order of 500% are possible.

Errors in other parameters such as wave period or wave orbital velocity amplitude have a much smaller effect on the shear stress produced by the models, errors of less than 10%. However, it is interesting to note that the Soulsby et al. (1994) model which is based on

field data (section 2.4.1) is more affected by the wave period than any of the other models. Reasons for this difference are unclear and, perhaps, would warrant further investigation.

## **7.4 Comparison of Model and Field Results**

Shear stresses from model runs using the observed and measured parameters were compared with the shear stress estimates made using the three methods described .

Observed and modelled bed roughness model predictions from the Huynh Thanh and Temperville (1992) model were used in the comparison. This model was chosen as it was one of the two models which gave the intermediate values from amongst those studied. The model estimates encompassed the mean shear stresses for the first four tidal cycles and most of the fifth as well as the penultimate tidal cycle. However, the other five tidal cycles were much less good. Reasons for this discrepancy were sought. Reviewing figure 4.1 shows that for all the tidal cycles in which the shear stress estimates were greater than the modelled estimates were tidal cycles in which the wave orbital velocity amplitude was greater than the mean current. Also, the period of the waves during these tidal cycles was shorter, typically 5-6 second waves as compared with 8-9 second waves in the other tidal cycles.

## **7.5 Future work**

This project has highlighted the need for accurate observations and estimates of bed roughnesses. Investigations into the effects of bed roughnesses on wave and current interaction could prove to be very interesting and perhaps, looking into new and improved ways to record bedforms, bedload and suspended sediment transport would be beneficial.

In modelling wave and current interaction the inclusion of more realistic waves, non-linear waves, for the shallow water environment of the nearshore zone would increase the range of conditions under which the models could be used. If the turbulence added to the water column by breaking and spilling waves was also included the whole of the surf zone could be modelled. This would enable wave and current interaction effects to be used in the modelling of longshore currents and the resulting sediment transport.



It might also prove to be interesting to use equation 6.12, for the wave and current drag coefficient, to provide curves using the  $b$ ,  $p$  and  $q$ , for each model and appropriate  $C_d$ , and  $f_w$  values to calculate  $C_{dwc}$  for comparison with the data. Alternatively, the data could be fitted to the parameterised model equation, instead of the exponential equation used, for the values of roughnesses, and velocities associated with each data point.

Another large scale method for calculating the drag coefficient was introduced in chapter 2, this method was not used due to difficulties fitting sinusoids to the small amounts of data available over each tidal cycle. It would be very interesting to be able to use this model in conjunction with data collected perhaps in deeper water to compare the results of the model with other methods of estimating the drag on the seabed.

## APPENDIX

# SEABED STRESS DETERMINATIONS USING THE INERTIAL DISSIPATION METHOD AND THE TURBULENT KINETIC ENERGY METHOD

K. R. STAPLETON AND D. A. HUNTLEY

*Institute of Marine Studies, University of Plymouth, Plymouth, PL4 8AA, U.K.*

*Received 10 March 1995*

*Accepted 26 May 1995*

## ABSTRACT

Direct measurements of seabed stress are difficult, especially in field conditions. Several methods for estimating these stresses using current meter data are available. Two of these methods, the Inertial Dissipation Method and the Turbulent Kinetic Energy Method, are described below, and a Matlab program is used to analyse data from a wave-current environment.

**KEY WORDS** wave-current data; turbulence; seabed stress

## INTRODUCTION

Determination of bottom shear stresses in turbulent environments is difficult, if not impossible, by direct means. There are, however, several indirect methods available for estimating these stresses using current meter data. The logarithmic profile method (Soulsby, 1983) requires a vertical array of current meters measuring within the logarithmic layer. This can prove to be a problem, particularly in shallow water environments. The Reynolds stress, or 'eddy correlation' method (Soulsby, 1983) uses turbulent momentum flux to estimate stress at the instrument height. This method is particularly sensitive to sensor misalignment and can give errors of as much as 156 per cent per degree of misalignment in wave-dominated conditions, (Soulsby and Humphrey, 1989).

The two methods described below use the spectra of the turbulent fluctuations to make estimates of the bottom stress. The inertial dissipation method uses the well known  $k^{-5/3}$  relationship between wavenumber ( $k$ ) and spectral energy, ( $\phi$ ) within a sub-range of the spectrum (Huntley, 1988) to infer turbulence. Soulsby and Humphrey (1989) uses the premise that the variance of a current meter time series can be separated into fluctuations due to waves and fluctuations due to turbulence, and infer bed stress from the level of turbulent energy. These two methods were chosen as they require instruments at only one height and the methods are far less sensitive to alignment errors. In an empirical test of sensitivity to alignment errors, the inertial dissipation method was shown to have errors of only 0.8 per cent in stress per degree of misalignment (Huntley and Hazen, 1988).

## DATA COLLECTION

Measurements were made at a variety of beach field sites using an array of electromagnetic current meters (EMCMs), pressure transducers (PTs) and optical backscatter sensors (OBSs). The data presented here were collected on a beach at Nieuwpoort, Belgium in February 1994, as part of the CSTAB experiment. Data were collected at a rate of 8 Hz; filtering of the EMCMs was at 2.4 Hz, to ensure minimal aliasing of the signal. Aliasing occurs when energy from frequencies higher than the Nyquist frequency (half the sampling

frequency) is interpreted as belonging to lower frequencies. This can distort the results of the spectral analysis. To prevent this, filtering is carried out at the time of data collection, prior to digitization.

### INERTIAL DISSIPATION METHOD (IDM)

If the wavenumbers at which turbulent energy is produced and dissipated are well separated, the region of separation is known as the inertial sub-range. In this range the flux of energy from low to high wavenumber is equal to the dissipation rate, as there are no sinks or sources of energy within the wavenumbers of the sub-range. The spectrum, in a given direction within this range, is given by:

$$\phi_{ii} = \alpha_i \epsilon^{2/3} k^{-5/3} \quad (1)$$

where  $k$  is the one-dimensional wavenumber,  $\alpha_i$  is the one-dimensional Kolmogorov constant,  $\epsilon$  is the energy dissipation rate and the subscript  $i$  represents a given direction. Equation 1 has been found using dimensional analysis and is not given in detail in this paper.

It is necessary to make two assumptions to order to estimate bottom shear stress from the above equation.

1. There is a local balance between production and dissipation of turbulent energy. The production rate of turbulent kinetic energy is given by  $\tau/\rho(\partial u/\partial z)$  and in the logarithmic layer  $\partial u/\partial z = u_*/\kappa z$ , where  $\tau = \rho u_*^2$  is the stress felt at the bottom,  $u$  is the velocity in the  $x$  direction,  $\rho$  is the density of the water (taken as  $1025 \text{ kg m}^{-3}$ )  $\kappa$  is von Karman's constant (taken as 0.4),  $u_*$  is a parameter known as the friction velocity and  $z$  is the height of measurement above the bottom. The friction velocity parameter has the dimensions of velocity but has no physical meaning.
2. The measurements are made within the constant stress part of the logarithmic boundary layer. Within this part of the boundary layer local stress is equal to the bottom stress.

These assumptions after some rearranging, give:

$$u_* = (\phi_{ii}(k)k^{5/3}/\alpha_i)^{1/2}(\kappa z)^{1/3} \quad (2)$$

Turbulence measurements are generally in the form of time series and therefore provide spectra as functions of frequency and not wavenumber. The Taylor concept of 'frozen turbulence' is used to convert wavenumber spectra to velocity spectra:

$$\phi_{ii}(k) = \phi_{ii}(f)\bar{u}/2\pi \quad (3)$$

where  $\bar{u}$  = mean velocity in the  $i$  direction and  $f$  = frequency. For this concept to be valid, the time scale of the eddy must be much longer than the time taken for the eddy to advect past the point of measurement. For this to be true it is required that:

$$k\phi_{ii}(k)/\bar{u}^2 \ll 1 \quad (4)$$

For an environment with significant oscillatory flows it has been suggested that Taylor's hypothesis would need to be significantly revised. Huntley (1988) suggests that for isotropic turbulence, horizontal wave velocities much greater than vertical wave velocities, and small values of the wave velocity/mean current ratio, the correction to friction velocity due to the wave advection is given approximately by:

$$\hat{u}_* = [1 - 0.16(u_{\text{rms}}/\bar{u})^2]^{1/2} u_* \quad (5)$$

where  $u_{\text{rms}}$  is the root mean square horizontal velocity. In the data set used here, this new approximation is less than 1 per cent smaller than the original estimate and, hence, is not a major source of error.

The inertial sub-range will only exist in flows where the low wavenumbers, (where energy is produced) are well separated from those where energy is dissipated. Tennekes and Lumley (1972) suggest that this will only occur in flows where the turbulent Reynolds number ( $Re$ ) is greater than some critical Reynolds number ( $Re_c$ ):

$$Re = u_* \kappa z / \nu > Re_c \quad (6)$$

Estimates for the critical Reynolds number range from 2500 to 4000 (Huntley, 1988).

## SEABED STRESS DETERMINATIONS

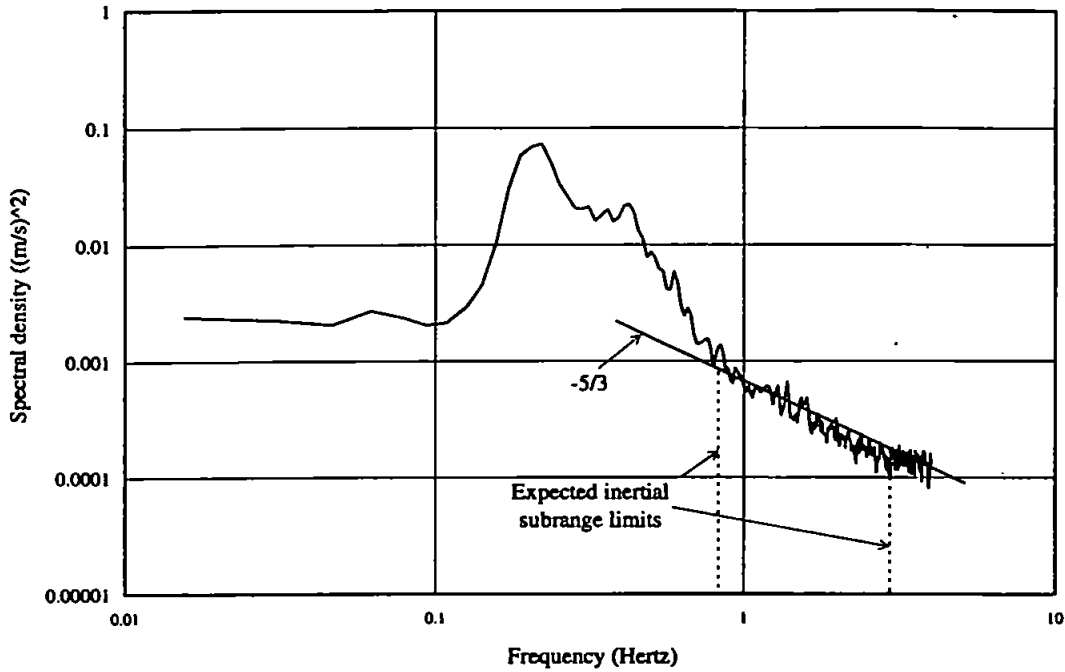


Figure 1. Spectrum of vertical velocity time series showing predicted limits of inertial sub-range and  $-5/3$  roll-off

Taking a different perspective of Equation 6, assuming that it is generally valid, it is possible to derive a critical height above which measurements must be made to ensure an inertial sub-range:

$$z_{cr} = Re_c \nu / (\kappa u_*^2) \quad (7)$$

However, it is also a requirement that the measurements are made within the constant stress part of the logarithmic layer (see assumption 2). It is possible that, in certain circumstances, these two height requirements cannot be satisfied, i.e. there is no height at which the instrument is high enough to satisfy the Reynolds number criterion whilst also being within the constant stress layer. If this is found to be true, Huntley (1988) suggests a modification to the inertial dissipation method so that this method may be used. In the data discussed further here, Equation 6 is readily achieved and an inertial dissipation range is therefore expected.

In the spectrum, (see Figure 1), the wind wave band can be seen and is indicated on the diagram. The limits marked on the spectrum are the theoretical limits within which the inertial sub-range is expected to occur. These will be explained in more detail in subsequent paragraphs. Within these limits, it is possible to see an approximate  $-5/3$  run-off as predicted by theory.

There is a limit to the physical size of the turbulent motions that the current meters can sense. This is due to the physical dimensions of the EMCM. This upper limit for the sub-range is given (Soulsby, 1980) as;

$$k = 2.3/d \quad (8)$$

where  $d$  is the distance between the electrodes on the sensing head of the EMCM.

There is also a lower limit to where the  $k^{-5/3}$  roll-off will occur. This is given by:

$$k = 2\pi/z \quad (9)$$

For a sensor at height  $z$  above the bed, the peak turbulent energy is expected close to  $k = \pi/z$ , but for the assumed value of the Kolmogorov constant to be valid, it has been suggested (Huntley and Hazen, 1988) that wavenumbers greater than twice the expected peak should be used. If effects of wave energy from the surface prevent the confirmation of the turbulent peaks, then the lower wavenumber limit can be chosen to be at or larger than the number found from Equation 9.

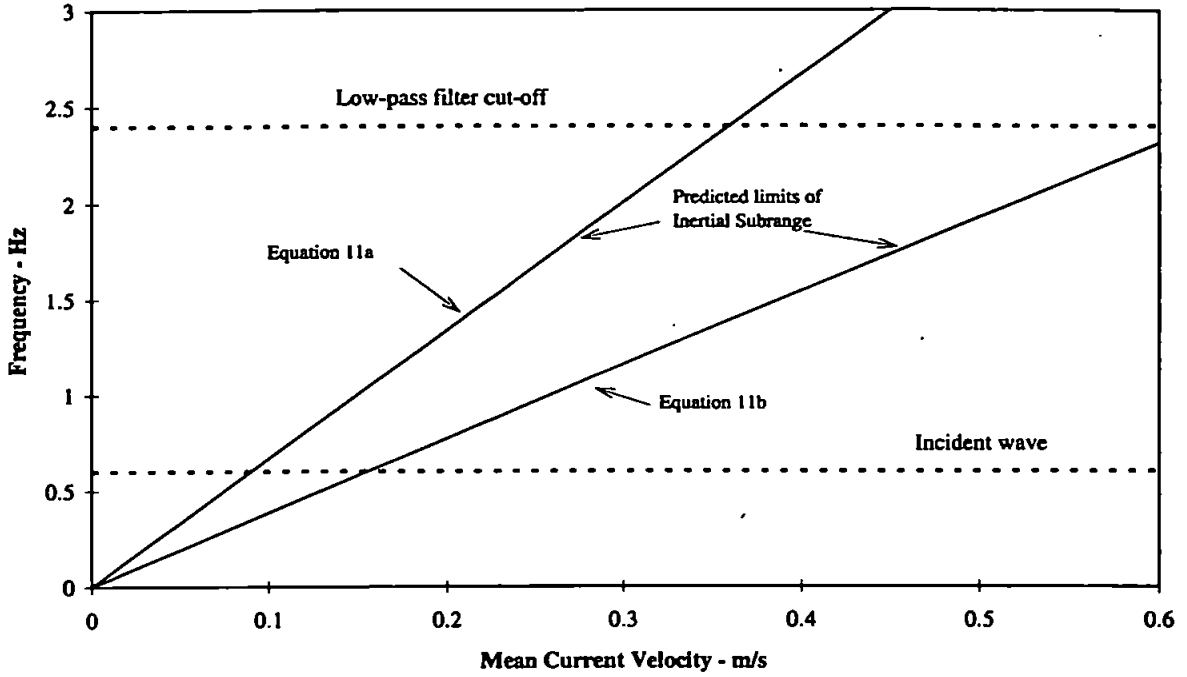


Figure 2. Limits on inertial sub-range for velocities between 0 and 0.6 m s<sup>-1</sup>

However, since frequency is measured and not wavenumber, it is necessary to convert wavenumber to frequency. This is done using the formula:

$$k = 2\pi f / \bar{u} \quad (10)$$

where  $f$  is the frequency. Substituting Equation 10 into Equations 8 and 9 and rearranging gives two new equations:

$$f = \bar{u}/z \quad (11a)$$

and

$$f = 2.3\bar{u}/2\pi d \quad (11b)$$

which are linearly dependent on the magnitude of the mean velocity at a given height. These are plotted in Fig. 2 as solid lines.

A very important consideration in measuring turbulence with electromagnetic current meters is the high frequency cut-off filter in the sensor. The current meters in this study contained a ninth order elliptical low pass filter and a -3 dB frequency was set at 2.4 Hz. This cut-off and the filter characteristics were verified by laboratory measurement. In Figure 2, the filter limit is shown as a single frequency boundary at 2.4 Hz (all data in this paper are collected with this type of filter), and the sharp roll-off of the ninth order filter ensures that spectral amplitudes are not reduced by more than 20 per cent for frequencies below 2 Hz.

The lower frequency limit for the turbulence is set by the upper frequency limit of the incident wave band, and will vary with conditions at the time of data collection. The lines defining the limits of the inertial sub-range are calculated using Equations 8 and 9.

### TURBULENT KINETIC ENERGY METHOD (TKEM)

Instantaneous velocity, at time  $t$ , in the  $x$  direction, for example, can be written as:

$$u(t) = \bar{u} + u_w(t) + u_1(t) \quad (12)$$

## SEABED STRESS DETERMINATIONS

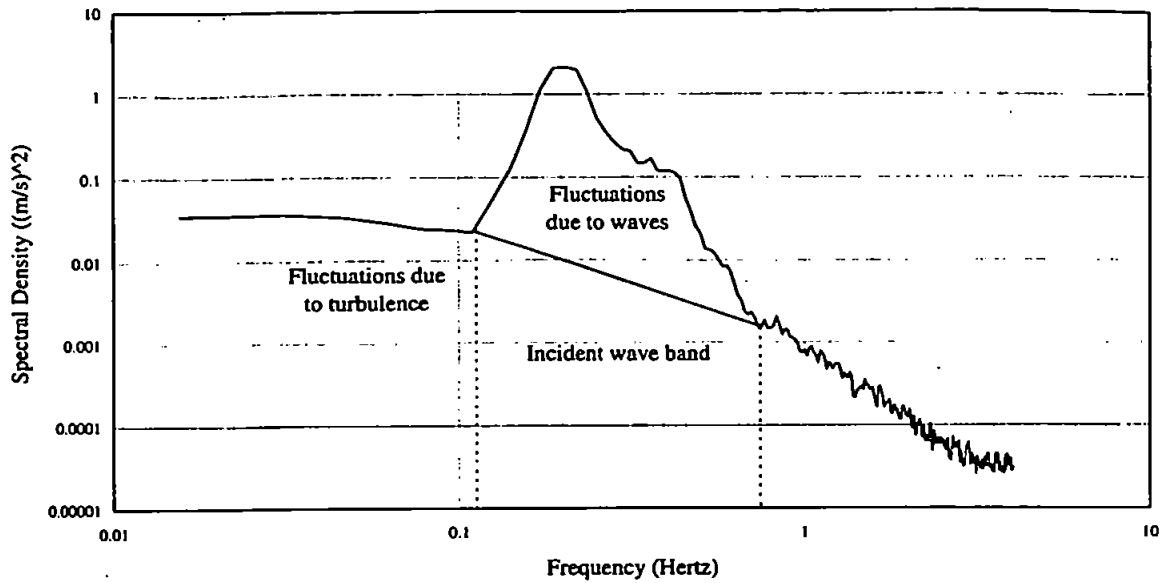


Figure 3. Spectrum of cross-shore velocity time series showing areas of variance due to waves and to turbulence

where  $\bar{u}$  is the mean (time averaged) velocity and the subscripts w and t refer to fluctuations due to waves and turbulence respectively. Since  $u_t(t)$  is, by definition, not correlated with  $u_w(t)$  then it can be seen from the equation that the variance of a time series can be attributed to either waves or turbulence, i.e.  $\bar{u}^2 = \bar{u}_w^2 + \bar{u}_t^2$ , where  $\bar{u}^2$  is the total variance of the time series. There is no hard and fast rule for separating these fluctuations in frequency space but Soulsby and Humphrey (1989) suggest that it can be done by interpolating across the base of the wave band, as shown in Figure 3.

The area above the line in Figure 3 is taken to be the wave variance and the area below, the variance due to turbulence. The same procedure can be applied to both the  $u$  and  $v$  components of flow. The vertical component,  $w$  is assumed to be uncontaminated by waves and consequently all fluctuations are taken to be due to turbulence. When the velocity measurements are made well above the seabed it is possible that the wave motion will have an effect on the vertical velocity time series and, if this is found to be the case, the fluctuations due to the waves can be removed in the way described above.

The turbulent kinetic energy density,  $E$  is calculated from the definition:

$$E = 1/2\rho(\bar{u}_t^2 + \bar{v}_t^2 + \bar{w}_t^2) \quad (13)$$

From this it is possible to calculate the bed shear stress. In the region close to the bed, where energy production equals energy dissipation, the bed shear stress is proportional to the turbulent kinetic energy density. Using the constant of proportionality observed in a wide range of flows (Soulsby, 1983) the bed shear stress can be calculated:

$$\tau = 0.19E \quad (14)$$

The value 0.19 is assumed constant under diverse conditions (Soulsby, 1983).

## MATLAB PROGRAMS

Matlab is a commercially available mathematical package which can deal with very large data sets easily. Macros for Matlab are simple to run from within the package, and using a language related to C it is possible to write programs and macros. Two of these are listed below. The first calculates the bottom shear stress using the inertial dissipation method and the second uses the turbulent kinetic energy method. In both cases the inputs are three vectors of current meter data, one for each component of the flow, and  $z$ , the height of

the instrument above the bottom. For this data set we take the vertical Kolmogorov constant  $\alpha_3 = 0.69$ , and the height of the instrument above the bottom  $z = 0.545$  m.

In the inertial dissipation method the spectrum of the vertical time series is used, because it is less affected by wave motion than the horizontal components of the flow. The frequency limits between which the inertial dissipation sub-range is predicted to occur are calculated, and from this  $u_*$  is predicted. The following algorithm gives the method in more detail.

1. Check for the validity of Equation 4; in this case the inequality is valid at all frequencies.
2. Calculate the spectrum of the time series (see Hardisty, 1993); averaging is done automatically within Matlab dividing the time series into segments of a specified length (usually a power of 2 for simplicity when calculating using fast Fourier transforms) which overlap by 50 per cent of the length of the segment. For example, if the time series has 8192 points, it can be divided into 15 shorter series of 1024. This overlapping is done to increase the number of degrees of freedom of the spectrum.
3. Calculate predicted limits of inertial sub-range from Equations 11a and 11b.
4. Plot the spectrum on log-log axes to check for  $-5/3$  roll-off.
5. Calculate the mean of logarithm of the inertial sub-range frequency and amplitude,  $\phi(f)$ . This gives a mean point within the inertial sub-range through which a line with a gradient of  $-5/3$  may be plotted. The intercept of this line with the log  $\phi$  (i.e. where  $\log f = 0$ ) axis gives a value for  $\log \alpha_i \epsilon^{2/3} (2\pi/\bar{u})^{-2/3}$ , i.e.

$$\phi_{ii}(f) = \alpha_i \epsilon^{2/3} (2\pi/\bar{u})^{-2/3} f^{-5/3}$$

taking logs gives:

$$\log[\phi_{ii}(f)] = \log[\alpha_i \epsilon^{2/3} (2\pi/\bar{u})^{-2/3}] - 5/3 \log(f)$$

so where  $\log(f) = 0$ , (i.e.  $f = 1$ ):

$$\log(\phi_{ii}) = \log[\alpha_i \epsilon^{2/3} (2\pi/\bar{u})^{-2/3}]$$

6. Use the value found in step 4 to calculate a value for  $u_*$  using Equation 2, and the given values for  $z$  and  $\kappa$ . Since, within the inertial sub-range,  $\phi_{zz}(k) \propto k^{-5/3}$ , then the  $k$ 's cancel out.
7. Use Equation (5) to correct  $u_*$  for wave advection.
8. Calculate bottom stress using the relationship  $\tau = \rho u_*^2$ .

Matlab program for the inertial dissipation method:

```
function [tau]=idm(cross,long,vertical, height);

% program to calculate a value for ustar using the
% Inertial Dissipation Method (Huntley,1988).

% Calculate mean speed
a=mean(cross);
b=mean(long);
c=mean(vertical);
magvel=(a^2+b^2+c^2)^.5;
urms=std(cross);

% Calculate predicted limits on inertial subrange
f1=magvel/height;
f2=2.3*magvel/(2*pi*.055);

% Calculate spectrum of vertical time series
[p,f]=spectrum(vertical,512,256,512,8);

g=256;
p=p(:,1)/4;
ef1=(ceil(f1*64))+1;
ef2=(floor(f2*64))+1;
```



## SEABED STRESS DETERMINATIONS

```

if cf2>g
    cf2=g;
end

meanfreq=mean(log10(f(cf1:cf2)));
meanphi=mean(log10(p(cf1:cf2)));
logconst=(meanphi)+5/3*(meanfreq);
uhat=(10^(logconst)*(2*pi/magvel)^(2/3)/.69)^.5*(.4*height)^(1/3);
ustar=(1-.16*(urms/magvel)^2)^.5*uhat;

tau=1025*ustar^2;
zcr=3000*.000001/(.4*ustar)

```

To run this program load cross.asc, long.asc and vertical.asc into the Matlab workspace. Type `tau = idm(cross,long,vertical,.545)` into the workspace. The estimate for the stress will then be produced.

For the kinetic energy method it is necessary to calculate the spectra for all three components of the flow. From the cross-shore spectra the incident wave band is found and is used to remove the turbulence due to the waves. The algorithm is as follows.

1. Calculate the spectrum of the cross-shore time series.
2. From this spectrum estimate the limits of the incident wave band.
3. Split the spectrum into four parts: the low frequency turbulence, the variance due to waves, the variance within the wave band not due to waves, and the higher frequency turbulence.
4. Calculate the area under the spectrum due to turbulence.
5. Repeat steps 1, 3 and 4 for the other horizontal component of flow.
6. Calculate area under spectrum of vertical fluctuations.
7. Add areas found in steps 4, 5 and 6 together and divide by 2, as in Equation (13).
8. Calculate bottom stress using Equation (14).

Matlab program to calculate bottom stress using the turbulent kinetic energy method:

```

function [tau]=tkesouls(cross,long,vertical,height)
% Calculation of friction velocity (shear stress) using Soulsby
% method of splitting the spectrum.
fclose('all');
energy=0;
% Calculate spectrum of cross shore data
[p,f]=spectrum(cross,512,256,512,8);
loglog(f,p(:,1)/4)
hold on

% Choose the incident wave band using graphical input, click
% on the plot at the extremes of the incident
% wave band with the mouse.
[x1,y1]=ginput(2);

% Plot line separating turbulence and wave fluctuations
loglog(x1,y1)
x2=floor(x1*64);

% Calculate turbulent kinetic energy using the trapezium rule.
energy=1/256*(.5*(p(1,1)+p(x2(1),1))+sum(p(2:x2(1)-1,1)));

```

```

energy=energy+.25*(f(x2(2))-f(x2(1)))*(p(x2(1),1)+p(x2(2),1))/2;
energy=energy+1/256*(.5*(p(x2(2),1)+p(256,1))+sum(p(x2(2)+1:255,1)));
hold off

% Calculate spectrum of long shore data
[p,f]=spectrum(long,512,256,512,8);
energy=energy+1/256*(.5*(p(1,1)+p(x2(1),1))+sum(p(2:x2(1)-1,1)));
energy=energy+.25*(f(x2(2))-f(x2(1)))*(p(x2(1),1)+p(x2(2),1))/2;
energy=energy+1/256*(.5*(p(x2(2),1)+p(256,1))+sum(p(x2(2)+1:255,1)));

% Calculate spectrum of vertical data
[p,f]=spectrum(vertical,512,256,512,8);
energy=energy+1/256*(.5*(p(1,1)+p(x2(1),1))+sum(p(2:x2(1)-1,1)));
energy=energy+.25*(f(x2(2))-f(x2(1)))*(p(x2(1),1)+p(x2(2),1))/2;
energy=energy+1/256*(.5*(p(x2(2),1)+p(256,1))+sum(p(x2(2)+1:255,1)));
fclose('all');
end
tau=(0.19*.5*energy)*1025;

```

Use in the same way as the inertial dissipation program.

The two methods give estimates for the bottom stress which are very similar,  $\tau = 1.99 \text{ Nm}^{-2}$  for IDM and  $\tau = 1.77 \text{ Nm}^{-2}$  for TKEM, but it is necessary to check for the validity of the methods before using them.

It is not always possible to collect data with the necessary three orthogonal time series. With the IDM only an estimate of the mean current and a time series are required, not necessarily the vertical. If one of the two other components of flow is used, the appropriate Kolmogorov constant should be used. Three components of flow are required for the TKEM. However, it might be possible to estimate a value for any one component of the flow from the others. This could be done either by using the ratio of components found from the steady boundary layer ratios:

$$\bar{u}_t^2 : \bar{v}_t^2 : \bar{w}_t^2 = 2.4^2 : 1.9^2 : 1.2^2 \quad (15)$$

It might also be possible to use components of flows at different heights above the bottom to interpolate flows at the necessary height.

#### ACKNOWLEDGEMENTS

The fieldwork was funded as part of the MAST II Programme by the Commission of the European Union under contract MAS2-CT92-0024.

#### REFERENCES

- Hardisty, J. 1993. 'Time series analysis using spectral techniques: oscillatory currents', *Earth Surface Processes and Landforms*, 18, 855–862.
- Huntley, D. A. 1988. 'A modified inertial dissipation method for estimating seabed stresses at low Reynolds numbers, with application to wave/current boundary layer measurements', *Journal of Physical Oceanography*, 18, 339–346.
- Huntley, D. A. and Hazen, D. G. 1988. 'Seabed stresses in combined wave and steady flow conditions on the Nova Scotia Continental Shelf: Field measurements and predictions', *Journal of Physical Oceanography*, 18, 347–362.

#### SEABED STRESS DETERMINATIONS

- Lumley, J. L. and Terray, 1983. 'Kinematics of turbulence convected by a random wave field', *Journal of Physical Oceanography*, 13, 2000-2007.
- Soulsby, R. L. 1980. 'Selecting record length and digitization rate for near-bed turbulence measurements', *Journal of Physical Oceanography*, 10, 208-219.
- Soulsby, R. L. 1983. 'The bottom boundary layer of shelf seas', in Johns, B. (Ed.), *Physical Oceanography of Coastal and Shelf Seas*, Elsevier Oceanography Series, 35, Amsterdam, Ch. 5B.
- Soulsby, R. L. and Humphrey, J. D. 1989. 'Field observations of wave and current interaction at the sea bed', in Torum, A. (Ed.), *Proc. of NATO Advanced Research Workshop of water wave Kinematics, Norway*, Pub. B. V., Dordrecht, The Netherlands.
- Tennekes, and Lumley, J. L. 1973. *A First Course in Turbulence*, MIT Press, London.

## References

- Allen J.R.L. and Leeder M.R., 1980, Criteria for the instability of upper-stage plane beds. *Sedimentology* 27: 209-217.
- Allen J.S., Beardsley R.C., Brown W.S., Cacchione D.A., Davis R.E., Drake D.E., Friehe C., Grant W.D., Huyer A., Irish J.D., Janopaul M.M., Williams A.J. and Winant C.D., 1982, A preliminary description of the CODE-1 field program, Code Tech. Report No. 9 WHOI Tech. Rep. No. 82-51 pp 44.
- Amos C.L., Bowen A.J., Huntley D.A., Judge J.T. and Li M.Z., 1995,. Ripple migration and sand transport under quasi-orthogonal combined flows on the Scotian shelf. (Submitted Marine Geology).
- Bagnold R.A., 1966. An approach to sediment transport from general physics. U.S. Geological Survey Professional Paper 4421: 37p
- Bakker W.T. and Van Doorn T., 1978. Near bottom velocities in waves and current. Proc 16th Conf. Coastal Engineering, Hamburg, 1394-1413.
- Bijker E.W., 1967, Some considerations about scales for coastal models with moveable bed. Publ. 50, Delft Hydraulics Lab., Delft, Netherlands, pp 142.
- Bradshaw P., Cebeci T. and Whitelaw J.H., 1981, Engineering calculation methods for turbulent flow. Academic Press, London, 331pp.
- Boussinesq J., 1877, Essai sur la theorie des eaux courantes. Mem. pres.par div. savants a l'academie Sci., Paris, 23, 1-680.
- Bowden K.F., 1978, Physical problems of the benthic boundary layer. *Geophys. Surv.*, 3: 255-296.
- Cacchione D.A. and D.E Drake, 1982, Measurements of storm generated bottom stresses an the continental shelf. *J. Geophys. Res.*, 87, 1952-1961.
- Chatwin P.G., 1996, Near bed flows and sediment movement on the continental slope. PhD Thesis.
- Crapper G.D., 1984, Introduction to water waves. Ellis Horwood, 224pp
- Christoffersen J.B., and Jonnson I.G., 1985, Bed friction and dissipation in combined current and wave motion, *Ocean Engng.*, Vol. 12, No 5, 387-423,
- Davies A.G., Soulsby R.L. and King H.L., 1988, A numerical model of the combined wave and current bottom boundary layer. *J. Geophys. Res.* Vol. 93, No. C1 pp 491-508.

- Dutoit C.G. and Sleath J.F.A., 1981, *J. fluid Mech.*, 112 pp 71-96.
- Dyer K.R., 1986, *Coastal and Estuarine Sediment Dynamics*, John Wiley and Sons, pp 342.
- Folk R.L. and Ward W.C., 1957, Brazos river Bar: A study in the significance of grain size parameters. *J. Sediment. Petrol.*, 27 3-26.
- Forestell G.Z., Hamilton R.C., and Cardone V.J., 1977, Continental shelf currents in tropical storm Delia: observations and theory, *J. Phys. Oceanogr.*, 7, 532-546.
- Fredsoe J., 1984, Turbulent boundary layer in wave and current motion. *J. Hydr. Eng.* Vol. 110, No. 8 1103-1120.
- Glen S.M. and Grant W.D., 1987, A suspended sediment stratification correction for combined wave and current flows. *J. Geophys. Res.*, Vol. 92, No. C6, pp 8244-8264
- Grace R.A., 1976, Near-bottom water motion under ocean waves. *Proc. 15th Coastal Eng. Conf, Honolulu 3: 2371-2386.*
- Grant W.D. and Madsen O.S., 1979, Combined Wave and Current Interaction with a Rough Bottom, *J. Geophys. Res.*, 85, C4 1797-1808.
- \_\_\_\_\_, 1982, Moveable bed roughness in unsteady oscillatory flow, *J. Geophys. Res.*, 87, C1, pp469-481.
- Grant W.D., Williams A.J. and Glenn S.M., 1983, Bottom stress estimates and their prediction on the Northern Californian continental shelf during CODE-1: The importance of wave-current interaction. *J. Phys. Oc.* Vol. 14 pp 506-527.
- Grant W.D. and Williams A.J., 1985, Replies to Comments on "Bottom stress estimates and their prediction on the Northern Californian continental shelf during CODE-1: The importance of wave-current interaction. *J. Phys. Oc.* Vol. 15 pp 1219-1228 and 1238-1243.
- Gill A.E., 1982. *Atmosphere- Ocean Dynamics*. Academic Press New York, N.Y., pp xiii + 662.
- Green M.O., Rees J.M. and Pearson N.D., 1990, Evidence for wave -current interaction in a tidal boundary layer. *J. Geophys. Res.*, Vol. 95, No. C6, pp 9629-9644.
- Green M. O. and McCave I.N., 1995, Seabed drag coefficient under tidal currents in the eastern Irish Sea, *J. Geophys. Res.*, 100, 16,057- 16,069.
- Gust G., 1985, Comments on "Bottom stress estimates and their prediction on the Northern Californian continental shelf during CODE-1: The importance of wave-current interaction. *J. Phys. Oc.* Vol. 15 pp 1229-1237.

- Guza R.T. and Thornton E.B., 1980, Local and shoaled comparison of sea surface elevations, pressures and velocities, *J. Geophys. Res.* 85 C3 1524-1530.
- Huntley, D.A., 1985, Comments on "Bottom stress estimates and their prediction on the Northern Californian continental shelf during CODE-1: The importance of wave-current interaction. *J. Phys. Oc.* Vol. 15 pp 1217-1218.
- Huntley, D.A., 1988, A modified inertial dissipation method for estimating seabed stresses at low Reynolds numbers, with application to wave/current boundary layer measurements. *J. Phys. Oc.* Vol. 18 pp 339-346
- Huntley, D.A. and Hazen, D.G., 1988, Seabed stresses in combined wave and steady flow on the Nova Scotia continental shelf: Field measurements and predictions. *J. Phys. Oc.* Vol. 18 pp 347-362.
- Huyth-Thanh S. and Temperville A., 1992, A numerical model of the rough turbulent boundary layer in combined wave and current interaction. *Proc. 22nd Coastal Eng. Conf.* pp 853-866.
- Jones W.P. and Lauder B.E., 1972, The prediction of laminarization with a two-equation model of turbulence. *Int. J. Heat Mass Transf.* 15, p301.
- Kemp P.H. and Simons R.R., 1982, The interaction between waves and a turbulent current: Waves propagating with the current. *J. Fluid Mech.* 116, 227-250.
- Komar P.D. and Miller, M.C., 1975, Sediment threshold under oscillatory wave. *Proc. 14th Coastal Eng. Conf.* pp 756-775.
- Lanckneus J., De Moor G. and Stolk A., 1994, Environmental setting, morphology and volumetric evolution of the Middelkerke Bank (southern North Sea), *Marine Geology* 121, 1-21.
- Landahl M.T. and Mollo-Christensen, 1986, *Turbulence and random processes in fluid mechanics.* Cambridge University Press, pp154.
- Le Méhauté B., 1976, *An introduction to hydrodynamics and water waves,* Springer - Verlag, New York Heidelberg Berlin, pp315.
- Long C.E., 1981. A simple model for time dependent stably stratified turbulent boundary layers, *Dep. Oceanography, Spec. Rep., 95, Univ. Seattle Wash., 170pp.*
- Lumley J.L. and Terray E.A., 1983, Kinematics of turbulence by a random wave field, *J. Phys Oceanog.,* 13, 2000-2007.
- Lyne V.D., Butman B. and Grant W.D., 1990, Sediment movement along the U.S. east coast continental shelf - 1. Estimates of bottom stress using the Grant and Madsen model and Near bottom wave and current measurements. *Continental Shelf Research,* Vol. 10, No.5, 397-428.
- Madsen O.S., 1993, *Sediment Transport on the Shelf, 2nd draft,* pp 160.

- Myrhaug D. and Slaatelid O.H., 1990, A rational approach to wave-current friction coefficients for rough, smooth and transitional flow, *Coastal Engineering*, 14 265-293.
- Nielsen P., 1986, Suspended sediment concentrations under waves. *Coastal Engineering* 10:23-31
- Nuttal A.H., 1979, Spectral estimation by means of overlapped fast Fourier transforms of windowed data, NUSC Report No. 4169 Dept. Navy U.S.A.
- O'Connor et al., 1995, CSTAB Handbook, EU MAST II Contract, (full title not yet released).
- Prandtl, L. 1925, Bericht uber Untersuchungen zur ausgebildeten Turbulenz. *Z. ang. Math. Mech.* 5, 136-7.
- \_\_\_\_\_, 1945 Uber ein neues Formelsystem fur die ausgebildete Turbulenz. *Nachr. Ges. Wiss. Gottingen, Math.-phys. Kl.*, 6-19.
- Press W.H., Teukolosky S.A., Vetterling W.T. and Flannery B.P., 1992, *Numerical Recipes in FORTRAN: The Art of Scientific Computing*. 2nd Ed. Cambridge University Press.
- Reynolds O., 1883, An experimental investigation of the circumstances which determine whether the motion of water shall be direct or sinuous, and of the law of resistance in parallel channels. *Philos. Trans. R. Soc., London* 174, 935-982.
- \_\_\_\_\_, 1894, On the dynamical theory of incompressible viscous fluids and the determination of the criterion. *Philos. Trans. R. Soc., London* 186, 819-832.
- Simons R.R, Soulsby R.L., Davies A.G., Fredsoe J., Huntley D.A., Jonsson I.G., Myrhaug D., Temperville A. and Zitman T., September 1995, Wave-current bottom shear stresses task force, report to Final Overall Meeting MAST G8M Coastal Morphodynamics, Gdynia, Poland. pp2-38 - 2-41.
- Smith J.D., 1977, Modelling of sediment transport on continental shelves, In: *The Sea* Vol. 6 E.D. Goldberg (editor), Wiley- Interscience, New York, pp 538 - 577.
- Smith J.D. and McLean S.R., 1977, Spatially averaged flow over a wavy surface, *J. Geophys. Res.*, 82 1735-1746.
- Soulsby R.L., 1983, The bottom boundary layer of shelf seas. In: B. Johns (Editor), *physical oceanography of coastal and shelf seas*. Elsevier, New York, N.Y. 189-266.
- \_\_\_\_\_, Davies A.G., Fredsoe J., Huntley D.A., Jonsson I.G., Myrhaug D., Simons R.R, Temperville A. and Zitman T., 1994, Bed shear stresses due to combined waves and currents, Abstracts G8M Overall Workshop Gregynog, September.

- \_\_\_\_\_ and Humphery J.D., 1989, Field observations of wave-current interaction at the sea bed. In A. Torum and O.T. Gudmestad (Editors), Proc. NATO Advanced Research Workshop on Water Wave Kinematics. Kluwer Academic Publ. B.V., Dordrecht, 423-428.
- Swart D.H., 1974, Offshore sediment transport and equilibrium beach profiles. Delft Hydraulics Lab., Publ. 131.
- Taylor G.I., 1915, Eddy motion in the atmosphere. Proc. R. Soc., London Ser. A215, 1-26.
- \_\_\_\_\_, 1935, Statistical theory of turbulence. Proc. R. Soc., London Ser. A151, 421-478.
- Tennekes H. and Lumley J.L., 1972, A First Course in Turbulence, MIT Press.
- Thompson J.M.T. and Stewart H.B., 1986, Non-linear dynamics and Chaos, John Wiley and Sons, 376pp
- Van Cauwenberghe C., 1977, Overesicht van de tijwaarnemingen langs de Belgische kust. Periode: 1941-1970 voor Oostende, 1959-1970 voor Zeebrugge en Nieuwpoort. Tijdschr. der Openbare Werken van België, 1977/4, pp12.
- \_\_\_\_\_, 1985, Overesicht van de tijwaarnemingen langs de Belgische kust. Periode: 1971-1980 voor Nieuwpoort, Oostende en Zeebrugge. Tijdschr. der Openbare Werken van België, 1977/4, pp12.
- \_\_\_\_\_, 1992, Stroomatlas 1992 Noordzee Vlaamse Banken. Dienst der Kunsthavens, Hydrografie Oostende, Ministerie van de Vlaamse Gemeenschap, Dep. Leefmilieu en Infrastructuur, pp26.
- van Kesteren W.G.M. and Bakker W.T., 1984, Near bottom velocities in waves with a current : Analytical and numerical computations, Proc. 19th Coastal Engineering Conf, pp 1161-1177.
- Wiberg P. and Smith D.J., 1983, A comparison of field data and theoretical models for wave-current interactions at the bed on the continental shelf. Continental Shelf Res. Vol. 2 Nos. 2/3, pp 147-162.
- Wikramanayake P.N. and Madsen O.S., 1990, Calculation of moveable bed friction factors, Technical Progress Report No. 2, Dredging Research Program, U.S. Army Corp of Engineers, Coastal Engineering Research Centre.
- Yalin, M.S., 1977, Mechanics of sediment transport. Pergamon Press, Oxford pp298.
- Young A.D., 1989, Boundary layers,; Blackwell Scientific, Oxford.